UNIVERSITY OF SASKATCHEWAN
College of Graduate Studies and Research

SUMMARY OF DISSERTATION

Submitted in partial fulfillment
of the requirements for the
DEGREE OF DOCTOR OF PHILOSOPHY

by

Erik Eberhardt

Department of Geological Sciences
University of Saskatchewan

Spring 1998

Examining Committee:

Dr. S.L. Barbour	Dean's Designate, Chair, College of Graduate Studies and Research
Dr. J.F. Basinger	Chair of Advisory Committee, Department of Geological Sciences
Dr. D. Stead	Co-supervisor, Camborne School of Mines, University of Exeter
Dr. B. Stimpson	Co-supervisor, Department of Civil and Geological Engineering, University of Manitoba
Dr. M.J. Reeves	Department of Geological Sciences
Dr. J. Merriam	Department of Geological Sciences
Dr. D. Milne	Department of Geological Sciences
Dr. J. Wilson	Department of Mechanical Engineering
Dr. B. Rostron	Department of Earth and Atmospheric Sciences, University of Alberta
Dr. M. Aubertin	External Examiner, Département de Génie Minéral, École Polytechnique de Montréal, C.P. 6079, succursale Centre-ville, Montréal, PQ, H3C 3A7

Brittle Rock Fracture and Progressive Damage in Uniaxial Compression

A thesis submitted to the
College of Graduate Studies and Research
in partial fulfillment of the requirements
for the degree of Doctor of Philosophy
in the Department of Geological Sciences
University of Saskatchewan
Saskatoon

by

Erik Eberhardt

April 1998

Permission to Use

In presenting this thesis in partial fulfillment of the requirements for a Postgraduate degree from the University of Saskatchewan, I agree that the Libraries of this University may make it freely available for inspection. I further agree that permission for copying of this thesis in any manner, in whole or in part, for scholarly purposes may be granted by the professor or professors who supervised my thesis work or, in their absence, by the Head of the Department or the Dean of the College in which my thesis work was done. It is understood that any copying or publication or use of this thesis or parts thereof for financial gain shall not be allowed without my written permission. It is also understood that due recognition shall be given to me and the University of Saskatchewan in any scholarly use which may be made of any materials in my thesis.

Requests for permission to copy or make other use of material in this thesis in whole or in part should be addressed to:

Head of the Department of Geological Sciences
University of Saskatchewan
Saskatoon, Saskatchewan
S7N 5E2 CANADA

ABSTRACT

Recent work at Atomic Energy of Canada Limited's Underground Research Laboratory in Pinawa, Manitoba, has shown that high compressive stresses near the tunnel face significantly contributes to the loss of strength, and eventual failure of the rock, through stress-induced brittle fracturing. These processes are commonly observed around excavations in highly-stressed massive brittle rock in forms ranging from minor spalling or slabbing to violent breakouts or rockbursts. The research presented in this thesis was undertaken to investigate the mechanisms responsible for these failures: i.e. stress-induced brittle fracturing and the progressive degradation of rock strength.

Through the combined use of laboratory strain gauge and acoustic emission techniques, rigorous methodologies were developed to aid in the identification and characterization of the brittle fracture process. Uniaxial compression testing of pink Lac du Bonnet granite from the 130 m level of the URL revealed that several stages of crack development could be resolved. These include: crack closure (σ_{cc}), crack initiation (σ_{ci}), secondary cracking (σ_{ci2}), crack coalescence (σ_{cs}), crack damage (σ_{cd}), and peak strength (σ_{UCS}). Elements of numerical modelling were further used to aid in the conceptualization of the internal mechanisms acting during microfracturing processes.

The versatility and full potential of the laboratory methodologies developed for this thesis study was further established through tests involving rock types of varying grain size, mineralogy, sampling disturbance and rheological behaviour. Through these tests, it was found that the mineralogy of the sample had the greatest influence on the initiation of cracking. Increasing grain size and sampling disturbance was found to provide longer paths of weakness for growing cracks to propagate along, resulting in lower strengths due to the coalescence and unstable propagation of cracks at lower

stresses. Brittle fracture processes were also observed and quantified for Saskatchewan potash and Berea sandstone.

Insights into the processes and mechanisms relating to brittle fracture were further utilized to derive empirical relationships describing the progressive accumulation of stress-induced fracture damage. Results from monotonic loading tests were used to quantify the state of microfracturing damage with respect to stress, strain, acoustic velocity and acoustic emission. Cyclic loading techniques were used in a series of damage-controlled tests to investigate the effects of load path and time-dependency on the accumulation of microfracturing damage.

The insights gained through this study provide major contributions into understanding how stress-induced microfracturing results in the degradation of material strength leading up to failure. The correlation of these findings to *in situ* observations will allow for the improved assessment of damage and excavation stability in brittle rock.

ACKNOWLEDGEMENTS

I would like to thank a number of people who were instrumental in the completion of this thesis. First I would like to thank my thesis advisors, Profs. Doug Stead of the Camborne School of Mines and Brian Stimpson of the University of Manitoba for their steady support and guidance. I would also like to thank them for creating the opportunity for me to carry out this research.

Special thanks are also extended to Prof. Malcolm Reeves for watching over me at the University of Saskatchewan, Zig Szczepanik for his valuable expertise in the lab and Prof. Emery Lajtai of the University of Manitoba for teaching me my first fracture mechanics course. I would also like to thank Prof. Lajtai for his valuable insights into the initial stages of this work and for the use of his program EZGRAPH.

I also wish to express my thanks to Drs. Rod Read and Derek Martin, formerly of AECL Research, for initiating this thesis study and for their recommendations during the early stages of the research. Thanks are also extended to AECL Research for providing financial support and to the staff of the URL for supplying the test materials.

I would also like to acknowledge and thank my thesis committee, Profs. Malcolm Reeves, Ben Rostron, Jim Merriam, Jim Wilson, Doug Milne, Jim Basinger and my external examiner, Michel Aubertin of École Polytechnique. Special thanks are also extended to Rob Tanner for his programming assistance, Blaine Novakovski for preparing my thin-sections, Tom Bonli for helping me to use the SEM, Ed Dzik for the use of his program EJBEM and Prof. Don Gendzwill for his insights into energy calculations.

Finally, I would especially like to thank my parents, family and friends for all their support during my academic pursuits. In answer to their numerous inquiries, yes this is as far as I can go in university and still be classified as a student.

TABLE OF CONTENTS

Abstract iii

Acknowledgements v

List of Tables x

List of Figures xiii

List of Symbols and Notations xxiii

Chapter 1 Introduction **1**

1.1 Statement of Problem 2

1.2 Scope of Work and Thesis Layout 4

Chapter 2 Deformation and Fracture in Brittle Rock **7**

2.1 Mechanistic Theories of Brittle Fracture 7
2.1.1 Griffith's Theory 9
2.1.2 Linear Elastic Fracture Mechanics Approach 11
2.1.3 Crack Geometries 14

2.2 Initiation and Propagation of a Griffith Crack 18
2.2.1 Critical Crack Length: Influence of Grain Size on Rock Strength 18
2.2.2 Critical Crack Orientation 19
2.2.3 Direction of Crack Propagation 19
2.2.4 Stable Crack Propagation and the Griffith Crack Locus 21

2.3 Laboratory Derived Stages in the Brittle Failure Process 26

2.4 Damage Mechanics and the Quantification of Stress-Induced Microfracturing 28

2.5 Chapter Summary 32

Chapter 3 Detection of Stress-Induced Microfracturing During Laboratory Testing 33

3.1 Strain Gauge Measurements 33
3.1.1 Moving Point Regression Technique 34
3.1.2 Sensitivity of Moving Point Regression Technique 37

3.2 Acoustic Emission Response in Rock 37
3.2.1 Correlation of Fracture with Acoustic Emission 39
3.2.2 Acoustic Emission Detection 39
3.2.3 Acoustic Event Properties 41
3.2.4 Acoustic Event Energy 44

3.3 Laboratory Testing Setup 45
3.3.1 Acoustic Emission Detection Settings 48
3.3.2 Processing of Acoustic Emission Data 53

3.4 The URL and Pink Lac du Bonnet Granite 53

3.5 Chapter Summary 54

Chapter 4 Identification of Brittle Fracture Thresholds for Lac du Bonnet Granite 57

4.1 Crack Closure 57

4.2 Linear Elastic Behaviour 62

4.3 Crack Initiation 64
4.3.1 Stress-Strain and Acoustic Emission Response to Crack Initiation 68
4.3.2 Generation of Microcracks and the Secondary Cracking Threshold 76

4.4 Crack Coalescence 81

4.5 Crack Damage and Peak Strength 85

4.6 Chapter Summary 86

Chapter 5 Numerical Analysis of Crack Initiation, Propagation and Interaction 89

5.1 Background and Methodology 89

5.2 Stress Shadow Effects in a Uniaxial Stress Field 96

5.3 Stress Shadow Effects in a Triaxial Stress Field 100
5.3.1 Correlation of Modelling Results with Laboratory Observations 105

5.4 Zone of Influence of Adjacent Cracks 106

5.5 Chapter Summary 111

Chapter 6 Extension of Brittle Fracture Thresholds for Varied Material States 113

6.1 Effects of Grain Size 113
6.1.1 Geological Description of URL Granite, Granodiorite and Pegmatite 115
6.1.2 Grain Size Dependent Deformation and Fracture Characteristics 118

6.2 Effects of Sample Disturbance 129
6.2.1 SEM Observations and Acoustic Velocity Results 130
6.2.2 Effect of Increasing Sample Disturbance on Deformation and Fracture 134
6.2.3 Effects of Grain Size on the Degree of Sample Disturbance 144

6.3 Ductility and Porosity Effects 148
6.3.1 Deformation and Brittle Fracture Characteristics of Potash 148
6.3.2 Deformation and Brittle Fracture Characteristics of Sandstone 161

6.4 Chapter Summary 176

Chapter 7 Degradation of Rock Strength through Stress-Induced Damage **179**

7.1 Monocyclic Loading Tests 180
7.1.1 Normalized Stresses and Strains 181
7.1.2 Acoustic Velocities 186
7.1.3 Normalized Acoustic Emission 191

7.2 Cyclic Loading Tests 195
7.2.1 Damage-Controlled Testing Above the Crack Damage Threshold 200
7.2.2 Damage-Controlled Testing Below the Crack Damage Threshold 213

7.3 Incremental Damage Tests 222
7.3.1 Incremental Cyclic Loading 222
7.3.2 Incremental and Constant Load Test 230

7.4 Chapter Summary 242

Chapter 8 Summary and Conclusions **245**

8.1 The Brittle Fracture Process 246

8.2 Rock Microstructure and the Brittle Fracture Process 249

8.3 Quantifying Stress-Induced Damage 254

8.4 Future Research 260

Bibliography **262**

Appendix I Strain Gauge Analysis for Individual Test Results **276**

Appendix II Acoustic Emission Response for Individual Tests **314**

LIST OF TABLES

3.1	Definition of acoustic emission event properties.	43
4.1	Average static elastic moduli for the 130m level URL pink granite.	64
4.2	Average Poisson's ratio as calculated per ASTM standards and over the stress interval between crack closure and crack initiation for the 130m level URL pink granite.	68
4.3	Average threshold values for the different stages of crack development for the 130 m level URL pink granite.	86
5.1	Material properties for Lac du Bonnet granite used in modelling study.	94
6.1	Methodology used to establish the different thresholds of crack development.	114
6.2	Composition and average grain sizes for URL granite and granodiorite.	117
6.3	Summary of density and acoustic velocity values for 240 m level URL samples.	118
6.4	Average elastic constants for 240 m level URL samples.	119
6.5	Average crack thresholds for the 240 m level URL samples.	121
6.6	Approximate major and minor principal stress magnitudes for the three *in situ* stress domains of the URL.	130
6.7	Estimates of crack density from SEM observations of 130, 240 and 420 m level URL granite.	131
6.8	Summary of density and acoustic velocity values for URL 130, 240 and 420 m level granite samples.	134

6.9	Average elastic parameters for URL 130, 240 and 420 m level granites.	135
6.10	Average fracture parameters for 130, 240 and 420 m level URL granites.	137
6.11	Average index and deformation parameters for samples of 420 m level granite and granodiorite and 240 m level granodiorite from the URL.	146
6.12	Average fracture parameters for 420 m level URL grey granite and granodiorite, and 240 m level URL granodiorite.	146
6.13	Average index and deformation parameters for Saskatchewan potash samples	150
6.14	Average strength parameters for Saskatchewan potash samples.	159
6.15	Average index parameters for Berea sandstone samples.	167
6.16	Average elastic constants for Berea sandstone samples.	169
6.17	Average crack threshold and strength values for Berea sandstone samples.	175
7.1	Stresses, normalized with respect to uniaxial compressive strength, recorded for the various stages of crack development in the 130 m level URL pink granite.	181
7.2	Axial and lateral strains, normalized with respect to the maximum strains recorded at failure, corresponding to the various stages of crack development in the 130 m level URL pink granite.	182
7.3	Percentage of strains associated with each stress interval of crack development for the 130 m level URL pink granite.	182
7.4	Deformation characteristics of the 130 m level URL pink granite equated in terms of an axial deformation modulus and a ratio of the lateral to axial deformation.	186
7.5	Cumulative AE event count, normalized with respect to the event count recorded at the peak load and the crack damage threshold, for the 130 m level URL pink granite.	194

7.6 Comparison of permanent axial and lateral strains from monotonic loading tests and the incremental cyclic loading test for the 130 m level URL pink granite. 230

7.7 Comparison of permanent axial and lateral strains from monotonic loading tests, the incremental cyclic loading test and the incremental/constant load for the 130 m level URL pink granite. 241

LIST OF FIGURES

1.1	Phenomenological and mechanistic theories of rock failure.	4
1.2	Development of thin slab failure zone through stress-induced brittle microfracturing.	4
2.1	Elastic tensile stresses, σ_t, at a crack tip in an arbitrary body.	8
2.2	Normal and frictional shear stresses acting on a closed crack under compressive loading conditions.	12
2.3	Modes of crack tip loading and displacement.	12
2.4	Depiction of the non-linear process zone ahead of a crack tip and the development of the process zone and its influence on macrocrack extension.	15
2.5	Conceptual models for the inclined ellipse, the inclined zero-width ellipse and the axial ellipse crack geometries.	16
2.6	Critical crack orientations for tensile and compressive loading.	20
2.7	Stress concentrations along the periphery of an elliptical crack for varying crack angles with respect to the direction of uniaxial compressive loading.	20
2.8	Crack propagation in the direction of the major principal stress.	22
2.9	Griffith crack locus for compression showing stable and unstable regions.	25
2.10	Demonstration of the Griffith crack locus.	25
2.11	Stress-strain diagram showing the elements of crack development including the crack closure, crack initiation and crack damage thresholds.	27

2.12	Characteristics and extent of the disturbed and damaged zone surrounding a tunnel in a plane perpendicular to the tunnel axis.	31
3.1	Determination of the crack initiation point using the lateral strain curve and showing the subjectivity incorporated into the picking of the point due to low resolution stress-strain data.	35
3.2	Illustration of the moving point regression technique.	35
3.3	Moving point regression analysis of an axial stress -*vs*- axial strain curve showing the changes in the axial stiffness throughout loading.	36
3.4	Variation in axial stiffness calculations for different regression intervals	38
3.5	Typical acoustic emission response for granite showing the cumulative number of events with axial load.	40
3.6	The use of threshold settings to filter out continuous background noise.	42
3.7	Illustration of common AE event waveform parameters.	42
3.8	Typical sample instrumentation and setup used for uniaxial compression tests.	46
3.9	Schematic of strain gauge and acoustic emission instrumentation, and data collection systems.	47
3.10	Uniaxial compression test setup showing load frame and data logging systems.	47
3.11	Logarithmic AE event counts for Lac du Bonnet granite samples using gains of 60 and 40 dB.	50
3.12	AE event ringdown counts for Lac du Bonnet granite samples using gains of 60 and 40 dB.	51
3.13	Logarithmic AE event counts for Lac du Bonnet granite samples using thresholds of 0.25, 0.10, 0.05 and 0.02 V.	52
3.14	Location and layout of AECL’s Underground Research Laboratory.	56

4.1	Plots of axial strain and axial stiffness -*vs*- axial stress for a 130 m level URL pink granite showing the crack closure threshold.	59
4.2	Plots of lateral strain and lateral stiffness -*vs*- axial stress for a 130 m level URL pink granite.	59
4.3	Directions of crack face movement during closure for different crack orientations.	60
4.4	Stress relief cracking in cores drilled at different orientations with respect to the *in situ* principal stresses.	61
4.5	Method for calculating the Young's, tangent and secant modulus from axial stress -*vs*- axial strain curves.	63
4.6	Determination of crack initiation using crack volume.	66
4.7	Variability of crack volume stiffness with Poisson's ratio for a 130m level URL pink granite.	67
4.8	Plots of volumetric strain and volumetric stiffness -*vs*- axial stress for a 130m level URL pink granite.	69
4.9	Breakdown and correlation of volumetric stiffness with brittle fracture showing the crack closure, crack initiation, crack damage and peak strength thresholds for a 130m level URL pink granite.	69
4.10	Typical acoustic emission response of a 130m level URL pink granite showing AE event count -*vs*- axial stress.	71
4.11	Plot of log acoustic emissions -*vs*- axial stress showing the crack initiation, secondary cracking and crack damage thresholds for a 130m level URL pink granite loaded to failure.	71
4.12	Plot of ringdown count -*vs*- axial stress for a 130m level URL pink granite.	73
4.13	Plot of event duration -*vs*- axial stress for a 130m level URL pink granite.	73
4.14	Plot of peak amplitude -*vs*- axial stress for a 130m level URL pink granite.	74
4.15	Plot of rise time -*vs*- axial stress for a 130m level URL pink granite.	74

4.16	Plots of cumulative elastic impulse “energy” -*vs*- axial stress for a 130m level URL pink granite.	75
4.17	Log acoustic emission event count showing what appears to be a normal distribution of critical crack initiation loads with a mean value equal to the crack initiation threshold.	77
4.18	Scanning electron microscope image of a stress-induced crack originating along a quartz-feldspar grain boundary in a 130 m level URL pink granite.	79
4.19	SEM image of a feldspar grain with stress induced cracks aligned parallel to the direction of loading.	80
4.20	Plot of the stress dependent elastic impulse “energy” rate -*vs*- axial stress for a 130m level URL pink granite.	82
4.21	Axial stiffness plot indicating a significant change in the axial strain rate prior to the crack damage threshold for a 130m level URL pink granite.	83
4.22	Volumetric stiffness plot showing a major strain rate change at the crack coalescence threshold for a 130m level URL pink granite.	83
5.1	Examples of “zero-width Griffith” and “elliptical axial” cracks.	91
5.2	USR equivalent strength fracture criterion.	93
5.3	Problem geometry used for single crack boundary element models.	95
5.4	Applied axial stress -*vs*- stable crack length relationship for a single crack in a uniaxial stress field.	95
5.5	Problem geometry used in multiple crack array models for determination of stress shadow effects.	97
5.6	Applied axial stress -*vs*- stable crack length relationships for both single and multiple crack arrays in a uniaxial stress field.	98
5.7	Minimum principal stress contours surrounding adjacent crack tips in a multiple crack array under uniaxial loading conditions.	99
5.8	Applied axial stress -*vs*- stable crack length relationships for a multiple crack array with and without an applied confining pressure.	101

5.9	Minimum principal stress contours surrounding adjacent crack tips in a multiple crack array under uniaxial and triaxial loading conditions.	103
5.10	Effect of confining stress on crack initiation for a central crack in a multiple crack array.	104
5.11	Zone of influence of peripheral cracks on the crack initiation stress for a central crack in a uniaxial stress field.	108
5.12	Influence of peripheral crack length on the crack initiation stress level for a central crack in a uniaxial stress field.	109
5.13	Zone of influence of peripheral cracks on the crack initiation stress for a central crack in a uniaxial and triaxial stress field.	110
6.1	240 m level URL samples showing varying grain size: granodiorite, grey granite and pegmatite.	116
6.2	Plots of axial stiffness -*vs*- axial stress for URL 240 m level samples of granodiorite, grey granite and pegmatite.	120
6.3	Plots of volumetric stiffness -*vs*- axial stress for URL 240 m level samples of granodiorite, grey granite and pegmatite.	122
6.4	Plots of log AE event count -*vs*- axial stress for URL 240 m level samples of granodiorite, grey granite and pegmatite.	123
6.5	Plots of the stress dependent AE event rate -*vs*- axial stress for URL 240 m level samples of granodiorite, grey granite and pegmatite.	124
6.6	Plots of the AE elastic impulse “energy” rate -*vs*- axial stress for URL 240 m level samples of granodiorite, grey granite and pegmatite.	127
6.7	The Griffith criterion, for a plate with fixed ends, showing the elastic energy released upon crack elongation.	128
6.8	SEM image of two highly fractured quartz grains. Images are taken from sections prepared from untested samples of the 420 m level URL granite.	132
6.9	P- and S-wave velocities for granite samples from the URL 130, 240 and 420 m levels in comparison with *in situ* values.	133

6.10	Plots of secant modulus and crack closure thresholds -*vs*- sampling depth for granite samples from the URL 130, 240 and 420 m levels.	136
6.11	Plot of axial stiffness -*vs*- axial stress for granite samples from the URL 130, 240 and 420 m levels.	138
6.12	Plots of log AE event count -*vs*- axial stress for granite samples from the URL 130 m, 240 m and 420 m levels.	139
6.13	Plots of volumetric stiffness -*vs*- axial stress for granite samples from the URL 130 m, 240 m and 420 m levels.	141
6.14	Plot of axial stiffness -*vs*- axial stress for a 420 m level URL granite sample which never truly reaches a stage of linear elastic behaviour.	143
6.15	Plots of log AE event count -*vs*- axial stress for URL samples of 420 m level grey granite, 420 m level granodiorite and 240 m level granodiorite.	147
6.16	Plots of volumetric stiffness -*vs*- axial stress for URL samples of 420 m level grey granite, 420 m level granodiorite and 240 m level granodiorite.	149
6.17	Coarse grained Saskatchewan potash sample prior to testing.	151
6.18	Stress -*vs*- strain plot for a uniaxial compression test performed on a Saskatchewan potash sample.	153
6.19	Plots of axial stiffness and axial strain -*vs*- axial stress for a Saskatchewan potash sample.	154
6.20	Plots of lateral stiffness and lateral strain -*vs*- axial stress for a Saskatchewan potash sample.	154
6.21	Plot of the AE event count -*vs*- axial stress for a Saskatchewan potash sample.	155
6.22	Plot of the AE event elastic impulse “energy” rate -*vs*- axial stress for a Saskatchewan potash sample.	155
6.23	Tensile cracks opening perpendicular to the applied load.	157
6.24	Plots of volumetric strain and stiffness -*vs*- axial stress for a Saskatchewan potash sample.	158

6.25	Plot of AE event ringdown count -*vs*- axial stress for a Saskatchewan potash sample.	160
6.26	Plot of AE event rise time -*vs*- axial stress for a Saskatchewan potash sample.	160
6.27	Large tensile axial cracks coalescing and extending though most of the failed Saskatchewan potash sample.	162
6.28	Berea sandstone samples prior to testing showing bedding parallel and perpendicular to the core axis.	164
6.29	Axial stiffness and axial strain -*vs*- axial stress for a Berea sandstone sample.	165
6.30	Lateral stiffness and lateral strain -*vs*- axial stress for a Berea sandstone sample showing the stiffening and softening of the lateral strain curve before the crack closure threshold is reached.	166
6.31	Log AE event count -*vs*- axial stress for a Berea sandstone sample.	170
6.32	Volumetric stiffness -*vs*- axial stress for a Berea sandstone sample.	172
6.33	AE event count -*vs*- axial stress for a Berea sandstone sample showing several bursts of AE activity prior to failure.	174
6.34	Typical mode of failure observed for the Berea sandstone showing large axial cracks and spalled pieces around the sample boundary.	175
7.1	Normalized plot of axial stress -*vs*- strain comparing laboratory test data to a simple analytical deformation model for 130 m level URL pink granite.	185
7.2	P- and S-wave velocities -*vs*- axial stress for a 130 m level URL pink granite.	189
7.3	Peak S-wave amplitudes and axial stiffness -*vs*- axial stress showing the crack closure and crack coalescence thresholds for a 130 m level URL pink granite.	190
7.4	Plots of normalized damage and critical cohesion -*vs*- axial stress for the 130 m level URL pink granite.	193

7.5	Plot of AE derived damage -*vs*- axial stress normalized with respect to the total number of events recorded at failure for the 130 m level URL pink granite.	196
7.6	The mobilization of friction and cohesion as a function of damage.	198
7.7	Axial stress -vs- lateral strain showing the first three cycles of a cyclic loading test and the resulting permanent lateral strain damage with respect to the damage increment.	201
7.8	Axial stress -*vs*- time showing the load history of a damage-control test performed on a 130 m level URL pink granite.	202
7.9	Axial stress -*vs*- volumetric strain showing the migration of the volumetric strain curve with each damage increment for a 130 m level URL pink granite.	204
7.10	Damage -*vs*- damage increment showing the permanent axial, lateral and volumetric strain damage with each cycle normalized with respect to the total damage at failure for a 130 m level URL pink granite.	205
7.11	Crack damage and crack coalescence threshold stresses -*vs*- damage increments for a 130 m level URL pink granite.	206
7.12	Absolute axial strain damage -*vs*- damage increment showing the damage induced for each load-unload cycle normalized with respect to the total damage at failure for a 130 m level URL pink granite.	206
7.13	Conceptual model of crack coalescence accompanied by large permanent axial strains.	207
7.14	Plots of Young's modulus and Poisson's ratio -*vs*- cyclic damage increments for 130 m level URL pink granite.	209
7.15	Crack damage threshold recorded for each damage increment -*vs*- axial and lateral cumulative strain damage for a 130 m level URL pink granite.	210
7.16	Axial stress -*vs*- damage increments showing the stress levels at which new and significant cracking was detected through AE monitoring for a 130 m level URL pink granite.	212

7.17 Permanent lateral strain -*vs*- damage increments showing the damage induced by each load-unload cycle for a 130 m level URL pink granite. 214

7.18 Axial stress -*vs*- time showing the load history for a damage-controlled test in which the maximum loads were kept below the crack damage threshold as performed on a sample of 130 m level URL pink granite. 215

7.19 Damage -*vs*- damage increments for load cycling below the crack damage threshold. 217

7.20 Plot of AE event count -*vs*- damage increments for load cycling below the crack damage threshold for a 130 m level URL pink granite. 219

7.21 Axial stress -*vs*- damage increments for load cycling below the crack damage threshold showing the stress levels at which new and significant cracking was detected through AE monitoring for a 130 m level URL pink granite. 220

7.22 Plots of Young's modulus and Poisson's ratio -*vs*- cyclic damage increments for load cycling below the crack damage threshold in a 130 m level URL pink granite. 221

7.23 Axial stress -*vs*- time showing the load history for an incremental cyclic loading test performed on a sample of 130 m level URL pink granite. 224

7.24 Axial stress -*vs*- volumetric strain showing the migration of the volumetric strain curve with each cycle and load increment for a 130 m level URL pink granite. 225

7.25 Cumulative strain damage -*vs*- damage increment and peak cyclic axial stress for an incremental cycling test performed on a 130 m level URL pink granite. 226

7.26 Permanent lateral strains -*vs*- peak cyclic axial load showing the correlation between absolute lateral strain damage and the crack thresholds for a 130 m level URL pink granite. 227

7.27 Permanent axial strains -*vs*- peak cyclic axial load showing the correlation between absolute axial strain damage and the crack thresholds for a 130 m level URL pink granite. 228

7.28 Absolute AE event damage -*vs*- peak cyclic axial stress showing the correlation between absolute AE damage and the crack thresholds for a 130 m level URL pink granite. 229

7.29 Plots of Young's modulus and Poisson's ratio -*vs*- peak cyclic axial stress for a 130 m level URL pink granite. 231

7.30 Axial stress -*vs*- time showing the load history for an incremental constant loading test performed on a 130 m level URL pink granite. 233

7.31 Axial stress -*vs*- axial, lateral and volumetric strain showing the development of creep strains with each constant load increment for a 130 m level URL pink granite. 234

7.32 Axial and lateral creep strains -*vs*- constant load for a 130 m level URL pink granite. 236

7.33 Cumulative damage -*vs*- constant load showing the axial and lateral creep strain damage for a 130 m level URL pink granite. 237

7.34 Plots of the axial deformation modulus and Poisson's ratio -*vs*- load increment for a 130 m level URL pink granite. 238

7.35 Plot of AE event count -*vs*- axial stress showing the breakdown of AE events recorded during load increments and constant loads for a 130 m level URL pink granite. 239

7.36 Total AE event "energy" -*vs*- constant load for a 130 m level URL pink granite. 240

LIST OF SYMBOLS AND NOTATIONS

a	long axis of an ellipse
α	surface energy per unit area
b	short axis of an ellipse
c	crack half-length
E	elastic modulus
E_{AVG}	average Young's modulus
E_S	secant modulus
E_T	tangent modulus
ε_{axial}	axial strain
ε^p_{ax}	permanent axial strain
$\varepsilon_{lateral}$	lateral strain
ε^p_{lat}	permanent lateral strain
ε_V	volumetric strain
$\varepsilon_{V\ crack}$	crack volume strain
$\varepsilon_{V\ elastic}$	linear elastic component of the volumetric strain
ε^p_{vol}	permanent volumetric strain
ϕ_b	basic or residual friction angle
ϕ_i	angle of friction caused by roughness or the interlocking of asperities
η	angular coordinate along ellipse boundary
i	damage increment
K_I, K_{II},K_{III}	stress intensity factor (modes I, II and III)
K_{Ic}	critical stress intensity factor (mode I)
ν	Poisson's ratio
R	Rocker exponent

SF	factor of safety
σ	stress
σ_1	major principal stress
σ_{1f}	major principal stress at failure
σ_3	minor principal stress
σ_{axial}	axial stress
σ_c	compressive stress
σ_C	compressive strength
σ_{cc}	crack closure stress threshold
σ_{cd}	crack damage stress threshold
σ_{ci}	crack initiation stress threshold
σ_{ci2}	secondary cracking stress threshold
σ_{cs}	crack coalescence stress threshold
σ_f	frictional shear stress
σ_n	normal stress
σ_{spall}	stress-induced sample spalling threshold
σ_τ	tensile stress
σ_T	tensile strength
σ_{UCS}	uniaxial compressive strength
W	total potential energy
W_e	stored elastic strain energy
W_s	surface energy
ω_{AE}	AE event damage parameter
ω_{ax}	axial damage parameter
ω_{lat}	lateral damage parameter
ω_{vol}	volumetric damage parameter
ψ	crack inclination with respect to σ_1

CHAPTER 1

INTRODUCTION

The excavation of an underground opening in a stressed rock mass results in a redistribution of stresses and the deformation of the near field rock. This stress redistribution increases strain energy in zones of increased compression. If the resulting imbalance in the energy of the system is severe enough, it can result in the progressive degradation of the rock mass strength through stress-induced brittle fracturing. This is especially true for cases where the excavation is housed in massive intact rock (referred to as a CHILE material - continuous, homogeneous, isotropic, and linear elastic). If discontinuities are present (i.e. DIANE – discontinuous, inhomogeneous, anisotropic, and non-linear elastic), a significant proportion of the excess energy will be released through shear displacements along discontinuity surfaces. A number of conditions exist between these two ideal states where at depth, under high confining stresses, jointed rock can fail through elements of both sliding on discontinuity surfaces and brittle fracture.

Canada's concept for the permanent disposal of nuclear fuel waste involves just such a host environment. The concept proposes that a disposal facility and vault be located at a depth of 500 to 1000 m in the plutonic rock of the Canadian Shield (Simmons and Baumgartner, 1994). Some of the key concerns regarding the design of the facility include the implications of potential ground disturbance by the excavation method and the redistribution of *in situ* stresses around the excavation. Both of these factors relate to the extent of brittle fracture related damage which could adversely affect the stability of the excavation boundary and could increase the permeability of the near-field host rock.

These concerns, however, are not restricted to the design of nuclear waste repositories. Although a disposal vault is a unique underground facility, the design,

excavation and construction of the facility is similar to that required for many other major underground engineering projects. Numerous studies have concentrated on assessing the stability of these excavations and the role stress-induced fractures play in instigating failure of the material. Recent work at Atomic Energy of Canada Limited's Underground Research Laboratory (AECL's URL) has shown that areas of high tangential stress near the tunnel face significantly contributes to the strength degradation of the rock through brittle fracturing (Martin, 1993). Furthermore, this work has shown that strength degradation begins with the initiation of the microfracturing process and can end in failure at stresses well below the short-term uniaxial compressive strength of the material. Thus, the identification of these processes and their associated mechanisms are of key interest in predicting both the short- and long-term stability of an excavation.

1.1 Statement of Problem

The design of most underground openings, in cases where discontinuities play an insignificant factor in terms of stability, have concentrated on assessing the state of stress surrounding the excavation relative to the intact strength of the host rock. Two different approaches have typically been used to investigate *in situ* rock strength: the phenomenological approach and the mechanistic approach (Lajtai and Lajtai, 1974; Andreev, 1995). Most of the design theories used to evaluate rock strength fall under the classification of one of these approaches (Figure 1.1).

The phenomenological approach is based on integrating large-scale observations into a practical form for engineering design. For example, the Hoek-Brown failure criteria (Hoek and Brown, 1980) represents an interpretation of practical and laboratory experience gained over time. Largely based on observations of peak strength, phenomenological theories represent a simplistic interpretation of practical experience with the sole purpose of translating such observations and experiences into a useable form for engineering design.

Such criteria are limited in that they do not explicitly consider the micro-mechanisms involved in the deformation and gradual degradation of strength in a material leading up to failure. Numerous brittle failure processes, including those

observed around the test tunnels at the URL, clearly indicate that stress-induced microfractures play a controlling factor in the failure of the rock (Figure 1.2).

Mechanistic approaches, on the contrary, are better suited to the study of the microfracturing process and its influence on brittle failure. These approaches are generally related to the study of "fracture mechanics" which derives its concepts from processes ongoing at the atomic or microscopic scale. Largely based on the presence of microscopic flaws or "Griffith" cracks in a solid material, mechanistic theories try to explain and predict the behaviour of a material throughout the entire loading process leading up to failure. In terms of scale, these flaws can appear in rock as intracrystalline imperfections (atomic scale), grain boundaries and pores (microscopic scale), or faults and joints (meso-, macro- and megascopic scales).

Work at the URL has concentrated on using a mechanistic-based approach to better quantify rock damage through the identification of stress-induced crack generation. Martin (1993) has shown that material parameters determined through such an approach are more of an intrinsic characteristic of the rock's strength, whereas laboratory derived values of peak strength are dependent on a number of external factors, for example the loading rate. Martin (1993) found that the initiation of cracking in laboratory tested samples was independent of loading conditions and can be considered a material property.

Establishing the parameters associated with the initiation and propagation of microfractures, however, has proven difficult as existing methods based on laboratory testing incorporate a high degree of error and subjectivity (Eberhardt *et al*., 1996). Uncertainties also exist with respect to the mechanisms acting during the microfracturing process and how these processes contribute to the progressive degradation of material strength. These issues prompted the research presented in this thesis.

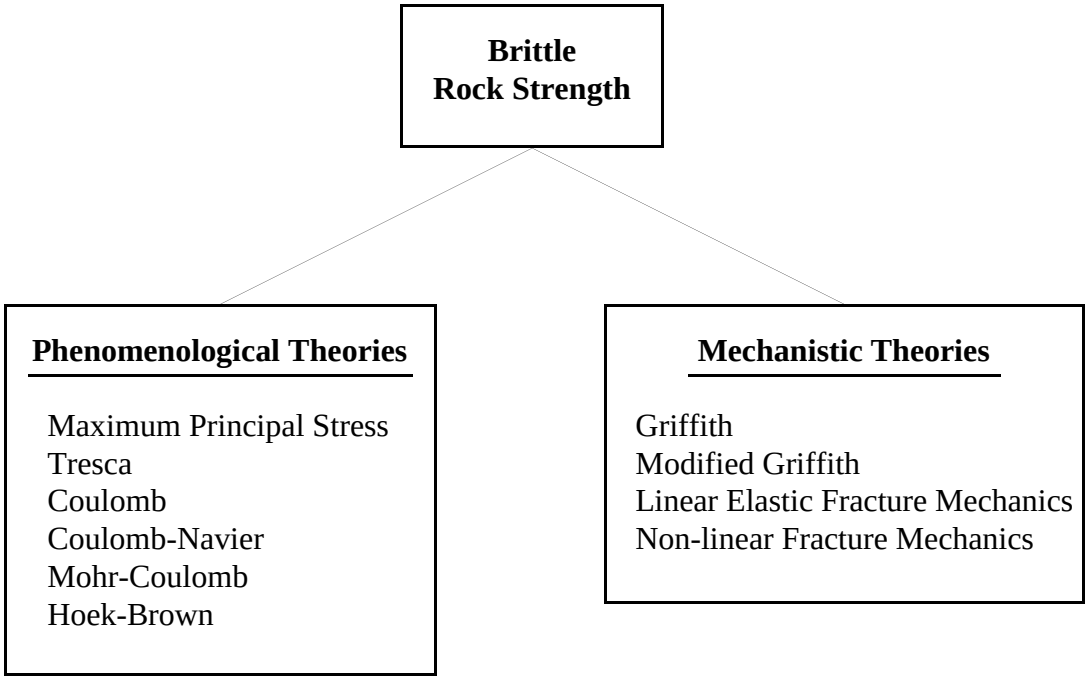

Figure 1.1 Examples of phenomenological and mechanistic theories of rock failure.

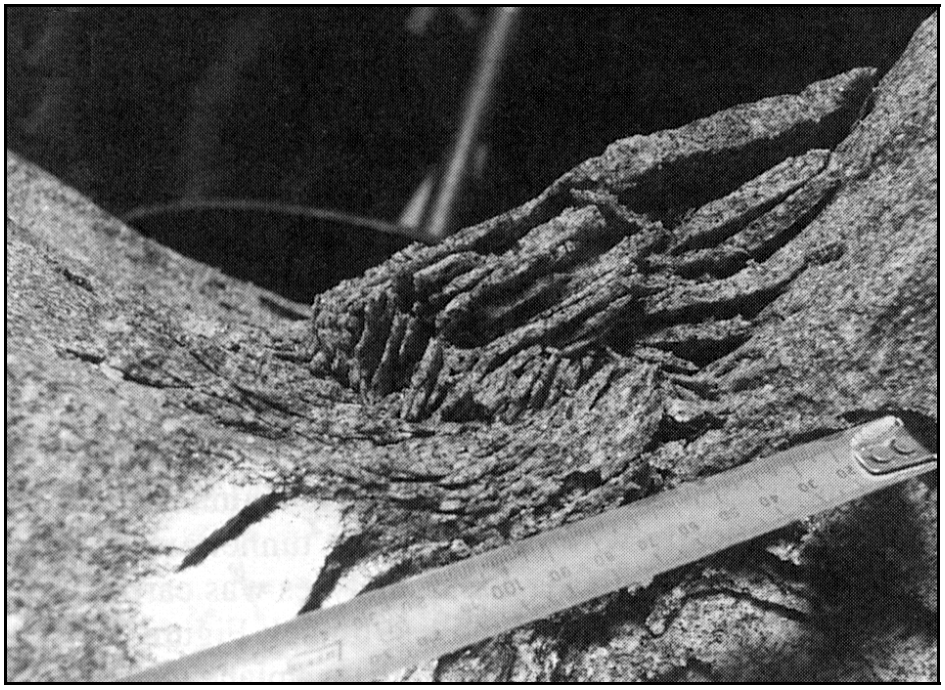

Figure 1.2 Development of thin slab failure zone through stress-induced brittle microfracturing (after Martin, 1997).

1.2 Scope of Work and Thesis Layout

The development of a mechanistic-based criterion describing the gradual loss of cohesion in a material through progressive fracturing is of primary interest to the *in situ* analysis of brittle rock failure around underground excavations. The work described in this thesis involves the development of rigorous methodologies to analyze laboratory stress-strain and acoustic emission data. In turn, these methodologies are used to characterize the processes and mechanisms responsible for the different stages of crack development, most notably crack initiation and the intermediate stages leading up to critical crack propagation. Furthermore, elements of laboratory testing and numerical modelling are used to help quantify the gradual loss of cohesion in a material through progressive fracturing.

The thesis begins with an introduction and overview of its contents. Chapter 2 reviews existing theories concerning the development of fractures in brittle solids, and includes discussions on: Griffith's theory, the initiation and propagation of microfractures in a stressed medium, the dependence of strength on grain size, the correlation of brittle fracturing with laboratory stress-strain data, and the quantification of stress-induced microfracturing damage.

Chapter 3 provides an account of current techniques used to monitor the development of microfractures in laboratory test samples. New methodologies developed to enhance existing strain gauge and acoustic emission techniques are introduced. Chapter 3 concludes with a description of the laboratory equipment and testing procedures, as well as a description of the primary testing material used, pink Lac du Bonnet granite from the 130 m level of the URL.

Chapter 4 presents the results obtained from initial laboratory tests designed to isolate the different stages of crack development. The mechanisms acting during these stages are identified and interpreted using the new techniques described in Chapter 3. Scanning electron microscope images are also presented and used to aid in the interpretation of laboratory data.

Chapter 5 examines the initiation, propagation and interaction of multiple cracks using numerical modelling techniques. Results from these models are used to

demonstrate the complexities of crack interaction and the effects neighbouring cracks have on one another in terms of inhibiting or promoting crack growth. In addition, the roles of crack density, crack length and confining stresses are examined.

The techniques and findings established in Chapters 4 and 5 are then extended in Chapter 6 to include several different material states. The effects of grain size and sample disturbance on crack development are investigated and laboratory test results are presented. In addition, the characteristics of deformation and fracture are investigated for ductile and porous rock types.

Chapter 7 explores the relationship between stress-induced microfracturing and the degradation of material strength. Results from monotonic loading tests are used to quantify the state of microfracturing damage with respect to stress, strain, acoustic velocity and acoustic emission. Cyclic loading techniques are then used in a series of damage-controlled tests designed to investigate the effects of load path on the accumulation of microfracturing damage. These relationships are further clarified and the influences of time-dependent fracture mechanisms are explored through the use of specially designed incremental loading tests.

Chapter 8 provides a summary and the major conclusions of the work performed in this thesis with recommendations for further research. Comprehensive appendices are included with full details of the laboratory testing and numerical modelling data.

CHAPTER 2

DEFORMATION AND FRACTURE IN BRITTLE ROCK

The study of brittle fracture and its relationship to deformation and strength is a fundamental part of rock mechanics and a number of other engineering disciplines. Fracturing is considered to be a process through which bonds are broken, forming new surfaces as a new or existing crack in an otherwise intact material propagates. The initiation, propagation and coalescence of these cracks result in the degradation of material strength which eventually leads to failure. Since most rock masses show some signs of brittle fracture (e.g. jointing, spalling, rockbursts), the interpretation of the conditions and mechanisms behind crack initiation and propagation is essential.

2.1 Mechanistic Theories of Brittle Fracture

Mechanistic theories of failure start from the premise that fractures initiate from existing flaws acting as stress concentrators through which the brittle fracture process in solid materials can be controlled. Griffith (Griffith, 1920) postulated that in the case of a linear elastic material, brittle fracture is initiated through tensile stress concentrations at the tips of small, thin cracks randomly distributed within an otherwise isotropic material (Figure 2.1). These cracks were used by Griffith to explain the discrepancy between the observed tensile strength of materials and the theoretical tensile strength based on molecular cohesion.

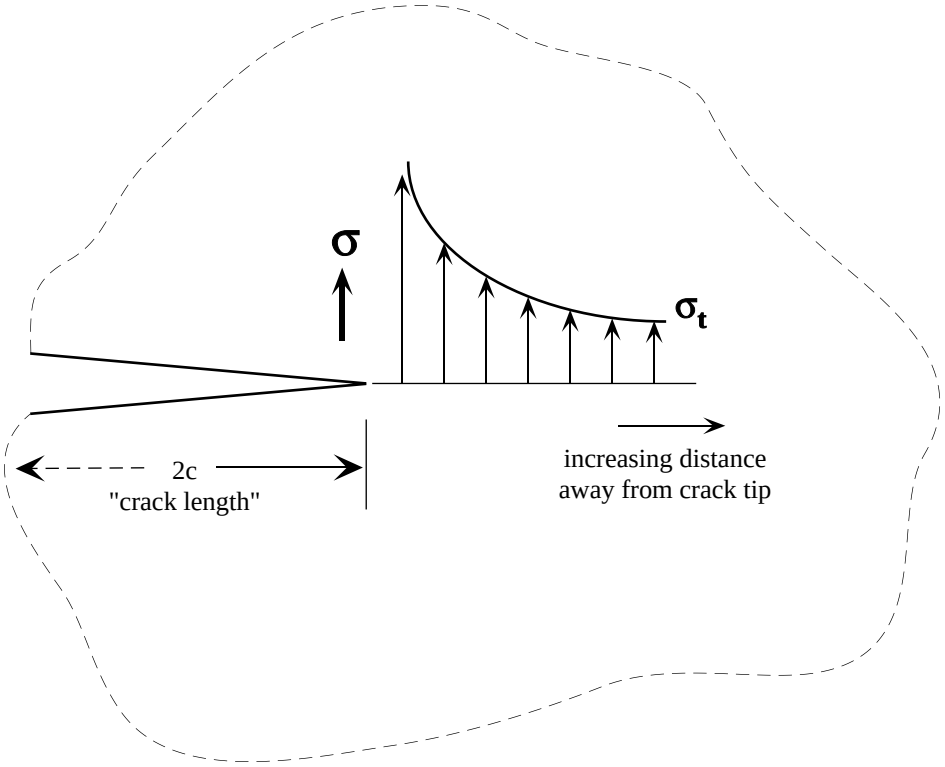

Figure 2.1 Elastic tensile stresses, σ_t, at a crack tip in an arbitrary body (after Broek, 1986).

2.1.1 Griffith's Theory

In what has become known as Griffith's crack theory, Griffith determined the energy condition necessary for cracks to grow. Using the "Theorem of Minimum Potential Energy", Griffith (1920) established that :

> The equilibrium state of an elastic solid body, deformed by specified surface forces, is such that the potential energy of the whole system is a minimum. The equilibrium position, if equilibrium is possible, must be one in which rupture of the solid has occurred, if the system can pass from the unbroken to the broken condition by a process involving a continuous decrease in potential energy.

The passage from an unbroken to a broken state occurs through the lengthening of the "Griffith" crack. Crack extension will therefore occur if the surface energy gained through the rupturing of molecular bonds along the crack path equals the net reduction in strain energy. In other words, the system is in equilibrium if the condition is such that the total potential energy of the system is balanced by the elastic strain energy stored in the structure and the surface energy in the free faces of the crack:

$$W = W_e + W_s \tag{2.1}$$

where : W = total potential energy;
W_e = stored elastic strain energy;
W_s = surface energy in the free faces of the Griffith's crack.

If the stresses around a Griffith crack increase due to an additional load, the corresponding increase in the potential energy may be balanced by either an increase in the strain energy or by an increase in the crack surface energy, or through a combination of both. Solving for the two-dimensional case of an elliptical crack subjected to uniaxial

tension in an elastic plate of uniform thickness (i.e. plane stress conditions), the strain energy and the surface energy can be calculated as:

$$W_e = \frac{\pi c^2 \sigma_T^2}{E} \tag{2.2}$$

and,

$$W_s = 4 \alpha c \tag{2.3}$$

where : σ_T = applied uniaxial tensile stress;

E = elastic or Young's modulus;

α = surface energy per unit area of the crack surfaces;

c = crack half-length.

Although Griffith's theory should be approached in terms of energy, a lack of energy-based experimental testing techniques has resulted in the development of numerous stress-based relationships. Solving for a uniaxial tensile load, Griffith (1920) established that crack extension will occur when:

$$\sigma_T \geq \sqrt{\frac{2E\alpha}{\pi c}} \tag{2.4}$$

where : σ_T = applied uniaxial tensile stress required for crack propagation (i.e. tensile strength).

E = elastic or Young's modulus;

α = surface energy per unit area of the crack surfaces;

c = crack half-length.

Modifications to this derivation have been made by a number of author's including those for two-dimensional plane strain (Hoek, 1965) and three-dimensional loading of penny shaped cracks (Sack, 1946).

Griffith-based relationships derived for tensile stress fields have proven practical for fracture studies involving such solid materials as metals, glass and ceramics. However, these relationships are less relevant in rock engineering problems which predominantly involve compressive stress fields. Griffith (1924) expanded his original formulation to include uniaxial and biaxial compressive stress fields acting on an open elliptical crack. Griffith suggested that although the applied stress may be compressive, the local stresses at the tips of the crack would be tensile. Reformulating his original equation, Griffith surmised that the applied compressive stress required for crack growth was eight times that required for tension, or:

$$\sigma_C \geq 8 * \sqrt{\frac{2E\alpha}{\pi c}} \tag{2.5}$$

where : σ_C = applied compressive stress required for crack propagation (i.e. compressive strength);

E = elastic or Young's modulus;

α = surface energy per unit area of the crack surfaces;

c = crack half-length.

This relationship was later modified by McClintock and Walsh (1962) to allow for normal and frictional stresses acting across the surface of the closing crack (Figure 2.2).

2.1.2 Linear Elastic Fracture Mechanics Approach

Griffith's theory assumes that fracture is initiated when the maximum tensile stress concentration, occurring on a critical flaw boundary, reaches the tensile strength of the material surrounding the flaw (this criterion in itself is an expression of the phenomenological minimum principal stress failure theory). Based on this stress-strength relationship, a discipline known as linear elastic fracture mechanics (LEFM) has evolved. Fracture mechanics concepts assume that cracks in a solid material can be stressed in three different modes (Figure 2.3). The response of the crack to these

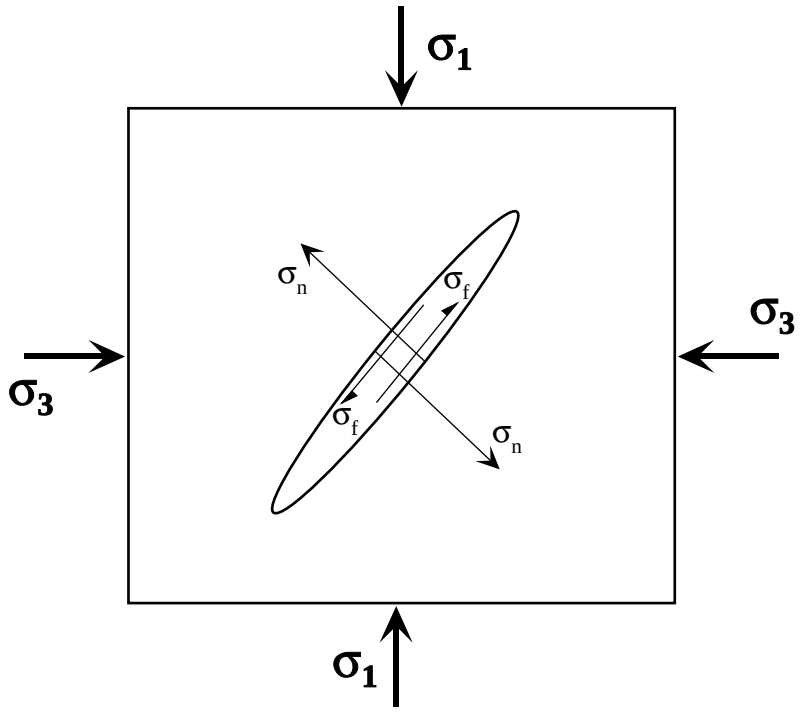

Figure 2.2 Normal, σ_n, and frictional shear, σ_f, stresses acting on a closed crack under compressive loading conditions (after McClintock and Walsh, 1962).

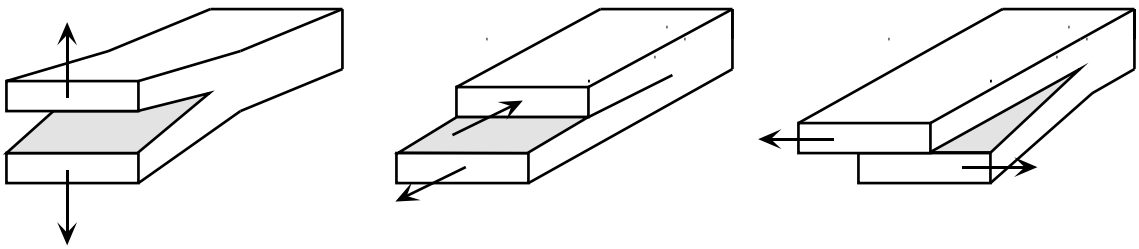

mode I tensile opening

mode II in-plane shear

mode III out-of-plane tearing

Figure 2.3 Modes of crack tip loading and displacement (after Broek, 1986).

stresses, in terms of crack tip displacements, includes tensile opening (mode I), in-plane shear (mode II) and out-of-plane tearing (mode III). Using these models, Ingraffea (1987) summarized the basic tenants of linear elastic fracture mechanics as follows:

1) Associated with a crack tip in a loaded material is a stress intensity factor, K_I corresponding to the induced stress state surrounding the crack (and likewise K_{II} and K_{III} depending on the mode of crack displacement).

2) For a given crack, the boundary material will have a critical stress intensity factor, K_{Ic}, corresponding to the material strength at the crack tip.

3) The criterion for crack propagation can then be written as :

$$K_I = K_{Ic} \, . \tag{2.6}$$

(testing for the K_{Ic} parameter is referred to as fracture toughness testing, the procedures for which have been standardized for various load geometries by both the ASTM, Designation E1820-96, and ISRM, anon. 1997).

4) The crack will continue to propagate as long as the above expression is met, and won't stop until :

$$K_I < K_{Ic} \, . \tag{2.7}$$

By focusing only on the boundary stresses, LEFM and most Griffith-based theories ignore the nature of the stress field beyond the flaw periphery, thus ignoring any stress field disturbances related to the existence of inhomogeneities or plastic deformation beyond the crack surface. The validity of this assumption is based on whether the disturbed non-linear region surrounding the crack tip, otherwise known as the "process zone", is small relative to the dimensions of the crack and specimen geometry (Rossmanith, 1983). If these scale conditions are not met, then a non-linear

approach should be taken to properly model the effects of the process zone (Figure 2.4). In either case, mathematical relationships have been derived in an attempt to realistically model the behaviour of an isolated, propagating crack.

2.1.3 Crack Geometries

In order to develop a series of mathematical expressions based on the principal of an existing crack or flaw acting as a stress concentrator, a number of simplifications are required in terms of the ideal crack geometry. The three more commonly used geometries are the inclined ellipse, the inclined zero-width ellipse and the axial ellipse (Figure 2.5). The inclined ellipse has primarily been used in Griffith-based studies involving physical modelling of crack propagation (Brace and Bombolakis, 1963; Hoek and Bieniawski, 1965; Bombolakis, 1968; Lajtai, 1971; Adams and Sines, 1978). Based on the solution of an ellipse in a homogenous, isotropic, elastic continuum, this crack geometry develops tensile tangential stresses near the crack tip dependent on the loading conditions and the ellipse's aspect ratio (Einstein and Dershowitz, 1990).

A similar inclined ellipse, but flat with zero-width, has been adopted by the LEFM approach. The closed ellipse allows stresses normal to the plane of the crack in excess of that required for closure to be transmitted across the crack faces, thus preventing the stresses from abnormally concentrating at the crack tips (Adams and Sines, 1978). Sliding may also be permitted along the closed crack faces, allowing a mixed mode of crack tip displacement through which friction is incorporated into the formulation. This crack geometry has been extensively used in numerical modelling simulations (Ingraffea and Heuze, 1980; Rossmanith, 1983; Kemeny and Tang, 1990; Shen and Stephansson, 1993; Dyskin *et al*., 1994; Carpinteri *et al*., 1996).

In both cases, these cracks must be inclined to the direction of loading in order to disturb the stress field and produce stress concentrations. The third type of crack geometry, axial ellipses, differs from the previous two geometries in terms of its alignment. Axial elliptical cracks are straight tensile cracks which are aligned with the major principal stress. These cracks are based on visual observations and scanning electron microscope (SEM) studies where the inclined crack geometries are seldom

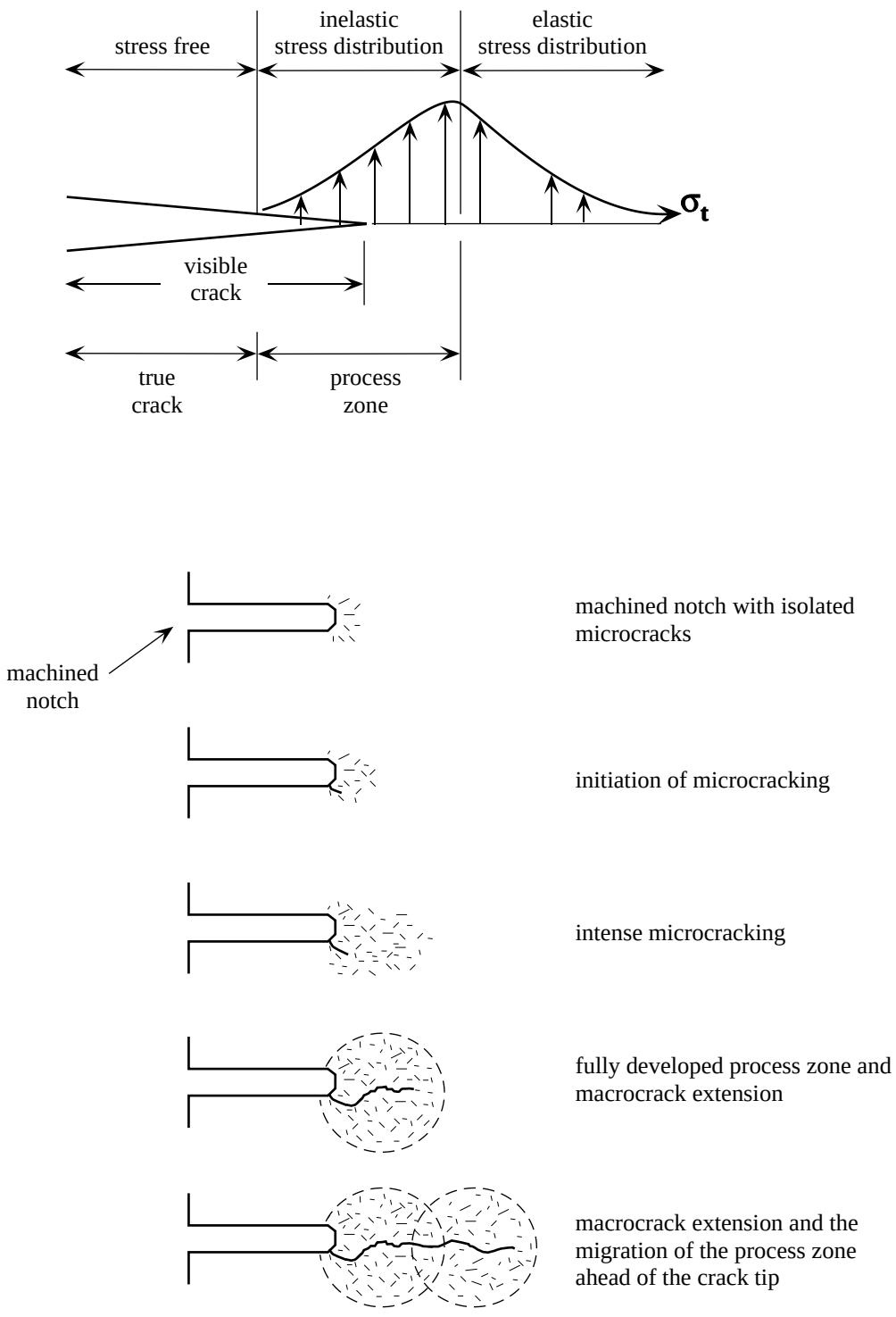

Figure 2.4 Depiction of the non-linear process zone ahead of a crack tip (top) and the development of the process zone and its influence on macrocrack extension (bottom) after Ingraffea (1987) and Atkinson (1987).

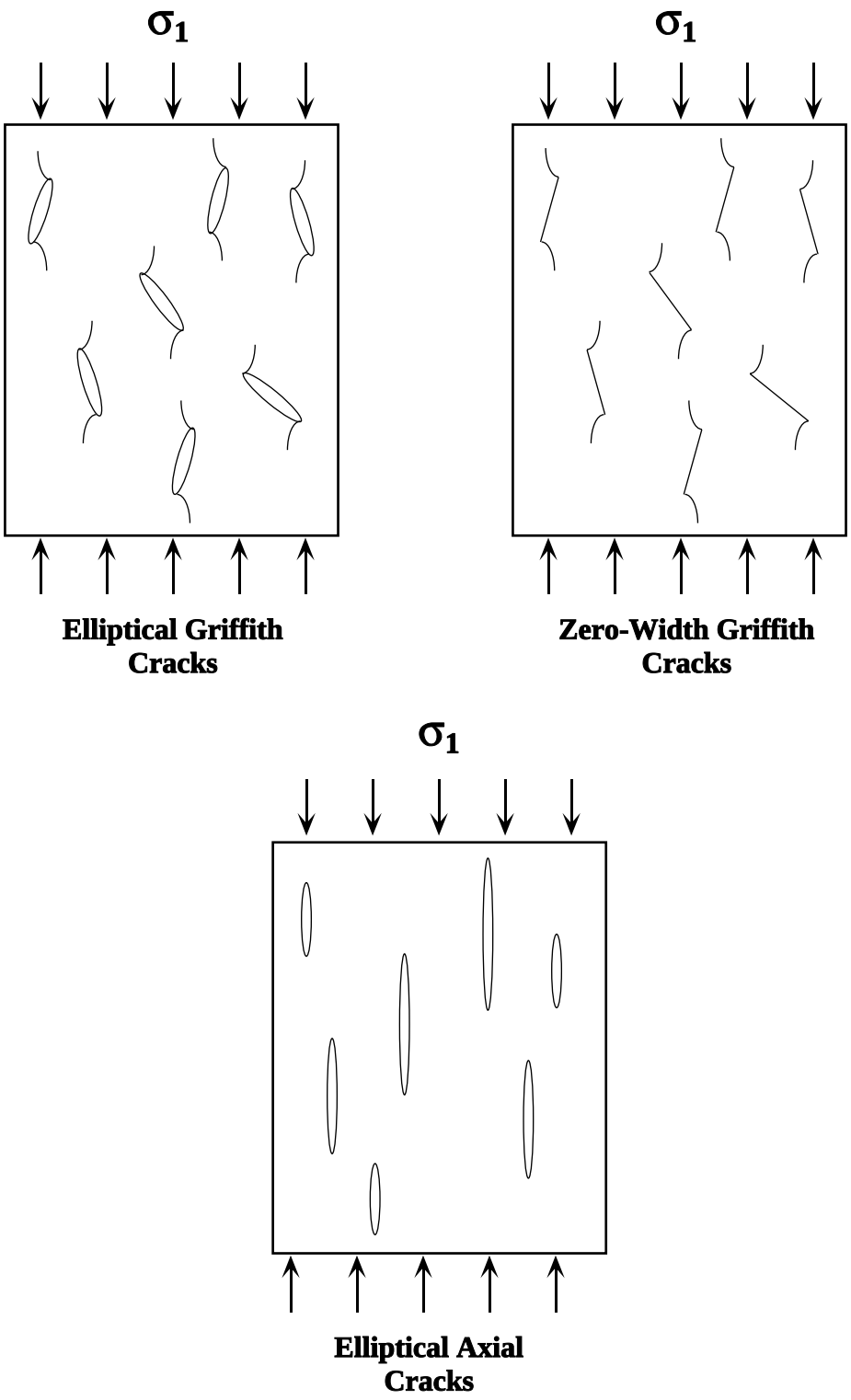

Figure 2.5 Conceptual models for the inclined ellipse, the inclined zero-width ellipse and the axial ellipse crack geometries.

observed (Wawersik and Fairhurst, 1970; Hallbauer *et al*., 1973; Peng and Oritz, 1973; Tapponnier and Brace, 1976; Batzle *et al*., 1980; Zhao *et al*., 1993).

The question as to the presence and origin of these different crack types has been studied thoroughly by a number of researchers. In crystalline materials, it may be assumed that grain boundaries act as stress concentrating cracks and that the crack lengths will be on the order of scale of the materials grain size. Simmons and Richter (1976) and Kranz (1983) divide the petrographic characteristics of microcracks into four types:

- grain boundary cracks (cracks associated with grain boundaries);
- intragranular cracks (cracks which lie totally within the grain);
- intergranular cracks (cracks which extend from a grain boundary crossing into another grain);
- and multigranular cracks (cracks which cross several grains and grain boundaries).

Direct observations of microfractures using either optical microscopes, SEM (scanning electron microscopes) or other petrographic methods have drawn various conclusions as to which crack type constitutes the weakest plane and is therefore prone to fracture propagation. Brace (1961) found that in the case of anhydrites, limestones and quartzites, the first detectable fracturing starts at the grain boundaries. In terms of crystalline, igneous rock, Brace *et al*. (1972), determined that although grain boundaries are the preferred site of microcracks, intergranular cracks also occur in some of the weaker mineral constituents such as in feldspar and biotite grains. Numerous studies have found that the majority of fracturing occurs between grain boundaries with secondary fracturing occurring within weaker grains along cleavage planes and at points where harder minerals induce a point load in neighbouring softer minerals (Wawersik and Brace, 1971; Bombolakis, 1973; Sprunt and Brace, 1974; Mosher *et al*., 1975; Tapponnier and Brace, 1976; Kranz, 1979).

2.2 Initiation and Propagation of a Griffith Crack

The practical application of Griffith's theory and LEFM primarily involves the determination of the stress threshold at which a crack will begin to propagate. This stress level is referred to as crack initiation. Once a crack initiates, the crack will then propagate in either a stable or unstable fashion depending on how much energy is available to drive the crack extension onwards. Examination of Griffith's criterion (Equation 2.5) reveals that a number of factors may influence the strength threshold of a Griffith crack, most notably crack size and crack orientation. This was confirmed by Mosher *et al*. (1975) who found that grain size (i.e. crack length) and crack orientation determines which cracks propagate and which do not.

2.2.1 Critical Crack Length: Influence of Grain Size on Rock Strength

Applying Griffith's theorem (Equation 2.5), one can see that the smaller the crack length, the stronger the material should be. This implies that the longest crack in a material will determine its strength (Brace, 1961). Numerous studies have confirmed that the peak strength decreases inversely with the square root of the grain size in cases where the grain boundary acts as a stress concentrating crack. This relationship has been observed in a number of materials including ceramics (Knudsen, 1959) and ice (Schulson, 1990). It has also been observed in various rock types of different lithology such as quartzite (Brace, 1961), marble (Fredrich and Evans, 1990; Wong *et al*., 1996), dolomite (Hugman and Friedman, 1979), limestone (Brace, 1964; Olsson, 1974) and basalt (Brace, 1961).

In addition to constraining the initial crack size, Fredrich *et al*. (1990) observed that the increase in crack density that would be expected with fine-grained materials can be equated to an increase in the spatial heterogeneity of the local stress field. Such heterogeneity will clearly have strong effects on the crack propagation behaviour, and may cause crack arrest at stages earlier than those predicted. This effect is later demonstrated in Chapter 5.

2.2.2 Critical Crack Orientation

Griffith's (1920, 1924) examination of the stress concentrations forming along the crack boundary near the crack tip were largely based on Inglis' (1913) solution for an ellipse in a stressed plate. Inglis demonstrated that the stresses forming on the boundary of an ellipse will vary depending on the orientation of the ellipse with respect to the applied load and the type of load applied. Tensile stress concentrations resulting from uniaxial tensile loading conditions were found to be at their greatest for a crack aligned perpendicular to the applied load and at their lowest for a crack aligned parallel to the load.

This condition changes for the case of a compressive stress field (Figure 2.6). Lajtai (1971) showed that under uniaxial compressive loading conditions the highest tangential stress concentration on an elliptical boundary (frictional effects between closing crack faces were ignored), was inclined to the major principal stress at approximately 30° (Figure 2.7). Although these cracks may be the first to propagate, it may be assumed that the crack population is randomly distributed and orientated, so that with incremental increases in the applied load, other crack angles will become critical.

2.2.3 Direction of Crack Propagation

In terms of crack initiation and propagation, one of the more significant differences between tensile and compressive stress fields is the location of the zone of maximum tension along the crack periphery. For a crack aligned perpendicular to a uniaxial tensile load, the maximum tensile stress concentration on the crack boundary is at the tip of the long axis. This results in crack growth occurring in the direction of its long axis (i.e. perpendicular to the direction of the applied tension), enlarging the crack continuously until a free surface is reached (Brace and Bombolakis, 1963). Assuming that the solid is isotropic, the orientation of the growing crack remains constant and the magnitude of the local stress at the most highly stressed point on the crack surface increases as the crack lengthens.

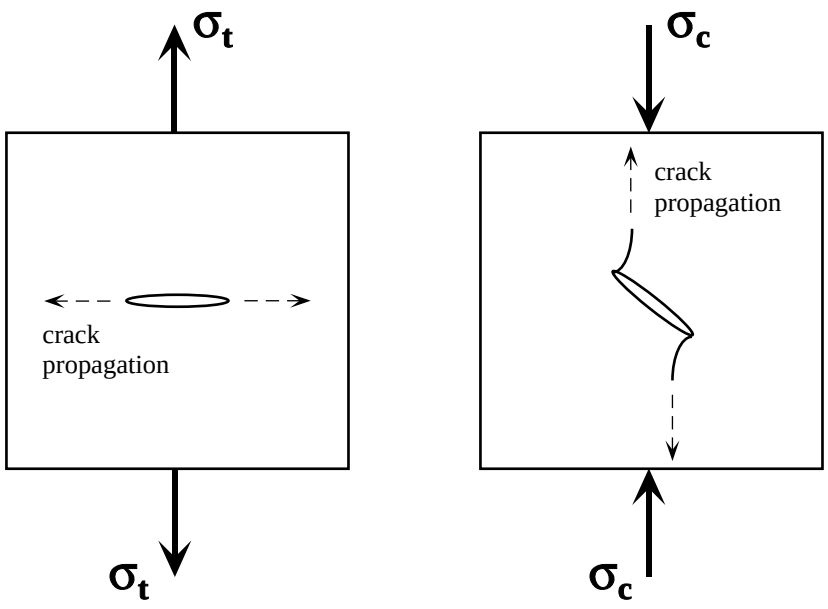

Figure 2.6 Critical crack orientations for tensile (σ_t) and compressive loading (σ_c).

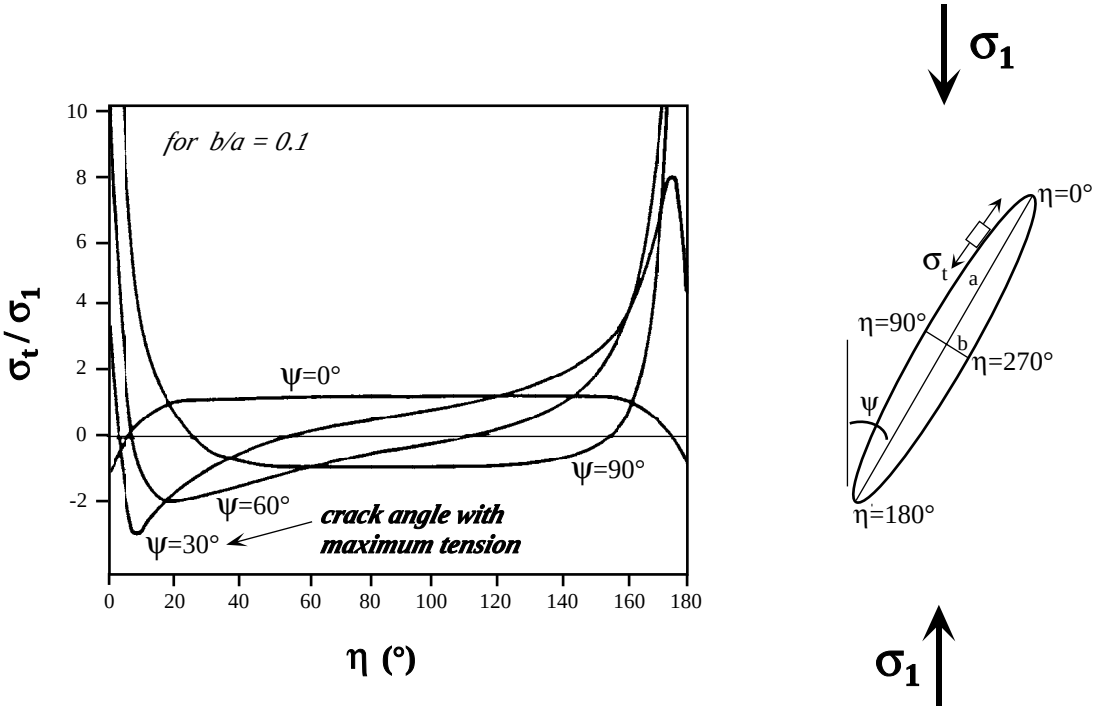

Figure 2.7 Stress concentrations along the periphery of an elliptical crack for varying crack angles with respect to the direction of uniaxial compressive loading (after Lajtai, 1971).

This behaviour changes for the case of an inclined crack. Inglis (1913) and Lajtai (1971) have shown that, for the respective cases of tensile and compressive loading of an inclined crack, the highest tensile stress concentrations do not form at the crack tips but in the sector between the long axis and the direction of applied load (Figure 2.7). Since the critical orientation of a crack in a compressive stress field is inclined to the direction of loading, the maximum tensile stress is offset from the crack tip. This means that unlike the case of crack growth in a tensile stress field, crack growth will not occur in the direction of the long axis. In fact, a number of researchers have shown that it will deviate until it reaches a direction parallel to the major principal stress (Figure 2.8). This phenomenon has been observed in a number of laboratory studies using glass (Hoek and Bieniawski, 1965), hard plastics (Brace and Bombolakis, 1963; Nemat-Nasser and Horii, 1982; Cannon *et al*., 1990), plaster (Lajtai, 1971), ice (Schulson *et al*., 1991), clay (Vallejo, 1987) and rock (Wawersik and Fairhurst, 1970; Peng and Johnson, 1972; Bombolakis, 1973; Huang *et al*., 1993) as the test materials.

2.2.4 Stable Crack Propagation and the Griffith Crack Locus

In formulating the critical condition for fracture, Griffith made assumptions which effectively ignored the behaviour of the moving crack. Griffith's energy balance accounted for the stored elastic strain energy and the crack surface energy only. Several other forms of energy losses into which part of the elastic strain energy is transformed must be considered. Bieniawski (1967a) cites these as including:

- kinetic energy;
- plastic energy (including visco-elastic losses);
- energy dissipated on the breakdown of atomic bonds at the tips of extending cracks;
- energy changes due to mining (artificial rock breaking, heat removal due to ventilation, etc.).

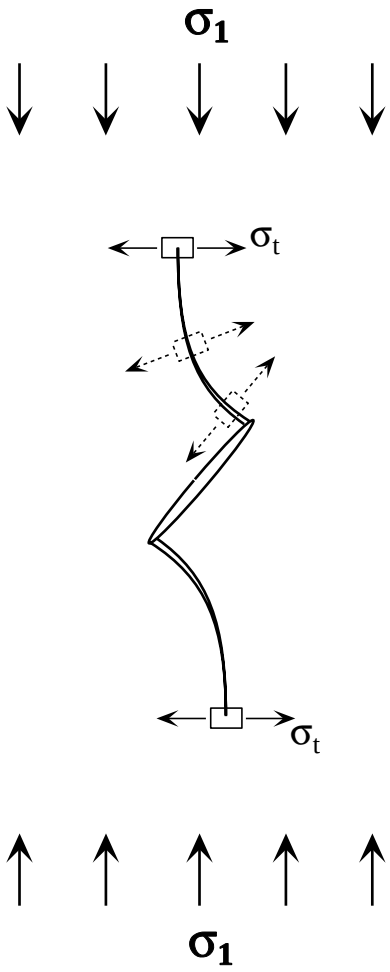

Figure 2.8 Crack propagation in the direction of the major principal stress (σ_1).

In terms of brittle rock, both plastic losses and those associated with interatomic breakdown can be neglected, leaving kinetic energy as the remaining factor outside the control of the excavation operation.

Berry (1960a) reexamined the Griffith problem by considering the presence of both potential and kinetic energy beyond the critical point defined by Griffith, and hence the non-elastic behaviour of a material. Up to the critical point, a solid body containing numerous cracks will deform linearly but with a lower elastic modulus than a solid containing no cracks. Once the critical stress is reached for a particular crack length and orientation, crack growth will begin. Berry (1960a) derived the relationship describing this point, defining a relation between the stress at which the crack becomes unstable and the corresponding strain at that time. This relation, known as the Griffith crack locus, identifies the stress-strain path along which crack extension for a given crack length occurs (Figure 2.9).

Based on work by Berry (1960b), Cook (1965) and Martin (1993), the Griffith crack locus for compression can be interpreted as follows:

- Line OA (Figure 2.10) represents the effective elastic behaviour of a sample containing a crack of zero length (i.e. c = 0). Upon loading, the material will deform elastically following the relationship described by its elastic stiffness, E_c. The critical condition for crack propagation is satisfied when the axial stress reaches σ_A (point A), at which point the crack length begins to increase.

- Segment AB on the Griffith crack locus represents the early stages of crack growth where a rapid loss in strength with no increase in axial strain occurs. Unless the strain energy released from the elastically strained regions around the propagating crack is removed from the system, the excess energy will be converted to kinetic energy. However, most rock systems are unable to unload along the path AB, due to the presence of some finite unloading

stiffness, and therefore unload along the path AC. Thus a crack starting at σ_A will propagate dynamically.

- As the system unloads towards point C, the critical condition is maintained (i.e. the path remains in the unstable region), the elastic modulus decreases and the stress also decreases as the crack grows. The triangle ABC represents the excess strain energy which will cause the crack growth to accelerate, and hence, crack growth will continue even as the stress drops below σ_C (corresponding to point C on the crack locus).

- As the crack continues to advance below σ_C, the surface energy increases at the expense of the strain energy and the kinetic energy. Eventually the kinetic energy will be reduced to zero and the crack will stabilize. At this point the excess strain energy ABC is equal to the strain energy CDE. The material containing the longer crack is now represented by the line OD with a reduced modulus E_{c+dc}.

- These cracks now exist at a subcritical stress level σ_E and will not propagate until the stress level once again reaches the locus at σ_D.

It thus follows that the Griffith locus has two key elements: the stiffness of the initial material, E_c, which controls the position of OA, and the crack properties which controls the shape and position of the locus segment BCD (Martin, 1993). The conditions for crack initiation and stable propagation are satisfied at the point where the stress-strain curve for the sample intersects the locus.

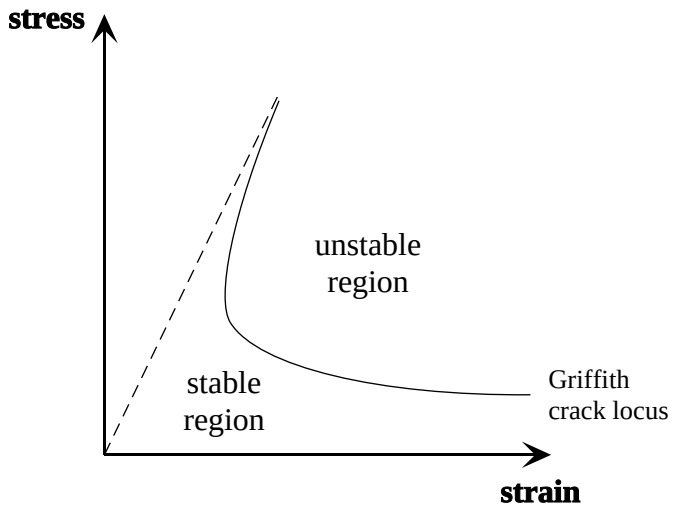

Figure 2.9 Griffith crack locus for compression showing stable and unstable regions.

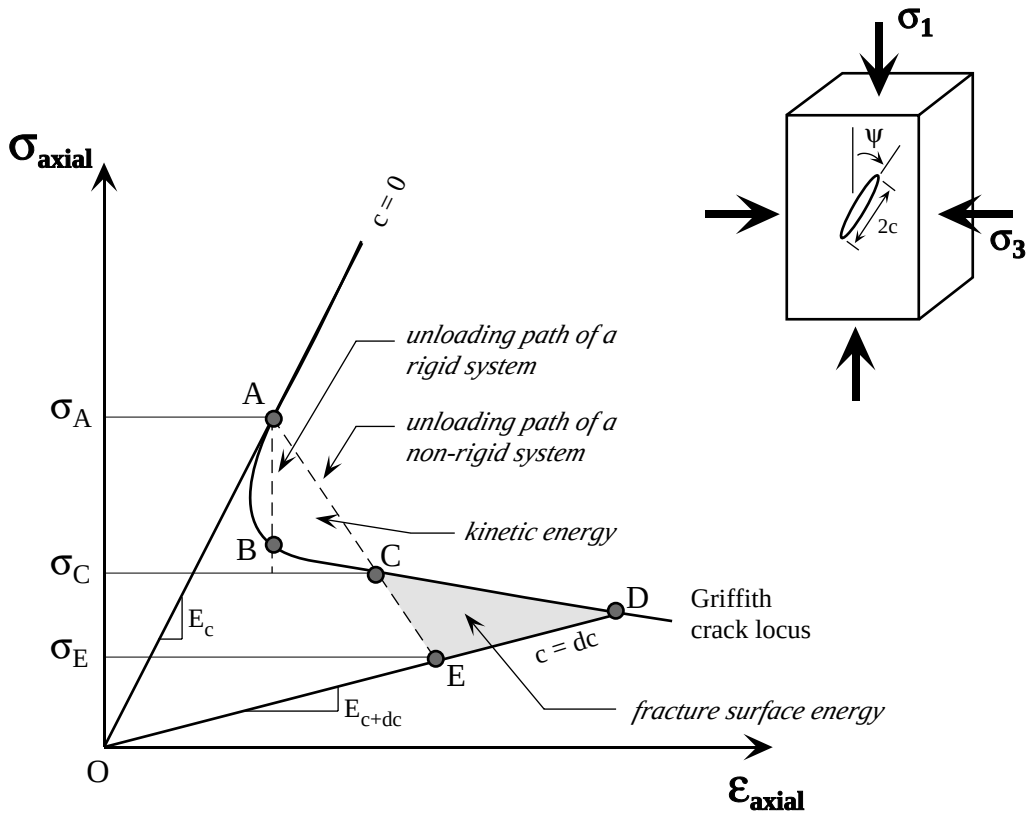

Figure 2.10 Demonstration of the Griffith crack locus (after Martin, 1993).

2.3 Laboratory Derived Stages in the Brittle Failure Process

The deformation and fracture characteristics of laboratory tested brittle rock have been studied by numerous researchers over the past thirty years (Brace, 1964; Bieniawski, 1967a; Wawersik and Fairhurst, 1970; Lajtai and Lajtai, 1974; Tapponnier and Brace, 1976; Martin and Chandler, 1994). The general consensus of these studies has been that the failure process can be broken down into a number of stages based largely upon the stress-strain characteristics displayed through axial and lateral deformation measurements recorded during uniaxial and triaxial laboratory tests. Correlating the measured stress-strain behavior of a loaded material to the opening and closing of "Griffith" cracks in the material (Figure 2.11), Brace (1964) and Bieniawski (1967a) defined these stages as being:

1) crack closure;
2) linear elastic deformation;
3) crack initiation and stable crack growth;
4) critical energy release and unstable crack growth;
5) failure and post peak behaviour.

Crack closure occurs during the initial stages of loading when pre-existing cracks orientated at an angle to the applied load close. During crack closure, the stress-strain response is non-linear, exhibiting an increase in axial stiffness (i.e. Young's modulus). The extent of this non-linear region is dependent on the initial crack density and geometrical characteristics of the crack population. Once the majority of pre-existing cracks have closed, linear elastic deformation takes place. The elastic constants of the rock are calculated from this linear portion of the stress-strain curve.

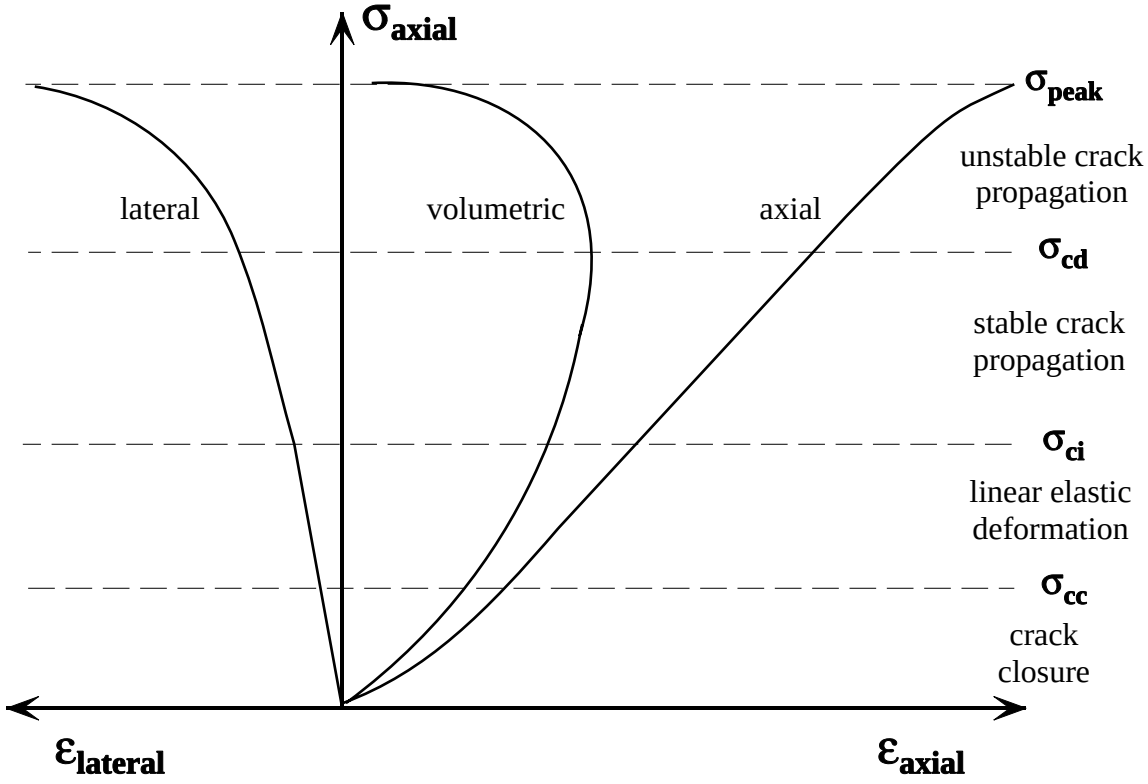

Figure 2.11 Stress-strain diagram showing the elements of crack development including the crack closure (σ_{cc}), crack initiation (σ_{ci}) and crack damage (σ_{cd}) thresholds. Note that only the axial and lateral strains are measured and the volumetric strain is calculated.

Crack initiation represents the stress level where microfracturing begins and is marked as the point where the lateral and volumetric strain curves depart from linearity (Figure 2.11). Crack propagation at this point is considered as being stable where controlling the applied load can stop crack growth. Bieniawski (1967a) defines unstable crack propagation as the condition that occurs when the relationship between the applied stress and the crack length ceases to exist and other parameters, such as the crack growth velocity, take control of the propagation process. Under such conditions, crack propagation would be expected to continue even if loading was stopped and held constant. Bieniawski (1967a) correlated the threshold for unstable crack growth, also referred to as the point of critical energy release and the crack damage threshold, with the point of reversal in the volumetric stress-strain curve.

Unstable crack propagation continues to the point where the numerous microcracks coalesce into larger cracks and the rock can no longer support an increase in load. This point is considered as being the peak strength of the rock sample. Martin (1993) notes, however, that the peak strength of granite (including the uniaxial compressive strength in unconfined tests) is not a unique material property but is dependent on loading conditions such as the loading rate. Instead, Martin (1993) found that the crack initiation and crack damage stress thresholds were more characteristic of the rocks' long-term strength, and are essentially independent of loading conditions.

2.4 Damage Mechanics and the Quantification of Stress-Induced Microfracturing

Identifying the stages of crack development through laboratory testing allows for an improved understanding of the *in situ* failure process. Martin and Read (1996) have observed that the microfracturing process can be correlated to the progressive failure of a circular opening in brittle rock. Munson *et al*. (1995) made similar observations with respect to a vertical shaft in salt. In general, microfractures contribute to the failure process by altering the mechanical properties of the material. The propagation of a microfracture can be equated with the irreversible destruction of molecular cohesion along the generated fracture path. In this sense, the microfracturing process acts to "damage" the material. As

the number of propagating fractures multiply, damage can be viewed as accumulative and can be correlated to observed decreases in the elastic stiffness and cohesive strength of the material. Rock deformation and failure, therefore, can be attributed to the continuous accumulation of stress-induced fracture damage.

The notion of fracture damage and the quantification of its effects on the mechanical properties of a material has developed into its own field of study known as damage mechanics. Mazars and Pijaudier-Cabot (1996) define damage mechanics as the description of the local effects of microfracturing and the evolution of the mechanical properties of the continuum as microfractures develop. These effects include elastic stiffness degradation, induced anisotropy, anelastic strains and cohesion loss. The theory of damage, therefore, describes the evolution of material behaviour between the virgin state and the fracture-induced failed state. Damage mechanics acts to quantify these changes by introducing a continuous internal state variable called the "damage", which may be regarded as a continuous measure of the state of internal degradation of the stiffness of the material considered (Singh and Digby, 1989).

The concept of a continuous measure of damage has been used extensively to describe various types of failure in metals and other types of solids. Lemaitre and Chaboche (1990) review these damage models which include damage formulation based on ductile plastic, creep and fatigue failures. Singh and Digby (1989) review a number of similar damage relationships developed for brittle materials. In each of these cases, the effects of microfracturing are quantified through the development of a damage variable within a constitutive relationship criteria which, in turn, acts to describe the degradation of elastic stiffness for a given material. One of the simplest of these relationships, the uniaxial linear elastic damage law, can be written as:

$$\varepsilon_e = \frac{\sigma}{(1-D)E} \tag{2.8}$$

where : ε_e = elastic strain;

σ = uniaxial stress;

D = damage;

E = elastic or Young's modulus.

Although this model assumes all material behaviour (i.e. elasticity, plasticity, viscoplasticity) is affected in the same way by damage defects, the formulation provides a coherent and efficient stress-strain relationship (Lemaitre and Chaboche, 1990).

The measurements required for these formulations have for the most part involved the coupling of deformation with damage (Lemaitre and Chaboche, 1990). Shao and Khazraei (1994) have demonstrated that laboratory stress-strain data can be used to both establish the required damage parameters and to calibrate the derived damage models. The versatility of laboratory stress-strain data is also demonstrated through its ability to measure a wide range of rock behaviour. This has allowed for the development of damage models for such complex behaviour as creep deformation in rocksalt (Aubertin *et al*., 1993; Munson *et al*., 1995) and subcritical crack growth (Horii and Okui, 1994). To a lesser extent, the development and calibration of damage models have also been achieved using acoustic velocities (Munson *et al*., 1995; Lemaitre and Chaboche, 1990) and acoustic emission (Cox and Meredith, 1993; Shah and Labuz, 1995).

The quantification of microfracturing damage has proven to be a valuable consideration in the design of underground openings. The application of a damage criterion allows for the practical implementation of fracture processes derived through laboratory experiments. Simple relationships such as those proposed by Martin and Read (1996) can be used to correlate the microfracturing process observed in laboratory tests to the extent and characteristics of the damaged zone surrounding an underground excavation in brittle rock (Figure 2.12). Similarly, damage models have been used to model the extent of borehole failure (Shao *et al*., 1996), the degree of damage surrounding salt-hosted nuclear waste repositories (Munson *et al*., 1995) and the damage induced by blasting (Li and Nordlund, 1993). In general, damage based relationships can be applied to any rock engineering problems in which brittle fracturing has a significant influence on the observed behaviour of the material.

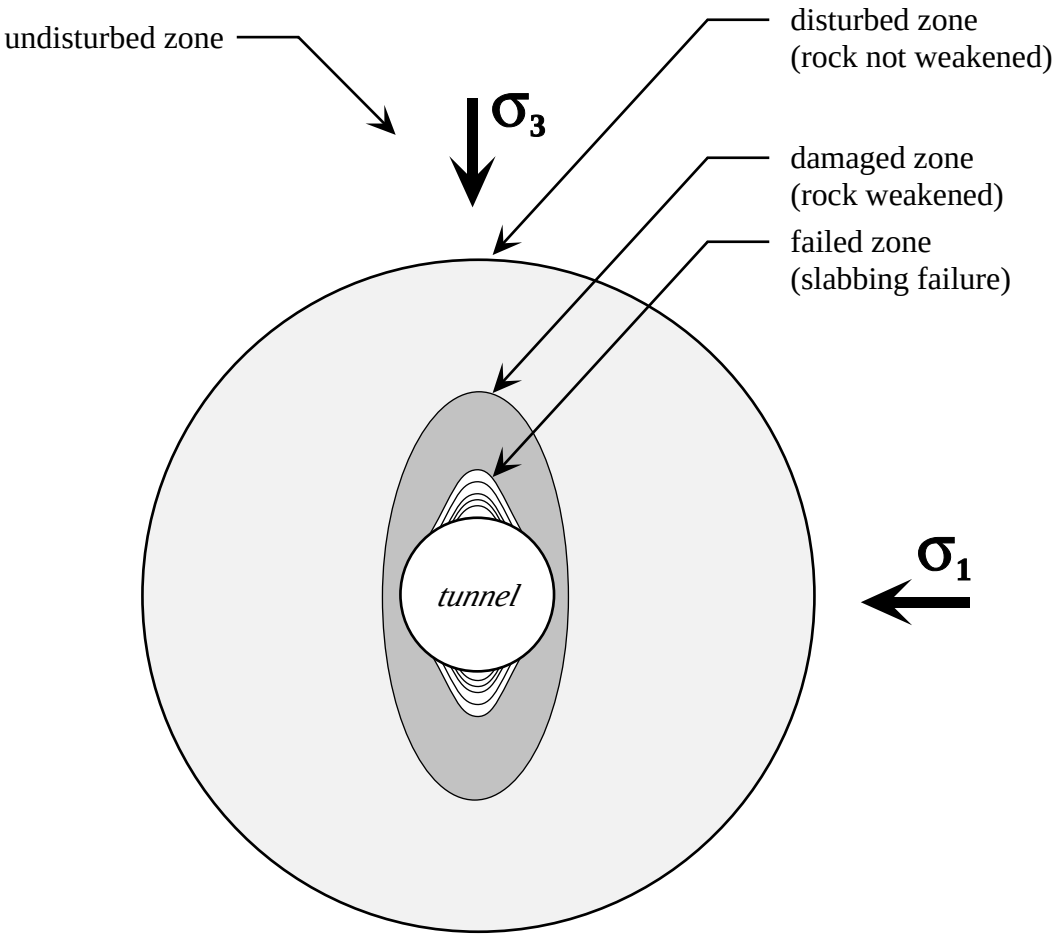

Figure 2.12 Characteristics and extent of the disturbed and damaged zone surrounding a tunnel in a plane perpendicular to the tunnel axis (after Martin and Read, 1996).

2.5 Chapter Summary

The deformation and failure of brittle materials can be attributed to the development of stress-induced microfractures. This process has been studied through the application of mechanistic-derived criteria based on the premise that fractures initiate from existing flaws acting as stress concentrators. The practical application of these theories (e.g. Griffith's theory, linear elastic fracture mechanics) primarily involves the determination of the stress threshold at which a crack will begin to propagate. Factors, which can influence this process, include the crack length (which in turn can be correlated to grain size), crack density and crack orientation.

Once a crack begins to propagate, it will do so under either stable or unstable conditions. The direction of propagation will follow an approximate path parallel to the direction of the applied load (i.e. maximum principal stress, σ_1). This phenomenon has been observed in a number of brittle materials. Laboratory measurements of stress and strain have allowed for the detection of several stages of crack development based on the opening and closing of these cracks. These stages include: crack closure; linear elastic deformation; crack initiation and stable crack growth; crack damage and unstable crack growth; and failure and post peak behaviour.

The identification of these stages has allowed for the correlation of the microfracturing process with the progressive failure of brittle rock. Microfracturing can be equated with irreversible damage and applied in a criterion that quantifies the internal degradation of elastic stiffness and cohesive strength in a material. These relationships can then be used to model the zone of damage surrounding an underground excavation.

CHAPTER 3

DETECTION OF STRESS-INDUCED MICROFRACTURING DURING LABORATORY TESTING

A number of techniques have been developed to detect and study crack growth in brittle materials. The most common of these involves the use of electric resistance strain gauges to measure slight changes in sample deformation that can be correlated to the closing, opening and coalescence of cracks (Brace *et al*., 1966; Bieniawski, 1967b; Martin, 1993). More recently, acoustic emission monitoring has been used to correlate the number of acoustic events to various strain gauge responses (Scholz, 1968; Ohnaka and Mogi, 1982; Khair, 1984). Other techniques have involved the use of photoelastic materials (Brace and Bombolakis, 1963; Hoek and Bieniawski, 1965), optical diffraction patterns (Wawersik and Fairhurst, 1970), sections (Peng and Johnson, 1972; Mosher *et al*., 1975), scanning electron microscopes (Kranz, 1979; Batzle *et al*., 1980; Zhao *et al*., 1993), laser speckle interferometry (Chengyong *et al*., 1990), ultrasonic probing (Swanson and Spetzler, 1984; Walsh, 1984), electrical resistivity (Walsh, 1984; Tomecka-Suchon and Rummel, 1992) and numerical modelling (Ingraffea, 1979; Hamajima *et al*., 1984; Li, 1995).

3.1 Strain Gauge Measurements

Strain gauge measurements have provided the most insight into delineating the stages of crack development in rock. The use of strain gauges in past studies, however, has been somewhat limited by data sampling, computing and storage capabilities. The work performed in this thesis has been directed towards using more powerful computers with larger data storage capabilities in conjunction with faster data logging systems. These capabilities have allowed for tests to be conducted in which the sampling rate has

been increased 5 to 10 times that permitable with conventional testing systems (i.e. capable of 5 measurements per second). Thus, more data points for educing the axial and lateral stress-strain curves can be collected and examined for indications of crack growth. In essence, higher resolution of sample deformation relating to crack initiation and growth is achieved.

Improvements can also be achieved in the way strain gauge data is analyzed. Stress-strain data analysis has traditionally concentrated on picking noticeable slope changes in the plotted stress-strain curves (i.e. axial, lateral and the calculated volumetric) which may then be correlated to several of the theoretical stages in crack development (for example, Lajtai and Dzik, 1996). However, a high degree of error and subjectivity is incorporated into this procedure when one considers the combined use of poor data resolution and the manual picking of points (Figure 3.1). Bearing in mind that certain inflections, some of which may be undetectable to the unaided eye, in the stress-strain curves are of key interest, a moving point regression technique, which uses the first derivative of the curves to highlight any slope or rate changes in the curves, was developed.

3.1.1 Moving Point Regression Technique

The moving point regression technique uses a “sliding window” approach to scan through an x,y data set, superimposing a straight line over a user-defined regression interval. The slope at each point is calculated over the interval and recorded, the process being repeated at successive points (Figure 3.2). The least squares method is used in calculating the best fit line through the data. When plotted against the parameter of interest, inflections in the original x,y data curve are highlighted. For example, when using an axial stress -*vs*- axial strain curve, this technique produces a moving average of the changes in Young’s modulus throughout loading (Figure 3.3). This is referred to as the average axial stiffness, therefore avoiding problems in terminology when calculating the slope outside the range of linear elastic behaviour. Similarly, moving point regression curves of lateral and volumetric stress-strain data are hereafter referred to as lateral and volumetric stiffness plots.

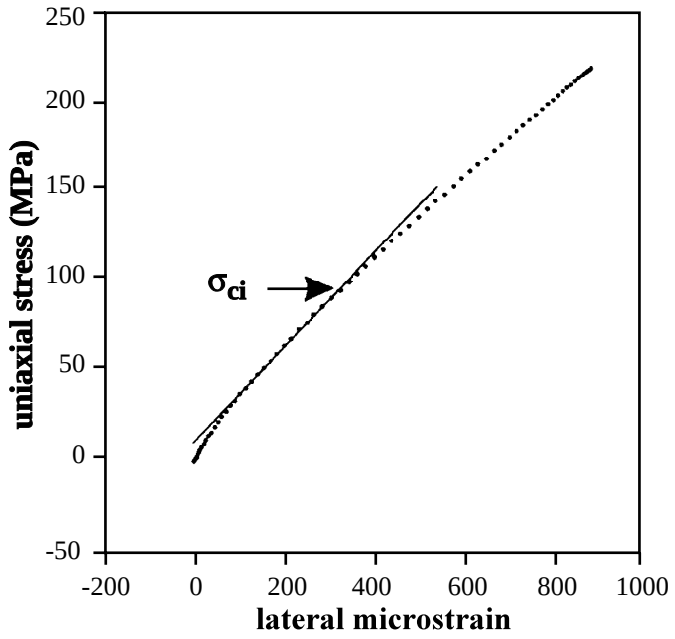

Figure 3.1 Determination of the crack initiation point using the lateral strain curve (after Lajtai and Dzik, 1996). Note the subjectivity incorporated into the picking of the point due to the low resolution of the stress-strain data.

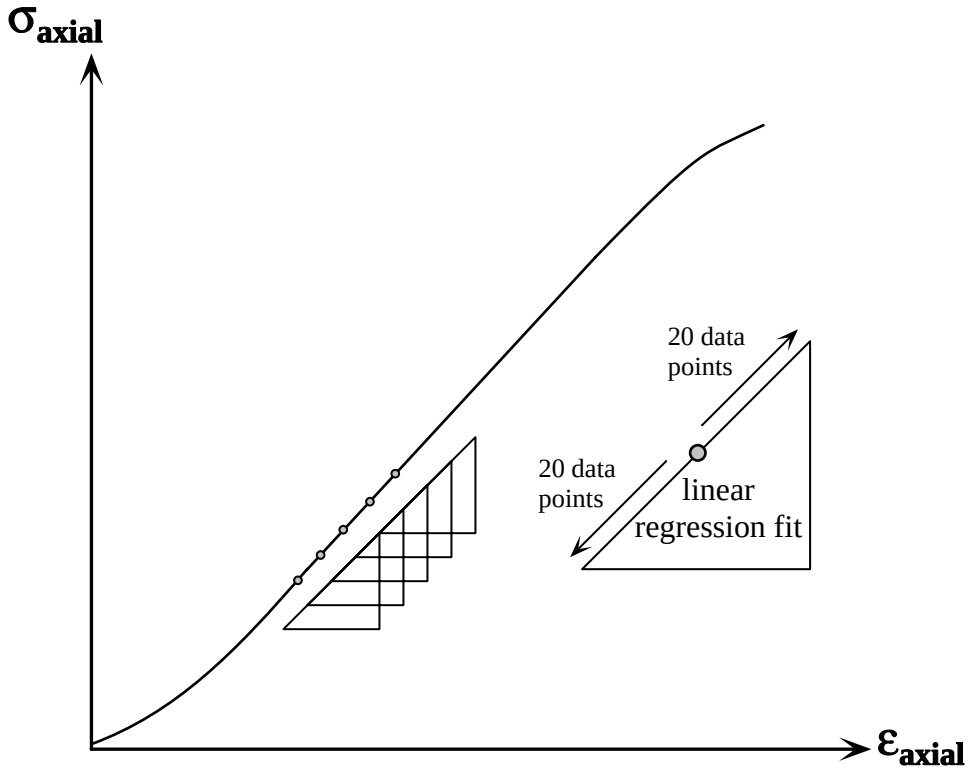

Figure 3.2 Illustration of the moving point regression technique.

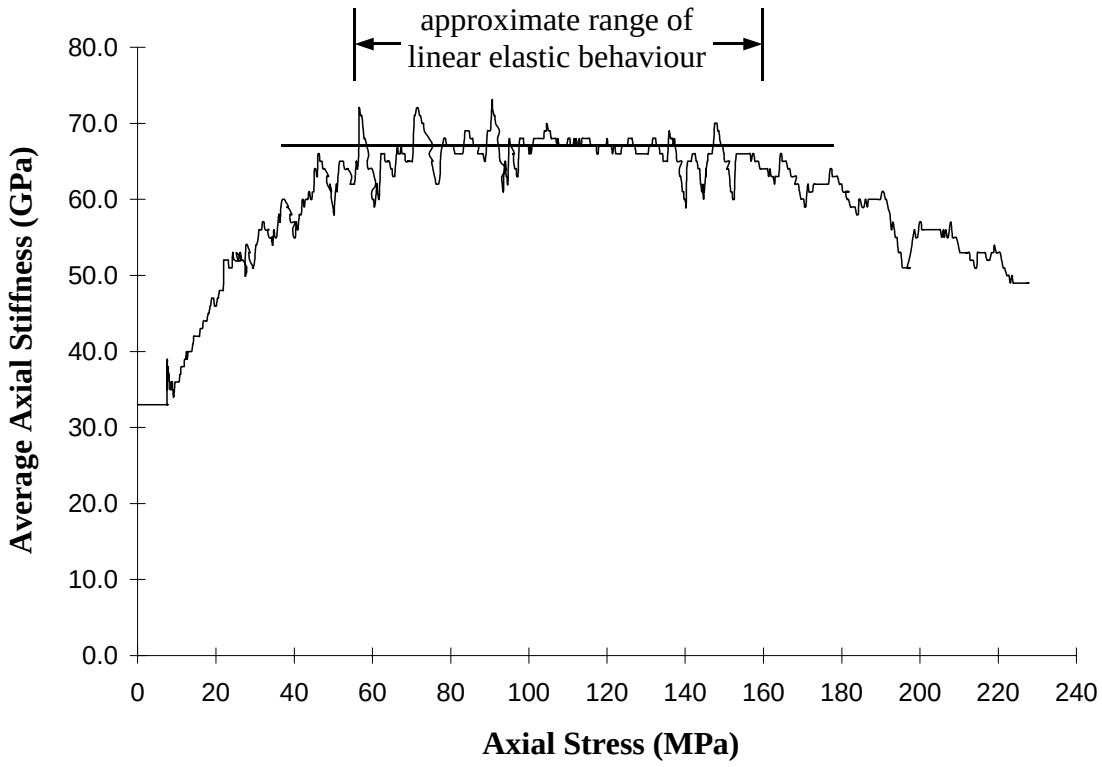

Figure 3.3 Moving point regression analysis of an axial stress -*vs*- axial strain curve showing the changes in the axial stiffness (i.e. modulus of deformation or Young's modulus over the elastic interval) throughout loading.

The moving point regression analysis performed in this thesis requires a user defined “sliding” window interval for which the least squares best-fit calculation is performed. To examine the influence the user-defined interval has on the measured response, a sensitivity analysis was conducted, the results for which are shown in Figure 3.4. The analysis indicates that if too few points are used, the results will widely fluctuate giving a rough appearance to the results. Conversely, too many points will cause excessive smoothing. In each case, the general shape of the stiffness curve remains the same, only the small scale fluctuations in the measured deformation response are filtered out when the largest regression interval is used. Analysis results indicate that the size of the regression interval should be approximately 5% of the total number of x,y data pairs. However, this ratio is highly dependent on the speed of the data logging equipment used (i.e. a slower logging system would require a smaller regression interval, whereas a faster logger would require a larger user-defined interval). For the testing performed in this thesis, a regression interval of 40 x,y data pairs was chosen (the average tests consists of approximately 1000 x,y data pairs). This window represents approximately 5 MPa of load (i.e. the least squares fit was performed for the change in strain over a stress interval of approximately 5 MPa).

3.2 Acoustic Emission Response in Rock

Existing cracks (i.e. “Griffith” cracks) and other flaws in a loaded material produce local concentrations of strain energy, which, through the deformation process, results in the conversion of energy into other forms. In the preceding chapter, it was shown that some of this surplus energy is absorbed through the creation of new crack surfaces and through plastic deformation. In addition, excess energy may also be absorbed through the heating of the material surrounding the crack tip. The final element of energy release takes the form of kinetic energy. Through the use of the Griffith crack locus, Berry (1960a) and Cook (1965) have shown that kinetic energy can have a significant influence on the stages of crack growth. More specifically, kinetic energy may be partially absorbed by the propagating crack to help meet some of the

Regression Interval:

10 x,y pairs

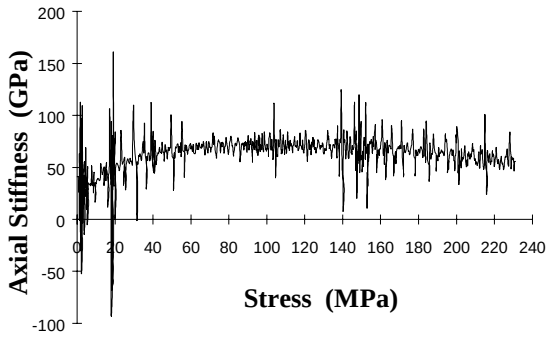

Regression Interval:

20 x,y pairs

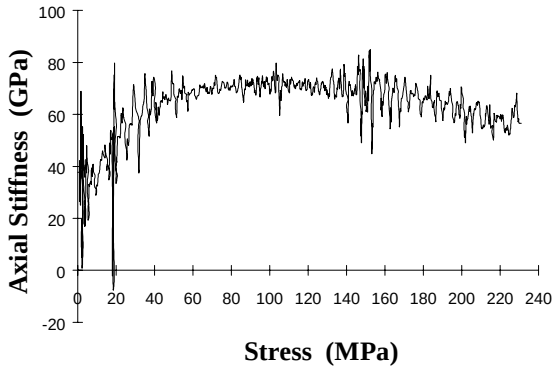

Regression Interval:

40 x,y pairs

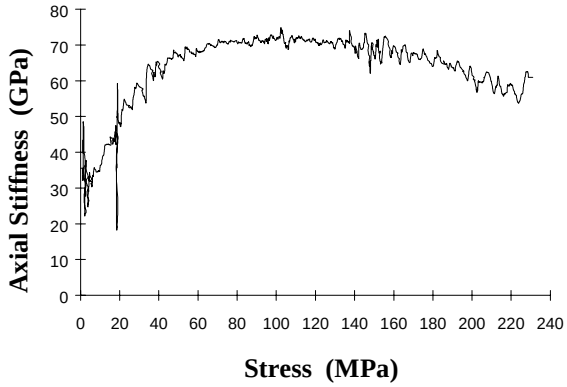

Regression Interval:

100 pairs

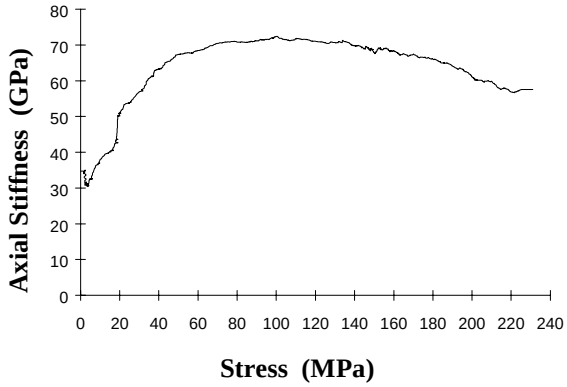

Figure 3.4 Variation in axial stiffness calculations for different regression intervals.

crack's energy needs and sustain its growth. This release of kinetic energy has been identified as acoustic emissions (Pollock, 1977).

3.2.1 Correlation of Fracture with Acoustic Emission

Acoustic emissions (AE), in polycrystalline rock, originate as a result of dislocations, grain boundary movement, or initiation and propagation of fractures through and between mineral grains. The sudden release of stored elastic strain energy accompanying these processes generates an elastic stress wave which travels from the point of origin within the material to a boundary where it is observed as an acoustic event (Hardy, 1977). This phenomenon of AE response provides a unique method for studying the processes behind rock deformation and failure.

Acoustic emission techniques have been used with some success in identifying microfracturing in brittle materials. Scholz (1968) found that characteristic AE patterns in rock correlate closely with stress-strain behaviour. However, most of the success in correlating AE activity to microfracturing has involved the latter stages of crack development (Scholz, 1968; Sondergeld *et al*., 1984; Rao, 1988; Xiao *et al*., 1991; Shah and Labuz, 1995). This is due to the fact that the majority of AE events occur just prior to failure (Figure 3.5). The lack of significant AE activity in the initial stages of loading makes it more difficult to distinguish background noise from fracture-related acoustic events. A balance must be struck between setting event threshold limits high enough to filter out the majority of the background noise, yet low enough to pick up the beginning of the microfracturing process.

3.2.2 Acoustic Emission Detection

When an acoustic event wavefront reaches the surface of a test object, the AE transducer detects the mechanical movements of the surface molecules and converts it into a specific, useable, electric signal. These signals are often complex since naturally occurring acoustic emission contain a mixture of wave modes (Spanner *et al*., 1987).

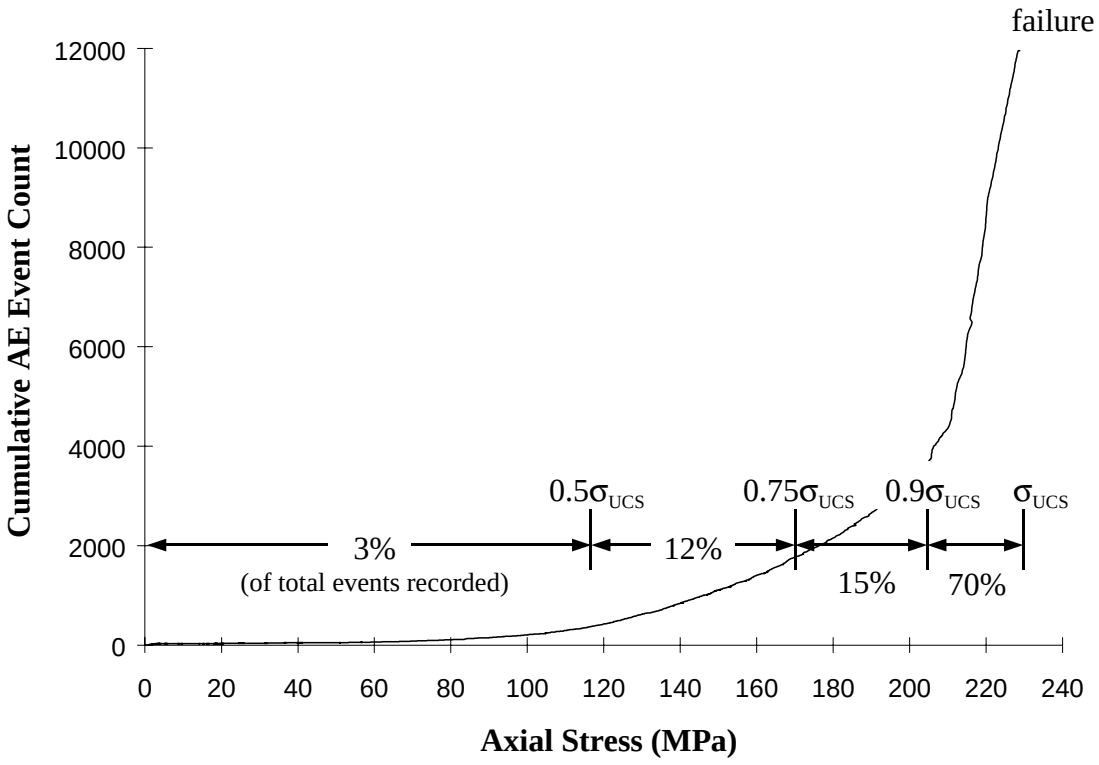

Figure 3.5 Typical acoustic emission response for Lac du Bonnet granite showing the cumulative number of events with axial load.

There are two basic types of AE signals to be processed: continuous and burst-type (Figure 3.6). Continuous signals may originate from such sources as leaks in pressurized systems and hydraulic noises. These signals are termed invalid or mechanical noise. Burst-type emissions originate from a variety of sources, but primarily involve some form of crack growth as observed in metals, composites and geological materials. These signals are usually characterized by a fast rise time to the signal's peak amplitude, followed by an exponential signal decay (Figure 3.7). Acoustic emission monitoring is usually carried out in the presence of both types of emission (continuous and burst) so a threshold detection level is set somewhere above the background level to filter out the continuous background noise.

3.2.3 Acoustic Event Properties

To date, most AE studies have concentrated on using event counts, event rates and source location to analyze sample deformation and failure. However, it is also possible to record certain properties of the individual AE event waveforms. Several of these simple waveform parameters, measured with respect to the threshold setting, are depicted in Figure 3.7 and defined in Table 3.1. In general, larger parameter values correlate to larger AE events. For instance, plots of the amplitude distribution (described in Sun *et al*., 1991) have been widely used to correlate gradual changes in AE event magnitudes with fracture processes precursory to failure. In this sense, measured changes in the waveform properties can be used to infer the mechanisms involved in the generation of an AE event. More recent studies have involved the development of techniques directed at obtaining the source mechanism of the events (i.e. tensile or shear fractures). Shah and Labuz (1995) relate the seismic moment tensor to crack displacements to sort AE events as either opening (i.e. tensile or Mode I) or sliding (shear or Modes II and III). Similarly, Meglis *et al*. (1995) derived mechanisms for AE events by classifying the sources as being either compressional if the first motion direction of the event was away from the AE sensor, tensile if it was towards, and shear if the distribution of the first motions fit a double couple dipole model.

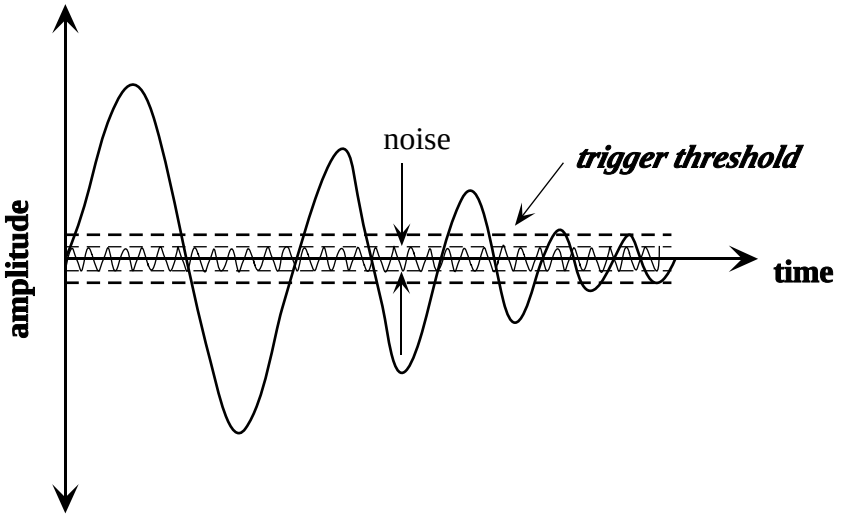

Figure 3.6 The use of threshold settings to filter out continuous background noise (after Spanner *et al*., 1987).

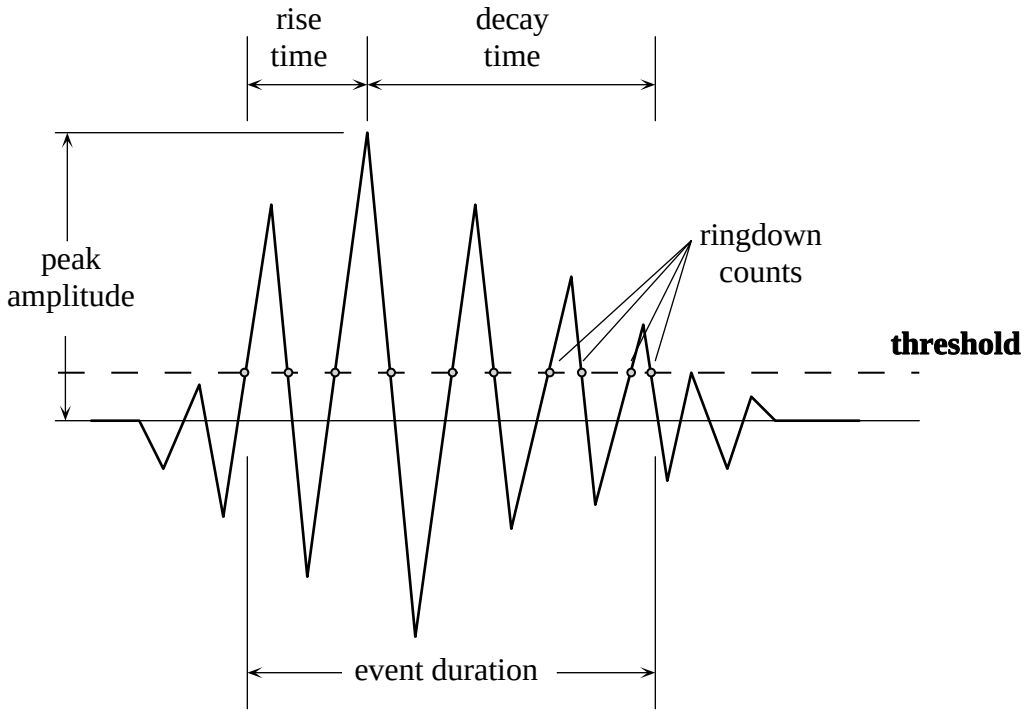

Figure 3.7 Illustration of common AE event waveform parameters.

Table 3.1 Definition of acoustic emission event properties (as shown in Figure 3.7).

AE Event Property	Description
Ringdown Count	The number of times a signal crosses a preset threshold datum; in general, large events require more cycles to "ring down" to the threshold level and will produce more counts than a smaller event; provides a measure of the intensity of the acoustic emission event; measured values range from 0 to 4095 counts/event.
Peak Amplitude	Related to the intensity of the source in the material producing an AE event; values are generally recorded in log units (decibels, dB) to provide measurement of both large and small signals; dynamic range of 64 dB.
Event Duration	When an acoustic event first crosses the preset threshold, an event detector measures the time that the waveform amplitude remains above the threshold thereby giving the event duration; event durations ranging from 0 to 65,520 μs measurable.
Rise Time	Measures the time it takes to reach the peak amplitude of an event; provides an account of the positive-changing AE signal envelope; rise times ranging from 0 to 65,520 μs measurable.

The signal waveform of an acoustic event, however, can also be affected by a number of factors including the characteristics of the source, the nature of the medium, the path the waveform travels prior to detection, the sensor characteristics and the recording system. Generally, these waveforms are complex and using them to characterize the source can be difficult. Due to these complexities, AE waveform

analysis can range from simple parameter measurements to more intricate pattern recognition. However, outside the previously mentioned studies and the results presented in this thesis, relatively little work has been done in the area of waveform analysis with respect to rock mechanics and the progressive degradation/failure process in rock.

3.2.4 Acoustic Event Energy

Since acoustic emission activity is attributed to the rapid release of kinetic energy in a material, the energy content of the acoustic emission signal can be related to the total energy released. The true energy is directly proportional to the area under the acoustic emission waveform which in turn can be measured by digitizing and integrating the waveform signal. However, this can be both difficult and time consuming. As a simplification, the event energy can be approximated as the square of the peak amplitude (Spanner *et al*., 1987; Lockner *et al*., 1991), or the square of the peak amplitude multiplied by the event duration (Beattie, 1983; Mansurov, 1994). The resulting values are actually more representative of the intensity of the event but are commonly referred to as energy calculations in the AE literature. This is due to their approximately linear relationship with energy (the units of this term are given in decibels, or dB, which can be defined as 10 times the logarithm, to the base 10, of the ratio of two mean square values of voltage). Beattie (1983) notes that when considering measurement inaccuracies, damping factors or other changes in parameters related to the signal shape, these calculations provide no closer a relationship to the event energy than does the AE count. The main reason to perform this type of "energy" analysis is to accentuate events with either abnormally large amplitudes or durations. In effect, squaring the peak amplitudes for an "energy" measurement produces a simple pulse from a burst signal and leads to a simplification of AE event counting. Regardless of the type of energy measurement used, neither is an absolute energy quantity, but a relative quantity proportional to the true energy (Spanner *et al*., 1987).

3.3 Laboratory Testing Setup

A program of uniaxial compression testing was undertaken to investigate the effects of stress-induced brittle fracturing on the progressive degradation of rock strength. These tests concentrated on identifying the crack initiation (σ_{ci}) and crack damage (σ_{cd}) stress thresholds using both strain gauge and AE response. All testing was carried out in the Department of Geological Sciences' Rock Mechanics Laboratory at the University of Saskatchewan. Samples were prepared for testing according to ASTM standards (Designation D4543-85) by grinding the ends to create right angled cylinders with length to diameter ratios of approximately 2.25. Considerable care was taken in reducing any influence that end effects may have on strain gauge and AE transducer readings. This entailed the use of a specially constructed frame that allowed for the sample ends to be highly polished, resulting in measurements of end surface flatness and perpendicularity five times lower than those recommended by ASTM standards. Each sample was instrumented with six Micro-Measurement electric resistance precision strain gauges (3 axial and 3 lateral at 60° intervals, 12.7mm in length, with a 5% strain limit) to record sample deformation and four 175 kHz resonant frequency, lead zirconate titanate, piezoelectric transducers to record acoustic emissions (Figure 3.8). Strain gauges were epoxied directly to the cleaned sample surface to ensure a solid bond, whereas the AE transducers were mounted onto waveguides, which were in turn epoxied to the sample surface to provide a good acoustic coupling.

The AE monitoring system consisted of a bandpass filter with a frequency range of 125 kHz to 1 MHz and a pre-amplifier with 40 dB total gain and a dynamic range of 85 dB. The AE data was recorded using an AET 5500 six channel signal processing system. A schematic of the system used is provided in Figure 3.9. Applied axial load was measured using an Artech 900 kN range load cell. The load was applied to the samples at a constant rate of 0.25 MPa/s so that failure occurred between 5 and 10 minutes as recommended by the ISRM (Brown, 1981). Automatic data logging was performed using a 16 channel Sciemetric Instruments LLSYS3 data acquisition system, sampling at an average rate of 2-3 readings per second. A typical setup is shown in Figure 3.10.

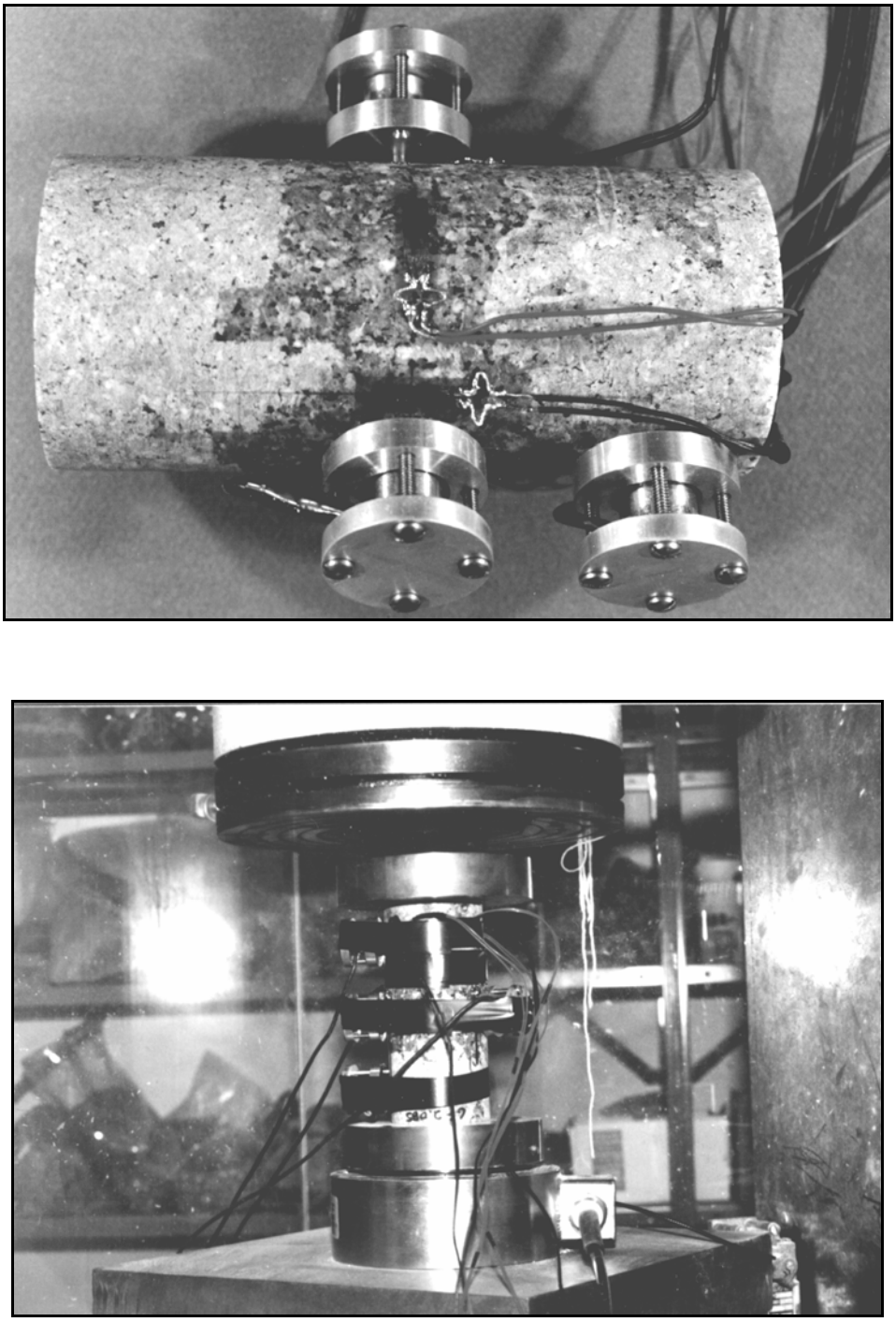

Figure 3.8 Typical sample instrumentation and setup used for uniaxial compression tests. Photos show a test sample with strain gauges and AE transducers (top) and the instrumented sample positioned in a load cell (bottom).

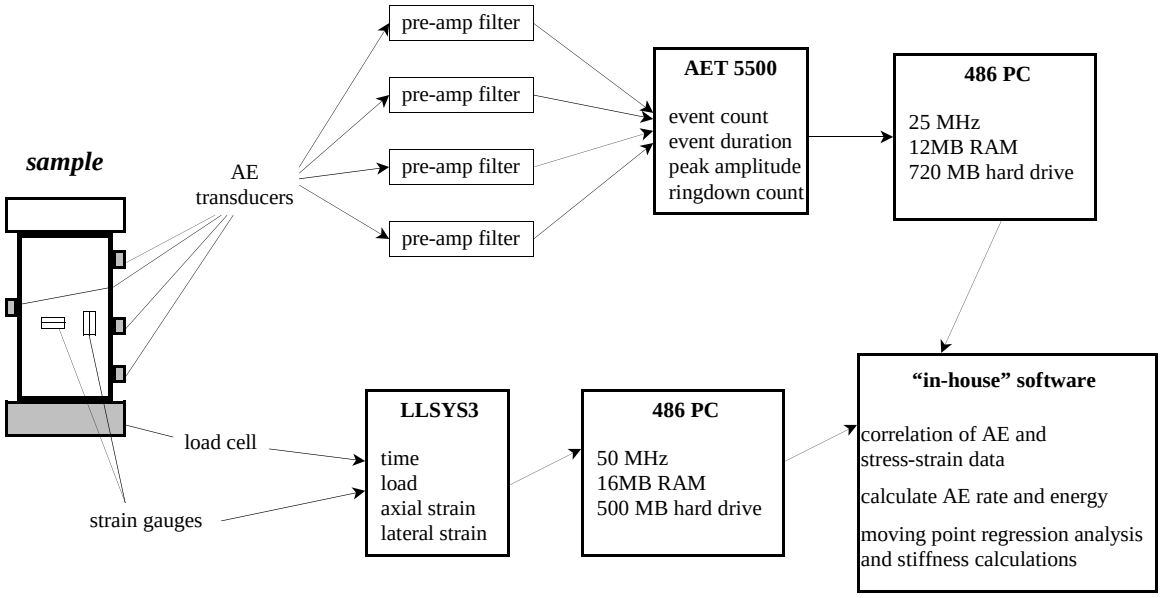

Figure 3.9 Schematic of strain gauge and acoustic emission instrumentation, and data collection systems.

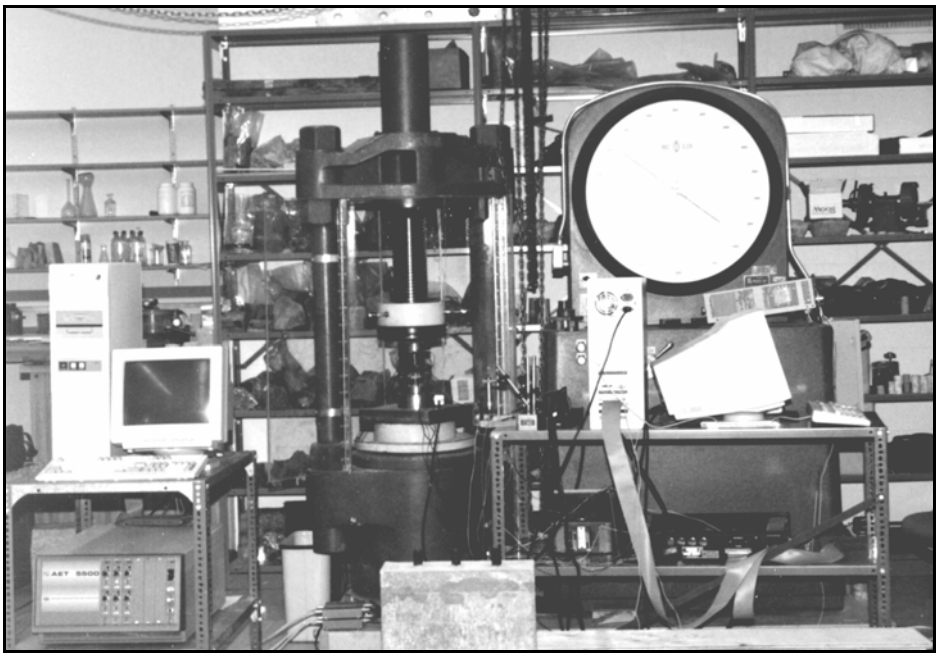

Figure 3.10 Uniaxial compression test setup showing load frame and data logging systems.

3.3.1 Acoustic Emission Detection Settings

The wide-band nature of AE sources require that the monitoring frequency used during acoustic emission testing be an operator defined function. Hardy (1981) reports the range over which AE and other associated studies have been conducted. For example, earthquakes usually fall within a frequency range of 0.01 to 1 Hz, whereas laboratory monitored acoustic emission fall within a range of 100 to 600,000 Hz. Typical range versus frequency tests show an inverse log-log relationship, in other words, as the AE signal monitoring frequency becomes higher, the range of detection becomes smaller (Hardy, 1981). Spanner *et al*. (1987) note that the most common frequency range for AE testing is 100 to 300 kHz. For laboratory sized samples, a higher frequency range may be required, thus a monitoring and filtering system with a frequency range of 125 kHz to 1 MHz was chosen for this study. Pollock (1977) found that frequencies lower than 100 kHz result in increasing problems with background noise and frequencies greater than 1 MHz are restricted by attenuation. Similar monitoring frequencies have been used in the testing of laboratory sized samples of granite and granodiorite (Sondergeld and Estey, 1981; Yanagidani *et al*., 1985; Dowding and Mueller, 1987; Mansurov, 1994). Mansurov (1994) notes that such a frequency range should be capable of detecting cracks with initial linear dimensions on the order of 0.1 - 10 mm.

The sensitivity of the AE test is also controlled by the gain and threshold of the system. Signal losses in the cables connecting the sensors to the detection and recording system may become excessive, requiring pre-amplification of the signal. The gain is a measure of the amplification provided by a system, whereas the threshold is a cut-off value used to filter out smaller signals. The majority of the systems reported in the literature use a gain within a range of 20 to 80 dB for the testing of granite, although 40 and 60 dB seem to be the more popular choices (as previously noted, decibels are logarithmic units). A compromise must be made when choosing this parameter since higher gains will result in the excessive recording of background noise and lower gains will filter out crack related events. During the initial stages of this study, tests were conducted using gains of 40 and 60 dB. As was expected, the results indicated a

significant increase in the number of recorded events for the higher gain of 60 dB (Figure 3.11). The disproportionate number and continuous nature of the recorded events implies that a significant amount of background noise was recorded, especially in the initial stages of loading during the coupling of the sample with the loading platens. This extreme number of recorded events obscures the existence of any significant increases in the AE event count which may be correlated to the initiation and propagation of cracks. This is especially true when examining the acoustic event properties (Figure 3.12). It was concluded that a gain of 60 dB was too sensitive and that a gain of 40 dB helped to filter out much of the background noise.

A second sensitivity analysis was conducted to determine an optimum sampling threshold value to be used for the given gain of 40 dB. The threshold value also acts to filter out background noise by establishing which of the detected events should be recorded and which should be rejected as insignificant. The threshold settings, however, work on a linear voltage scale and were found to be significantly less sensitive than adjustments to the gain (which works on a logarithmic scale). Four different threshold values of 0.25, 0.10, 0.05 and 0.02 volts were used. Figure 3.13 shows that by decreasing the threshold value, the number of recorded events increases but the overall shape of the plot remains the same. This suggests that the pattern of AE events associated with crack development is not sensitive to the threshold value but the measured event magnitudes are. Given that the detected events and their individual properties are measured relative to the threshold value (i.e. the threshold voltage is subtracted from the amplified signal voltage), it was found that values of 0.25 V reduced the measured events below a practical and meaningful limit. Effectively, signal voltages were reduced to the point where many of the events associated with the initial stages of crack development were filtered out. Conversely, threshold values of 0.02 V were found to include too many events associable with background noise and the coupling of the loading platens to the sample during the initial stage of loading. Threshold values of 0.05 to 0.1 V were found to be an appropriate compromise, detecting all significant events related to crack development. Subsequent tests were

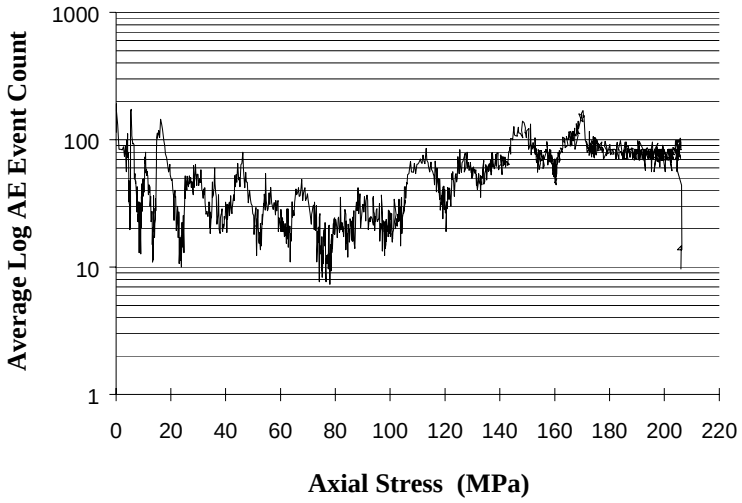

Sample 130-1-14
Gain = 60 dB
Threshold = 0.10 v

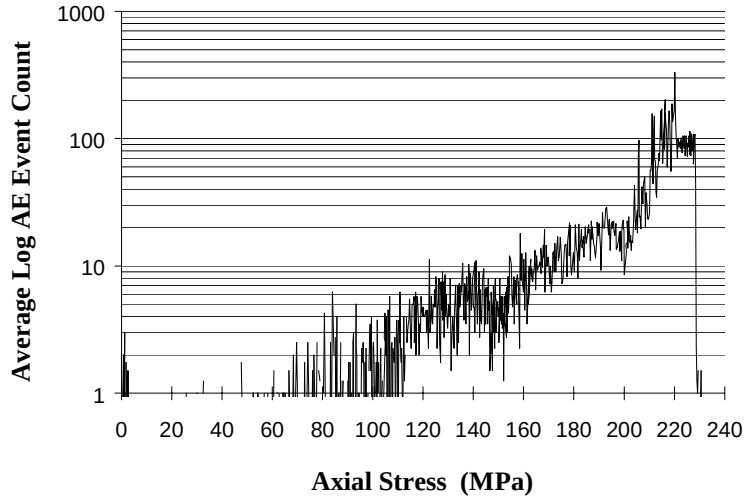

Sample 130-1-3
Gain = 40 dB
Threshold = 0.10 v

Figure 3.11 Logarithmic AE event counts for Lac du Bonnet granite samples using gains of 60 and 40 dB.

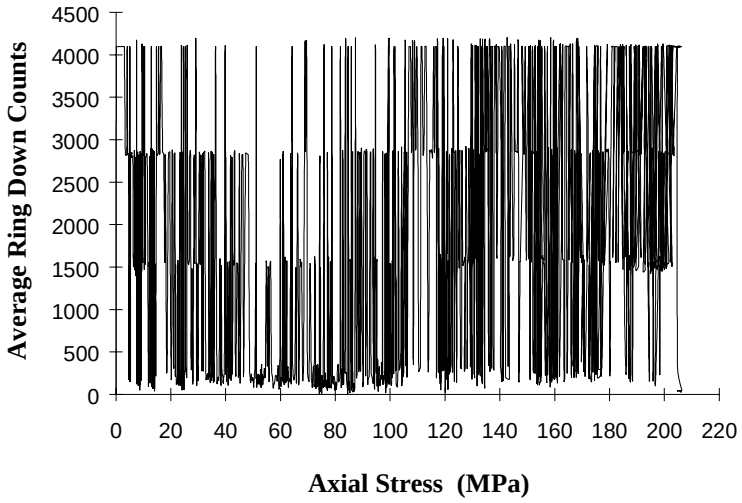

Sample 130-1-14
Gain = 60 dB
Threshold = 0.10 v

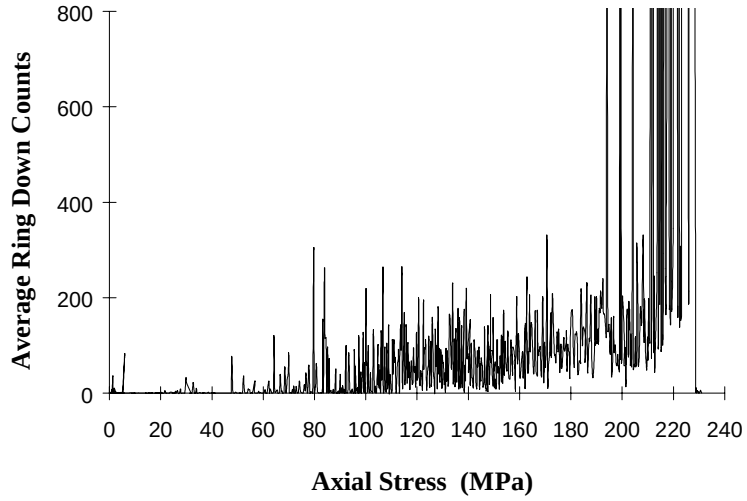

Sample 130-1-3
Gain = 40 dB
Threshold = 0.10 v

Figure 3.12 AE event ringdown counts for Lac du Bonnet granite samples using gains of 60 and 40 dB.

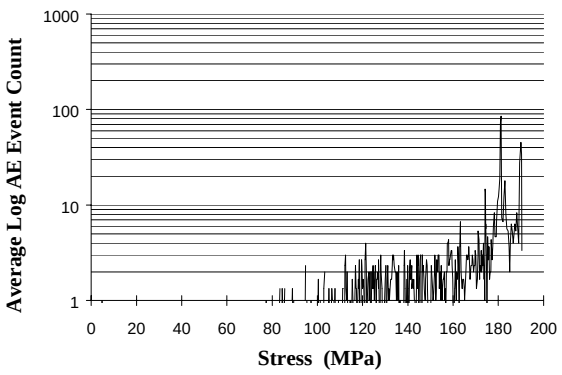

Sample 130-1-7
Gain = 40 dB
Threshold = 0.25 v

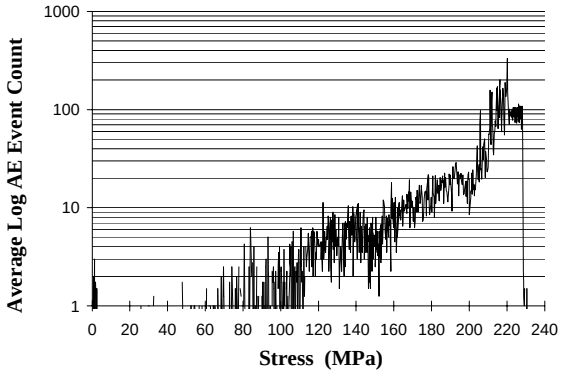

Sample 130-1-3
Gain = 40 dB
Threshold = 0.10 v

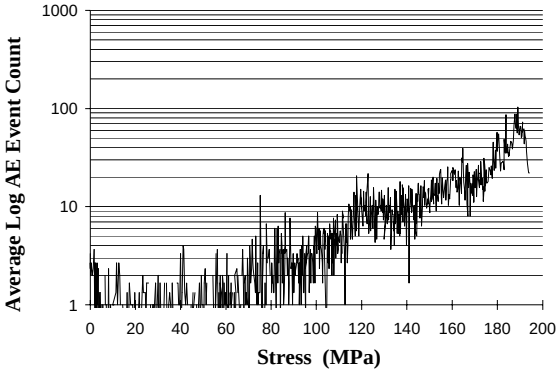

Sample 130-1-4
Gain = 40 dB
Threshold = 0.05 v

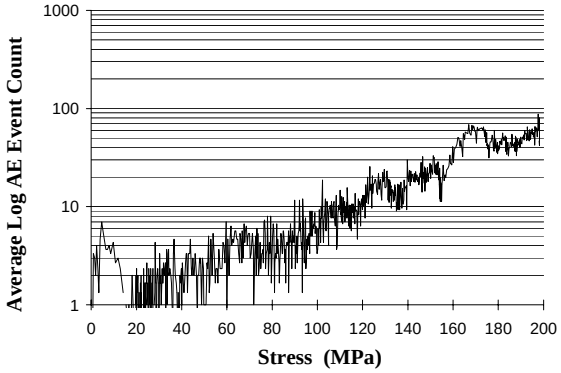

Sample 130-1-2
Gain = 40 dB
Threshold = 0.02 v

Figure 3.13 Logarithmic AE event counts for Lac du Bonnet granite samples using thresholds of 0.25, 0.10, 0.05 and 0.02 V.

conducted using both threshold settings, the results for which are presented and interpreted in Chapter 4.

3.3.2 Processing of Acoustic Emission Data

AE events are individual elastic stress waves or "signal bursts" produced by local changes in the material such as the formation and propagation of cracks in stressed rock. These stress waves excite the system's sensors where they are amplified and compared to the set threshold. AE data loggers record the occurrence of each event as an event time followed by the waveform properties of that event. These systems usually process the data with respect to time and not in terms of axial load since the load is measured with a separate logging system. In addition, the volume of AE data can be extremely difficult to handle.

To overcome these difficulties and limitations a program was specifically written to process the data and correlate the AE count with stress (as opposed to time). The program was written with several functions that would sort the AET 5500 data output and correlate the event counts and several waveform characteristics with stress and time. This enabled the AE data to be directly compared to stress-strain data and plotted with respect to the applied load.

3.4 The URL and Pink Lac du Bonnet Granite

To properly establish and calibrate the abilities of the fracture detection techniques discussed above, a near ideal material was required to allow for a straightforward interpretation of the measured response. The material chosen was pink Lac du Bonnet granite taken from the 130m level of AECL's Underground Research Laboratory (URL). This material was selected since it was retrieved from relatively shallow depths where the degree of stress-induced sampling damage would be minimal and because the mechanical properties of Lac du Bonnet granite have been well established through numerous test studies. The pink granite was therefore used as the reference material for which most of the principles and methodologies regarding the detection of crack initiation and propagation were established.

The URL is located within the Lac du Bonnet batholith in southeastern Manitoba (Figure 3.14). The geology of the site is representative of many granitic intrusions of the Precambrian Canadian Shield (Martin and Stimpson, 1994). Detailed descriptions of the site geology can be found in Brown *et al*. (1989) and Everitt *et al*. (1990). The granites are crystalline by nature and are generally coarse-grained and inequigranular. The pink granite is considered medium- to coarse-grained with an average grain size between 3 and 4 mm. Samples contain approximately 30% quartz, 30% potassium feldspar, 35% plagioclase feldspar and 5% biotite. The colouring of the pink granite is due to alteration by moving groundwater (Martin and Stimpson, 1994). Based on studies by Jackson and Lau (1990), 61mm diameter cores were chosen to minimize size effects. Jackson and Lau had found that samples with smaller diameters were more sensitive to factors influencing the observed mechanical behaviour of the rock.

3.5 Chapter Summary

Electric resistance strain gauges have been widely used to measure slight changes in sample deformation, which can be correlated with the closure and opening of microfractures. The use of strain gauges in past studies, however, has been somewhat constrained by poor data resolution and a high degree of error and subjectivity incorporated into the analysis procedure. The testing performed in this thesis incorporates the use of more powerful computers and faster data logging systems to provide higher resolution stress-strain measurements. In addition, a moving point regression technique has been introduced to aid in the interpretation of the test data.

Acoustic emission techniques have been used with some success in identifying microfracturing in brittle materials. Most of this success has involved the characterization of latter stages of crack development due to the high proportion of events that accompany failure. Several parameters relating to the characteristics of an AE event can also be used to identify different mechanisms relating to crack development, especially in the early stages. These parameters include the ring down

count, event duration, peak amplitude and rise time. In addition, approximations of the AE event energy can be used to accentuate large events.

Care was taken in the setup of laboratory test equipment to remove any external factors that may have a significant effect on the test results. Sample ends were highly polished to increase surface flatness and perpendicularity, AE transducers were mounted using wave guides to ensure a solid acoustic coupling, and AE settings for monitoring gain and threshold were tested for sensitivity and optimum levels. In addition, "in-house" software was specifically developed to process and correlate large volumes of AE data with the measured stress-strain response.

To rigorously establish and calibrate the fracture detection techniques and methodologies developed, a near isotropic, homogeneous, linear elastic brittle material was chosen - Lac du Bonnet pink granite from the 130m level of the URL. The granite is crystalline by nature with an average grain size between 3 and 4 mm and contains approximately 30% quartz, 30% potassium feldspar, 35% plagioclase feldspar and 5% biotite. Samples were obtained from a relatively low *in situ* stress regime and were considered to embody a low degree of sampling disturbance.

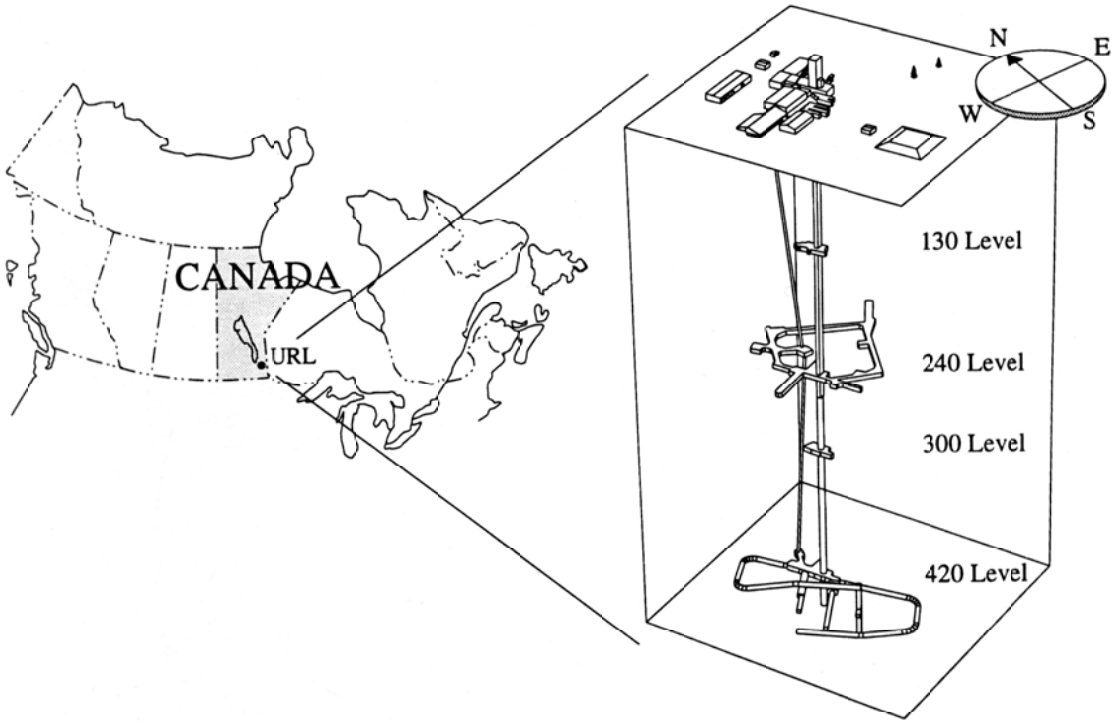

Figure 3.14 Location and layout of AECL's Underground Research Laboratory (after Read, 1994).

CHAPTER 4

IDENTIFICATION OF BRITTLE FRACTURE THRESHOLDS FOR LAC DU BONNET GRANITE

The mechanical properties of Lac du Bonnet granite have been determined and reported through numerous testing programs initiated by AECL as part of their nuclear waste disposal studies at the URL. The majority of this testing was performed between 1980-1993 by the Canadian Centre for Mineral and Energy Technology (CANMET) and the University of Manitoba (Martin, 1993). These tests concentrated on deriving the standard laboratory properties of Lac du Bonnet granite. Further testing of the Lac du Bonnet granite (more specifically, pink granite from the 130 m level of the URL) was undertaken through this thesis study to seek new techniques and refine existing methods for monitoring the development of stress induced microcracking in laboratory samples during uniaxial loading. Analysis of laboratory data obtained during this stage of the research concentrated on establishing stress thresholds for the different stages of crack development (as reviewed in Chapter 2). The following sections highlight some of the key observations and findings.

4.1 Crack Closure

The crack closure stress threshold (σ_{cc} in Figure 2.11) indicates the load at which a significant percentage of existing cracks have closed and near linear elastic behaviour begins. This point is approximated by determining the point on the stress-strain curve where the initial axial strain appears to change from non-linear to linear behaviour. Crack closure stresses were picked for each test using the moving point regression analysis (Figure 4.1). As was expected, a rapid increase in axial stiffness was observed before values leveled off and behaved more linearly. This pattern and the corresponding

values were consistent for each test (results for individual tests are provided in Appendix I).

Examination of the lateral stiffness curve over this region reveals relatively high stiffness values when the load is first applied to the sample (the lateral stiffness term represents the change in the lateral strain rate with uniaxial loading). Artificially high values of this term during the initial stages of loading represent a point in the load history where there is not a continuous transmission of stresses due to the presence of open microcracks, therefore the lateral and axial strain responses are not fully coupled. These initially high values are followed by a large drop (approximately 35%) during the first 25 MPa of loading (Figure 4.2). The initial stages of crack closure appear to predominantly involve the simple movement of preferentially aligned crack walls towards one another, parallel to the direction of applied load (Figure 4.3). This would have a significant effect on the axial strain but little effect on the lateral strain since the displacement is in the axial direction. With increasing load, values of lateral stiffness begin to rapidly decrease possibly signifying shear or sliding movement between the faces of closing or closed cracks (Figure 4.3). This behaviour has been observed in glass plates by Bieniawski (1967b) who noted that the sliding deformation demonstrated by single closed cracks continues even during linear elastic behaviour.

Crack orientation plays a key role in the observed closure behaviour necessitating close control over the direction along which core samples are taken with respect to the principal stress field. Stress relief cracking in cores drilled perpendicular to the major principal stress (σ_1) will predominantly occur perpendicular to the core axis resulting in crack orientations that are favorably aligned to display a large degree of crack closure when tested. The opposite is true for cores drilled parallel to σ_1 (Figure 4.4). In cases where sampling occurs within the disturbed zone of a nearby excavation, for example a circular tunnel, the major principal stress will be tangential to the opening. Stress induced cracking in such a case will likely be perpendicular to the core axis. Furthermore, Guessous *et al*. (1984) have shown through numerical models that the coring operation can result in the superposition of radial compressive stresses over the *in situ* stress state acting on the core. Sampling direction, therefore, becomes a major

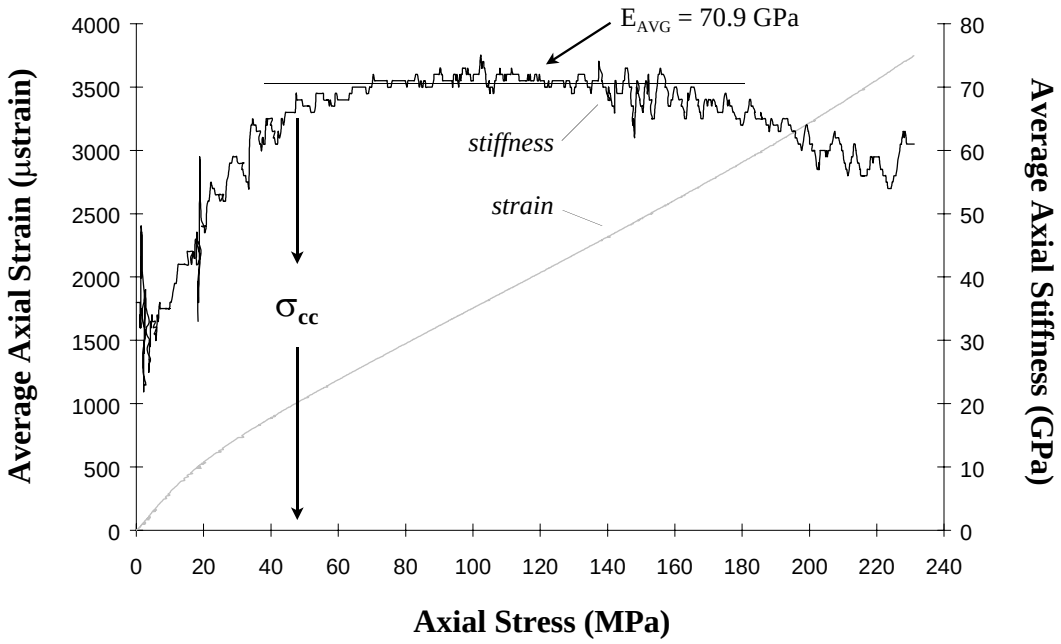

Figure 4.1 Plots of axial strain and axial stiffness -*vs*- axial stress for a 130 m level URL pink granite showing the crack closure threshold (σ_{cc}). Axial strain and stiffness are taken as an average of the three axial strain gauges used.

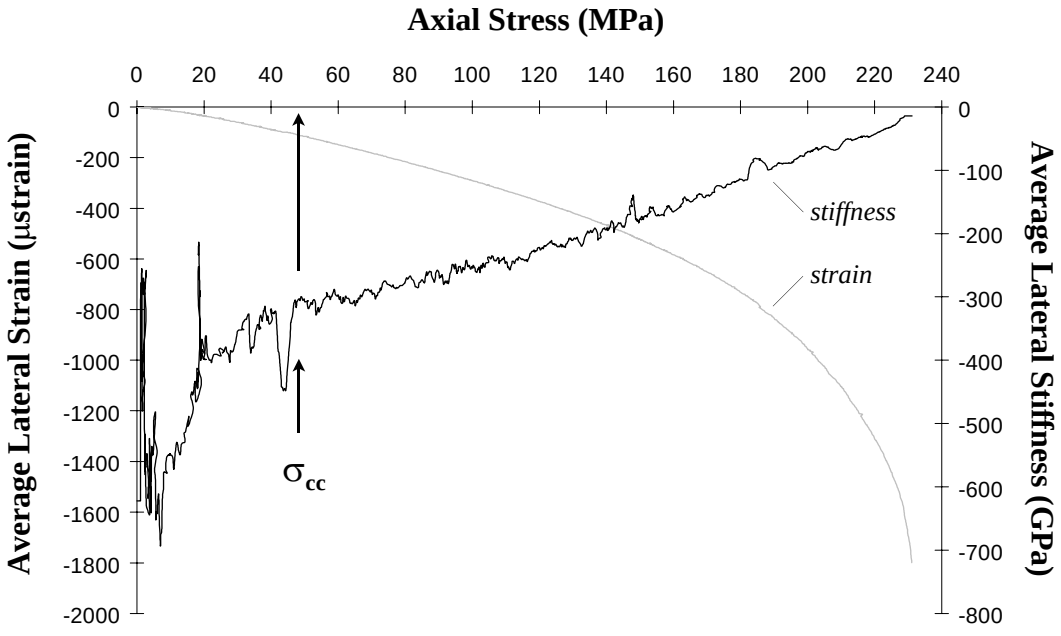

Figure 4.2 Plots of lateral strain and lateral stiffness -*vs*- axial stress for a 130 m level URL pink granite. Lateral strain and stiffness are taken as an average of the three lateral strain gauges used.

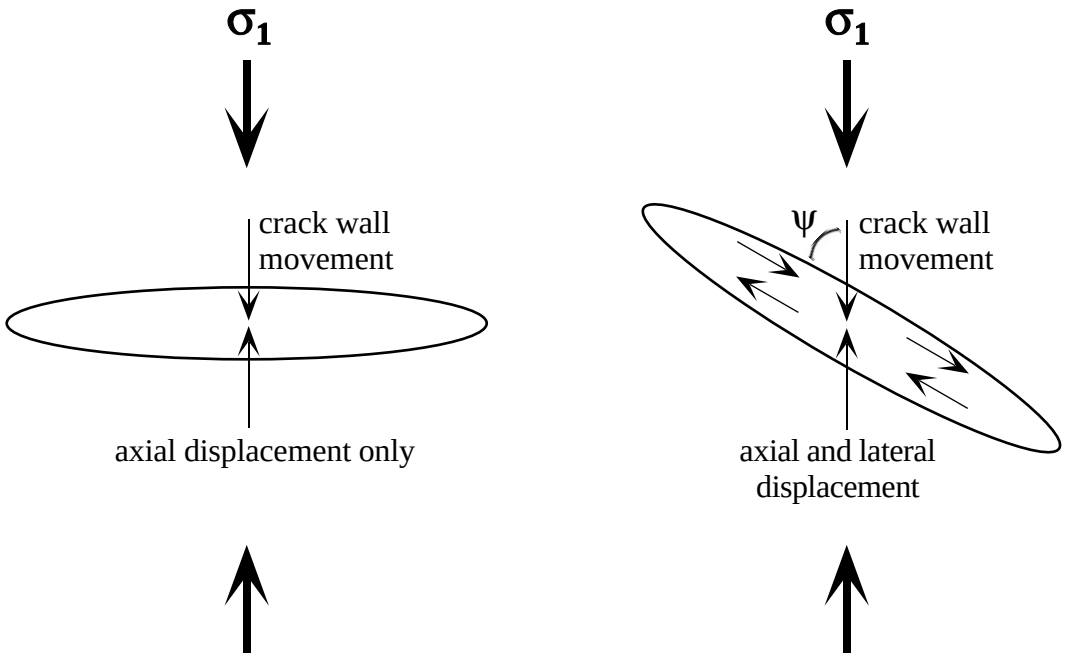

Figure 4.3 Directions of crack face movement during closure for different crack orientations.

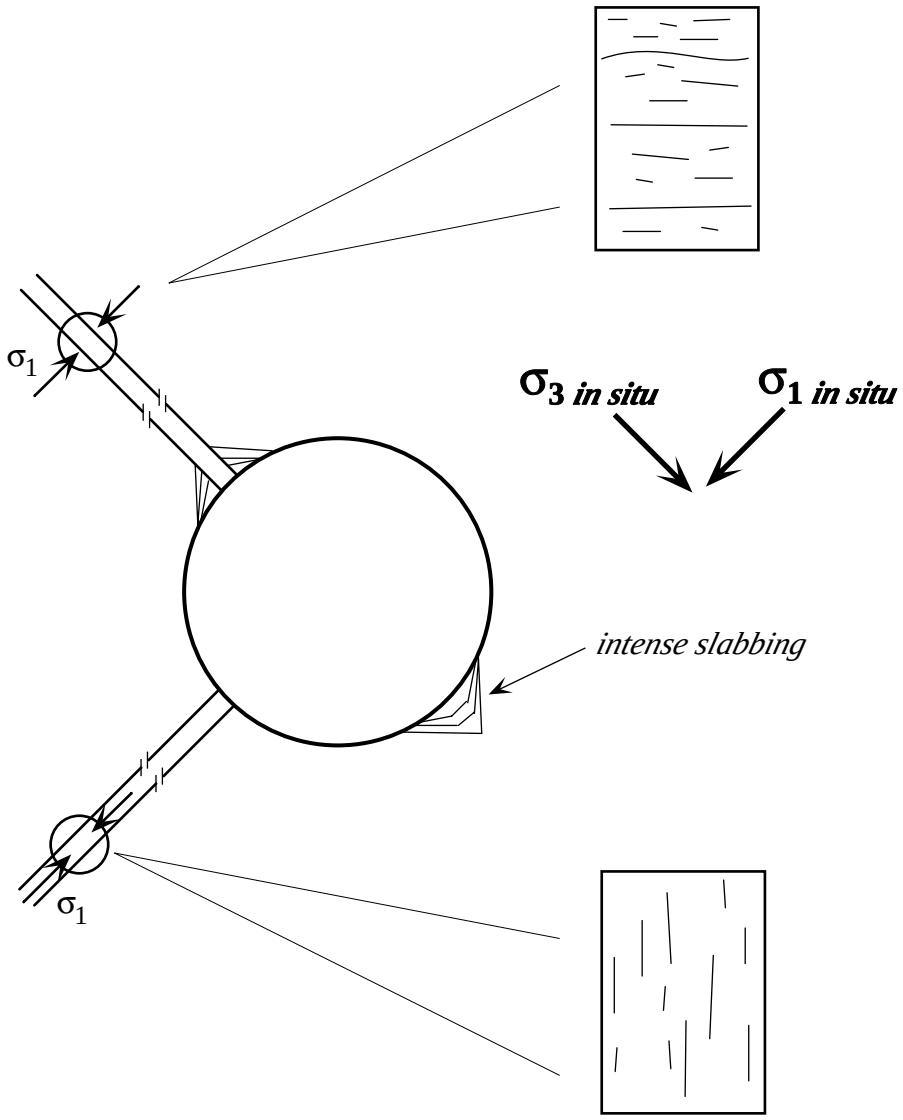

Figure 4.4 Stress relief cracking in cores drilled at different orientations with respect to the *in situ* principal stresses.

concern when testing samples from high stress regions since the observed crack behaviour can be markedly different between samples of the same lithology taken from the same depth but at different orientations.

4.2 Linear Elastic Behaviour

Figure 4.1 shows that after crack closure is reached, a period of relatively linear axial strain occurs. The average Young's modulus was taken as a least squares fit along this region. In terms of lateral stiffness, linear behaviour is never truly reached. Instead, the lateral stiffness continuously decreases from values of approximately 300 GPa to values less than 20 GPa prior to failure (Figure 4.2). This would seem to indicate that a number of processes may be contributing towards the gradual but continual loss of lateral stiffness in the specimens tested. These may include sliding (i.e. shear) between faces of closing cracks, tensile opening of cracks during crack initiation and possibly further shear movement related to crack coalescence/columnar buckling during the latter stages of rock deformation. Following ASTM standards (Designation D3148-93), Poisson's ratio was calculated using a least squares fit over the same interval as that used in calculating the average Young's modulus (i.e. linear region of the axial stress-strain curve). It will be later shown that this may not be the most appropriate interval over which to calculate Poisson's ratio.

Static elastic properties were determined from the stress-strain data and include the Young's, tangent and secant modulus as well as Poisson's ratio (Table 4.1). As described above, the Young's modulus and Poisson's ratio were taken from the approximately linear portion of the axial stress-strain curve. The tangent and secant moduli were calculated using the point of volumetric strain reversal, or crack damage threshold (σ_{cd}), as a reference limit as opposed to the peak load since, in most cases, the samples were not loaded to failure. The tangent modulus was determined at 50% of σ_{cd} and the secant modulus was taken from 0 to σ_{cd} (Figure 4.5).

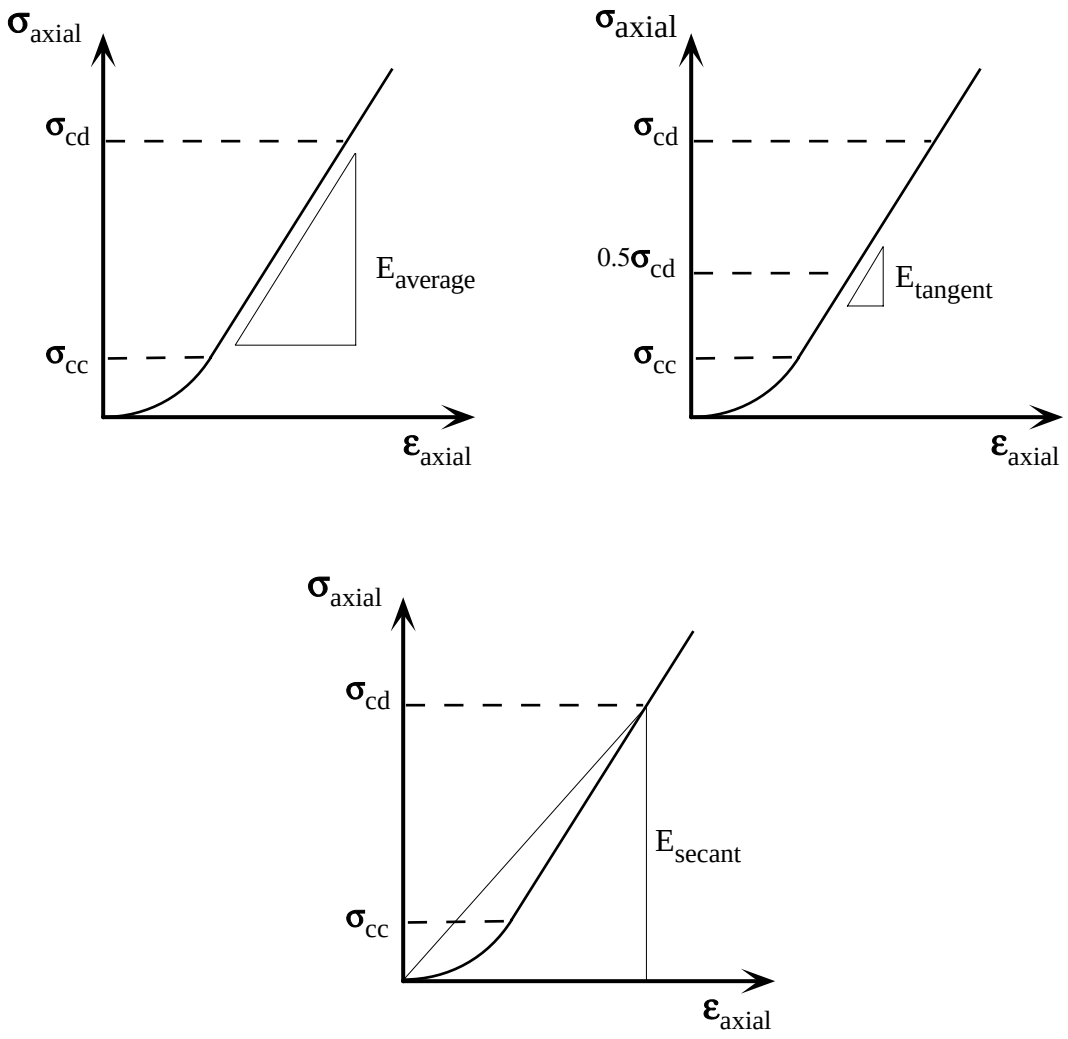

Figure 4.5 Method for calculating the Young's (i.e. average), tangent and secant modulus from axial stress -*vs*- axial strain curves.

Table 4.1 Average static elastic moduli for the 130m level URL pink granite (standard deviation is provided in parentheses).

Material Parameter	Value
Number of Tests	20
Young's Modulus, E_{AVG} (GPa)	66.5 (± 3.0)
Tangent Modulus, E_T (GPa)	66.2 (± 3.1)
Secant Modulus, E_S (GPa)	61.0 (± 3.4)
Poisson's Ratio, ν_{AVG}	0.31 (± 0.04)

4.3 Crack Initiation

The crack initiation stress threshold, as determined through laboratory testing, has been defined as the point where the lateral strain curve departs from linearity (Brace *et al*., 1966; Bieniawski, 1967a; Lajtai and Lajtai, 1974). Examination of the lateral strain curve (Figure 4.2) reveals that the identification of this point can be very subjective. This is clear from the analysis of the lateral stiffness curve which indicates that at no time is the lateral stress-strain curve truly linear. Noting the difficulty in using lateral strain gauge data, especially in highly damaged samples, Martin (1993) suggested using the calculated crack volumetric strain to identify crack initiation. For a cylindrical sample loaded uniaxially, crack volume is determined by subtracting the linear elastic component of the volumetric strain, given by:

$$\varepsilon_{V\,elastic} = \frac{1-2\nu}{E}\sigma_{axial} \tag{4.1}$$

where E and ν are the elastic constants, from the volumetric strain calculated from the measured axial and lateral strain, given by:

$$\varepsilon_V = \varepsilon_{axial} + 2 \cdot \varepsilon_{lateral} \tag{4.2}$$

The remaining volumetric strain is attributed to axial cracking, i.e.:

$$\varepsilon_{V\,crack} = \varepsilon_V - \varepsilon_{V\,elastic} \tag{4.3}$$

Martin (1993) defines crack initiation as the stress level at which dilation (i.e. crack volume increase) begins in the crack volume plot (Figure 4.6).

This method is limited, however, due to its dependence on the use of the elastic constants E and ν. Although the Young's modulus, E, can be determined with a reasonably high degree of confidence and consistency, the non-linearity of the lateral strain response complicates the measurement of Poisson's ratio. The resulting value is the ratio of lateral to axial strain magnitudes based on the linear elastic axial strain behaviour and the "best approximation" of a straight line through a non-linear region of lateral strain over the same stress interval. Table 4.2 lists the respective Poisson's ratio values calculated over the same stress interval as the average Young's modulus (as per ASTM standards) and over the stress interval between crack closure and crack initiation as determined using the moving point regression analysis. This variability introduces a large degree of uncertainty into the crack volume calculation used to determine crack initiation. Figure 4.7 demonstrates the sensitivity of crack initiation values to changes in the Poisson's ratio using crack volume strain reversal as the indicator (for example, a change of ±0.05 in the Poisson's ratio, results in a ±40% change in the σ_{ci} value). The crack volume stiffness plot in Figure 4.7 is calculated as the change in slope of the crack volume strain curve, the reversal of which is noted by the change from a positive to a negative slope.

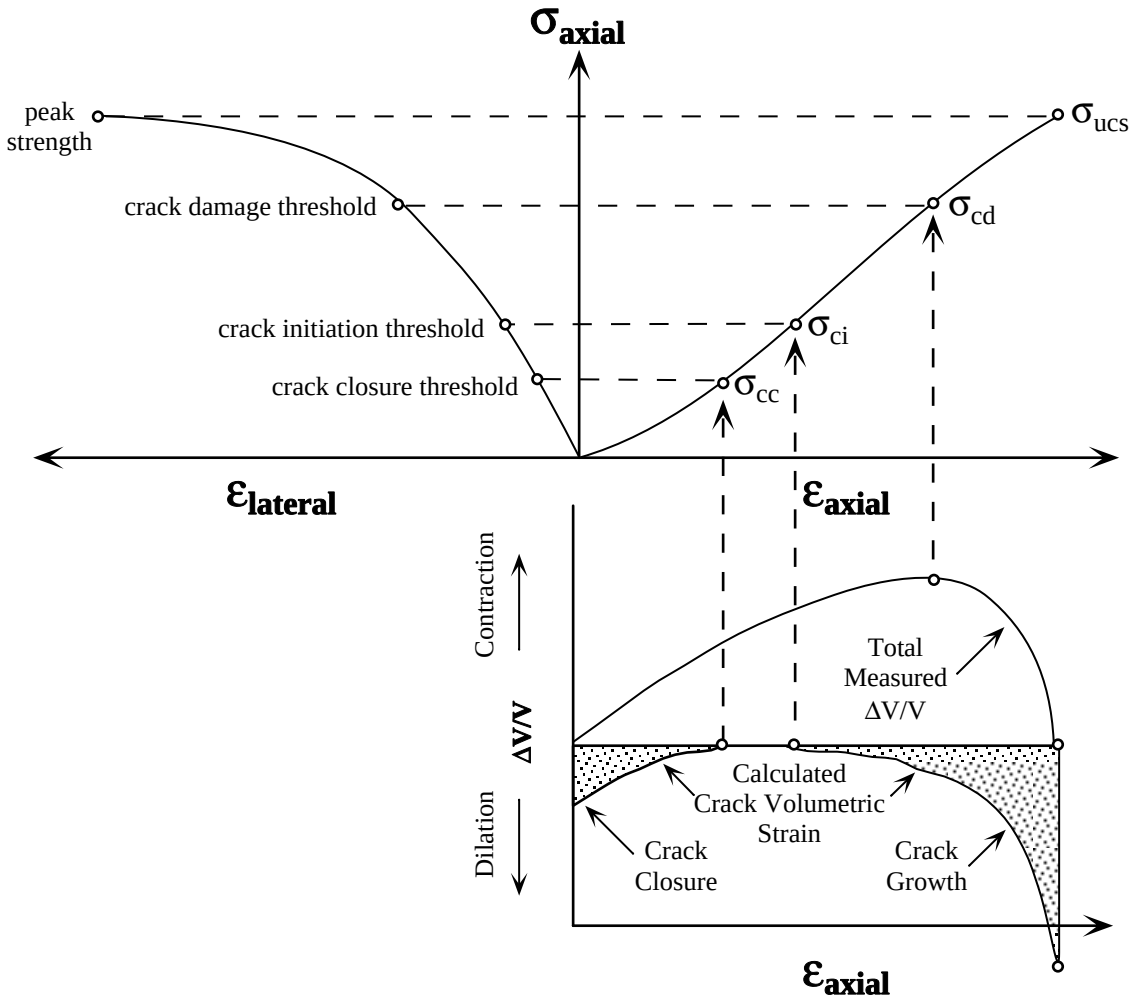

Figure 4.6 Determination of crack initiation using crack volume (after Martin, 1993).

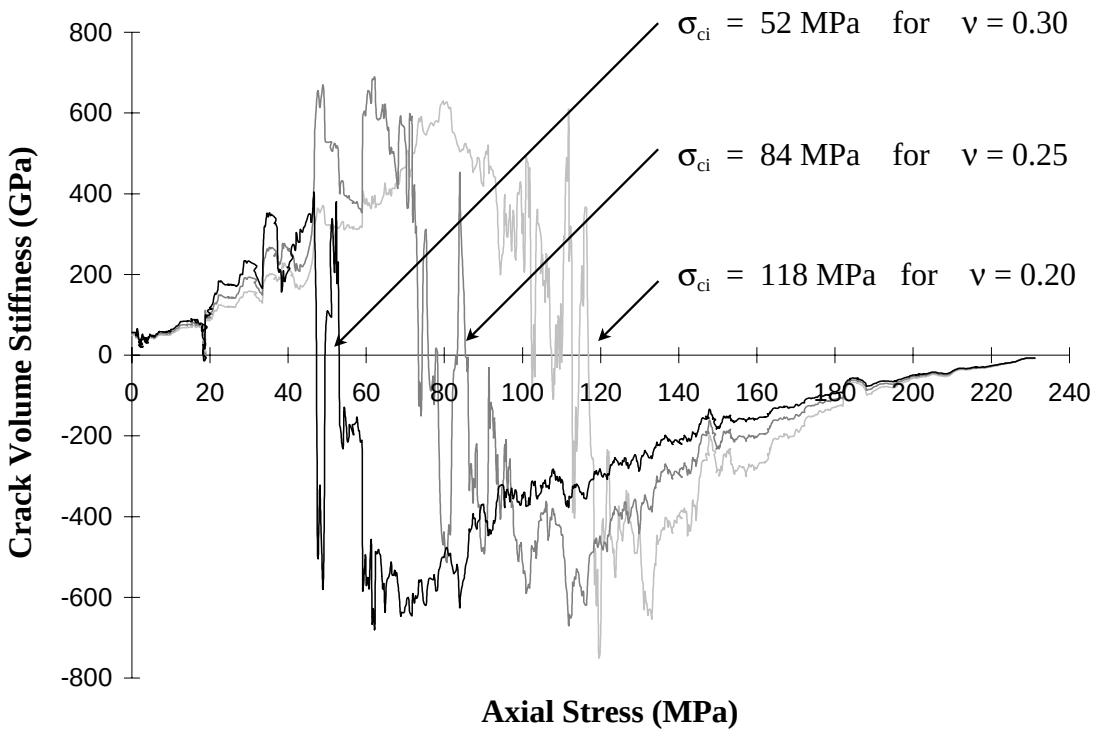

Figure 4.7 Variability of crack volume stiffness with Poisson's ratio for a 130m level URL pink granite. Crack volume stiffness is calculated as the change in slope of the crack volume strain curve, the reversal of which is noted by the change from a positive to a negative slope.

Table 4.2 Average Poisson's ratio as calculated per ASTM standards and over the stress interval between crack closure and crack initiation for the 130m level URL pink granite (standard deviation is provided in parentheses).

Material Parameter	Value
Number of Tests	20
Poisson's Ratio, ν (as per ASTM)	0.31 (± 0.04)
Poisson's Ratio, ν (between σ_{cc} and σ_{ci})	0.25 (± 0.04)

4.3.1 Stress-Strain and Acoustic Emission Response to Crack Initiation

Using an approach that involved the combined use of the moving point regression analysis and acoustic emission response, it was found that the crack initiation stress threshold could be more accurately determined. From the strain gauge data it was found that, although the lateral strain is non-linear, rate changes do occur and can be correlated to the growth of cracks in the sample. These rate changes are most evident when analyzing the volumetric strain and stiffness curves (Figure 4.8). The volumetric stiffness curve is based on the stress-dependent rate of change in the volumetric strain. Volumetric strain is defined in Equation 4.2. The volumetric stiffness is calculated as the slope of the volumetric strain -*vs*- axial stress curve. The rate at which the volumetric strain curve changes is dependent on the rate of change in the measured axial and lateral strain.

Examination of the volumetric stiffness curve indicated a series of characteristic patterns (Figure 4.9) that recur in each of the uniaxial tests performed (Appendix I). During the initial stages of loading, the axial strain controls the shape of the volumetric strain curve. The non-linear behaviour of the axial strain during crack closure distinguishes itself as an irregular region along the volumetric stiffness curve (Figure 4.9). This irregular region is followed by a linear region marked by a small break in slope signifying a rate change. This break in slope represents the transition from crack

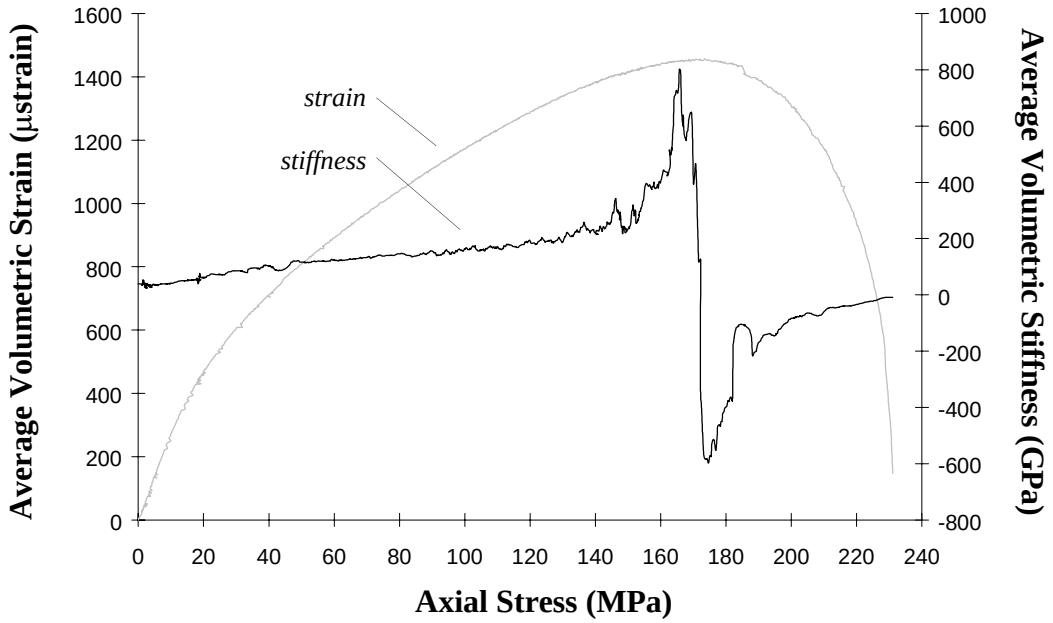

Figure 4.8 Plots of volumetric strain and volumetric stiffness -*vs*- axial stress for a 130m level URL pink granite. Volumetric strain and stiffness are calculated from the average axial and lateral strain gauge response.

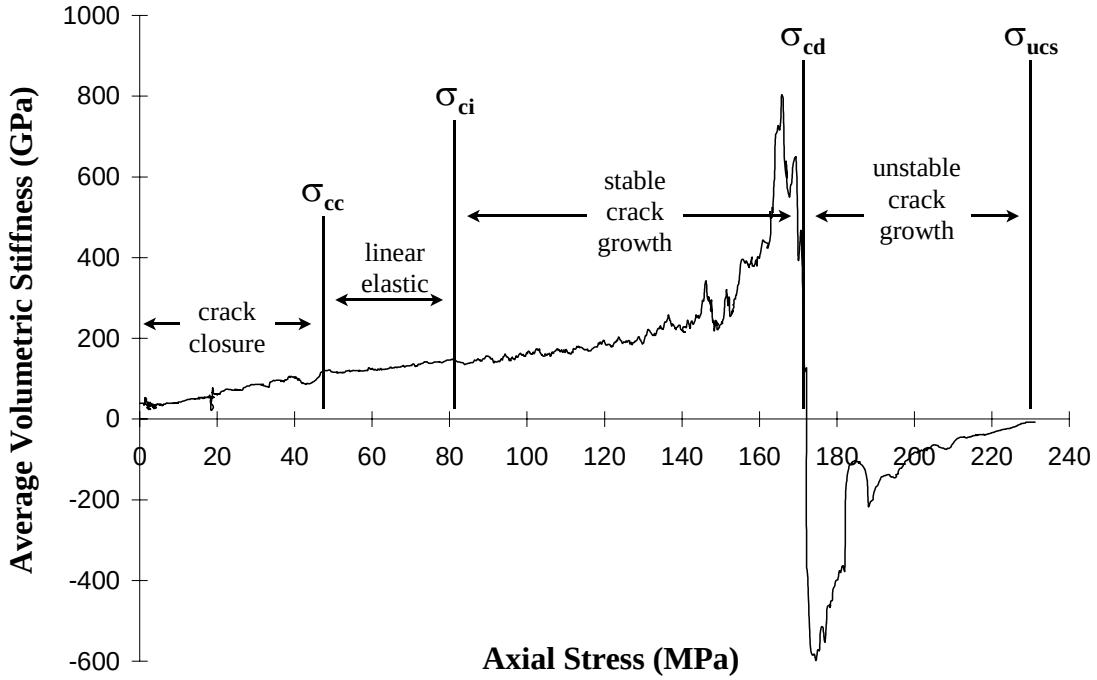

Figure 4.9 Breakdown and correlation of volumetric stiffness with brittle fracture showing the crack closure (σ_{cc}), crack initiation (σ_{ci}), crack damage (σ_{cd}) and peak strength (σ_{UCS}) thresholds for a 130m level URL pink granite.

closure to near linear elastic behaviour. This linear region also marks the stress interval in which the lateral strain achieves its most linear behaviour (i.e. the Poisson's ratio should be calculated in this region as shown in Table 4.2). The volumetric stiffness curve then makes a transition to a less regular region with another small break in the slope at approximately 80 MPa. Throughout this region the stress dependent axial strain rate maintains a near constant level, therefore any change in the volumetric stiffness curve can be attributed to a change in the lateral strain rate. Changes in the stress dependent lateral strain rate result in slight slope changes in the volumetric strain curve. However, because the axial strain rate still dominates in controlling the shape of the volumetric strain curve, no noticeable slope change occurs in the volumetric stiffness curve. Although these changes in lateral strain do not contribute to the overall volumetric strain enough to cause a major change in the slope of the volumetric stiffness curve, they do contribute enough to cause irregularities in it. These changes in the lateral strain rate, and consequently the volumetric stiffness curve, signify crack initiation at approximately 80 MPa or $0.35\sigma_{peak}$.

Correlation between the behaviour of the volumetric stiffness curve and crack initiation can also be validated through acoustic emission analysis. A typical acoustic emission response for the 130 m level URL pink granite is presented in Figure 4.10. The average response from the four AE transducers shows that the majority of activity occurs towards the end of the test. Although AE activity occurs continuously throughout the test, the log plot in Figure 4.11 shows that the beginning of significant AE activity begins at approximately 80 MPa. This coincides with the crack initiation stress threshold of 80 MPa as determined using the volumetric stiffness curve in Figure 4.9. AE activity prior to this point can be attributed to movement along crack faces during crack closure, as recognized in the lateral stiffness curves and previously discussed. It is also likely that small cracks may form at lower stresses in areas already weakened prior to or during the sampling process.

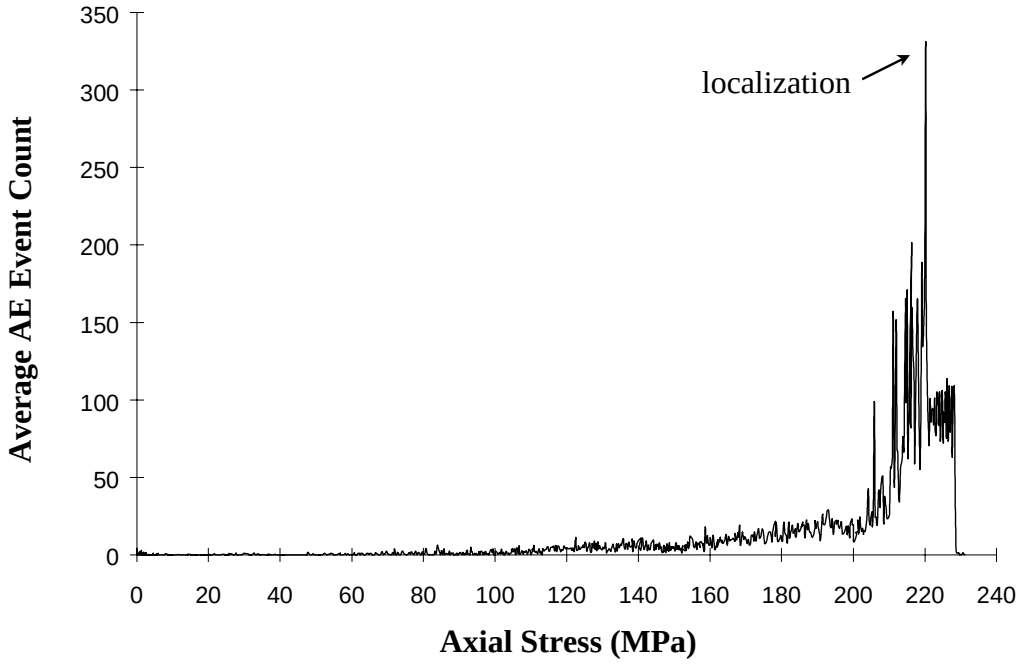

Figure 4.10 Typical acoustic emission response of a 130m level URL pink granite showing AE event count -*vs*- axial stress. Results are plotted as an average of the response recorded from four AE transducers.

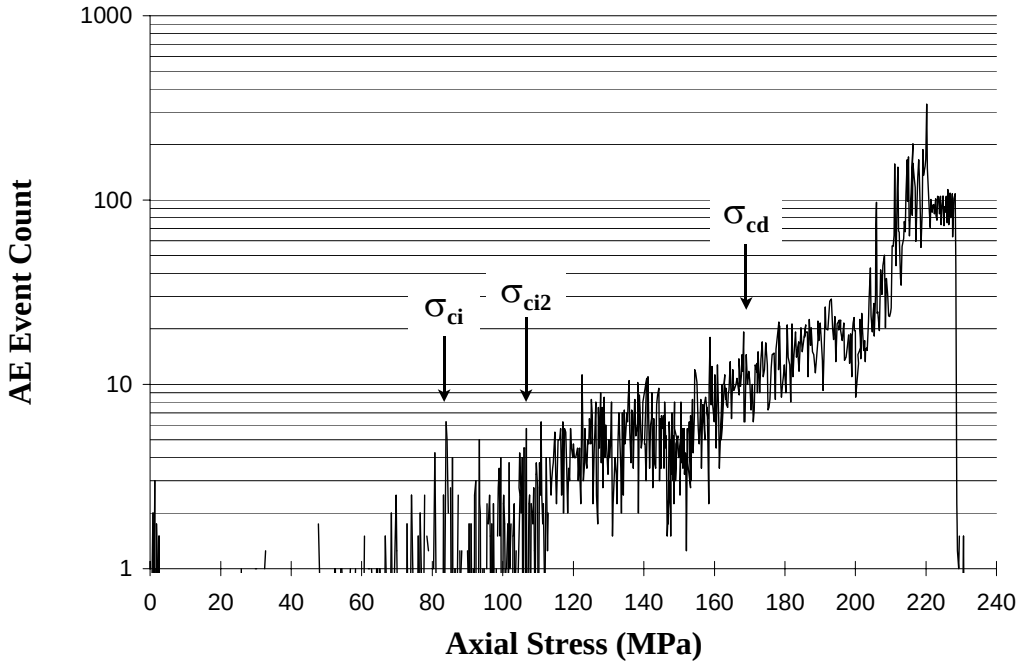

Figure 4.11 Log plot of AE event count -*vs*- axial stress showing the crack initiation (σ_{ci}), secondary cracking (σ_{ci2}) and crack damage (σ_{cd}) thresholds for a 130m level URL pink granite loaded to failure. Results are plotted as an average of the response recorded from four AE transducers.

In addition to the acoustic emission response, the properties of the acoustic events themselves are markedly different before and after crack initiation. This proves valuable in substantiating observations made using strain gauge data. Figures 4.12 and 4.13 contain plots of the ringdown count and event duration with loading, respectively. From these plots it can be seen that a marked increase in their respective magnitudes occurs at approximately 80 MPa coinciding with crack initiation. As a qualitative measure, larger ringdown counts and event durations both signify larger acoustic events. Although acoustic activity occurs prior to this point, the sizes of the events are relatively small (in terms of event duration, these events are 70% shorter than those occurring above 80 MPa). This may indicate that the acoustic events generated through closure are much smaller than those generated through stress-induced tensile cracking.

Comparable results are obtained in plots of the event peak amplitudes (Figure 4.14) and rise times (Figure 4.15). These plots show that significant increases in their respective values occur at the crack initiation threshold of 80 MPa. These increases can be more clearly seen in calculations of the acoustic event “energy” based on peak amplitude and event duration values (herein referred to as the elastic impulse “energy” so as not to confuse it with the true energy). Plots of the elastic impulse “energy” and its stress dependent rate of change (Figure 4.16) show that the size of the events in terms of “energy” dramatically increases shortly after crack initiation begins. Beattie (1983) remarked that increases in event amplitude may provide significant warning of increasing crack growth rate. Accordingly, these results demonstrate the effectiveness of using peak amplitude values to provide an additional means to corroborate stress-strain data in tracking crack initiation and propagation.

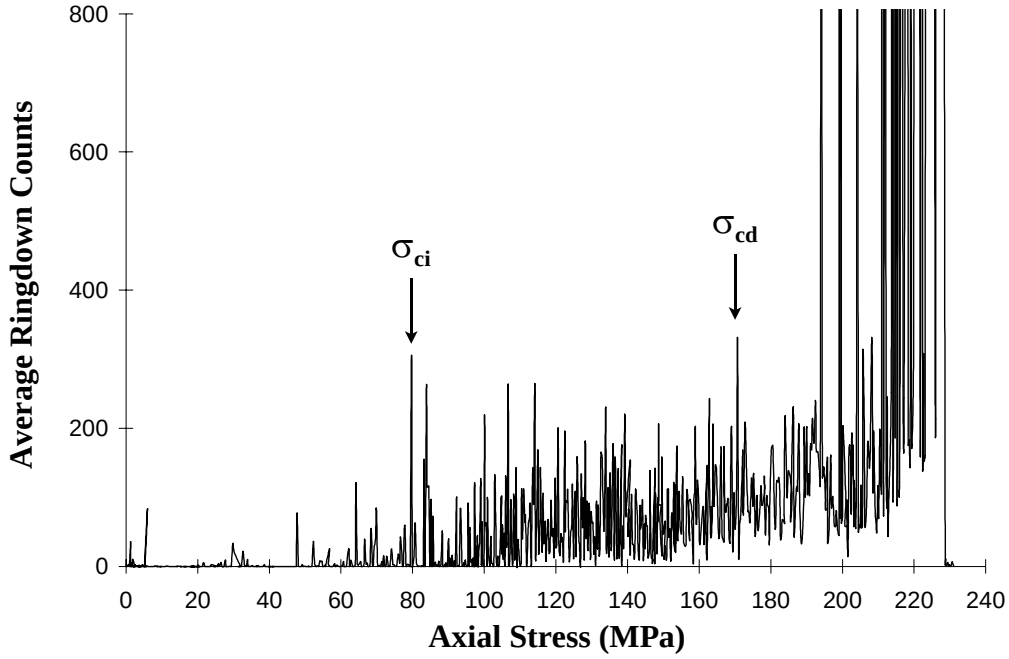

Figure 4.12 Plot of ringdown count -*vs*- axial stress for a 130m level URL pink granite. Ringdown count is taken as the average of the maximum values recorded by the four AE transducers for those events that occur during the same loading increment.

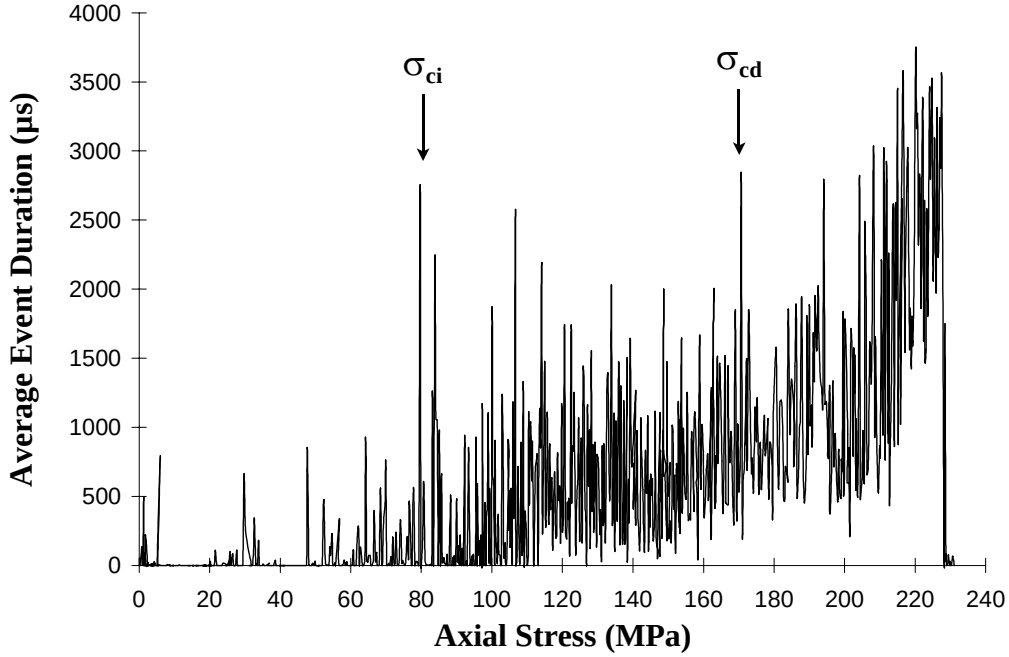

Figure 4.13 Plot of event duration -*vs*- axial stress for a 130m level URL pink granite. Event duration is taken as the average of the maximum values recorded by the four AE transducers for those events that occur during the same loading increment.

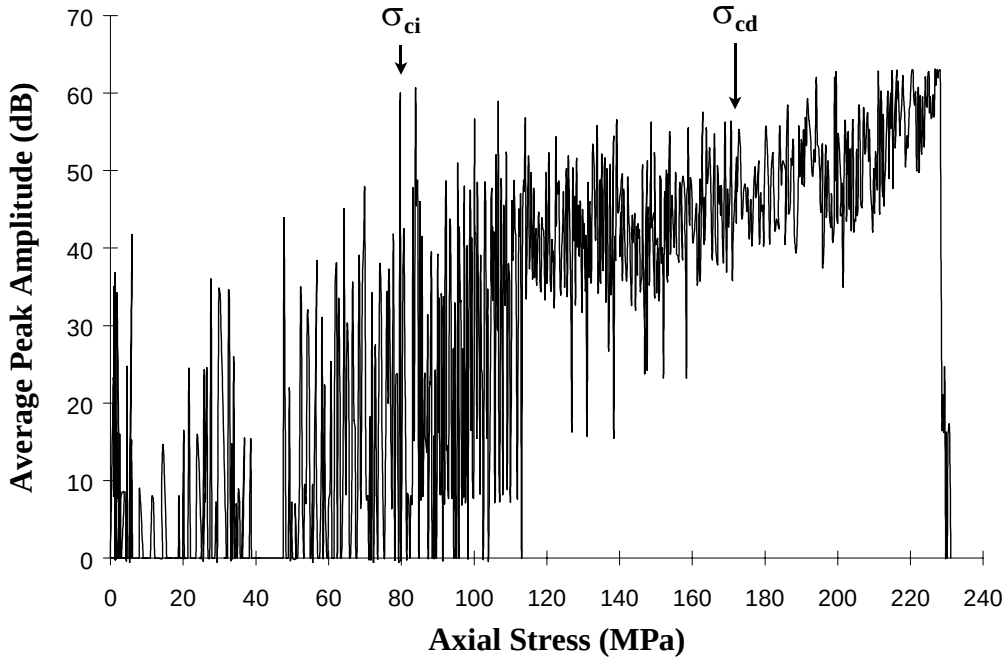

Figure 4.14 Plot of peak amplitude -*vs*- axial stress for a 130m level URL pink granite. Peak amplitude is taken as the average of the maximum values recorded by the four AE transducers for those events that occur during the same loading increment.

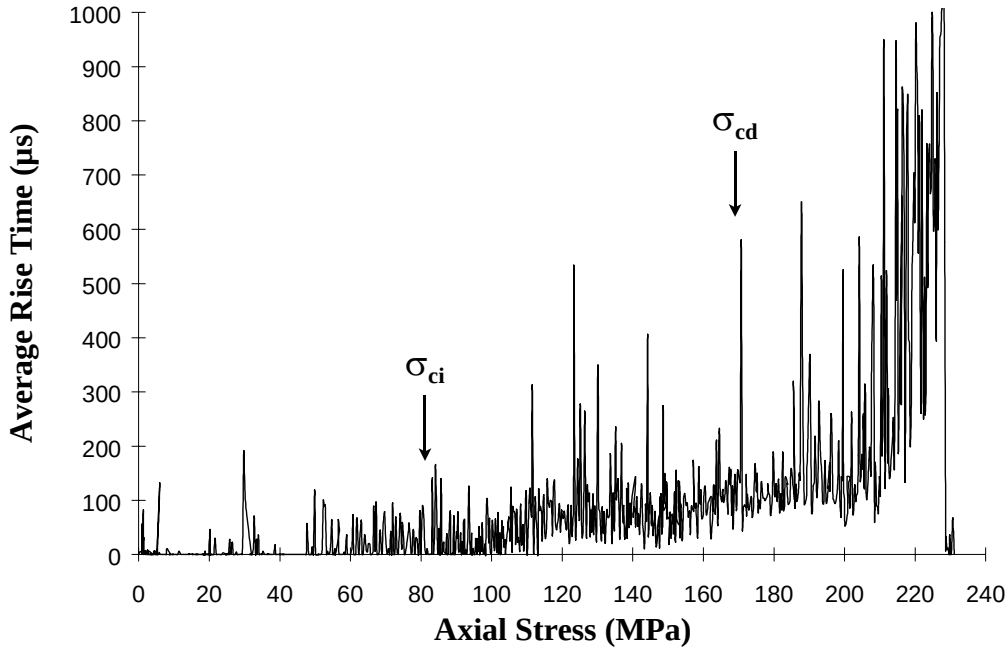

Figure 4.15 Plot of rise time -*vs*- axial stress for a 130m level URL pink granite. Rise time is taken as the average of the maximum values recorded by the four AE transducers for those events that occur during the same loading increment.

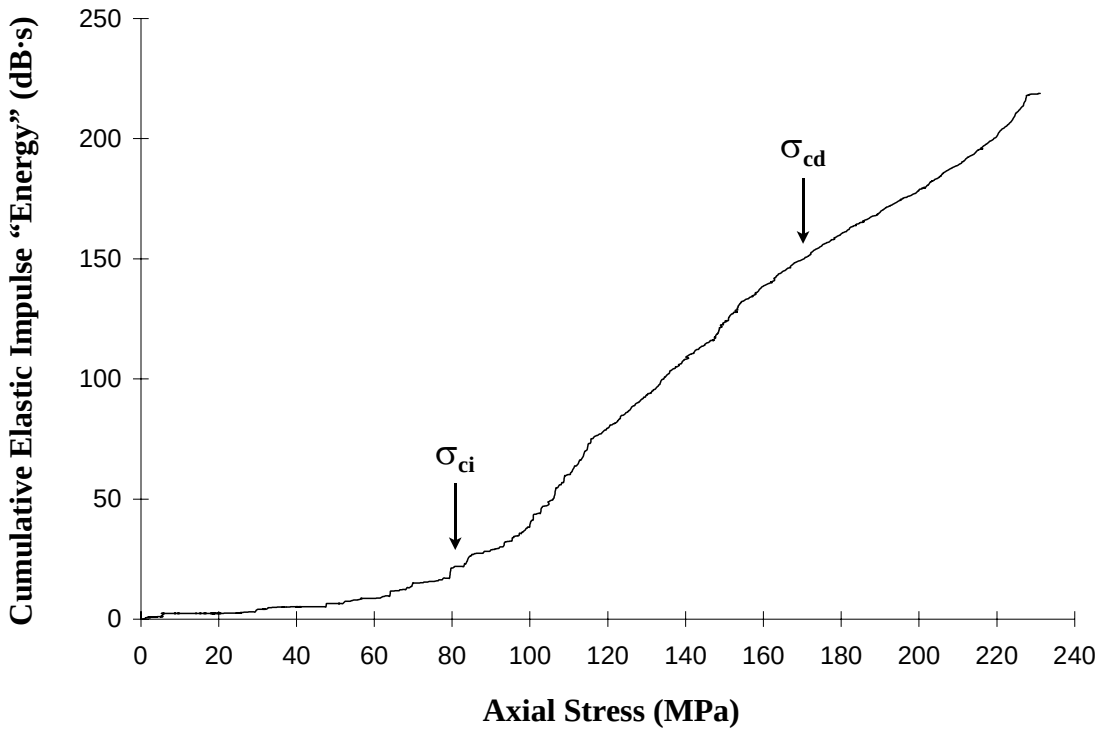

Figure 4.16 Plot of the cumulative elastic impulse "energy" -*vs*- axial stress for a 130m level URL pink granite. Elastic impulse "energy" is calculated as the square of the event amplitude multiplied by the event duration for each AE event.

4.3.2 Generation of Microcracks and the Secondary Cracking Threshold

The crack initiation threshold for the pink granite was chosen as the point where significant cracking begins. However, it is unlikely that this point represents a threshold where the entire crack population simultaneously initiates and propagates. Instead, heterogeneities in the rock matrix must be considered. The initiation of a propagating crack, as discussed in Chapter 2, is dependent on the stresses that form at the tips of the crack and the strength of the material at the crack's tip. In the first instance, the stress anomaly at the crack tip can be associated with the length of the crack and the angle it's orientation makes with the applied load. However, numerous combinations of crack lengths and orientations potentially exist in a randomly distributed population throughout the rock sample. The crack tip stresses available to initiate crack extension, therefore, will vary on a localized scale depending on the length and orientation of the individual cracks. Bortolucci and Celestino (1996) and Gorelic *et al*. (1996), for example, both cite statistical variations in crack length and orientation as controlling factors in the modelled behaviour of propagating cracks. Analysis of acoustic emission data suggests that the initial detection of cracking in the 130 m level URL pink granite appears to follow a normal distribution with a mean equal to the crack initiation threshold (Figure 4.17). The detection of minor AE activity prior to and following the crack initiation threshold suggests that these events can be attributed to cracks with lower or higher initiation thresholds. Comparable results were obtained by Chudnovsky and Kunin (1987), who used probabilistic models to calculate the extent of brittle crack propagation. Using critical crack length as a random variable, their models produced similarly shaped probability density functions as the conceptual model depicted in Figure 4.17.

The second, and more significant, component of crack initiation involves the strength of the material surrounding the crack tip. The 130 m level URL pink granite is primarily made up of feldspar and quartz grains with minor mica and other accessory minerals. Grain-sized heterogeneities in the rock will therefore exist since individual quartz and feldspar grains have contrasting elastic moduli and hardness values. In terms of the mismatch in elastic moduli, Dey and Wang (1981) found that the modelled response

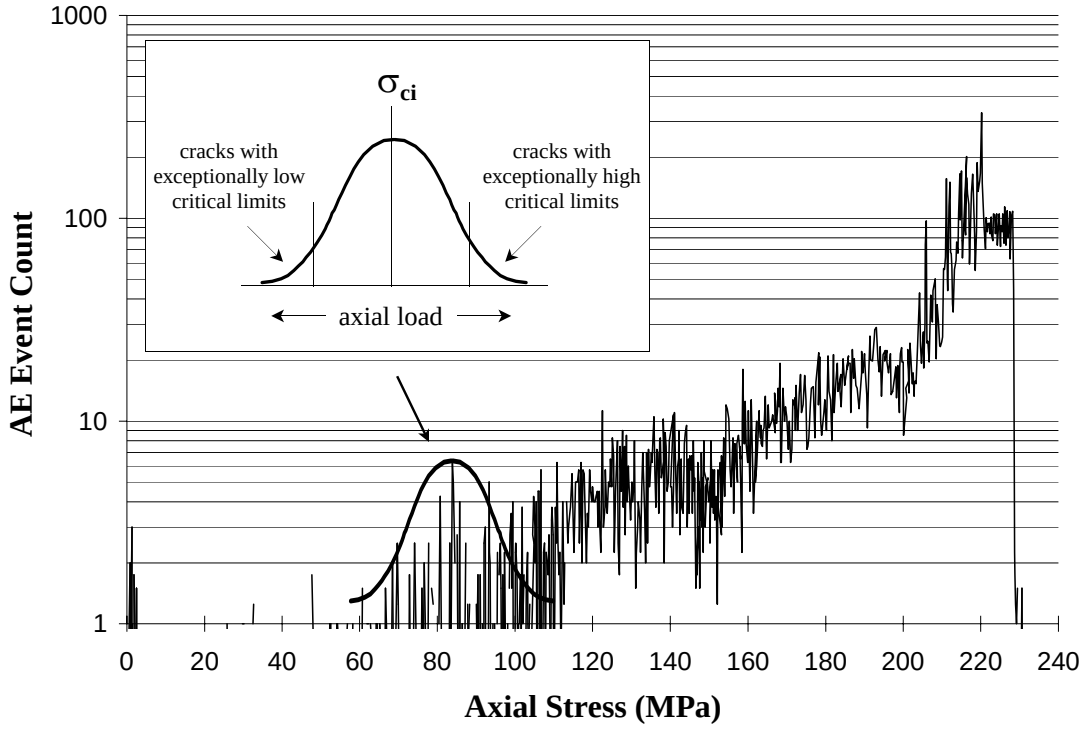

Figure 4.17 Log plot of the AE event count showing what appears to be a normal distribution of critical crack initiation loads with a mean value equal to the crack initiation threshold (σ_{ci}).

between two different minerals in welded contact with each other and subjected to the same external loading, will result in additional boundary tractions between the two minerals. In other words, as neighbouring grains of quartz and feldspar deform under load, their respective rates of deformation will vary resulting in the formation of tensile stresses acting across the grain boundary and shear stresses acting parallel to it. These localized stress inhomogeneities could in turn induce boundary cracks to initiate and propagate. The development of these fractures were confirmed through the analysis of thin-sections taken from two samples of 130 m level URL pink granite loaded past the crack initiation threshold. Scanning electron microscope (SEM) observations revealed that approximately 50% of the observed microcracks occurred along grain boundaries between neighbouring feldspar and quartz grains (Figure 4.18).

SEM observations from these samples also suggest that the remaining 50% of observable cracks are primarily located within feldspar grains (Figure 4.19). The feldspar grains, which include both plagioclase and potassium feldspar, have a lower hardness value than quartz (6 compared to 7 on the Moh's scale, respectively). It was noted in Chapter 2 that hardness can play a contributing role with respect to the initiation of fractures where harder minerals induce a point load in softer neighbouring minerals. For example, Hallbauer *et al*. (1973) found that point loading of grains by other grains was a frequent source of cracks in triaxial tested samples of quartzite. Hardness can also be loosely correlated with strength (Franklin and Dusseault, 1989). It then follows that the weaker feldspar grains will be the source of the first intergranular cracks to initiate and propagate. Eventually, at higher loads, the harder and stronger quartz grains will begin to crack thereby resulting in a second crack initiation interval.

These deductions can be substantiated through the detected AE response, which shows two separate bursts of AE activity. The initial burst coincides with the crack initiation threshold at 80 MPa as cracks begin to propagate along grain boundaries and through feldspar grains. Similar observations have been made by Svab and Lajtai (1981) who found that grain boundaries and feldspar cleavage act as the primary microstructural path controllers for a propagating crack in Lac du Bonnet granite. A second crack initiation threshold then follows at approximately 105 MPa as cracking

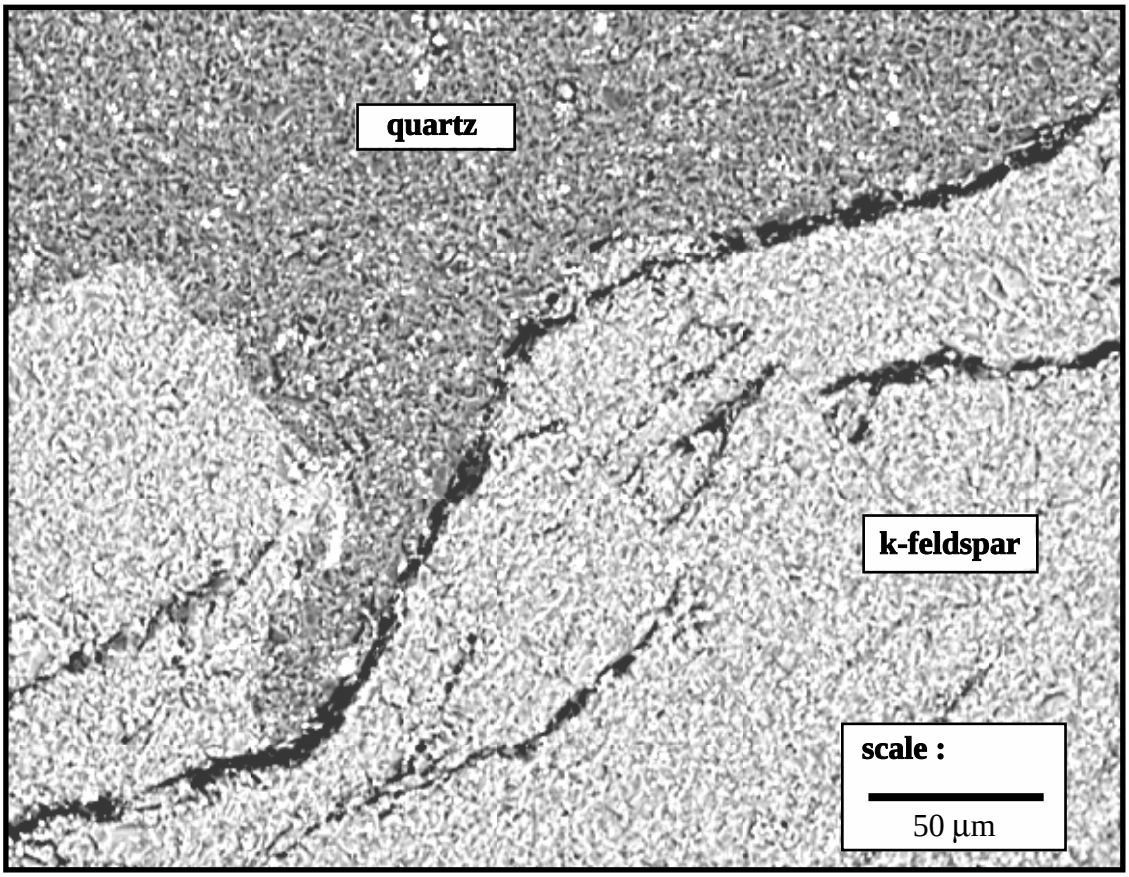

Figure 4.18 Scanning electron microscope (SEM) image of a stress-induced crack originating along a quartz-feldspar grain boundary in a 130 m level URL pink granite.

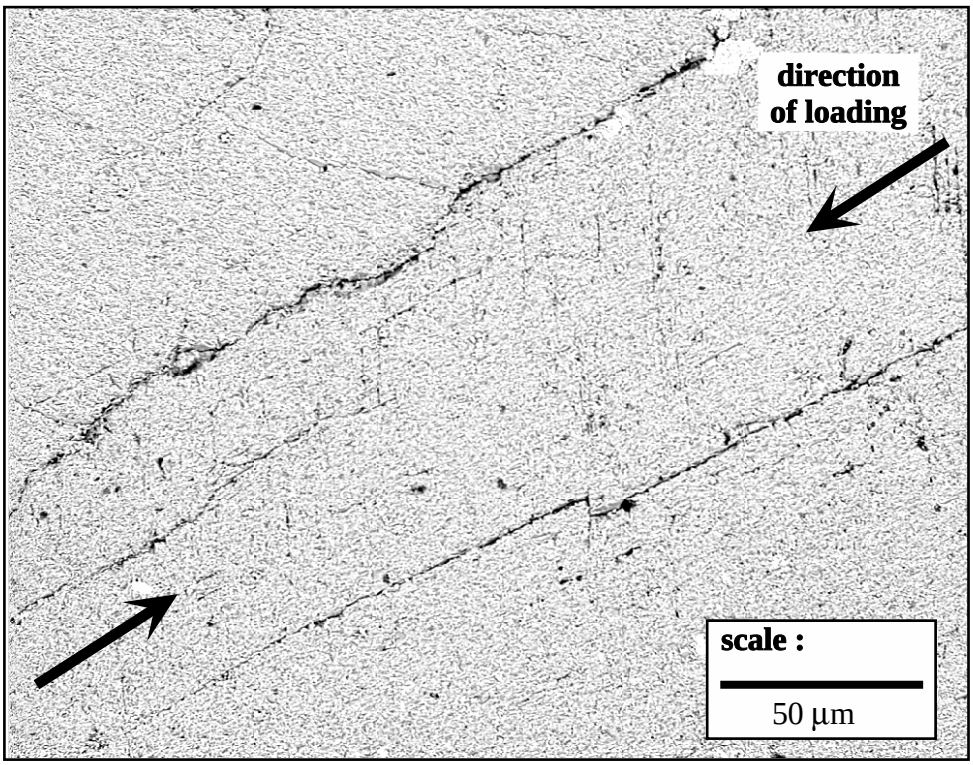

Figure 4.19 SEM image of a feldspar grain with stress induced cracks aligned parallel to the direction of loading (i.e. σ_1).

begins in the quartz grains. This threshold, referred to as the secondary cracking threshold (σ_{ci2}), also marks the point where continuous AE activity is recorded as cracking takes place in all of the constituent minerals of the granite (Figure 4.11). Furthermore, large increases are seen in the calculated acoustic event "energy" at this threshold. This implies that the energy of the events originating from the harder quartz grains is somewhat greater than those seen at the crack initiation threshold arising from feldspar grains and quartz/feldspar grain boundaries (Figure 4.20).

4.4 Crack Coalescence

In defining the stages of crack behaviour, Brace (1964), Bieniawski, (1967a) and Martin (1993) interpret stable crack growth as one stage bounded at the lower end by the crack initiation threshold (σ_{ci}) and at the upper end by the crack damage threshold (σ_{cd}). Analysis of laboratory data obtained in this study, however, indicates that this region may consist of two stages distinguished by a major change in the volumetric strain rate. Examination of both the axial and lateral stiffness curves indicates that a large rate change occurs in strain well before volumetric strain reversal (i.e. crack damage threshold). During stable crack growth, rate changes are believed to occur solely in terms of lateral strain since crack growth is predominantly in the direction of uniaxial loading. Test results indicate, however, that the stress dependent axial strain rate (i.e. stiffness) is not constant but decreases well before the crack damage threshold. Figure 4.21 demonstrates that although the axial stiffness remains constant after crack initiation (i.e. only the lateral stiffness is affected) it begins to decrease at approximately 140 MPa. These changes can be more clearly seen in the volumetric stiffness plot, where large increases in the lateral strain rate combined with the changes in the axial strain rate cause large irregularities as the volumetric strain curve approaches reversal (Figure 4.22).

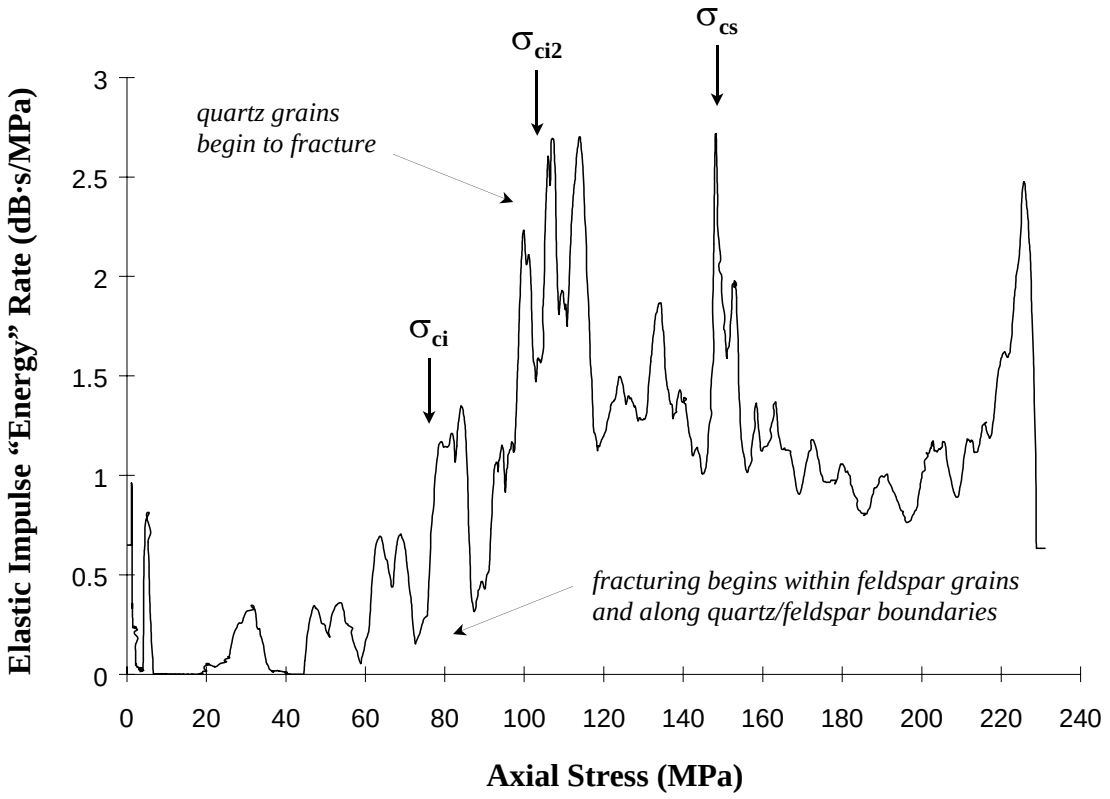

Figure 4.20 Plot of the stress dependent elastic impulse "energy" rate -*vs*- axial stress for a 130m level URL pink granite.

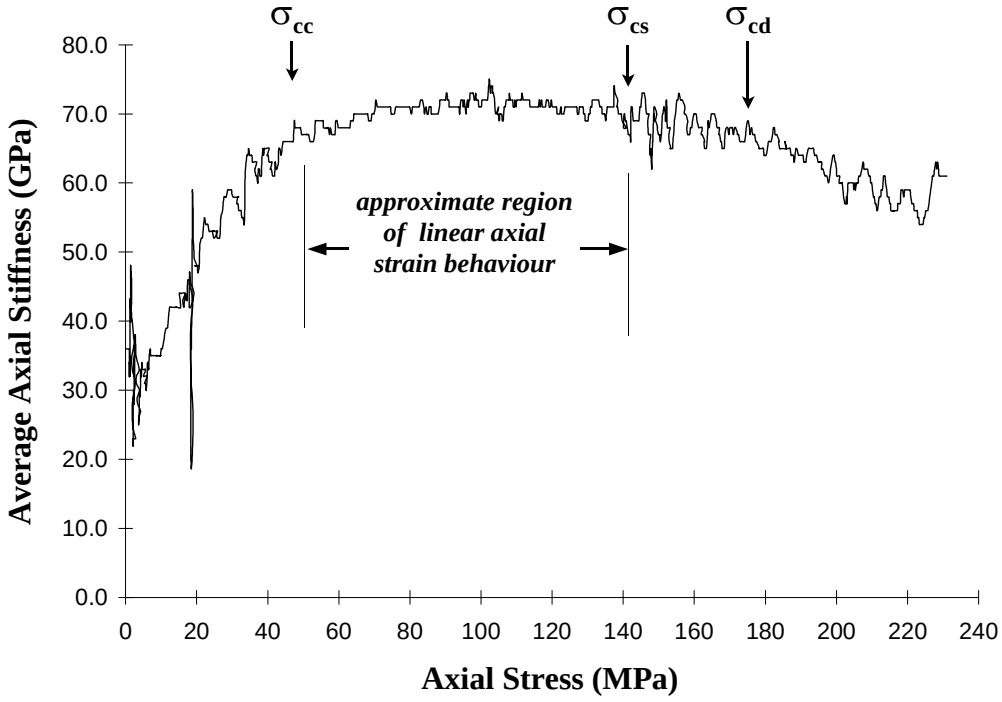

Figure 4.21 Axial stiffness plot indicating a significant change in the axial strain rate prior to the crack damage threshold for a 130m level URL pink granite.

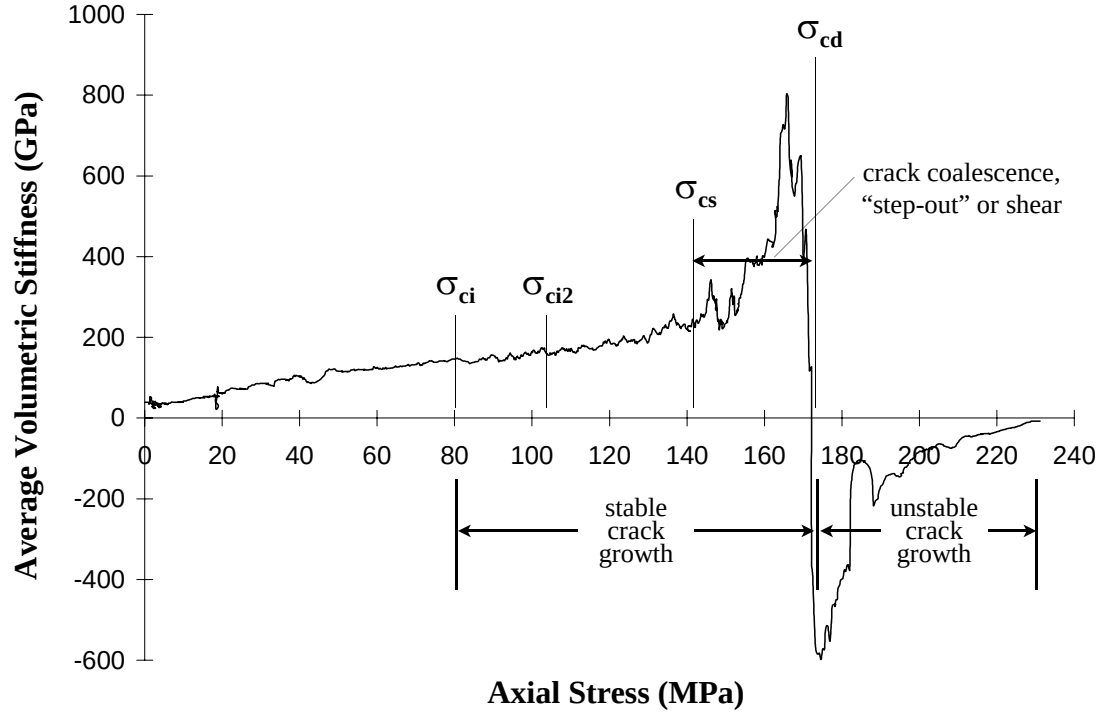

Figure 4.22 Volumetric stiffness plot showing a major strain rate change at the crack coalescence threshold (σ_{cs}) for a 130m level URL pink granite.

The unexpected departure from linear behaviour seen in the axial strain response prior to the crack damage threshold may be explained through the coalescence of propagating cracks in a loaded sample. At the beginning of crack initiation, small tensile cracks critically aligned to the loading direction begin to grow parallel to the applied load. The cracks are assumed to appear randomly throughout the sample and, for the most part, are isolated from one another. Such cracks would have very little effect in decreasing the overall competency of the rock. As the load is increased additional cracks will begin to grow as their individual strengths are exceeded, incrementally contributing to the degradation of the inherent rock strength (i.e. loss of cohesion). For example, test results presented in the previous section indicate that continuous AE activity does not occur until a load of 110 MPa is reached, well after the crack initiation threshold has been exceeded (Figure 4.11).

As cracks increase, both in number and size, they will eventually begin to interact with one another. Crack interaction then becomes extremely complex as induced stresses localized at the tips of the propagating cracks overlap (this process is examined in greater detail in Chapter 5 using numerical modelling techniques). Eventually cracks will begin to "step-out" and coalesce (i.e. develop en-echelon, Lajtai *et al*., 1994). This process has been observed and modelled for contrived Griffith wing crack geometries in gypsum (Reyes and Einstein, 1991; Bobet and Einstein, 1996). Furthermore, Bobet and Einstein (1996) propose four different modes of coalescence, dependent on the initial crack patterns, which in turn show some form of crack growth at oblique angles to the loading direction. The oblique coalescence of these cracks with perhaps an element of shearing, and therefore friction, and the breakdown of bridging material would result in changes to the axial strain rate. Thus, the changes seen in the axial and volumetric stiffness curves may be attributed to a stage of crack coalescence (σ_{cs}) prior to the crack damage stress threshold. It should also be noted that a significant increase in the event "energy" and "energy" rate (Figures 4.16 and 4.20, respectively) occurs between 140 and 150 MPa, coinciding with crack coalescence values seen in the strain gauge data.

4.5 Crack Damage and Peak Strength

Following crack coalescence, determination of the crack damage stress threshold (σ_{cd}) is relatively straightforward. When the lateral strain rate surpasses the axial strain rate as the dominant component in the volumetric strain calculation, the slope of the volumetric strain curve changes from positive to negative thus signifying volumetric strain reversal and the crack damage threshold. Although a certain degree of subjectivity may be introduced by picking the point of volumetric strain reversal directly off the volumetric strain curve, the point stands out very clearly on a volumetric stiffness plot (Figure 4.22). Martin and Chandler (1994) considered this threshold point to be the true peak strength of a rock monotonically loaded in uniaxial compression. However, it should be noted that the reversal of the volumetric stress-strain curve is dependent on how the volumetric strain is calculated (e.g. applying Equation 4.2, reversal occurs when the lateral strains measured exceed half of the axial strains).

In terms of AE response, the majority of detected events are recorded between the crack damage threshold and peak strength. Further increases in the event amplitudes, as seen at the crack coalescence threshold, are experienced at the crack damage threshold (Figure 4.14). These results concur with observations made by Watters and Chuck (1989) who found that the peak amplitude of acoustic events in welded tuff gradually increased throughout loading followed by a significant increase prior to failure. Similar observations were made by Mlakar *et al*. (1993) on samples of potash where increases in event amplitude occurred predominantly at the yield point of the material. In effect, low amplitude AE activity was observed during elastic deformation of the sample followed by high amplitude events after the elastic limit was exceeded. Comparing their results with SEM observations, Mlakar *et al*. (1993) concluded that intergranular phenomena present in the early stages in the loading cycle could be associated with low amplitude events. High amplitude events present in the later stages of the loading cycle were associated with intragranular microcracking and transgranular cracking. Test results from the 130m level granite reflect these observations, not only in terms of the recorded event amplitudes but also with respect to the other event properties. Significant increases in the waveform properties are observed at the crack

damage threshold and even larger increases are experienced prior to failure possibly marking the onset of plastic yield in the sample.

Unstable crack growth continues to the point where the numerous microcracks have coalesced and the rock can no longer support an increase in load. The material strain-softens with deformations occurring not so much in the rock matrix but among structural blocks delineated by propagating cracks. A large AE spike recorded at approximately $0.95\sigma_{UCS}$ may coincide with microcrack localization resulting in the formation of a critical failure plane (Figure 4.10). Failure then occurs in a violent fashion as columnar pieces of intact rock appear to buckle. Values of peak strength, in addition to the intermediate stages of crack development, for the 130 m level pink granite are given in Table 4.3.

Table 4.3 Average threshold values for the different stages of crack development in uniaxial compression for the 130 m level URL pink granite (standard deviation is provided in parentheses).

Threshold Parameter	Value (MPa)
Number of Tests	20
Crack Closure, σ_{cc}	47.3 (± 2.7)
Crack Initiation, σ_{ci}	81.5 (± 3.7)
Secondary Cracking, σ_{ci2}	103.9 (± 5.0)
Crack Coalescence, σ_{cs}	132.8 (± 9.0)
Crack Damage, σ_{cd}	156.0 (± 13.2)
Peak Strength, σ_{UCS}	206.9 (± 13.5)

4.6 Summary

A series of uniaxial compression tests were performed on 20 samples of 130 m level URL pink granite. Using the techniques developed in Chapter 3, the analysis of these tests concentrated on establishing stress thresholds for the different stages of crack development. Crack closure thresholds (σ_{cc}) were picked as the point where the axial

stiffness curve leveled off and behaved in a relatively linear fashion (i.e. following sharp increases in stiffness corresponding to the closure of cracks). The average value for the crack closure threshold was determined to be 47 MPa or approximately $0.23\sigma_{UCS}$.

The crack initiation threshold (σ_{ci}) was determined using an approach that involved the combined use of the moving point regression analysis and acoustic emission response. It was found that this method was more accurate than techniques used by Martin (1993) and Lajtai and Dzik (1996) which incorporated large errors due to subjectivity and assumptions regarding the elastic constants. Crack initiation was determined as the point where variations in the lateral and volumetric stiffness curve indicated a significant change in the stress dependent rate of strain. These values were confirmed using the stresses at which significant AE activity was detected and where values of the ringdown count, event duration, rise time and elastic impulse "energy" dramatically increased. The average value for the crack initiation threshold was determined to be 82 MPa or approximately $0.40\sigma_{UCS}$.

SEM analysis further suggested that the initial AE bursts observed at the crack initiation threshold coincided with the development of cracks along grain boundaries and within feldspar grains. A second crack initiation threshold was subsequently detected at approximately 105 MPa relating to the initiation of cracking in the quartz grains. This threshold was referred to as the secondary cracking threshold (σ_{ci2}) and marked the point where continuous AE activity was recorded.

A stage of crack coalescence (σ_{cs}) was identified coincident with an unexpected departure from linear axial strain behaviour prior to the crack damage threshold. Crack coalescence was defined as the point where the crack population reaches a limiting state, both in number and size, and localized stresses at the tips of the propagating cracks begin to interact with one another. This coalescence appears to involve elements of oblique crack growth due to shearing and the weakening and destruction of bridging material between coalescing cracks. This threshold was subsequently picked as the point where the axial stiffness curve began to decrease and the volumetric stiffness curve began to sharply increase. The average value of the crack coalescence threshold was determined to be 133 MPa or approximately $0.64\sigma_{UCS}$.

The crack damage threshold (σ_{cd}) was picked as the point where the volumetric stiffness curve sharply shifted from positive values to negative values indicating a reversal in the volumetric strain curve. This occurred at an average value of 156 MPa or approximately $0.75\sigma_{UCS}$. Unstable crack propagation ensued followed by the failure of the rock at an average uniaxial compressive strength value of 207 MPa.

For each of the 20 tests, the patterns used to pick these threshold values remained consistent. Results of the analysis for each test are included in Appendices I and II.

CHAPTER 5

NUMERICAL ANALYSIS OF CRACK INITIATION, PROPAGATION AND INTERACTION

Laboratory test results presented in Chapter 4 revealed that the degradation of material strength through stress-induced microfracturing follows a complicated process of crack initiation, propagation and coalescence leading to the failure of the material. Furthermore, the crack coalescence threshold appears to signify a noticeable change in the deformation and fracture characteristics of the 130 m level URL pink granite samples as cracks begin to interact. Attempts have been made by other researchers to gain a better understanding of the processes involved in the propagation of multiple cracks through analytical and numerical techniques. Analysis of crack behaviour in a compressive stress field has progressed from the simple case of a single crack, to en echelon arrays of cracks, to multiple random crack arrays. Few studies, however, have examined how multiple cracks, and more specifically the localized stresses surrounding the tips of multiple cracks, interact in either promoting or inhibiting the growth of adjacent cracks. A study was therefore conducted in an attempt to gain insight into the complexities of the crack coalescence process. The work presented in this chapter utilizes boundary element techniques to model the interaction of multiple cracks and the mutual influence neighbouring cracks have on crack initiation and propagation.

5.1 Background and Methodology

Numerical modelling to simulate crack initiation and propagation in rock has been used by a number of researchers. Ingraffea (1979), Kemeny and Cook (1991) and Dyskin *et al*. (1994) focused on the use of linear elastic fracture mechanics (LEFM) to model crack stability and propagation trajectories by incorporating a stress intensity

factor into the numerical formulation to dictate whether crack propagation would occur or not. Additional studies have concentrated on the concept of a process zone at the crack tip to model non-linear effects (Rossmanith, 1983; Ingraffea and Wawrzynek, 1985). To a lesser extent the effects of crack interaction have been studied. Studies have been conducted on the modelling of crack coalescence (Reyes and Einstein, 1991; Shen and Stephansson, 1993), however, little work has been done with respect to how the stresses surrounding these coalescing cracks interact in terms of promoting or inhibiting crack propagation.

Crack initiation and propagation were modelled following a similar process to that outlined by Ingraffea *et al*. (1993). The sequence of events begins by computing the stress intensity factors for a given crack length and determining crack stability under a pre-specified load. If the crack is unstable the crack length is increased, and if the crack is stable the load is increased. This process is repeated, thereby producing a relationship between stable crack length and applied stress. One of the limitations in this methodology is that the problem geometry requires remeshing for each crack length increment and reanalysis for each load increment. In cases where a large number of model runs are required, the boundary element method can be an efficient tool since only the boundary of the problem geometry requires discretization. To model the effects of crack interaction, Dyskin *et al*. (1995) note that a high number of crack models must be run, thus making the use of the boundary element method more attractive than the finite element method. For these reasons, a boundary element approach was chosen as it allowed for the quick analysis of numerous crack models.

The nature of the boundary element approach chosen, however, required a number of assumptions and modifications to be made to the LEFM approach summarized by Ingraffea *et al*. (1993). For example, crack geometries were modelled as axial cracks represented by ellipses of finite width. Most LEFM approaches assume a zero-width Griffith type crack (Figure 5.1). In cases where the crack is aligned parallel to the principal stress direction, the zero-width crack is unaffected by the applied compressive stress field and, therefore, cannot be propagated. To propagate, the zero-width crack must be inclined to the principal stress direction. Dzik and Lajtai (1998)

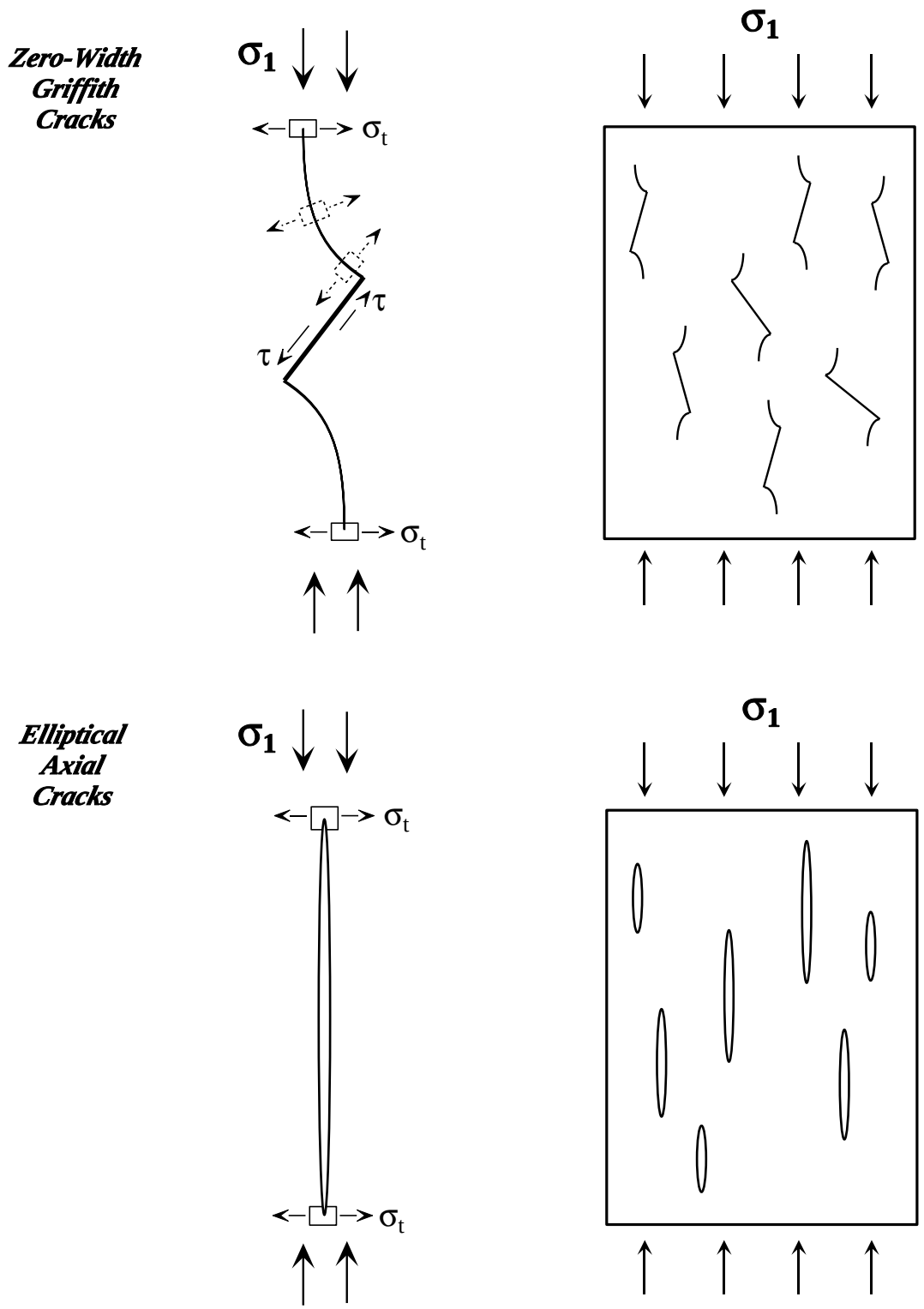

Figure 5.1 Examples of "zero-width Griffith" and "elliptical axial" cracks.

note that, theoretically, an axial crack can only be propagated in the axial direction by removing the zero-width simplification or by allowing a finite deformation in the lateral direction. In either case, the latter stages of crack development involve the interaction of crack tips propagating in the axial direction.

Another modification to Ingraffea *et al.*'s (1993) approach was to replace the stress intensity formulation to model crack tip failure with an empirical fracture criterion. The Uniaxial Strength Ratio (USR) failure criterion calculates a safety factor in terms of the ratio of material strength to the induced stresses surrounding the crack tip. Described in detail by Dzik and Lajtai (1998), the USR criterion is derived through the Rocker function (Johnston, 1985; Carter *et al.*, 1991) which describes material strength, σ_{1f}, as a function of its compressive, σ_C, and tensile, σ_T, strength :

$$\sigma_{1f} = \sigma_C \left(1 - \frac{\sigma_3}{\sigma_T}\right)^R \tag{5.1}$$

where R is a fitting constant which typically has a value of 0.5 (Dzik and Lajtai, 1998). The Rocker function represents an equivalent strength curve passing through the stress point (σ_3, σ_1) as shown in Figure 5.2. Assuming an initial crack length, crack initiation is defined as the stress level required to produce a factor of safety, SF, below 1.0 (i.e. tensile failure of the crack tip material):

$$SF = \frac{\sigma_{1f}}{\sigma_1} \tag{5.2}$$

The use of the boundary element formulation also required the incorporation of an averaging distance to correctly portray the critical stress concentrations required at the crack tip to initiate crack propagation. Since elements are located only along the periphery of the crack ellipse, high stress concentrations are calculated that do not take into account the redistribution of stresses around the crack tip due to material yield. In other words, the largest tensile stress concentration must coincide with the crack tip

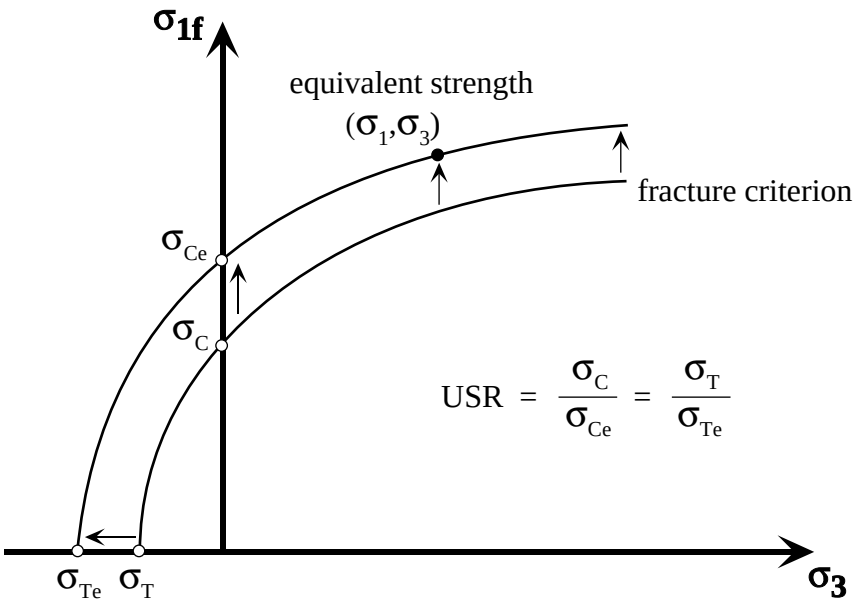

Figure 5.2 USR equivalent strength fracture criterion (after Dzik and Lajtai, 1998).

boundary, with a steep stress gradient away from the crack tip. A very small averaging radius is required to accurately represent the redistribution of stresses in this region. This procedure is somewhat analogous to incorporating a process zone into the analysis. Dzik and Lajtai (1998) found that in order to obtain results that match experimental data, the averaging distance should be approximately 2-3 times the minor axis width of the elliptical crack.

Modelling proceeded such that, if fracture was indicated near the crack tip, the crack was extended parallel to the applied load. This process of crack extension was continued until the crack length became stable. By following the routine of incrementally increasing stress levels and crack length until stability was reached, a stable crack length curve can be constructed. Using the single crack geometry shown in Figure 5.3, simulation of uniaxial loading produced a stable crack length -*vs*- applied axial stress curve with a decreasing slope with increasing load (Figure 5.4). This indicates that as the axial load is increased, the crack length required to stabilize crack propagation for the same stress increment increases. Material properties for these models were chosen to represent the Lac du Bonnet granite (Table 5.1).

Table 5.1 Material properties for Lac du Bonnet granite used in modelling study.

Material Property	Value
Young's Modulus	70 GPa
Poisson's Ratio	0.2
Uniaxial Compressive Strength	225 MPa
Tensile Strength	10 MPa
Rocker Exponent	0.5

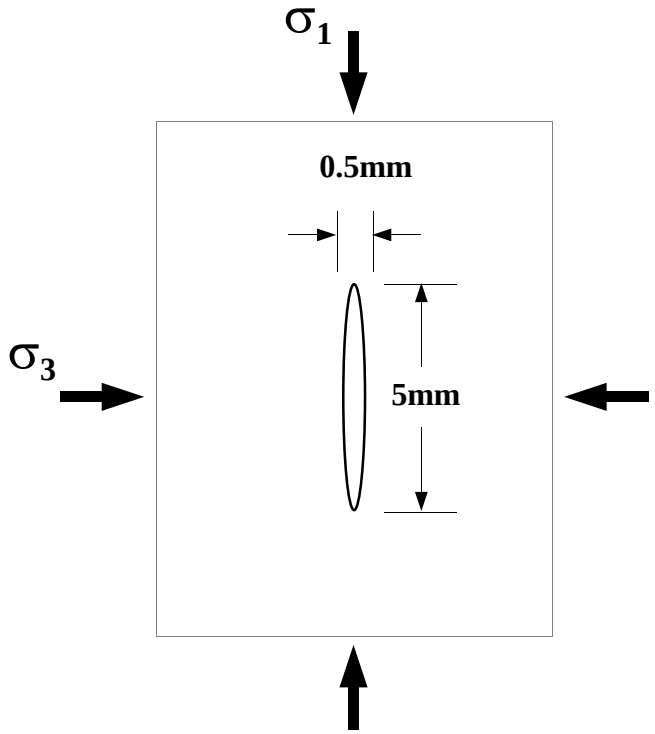

Figure 5.3 Problem geometry used for single crack boundary element models.

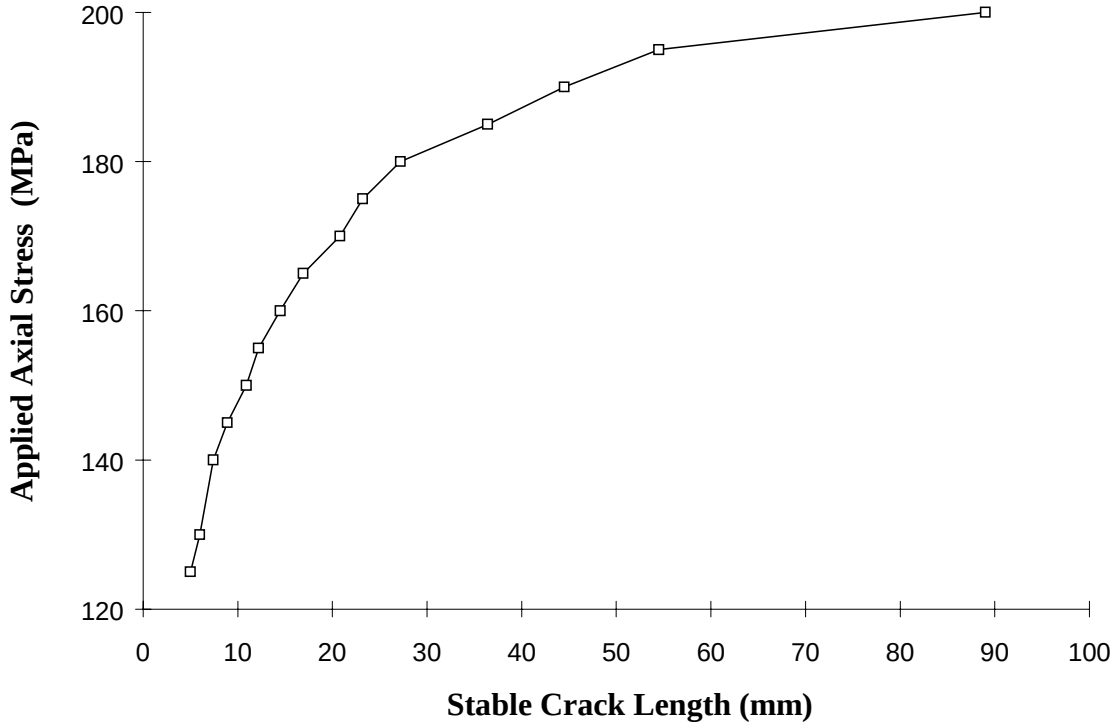

Figure 5.4 Applied axial stress -*vs*- stable crack length relationship for a single crack in a uniaxial stress field.

5.2 Stress Shadow Effects in a Uniaxial Stress Field

Two axial cracks were added to the single crack geometry to examine the influence of their respective stress shadows on the initiation and growth of the central crack (Figure 5.5). With the addition of these cracks, crack initiation and propagation differ from the case of a single crack in that crack initiation occurs at a higher stress level for the single crack case (Figure 5.6). This conflicts with observations presented by Hoek and Bieniawski (1965) who found that crack initiation in glass plates occurred at lower stresses when multiple cracks were present. Du and Aydin (1991) found that crack interaction depends both on the distance between cracks and the relative position of the cracks, with the strongest interaction occurring when cracks are offset such as in an en echelon array. Depending on the geometry of the array, this interaction may result in stress conditions that either inhibit or promote crack initiation. It is apparent that for the particular two-dimensional crack arrangement used in this study, crack initiation is inhibited by the presence of the adjacent cracks.

A second effect of the addition of neighbouring cracks is in terms of crack propagation. Initially, induced stresses retard crack growth, but at about 150 MPa they appear to greatly enhance crack growth (Figure 5.6). This agrees well with modelling results provided by Kachanov and Laures (1989) who noted that shielding or amplification of stresses can occur in a uniaxial stress field when multiple cracks are used. They found that a major crack produces shadows normal to its major axis which may shield nearby microcracks. Crack growth then continues at approximately the same rate as without the stress shadows, but at a lower stress for a given crack length, indicating that the stress field continues to influence propagation (Figure 5.6). Due to the nature of the elastic solution, as the central crack lengthens and moves farther away from the two neighbouring cracks' zone of influence, the two curves will eventually converge.

These differences can be best explained by noting that in a uniaxial stress field a tensile stress zone exists around each of the three crack tips if the cracks are aligned approximately parallel to the applied compressive load (Figure 5.7). When the propagating crack is small its zone of influence is not within the zone of influence of the

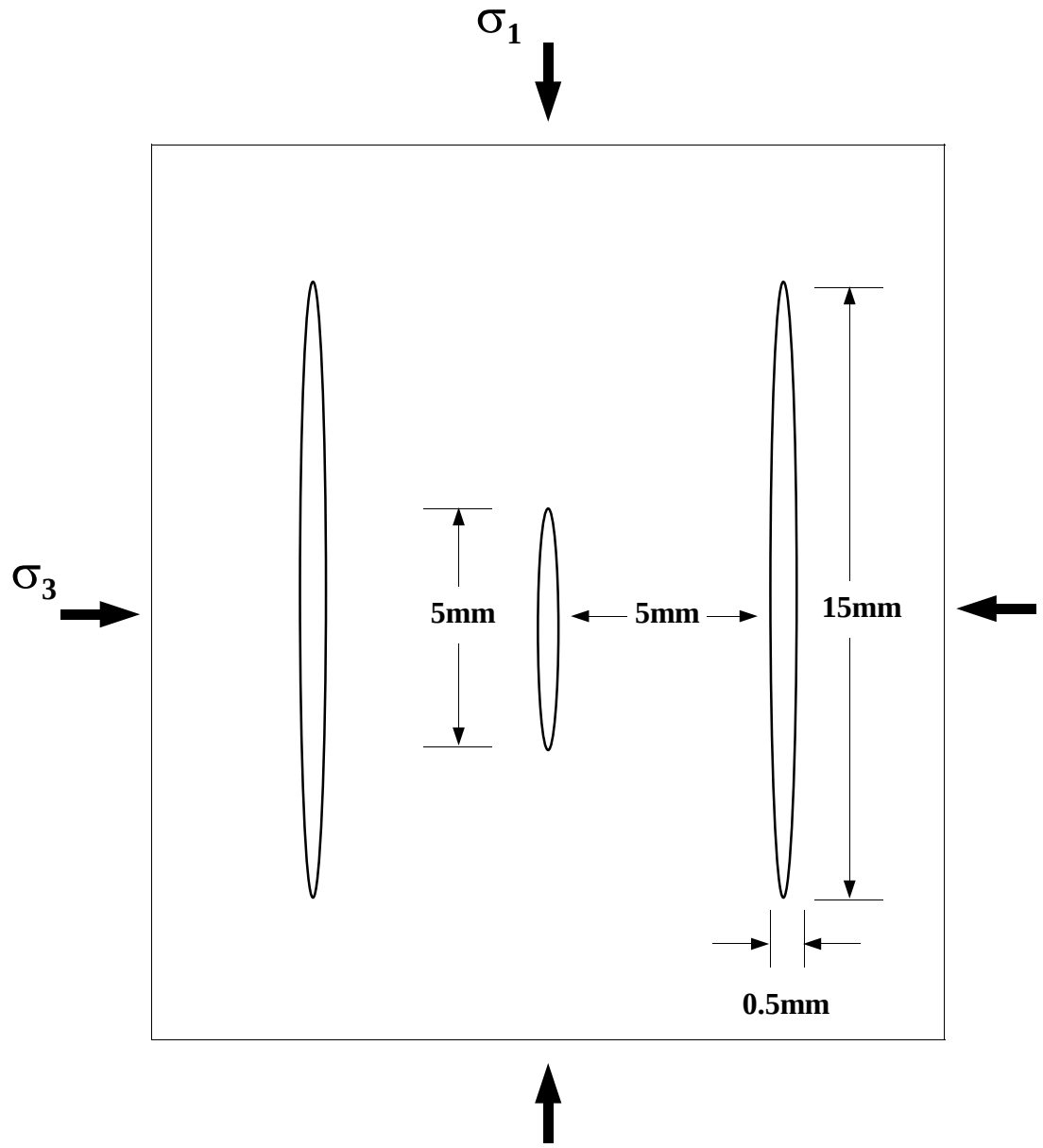

Figure 5.5 Problem geometry used in multiple crack array models for determination of stress shadow effects.

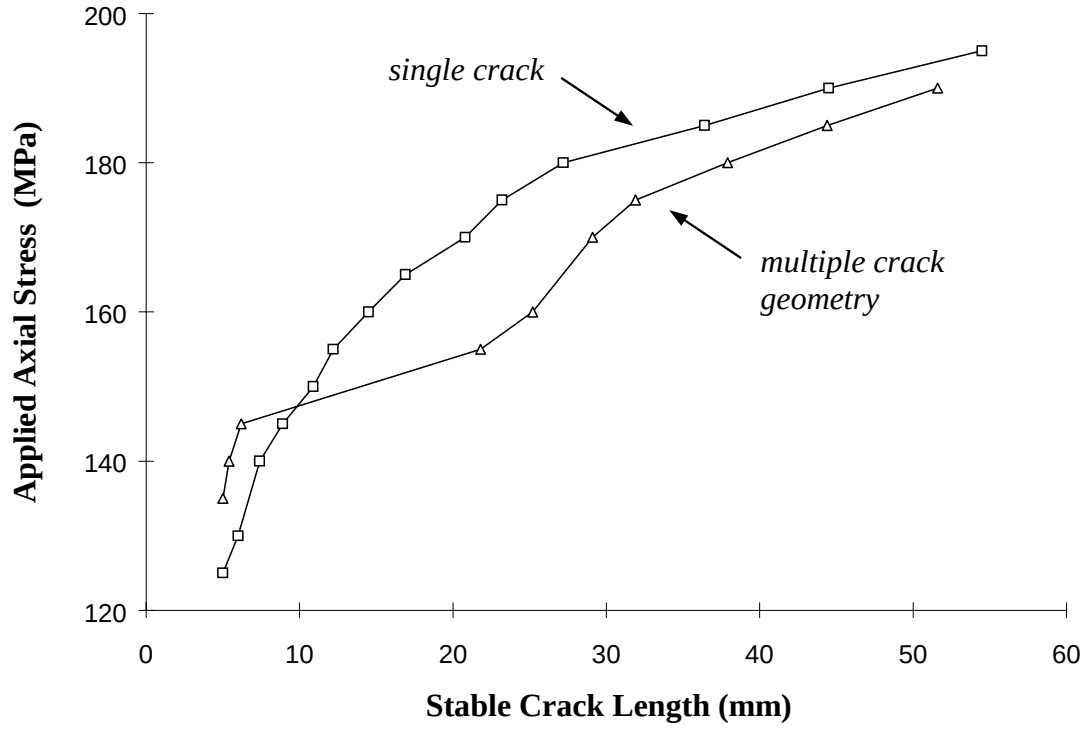

Figure 5.6 Applied axial stress -*vs*- stable crack length relationships for both single and multiple crack arrays in a uniaxial stress field.

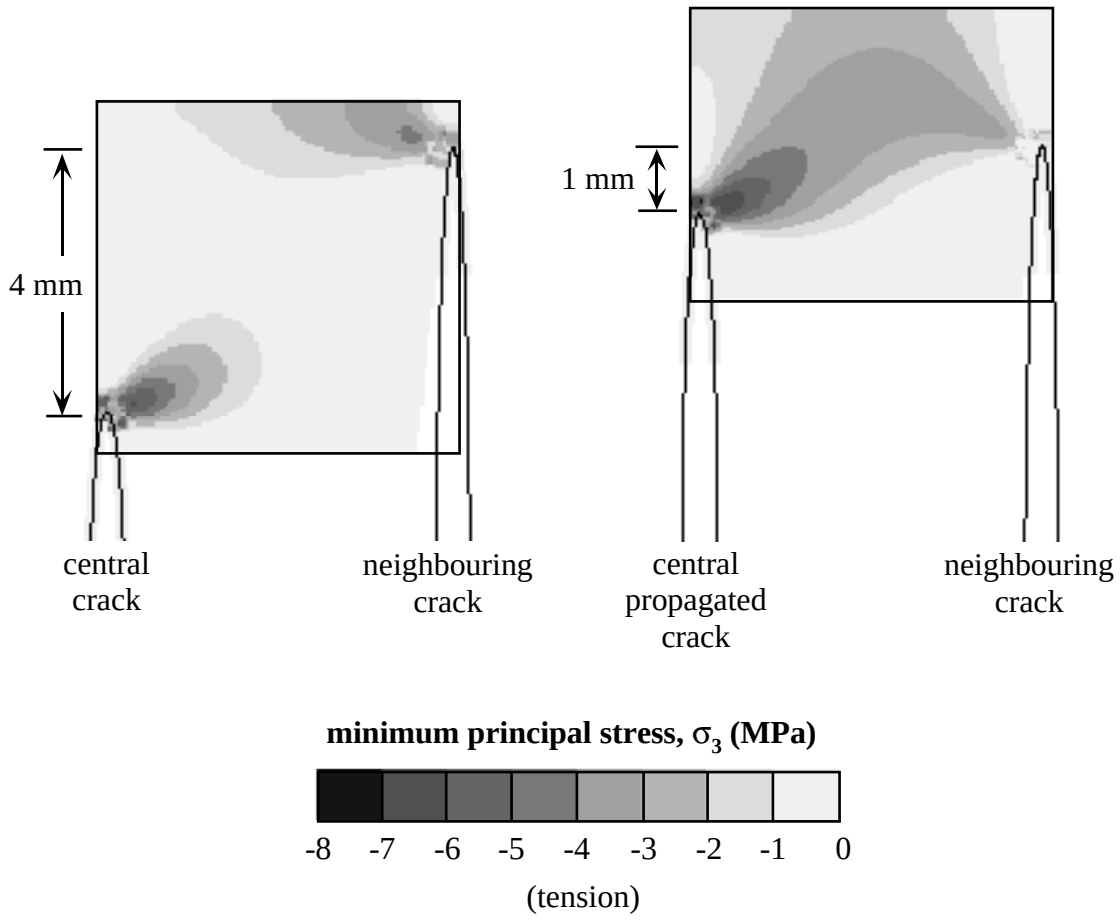

Figure 5.7 Minimum principal stress (σ_3) contours surrounding adjacent crack tips in a multiple crack array under uniaxial loading conditions.

larger neighbouring cracks. Therefore, although crack growth is promoted, the interaction between neighbouring cracks is small. As the crack grows, due to increased loading, its tensile stress shadow gradually approaches the tensile stress shadows produced by the other cracks and this development accelerates crack propagation. After the crack extends past the zone of influence of the two peripheral cracks, crack growth decelerates. The zone in which the propagating crack is most influenced by the induced stresses, as shown in Figure 5.6, is between a central crack length of 10-20 mm, coinciding with the location of the neighbouring crack tips.

5.3 Stress Shadow Effects in a Triaxial Stress Field

The addition of confining stress to the single crack model results in a reduction of the tensile stresses near the crack tip. Therefore, crack initiation occurs at much lower stresses for a single crack loaded uniaxially than for one loaded triaxially. Similar results were found by Adams and Sines (1978) through the testing of polymethylmethacrylate (PMMA) plates with an embedded crack. Modelling results indicate the opposite effect when peripheral cracks are included in the model. Confinement was added to the multiple crack array model (Figure 5.5) by simulating 20 MPa in the σ_3 and σ_2 (out-of-plane) directions. Both the applied out-of-plane stress and the intermediate principal stress were identical in magnitude so as to avoid any crack propagation in the out-of-plane direction.

With the addition of triaxial loading to the multiple crack array, results show that the predicted tensile stress zone which forms around the central crack tip is enhanced and appears at a lower σ_1 than in the uniaxial case. The development of larger tensile stresses results in a crack initiation stress 40 MPa lower than in the uniaxial case (Figure 5.8). Although crack initiation begins sooner in the triaxial case than in the uniaxial case, crack propagation in the triaxial case is much slower with crack growth occurring on the scale of only a few millimeters over a change in applied stress of 140 MPa (Figure 5.8). In comparison, total crack propagation in the uniaxial multiple crack model is approximately 35 mm over only 40 MPa of applied axial stress. This indicates that stress shadows resulting from the addition of peripheral cracks and the addition of a

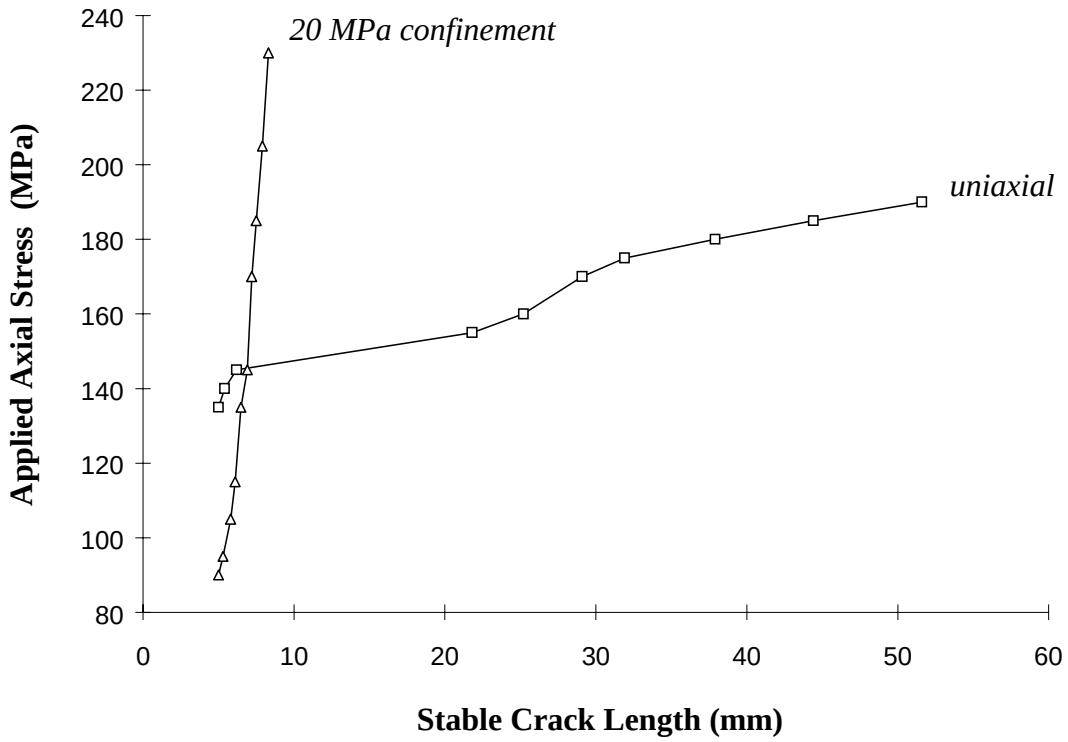

Figure 5.8 Applied axial stress -*vs*- stable crack length relationships for a multiple crack array with and without an applied confining pressure.

confining load seriously retards crack growth. In the uniaxial case, the stress zones around the tips of the neighbouring cracks are tensile and were shown to promote crack propagation. Examination of the stress zones around the neighbouring crack tips in the triaxial case reveal that not only are these stresses not tensile, but the minimum principal stresses are consistently around 30 MPa compressive (Figure 5.9) regardless of the applied axial load. This phenomenon accounts for the extremely slow crack propagation that occurs. Whereas peripheral cracks in a uniaxial stress field enhance crack growth due to the interaction of the tensile stress shadows which form around all three crack tips, the compressive stress shadows that form around the neighbouring crack tips in a triaxial stress field suppress the tensile stress zone around the central crack, effectively restricting crack growth to only a few millimeters. Initially, large tensile stress zones form around the middle crack tip early on so that crack initiation occurs sooner in a triaxial stress field. However, as the crack grows and approaches the compressive stress zones surrounding the tips of the neighbouring cracks, crack growth is essentially halted (Figure 5.8).

Additional modelling shows that as the confining stress applied to the multiple crack array is varied its influence on promoting crack initiation changes. Models of a multiple crack array with varying confining stress show that central crack initiation occurs at decreasing applied axial compressive stresses with increasing confining stress (Figure 5.10). Crack initiation stress decreases from 140 MPa for the uniaxial condition to 45 MPa at 30 MPa of confinement. Similar findings were made by Hamajima *et al*. (1984) using discrete element modelling. These models also reinforce observations made for the case of 20 MPa confinement regarding crack propagation. With increasing confining pressure, the magnitude of compressive stresses surrounding the peripheral crack tips increases, thereby increasing the restraint on propagation of the central crack. With an increase in confining pressure from 10 to 20 MPa, the compressive stress magnitudes around the tips of the peripheral cracks increase from an approximate range of 10-15 MPa to 20-30 MPa.

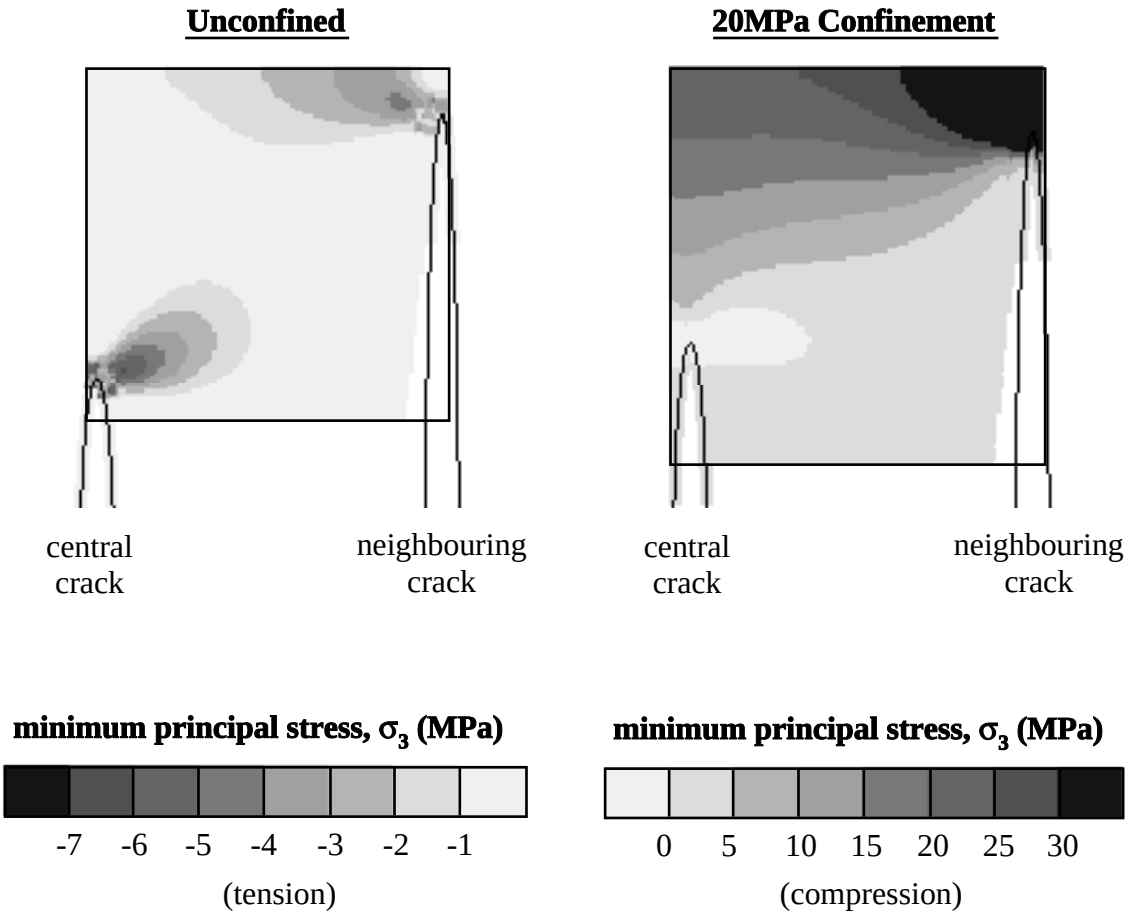

Figure 5.9 Minimum principal stress (σ_3) contours surrounding adjacent crack tips in a multiple crack array under uniaxial and triaxial loading conditions.

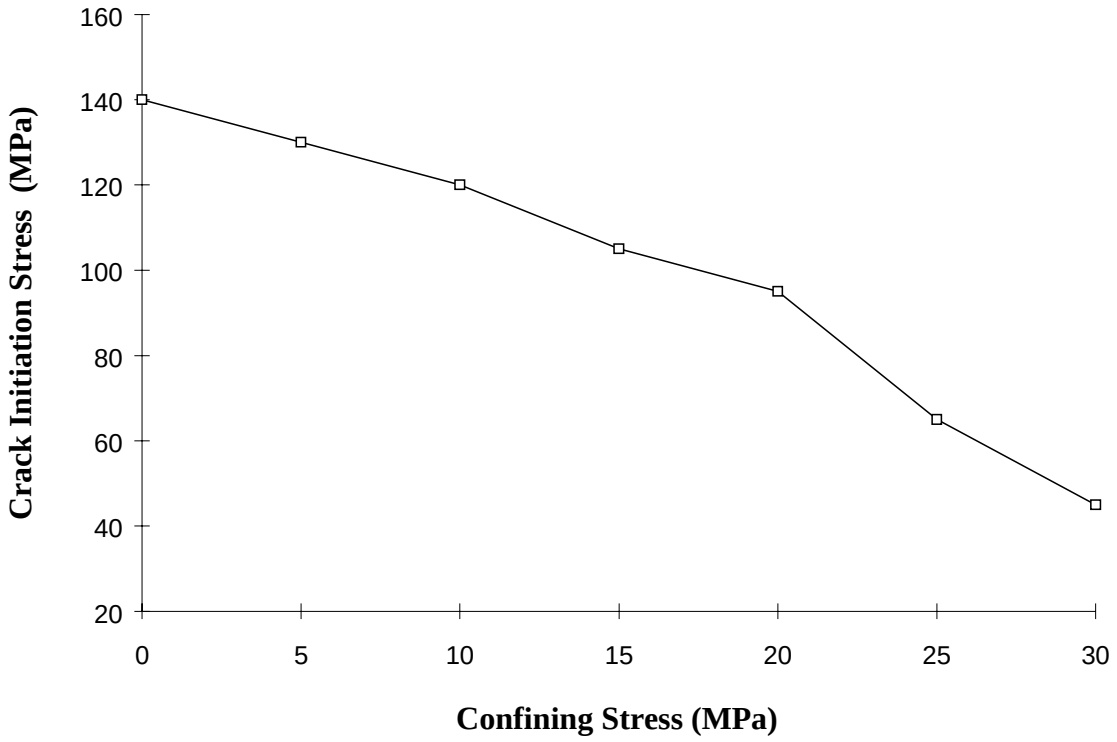

Figure 5.10 Effect of confining stress on crack initiation for a central crack in a multiple crack array.

5.3.1 *Correlation of modelling results with laboratory observations*

The modelling results suggest that with the addition of confining stress the stress level required to achieve crack initiation should be lower than that required under uniaxial loading. It would also appear that, although cracks growing in a triaxial stress field may be smaller in length due to the restraining effect compressive stress shadows have on crack growth, the number of cracks, or crack density, would be greater than that in a uniaxial stress field due to the ease with which they initiate. These findings are supported by crack counting studies using optical microscopes and scanning electron microscopes (SEM) on thin sections taken from rock samples previously loaded through uniaxial and triaxial laboratory testing. Thin section studies by Kwong (1983) and Bezys (1984) indicate that crack density is higher in samples tested triaxially than those tested uniaxially. Wawersik and Brace (1971) and Kranz (1983) both observed an increase in crack density with the addition of confining stress. Hugman and Friedman (1979) noted that as the confining pressure is increased the density of microcracks developing before failure also increases.

Studies comparing the lengths of cracks in samples tested uniaxially and triaxially are more limited. Model studies indicate that, due to the adverse conditions created by stress shadows under triaxial conditions, crack lengths will be small relative to those found for the uniaxial case. Similar results were found by Dey and Wang (1981) using two-dimensional, analytical, stress inhomogeneity models. They noted that with the addition of confining pressure, axial crack growth was strongly suppressed. Observations made on Indiana limestone by Myer *et al*. (1992) also substantiate these results. In their studies, visual inspection revealed that the dominant micromechanical process associated with failure under uniaxial conditions was the growth of long extensile cracks. They found that the addition of confining pressure limited the extent of stable crack growth and limited the amount of crack interaction. Based on these observations, Myer *et al*. (1992) concluded that lack of confinement results in lower densities of longer extensile cracks which eventually interact to form macrofractures, while confined compression produces more uniform populations of shorter cracks due to a lack of crack interaction. Modelling results presented earlier demonstrate that in a

multiple crack array under triaxial loading conditions, stresses around a crack tip may be compressive and inhibit other cracks extending into their localized compressive stress field.

5.4 Zone of Influence of Adjacent Cracks

The zone of influence of adjacent cracks depends upon their relative size and position (or distance away) from each other. Using the multiple crack geometry (Figure 5.5), cases for varying crack lengths and crack distances were analyzed for both uniaxial and triaxial loading conditions. In terms of uniaxial loading, results show that as the peripheral cracks are moved away from the central crack, the tensile stresses surrounding the middle crack tip decrease. This reduction increases the applied axial stress required to initiate cracking (Figure 5.11). When the peripheral cracks are between 5 and 10 mm from the central crack, a compressive stress shadow forms between the middle and peripheral cracks and results in a higher crack initiation stress than that for a single crack (i.e. an isolated crack without preexisting cracks). With no peripheral cracks, the crack initiation stress for a single 5mm crack under uniaxial loading is approximately 130 MPa (Figure 5.6). This uniaxial crack initiation stress is once again achieved under the multiple crack conditions when the peripheral cracks are separated approximately 45 mm from the middle crack. These results indicate that the zone of influence of the stress shadows resulting from the inclusion of two cracks 15 mm in length and 0.5 mm in width is approximately 45 mm on either side of the central crack.

Shortening or lengthening of the peripheral cracks also effects crack initiation. The effect is dependent on the interaction between the stress shadows surrounding the middle crack and peripheral cracks. Under uniaxial loading conditions, tensile stress zones form around both the middle and outer crack tips when the peripheral crack lengths are small relative to the middle crack length resulting in reduced crack initiation stresses (Figure 5.12). As the peripheral cracks are lengthened, the stresses around them change from tensile to compressive. The appearance of these compressive stress zones occurs between crack lengths of approximately 7 mm and 9 mm. At crack lengths

greater than 10 mm the stress shadows around the outer cracks become tensile again with a resulting drop in the required crack initiation stress.

These findings indicate that the relative position and size of peripheral cracks have a significant effect on the crack initiation and propagation process. Similar results have been described by other authors. Using photoelastic models, Bombolakis (1968) found that the stress required for initial crack growth depends strongly on the crack spacing. Similar to the results shown in Figure 5.11, Bombolakis (1968) showed that as the crack spacing decreased, the applied stress required to initiate crack growth also decreased. Peng and Oritz (1973) found in their studies that the initiation and propagation of individual cracks under compression was predominantly governed by the local configuration of the microstructure. Similarly, Kranz (1979) and Dey and Wang (1981) noted that significant changes in the tensile stresses near the crack tip occur as a function of both crack separation and relative orientation. In general, cracks can inhibit or promote the propagation of adjacent cracks depending on their relative positions, size, and the degree of interaction between the induced crack tip stress concentrations. These findings may help to provide insight into explaining grain size effects, with respect to the microfracturing process and rock strength, since grain boundaries effectively control the initial crack geometries (grain size effects are further explored through laboratory testing techniques in Chapter 6).

The application of confining pressure was seen to significantly alter the zone of influence and the behaviour of cracks within it. Initially, as the peripheral cracks move away from the central crack, the higher tensile stress zone surrounding the propagating crack resulting from the stress drop induced in between the two peripheral cracks remains, thus keeping the crack initiation stresses lower than in the uniaxial case (Figure 5.13). However, once the adjacent cracks are separated sufficiently for the pressure drop to disappear, triaxial loading has an adverse effect and requires a higher applied load to initiate cracking since the deviatoric stresses are lower than in the uniaxial case. The farther away the outer cracks are located, the more the triaxial load prevents crack initiation, thereby requiring higher axial loads for crack initiation.

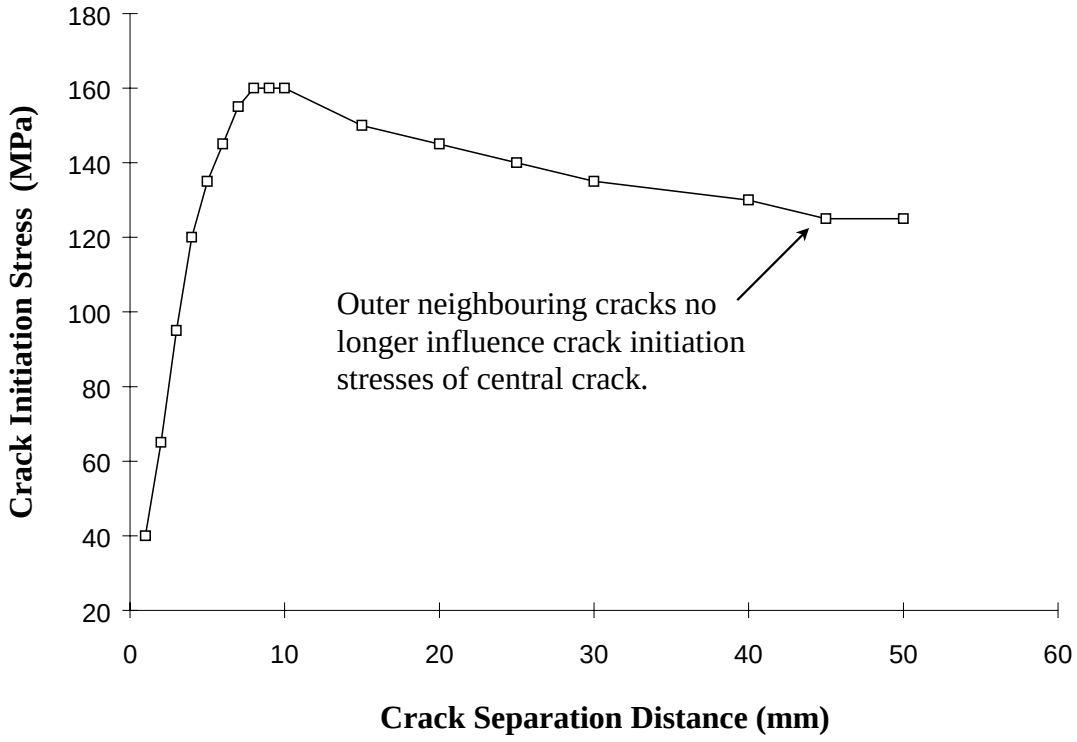

Figure 5.11 Zone of influence of peripheral cracks on the crack initiation stress for a central crack in a uniaxial stress field. Zone of influence is taken as the horizontal distance separating the central crack from the two neighbouring cracks.

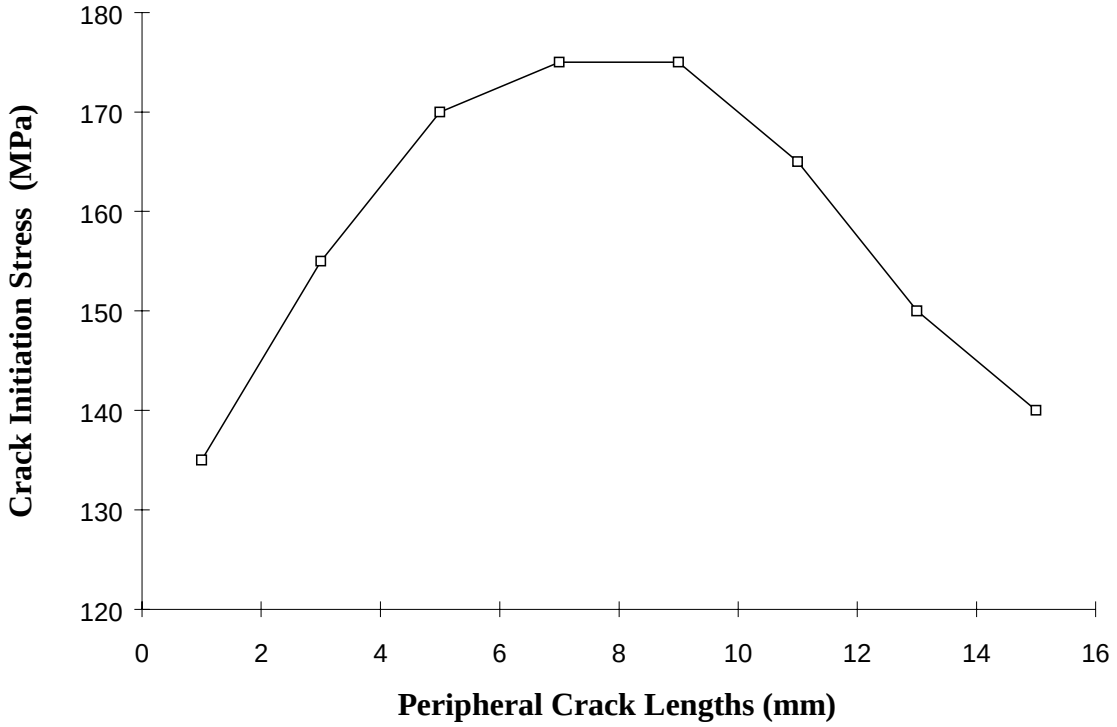

Figure 5.12 Influence of peripheral crack length on the crack initiation stress level for a central crack in a uniaxial stress field.

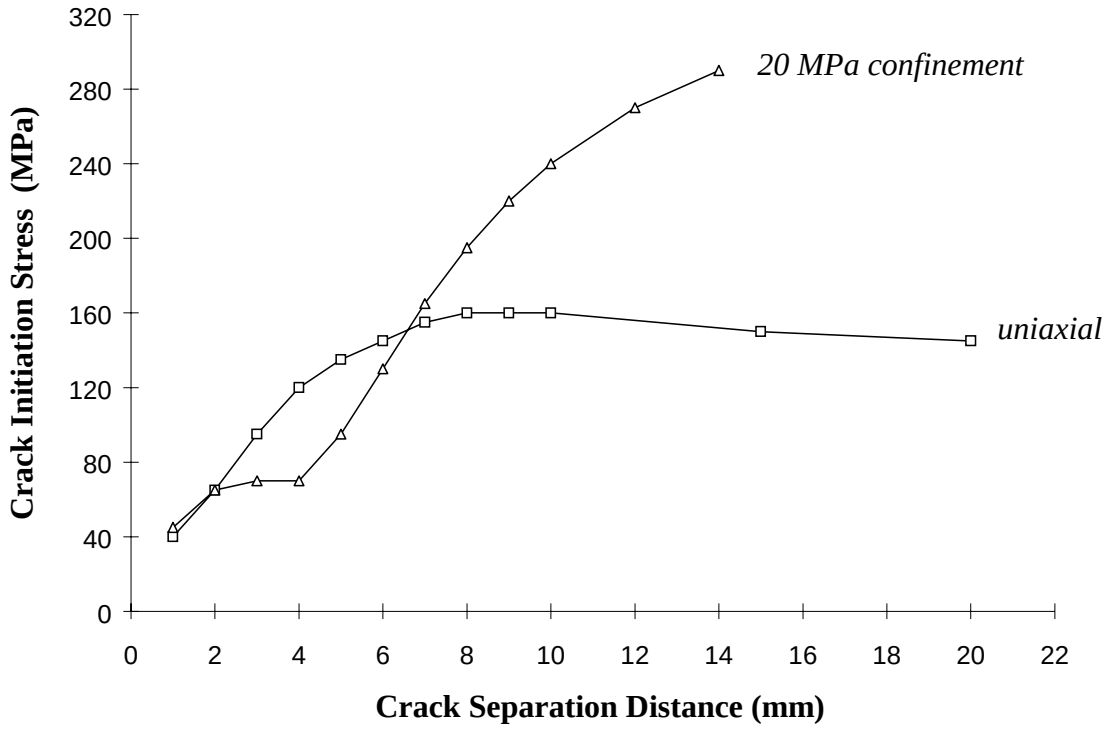

Figure 5.13 Zone of influence of peripheral cracks on the crack initiation stress for a central crack in a uniaxial and triaxial stress field. Zone of influence is taken as the horizontal distance separating the central crack from the two neighbouring cracks.

5.5 Chapter Summary

The brittle fracture process, established in Chapter 4, encompasses the initiation, propagation and coalescence of cracks leading up to rock failure. Boundary element techniques were used to model these processes, concentrating on the interaction of axial cracks. This analysis utilized a fracture criterion to develop relationships between stable crack length and applied stress for elliptical crack geometries involving both single and multiple cracks.

Results suggest crack initiation and propagation may either be inhibited or promoted depending on the geometry of the crack array used and the loading conditions applied. Under uniaxial loading conditions, the multiple crack geometry modelled required higher stresses to *initiate* cracking but lower stresses to *maintain* crack propagation, relative to the single crack geometry. These effects were found to be dependent on the interaction between localized crack tip stresses associated with the adjacent cracks.

The addition of confining stresses produced the opposite effects for the multiple crack array models. The localized stresses between adjacent cracks were seen to interact such that the initiation of a central crack between two neighbouring cracks occurred at lower applied loads than for the uniaxial case. However, higher applied loads were required for crack propagation to continue. These results suggest that although cracks growing in a triaxial stress field will be smaller in length due to the restraining effects confining stresses have on crack propagation, the number of cracks would be greater than that in a uniaxial stress field due to the ease with which they initiate. These findings are supported by crack counting studies, scanning electron microscope observations and other numerical modelling studies.

The zone of influence between adjacent cracks was seen to depend upon their relative size and separation distance. As with the previous models, neighbouring cracks would act to either inhibit or promote crack initiation and propagation depending on the degree of interaction between the induced crack tip stresses. These effects were also dependent on the loading conditions applied.

Results from this study are of relevance in resolving the effects grain size and sampling disturbance have on the brittle fracture process. Numerical crack array models using crack size and separation distance as variables can conceptually be related to grain size and crack density. These effects are to be explored in Chapter 6 using laboratory test data. It should be noted that the assumptions used in this analysis partially limit the modelled results to a number of specific cases. In terms of the crack model used (i.e. elliptical), further study would be required to determine the sensitivity of the boundary element results to the input geometry. It is conceivable that the elliptical crack geometry could also be used to represent the latter stages of crack development for a Griffith type crack (i.e. inclined) as the wings of the Griffith crack propagate in the axial direction. However, this assumption should be tested to ascertain its validity. The material properties used in this study should also be tested to determine the sensitivity of the model to a range of different input values. Given the nature of the boundary element solution, however, only the magnitudes of the modelled results should change and the general relationships regarding crack interaction should hold true.

CHAPTER 6

EXTENSION OF BRITTLE FRACTURE THRESHOLDS FOR VARIED MATERIAL STATES

Identifying and characterizing the stages of brittle fracture in a loaded test sample required that the methodologies and techniques adopted be first validated using a near ideal material. Subsequently, the findings presented in Chapter 4 were obtained through laboratory tests performed solely on samples of pink granite from the 130 m level of the URL. As a reference material, the pink granite behaved as a near isotropic, linear elastic, brittle material with relatively little stress-induced sampling disturbance. This provided a means to clearly demonstrate the ability of the detection techniques developed in Chapter 3 to identify and isolate the various thresholds of the brittle fracture process. However, in order to evaluate the versatility and full potential of these techniques, additional testing was required using less than ideal materials. Several series of laboratory tests were therefore conducted using rock types of varying grain size, mineralogy, sampling disturbance and rheological behaviour. Due to the large contrast in behaviour exhibited by the different materials tested, a rigorous methodology based on the results from Chapter 4 was defined to help in establishing the different thresholds of crack development (Table 6.1). The following sections present the results and analysis from these tests.

6.1 Effects of Grain Size

The structure of the Lac du Bonnet batholith is such that rock types of three different grain sizes may be encountered. Referred herein as Lac du Bonnet grey granite, granodiorite and pegmatite, these samples represent a large variation in grain size while still falling within the International Union of Geological Sciences (IUGS)

Table 6.1 Methodology used to establish the different thresholds of crack development.

Crack Threshold	Description
Crack Closure	The crack closure threshold was established using the axial stiffness curve. The threshold value was determined as the point where the axial stiffness curve shifted from incrementally increasing values (i.e. non-linear behaviour) to constant values (i.e. linear behaviour).
Crack Initiation	The crack initiation threshold was based on several criteria. The primary criterion involved picking the approximate interval in which the AE event count first rose above the background level of detected events with respect to the beginning of the test. The exact value within this interval was then picked at the point in the AE event rate and "energy" rate where values began to significantly increase. This point was also checked against any significant breaks in the volumetric stiffness curve.
Secondary Cracking	The secondary cracking threshold was taken as the first significant increase in the AE event rate following crack initiation, which in turn, coincided with the continuous detection of AE activity. This point was checked against any large increases in the event "energy" rate and notable breaks in the volumetric stiffness curve.
Crack Coalescence	Crack coalescence was taken from the approximate interval in which the axial stiffness curve departed from linear behaviour. This point was checked against large irregularities in the volumetric stiffness curve. In addition, changes in the AE event rate and the different event properties would sometimes coincide with this point.
Crack Damage	The crack damage threshold was taken as the point in the volumetric stiffness curve where stiffness values changed from positive to negative thereby marking the reversal of the volumetric strain curve.

classification of a granite (Read, 1994). Grain size, when equated with the theoretical crack length, has been shown through Griffith's formulation and the Griffith's locus (Chapter 2) to be related to the material cohesion and strength. This variation in grain size could therefore have a serious impact on tunnel stability when either two or three of these rock types are encountered in the same excavation.

6.1.1 Geological Description of URL Granite, Granodiorite and Pegmatite

Test samples of grey granite, granodiorite and pegmatite (Figure 6.1) were obtained from core retrieved from the 240 m level of the URL. This ensured that each rock type would have been exposed to similar *in situ* stress conditions and that any differences in material behaviour must be attributed to the individual strengths of each rock type. The grey granite has been described as homogeneous and equigranulaur (Brown *et al*., 1989), although some samples were found to be slightly porphyritic containing moderately larger feldspar phenocrysts. The average grain size was approximately 3 mm. Interspersed with the grey granite of the URL, primarily below 200 m, are granodiorite dykes which are similar in mineralogy with the exception that the granodiorite has slightly less feldspar and more biotite. The granodiorite is fine-grained and relatively equigranular with an average grain size of 1 mm. Descriptions of the mineralogy and grain sizes for these two rock types are given in Table 6.2. The third rock type tested appears on the 240 m level as pegmatitic granite dykes. These pegmatites are large grained and inequigranular hosting large phenocrysts of feldspar. Grain sizes in the pegmatite range from 10 to 40 mm with an approximate average of 20 mm.

Initial testing of these samples revealed that, although the samples are similar in terms of their mineralogical composition, the variation in grain size results in differing index properties. For example, a relationship between grain size and density was found where sample density decreases with increasing grain size (Table 6.3). A similar relationship can be found in terms of the measured acoustic velocities. P- and S-wave velocities for the granite samples were found to be approximately 15% smaller than those for the finer grained granodiorite (Table 6.3). This would be expected since

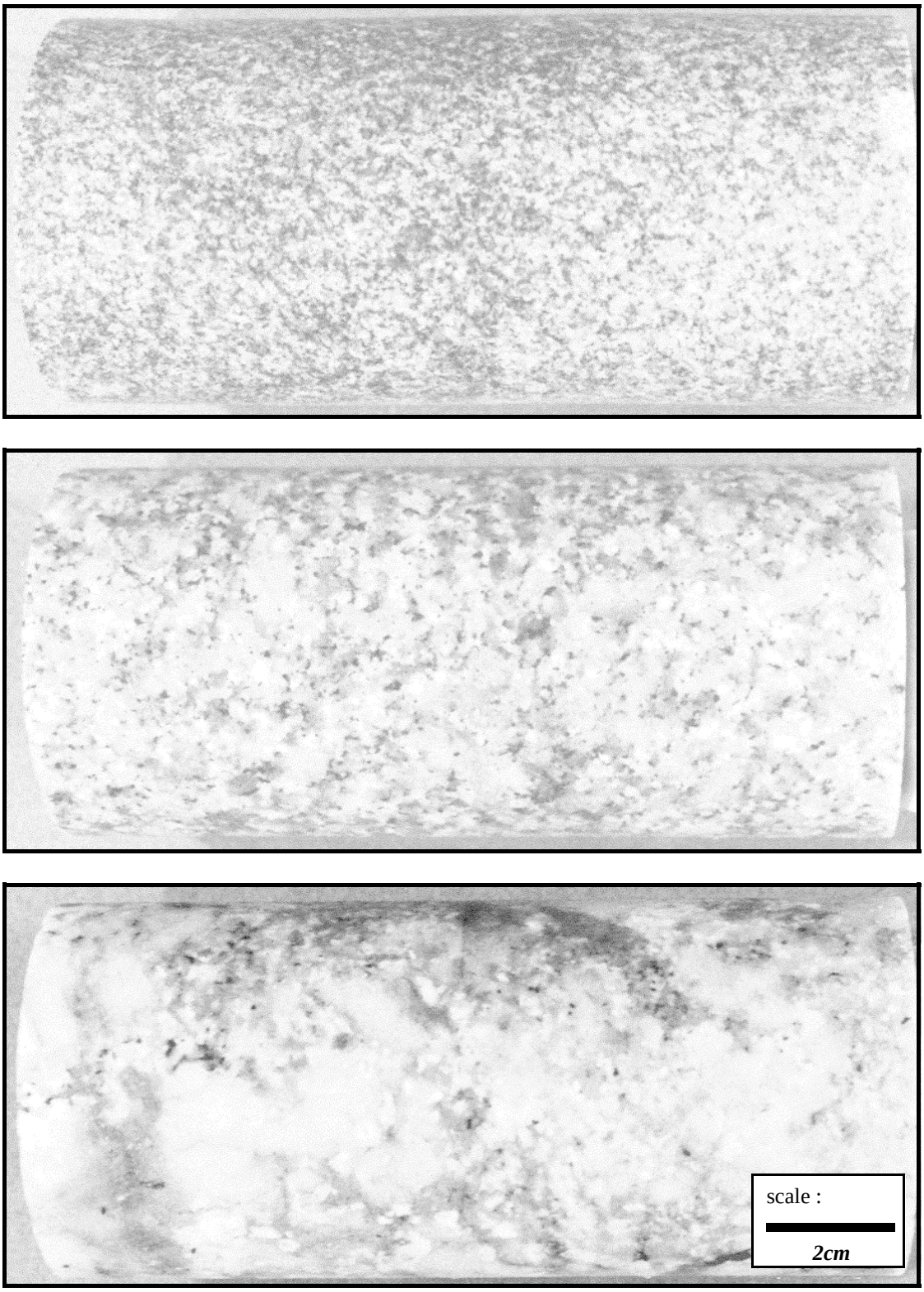

Figure 6.1 240 m level URL samples showing varying grain size: granodiorite (top), grey granite (middle), and pegmatite (bottom).

acoustic velocities generally increase with increasing sample density. Pegmatite test samples, however, contradict these findings. The pegmatite was found to have the lowest density of the three rock types tested yet had similar velocities to those of the granodiorite samples. These larger than expected velocities can be attributed to the much larger crystals found in the pegmatite, as can the large standard deviation seen in the test results. Larger crystals mean fewer grain boundaries which act to reduce the velocity of the acoustic pulse. For example, measured acoustic velocities of 6240 m/s (V_P) and 3180 m/s (V_S) were obtained for one of the pegmatite samples which contained two large feldspar crystals measuring over 40 mm in diameter and constituting half of the sample. In terms of P-wave values, the recorded velocity for the sample was approximately the same as that given by Goodman (1989) for a single crystal of the mineral plagioclase feldspar (V_P = 6250 m/s). Thus it should be noted that in such extreme cases, the physical properties of the individual minerals might control or partly control the overall behaviour of the sample.

Table 6.2 Composition and average grain sizes for URL granite and granodiorite (after Read, 1994).

	K-Feldspar		**Plagioclase**		**Quartz**		**Biotite**	
Rock Type	mineral (%)	grain size (mm)	mineral (%)	grain size (mm)	mineral (%)	grain size (mm)	mineral (%)	grain size (mm)
Granite	45	3.7	20	3.1	30	1.8	5	0.9
Granodiorite	35	1.0	25	1.1	30	0.7	10	0.6

Table 6.3 Summary of density and acoustic velocity values for 240 m level URL samples (standard deviation is in parentheses).

Material Parameter		Granodiorite	Grey Granite	Pegmatite
Samples Tested		5	5	5
Density	ρ (g/cm^3)	2.66 (± 0.00)	2.62 (± 0.01)	2.59 (± 0.02)
Acoustic Velocity	V_P (m/s)	5240 (± 70)	4445 (± 295)	5295 (± 545)
	V_S (m/s)	3245 (± 60)	2905 (± 85)	3025 (± 125)
	V_P / V_S	1.61	1.53	1.75

6.1.2 Grain Size Dependent Deformation and Fracture Characteristics

Strain gauge and acoustic emission data were subsequently analyzed to determine the effects grain size had on the mechanical properties of the rock types tested. The Young's modulus was found to decrease with increased grain size. Average values for the grey granite and pegmatite were found to be 5% and 11% lower, respectively, than those for the granodiorite (Table 6.4). This suggests that the degree of intercrystalline deformation, plastic flow, dislocation glide and other similar sliding mechanisms associated with more plastic type materials, slightly increases with increasing grain size. Similar observations, but with significantly higher strains, were made by Fredrich and Evans (1990) for marble where an association was found between grain size, semibrittle flow and plastic yielding.

Examination of secant modulus values provided further insight into the relationship between grain size and stress-induced fracturing. Calculations of the secant modulus, which includes the non-linearity in axial strain during initial loading and subsequent crack closure, can be used as an indicator of the crack density in the sample prior to testing. The larger the disparity between the secant and Young's modulus values, the greater the initial crack density. Test values provided in Table 6.4 show that the difference between secant and Young's modulus values for the fine-grained

granodiorite is less than 1%, whereas the differences in values for the grey granite and pegmatite are 22% and 14% respectively. Since all samples originated from the 240 m level, and in most cases the same core run (i.e. within 5 m of each other), the samples would have experienced similar *in situ* stress and sampling conditions. Therefore, any differences in the degree of stress-induced sampling damage must be attributed to the individual strengths of each rock type. It then follows that the granodiorite must be considerably stronger than the granite and pegmatite, thus substantiating Griffth's empirical relationships between crack length and strength.

Table 6.4 Average elastic constants for 240 m level URL samples (standard deviation is provided in parentheses).

Material Parameter	Granodiorite	Grey Granite	Pegmatite
Samples Tested	5	5	5
Young's Modulus, E_{avg} (GPa)	67.2 (± 3.5)	63.8 (± 2.2)	60.1 (± 1.7)
Tangent Modulus, E_T (GPa)	69.4 (± 1.3)	60.3 (± 1.1)	57.7 (± 3.0)
Secant Modulus, E_S (GPa)	66.8 (± 0.9)	49.7 (± 1.9)	51.6 (± 2.0)
Poisson' Ratio, ν_{avg}	0.30 (± 0.03)	0.33 (± 0.04)	0.29 (± 0.07)

Differences in the degree of stress-induced sampling damage between the three rock types were also discernable in plots of the axial stiffness. These plots show that initial axial stiffness values for the granodiorite are 2-3 times higher than values for the granite and pegmatite (Figure 6.2). In addition, crack closure was achieved at lower stresses in the granodiorite than the grey granite (Table 6.5), confirming acoustic velocity tests which showed that the granite had a higher initial crack density. However, crack closure threshold values for the pegmatite samples were approximately the same as those for the granodiorite. These similar crack closure thresholds can be attributed to

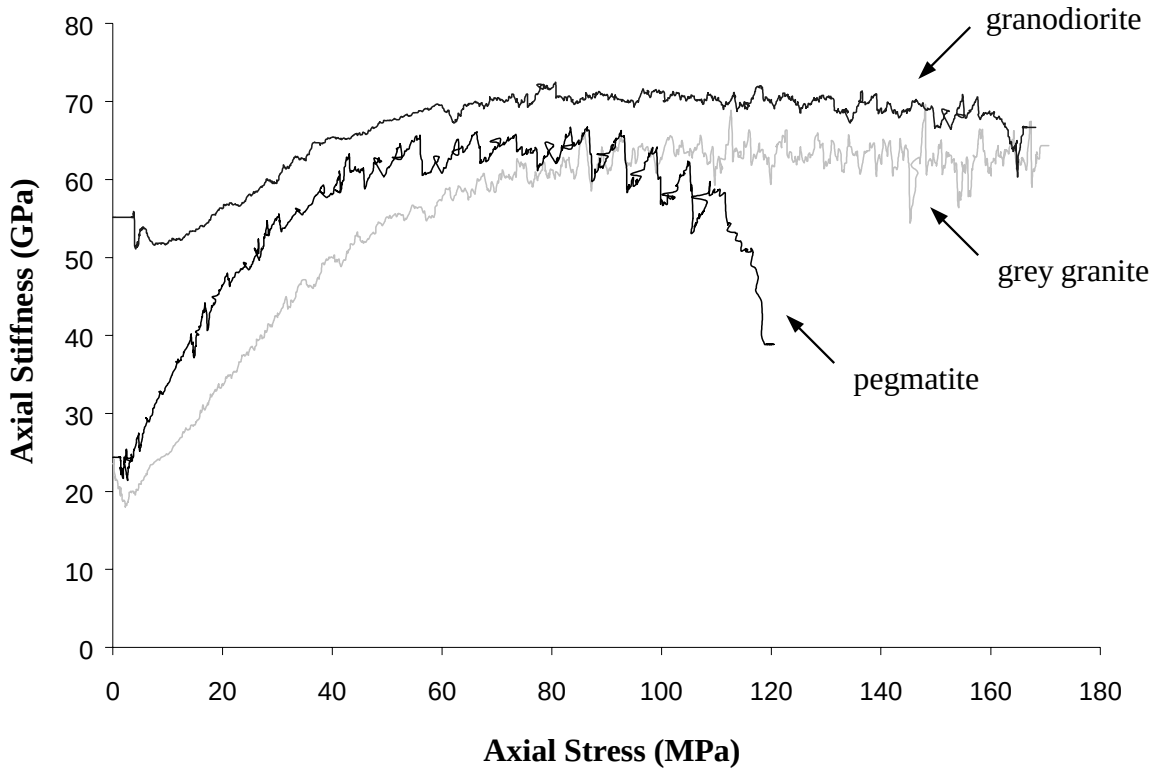

Figure 6.2 Plots of axial stiffness -*vs*- axial stress for URL 240 m level samples of granodiorite, grey granite and pegmatite.

the lower crack densities of the pegmatites, owing to their significantly larger grain sizes, as was reflected through measured P-wave velocity values. Furthermore, the lower initial axial stiffness values seen in the pegmatites attest to the longer crack lengths that would be expected with larger grains and grain boundaries.

Table 6.5 Average crack thresholds for the 240 m level URL samples (standard deviation is provided in parentheses).

Strength Parameter	Granodiorite	Grey Granite	Pegmatite
Number of Tests	5	5	5
Crack Closure, σ_{cc} (MPa)	45.6 (± 3.4)	55.6 (± 1.5)	45.2 (± 2.7)
Crack Initiation, σ_{ci} (MPa)	79.6 (± 2.7)	79.6 (± 2.3)	72.0 (± 5.9)
Secondary Cracking, σ_{ci2} (MPa)	102.8 (± 4.5)	102.8 (± 4.3)	96.0 (± 4.4)
Crack Coalescence, σ_{cs} (MPa)	164.7 (± 9.0)	127.6 (± 14.2)	104.8 (± 6.4)
Crack Damage, σ_{cd} (MPa)	194.0 (± 2.8)	147.4 (± 9.1)	113.2 (± 6.8)

The behaviour of the samples following crack closure and approximate linear elastic deformation continued in a similar pattern as observed in the 130 m level pink granites. Each of the thresholds of crack development seen in the pink granite samples were detectable in the strain gauge (Figure 6.3) and acoustic emission (Figures 6.4 and 6.5) data recorded during testing of the granodiorite, grey granite and pegmatite. Surprisingly, the crack initiation and secondary cracking thresholds for the granodiorite were the same as those seen in the grey granite. This would seem to suggest that the initial stages of cracking are partly independent of grain size and are more related to the feldspar and quartz mineralogy. In other words, the initial stages of detectable crack propagation are primarily intergranular as cracking begins (i.e. σ_{ci}) within the feldspar grains, followed by secondary cracking (i.e. σ_{ci2}) at higher loads within the quartz grains. A similar pattern is seen in the pegmatites, however threshold values are

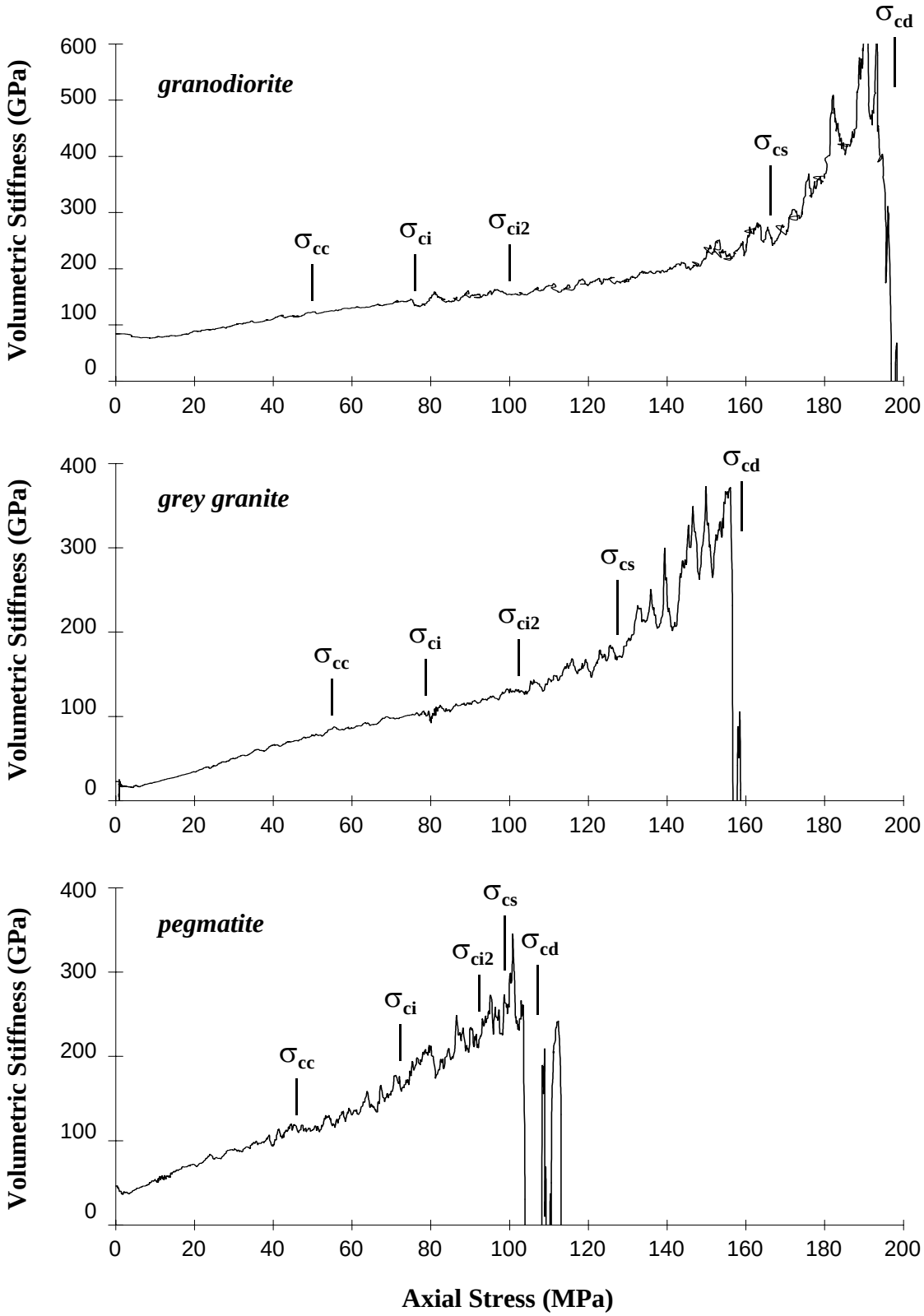

Figure 6.3 Plots of volumetric stiffness -*vs*- axial stress for URL 240 m level samples of granodiorite (top), grey granite (middle) and pegmatite (bottom).

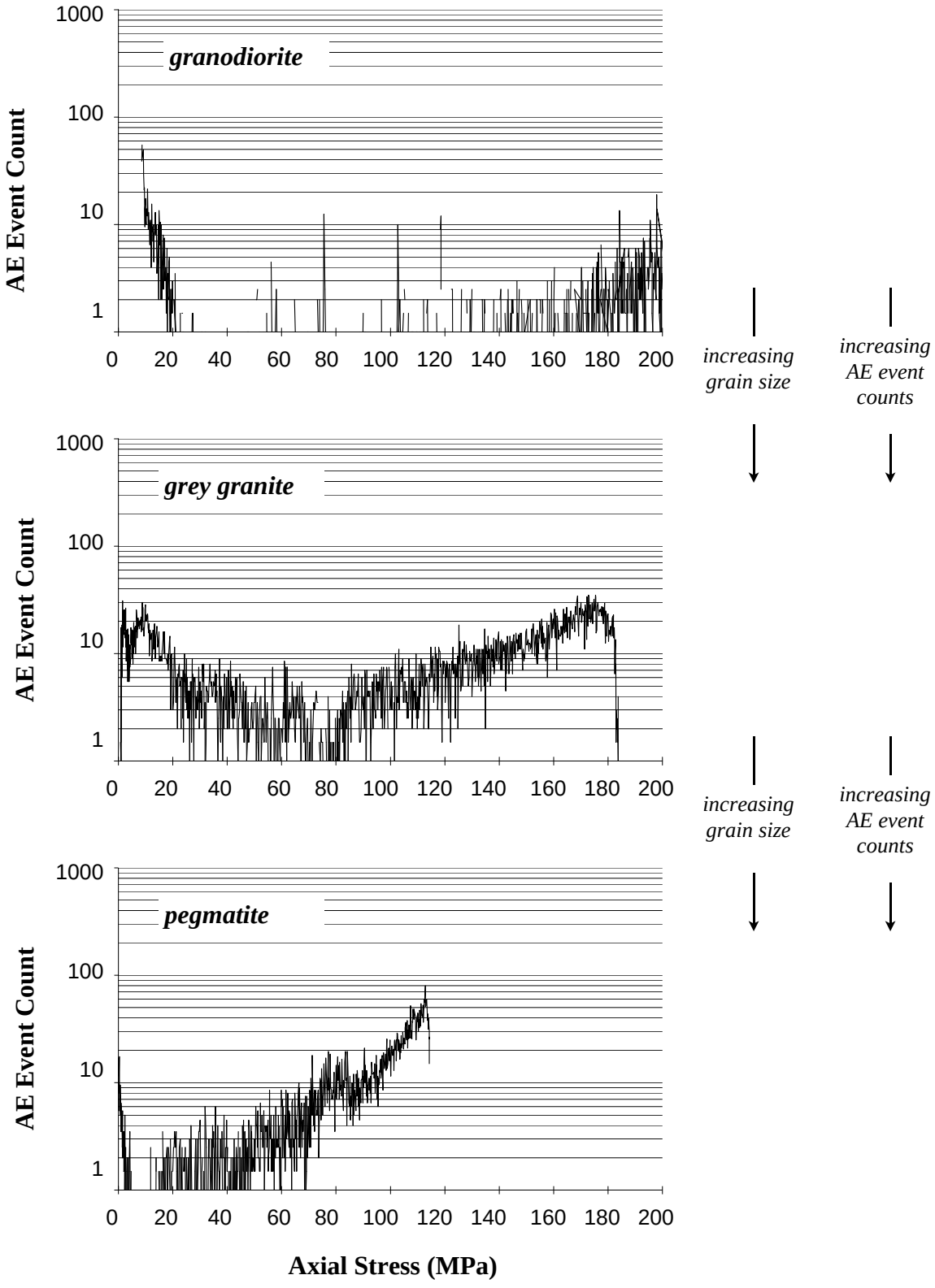

Figure 6.4 Log plots of AE event count -*vs*- axial stress for URL 240 m level samples of granodiorite (top), grey granite (middle) and pegmatite (bottom).

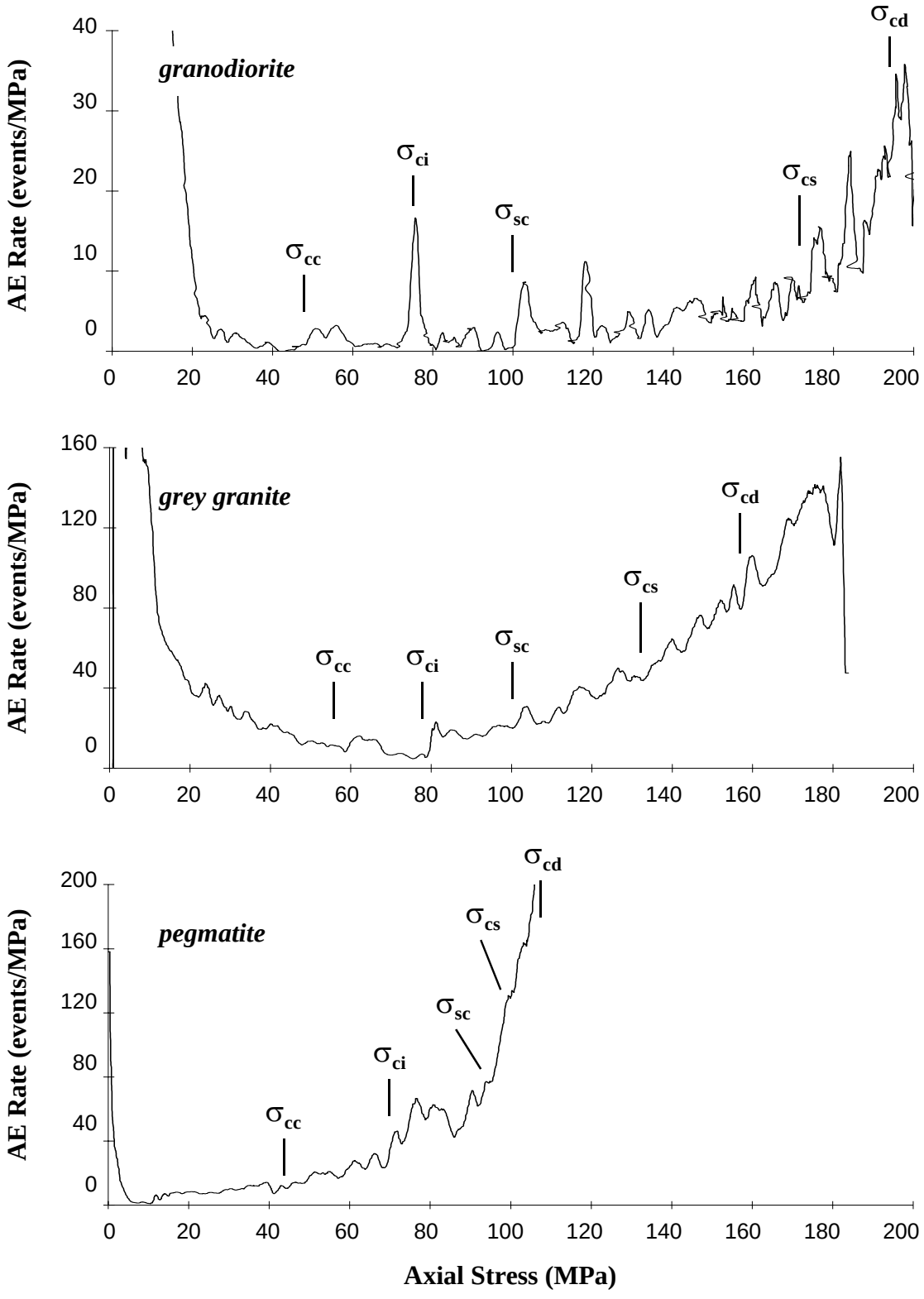

Figure 6.5 Plots of the stress dependent AE event rate -*vs*- axial stress for URL 240 m level samples of granodiorite (top), grey granite (middle) and pegmatite (bottom).

somewhat lower (approximately 10%) than those seen in the granodiorites and granites. This would seem to suggest that there exists an upper limit with respect to grain size and the strength of the individual minerals whereby the much larger grains in the pegmatites seem to induce fracturing at lower stresses. It should also be noted that this response may be related to the size of the sample relative to the maximum grain size (i.e. the measured response of samples in which the total diameter is less than 10 times the maximum grain size may be more indicative of the properties relating to the individual constituent minerals rather than the behaviour of the assemblage). The difference in grain size between the granodiorite and grey granite, on the other hand, does not seem to significantly influence when intergranular fracturing begins.

Grain size appears to have a significant effect in terms of the volume of AE events detected. Figures 6.4 and 6.5 show that the number of detected AE events drastically decreases with decreasing grain size. Tests involving the granodiorite produced approximately 90% fewer AE events than those for the pegmatites, and 60% fewer events in comparison to the grey granites. Testing of the grey granites resulted in approximately 60% fewer events than those recorded for the pegmatites. In all three cases, a significant number of events were recorded during crack closure and prior to the crack initiation threshold implying that events are being produced through grain boundary movements. SEM observations (Chapter 4) confirmed that an almost equal number of fractures originated within the feldspar grains at low stresses as along grain boundaries. According to Griffith's theories, these grain boundary cracks should be highly sensitive to grain size since the length of the grain boundary controls the magnitude of the stresses acting at the crack's tips. Larger grain boundaries critically aligned to the direction of loading will initiate before smaller ones. It then follows that the increase in the number of detected events with grain size is due to the increasing number of cracks originating along grain boundaries.

Further analysis reveals that grain size also has a significant effect on the crack coalescence (σ_{cs}) and crack damage (σ_{cd}) thresholds. Figure 6.3 and values in Table 6.5 show that the crack coalescence values for the grey granite and pegmatite decrease by 23% and 36%, respectively, when compared to values for the granodiorite. Likewise,

values for the crack damage threshold decrease by 21% and 42%, respectively, when comparing grey granite and pegmatite values to the granodiorite. These results contrast those obtained for the crack initiation and secondary cracking thresholds which remained relatively constant for all three rock types. In other words, grain size had minimal effects in terms of when intergranular cracking began, but the behaviour of the cracks during propagation was highly influenced by grain size.

Insight into crack behaviour following crack initiation may also be gained by examining plots of the calculated AE elastic impulse "energy" rate. Figure 6.6 shows that event "energy" values for the granodiorite are relatively small when compared to values for the grey granite and pegmatite. This provides valuable information with respect to extent that the cracks are propagating. According to Griffith's criterion and the Griffith crack locus (Chapter 2), the amount of elastic energy released during crack propagation increases with increasing crack length extension (Figure 6.7). AE event "energy" values in Figure 6.6 suggest that crack propagation in the granodiorite is more limited, whereas significant propagation in the grey granite and pegmatite samples occurs resulting in larger releases of kinetic energy. It would therefore appear that an important factor responsible for limiting crack propagation is grain size. Numerical modelling results presented in Chapter 5 showed that propagating cracks in close proximity to one another could interact in such a fashion as to inhibit crack propagation. Furthermore, this effect was seen to diminish with increasing crack separation distances, which in turn, can be related to increasing grain sizes. Decreasing crack coalescence and crack damage thresholds seen in the granite and pegmatite samples, therefore, could be reflecting the ease at which cracks are propagating and interacting leading up to crack coalescence and unstable crack propagation at respectively lower stress levels. Conversely, crack propagation and coalescence in the granodiorite would be more limited due to the smaller grain size and the closer proximity of the propagating cracks, thereby resulting in higher strengths.

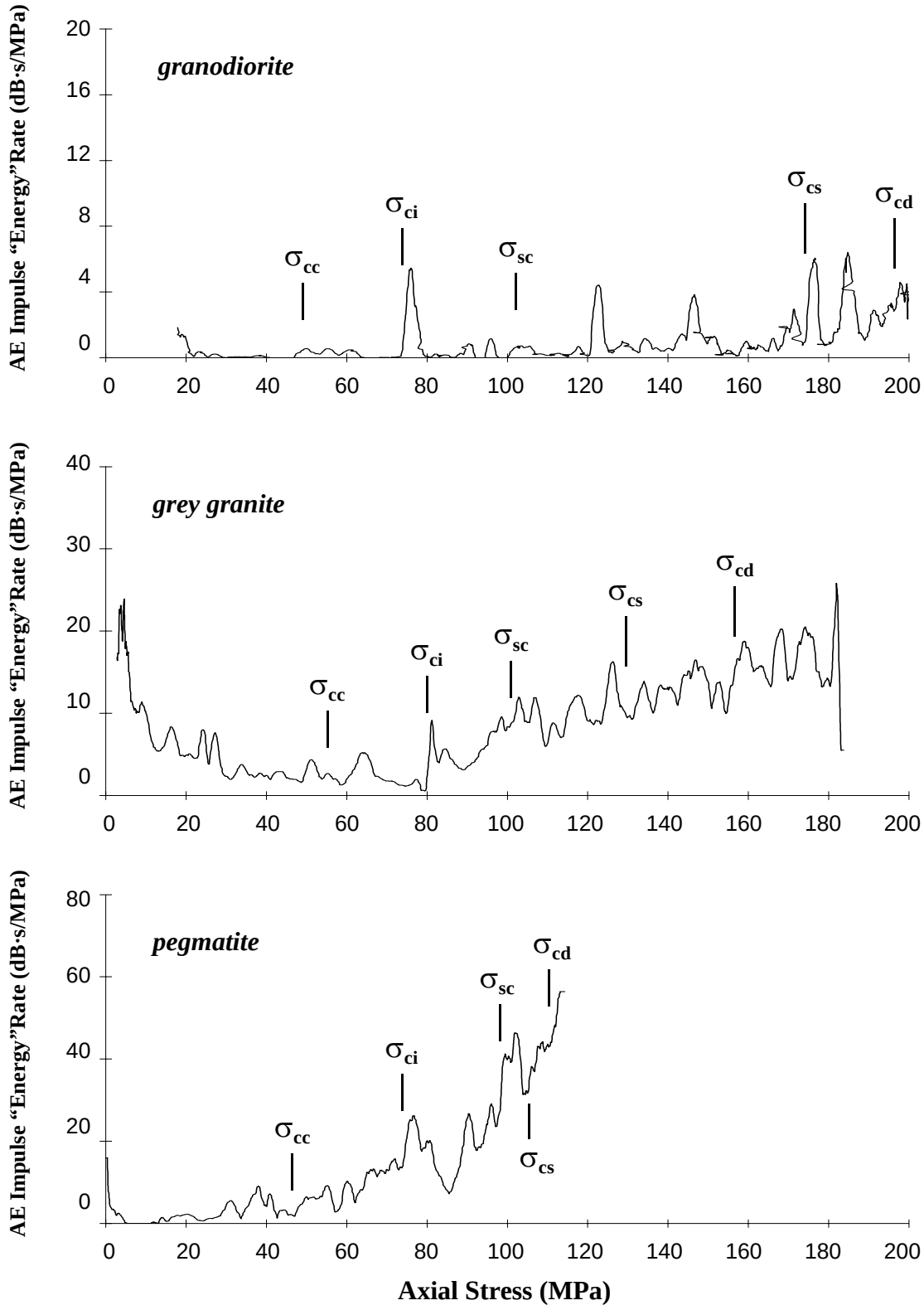

Figure 6.6 Plots of the AE elastic impulse "energy" rate -*vs*- axial stress for URL 240 m level samples of granodiorite (top), grey granite (middle) and pegmatite (bottom).

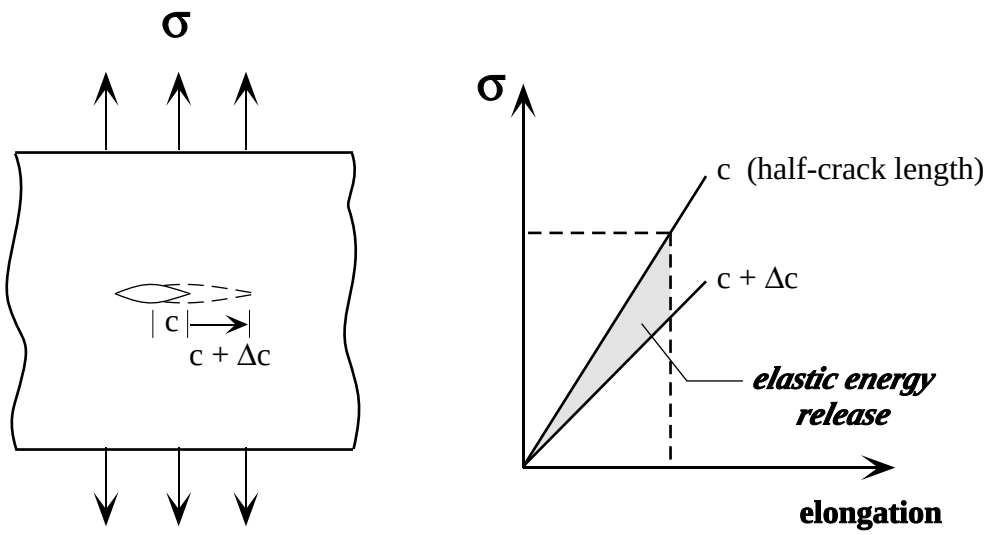

Figure 6.7 The Griffith criterion, for a plate with fixed ends, showing the elastic energy released upon crack elongation (after Broek, 1986).

6.2 Effects of Sample Disturbance

The process of drilling and recovering core for laboratory testing often results in sample disturbance through stress-induced microfracturing altering the physical properties of the rock. This disturbance may be the result of mechanical abrasion and vibration due to the drilling process itself, and/or through stress relief cracking in cases where the samples are retrieved from high *in situ* stress regimes. In general, the extent of this disturbance is often a function of drilling depth and, to a lesser degree, borehole orientation. For example, *in situ* stresses generally increase with depth resulting in higher crack densities in the retrieved samples. Martin and Stimpson (1994) note that it then becomes possible for samples of the same rock type, but obtained from different *in situ* stress regimes, to have drastically different mechanical properties. Furthermore, the mechanical properties of the rock can profoundly change whereby the properties of the tested samples are quite different from those of their *in situ* state. It was therefore decided that a series of laboratory tests be conducted to see what effects sample disturbance had on the brittle fracture characteristics of the Lac du Bonnet granites.

Test samples of Lac du Bonnet granite were obtained from three different working levels of the URL located at depths of 130, 240 and 420 m (Figure 3.14). These levels represent three different *in situ* stress domains each characterized by differing stress magnitudes and orientations. Martin (1993) and Read (1994) describe these regimes as varying from a low stress domain (130 m level) associated with stress relief jointing, to a transitional zone (240 m level) with moderate stresses, to a highly stressed region (420 m level) in unfractured rock. Values of the *in situ* stress magnitudes for these levels, as reported by Martin and Stimpson (1994), are provided in Table 6.6. In addition to the granites, samples of the finer grained granodiorite from the 240 and 420 m levels of the URL were also tested. These tests allowed for further comparisons to be made with respect to the effects of grain size on the degree of induced sampling disturbance.

Table 6.6 Approximate major (σ_1) and minor (σ_3) principal stress magnitudes for the three *in situ* stress domains of the URL (after Martin and Stimpson, 1994).

URL Level	σ_1 (MPa)	σ_3 (MPa)
130 m Level	10 - 20	5 - 10
240 m Level	25	12
420 m Level	55	14

6.2.1 SEM Observations and Acoustic Velocity Results

Prior to uniaxial compression testing, two samples each of 130 m, 240 m and 420 m level URL granite were set aside from which thin sections were prepared. SEM analysis of these sections showed that the density of observed microcracks significantly increased with sampling depth. Whereas visible cracks were difficult to find in thin sections of 130 m and 240 m level granite, numerous cracks were visible in sections of 420 m level granite. Estimates of crack density between these thin sections varied by three orders of magnitude (Table 6.7). Furthermore, thin sections of 420 m granite contained approximately five times more cracks than thin sections prepared from samples of 130 m level granite which had been previously loaded past the crack damage threshold. This was unexpected since the maximum loads experienced by the 130 m level granite samples during testing were approximately four times greater than those experienced by the 420 m level granite *in situ*.

The most notable difference between these granites, was the high proportion of fractured quartz grains seen in the 420 m level sections (Figure 6.8). Although intergranular fractures within quartz grains were observed in sections from the tested 130 m level samples, these fractures were often singular in number and long in length. In other words, the fractures induced by uniaxial compressive loading were few in number and grew parallel to the direction of loading until they coalesced with one or two other neighbouring cracks. Conversely, the fractures observed in sections taken

from the untested samples of the 420 m level have a shattered appearance to them. Although a preferred orientation can sometimes be seen in certain quartz grains, these cracks are often intersected by a number of other cracks orientated at a variety of angles (Figure 6.8). Overall, these fractures appear to have formed due to high tensile stress gradients which may have been acting in the sample during stress relief (i.e. anelastic expansion) following drilling and core retrieval. It should also be noted that a number of these cracks may have developed *in situ* due to high deviatoric stresses.

Table 6.7 Estimates of crack density from SEM observations of 130, 240 and 420 m level URL granite. Crack densities are calculated as the average number of cracks counted over a 1 mm by 1mm area.

URL Level	Minimum Count (cracks/mm^2)	Maximum Count (cracks/mm^2)
130 m Level	0.005	0.01
130 m Level *	1	5
240 m Level	0.01	0.05
420 m Level	10	20

* samples loaded in uniaxial compression prior to analysis.

The heavily fractured state of the 420 m level granite was further reflected in acoustic velocity measurements. Results from these measurements indicate a significant drop, approximately 30%, in both P- and S-wave velocities for the 420 m level samples relative to those from the 130 m level (Table 6.8). These results compare well with those presented by Martin and Stimpson (1994). Overall, P-wave velocities for the 130 m, 240 m and 420 m level samples decrease by 18%, 22% and 44%, respectively, when compared to the measured *in situ* value of 5900 m/s reported by Talebi and Young (1992). Similarly, S-wave values decrease by 12%, 16% and 38% when compared to the measured *in situ* value of 3440 m/s (Figure 6.9).

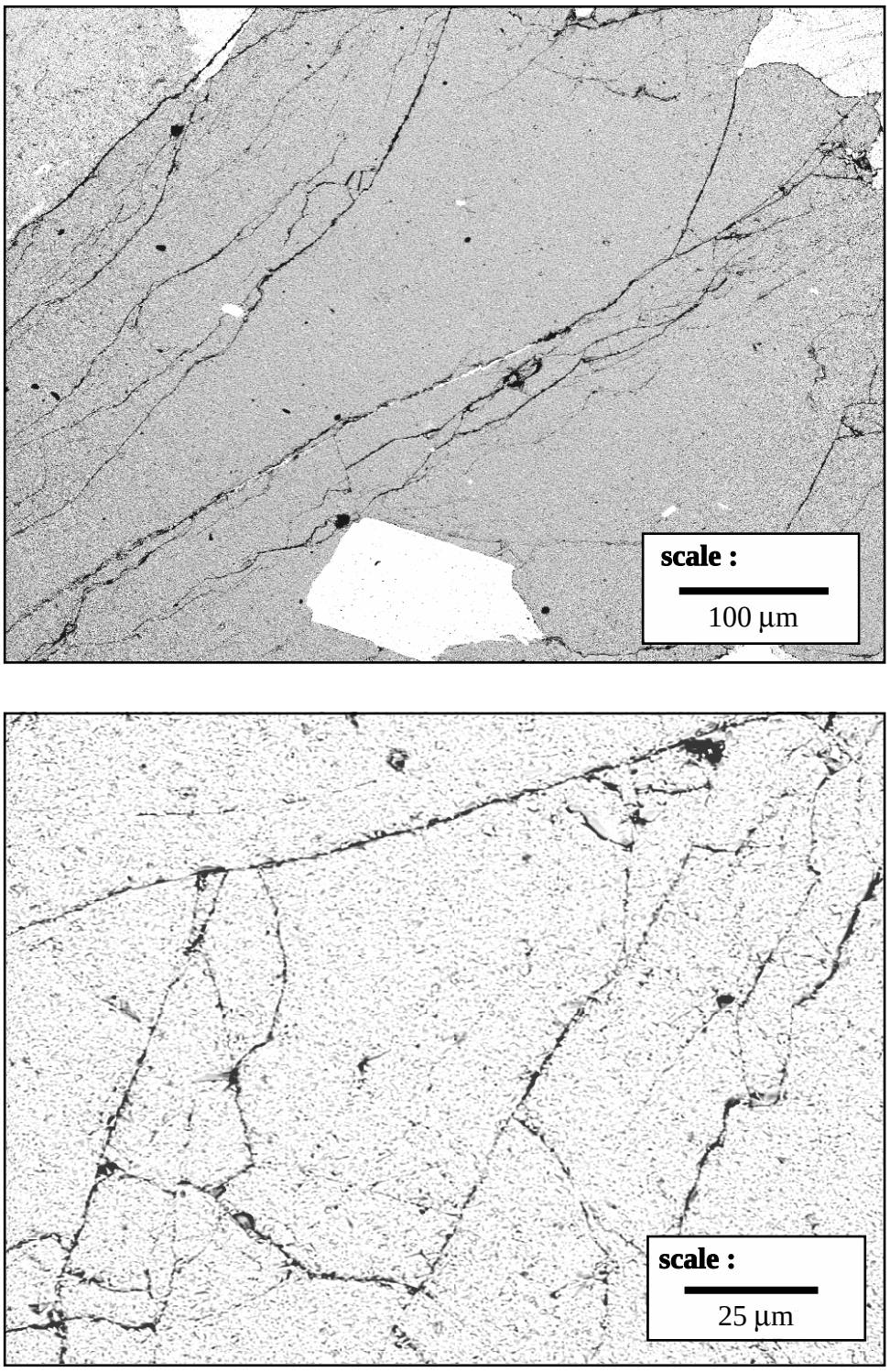

Figure 6.8 SEM image of two highly fractured quartz grains. Images are taken from sections prepared from untested samples of the 420 m level URL granite.

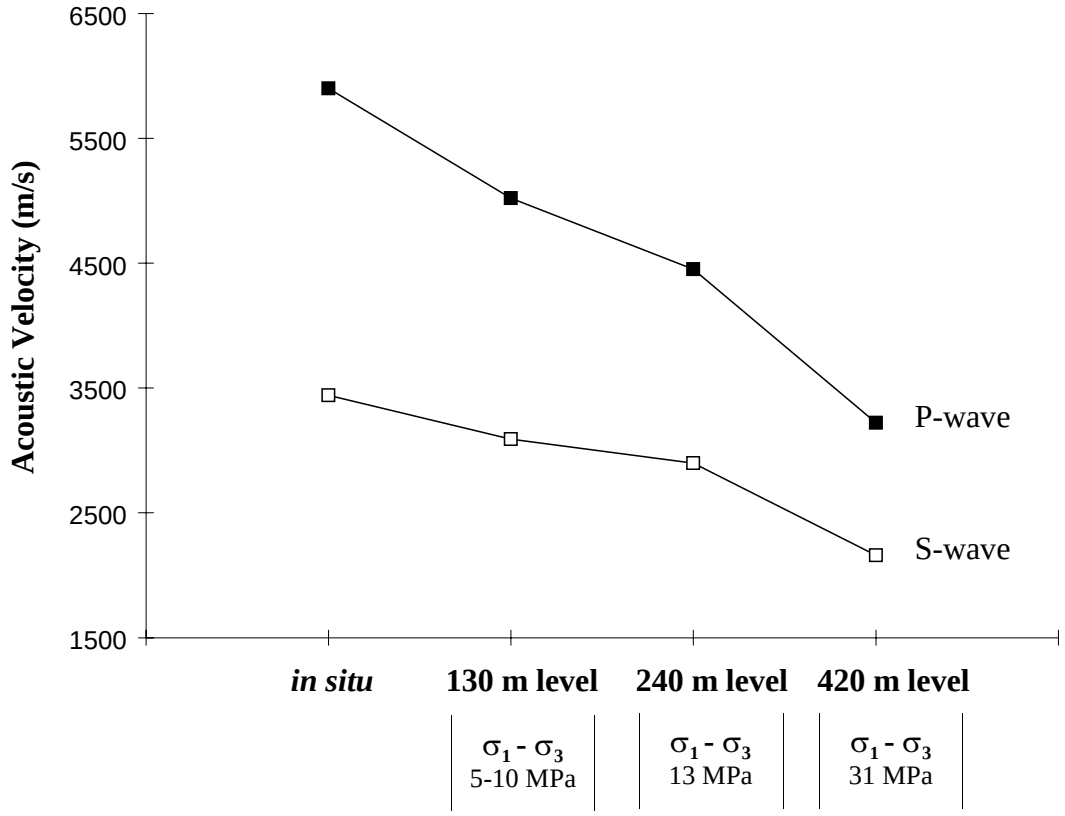

Figure 6.9 P- and S-wave velocities for granite samples from the URL 130, 240 and 420 m levels in comparison with *in situ* values.

Table 6.8 Summary of density and acoustic velocity values for URL 130, 240 and 420 m level granite samples (standard deviation is provided in parentheses).

Material Parameter		130 m Level	240 m Level	420 m Level
Density	ρ (g/cm^3)	2.62 (± 0.01)	2.62 (± 0.01)	2.59 (± 0.02)
Acoustic Velocity	V_P (m/s)	4885 (± 190)	4445 (± 295)	3220 (± 100)
	V_S (m/s)	3030 (± 115)	2905 (± 85)	2160 (± 55)
	V_P / V_S	1.61	1.53	1.49

6.2.2 Effect of Increasing Sample Disturbance on Deformation and Fracture

Previous studies by Jackson *et al*. (1989) and Martin (1993) have shown that the mechanical properties of Lac du Bonnet granite (e.g. the tangent modulus, Poisson's ratio and compressive strength), can vary significantly with increasing sample disturbance. Similarly, test results from this study indicated that significant changes in the deformation and fracture characteristics of the granite occur if the samples have previously experienced some form of stress relief microfracturing. Comparisons were first made between values of the secant and Young's modulus for granite samples from the 130 m, 240 m and 420 m levels of the URL. As previously shown (Figure 4.5), the secant modulus includes the initial non-linearity in axial strain attributable to the closure of existing cracks, whereas the Young's modulus is a measure of the approximate linear elastic behaviour of the sample assuming all cracks perpendicular to the applied load are closed. In other words, the more initial cracking induced during sampling the more non-linearity in the axial stress-strain curve and therefore the lower the secant modulus value. Test results show that secant modulus values for the 130 m level samples are only 8% lower than the average modulus values, whereas those for the 240 m and 420 m level samples are 22% and 39% lower, respectively (Table 6.9). These differences are

attributable to increasing sample disturbance, and therefore increasing crack densities, with depth. In direct comparison, secant modulus values for the 240 and 420m level samples are 19% and 48% lower than 130m level values.

Table 6.9 Average elastic parameters for URL 130, 240 and 420 m level granites (standard deviation is provided in parentheses).

Material Parameter	130 m Level	240 m Level	420 m Level
Samples Tested	20	5	5
Young's Modulus, E_{avg} (GPa)	66.5 (± 3.0)	63.8 (± 2.2)	51.9 (± 1.6)
Tangent Modulus, E_T (GPa)	66.2 (± 3.1)	60.3 (± 1.1)	40.5 (± 0.9)
Secant Modulus, E_S (GPa)	61.0 (± 3.4)	49.7 (± 1.9)	31.7 (± 1.2)
Poisson' Ratio, ν_{avg}	0.31 (± 0.04)	0.33 (± 0.04)	0.38 (± 0.04)

The extent of sample disturbance with sampling depth was further established through plots of the axial stiffness. As would be expected, increases in crack density due to higher degrees of stress relief cracking resulted in larger crack closure thresholds for the granite samples. This was reflected in decreasing secant modulus values (Figure 6.10). Crack closure thresholds for the 240 m and 420 m level granites were 18% and 58% higher, respectively, than the 130 m level threshold value (Table 6.10). Test results also revealed that sample disturbance acts to reduce the overall stiffness of the rock matrix. Average values of Young's modulus for the 420 m level granite decrease by 22 % when compared to 130 m level values (Table 6.9). Poisson ratio values were seen to increase by 23% when comparing 130 m and 420 m level measurements. In comparison, Young's modulus and Poisson ratio values for the 240 m level deviate by only 5% from 130 m level values. This emphasizes the relatively minor degree of sampling disturbance seen in the 240 m level samples compared to that incurred by the 420 m level samples. Axial stiffness plots further reveal that the general trends and

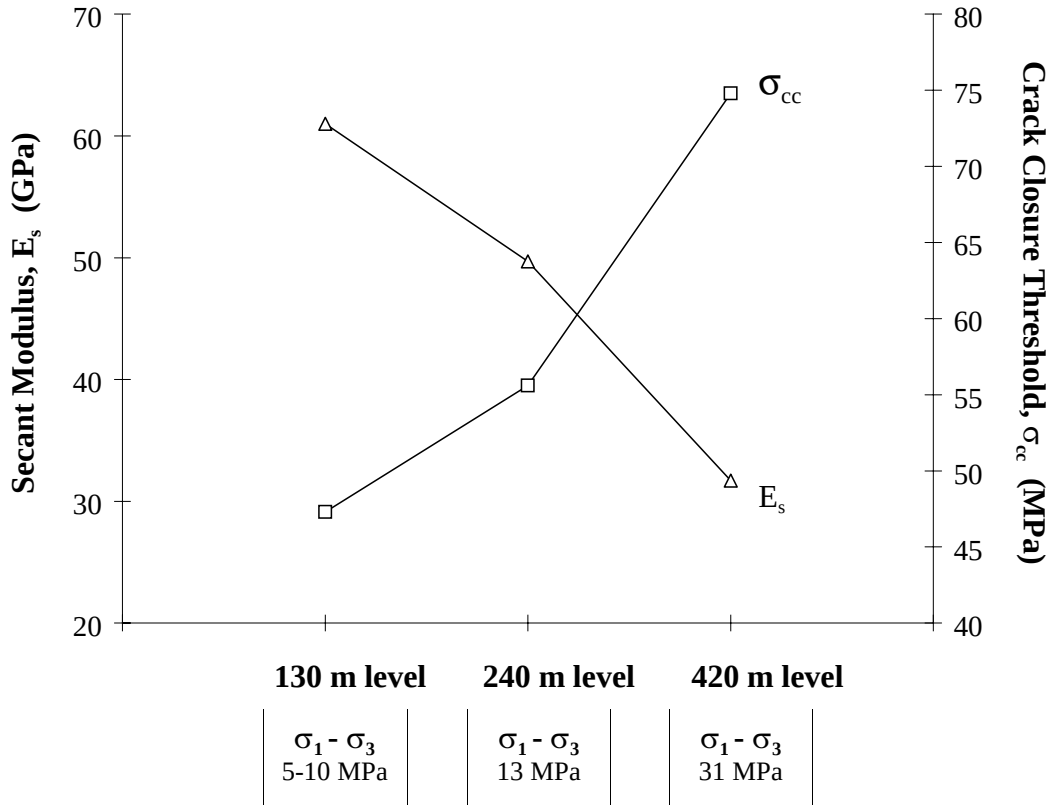

Figure 6.10 Plots of secant modulus and crack closure thresholds -*vs*- sampling depth for granite samples from the URL 130, 240 and 420 m levels.

magnitudes of the curves are reduced, with respect to increased sampling depth, even past the crack closure threshold (Figure 6.11). In other words, damage not only increases the degree of non-linear deformation exhibited during the initial stages of loading, but by destroying grains within the rock matrix (through intragranular cracking) also reduces the ability of the rock matrix to accommodate increases in load energy through elastic strain.

Table 6.10 Average fracture parameters for 130, 240 and 420 m level URL granites (standard deviation is provided in parentheses).

Strength Parameter	130 m Level	240 m Level	420 m Level
Number of Tests	20	5	5
Crack Closure, σ_{cc} (MPa)	47.3 (± 2.7)	55.6 (± 1.5)	74.8 (± 1.0)
Crack Initiation, σ_{ci} (MPa)	81.5 (± 3.7)	79.6 (± 2.3)	76.4 (± 3.7)
Secondary Cracking, σ_{ci2} (MPa)	103.9 (± 5.0)	102.8 (± 4.3)	102.0 (± 2.5)
Crack Coalescence, σ_{cs} (MPa)	132.8 (± 9.0)	127.6 (± 14.2)	85.5 (± 12.6)
Crack Damage, σ_{cd} (MPa)	156.0 (± 13.2)	147.4 (± 9.1)	100.4 (± 12.2)

The substantial effects sample disturbance had on the deformation and crack closure parameters were not seen in values for the crack initiation and secondary cracking thresholds. Values in Table 6.10 show that only minor decreases with increasing sampling depth were seen in these two fracture parameters. Crack initiation values for the 240 m and 420 m level samples decreased by only 2% and 6% when compared to 130 m level values. Secondary cracking values varied even less for the 240 m and 420 m level samples, decreasing by 1% and 2% from 130 m level values. These results indicate that sampling disturbance has little effect on the initiation of new fractures. Increased AE activity during crack closure was seen, however, with increasing sampling disturbance (Figure 6.12). These increases in AE activity are likely related to the closure and collapse of crack structures (i.e. bridging material), the number of which

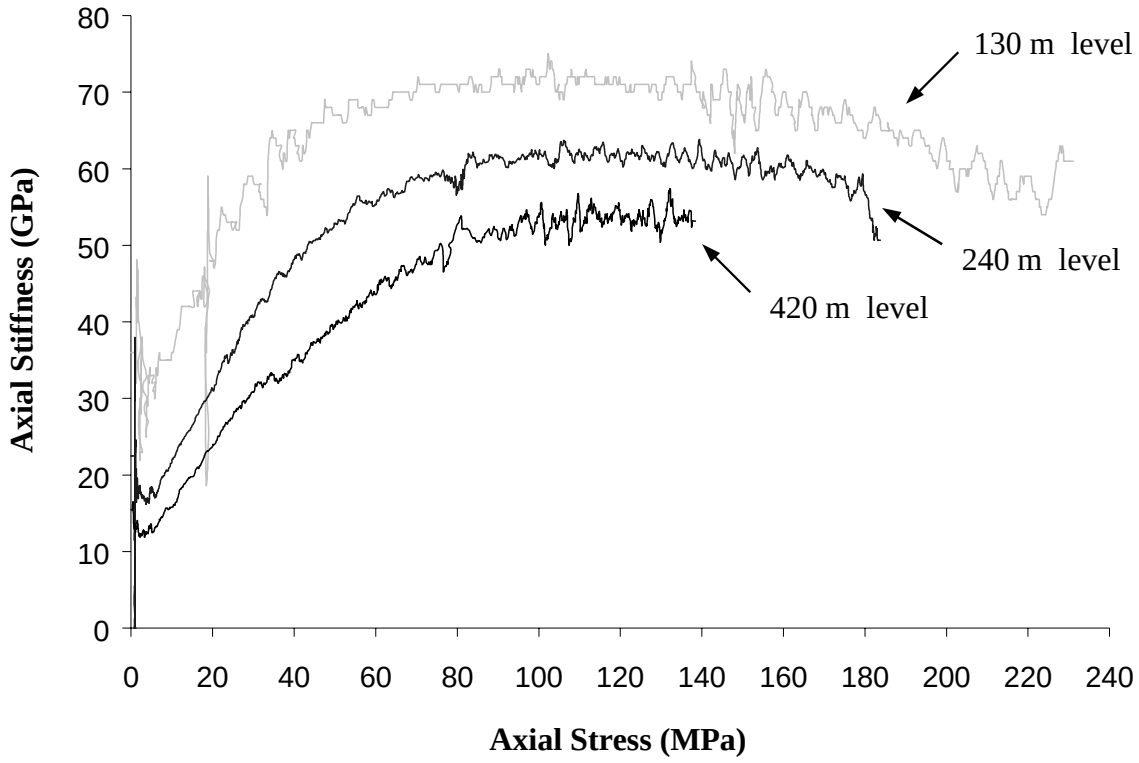

Figure 6.11 Plot of axial stiffness -*vs*- axial stress for granite samples from the URL 130, 240 and 420 m levels.

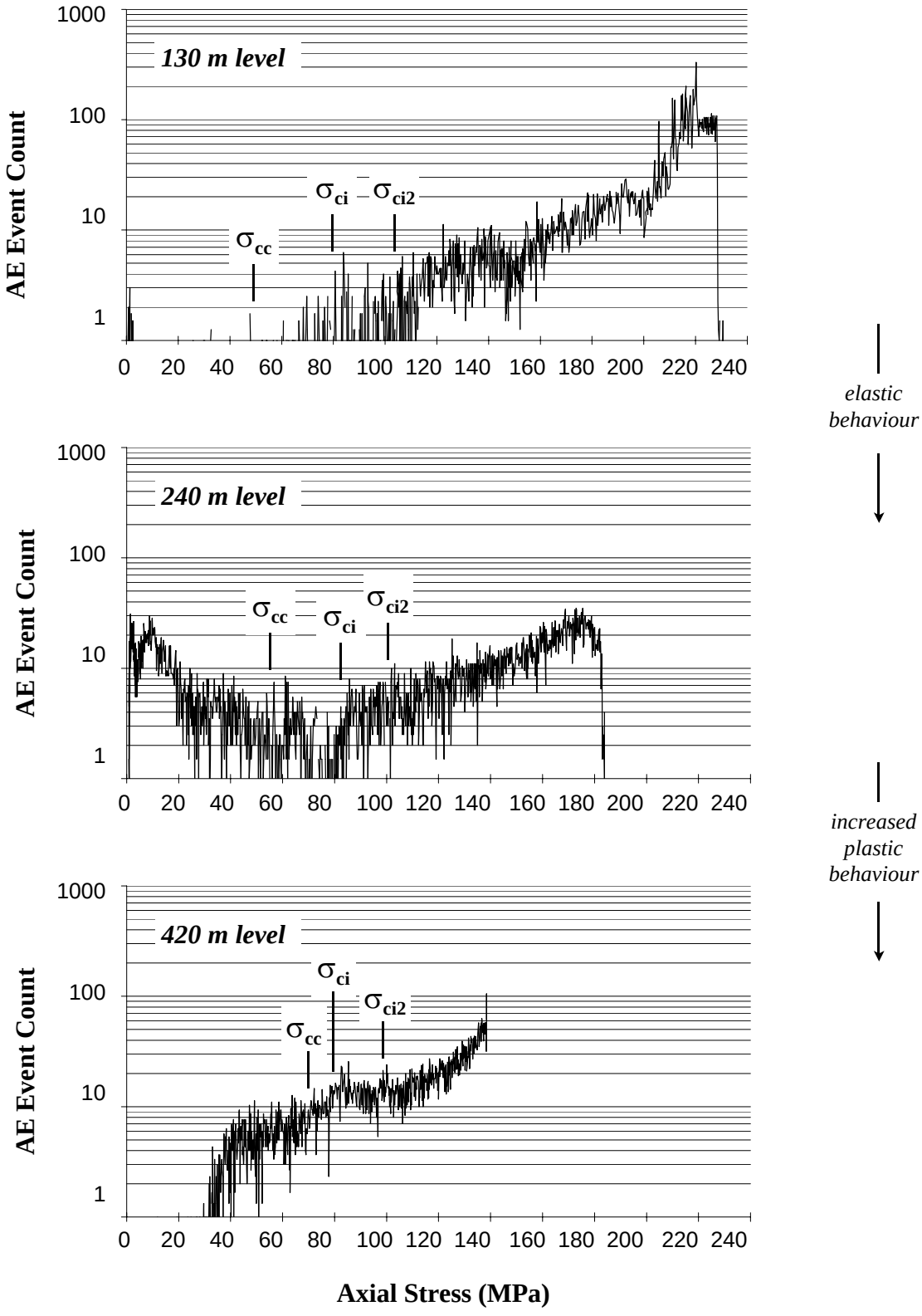

Figure 6.12 Log plots of AE event count -*vs*- axial stress for granite samples from the URL 130 m (top), 240 m (middle) and 420 m (bottom) levels.

increase with crack density and sampling disturbance. As loads approach the crack initiation and secondary cracking thresholds, new fracturing begins in those grains and grain boundaries that had not been damaged during sampling. In the case of the severely damaged 420 m level granite, the absence of any detected AE events prior to 40 MPa suggests that weaker grain structures had all but been destroyed or eliminated. Furthermore, the behaviour of these samples appear to incorporate more elements of plasticity during deformation. The different modes of cracking associated with this type of deformation may result in lower energy AE events below the detection limit. However, given that the *in situ* stress difference (i.e. σ_1-σ_3) on the 420 m level of the URL is also approximately 40 MPa (Table 6.6), the commencement of AE activity in the 420 m level granite is likely a reflection of its previous stress history, otherwise known as the Kaiser effect (the generalized theory of which is discussed by Holcomb, 1993).

The results presented above suggest that sample disturbance does not play a significant role in lowering the crack initiation and secondary cracking thresholds. The reduction in compressive strength with sampling depth at the URL, reported by Jackson *et al*. (1989) and Martin and Stimpson (1994), must therefore be associated with how these cracks behave and interact once they begin to propagate. Analysis of the volumetric stiffness plots for the test samples (Figure 6.13), show that the crack coalescence and crack damage thresholds significantly decrease with increased sampling disturbance. Variations in values for the 240 m level granite reflect the small increase in *in situ* stress magnitudes between the 130 m and 240 m levels (Table 6.6). Crack coalescence and crack damage thresholds for the 240 m level samples decrease by 4% and 6%, respectively, when compared to 130 m level values. The increase in *in situ* stress magnitudes on the 420 m level, however, is nearly two to three times that seen on the 130 m and 240 m levels. Crack coalescence and crack damage values for these samples decrease substantially, 36% and 37% respectively, when compared to 130 m level values.

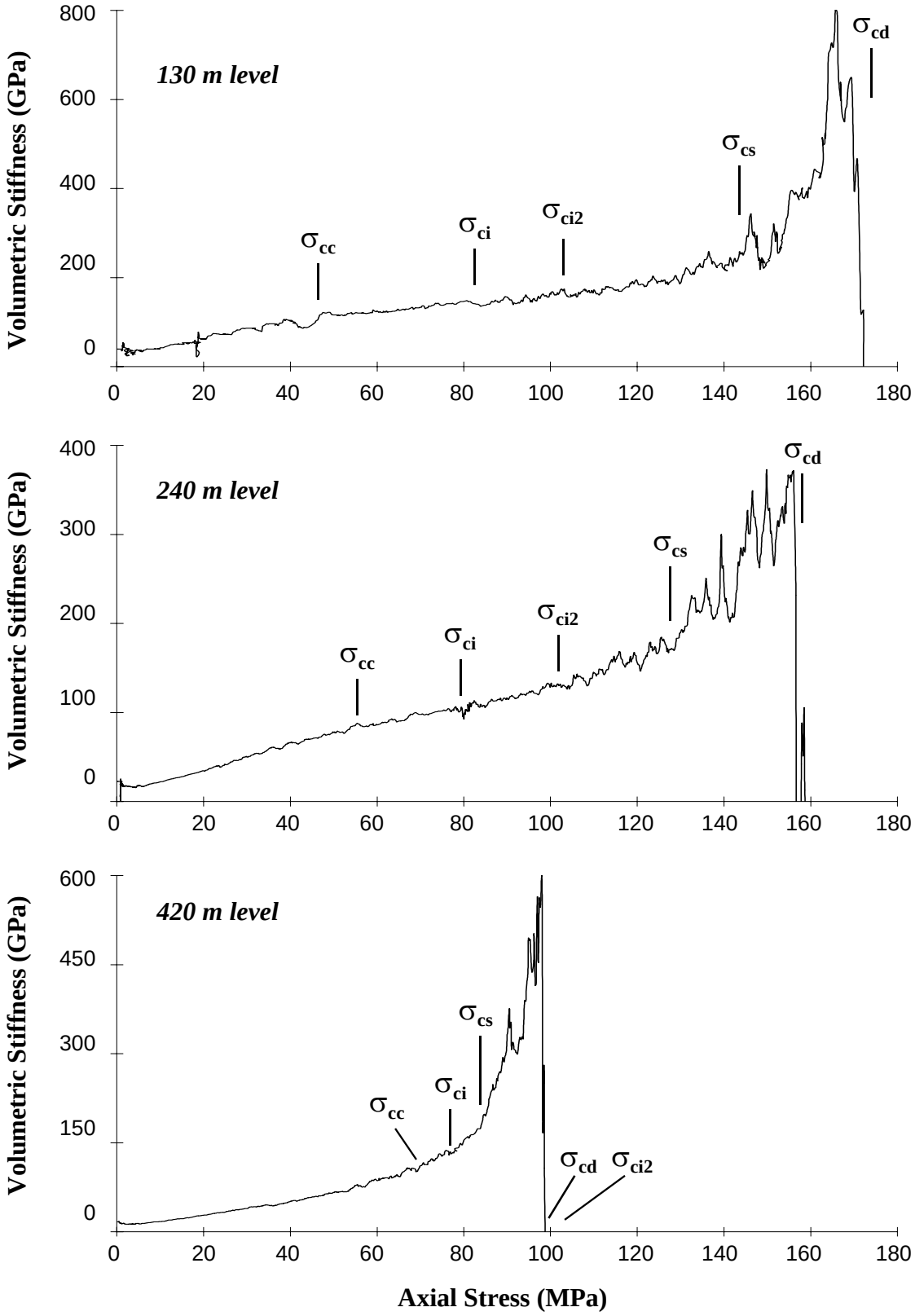

Figure 6.13 Plots of volumetric stiffness -*vs*- axial stress for granite samples from the URL 130 m (top), 240 m (middle) and 420 m (bottom) levels.

It would appear that the increased number of stress relief cracks present in the 420 m level samples, act to weaken the rock by providing a number of pre-existing planes of weakness for active cracks to propagate along. As a crack propagates there must be enough energy in the system to break the bonds located near and around it's tip. Cracks propagating in the 130 m and 240 m level samples would have fewer planes of weakness to follow thereby requiring higher stresses to break through intact grains and grain boundaries. The large number of failed grains and grain boundaries in the 420 m level samples, however, provide a significant number of paths for an active crack to propagate along which, in turn, have already had their cohesive bonds broken. Martin and Stimpson (1994) note that in highly disturbed samples, the cohesion can be reduced by as much as 70%. It therefore follows that in a highly damaged sample more cracks may propagate more easily, resulting in their coalescence and ultimately the failure of the sample at lower than expected compressive stresses.

The degree of sampling damage induced in the 420 m level samples further complicated the analysis. It should be recognized that the damaged granite samples are essentially a different material than those samples retrieved from lower *in situ* stress regimes (i.e. relatively low damage). Analysis of the damaged samples revealed that several of the stages of crack development appear to either overlap with one another or prematurely precede those thresholds that would have been expected to follow next. Part of this initial overlap was due to the high stresses required to achieve crack closure. Values in Table 6.10 show that the crack closure threshold for the 420 m samples was approximately the same magnitude as the crack initiation threshold (Table 6.10). Hence the "overlap" represents a transition where changes in the axial and lateral strain rate may be occurring due to both the initiation of new cracks and due to deformations in the form of grain boundary/crack sliding. If new cracks are forming while existing ones have yet to close, situations may exist where the axial stiffness of the sample never reaches linear elastic behaviour but continues to increase in a non-linear fashion throughout loading (Figure 6.14). In such cases, crack closure as it is presently defined is never truly reached and detection of the characteristic patterns for the crack initiation and secondary cracking thresholds are only discernable in the acoustic emission data.

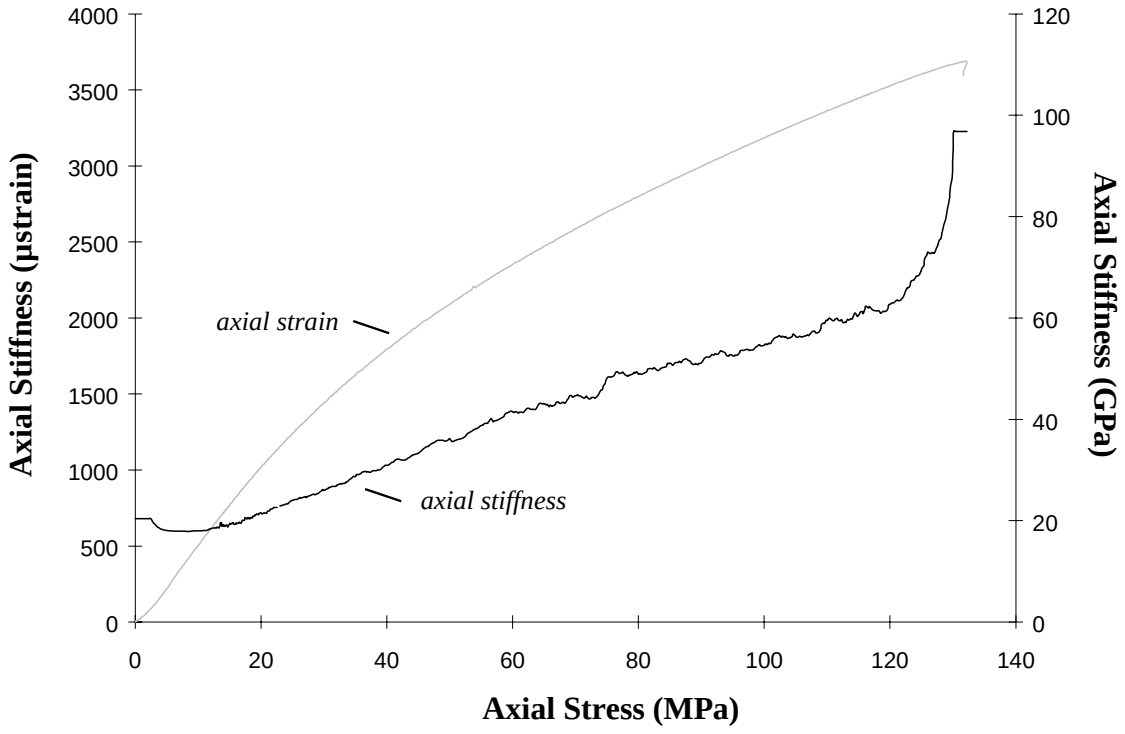

Figure 6.14 Plot of axial stiffness -*vs*- axial stress for a 420 m level URL granite sample which never truly reaches a stage of linear elastic behaviour (i.e. highly non-linear).

It was also observed that the secondary cracking threshold for the 420 m level granite appeared to be preceded by the crack coalescence and crack damage thresholds (Figures 6.12 and 6.13). In both the 130 and 240 m level granites, secondary cracking preceded both crack coalescence and crack damage. This would seem to indicate that the propagation and interaction of pre-existing cracks related to sample disturbance and new fractures initiated at the crack initiation threshold, was significant enough to lead to crack coalescence and volumetric strain reversal. The secondary cracking threshold was still detected in the AE data, however, the stress-induced fracturing of the intact quartz grains marked by this threshold likely only served to help accelerate the failure of the samples. Failure of the 420m level granite was also somewhat different from that of the 130m and 240 m granite, both of which exhibited some degree of strain softening leading up to failure. In the case of the weaker 420m level granite, signs of strain hardening were present as the final mode of failure seemed to follow a complex combination of shear and buckling among columnar pieces shaped by large cracks parallel to the loading direction. Movement of these interlocked columnar pieces may result in the appearance of strain hardening as irregularities lock up providing some additional short term strength.

6.2.3 Effects of Grain Size on the Degree of Sample Disturbance

Additional testing was also performed on samples of the fine-grained granodiorite taken from the 420 m level of the URL, so that the effects of grain size on the degree of sampling disturbance could be investigated. As previously demonstrated, a finer grain size increases the strength of the rock by making it more difficult for cracks to initiate and propagate. Thus, the degree of sample disturbance expected in the 420 m level granodiorite should be less than that seen in the 420 m level granite. SEM observations confirm that the density of microcracks attributable to sample disturbance in the granodiorite was significantly lower than that seen in the 420 m level granite (0.25 cracks/mm^2 as opposed to 10 cracks/mm^2). Observable cracks in the granodiorite thin sections were predominantly found along grain boundaries and within feldspar grains. Fractured or shattered quartz grains, which were frequently observed in thin

sections taken from the 420 m level granite, were not apparent in the 420 m level granodiorite sections.

SEM analysis of the 420 m level granodiorite also revealed that the crack density of the samples, although not as high as in the 420 m level granites, was still considerably higher than that seen in the 130 m and 240 m level samples. The damaged state of the granodiorite samples was reflected in density and acoustic velocity measurements prior to uniaxial compression testing. The granodiorite had slightly higher (5%) acoustic velocities than the grey granite but significantly lower (34%) values than the 240 m level granodiorites. Table 6.11 shows that the 420 m level granodiorite, as compared to the 420 m level granite, has a higher density, P- and S-wave velocity and Young's, tangent and secant modulus. Although these high values may be partially attributed to the difference in grain size, larger disparities exist when comparisons are made between 420 m and 240 m level granodiorite values. It can therefore be concluded that granodiorite samples from the 420 m level have been subjected to a large degree of microfracturing prior to testing.

In terms of strength, crack thresholds for the 420 m level granodiorite follow the same patterns of crack development as those seen in previous tests. Crack closure values are similar to those for the 420 m level granites (Table 6.12), thus reflecting the high degree of sample disturbance resulting from the high *in situ* stresses on the 420 m level of the URL. Values for the crack initiation and secondary cracking thresholds did not significantly vary between the different samples (Figure 6.15), once again showing that their values are more closely related to the strengths of the individual feldspar and quartz minerals than grain size. As was previously shown in testing of the 240 m level granite and granodiorite, grain size did have a significant effect on the crack coalescence and crack damage thresholds of the 420 m level samples. Crack coalescence and crack damage values for the finer grained 420 m level granodiorite were 30% and 34% higher, respectively, than values for the coarser grained 420 m level granite. Furthermore, a similar reduction in the number of detected AE events was seen between 420 m level granite and granodiorite samples as was seen in the 240 m level samples. The effects of sampling disturbance were also evident in that crack coalescence and crack damage

Table 6.11 Average index and deformation parameters for samples of 420 m level granite and granodiorite and 240 m level granodiorite from the URL (standard deviation is provided in parentheses).

Material Parameter	420 m Level Grey Granite	420 m Level Granodiorite	240 m Level Granodiorite
Samples Tested	5	5	5
Density, ρ (g/cm^3)	2.59 ($\pm$ 0.02)	2.63 ($\pm$ 0.01)	2.66 ($\pm$ 0.00)
P-wave Velocity, V_P (m/s)	3220 ($\pm$ 100)	3335 ($\pm$ 105)	5240 ($\pm$ 70)
S-wave Velocity, V_S (m/s)	2160 ($\pm$ 55)	2310 ($\pm$ 35)	3245 ($\pm$ 60)
V_P / V_S ratio	1.49	1.44	1.61
Young's Modulus, E_{avg} (GPa)	51.9 ($\pm$ 1.6)	57.7 ($\pm$ 0.9)	63.8 ($\pm$ 2.2)
Tangent Modulus, E_T (GPa)	40.5 ($\pm$ 0.9)	50.0 ($\pm$ 1.2)	60.3 ($\pm$ 1.1)
Secant Modulus, E_S (GPa)	31.7 ($\pm$ 1.2)	40.2 ($\pm$ 1.5)	49.7 ($\pm$ 1.9)
Poisson' Ratio, ν_{avg}	0.38 ($\pm$ 0.04)	0.34 ($\pm$ 0.01)	0.33 ($\pm$ 0.04)

Table 6.12 Average fracture parameters for 420 m level URL grey granite and granodiorite, and 240 m level URL granodiorite (standard deviation is provided in parentheses).

Strength Parameter	420 m Level Grey Granite	420 m Level Granodiorite	240 m Level Granodiorite
Number of Tests	5	5	5
Crack Closure, σ_{cc} (MPa)	74.8 ($\pm$ 1.0)	70.4 ($\pm$ 7.9)	45.6 ($\pm$ 3.4)
Crack Initiation, σ_{ci} (MPa)	76.4 ($\pm$ 3.7)	79.6 ($\pm$ 4.5)	79.6 ($\pm$ 2.7)
Secondary Cracking, σ_{ci2} (MPa)	102.0 ($\pm$ 2.5)	100.8 ($\pm$ 2.7)	102.8 ($\pm$ 4.5)
Crack Coalescence, σ_{cs} (MPa)	85.5 ($\pm$ 12.6)	122.0 ($\pm$ 11.5)	164.7 ($\pm$ 9.0)
Crack Damage, σ_{cd} (MPa)	100.4 ($\pm$ 12.2)	152.4 ($\pm$ 3.4)	194.0 ($\pm$ 2.8)
Peak Strength, σ_{UCS} (MPa)	157.1 ($\pm$ 17.7)	209.0 ($\pm$ 3.7)	221.5 ($\pm$ 21.3)

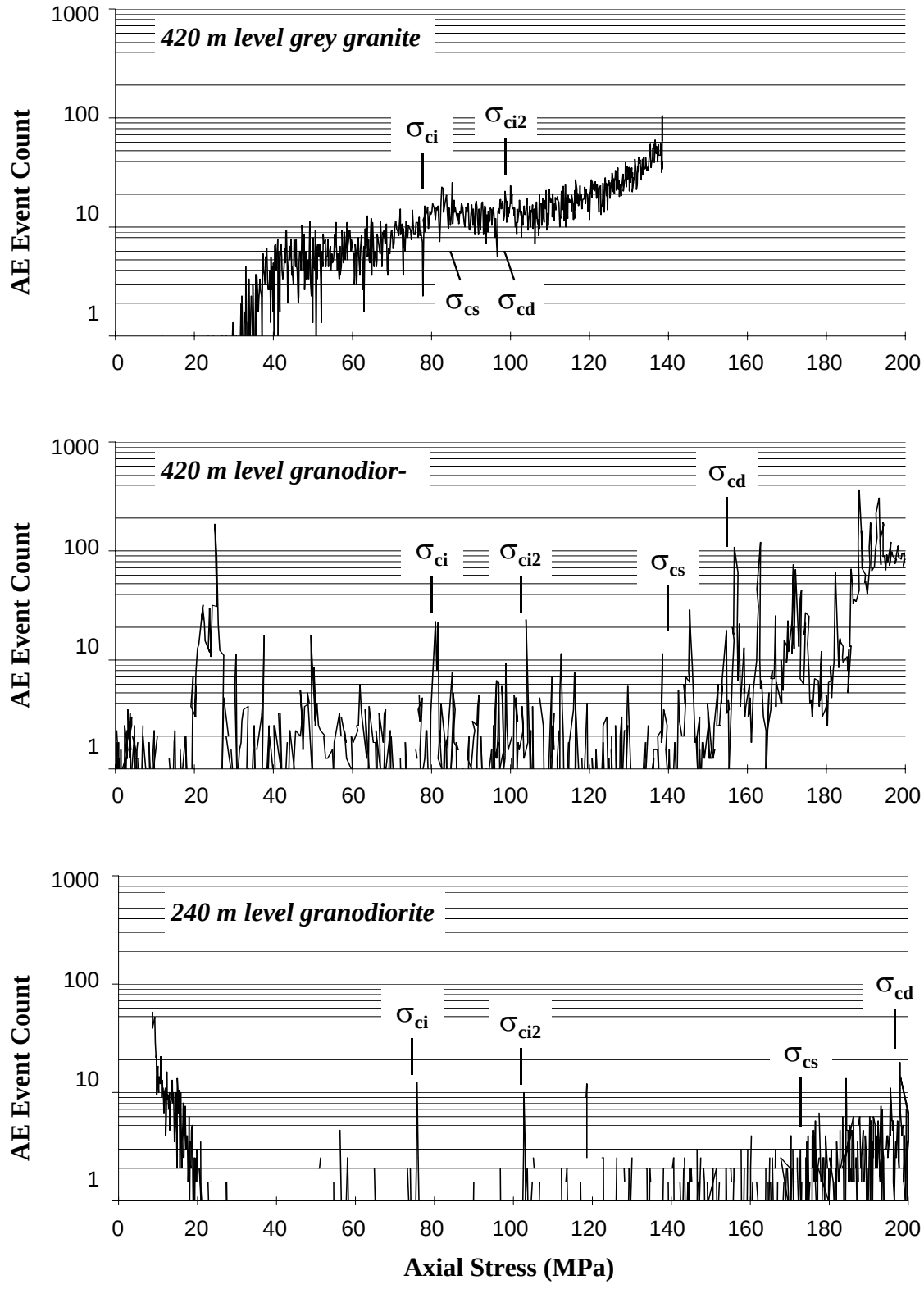

Figure 6.15 Log plots of AE event count -*vs*- axial stress for URL samples of 420 m level grey granite (top), 420 m level granodiorite (middle) and 240 m level granodiorite (bottom).

values for the 240 m level and 420 m level granodiorites differed by 26% and 21%, respectively (Figure 6.16). Overall, the fine-grained nature of the 420 m level granodiorite helps to limit the extent of crack propagation, thereby resulting in higher compressive strengths than the 420 m level granite, yet sampling disturbance acts to reduce its strength relative to the 240 m level granodiorite.

6.3 Ductility and Porosity Effects

The previous sections have concentrated on establishing the thresholds for crack development and strength degradation in brittle igneous rock. The application of these methods, however, becomes more difficult when considering more ductile materials such as potash. In addition, the pore structure present in sedimentary rocks such as sandstone also brings into question the application of the brittle fracture model. Yet theoretically, stress-induced brittle fracturing should follow the same general rules regardless of the material type. A study was therefore conducted to establish the different stages of material behaviour and crack development, under uniaxial loading conditions, for both a ductile (potash) and porous (sandstone) material.

6.3.1 Deformation and Fracture Characteristics of Potash

The mechanical behaviour of potash, and other salt rocks, has been studied extensively over the past thirty years for projects ranging from mining to the storage of petroleum and hazardous wastes (reviews of which are presented in Jeremic, 1994). These studies have primarily concentrated on the ductile yield, or creep, response of the rock. Stress-induced brittle fractures, however, are commonly observed in failing potash pillars as single, multiple or en echelon crack arrays (Lajtai *et al*., 1994). The failure of both laboratory samples and mine pillars often results in an hour glass shape indicating that extensive damage has occurred on the boundaries of the pillars. This damage can be attributed to stress-induced micro- and macro-scale cracking which significantly contributes to the loss of strength and eventual failure of the pillar.

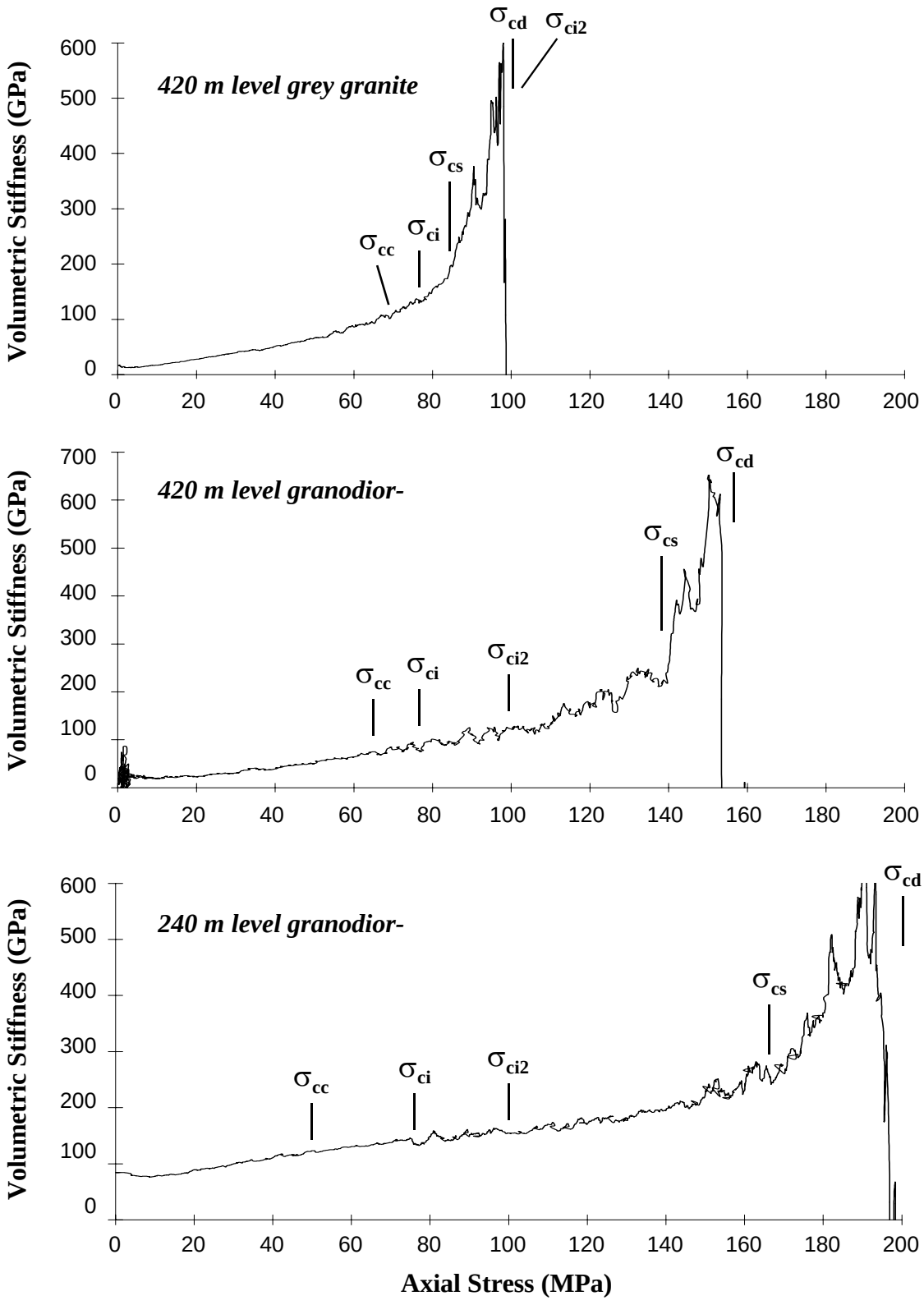

Figure 6.16 Plots of volumetric stiffness -*vs*- axial stress for URL samples of 420 m level grey granite (top), 420 m level granodiorite (middle) and 240 m level granodiorite (bottom).

Uniaxial compression testing was performed on 5 samples of Saskatchewan potash. Grain sizes in the samples varied from a minimum of 4 mm to a maximum of 40 mm, with an average grain size between 10 and 15 mm depending on the sample (Figure 6.17). Clay content was largely dispersed and varied visually from sample to sample. Cylindrical samples were prepared for testing according to ASTM standards with lengths of 230 mm and diameters of 110 mm. Each sample was instrumented with four 51 mm (2 inch) electric resistance strain gauges (2 axial and 2 lateral at 90° intervals) and two 175 kHz piezoelectric AE transducers. Prior to uniaxial testing, P- and S-wave travel times were recorded for each sample (Table 6.13). Samples were then loaded at an average rate of 4 MPa/minute.

Table 6.13 Average index and deformation parameters for Saskatchewan potash samples (standard deviation is provided in parentheses).

Material Parameter	Value
Samples Tested	5
Loading Rate (MPa/minute)	4.0 (± 0.4)
Density, ρ (g/cm^3)	2.09 (± 0.05)
P-wave Velocity, V_p (m/s)	3950 (± 70)
S-wave Velocity, V_s (m/s)	2520 (± 190)
Velocity Ratio, V_p / V_s	1.58 (± 0.11)
Young's Modulus, E_{avg} (GPa)	13.7 (± 3.5)
Poisson' Ratio, ν_{avg}	0.18 (± 0.04)

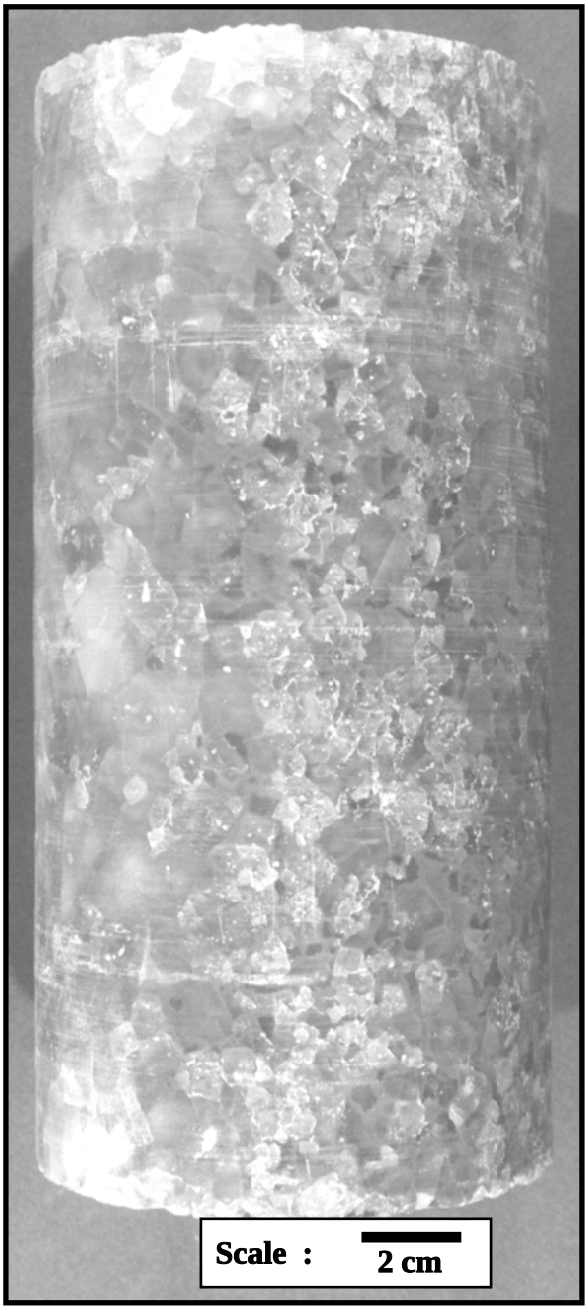

Figure 6.17 Coarse grained Saskatchewan potash sample prior to testing.

Figure 6.18 depicts a typical stress-strain response from one of the five uniaxial tests performed. Examination of the axial and lateral stiffness plots reveal that the potash displays its stiffest and most linear behaviour during the initial stages of loading. In other words, a stage of crack closure, as seen in the URL samples, was not detectable in the potash samples. Crack closure in the URL samples reflected the degree of sample disturbance induced during sample retrieval from high *in situ* stress regimes. In contrast, the potash exhibits elasto-plastic behaviour from the commencement of loading between 0 and 0.25 σ_{UCS}. The absence of the crack closure stage may be due to a number of factors. For example, the *in situ* and sampling related stresses, which the potash block experienced prior to retrieval, may not have exceeded the crack initiation strength threshold. It's also conceivable that any existing stress relief cracks healed or closed over time due to the potash's viscous nature. Another possibility is that the majority of these cracks closed during the first increments of loading before the sample, loading platen and strain gauges could become fully coupled. It is likely that some crack closure, as well as intercrystalline plastic strain, occurred during the initial stages of loading but not at significant enough levels to influence the measured strain response (although some indication is provided by the AE response). Regardless, the axial (Figure 6.19) and lateral (Figure 6.20) plots show that the potash material behaves in an elasto-plastic fashion during the initial stages of loading. The elastic constants were therefore calculated using a least squares fit over this interval (Table 6.13).

At approximately 6 MPa, or 0.25 σ_{UCS}, sample deformation departs from linearity. Examination of the acoustic emission response indicates that the onset of significant cracking begins at this point (Figure 6.21). This point was subsequently interpreted as being the crack initiation threshold (σ_{ci}). AE activity prior to this point can be attributed to movement along crack faces or minor cracking along planes previously weakened through the sampling process. In addition, plots of the AE elastic impulse "energy" rate show that the magnitudes of the events begin to increase at the crack initiation threshold (Figure 6.22). Similar observations were made by Mlakar *et al*. (1993) on samples of potash where increases in event amplitude occurred predominantly at the yield point of the material. In effect, low amplitude AE activity

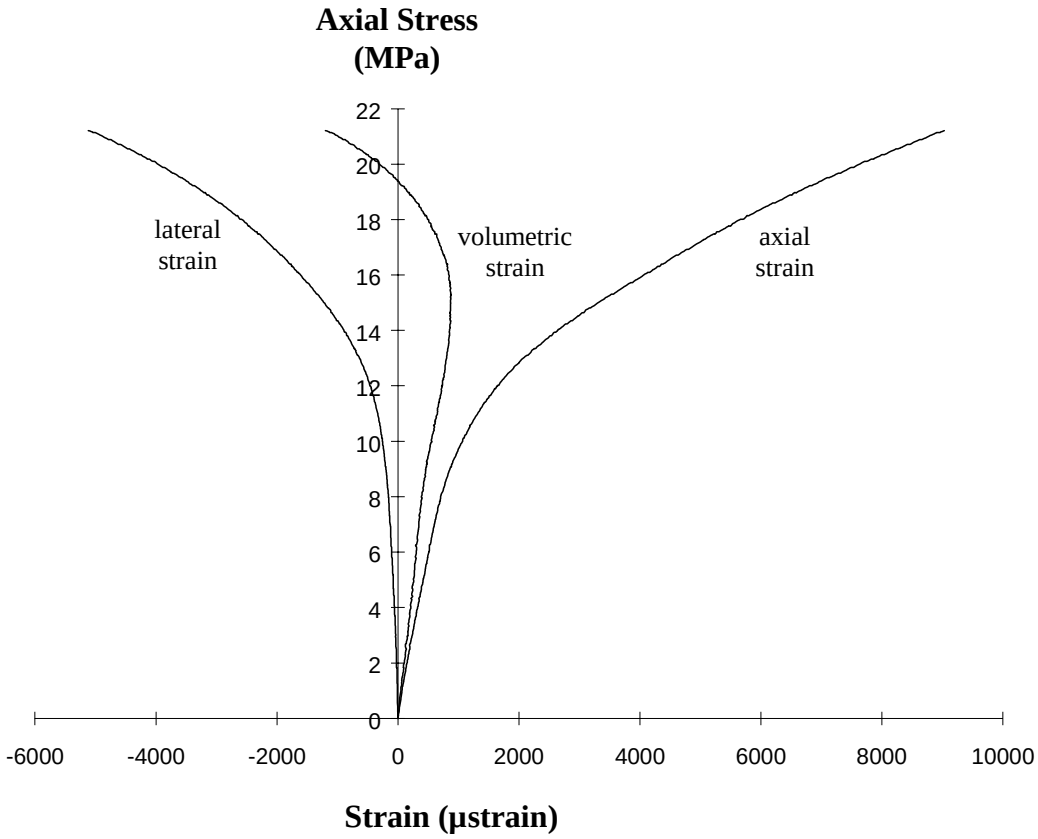

Figure 6.18 Stress -*vs*- strain plot for a uniaxial compression test performed on a Saskatchewan potash sample. Note that the volumetric strain is not measured but calculated from the axial and lateral strains.

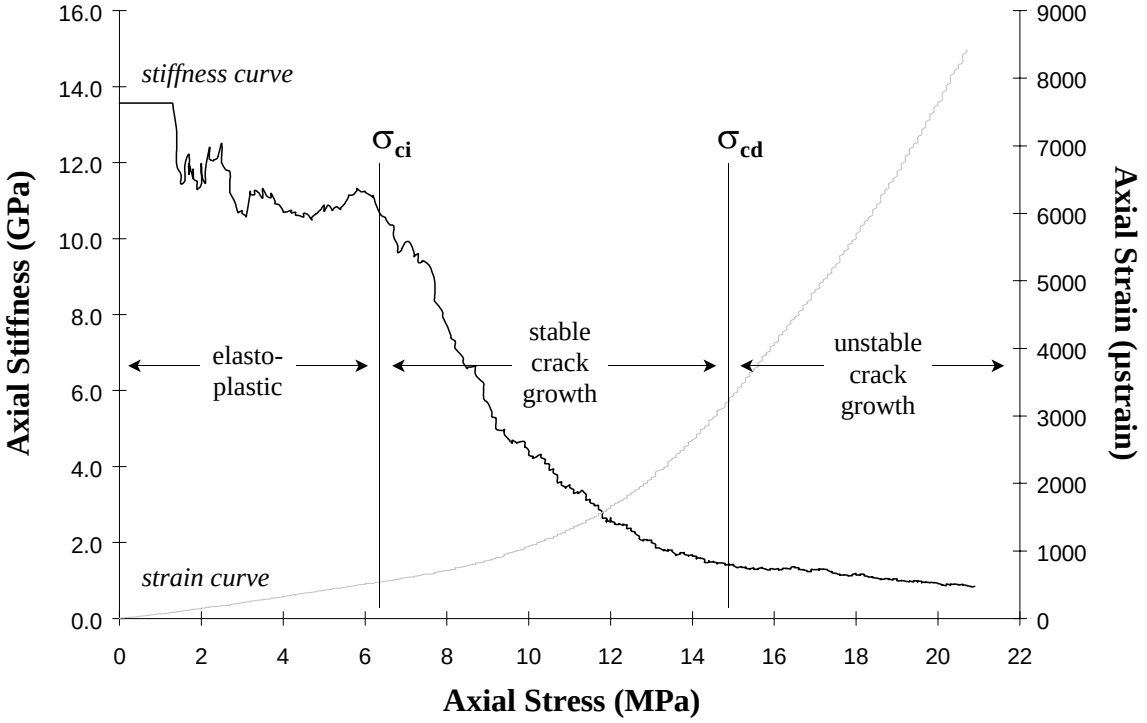

Figure 6.19 Plots of axial stiffness and axial strain -*vs*- axial stress for a Saskatchewan potash sample.

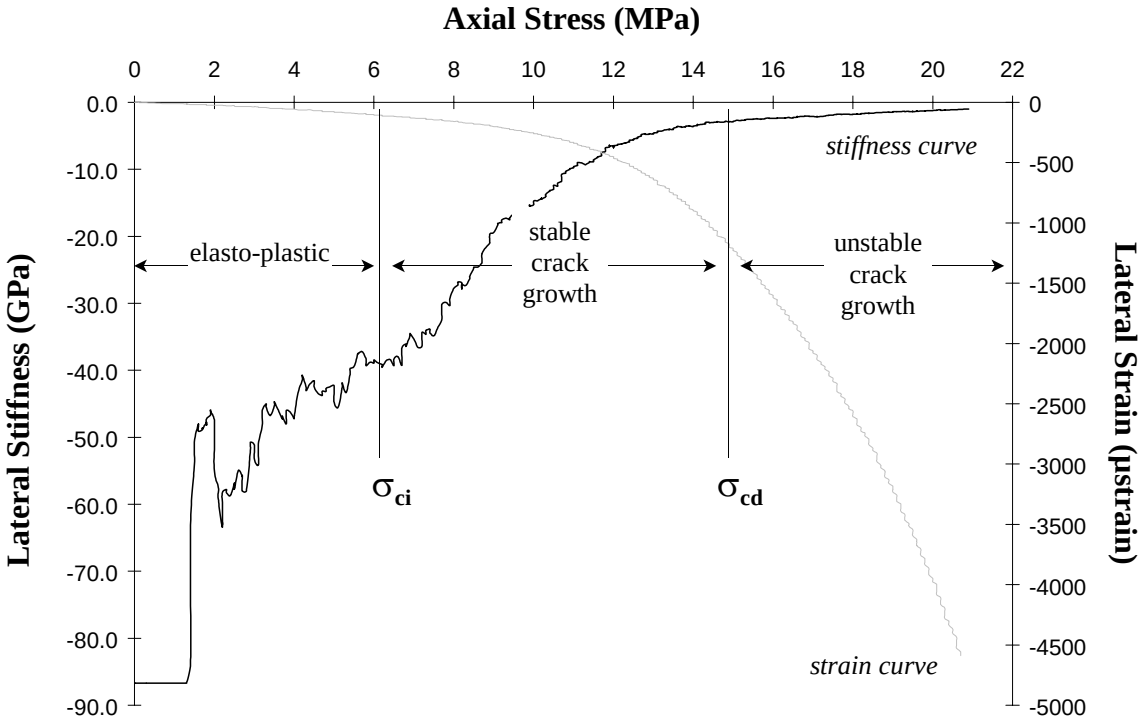

Figure 6.20 Plots of lateral stiffness and lateral strain -*vs*- axial stress for a Saskatchewan potash sample.

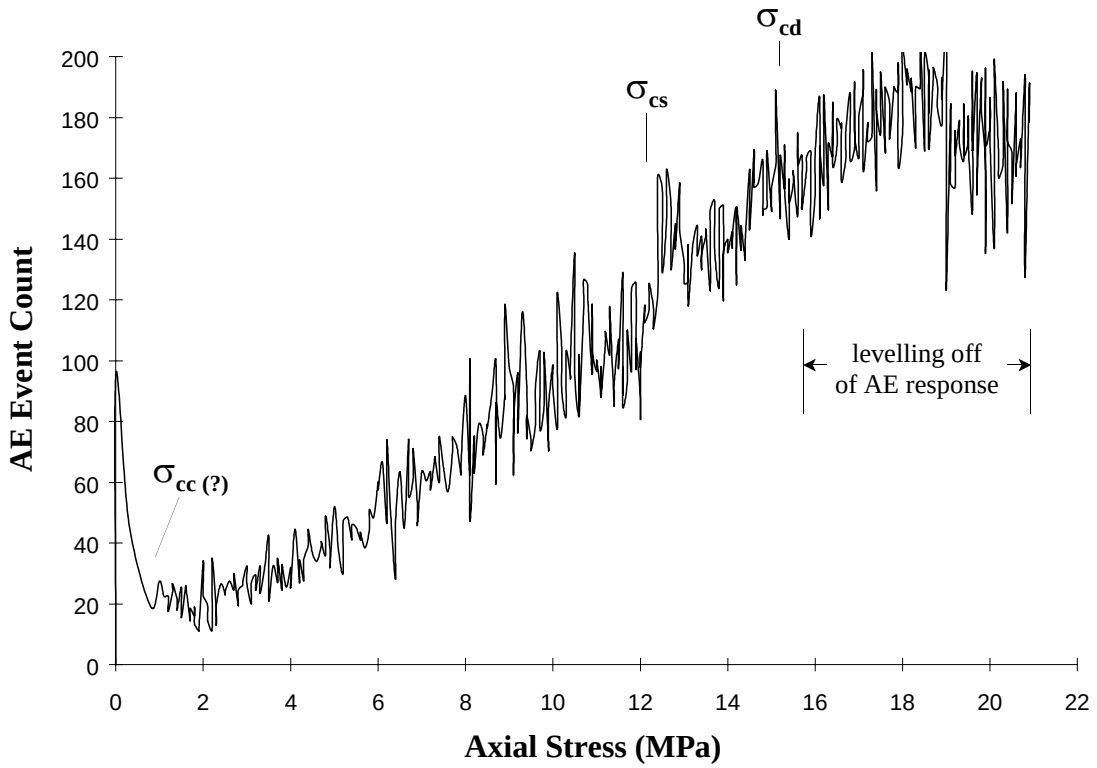

Figure 6.21 Plot of the AE event count -*vs*- axial stress for a Saskatchewan potash sample.

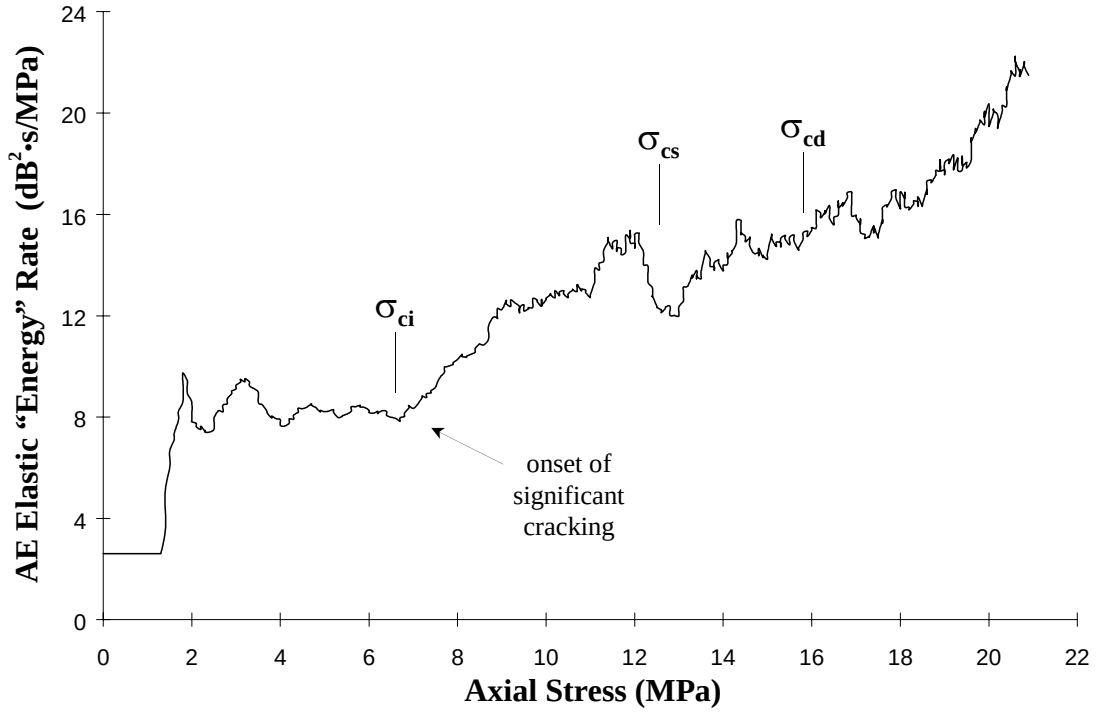

Figure 6.22 Plot of the AE event elastic impulse "energy" rate -*vs*- axial stress for a Saskatchewan potash sample.

was observed during elastic deformation of the sample followed by high amplitude events after the elastic limit was exceeded. It may therefore be reasoned that grain boundary movements in the early stages of loading are associated with lower amplitude events, while the higher amplitude events present in the later stages of the loading cycle result from intergranular and transgranular cracking. This was also found to be the case with the URL samples. Other changes in the acoustic emission rate and event "energy" rate following crack initiation, most notably around 9 MPa, may be associated with secondary cracking of different mineral grains (i.e. NaCl or KCl). However, more information regarding the mineralogy of the samples in conjunction with more in-depth testing would be required to make a more definite conclusion.

Examination of the stiffness plots further reveals that tensile brittle fracturing may not be the only active mechanism after the crack initiation threshold is exceeded. Figures 6.19 and 6.20 show that during stable crack propagation a continuous reduction in both the axial and lateral stiffness occurs. Theoretically, stress-induced cracking should only influence the lateral strain rate since crack propagation occurs in the σ_1 direction (i.e. the axial direction), and the opening of these cracks occurs perpendicular to this motion (i.e. in the lateral direction). The opening of these tensile cracks could be clearly seen on the surface of tested specimens (Figure 6.23). Significant reductions in the axial stiffness, therefore, were likely related to plastic yield of the large potash crystals coinciding with tensile microfracturing. Similar conclusions were made by Lajtai *et al*. (1994) who observed the same phenomenon in their potash tests.

Crack coalescence also contributes to unexpected axial deformations. As previously shown in the URL granites, the interaction and coalescence of cracks results in some crack growth at oblique angles to the loading direction and perhaps an element of shearing, thereby contributing to a change in the axial strain rate and stiffness. Lower "energy" AE events at the crack coalescence threshold (Figure 6.22), similar to those seen during crack closure, also suggests that an element of shearing is involved in the crack coalescence process. Stable crack propagation and coalescence continues past this point until volumetric strain reversal occurs thereby marking the crack damage threshold (Figure 6.24). Threshold values for these points are presented in Table 6.14.

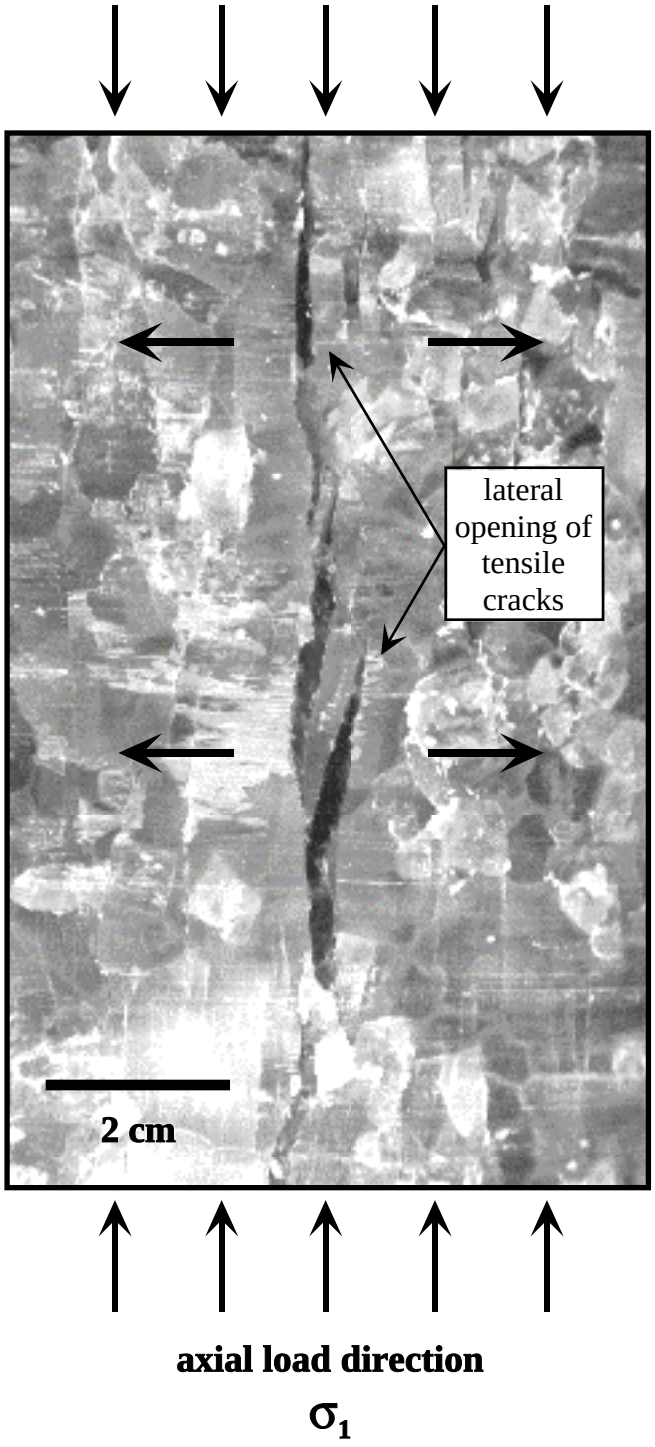

Figure 6.23 Tensile cracks opening perpendicular to the applied load.

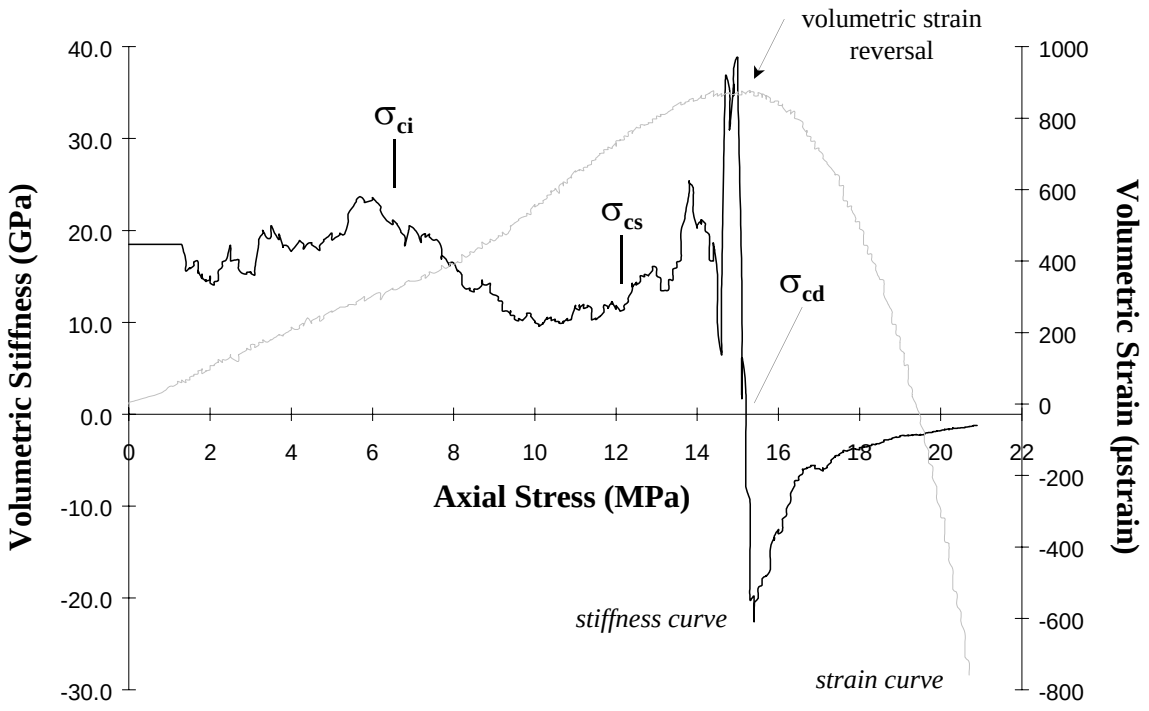

Figure 6.24 Plots of volumetric strain and stiffness -*vs*- axial stress for a Saskatchewan potash sample.

The crack damage threshold also marks an interval where the AE event count reaches a relatively constant level. Figure 6.21 reveals that throughout stable crack propagation, the number of detected events continuously increases. Once unstable crack propagation begins (i.e. after the crack damage threshold is reached), the number of events peak and remain constant until sample failure. Further examination of these events, however, reveals that even though the number of detected events remain constant, their properties continue to increase in magnitude. For example, plots of the event ringdown count (Figure 6.25) and rise time (Figure 6.26) seem to indicate that larger AE events are accompanying unstable crack propagation.

Table 6.14 Average strength parameters for Saskatchewan potash samples (standard deviation is provided in parentheses).

Material Parameter	Value
Samples Tested	5
Crack Initiation, σ_{ci} (MPa)	4.8 ($\pm$ 0.8)
Crack Coalescence, σ_{cs} (MPa)	11.0 ($\pm$ 1.7)
Crack Damage, σ_{cd} (MPa)	12.2 ($\pm$ 2.0)
Peak Strength, σ_{UCS}	23.2 ($\pm$ 2.3)

These larger events may also indicate the occurrence of different deformation and fracture mechanisms. For example, Sondergeld *et al*. (1984) noted that observations of larger events have been associated with plastic deformation in metals. This would be especially true in the case of potash where large plastic strains are expected. Figures 6.19 and 6.20 indicate that the stiffness of the potash reaches a relatively constant but significantly reduced level at the crack damage threshold. The large strains observed from this point until failure are likely due to plastic yield as well as the

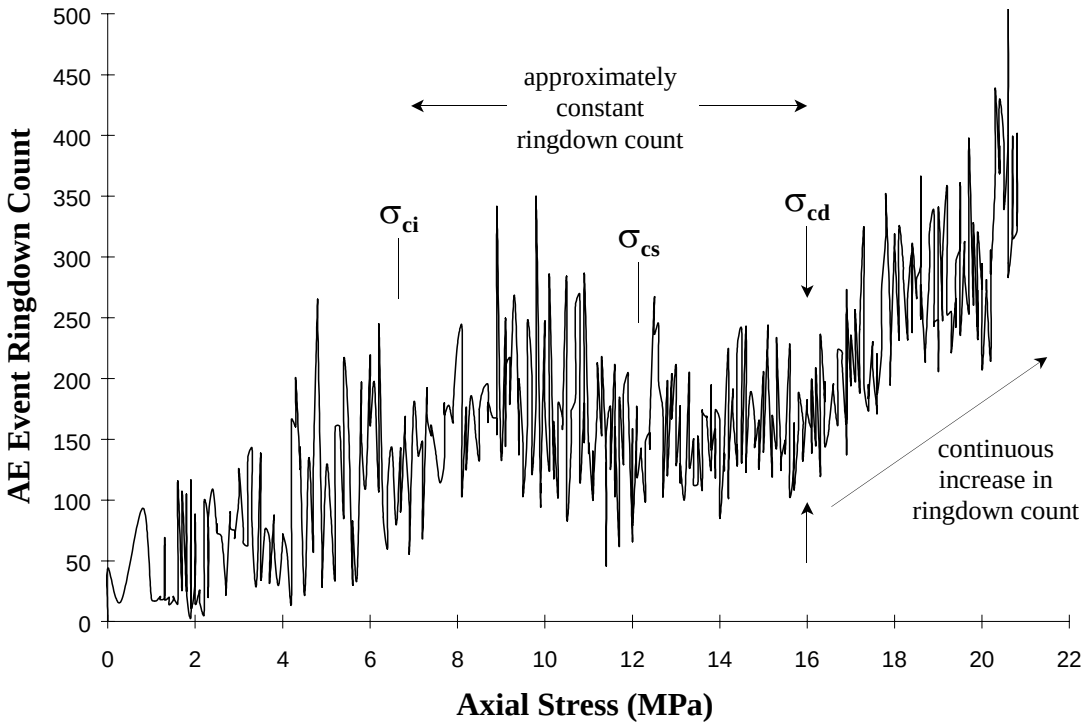

Figure 6.25 Plot of AE event ringdown count -*vs*- axial stress for a Saskatchewan potash sample.

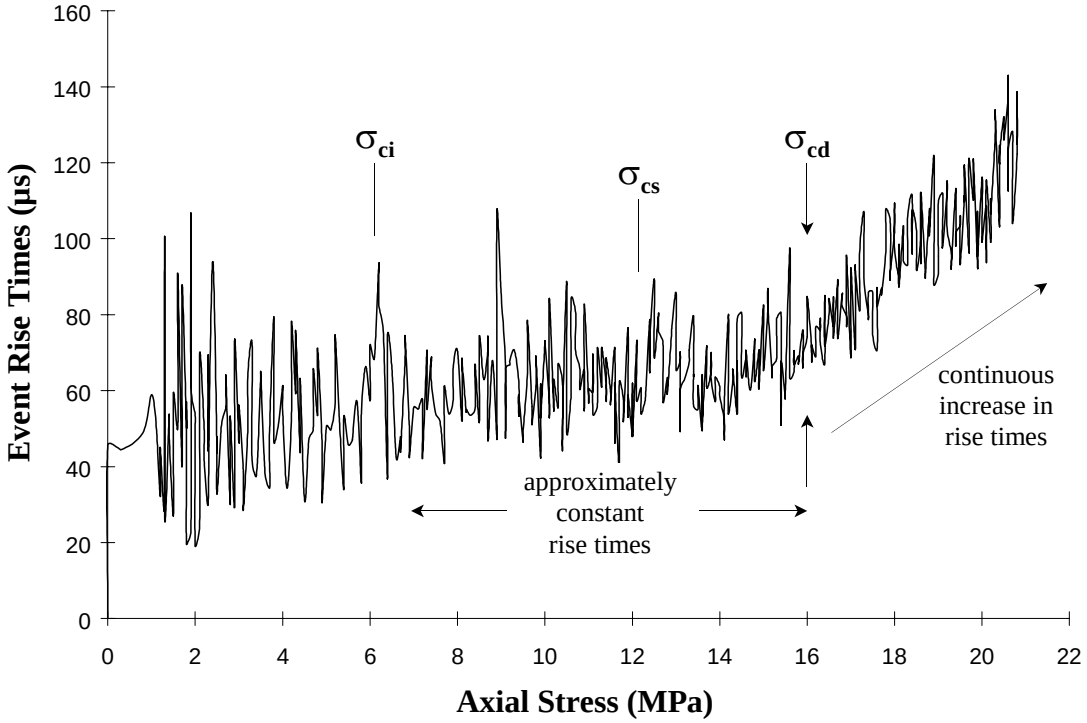

Figure 6.26 Plot of AE event rise time -*vs*- axial stress for a Saskatchewan potash sample.

movement/buckling of columnar pieces of intact material. Observations of the failed samples seems to indicate that the final mode of failure was linked to a complex combination of shear and buckling of columnar pieces shaped by large cracks parallel to the loading direction (Figure 6.27). These large cracks which extend from one end of the sample to the other are analogous to the large vertical tensile fractures, several meters in length, commonly observed in potash mines (Lajtai *et al*., 1994). It should also be noted that, unlike the results obtained for the URL samples, failure did not occur until well after the crack damage threshold was reached. In testing of the URL 130 m level pink granite, the crack damage threshold represented 75% of the total load applied to the sample prior to failure. Comparatively, the crack damage threshold for the potash appeared at 53% of peak strength. In other words, the ductile nature of the potash allowed samples to slowly yield and sustain a load throughout unstable crack propagation, whereas failure of the granite samples was relatively quick and explosive.

6.3.2 Deformation and Fracture Characteristics of Sandstone

Laboratory test results presented up to this point have concentrated on the fracture characteristics of crystalline materials where grain boundaries and intergranular mechanisms (i.e. elastic mismatch between grains, point loading contacts) act as the primary sources for crack nucleation. These tests have clearly shown that the microfracturing process is largely controlled by the microstructure of the material. Experimental observations involving porous siliclastic materials, have also shown that microstructure largely contributes to the development of stress-induced cracking but through a number of different mechanisms intrinsic to porous and cemented materials. For example, Sammis and Ashby (1986) have shown that concentrated stresses can form at pore boundaries resulting in the initiation of isolated cracks. Kranz (1983) notes that cemented grains in sedimentary rock may be wedged apart and rotated by neighbouring grains, producing cracks in the cement or along the grain boundary. A series of uniaxial compression tests were proposed to investigate these effects and the applicability of the developed strain gauge and acoustic emission techniques in establishing the fracture characteristics of porous cemented materials.

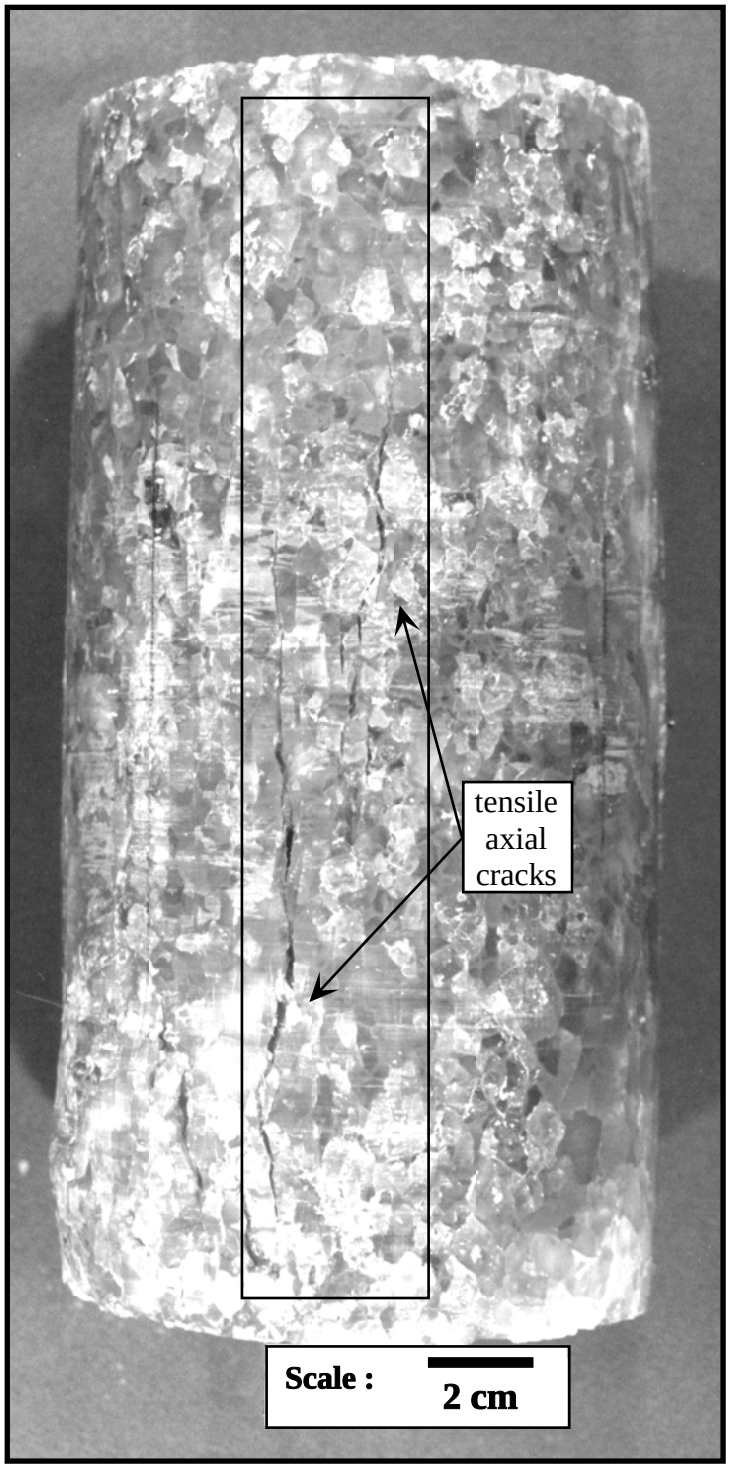

Figure 6.27 Large tensile axial cracks coalescing and extending though most of the failed Saskatchewan potash sample.

Samples of Berea sandstone were chosen for testing due to their wide use in similar experimental studies and their homogeneous texture. Samples were prepared from 55 mm diameter cores with length to diameter ratios of 2.1. Each sample was instrumented with four 12.7 mm (0.5 inch) electric resistance strain gauges (2 axial and 2 lateral at 90° intervals) and two 175 kHz piezoelectric AE transducers. Bedding was orientated perpendicular to the core axis in four of the five samples tested and parallel in one sample specially prepared to test the influences of transverse isotropy on the measured response (Figure 6.28). Petrophysical descriptions of Berea sandstone by Shakoor and Bonelli (1991) and Menendez *et al*. (1996), list the modal composition as being approximately 75% quartz, 10% feldspar, 10% cement and clays, and 5% feldspar. Grains are described as being angular in shape, well-sorted and intermediate in sphericity with a mean grain size of approximately 0.1 mm (Shakoor and Bonelli, 1991). This grain size is considerably smaller than that of the crystalline materials tested. Porosity values for the samples were obtained through saturation measurements, as described by Freeze and Cherry (1979), and are presented in Table 6.15. These values closely match those given by Bernabe and Brace (1990) and Dowla *et al*. (1990).

The mechanical behaviour of the Berea sanstone samples was found to be in good agreement with those observations made in other studies. Stress-strain measurements during the initial stages of loading indicate that a large degree of non-linearity occurs similar to the crack closure measurements seen in the crystalline materials. However, it would appear that in the case of the sandstone samples, this non-linearity could be attributed to both the closure of existing cracks and the compaction of the matrix. Figures 6.29 and 6.30 indicate that increases in both the axial and lateral stiffness are experienced up to a load of approximately 22 MPa or $0.33\sigma_{UCS}$. These values agree well with acoustic velocity measurements made by Sayers and van Munster (1991), who showed that increases in velocity measurements attributed to the closure of cracks and grain boundaries occurred up to values of approximately 20 MPa in Berea sandstone. Once this point was reached, however, values of lateral stiffness

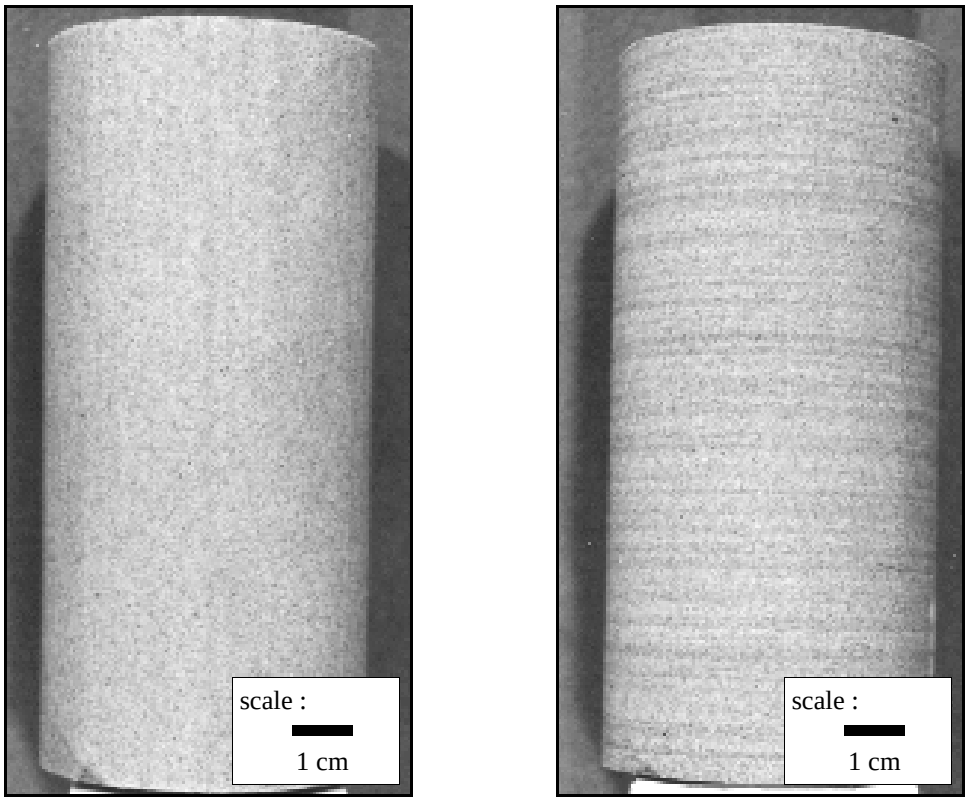

Figure 6.28 Berea sandstone samples prior to testing showing bedding parallel (left) and perpendicular (right) to the core axis.

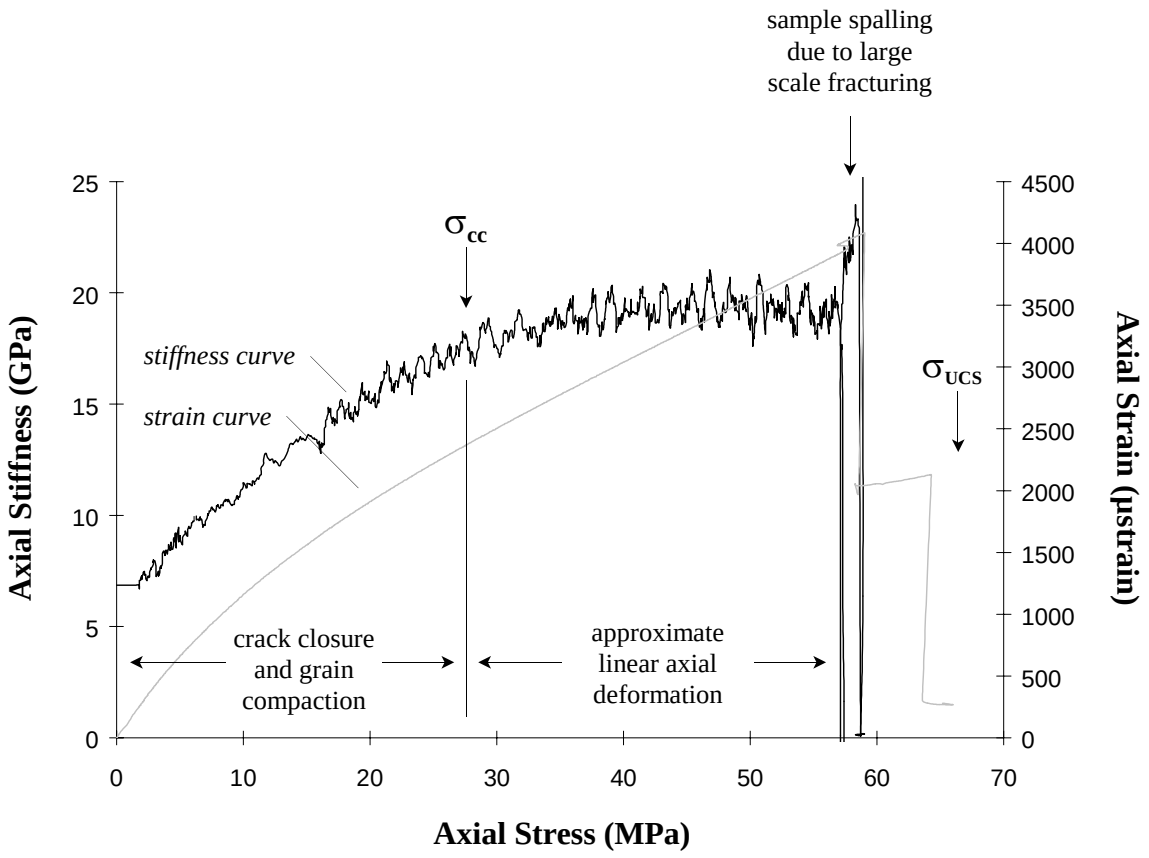

Figure 6.29 Axial stiffness and axial strain -*vs*- axial stress for a Berea sandstone sample.

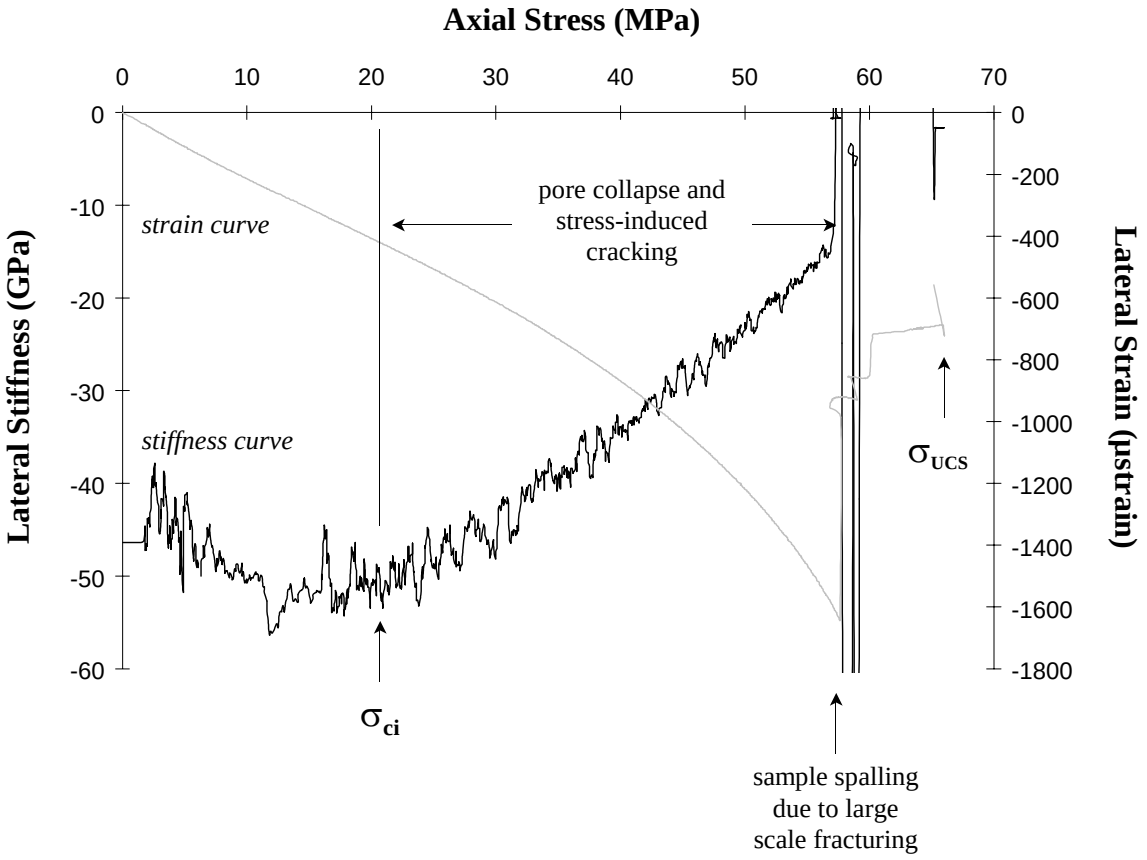

Figure 6.30 Lateral stiffness and lateral strain -*vs*- axial stress for a Berea sandstone sample showing the stiffening and softening of the lateral strain curve before the crack closure threshold is reached.

leveled off and began to decline suggesting the onset of permanent lateral strains (Figure 6.30). Values of axial stiffness, on the other hand, continued to increase past this point (Figure 6.29). This pattern was consistent for each of the samples tested (Appendix I).

Table 6.15 Average index parameters for Berea sandstone samples (standard deviation is provided in parentheses).

Material Parameter	Core Axis Parallel to Foliation	Core Axis Perpendicular to Foliation
Samples Tested	1	4
Dry Density, ρ_{dry} (g/cm^3)	2.11	2.15 (± 0.00)
Saturated Density, ρ_{sat} (g/cm^3)	2.31	2.34 (± 0.01)
Porosity, n (%)	18.6	19.0 (± 0.5)
Dry P-wave Velocity, $V_{P\,dry}$ (m/s)	3105	2993 (± 15)
Dry S-wave Velocity, $V_{P\,dry}$ (m/s)	1828	1881 (± 12)
Dry Velocity Ratio, V_P / V_S	1.7	1.6 (± 0.0)
Saturated P-wave Velocity, $V_{P\,sat}$ (m/s)	3448	3605 (± 10)
Saturated S-wave Velocity, $V_{S\,sat}$ (m/s)	1424	1648 (± 13)
Saturated Velocity Ratio, V_P / V_S	2.4	2.2 (± 0.0)

These results would seem to indicate that the internal mechanism responsible for reducing values of the lateral stiffness has the opposite effect with respect to the axial stiffness. It is believed that these effects can be attributed to an interval of pore collapse and grain compaction. Bessinger and Cook (1996) note that for high porosity materials, pore collapse is a dominant mechanism. Pore collapse and compaction would involve

both the development of axial cracks along grain boundaries, through the weaker segments of the cement matrix, and the rotation or movement of the intact grains into a tighter alignment parallel to the direction of loading (i.e. the axial direction). Electron microscope observations by Xiao *et al*. (1991) confirm that some cements in the sandstone matrix may be crushed due to high stress concentrations in the early stages of loading. Thus, decreases in lateral stiffness may be attributed to the lateral opening of grain boundary cracks through weakened cements, and increases in axial stiffness can be attributed to pore collapse and grain compaction. In addition, the collapse of pore structures can result in the offset of initiating cracks resulting in permanent lateral deformation.

Following grain compaction, contact is established between the constituent grains and an interval of approximate linear elastic behaviour is observed in the axial direction (Figure 6.29). The elastic constants for the sandstone were calculated over this interval (Table 6.16). Elastic modulus values demonstrate that there is a significant difference between the average value measured over the approximate range of linear behaviour and the secant value that incorporates the non-linearity of the crack closure and compaction processes (e.g. 27% difference). This difference was not as great, though, for the one sample in which the bedding was oriented parallel to the core axis (9% difference). This suggests that a degree of anisotropy, perhaps transverse isotropy, exists in the Berea sandstone. Poisson's ratio values for the sandstone were found to be relatively high and reflect the high degree of non-linearity in the lateral stiffness curve. Once again, this brings into question the appropriate stress interval over which to measure the elastic constants for a damaged material and the applicability of the values. Similar conclusions were made by Deflandre *et al*. (1995) for Fontainebleau sandstone, noting that elastic constants values taken at 50% of the compressive strength were questionable due to non-linearities caused by stress-induced microfracturing.

Acoustic emission activity during the initial stages of loading further established the initiation of cracks relating to the collapse of pore structures. AE numbers, subsequent to the high response related to the coupling of the loading platen with the sample, maintained a relatively constant rate during the crack closure interval (Figure

6.31). This activity was greater than that seen in the granites during crack closure. Furthermore, the detection of AE activity remained relatively constant until the crack damage threshold was reached, reflecting the continuous decrease seen in the lateral stiffness values. This would seem to suggest that the crack initiation threshold for the Berea sandstone is associated with pore collapse and therefore corresponds to the point where the lateral stiffness begins to decrease, i.e. 22 MPa or $0.33\sigma_{UCS}$ (Figure 6.30). The crack closure threshold, largely relating to axial compaction, then follows at 28 MPa or $0.42\sigma_{UCS}$.

Table 6.16 Average elastic constants for Berea sandstone samples (standard deviation is provided in parentheses).

Material Parameter	Core Axis Parallel to Foliation	Core Axis Perpendicular to Foliation
Samples Tested	1	4
Average Young's Modulus, E_{AVG} (GPa)	17.4	18.5 ($\pm$ 0.3)
Tangent Modulus, E_T (GPa)	16.3	15.4 ($\pm$ 0.5)
Secant Modulus, E_S (GPa)	15.8	13.5 ($\pm$ 0.6)
Poisson's Ration, ν	0.40	0.40 ($\pm$ 0.03)

Once a general state of compaction is reached and the axial stiffness begins to behave in a more linear fashion, stress-induced cracking due to grain contact loading would be expected. Wen *et al*. (1996) observed several mechanisms relating to the initiation of cracks in a sandstone including: fracture tip bridging, crack branching, the fragmentation of individual grains, and the spalling of grain assemblages. Similarly, petrographic observations by Bernabe and Brace (1990) established that the source of

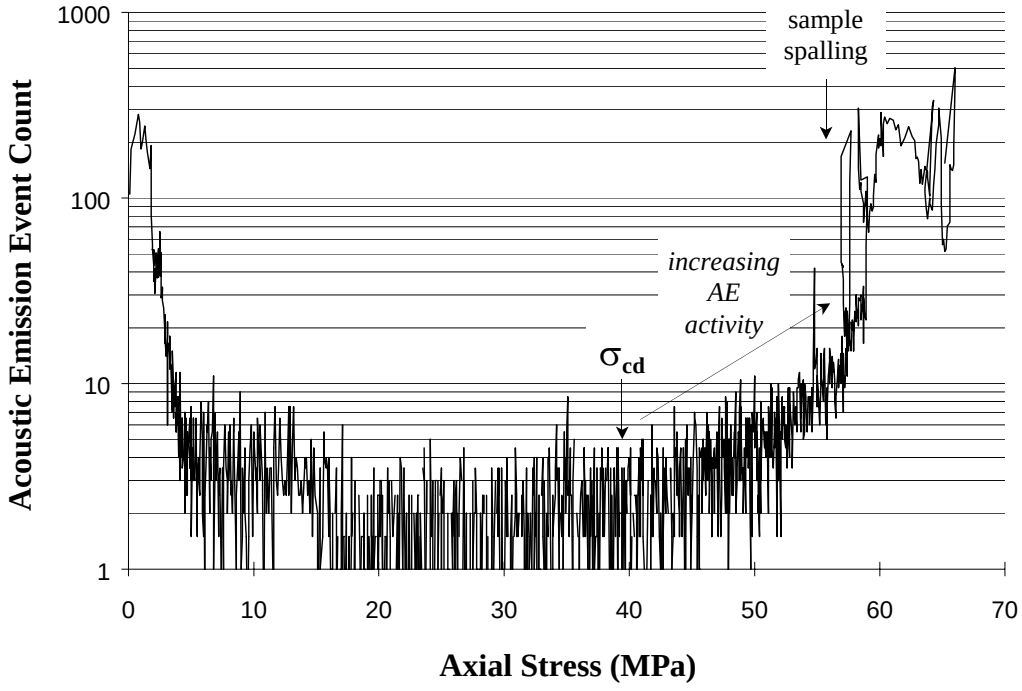

Figure 6.31 Log plot of the AE event count -*vs*- axial stress for a Berea sandstone sample.

permanent damage in stressed samples of Berea sandstone was caused by a combination of grain boundary cracking and the rotation and sliding of grains and grain fragments. In general, these mechanisms predominantly originate and act along grain boundaries resulting in cracks that propagate intergranularly through the cements. SEM observations by Menendez *et al*. (1996) on samples of Berea sandstone, confirm that very little in terms of stress-induced intragranular cracking occurred prior to failure.

Stable crack propagation and constant AE activity continued in the tested sandstone samples up to the point of volumetric strain reversal (i.e. the crack damage threshold). Similar trends were observed in the acoustic event properties. Figure 6.32 shows that the crack damage threshold was reached at approximately 38 MPa, or $0.58\sigma_{UCS}$ and coincides with a transition in the AE event rate (Figure 6.31). Unlike the granite samples tested no significant changes in the volumetric stiffness curve was detected prior to the crack damage threshold to indicate a stage of crack coalescence. Instead, Xiao *et al*. (1991) found that crack coalescence in sandstone occurs at volumetric strain reversal thus leading to unstable crack propagation and the development of fracture planes. It should also be noted that this threshold was reached at a much sooner point in the load history than that seen in the crystalline materials (i.e. $0.58\sigma_{UCS}$ as opposed to $0.75\sigma_{UCS}$).

Subsequent to the crack damage threshold, AE activity continued to increase until the unstable development and propagation of coalescing cracks resulted in the small scale spalling of the sample at $0.89\sigma_{UCS}$. This process occurred in all five samples of the Berea sandstone tested and involved the development of thin slabs of intact material delineated by coalescing cracks. As can be seen in the stiffness plots, the spalling of this material resulted in the partial to total loss of the strain gauges. Spalling on a much less significant scale was also seen in the URL rocks tested and appeared to be related to grain size (i.e. initial crack boundary length). In general, the degree of surface spalling in these rocks seemed to increase with decreasing grain size but did not occur on a large enough scale to allow for any explicit conclusions to be made. In the case of the Berea sandstone, grain sizes were several orders of magnitude smaller than those seen in the crystalline materials tested. Cracks initiating along grain boundaries,

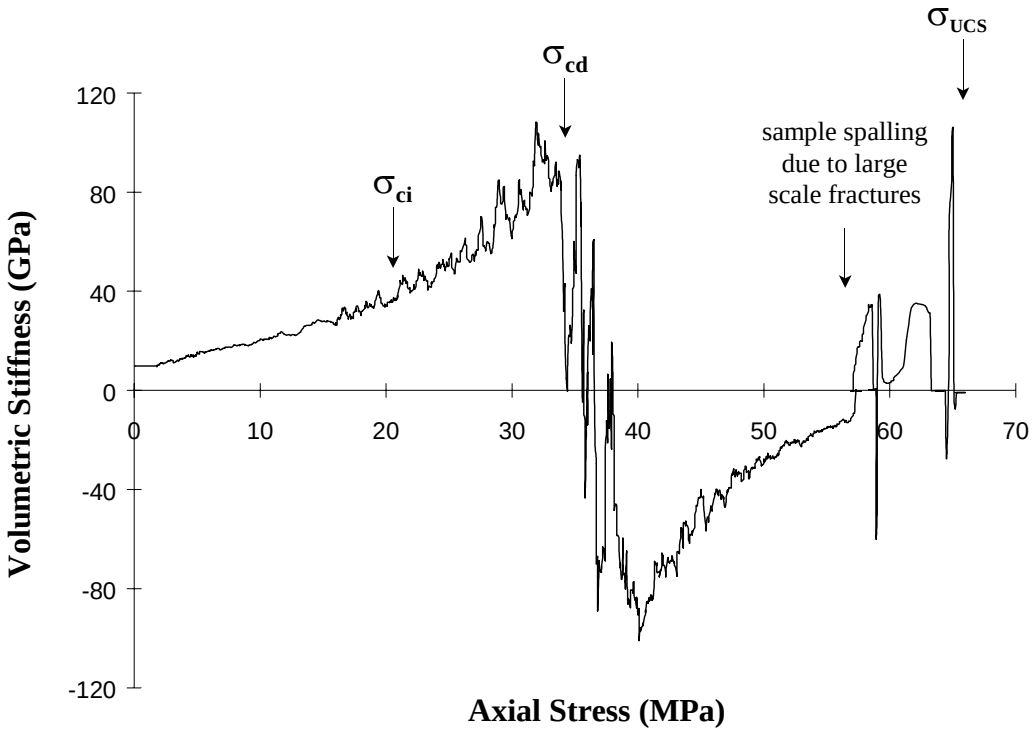

Figure 6.32 Volumetric stiffness -*vs*- axial stress for a Berea sandstone sample.

therefore, would be significantly smaller than those initiating in the granites but in terms of the number of cracks initiating, the crack density in the Berea sandstones would be much greater. In effect, the initiation of a large number of cracks on such a small scale would result in the development of confining pressures within the interior of the sample. For example, observations of stress-induced microstructural changes in limestone and sandstone sections, as reported by Myer *et al*. (1992), have shown that higher crack concentrations are observed near the boundary of the sample than in the interior, and the cracks near the boundary are more open than those in the interior of the sample. These observations suggest that interior cracks surrounded by intact rock material generate a confining stress as they open. Sammis and Ashby (1986) have shown through 2-D modelling studies of porous materials that unconfined samples tend to fail by vertical slabbing, as seen on the exterior of the Berea sandstone samples tested. The addition of low and intermediate confining pressures to their models resulted in a migration of the coalescing cracks from the centre of the material towards an outer boundary resulting in a failure plane that coincides along an apparent shear band. As was shown in the numerical modelling study presented in Chapter 5, confining stresses can act to significantly retard crack development. These observations closely match the behaviour seen in the Berea sandstone samples and suggests that the strength of the material could be drastically increased with the addition of confining stress due to its extremely fine grain size.

Subsequent to the sample slabbing, several large bursts of AE activity were detected prior to failure perhaps indicating the stick-slip development of a failure plane (Figure 6.33). The sample continued to support increases in load up until its explosive failure at 66 MPa (Figure 6.34). This value falls within the range of compressive strength values for Berea sandstone given by Shakoor and Bonelli (1991). It should also be noted that the threshold and strength values for the one sample in which the bedding was orientated parallel to the direction of loading were lower than those seen in the other sandstone samples. This would seem to suggest that the foliation acts as a plane of weakness along which cracks can more easily propagate and coalesce resulting in failure

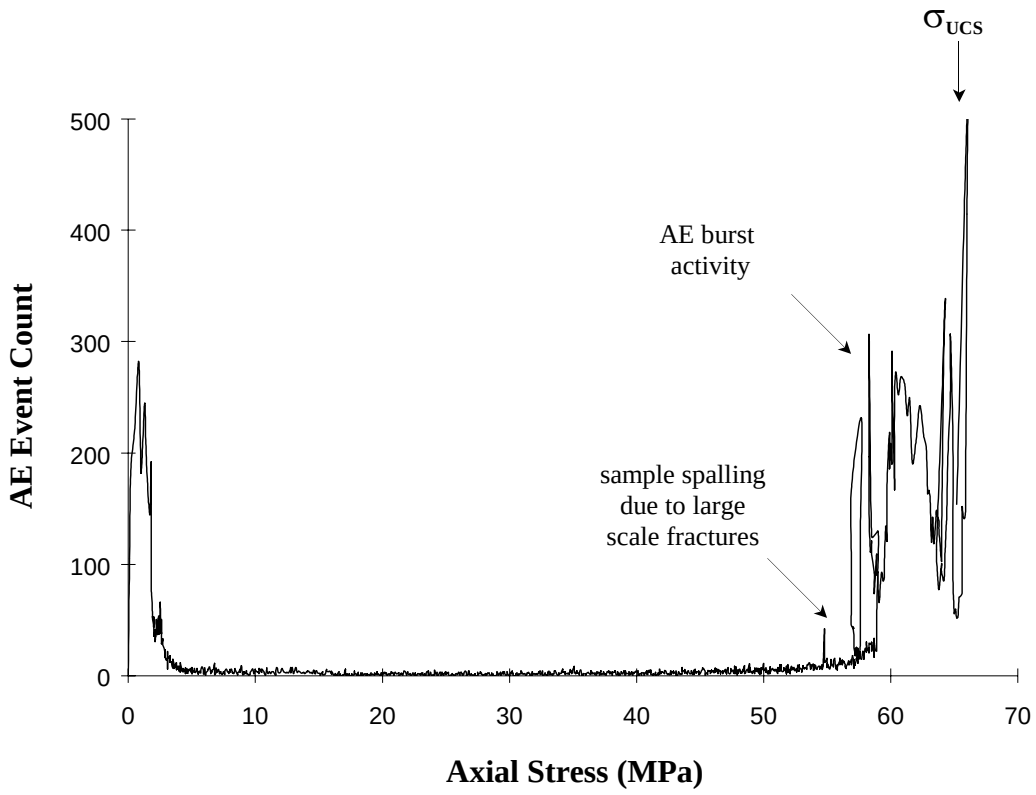

Figure 6.33 AE event count -*vs*- axial stress for a Berea sandstone sample showing several bursts of AE activity prior to failure.

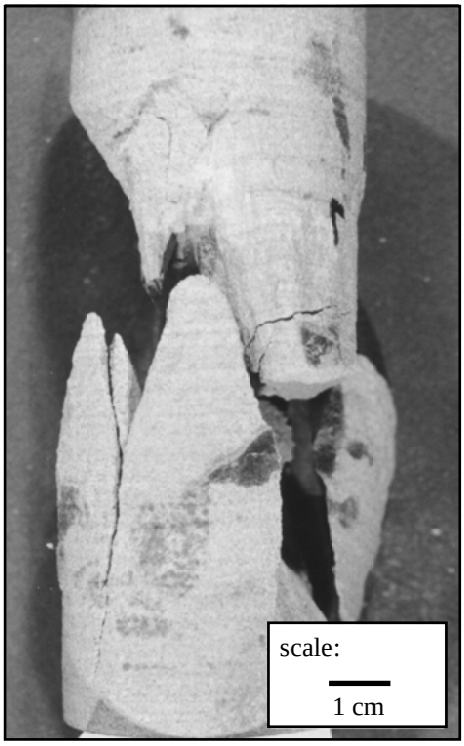

Figure 6.34 Typical mode of failure observed for the Berea sandstone showing large axial cracks and spalled pieces around sample boundary.

at lower loads. This is in agreement with observations by Wen *et al*. (1996) who observed that the fracture mechanisms of sandstone can be affected by bedding. Strength values for this sample and the four drilled horizontal to bedding are presented in Table 6.17.

Table 6.17 Average crack threshold and strength values for Berea sandstone samples (standard deviation is provided in parentheses).

Material Parameter	Core Axis Parallel to Foliation	Core Axis Perpendicular to Foliation
Samples Tested	1	4
Pore Collapse and Crack Initiation, σ_{ci} (MPa)	10.0	21.0 (± 1.2)
Crack Closure, σ_{cc} (MPa)	14.0	26.5 (± 0.9)
Crack Damage, σ_{cd} (MPa)	32.0	41.0 (± 2.1)
Sample Spalling, σ_{spall} (MPa)	43.0	62.3 (± 1.9)
Peak Strength, σ_{UCS} (MPa)	48.6	71.3 (± 3.0)

6.4 Chapter Summary

Several series of uniaxial compression tests were performed to determine the effects that varying material states may have on the development of stress-induced microfractures. Using a rigorous methodology, based on testing of the 130 m URL pink granite (Chapter 4), test results were analyzed to determine the influences grain size, sampling disturbance and rheological behaviour had on the different crack thresholds.

Grain size effects were tested using samples of fine-grained granodiorite, medium-grained grey granite and coarse-grained pegmatite from the 240 m level of the URL. In terms of the basic mechanical properties of these rocks, an inverse relationship

was found between grain size and acoustic velocity, Young's modulus and secant modulus. Analysis of the fracture characteristics of the samples showed that grain size had relatively little influence on the crack initiation and secondary cracking thresholds. These thresholds were found to be more dependent on the strength of the constituent minerals than their grain size. Grain size was found to have a detrimental effect on the crack coalescence and crack damage thresholds. Larger grain boundaries and intragranular cracks appeared to provide longer paths of weakness for growing cracks to propagate along. Rock strength was found to decrease with increasing grain size due to the presence of these longer planes of weakness which, in turn, allowed propagating cracks to coalesce at lower stresses resulting in premature failure of the samples.

Sampling disturbance effects were tested using samples taken from three different *in situ* stress regimes of the URL (i.e. 130 m, 240 m and 420 m levels). Acoustic velocity and elastic stiffness values were seen to decrease with depth of sampling. These decreases were attributable to increased stress induced sampling damage with increased *in situ* stresses. Analysis of the fracture characteristics of the samples revealed that sampling disturbance had only minor effects on the initiation of new fractures. As loads approached the crack initiation and secondary cracking thresholds, new fracturing was found to begin along those grains and grain boundaries that had not been previously damaged during sampling. Crack coalescence and crack damage thresholds, on the other hand, significantly decreased with increased sampling disturbance. The presence of numerous stress-relief cracks in the 420 m level samples were seen to weaken the rock by providing an increased number of planes of weakness for active cracks to propagate along. It was found that in the highly damaged sample more cracks may propagate more easily, resulting in their coalescence and ultimately the failure of the sample at lower than expected compressive stresses.

Ductility and porosity effects were tested using samples of Saskatchewan potash, representing a ductile material, and Berea sandstone, representing a porous material. Test results demonstrate that brittle fracture characteristics can be detected in potash under accelerated loading rates. Potash samples were seen to initially behave as an elastic material, followed by significant cracking and plastic deformation. Testing of the

Berea sandstone revealed that the behaviour and fracture characteristics of porous materials are dominated by mechanisms relating to pore collapse. In both cases, failure occurred through the initiation, propagation and coalescence of stress-induced microfractures.

CHAPTER 7

DEGRADATION OF ROCK STRENGTH THROUGH STRESS-INDUCED DAMAGE

The preceding chapters have shown how the brittle fracture process may be resolved during laboratory testing and how it may be applied to the analysis of the effects of varying grain size, sampling disturbance, and ductile and porous rock behaviour. For example, results from the preceding chapters have shown that those factors which effectively increase the number and length of weakness planes in the test sample (i.e. grain size, sampling disturbance) can have an adverse effect in terms of the ease in which propagating cracks interact, leading up to unstable crack propagation and ultimately failure of the rock. In effect, the tools and methodologies developed to perform these tasks may be used in a number of different manners to investigate the microscale mechanisms responsible for material behaviour and strength. Once these mechanisms are identified and understood, it then becomes important to quantify these processes so that they may be applied in a more practical fashion.

It has also been established in the previous chapters that the mechanical properties of the laboratory test samples vary throughout loading as the microfracturing network progressively develops. In other words, the engineering behaviour of rock is drastically different after microfracturing begins as compared to its pre-disturbed state. Martin (1993) observed through cyclic loading tests that the stress level at which the crack damage threshold was reached drastically decreased after a significant amount of damage was incurred by the sample. This becomes a critical issue since the crack damage threshold can be equated with the short-term strength of the rock (i.e. failure is imminent once crack propagation becomes unstable). If the short-term strength of the rock surrounding an excavation can decrease with increasing damage, then design limits

must be adjusted to account for this change in material behaviour. An attempt was therefore made to explore a number of means to quantify this stress-induced microfracturing damage. In addition to analyzing test results from the previously described series of monocyclic loading tests, supplementary testing involving acoustic velocity measurements and several series of cyclic loading tests were performed to better understand and quantify how the progressive accumulation of brittle fracturing changes sample deformation and reduces material strength.

7.1 Monocyclic Loading Tests

To quantify properly the effects of brittle fracture on material behaviour and strength, the process of rock failure must be defined. The initiation of a fracture, either along a grain boundary or within and through an individual crystal, may be thought of as the loss of molecular strength or cohesion in the immediate vicinity of that crack. The progressive accumulation of these fractures may therefore be thought of as damage incurred by the sample, which in turn acts to reduce its strength. However, observations of laboratory samples make it quite clear that brittle failure does not occur as the result of the complete loss of cohesion throughout the sample. Instead, failure occurs when propagating cracks coalesce into a series of larger cracks, which in turn become critical, splitting the sample along definable failure planes. Failure, in the brittle sense, is subsequently defined herein as the load sustained by the sample prior to the formation of these failure planes (i.e. post-peak behaviour is thus ignored). The gradual loss of cohesion due to stress-induced cracking may therefore be thought of as providing a number of weakened zones or planes along which coalescing cracks may more easily propagate. The following sections and analyses, therefore, are based on the assumption that the loss of cohesion leading to failure (i.e. zero cohesion) refers to the degree of microfracturing required to reach a critical state through which a number of failure planes are formed.

7.1.1 Normalized Stresses and Strains

One of the simpler options available - in terms of quantifying the results obtained through the monocyclic testing described in Chapter 4 - is to normalize the stresses and strains required to pass from one stage of crack development to another. Table 7.1 shows the relationship between axial stress, normalized with respect to the uniaxial compressive strength (σ_{UCS}), and the different stages of crack development for the 130 m level URL pink granite. Similarly, Tables 7.2 and 7.3 provide this relationship for strain, normalized with respect to the maximum recorded strains at failure. By normalizing these values an assumption is made that the threshold values for the granite will remain constant and therefore only uniaxial compressive strength or maximum strain values are required to derive their values.

Table 7.1 Stresses, normalized with respect to uniaxial compressive strength, recorded for the various stages of crack development in the 130 m level URL pink granite (standard deviation is provided in parentheses).

Crack Threshold	Normalized Relationship
Number of Tests	10
Crack Closure, σ_{cc}	0.23 σ_{UCS} ($\pm$ 0.02 σ_{UCS})
Crack Initiation, σ_{ci}	0.39 σ_{UCS} ($\pm$ 0.03 σ_{UCS})
Secondary Cracking, σ_{ci2}	0.51 σ_{UCS} ($\pm$ 0.03 σ_{UCS})
Crack Coalescence, σ_{cs}	0.65 σ_{UCS} ($\pm$ 0.04 σ_{UCS})
Crack Damage, σ_{cd}	0.75 σ_{UCS} ($\pm$ 0.05 σ_{UCS})

Table 7.2 Axial and lateral strains, normalized with respect to the maximum strains recorded at failure, corresponding to the various stages of crack development in the 130 m level URL pink granite (standard deviation is provided in parentheses).

Crack Threshold	Normalized Axial Strains	Normalized Lateral Strains
Number of Tests	10	10
Crack Closure, σ_{cc}	0.31 ε_{ax_max} ($\pm$ 0.04 ε_{ax_max})	0.07 ε_{lat_max} ($\pm$ 0.01 ε_{lat_max})
Crack Initiation, σ_{ci}	0.45 ε_{ax_max} ($\pm$ 0.04 ε_{ax_max})	0.16 ε_{lat_max} ($\pm$ 0.03 ε_{lat_max})
Secondary Cracking, σ_{ci2}	0.55 ε_{ax_max} ($\pm$ 0.05 ε_{ax_max})	0.23 ε_{lat_max} ($\pm$ 0.04 ε_{lat_max})
Crack Coalescence, σ_{cs}	0.68 ε_{ax_max} ($\pm$ 0.05 ε_{ax_max})	0.34 ε_{lat_max} ($\pm$ 0.05 ε_{lat_max})
Crack Damage, σ_{cd}	0.77 ε_{ax_max} ($\pm$ 0.05 ε_{ax_max})	0.44 ε_{lat_max} ($\pm$ 0.07 ε_{lat_max})

Table 7.3 Percentage of strains associated with each stress interval of crack development for the 130 m level URL pink granite.

Stress Interval	Percentage of Axial Strains	Percentage of Lateral Strains	$\Delta\varepsilon_{lateral} / \Delta\varepsilon_{axial}$
Number of Tests	10	10	10
0 to σ_{cc}	31 %	7 %	0.23
σ_{cc} to σ_{ci}	14 %	9 %	0.64
σ_{ci} to σ_{ci2}	10 %	7 %	0.70
σ_{ci2} to σ_{cs}	13 %	11 %	0.85
σ_{cs} to σ_{cd}	9 %	10 %	1.11
σ_{cd} to σ_{UCS}	23 %	56 %	2.43

The system of normalizing stress values for the crack initiation and crack damage thresholds has been widely used at the URL. Recent values reported by Martin (1997) include 0.3 - 0.4 σ_{UCS} for the crack initiation threshold and 0.7 σ_{UCS} for the crack damage threshold. These values closely correspond to those given in Table 7.1. Standard deviations for the normalized values also indicate that a relatively tight fit was obtained even though Martin (1993) reported that uniaxial compressive strength values for the granite were unreliable. Increasing standard deviations with increasing stress levels, however, does suggest that some degree of divergence exists, most likely relating to a degree of randomness in the crack propagation process. As stress levels increase different degrees of randomness are introduced, such as which cracks will initiate and when, how easily will they propagate along any number of possible paths (dictated by localized planes of weakness), and how will they interact and coalesce with similar advancing cracks. This increasing variation in the established crack thresholds values can be clearly seen in the form of increasing standard deviations for both normalized values (Table 7.1) and average values (Table 4.3). Larger deviations, therefore, will exist for peak strength values, thus suggesting that uniaxial compressive strength values may be unreliable. However, the act of normalizing helps to reduce the error introduced by random crack behaviour and allows these types of values to serve a useful purpose.

Normalized values also provide an easy means by which to constrain analytical, empirical or numerical models. Most design methods allow the user to have some control over the modelled material behaviour either through user-defined material properties, or in some cases user-derived constitutive models. For example, numerical modelling results from a simple parametric study can be used to obtain input parameters that will produce similar deformation and strength characteristics as those seen in the laboratory or *in situ*. In some cases specialized numerical codes, such as FLAC (Itasca, 1995), allow you to write your own subroutines through which normalized values can be used to dictate the modelled material behaviour. Normalized values thus provide a means by which to check modelled output and can be easily incorporated into any design methodology.

Further understanding and relationships may also be gained through normalized values by examining which threshold intervals incorporate different degrees of strains. Results shown in Tables 7.2 and 7.3 reveal that approximately 30% of the measured axial strain occurred during crack closure and nearly half occurred before any cracking was detected. In contrast, only 7% of the total lateral strains were recorded during the crack closure interval, reinforcing earlier assumptions that crack closure predominantly involves cracks preferentially aligned perpendicular to the applied load. The largest proportion of total lateral strain was recorded in the interval following crack coalescence. Approximately 66% of the lateral strains may be attributed to the coalescence and unstable propagation of growing cracks. It should be noted that these proportional relationships still hold true when the length of the associated stress interval is accounted for.

Similar to the normalized stress relationships, normalized strains can also be incorporated into numerical models. Table 7.4 shows the approximate strain rates in terms of an axial deformation modulus (E_{def}) and the ratio of lateral to axial deformation (ν_{def}) based on average normalized values for the 130 m level pink granite. It should be noted that unlike the elastic constants, E and ν, these parameters incorporate non-linear strains accumulated within the given stress interval (i.e. a ν_{def} parameter greater than 1 would indicate a material in which the lateral strains exceed the axial strains). These deformation parameters can be easily incorporated into numerical models and would allow for more accurate simulations in terms of changes in material behaviour with progressive microfracturing. Figure 7.1 illustrates the fit of the modelled deformation parameters to the normalized data recorded through a uniaxial compression test performed on a 130 m level URL pink granite. One advantage of using a simple design methodology such as this is that once the deformation parameters are determined the model provides a quick approximation of the material behaviour. However, this simple methodology only addresses the deformation characteristics of the rock observed in the laboratory, it does not address the loss of cohesion and material strength with progressive microfracturing.

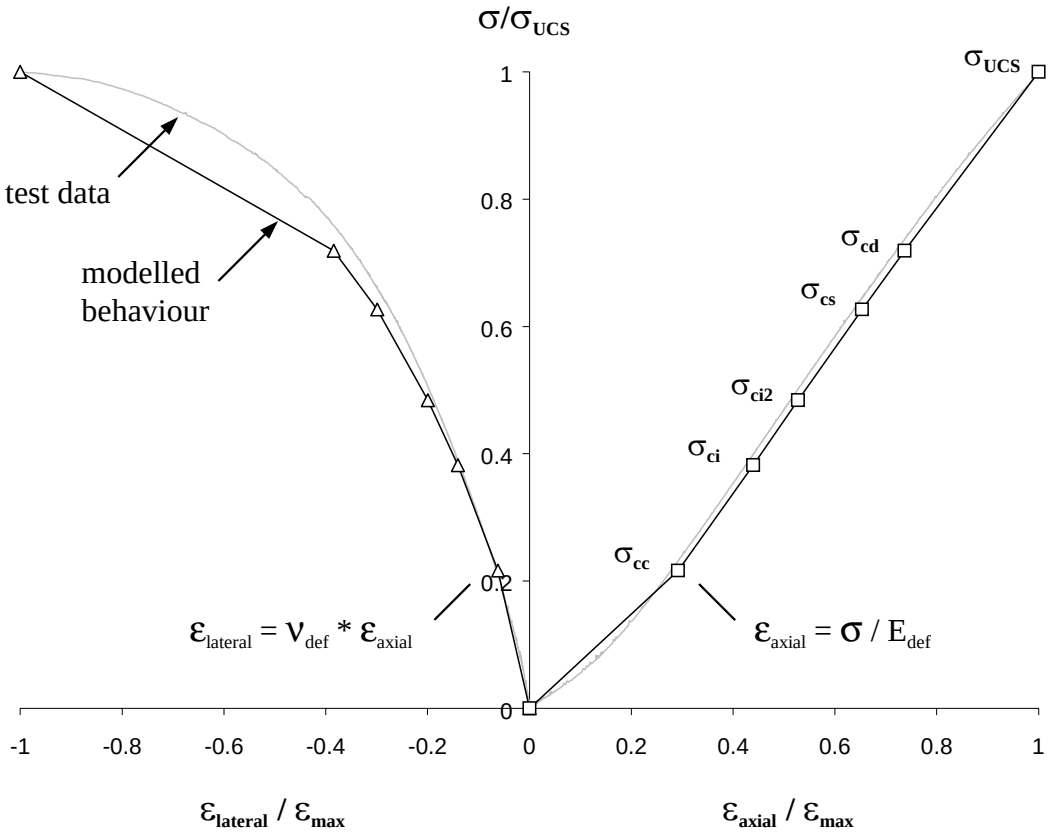

Figure 7.1 Normalized plot of axial stress -*vs*- strain comparing laboratory test data to a simple analytical deformation model for 130 m level URL pink granite. The modelled behaviour is derived using an axial deformation modulus, E_{def}, and the ratio of the lateral to axial deformation, ν_{def}.

Table 7.4 Deformation characteristics of the 130 m level URL pink granite equated in terms of an axial deformation modulus, E_{def}, and a ratio of the lateral to axial deformation, ν_{def}. It should be noted that some threshold intervals incorporate a large proportion of non-linear strains.

Stress Interval	E_{def} (GPa)	ν_{def}
Number of Tests	10	10
Crack Closure (0 to σ_{cc})	42.2	0.09
Elastic Deformation (σ_{cc}o σ_{ci})	63.8	0.23
Stable Cracking I (σ_{ci} to σ_{ci2})	65.6	0.29
Stable Cracking II (σ_{ci2} to σ_{cs})	64.7	0.34
Crack Coalescence (σ_{cs} to σ_{cd})	62.8	0.45
Unstable Cracking (σ_{cd} to σ_{UCS})	60.8	1.01

7.1.2 Acoustic Velocities

As demonstrated in Chapter 6, acoustic velocities can be used as an indicator of stress-induced damage. Acoustic, or sound, velocities are measurements of the speed at which stress waves are transmitted through the material and are highly dependent on the elastic properties and density of the host material. Microfractures change the localized elastic properties and density of the material, and hence the velocity and attenuation of the propagating waves. The closure of existing cracks increases acoustic velocities whereas the opening of cracks reduces velocity values from those expected for the intrinsic mineral matrix of the material. In both cases, velocity measurements are highly sensitive to the orientation of the crack with respect to the wave motion. Acoustic velocities have been widely used, both in the laboratory and *in situ*, as a measure of crack density and damage (Sayers and van Munster, 1991; Ma *et al*., 1995; Munson *et al*., 1995).

A series of uniaxial compression tests were performed using high frequency velocity transducers in an attempt to quantify stress-induced damage as a function of

measured velocity changes. The frequency of the compression and shear piezoelectric crystals (250 kHz) was chosen based on the grain size of the pink granites so as to ensure that the wavelength of the signal was at least three times that of the largest grains. This helped to minimize the degree of reflection and refraction experienced by the wave, thus providing a more coherent signal for analysis. The crystals were housed in a pair of specially designed loading platens to allow for the recording of acoustic pulse travel times during loading. Travel time measurements were made at 5 MPa increments and, subsequently, were analyzed to determine the P- and S-wave velocities, as well as the initial and peak S-wave amplitudes. Values were then correlated to the stress-strain behaviour of the samples as recorded using strain gauges. One drawback associated with the nature of these tests was that acoustic emissions could not be recorded at the same time. In addition, size limitations associated with the housings did not permit the addition of a second shear crystal orientated at 90° to the first, thereby allowing for comparisons to be made with respect to directional fracture anisotropy.

Results from these tests indicate that both the P- and S-wave velocities generally increased throughout loading (Figure 7.2). This was not expected since stress-induced microfracturing should be accompanied by decreases in the measured velocities. These results, however, may be somewhat misleading since velocity measurements were restricted to a plane parallel to the core axis due to limitations imposed by the test equipment used. Since both the P- and S-wave were generated to propagate along the sample axis, velocity values would be most sensitive to cracks orientated perpendicular, or at shallow angles, to the velocity path. It then follows that as cracks with normals aligned along the direction of loading preferentially close, P- and S-wave velocities will increase. The initiation and propagation of new cracks parallel to the direction of loading, and likewise the velocity path would, in contrast, have very little effect on the measured velocity values. The detection of these cracks through velocity measurements would be more readily achieved if the transducers were orientated perpendicular to the direction of loading. However this would require specialized equipment such as that described by Chow *et al*. (1995). Continued increases in the velocity values were observed up to the point where the material appears to yield, resulting in a sharp decline

in P- and S-wave values (Figure 7.2). These sharp velocity decreases likely reflect the onset of plastic yielding in the crystals and the lateral breakdown of bridging material and large scale coalescence of cracks leading up to sample failure. Overall, however, the progressive accumulation of brittle fractures throughout loading was undetectable using P- and S- wave velocity values.

Initial and peak S-wave amplitudes were subsequently analyzed to see if the initiation and propagation of cracks parallel to the direction of the generated acoustic velocity pulse could be detected through changes in the recorded waveform characteristics. Since S-waves oscillate perpendicular to the direction in which they are travelling, it was anticipated that the microfracturing processes undetectable through acoustic velocity values could be detected through the analysis of the waveform's amplitudes. Results from this analysis show that a drop in the peak S-wave amplitude occurs at the crack coalescence threshold (determined independently through strain gauge analysis). The lack of any changes in amplitude values following the crack initiation threshold would appear to indicate that the method is not sensitive enough to detect the development of smaller individual cracks. It is not until these cracks coalesce into larger cracks that they have some measurable effect on the S-wave properties. Large decreases were observed in the peak S-wave amplitudes following crack coalescence (Figure 7.3).

These results, however, did little more than to serve as another qualitative check with respect to identifying the various thresholds of crack behaviour. A number of difficulties were also encountered throughout testing as the explosive nature of the brittle failure process at high stresses had an adverse effect on the P- and S-wave crystals. Three tests were attempted and in each case the crystals would become unseated in their housings resulting in decreased sensitivity and poor signal quality. Due to the reduced effectiveness of these tests and the lack of any solid quantitative measurements, it was decided to discontinue this line of testing.

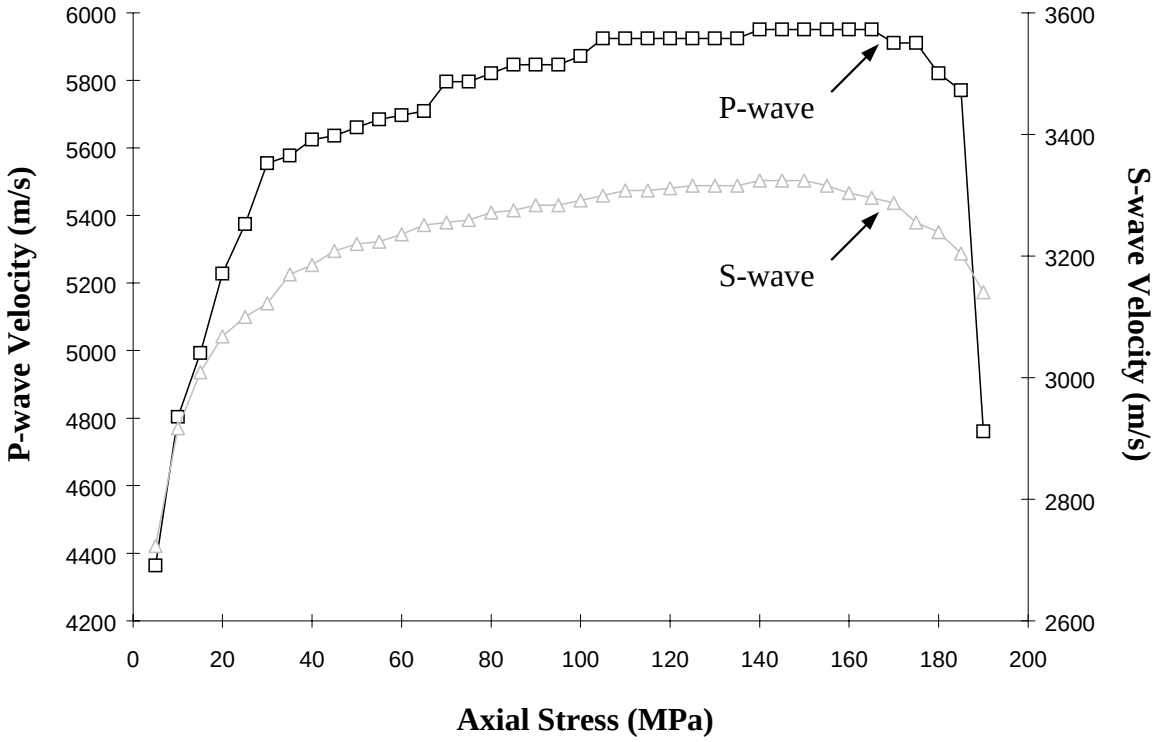

Figure 7.2 P- and S-wave velocities -*vs*- axial stress for a 130 m level URL pink granite.

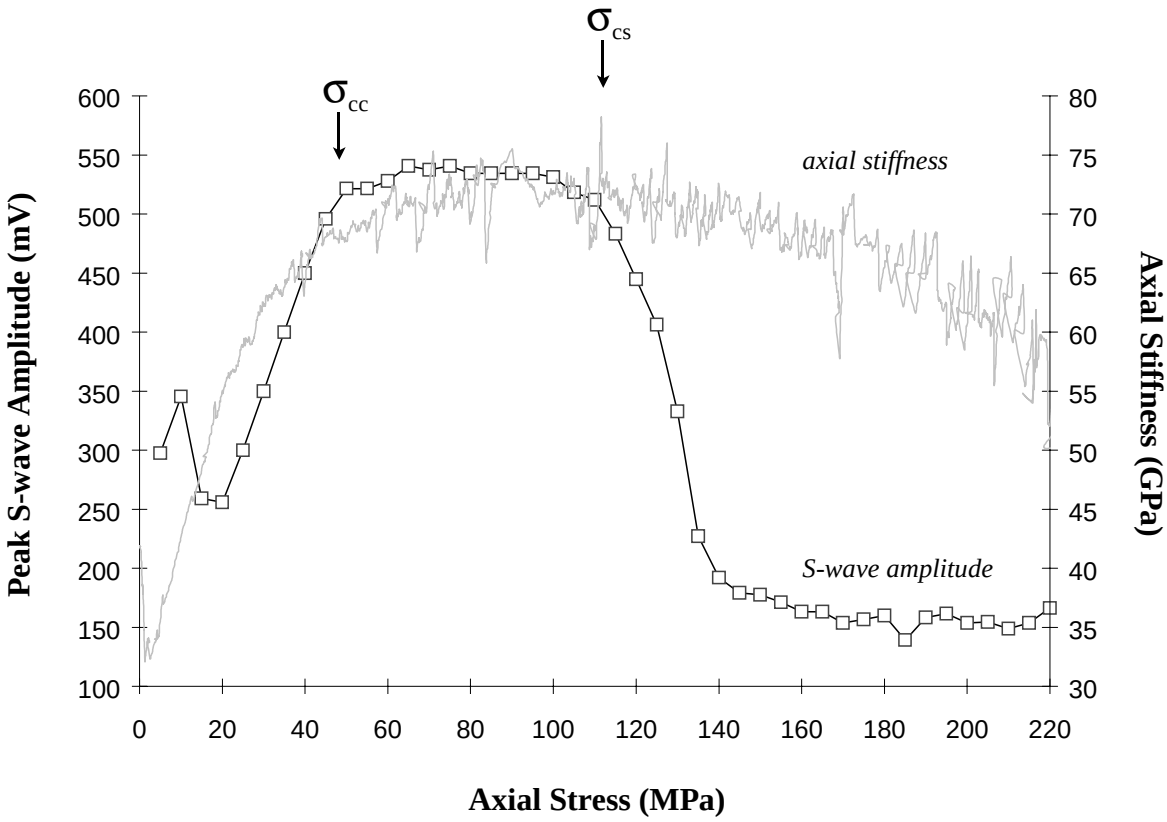

Figure 7.3 Peak S-wave amplitudes and axial stiffness -*vs*- axial stress showing the crack closure and crack coalescence thresholds for a 130 m level URL pink granite.

7.1.3 Normalized Acoustic Emission

Lockner (1993) describes the initiation and propagation of a microfracture as irreversible damage resulting in both plastic strain and an acoustic event. The use of normalized strain gauge measurements presented earlier provided a simple means to describe the deformation characteristics of the tested samples during the progressive accumulation of microfracturing damage. Although these measurements included the plastic strains associated with crack development, they also included elastic strains and plastic strains associated with the behaviour of the constituent minerals. Uncertainties in the elastic constants and the presence of large strains relating to the stick-slip movements between coalescing grains makes it difficult to correlate strain gauge measurements directly to the loss of cohesion resulting from the initiation and propagation of a crack.

Acoustic emissions, on the contrary, provide a direct measure marking the rapid release of energy associated with damage related mechanisms. In brittle materials, pore collapse, crack propagation and grain boundary movements are all readily accepted as damage related processes which produce AE events (Holcomb *et al*., 1990). Test results were therefore analyzed to develop a simple relationship correlating AE activity with the gradual loss of cohesion and the accumulation of damage. AE event counts for each crack threshold were normalized with respect to the total number of events recorded at failure so that comparisons could be made from test to test. This was necessary since a number of factors can influence the sensitivity of the AE transducers. For example the degree of coupling achieved between the sample and the transducers can have a significant effect on the total number of events recorded from test to test. However, these factors have relatively little influence on the relative proportions of events recorded throughout testing. AE counts were also normalized with respect to the total number of events at the crack damage threshold since an extremely high proportion of events are recorded during unstable crack propagation and prior to failure.

Results from this analysis indicated that the relative percentage of events recorded between the different thresholds of crack development remained fairly constant regardless of the AE detection thresholds used. One exception to this observation was with respect to the number of events recorded during the crack closure interval. Lower detection threshold values resulted in higher and disproportionate numbers of events from test to test. This was likely due to the increased sensitivity to lower energy events associated with the mechanisms acting during crack closure. To correct for this, events recorded during crack closure were subtracted from the total cumulative count. The total percentage of events recorded up to the crack initiation threshold, therefore, include only those events recorded between crack closure and crack initiation.

Results for this analysis are presented in Table 7.5. Assuming that the number of AE events detected can be directly correlated to damage, results indicate that the majority of damage causing mechanisms occur during unstable crack propagation prior to failure (approximately 83%). However, if it assumed that once crack propagation becomes critical and failure is inevitable, then the analysis can be normalized with respect to the crack damage threshold (as also shown in Table 7.5). In this respect, the results indicate that approximately 55% of the damage causing mechanisms leading up to unstable crack propagation occur prior to crack coalescence and 45% occur afterwards. From these values it becomes possible to develop simplified criteria which describe the gradual loss of cohesion along a critical plane resulting in the brittle failure of the sample. Once again, this analysis assumes that failure of the sample occurs not as a result of absolute cohesion loss throughout the sample but as a gradual loss of cohesion up to a point where complete cohesion loss occurs along a critical plane formed by coalescing cracks.

Similar to the normalized strain models presented earlier, it is possible to use the relationships shown in Table 7.5 to construct a simplified model describing the damage or loss of cohesion along a critical plane leading up to critical crack propagation (herein referred to as critical cohesion). Figure 7.4 demonstrates the fit of the model to test data for a 130 m level URL pink granite and also shows the progressive loss of critical

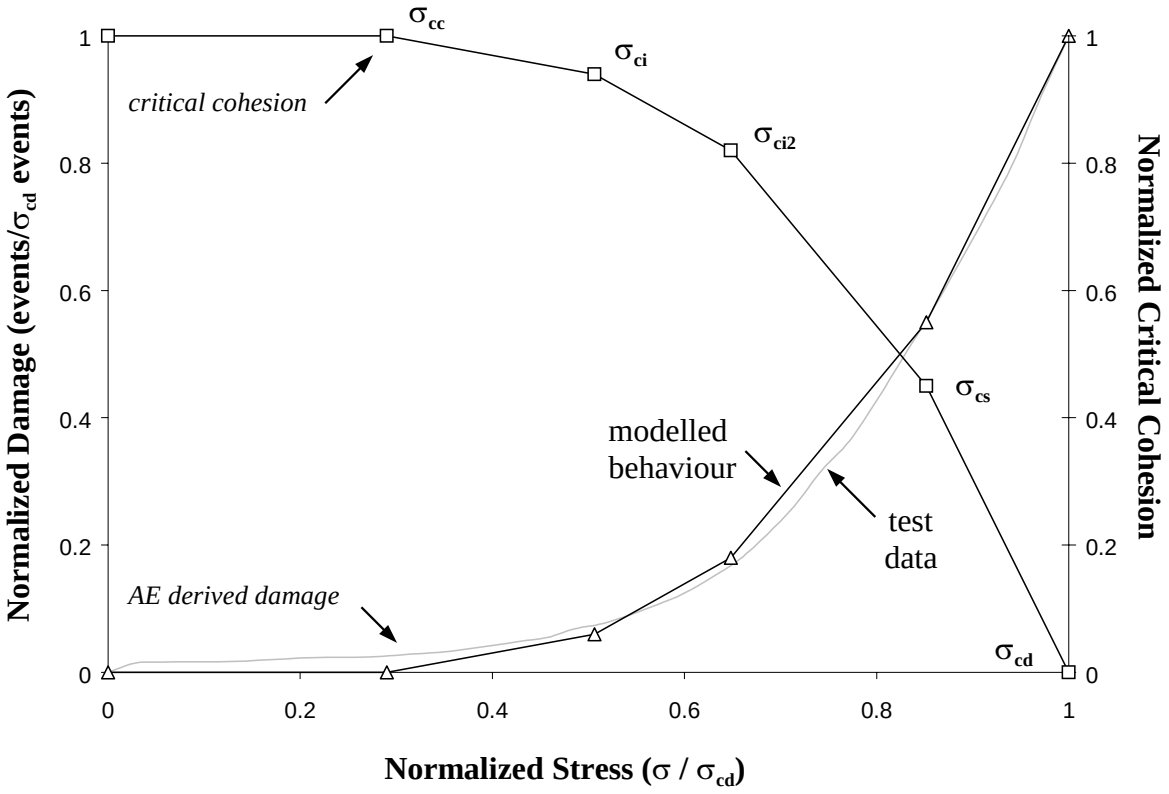

Figure 7.4 Plots of normalized damage and critical cohesion -*vs*- axial stress for the 130 m level URL pink granite. Damage and critical cohesion are derived from cumulative AE event data.

Table 7.5 Cumulative AE event count, normalized with respect to the event count recorded at the peak load and the crack damage threshold, for the 130 m level URL pink granite (standard deviation is provided in parentheses).

Crack Threshold	AE / (AE @ σ_{peak})	AE / (AE @ σ_{cd})
Number of Tests	5	10
Crack Initiation, σ_{ci}	0.006 AE_{total} ($\pm$ 0.002)	0.063 AE_{total} ($\pm$ 0.041)
Secondary Cracking, σ_{ci2}	0.024 AE_{total} ($\pm$ 0.011)	0.185 AE_{total} ($\pm$ 0.084)
Crack Coalescence, σ_{cs}	0.094 AE_{total} ($\pm$ 0.031)	0.552 AE_{total} ($\pm$ 0.090)
Crack Damage, σ_{cd}	0.175 AE_{total} ($\pm$ 0.024)	1.000 AE_{total} ($\pm$ 0.000)
Peak Strength, σ_{UCS}	1.000 AE_{total} ($\pm$ 0.000)	n/a

cohesion as a function of the normalized AE damage. It is also possible to fit a third order polynomial to the test data which would allow for the direct incorporation of a continuous function describing the accumulation of AE detected damage throughout loading. Derived with respect to the crack damage threshold this function can be written as:

$$\omega_{AE} = \frac{\sigma}{\sigma_{cd}} \left(\frac{2.2\,\sigma^2}{\sigma_{cd}^2} - \frac{1.5\sigma}{\sigma_{cd}} + 0.3 \right) \tag{7.1}$$

where : ω_{AE} = acoustic emission related cumulative damage parameter (AE count / AE count at σ_{cd}).

σ_{cd} = crack damage threshold (MPa);

σ = axial load (MPa).

The r-squared value (i.e. R^2) for the fit of this expression when compared to the average values obtained through laboratory testing was 0.9995. A similar relationship can be derived to include the acoustic events recorded between the crack damage and peak strength thresholds (i.e. normalizing the cumulative AE count with respect to the total number of events recorded at failure). However, due to the sharp increase in the number of events recorded prior to failure a sixth order polynomial is required to describe the full relationship (Figure 7.5). This essentially renders the relationship unusable due to the increased complexity required to describe the entire damage curve. In practical terms, it appears that the simplified relationships derived with respect to the crack damage threshold are more functional.

The simplest application of a damage criterion based on AE events would likely be in the form of a failure criterion incorporated into a numerical model. This would allow for a direct comparison between modelled stresses and the degree of microfracturing damage induced. It would also be possible to implement these relationships with respect to a constitutive model that allows for plastic deformation with increasing damage. The obvious deficiency of these simplified models, however, is that they are derived from laboratory based uniaxial compression tests. Further study would be required to determine the sensitivity of these models to confining stresses, thus taking into account the true nature of the stress state surrounding an underground opening.

7.2 Cyclic Loading Tests

The relationships previously described have all concentrated on characterizing the effects of microfracturing damage induced through monotonic loading tests. However, the load history of the near field rock surrounding an underground opening can sometimes be much more complex than that of a load incrementally increasing until the rock fails. Martin (1993) has shown that the state of stress at a point can increase, unload and then increase again as the tunnel advances towards the point and passes it. If these stresses induce microfracturing but not failure, then the mechanical properties of

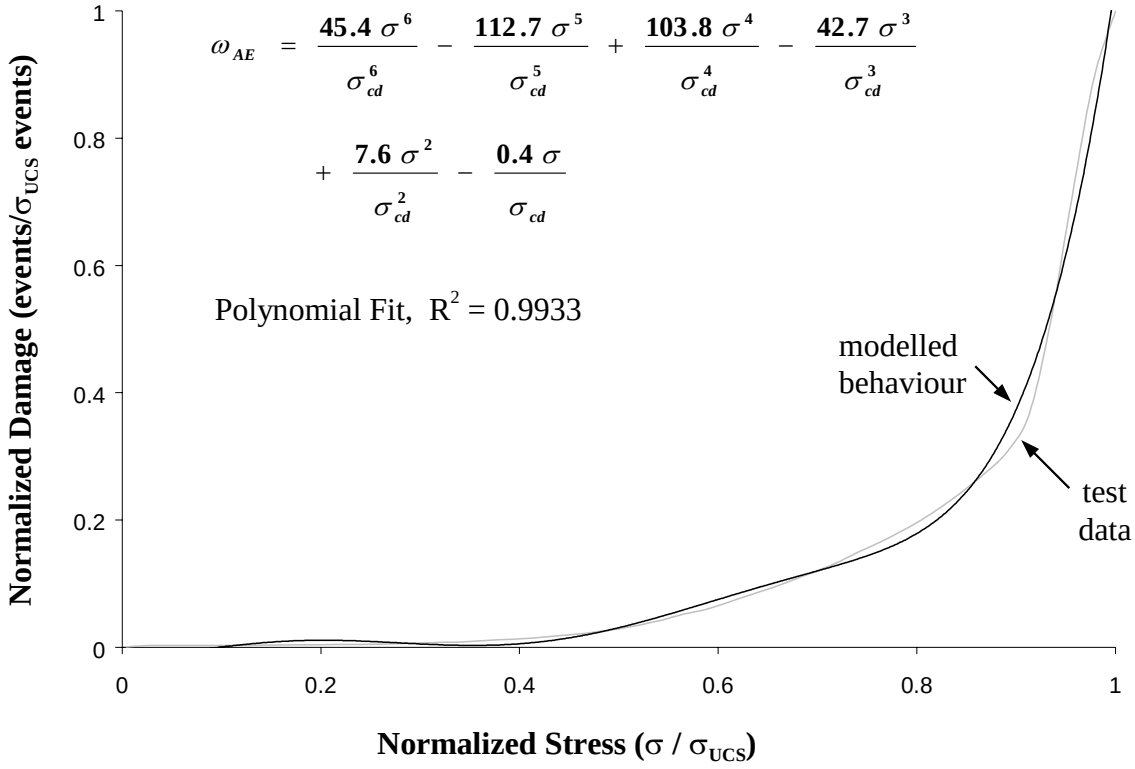

Figure 7.5 Plot of AE derived damage -*vs*- axial stress normalized with respect to the total number of events recorded at failure for the 130 m level URL pink granite. The AE based damage curve, in this case, requires a six order polynomial to properly describe the function.

the rock may significantly vary upon subsequent unloading and reloading, thus deviating from the expected behaviour determined for its initial state. Over time, these loading and unloading cycles may alter the properties of the rock to a point where it fails well below established strength values for the rock. This phenomenon has been confirmed through cyclic loading tests aimed at determining a “fatigue” strength for the tested rock.

Martin (1993) performed a series of cyclic loading tests, termed damage-control tests, to correlate increasing damage to the reduction in cohesion and increasing friction (Figure 7.6). In the development of these relationships, cohesion can be equated to the crack damage threshold and normalized it with respect to the peak strength of the rock. The friction angle was then calculated based on the crack damage threshold under the assumption that crack mobilization occurs at this point. Damage was defined as the permanent volumetric strain incurred during each load-unload cycle. These results greatly advanced the prevailing concepts of cohesion and mobilized friction in brittle rock, and showed that the prediction of failure around tunnels experiencing damage cannot be based on strength envelopes derived from traditional laboratory tests.

Martin's (1993) tests, however, primarily concentrated on the crack damage threshold to quantify cohesion and was thus limited to strain gauge measurements. Results presented in earlier chapters have shown that a number of other thresholds exist and have a marked influence on the overall behaviour of the rock. It was therefore decided that a similar series of cyclic loading tests be performed to examine the changes in the other detected crack processes and to use acoustic emission techniques to help quantify the induced damage. Traditionally, damage has been quantified as the accumulation of permanent axial strains with each cycle since microfracturing introduces an element of nonlinearity into the theoretical elastic behaviour of the sample. Martin (1993) defined damage, ω, as the permanent volumetric strain incurred with each cycle, noting that crack propagation involves a volumetric component as opposed to the one-dimensional measure provided by axial strain measurements.

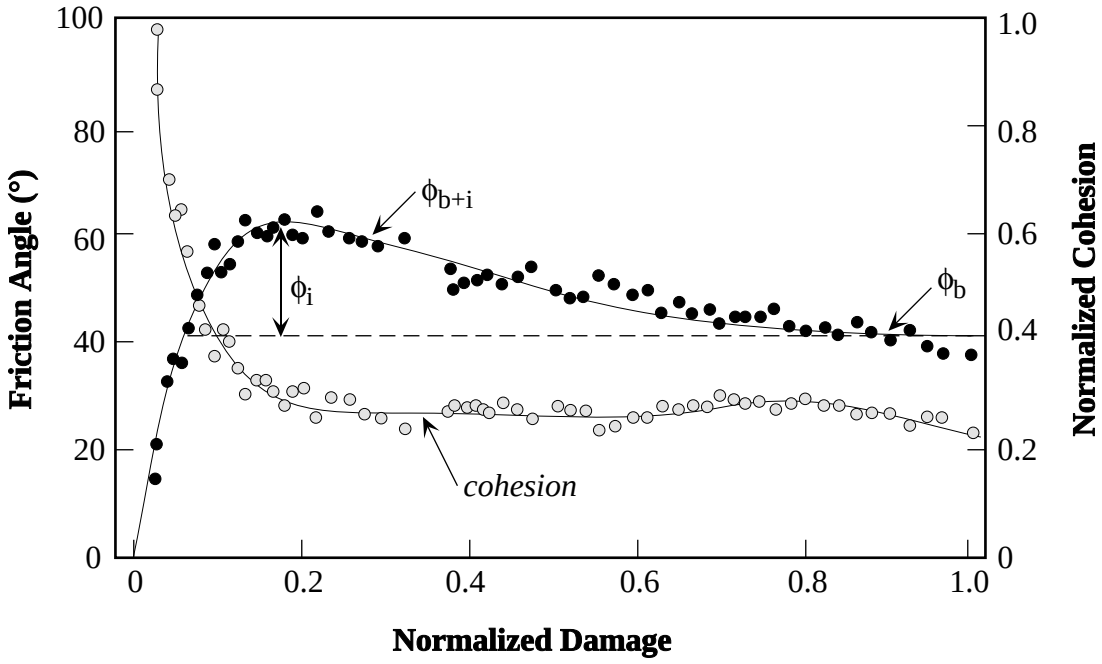

Figure 7.6 The mobilization of friction and cohesion as a function of damage, where ϕ_b represents the mobilized friction angle and ϕ_i is the angle of friction caused by roughness or the interlocking of asperities (after Martin, 1993).

It was found, however, that the different internal mechanisms relating to crack propagation and coalescence may induce axial and lateral displacements which could negate one another in terms of their use in the volumetric strain calculation (Equation 4.2). For example, the collapse of bridging material between cracks following the crack coalescence threshold could act to stiffen the material thereby reducing the permanent axial strain during the next cycle. This reduction in the permanent axial strain magnitude may result in negative damage values derived through volumetric strains even though cracks are still opening, in the lateral direction, thus inducing positive damage. Martin (1993) likely reduced this effect by loading the material to 75% of its peak strength with each cycle ensuring that crack propagation reached its critical limits and that enough damage had occurred in both the lateral and axial strain measurements to produce a positive damage value. Similar results were obtained in this study and are described in the following section, however, tests cycled to a lower load limit demonstrated that to accurately portray the development of microfracturing damage, separate damage parameters should be calculated for the permanent axial strain, ω_{ax}, and lateral strain, ω_{lat}. As well, a damage parameter was derived for the permanent volumetric strain, ω_{vol}, and the recorded number of acoustic events, ω_{AE}. For each case, the damage measured over a single load-unload cycle, or damage increment "*i*" (Figure 7.7), was normalized with respect to the total damage measured throughout the test. These parameters are thus defined as follows:

$$\omega_{ax} = \frac{\left(\varepsilon_{ax}^{p}\right)_i}{\sum_{i=1}^{n}\left(\varepsilon_{ax}^{p}\right)_i} \tag{7.2}$$

$$\omega_{lat} = \frac{\left(\varepsilon_{lat}^{p}\right)_i}{\sum_{i=1}^{n}\left(\varepsilon_{lat}^{p}\right)_i} \tag{7.3}$$

$$\omega_{vol} = \frac{\left(\varepsilon^{p}_{vol}\right)_i}{\sum_{i=1}^{n}\left(\varepsilon^{p}_{vol}\right)_i} \tag{7.4}$$

$$\omega_{AE} = \frac{\left(\text{events}\right)_i}{\sum_{i=1}^{n}\left(\text{events}\right)_i} \tag{7.5}$$

where : ω_{ax}, ω_{lat}, ω_{vol}, ω_{AE} = damage parameters;

ε^{p}_{ax}, ε^{p}_{lat}, ε^{p}_{vol} = permanent strain;

events = number of recorded AE events;

i = damage increment (i.e. one load-unload cycle).

7.2.1 Damage-Controlled Testing Above the Crack Damage Threshold

A damage-control test was performed whereby a sample of pink Lac du Bonnet granite was loaded in uniaxial compression to a stress level just above the crack damage threshold. The sample was then unloaded, completing one damage increment, and then loaded again up to the approximate crack damage threshold. This process was repeated until the sample failed at damage increment 46 (Figure 7.8). Load rates for these cycles were approximately 25 to 30 MPa/minute and the test took approximately eight hours to complete. In general, this test duplicated those reported by Martin (1993) with the exception that the test was not carried into the post peak region of sample behaviour. In addition, Martin (1993) used granite samples from the 420 m level of the URL which were shown in Chapter 6 to be highly disturbed in their initial state due to stress relief upon sample retrieval.

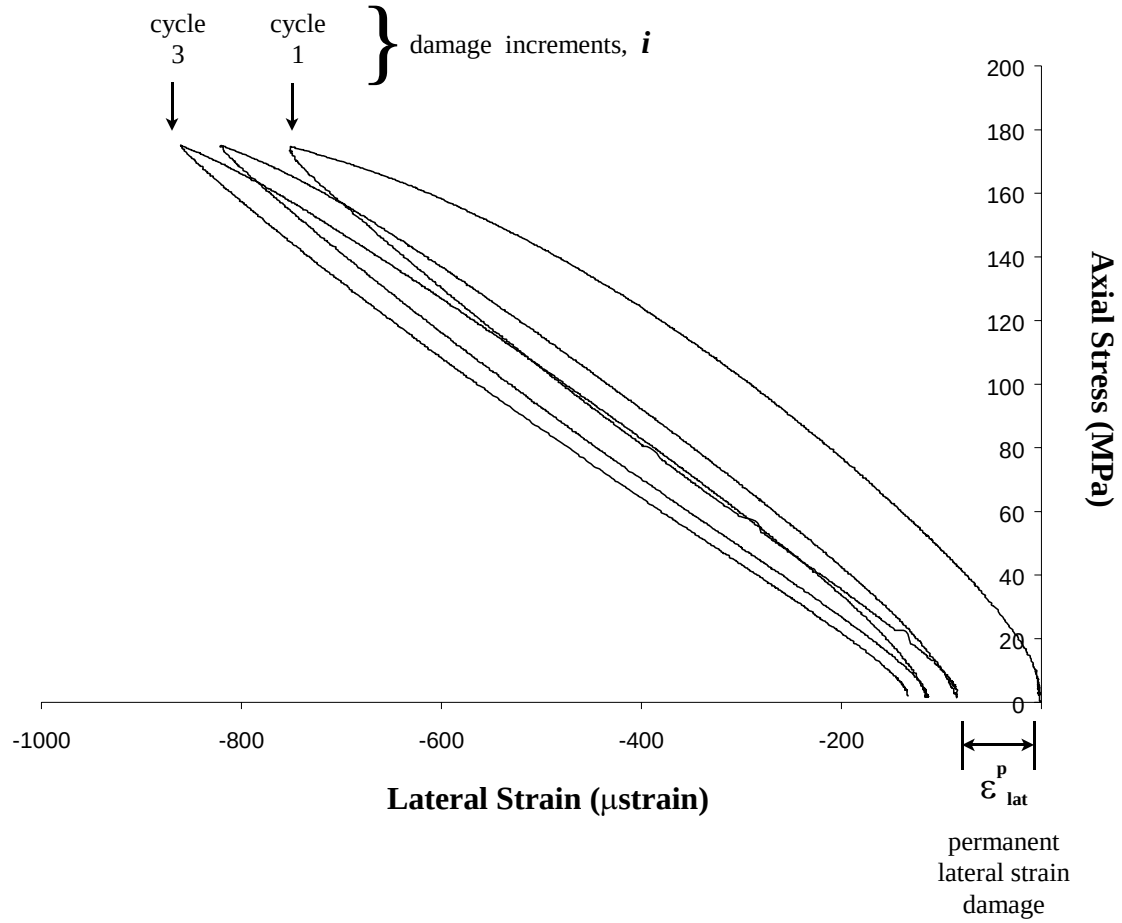

Figure 7.7 Axial stress *-vs-* lateral strain showing the first three cycles of a cyclic loading test and the resulting permanent lateral strain damage, ε^{p}_{lat}, with respect to the damage increment, *i*.

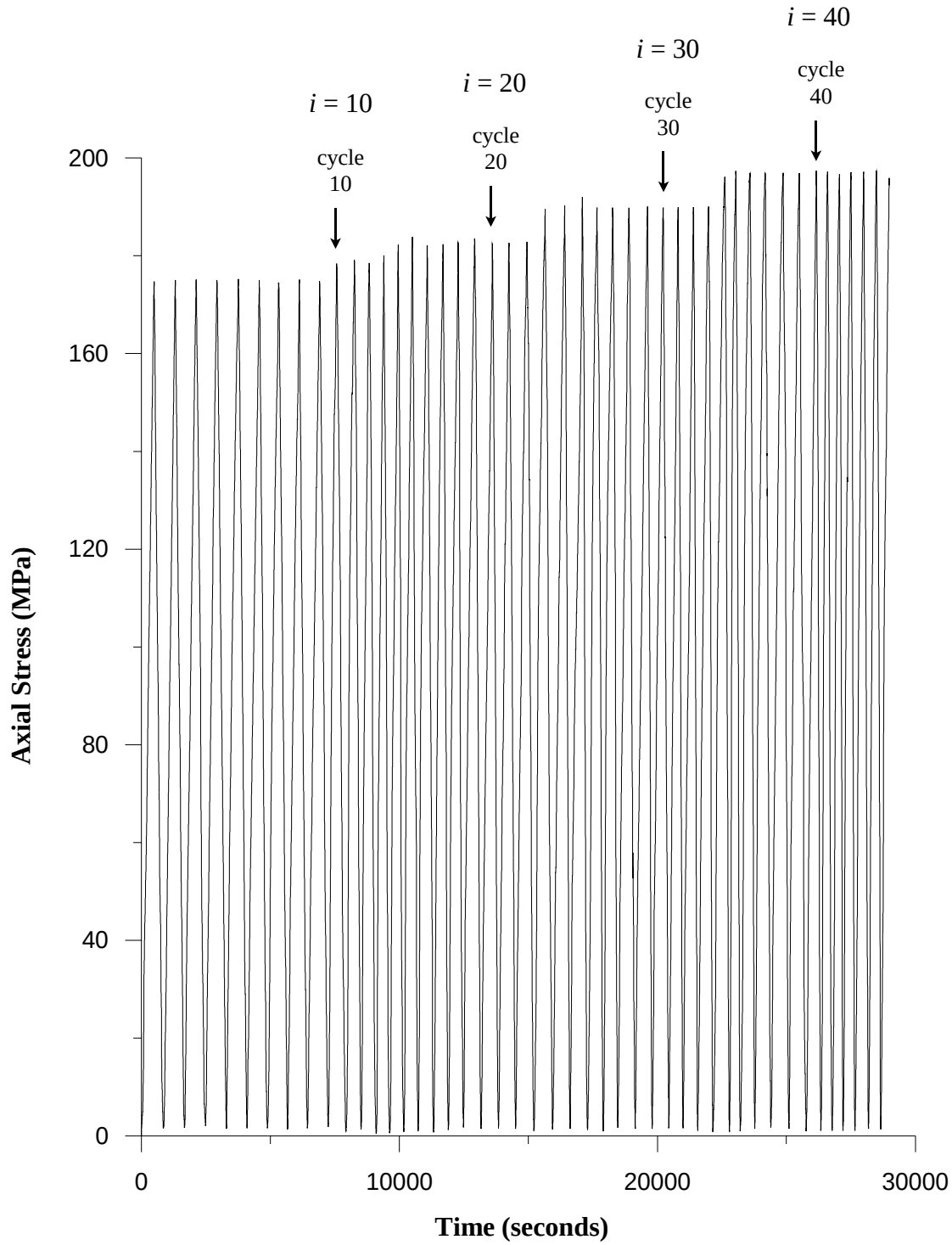

Figure 7.8 Axial stress -*vs*- time showing the load history of a damage-control test performed on a 130 m level URL pink granite.

Results from these tests concur with those obtained by Martin (1993). Figure 7.9 shows that with each damage increment, permanent strain damage attributable to microfracturing accumulated in the sample. This was true for both the axial and the lateral strain damage parameters as shown in Figure 7.10. The volumetric strain damage parameter, however, decreased between damage increments 12 and 24 even though positive damage was recorded in both the axial and lateral directions. This anomaly was due to the axial and lateral strain based derivation used to calculate volumetric strain (as previously discussed). In terms of material behaviour, these increases in damage over a number of load and unload cycles were seen to have a negative effect in terms of gradually reducing the strength of the rock. Figure 7.11 shows that the crack damage threshold for the sample slowly increased up to damage increment 26 before rapidly dropping to values well below the initial crack initiation threshold for the rock. Values for the crack coalescence threshold followed a similar pattern with the exception that a small-scale fluctuation could be seen throughout the test. These oscillations emulated a similar pattern to the absolute axial strain damage (Figure 7.12) and likely reflect the build-up and release of localized energy as cracks coalesce into one another. Figure 7.13 illustrates these mechanisms and suggests that the coalescence of interacting cracks would be accompanied by large plastic strains as the bridging material between the cracks weakens and collapses. The coalescence of these smaller cracks would result in the development of new, effectively longer cracks for which the crack tip material would be stiffer. Increased load energy (i.e. stresses) would be required during the next damage increment to develop the process zone around the tips of these newly formed cracks. As a result, the stresses required to reactivate the cracks during the next damage increment would increase (i.e. the crack coalescence threshold increases). This process appears to repeat itself several times during the test. These increases in the crack coalescence threshold, however, only occur over intervals of one or two damage increments at a time, whereas the decreasing trend of the curve alludes to the overall degradation of the material strength.

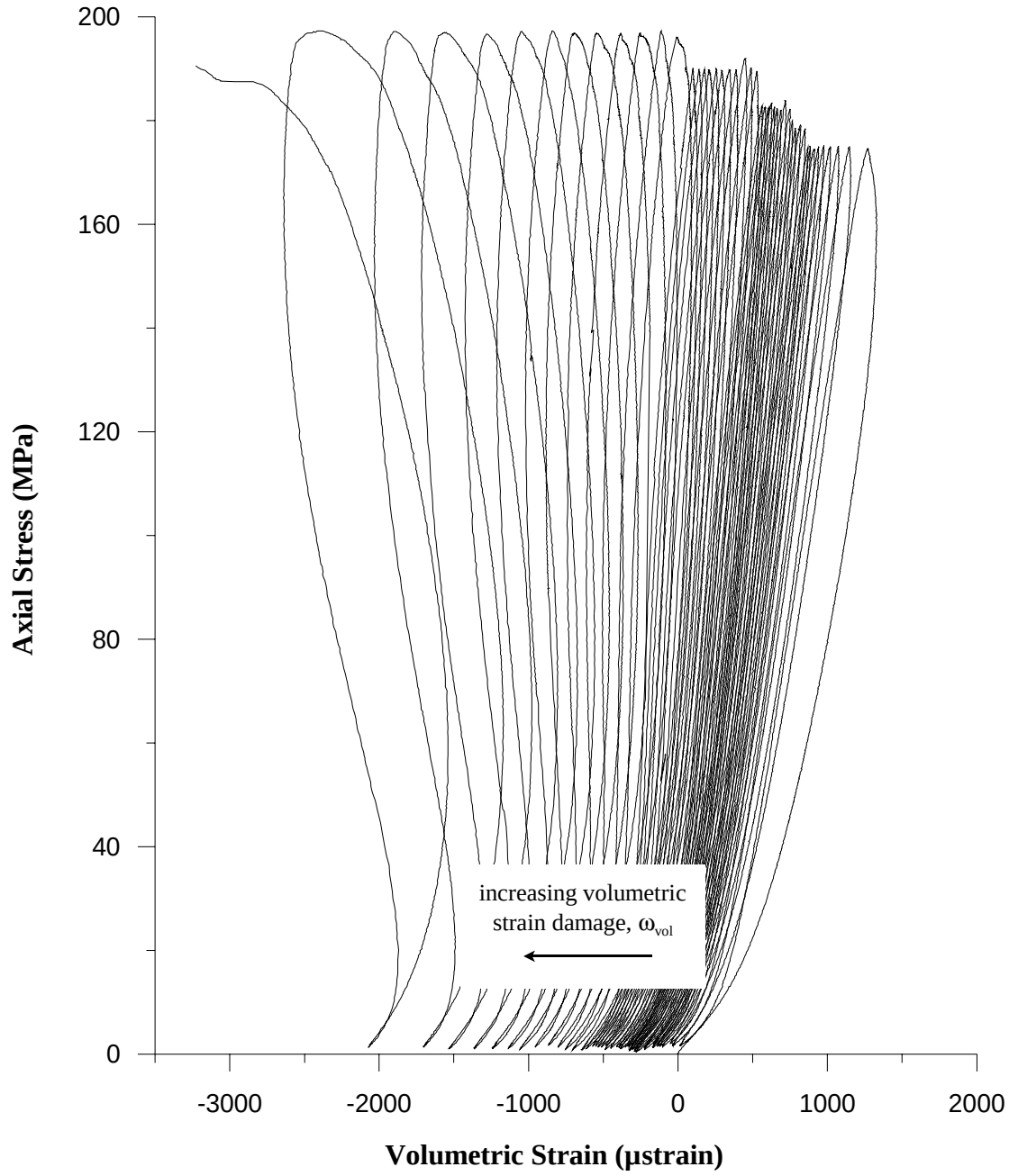

Figure 7.9 Axial stress -*vs*- volumetric strain showing the migration of the volumetric strain curve with each damage increment for a 130 m level URL pink granite.

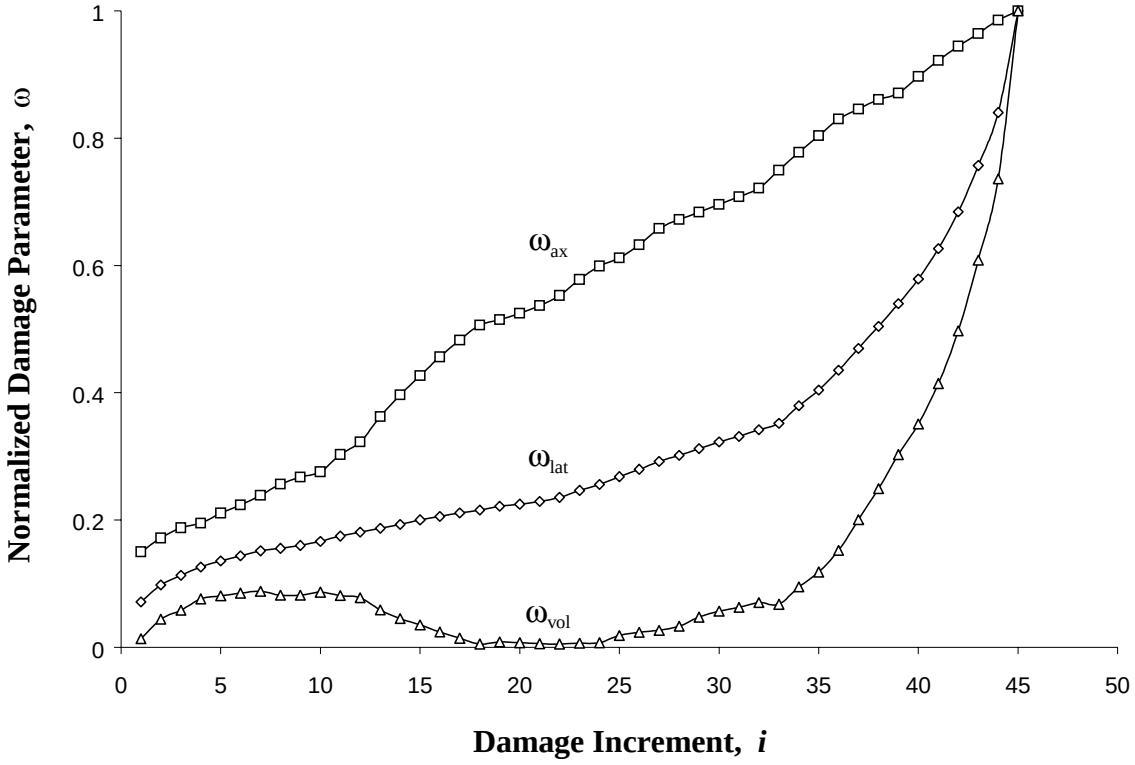

Figure 7.10 Damage -*vs*- damage increment showing the permanent axial (ω_{ax}), lateral (ω_{lat}) and volumetric (ω_{vol}) strain damage with each cycle normalized with respect to the total damage at failure for a 130 m level URL pink granite.

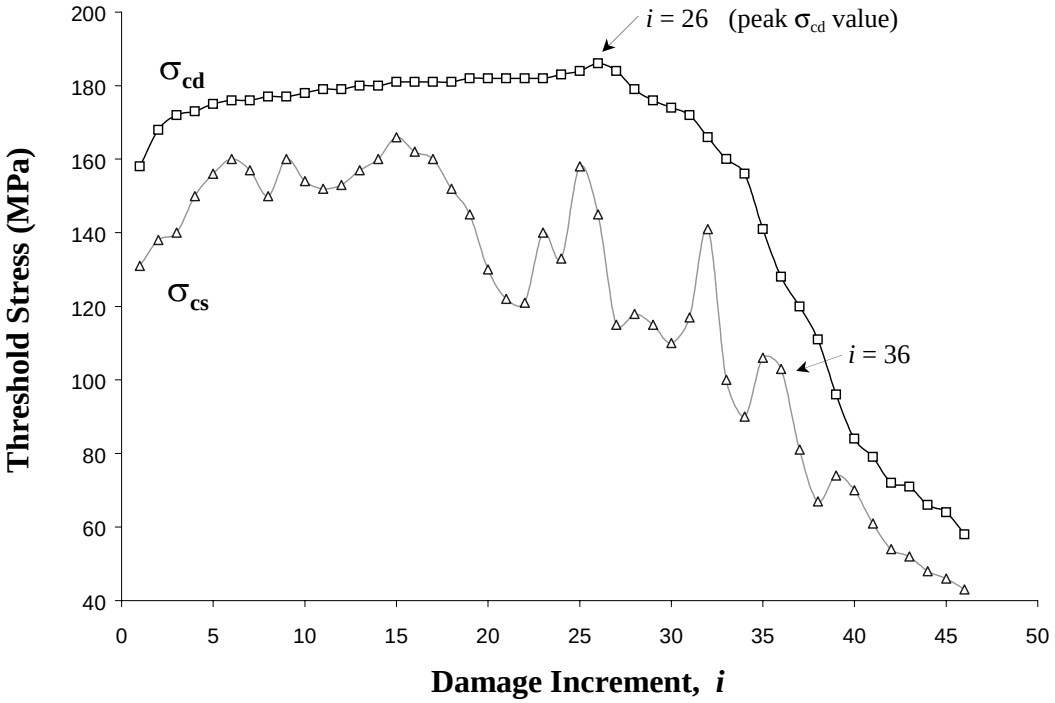

Figure 7.11 Crack damage and crack coalescence threshold stresses -*vs*- damage increments for a 130 m level URL pink granite.

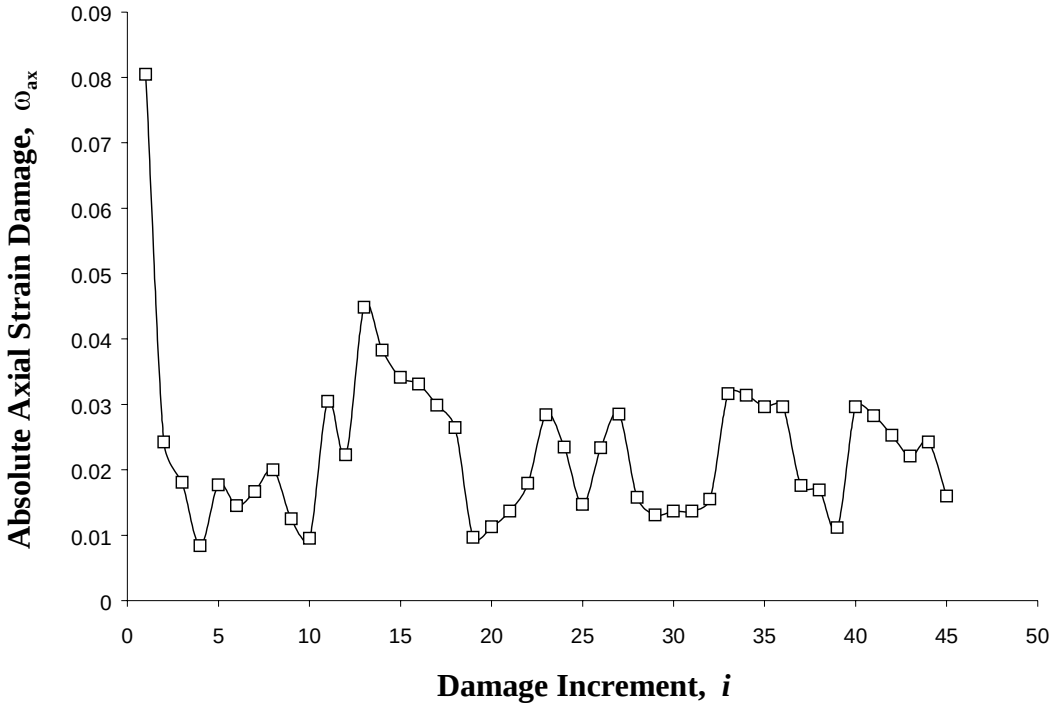

Figure 7.12 Absolute axial strain damage -*vs*- damage increment showing the damage induced for each load-unload cycle normalized with respect to the total damage at failure for a 130 m level URL pink granite.

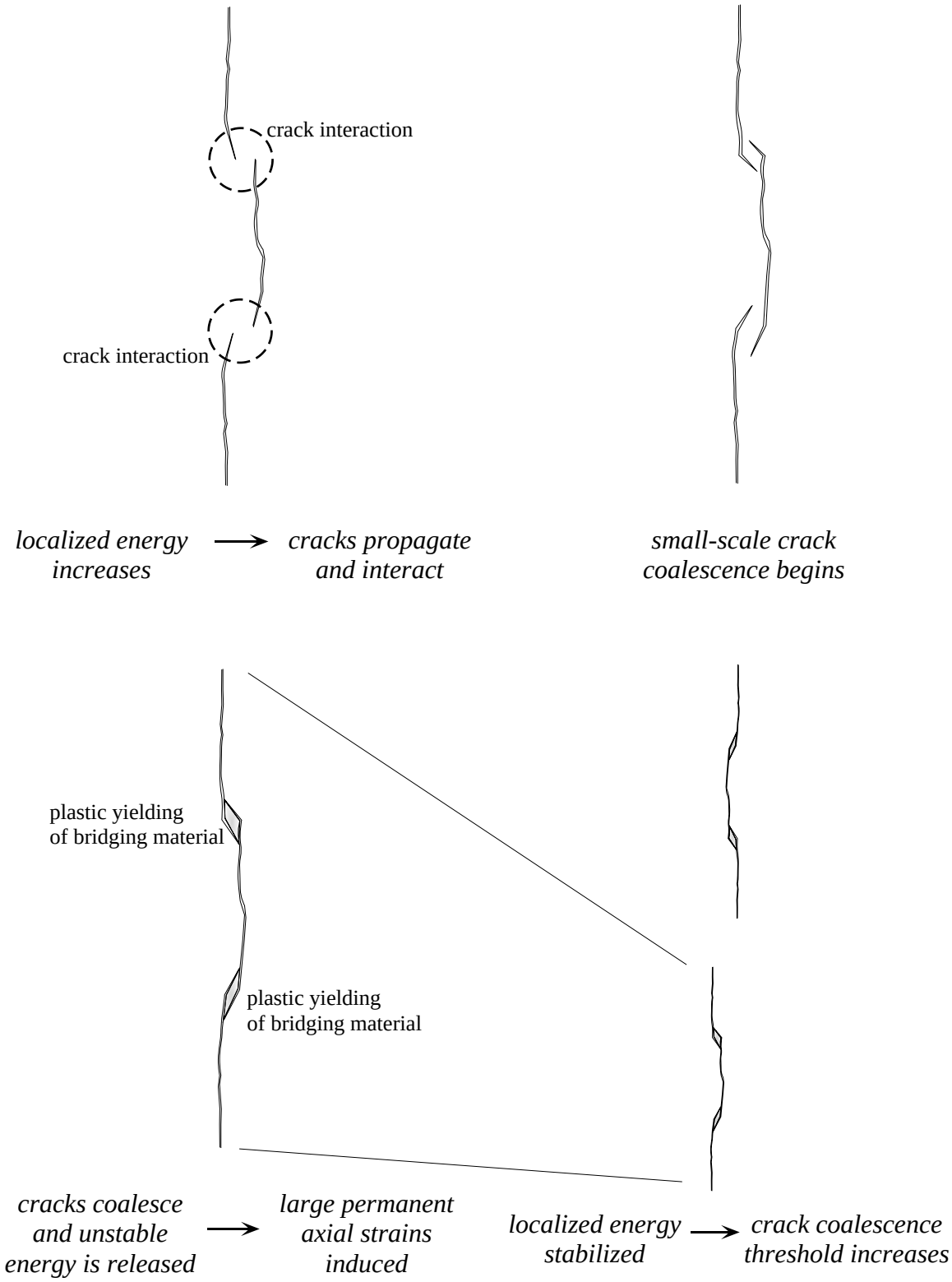

Figure 7.13 Conceptual model of crack coalescence accompanied by large permanent axial strains (i.e. axial strain damage).

The progressive accumulation of damage in the sample also resulted in the degradation of the material stiffness. Young's modulus and Poisson's ratio values were calculated for each cycle and taken as a linear regression fit between the crack closure and crack damage thresholds. Figure 7.14 shows that through the first 25 damage increments, Young's modulus and Poisson's ratio values show a gradual softening of the material. In general, Poisson's ratio values over these damage increments appear to have increased at a greater rate than the Young's modulus values decreased. This would seem to indicate that the predominant mechanism throughout these cycles is the steady growth of axial cracks. At damage increments 26 and 37, however, sharp increases in Poisson's ratio values were seen and were followed by sharp declines in the Young's modulus. It is interesting to note that damage increment 26 coincides with the peak crack damage threshold shown in Figure 7.11 and both damage increments 26 and 37 approximately coincide with decreases in the crack coalescence threshold.

Closer examination of the state of damage at increment 26 would appear to indicate that a correlation exists between the crack damage threshold and cohesion. Figure 7.15 shows that when broken down into its individual strain components, the permanent damage induced at this point widely varies. In terms of the lateral strain damage parameter, ω_{lat}, only 30% of the permanent lateral strains occurs before the peak crack damage threshold is reached at damage increment 26. In contrast, over 60% of the axial strain damage was induced prior to this point. Presumably, at some point in the load history of the sample, the state of crack development reaches a point whereby the continued inducement of damage results in a magnified effect in terms of reducing the cohesion of the sample. The magnitude of induced axial damage prior to this point, relative to lateral damage, suggests that crack interaction and coalescence plays a much larger part in the development of significant damage than does the initiation of new cracks.

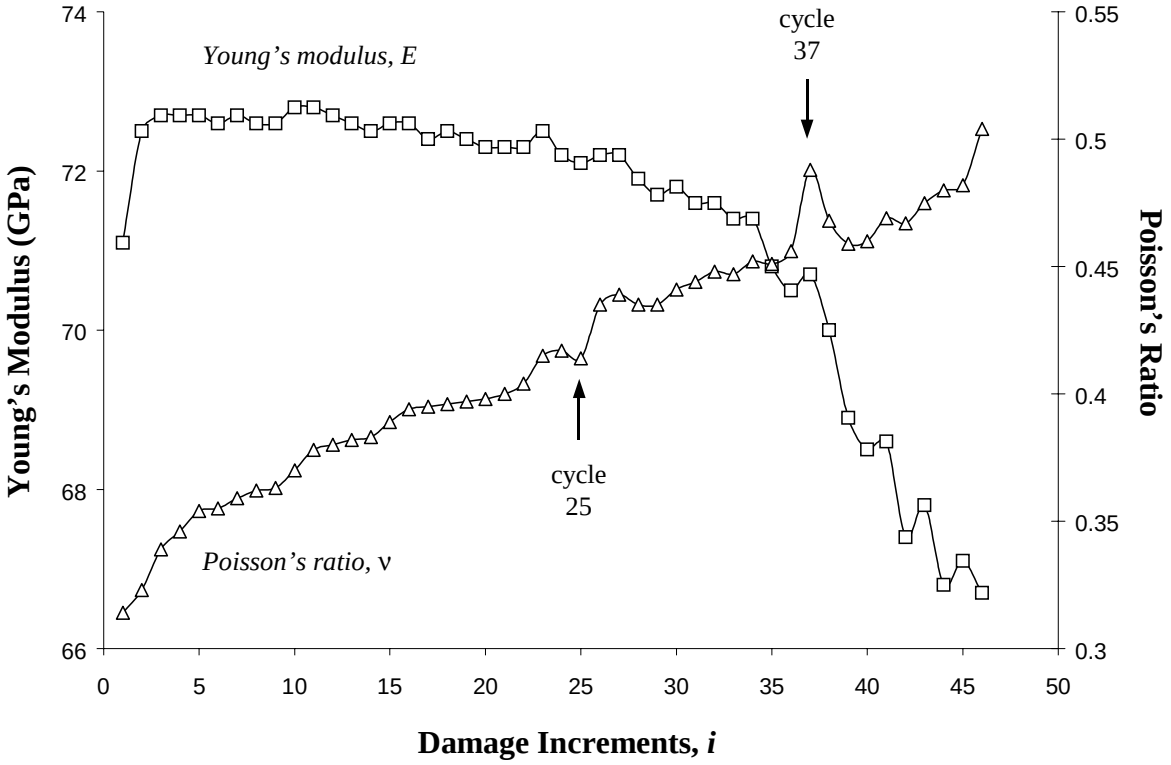

Figure 7.14 Plots of Young's modulus and Poisson's ratio -*vs*- cyclic damage increments for 130 m level URL pink granite.

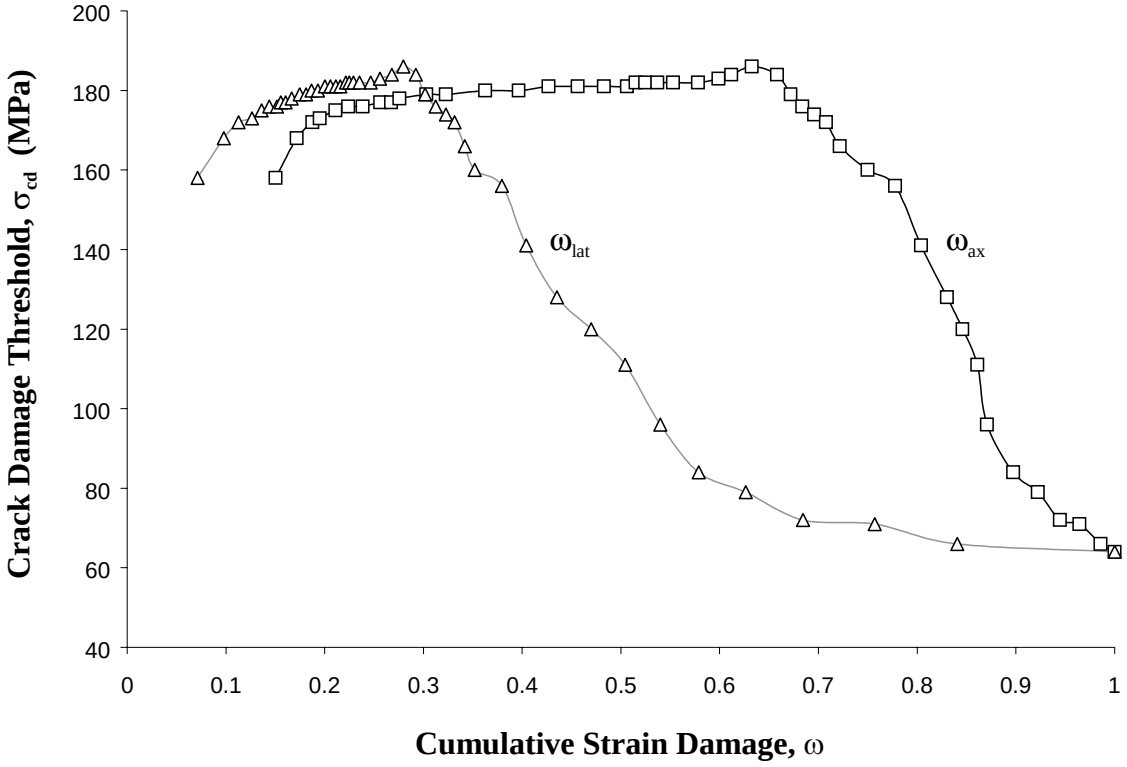

Figure 7.15 Crack damage threshold recorded for each damage increment -*vs*- axial and lateral cumulative strain damage for a 130 m level URL pink granite.

The influence crack interaction and coalescence have on the crack damage level can be assessed by relating observations made during the damage-control test to those presented in the previous chapters. Testing in Chapter 4 showed that the initiation of fractures in the Lac du Bonnet granite began at approximately 40% of the peak strength (i.e. 82 MPa). Continuous cracking associated with the secondary initiation of fractures in quartz grains was detected at 50% of peak strength (i.e. 102 MPa). These values coincide with the detected crack initiation and secondary crack thresholds determined for the first cycle of the damage-controlled test (82 and 106 MPa, respectively). In effect, the first cycle of the damage-controlled test closely matched observations of the damage process in the monotonic loading tests. During this first damage increment, therefore, it can be assumed that a population of cracks was initiated which in turn propagated and coalesced on a local level but without reaching an advanced state of coalescence as would be expected under prolonged unstable crack propagation conditions. Upon the second, third and ensuing load increments, the initiation of new fractures would be minimal but the development of existing fractures would be extensive. AE event counts and observations from the damage-control test confirm these hypotheses. In each of the cycles following the first cycle, no new AE events were detected until the crack coalescence value from the first cycle was reached. Furthermore, significant cracking in these cycles wasn't detected until the crack damage threshold from the first cycle was reached (Figure 7.16).

It would therefore appear that with each damage increment, very little in the form of new cracking transpires but at higher stresses existing cracks reactivate and once again continue to propagate and coalesce. The degree of axial damage also suggests that the weakening and breakdown of bridging material between these cracks at higher stresses contributes to a significant proportion of the recorded plastic strain. These observations also conform to the findings presented in Chapter 5 with respect to the numerical modelling of crack interaction. One of the observations from the numerical analysis suggested that cracks growing in a uniaxial stress field interact in such a fashion that the resulting crack population would consist of a relatively small number of long cracks as opposed to a large number of small cracks (as would be the

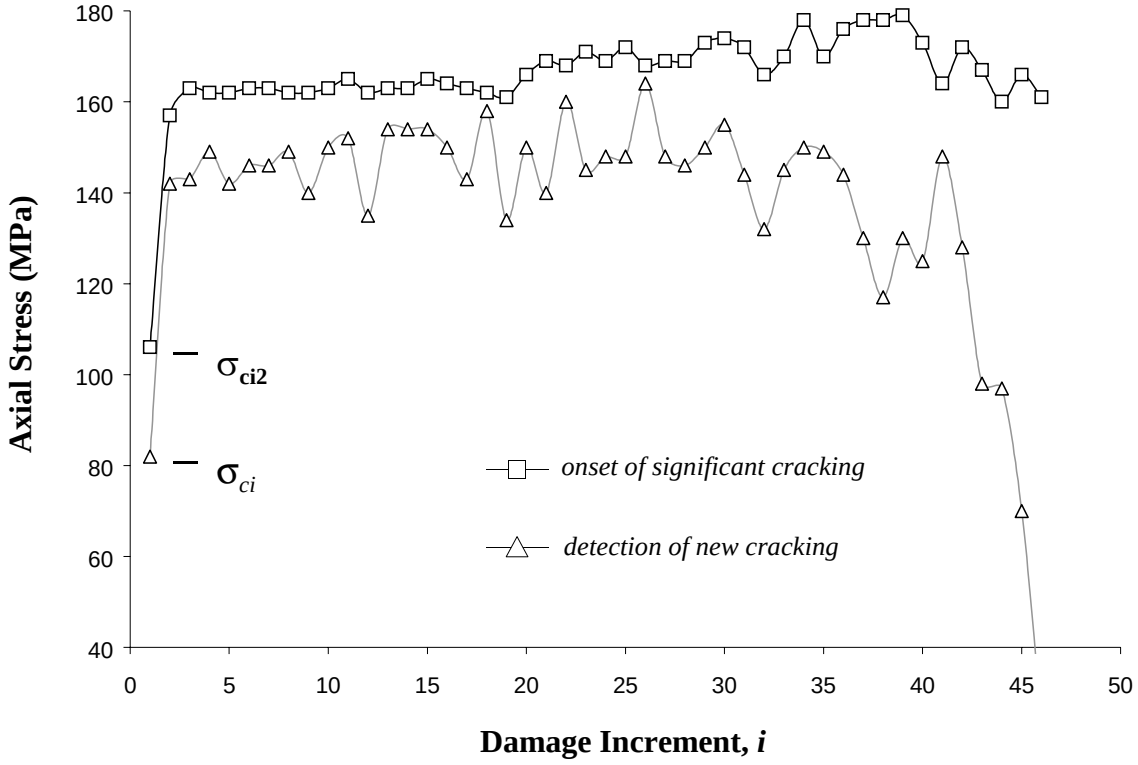

Figure 7.16 Axial stress -*vs*- damage increments showing the stress levels at which new and significant cracking was detected through AE monitoring for a 130 m level URL pink granite.

case under triaxial loading conditions). Results from the damage-control test appear to verify that with each damage increment, existing cracks reactivate and propagate until some critical stage in the overall development of the crack population is reached. Significant increases in lateral strain damage following maximum crack damage value suggests that the crack population reaches a state where smaller coalescing cracks combine to form larger cracks which, in turn, coalesce with one another until a critical plane is formed along which failure of the sample occurs (Figure 7.17). It should be noted that although significant damage was induced in the sample in the cycles leading up to failure and noticeable reductions were recorded with respect to cohesion and stiffness, failure still occurred in an explosive manner at a load of 196 MPa. In other words the effects of microfracturing damage, with respect to inducing failure at stresses below the peak strength of the sample, did not involve processes whereby the gradual reduction of cohesion resulted in a plastic, soil like failure. Instead, microfracturing acted to reduce the cohesion to a point whereby a series of critical cracks could more readily form a critical plane along which failure occurred.

7.2.2 Damage-Controlled Testing Below the Crack Damage Threshold

In the preceding section it was shown that the crack damage threshold of the material rapidly decreased at the point where the lateral and axial strain damage parameters reached values of 0.29 and 0.67, respectively. Interestingly, these values closely match damage values determined for the crack coalescence threshold through monotonic loading, 0.34 and 0.68 (Table 7.2). It appears quite evident that the interaction and coalescence of the propagating cracks plays a significant role in the degradation of material strength. This role was further explored through a second damage-control test. The setup and procedure for the test was identical to the first one described in the preceding section with the exception that the maximum load for each damage increment was kept below the crack damage threshold. In total the test took 12 hours to complete over which time 59 load-unload cycles were applied to the sample, pink Lac du Bonnet granite from the 130 m level of the URL, before the sample failed (Figure 7.18). An average loading rate of 24 MPa/minute was used.

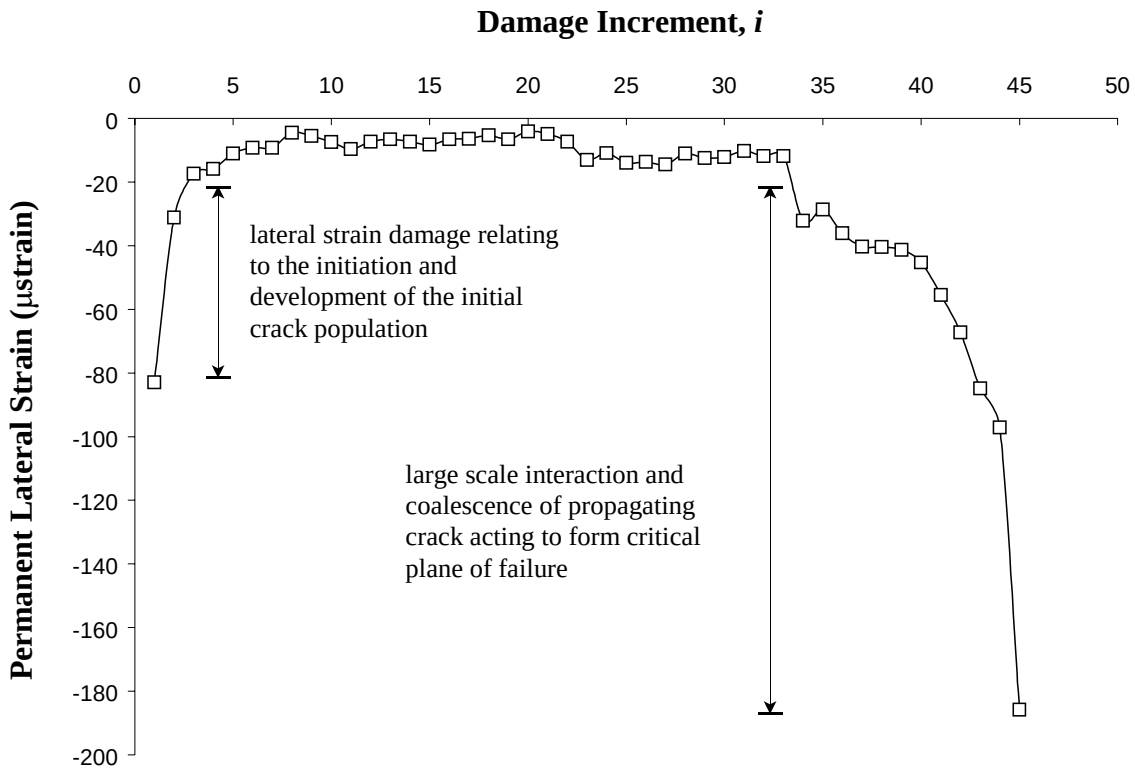

Figure 7.17 Permanent lateral strain -*vs*- damage increments showing the damage induced by each load-unload cycle for a 130 m level URL pink granite.

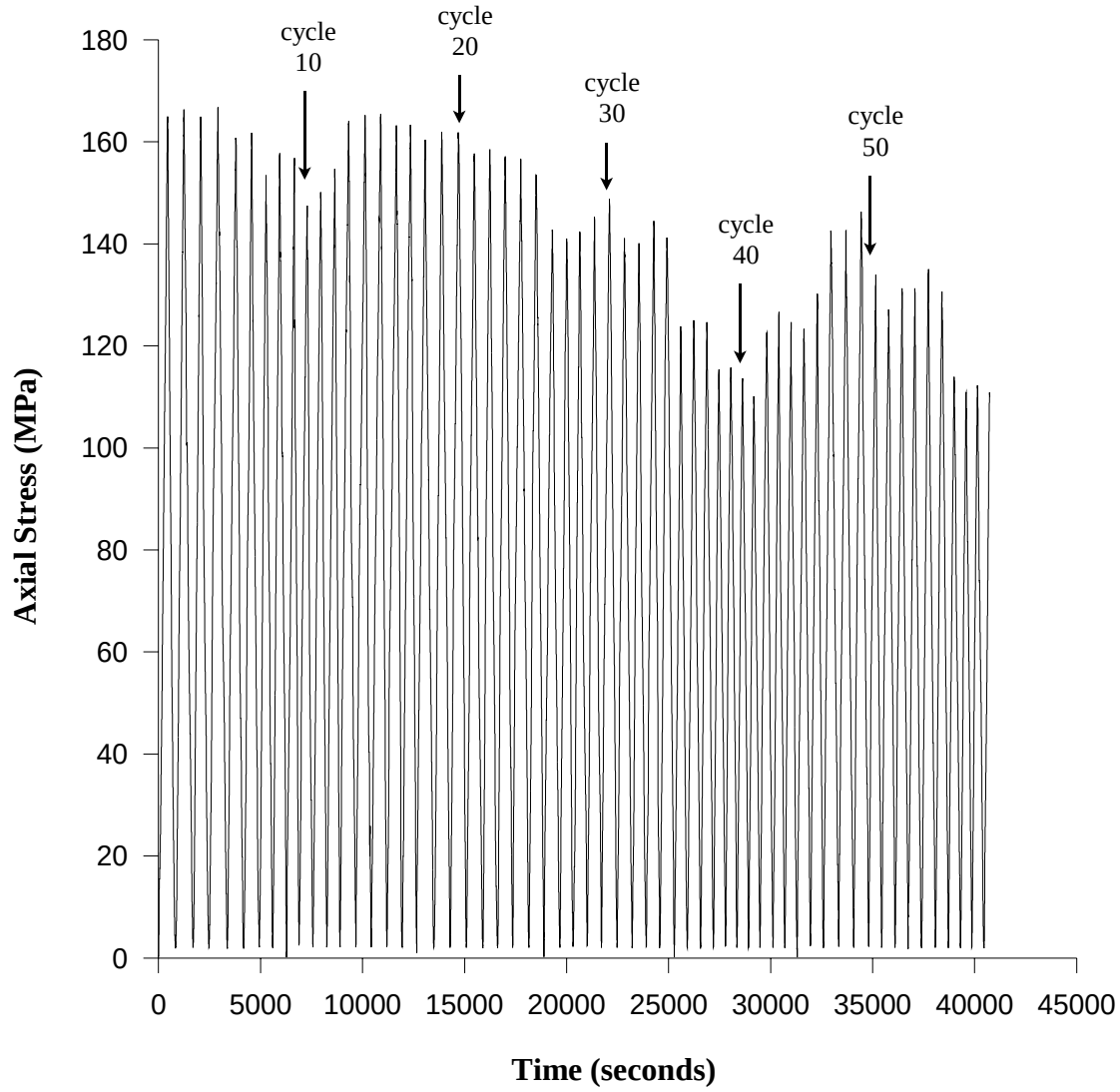

Figure 7.18 Axial stress -*vs*- time showing the load history for a damage-controlled test in which the maximum loads were kept below the crack damage threshold as performed on a sample of 130 m level URL pink granite.

Results from this test indicate that the behaviour of the sample, as controlled through the initiation and propagation of microfractures, was markedly different from that seen in the first damage-control test. In the first test, the maximum loads applied during the initial load cycles exceeded the crack damage threshold thus establishing a network of microfractures that required equally high stresses to reactivate and propagate during subsequent cycles. This was not the case when the maximum loads were kept below the crack damage threshold. Although both the crack initiation and secondary crack thresholds were exceeded during the first cycle, the load was removed before the cracks reached their unstable propagation state (this was achieved through real-time monitoring of the AE event rate). It then appears that with each subsequent damage increment, both new cracks and existing cracks initiated and propagated. Figure 7.19 shows the progressive accumulation of permanent strain damage measured throughout the test. Although the axial damage curve shows a steady rate of increase similar to the one seen in the first test (Figure 7.10), the lateral damage curve follows a different pattern. In the first test, a high degree of lateral damage was observed during the first cycle as new cracks initiated and propagated, but a relatively low amount of damage was seen in the subsequent cycles. The damage curve maintained a low rate of increase even though loads exceeding the crack damage threshold were being applied. It wasn't until the lateral strain damage parameter reached an approximate value of 0.3, at damage increment 33, that the rate of damage drastically increased (Figure 7.10 and 7.17). In the second damage-control test, the lateral damage curve was seen to follow a steady rate of increase throughout each cycle, although it should be noted that a relatively large increase in the lateral damage parameter was also seen at a normalized damage value of 0.3. Since lateral damage is indicative of the opening (i.e. initiation and propagation) of new cracks parallel to the direction of loading, it would appear that new cracks are generated with each damage increment.

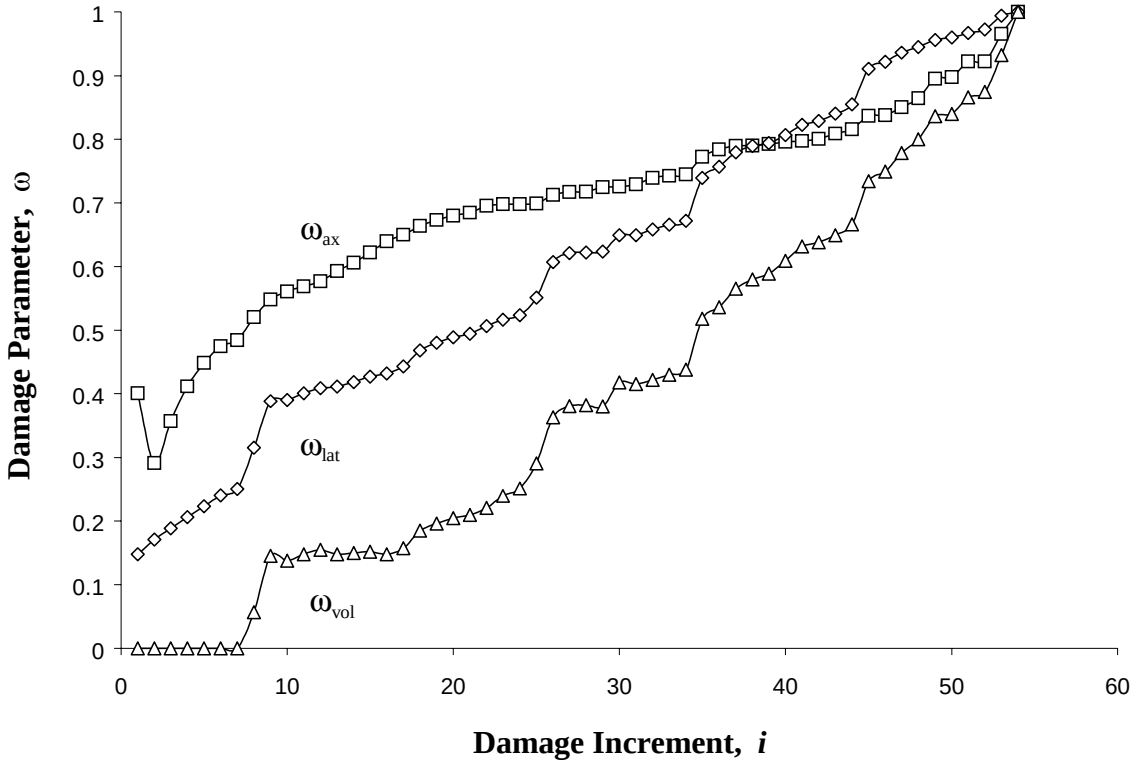

Figure 7.19 Damage -*vs*- damage increments for load cycling below the crack damage threshold. The plot shows the permanent axial (ω_{ax}), lateral (ω_{lat}) and volumetric (ω_{vol}) strain damage with each cycle normalized with respect to the total damage at failure for a 130 m level URL pink granite.

These observations can be validated through the measured AE event counts. Figure 7.20 shows that a constantly increasing trend can be seen in the number of AE events detected with each damage increment. The plot also shows that damage increments with increased AE activity correlate to large increases in the lateral damage curve but not the axial damage curve. It was also observed that the loads at which significant AE events were detected generally decreased throughout most of the test (Figure 7.21). In the damage-control test with loading exceeding the crack damage threshold, these values were seen to remain fairly constant (Figure 7.16). This would seem to imply that with each damage increment a crack population of both new and existing cracks develops and enlarges. This pattern continued right up to failure at damage increment 59. Failure of the sample occurred in a brittle manner at a load of 110 MPa (approximately $0.5\sigma_{UCS}$), well below the crack damage threshold.

Limiting the damage increments to loads below the crack damage threshold was also seen to have a pronounced effect on the measured stiffness of the sample. Results from the previous section showed that the deformation constants, E and ν, progressively decreased (Figure 7.14). In contrast, the deformation constants calculated for the second damage-control test showed very little in the terms of strain softening. Young's modulus and Poisson ratio values for this test remained fairly constant with each damage increment with the exception of a large jump in the Young's modulus between damage increments 27 and 33 (Figure 7.22). This rapid increase in material stiffness suggests that some form of strain hardening may have occurred within the sample, possibly as angular asperities along coalesced crack faces locked-up. Test results suggest that by limiting the cyclic loads to stresses below the crack damage threshold, the degree of plastic yielding exhibited by bridging material (as depicted in Figure 7.13) was greatly reduced. The breakdown of this material during crack coalescence and unstable crack propagation in the first test was seen to contribute to a large proportion of the plastic axial strains. It can thus be conjectured that the internal breakdown in material stiffness does not occur until the crack population reaches a state, both in density and size, through which large scale crack interaction and coalescence can occur. This was not observed until the last four or five damage increments of the test.

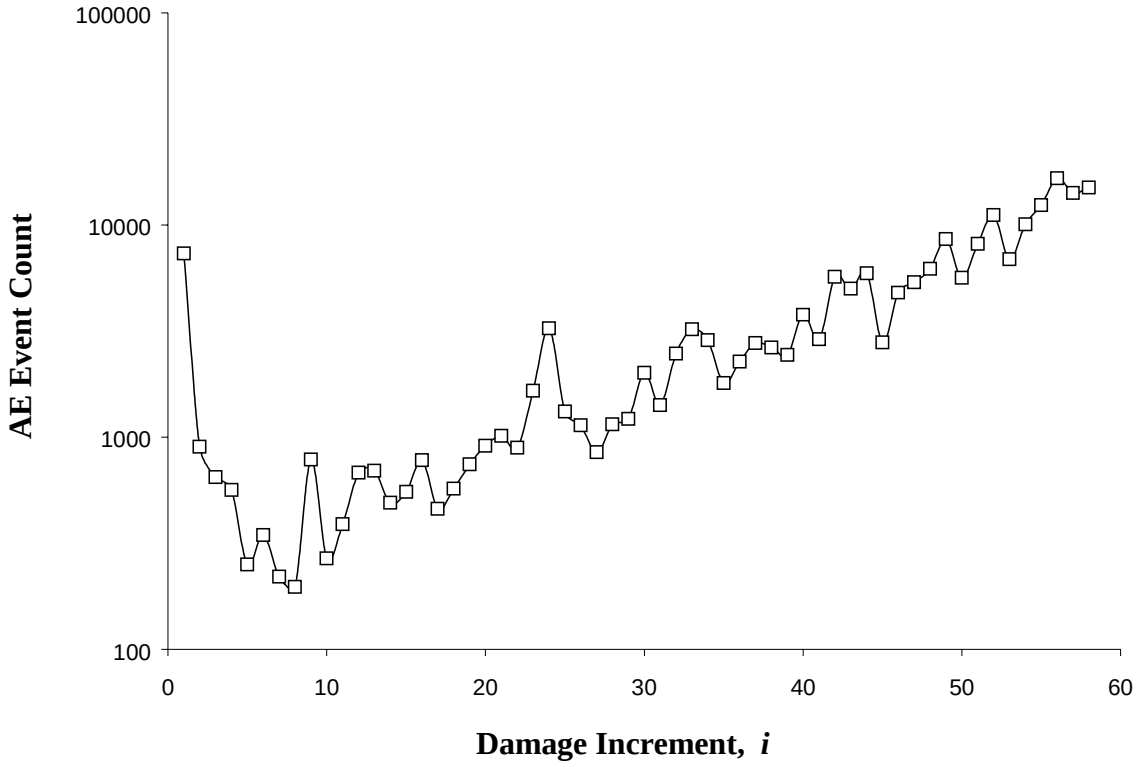

Figure 7.20 Log plot of the AE event count -*vs*- damage increments for load cycling below the crack damage threshold for a 130 m level URL pink granite.

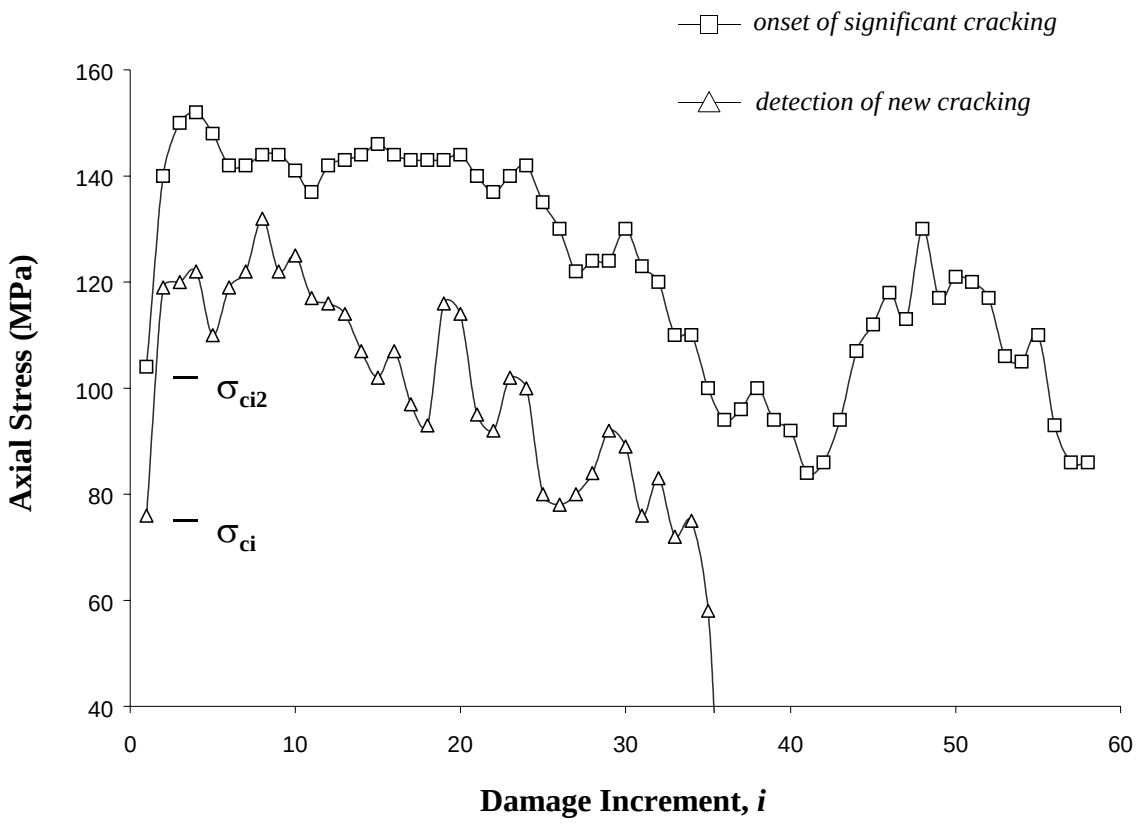

Figure 7.21 Axial stress -*vs*- damage increments for load cycling below the crack damage threshold showing the stress levels at which new and significant cracking was detected through AE monitoring for a 130 m level URL pink granite.

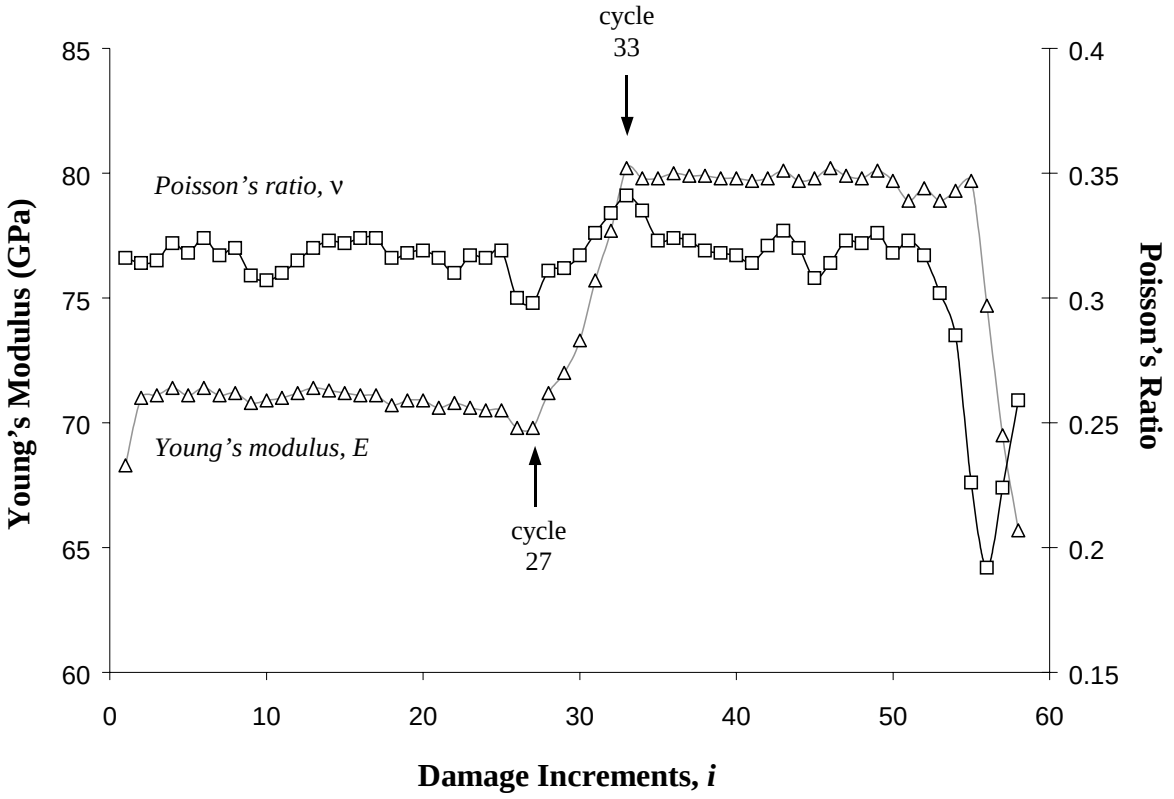

Figure 7.22 Plots of Young's modulus and Poisson's ratio -*vs*- cyclic damage increments for load cycling below the crack damage threshold in a 130 m level URL pink granite.

7.3 Incremental Damage Tests

Test results presented in the previous sections have demonstrated how damage may be quantified either as a function of continuous stress and strain, as seen in the monotonic tests, or in the form of accumulated permanent strain with increasing damage increments, as seen through the cyclic loading tests. Furthermore, results from the two damage-control tests suggest that the maximum loads applied to the sample can have a significant effect on the rate and type of damage induced in the test sample. Cyclic loading tests constrained by a maximum load below the crack damage threshold were seen to permit the slow development of the microfracturing population resulting in cracks that increased both in number and size with each damage increment. On the other hand, cyclic tests in which the maximum loads were allowed to exceed the crack damage threshold resulted in the quick development of the crack population establishing a smaller network of larger cracks which would remain dormant until loads approached critical levels.

The final tests performed for this study were designed to use incremental loading paths to quantify the damage induced in the test sample for a given change in the state of stress. In effect, these tests were contrived to include elements of both the monotonic and cyclic tests in an attempt to isolate the degree of microfracturing in the sample and the resulting permanent damage as seen with each increment of applied load. Tests were also devised to isolate time-dependent fracture characteristics that may be related to the changing state of stress and the added energy available to drive crack propagation.

7.3.1 Incremental Cyclic Loading

The first of two incremental loading tests performed was devised to increase the load applied to the sample with each cycle. The test procedure followed a load history whereby the test sample, 130 m level URL pink granite, would be loaded up to a pre-determined load and then unloaded. A maximum load of 40 MPa was used for this first cycle. Each subsequent cycle then saw the maximum load increased by 10 MPa. This process was repeated up to a maximum load of 180 MPa (Figure 7.23). With each cyclic

load increment the permanent strains and the number of acoustic events attributable to the increase in stress over the load interval were recorded.

Results from this test indicate that with each cycle and load increment additional damage is incurred in the sample (Figure 7.24). Plots of the permanent strain damage show that both the axial and the lateral strain damage increases with increasing damage increments but at different rates (Figure 7.25). In terms of damage measured through the permanent axial strains, a relatively linear increase in damage was seen with increasing load increments. The lateral damage, on the other hand, did not begin to increase until the approximate crack initiation threshold for the pink granite (as reported in Chapter 4) was reached. The lateral damage curve then appears to increase at a steadily increasing rate. In terms of absolute damage values, many of the trends observed in the data correspond to threshold values determined in the monotonic tests for the 130 m level URL pink granite. Load intervals over which the rate of permanent lateral strain increased correspond to the crack initiation, secondary cracking and crack coalescence thresholds, i.e. crack thresholds marking the initiation and opening of cracks (Figure 7.26). Increases in measurements of permanent axial strain coincide with those thresholds which were observed to significantly influence the axial component of deformation, i.e. crack closure, crack coalescence and crack damage (Figure 7.27).

The acoustic emission data showed similar trends and correlations with respect to thresholds of crack development (Figure 7.28). These results suggest that in many ways the sample responded to cyclic incremental loads in the same manner as samples loaded monotonically. For example, the cyclic volumetric strain curve shown in Figure 7.24 resembles that derived from a monotonic loading test and shows volumetric strain reversal at approximately 160 MPa, thus coinciding with the average crack damage threshold value derived for the same material in the monotonic loading tests of Chapter 4. In terms of the total permanent damage recorded at the end of the incremental cyclic load test, values resembled those obtained from monotonic loading tests in which loading was stopped prior to sample failure (Table 7.6).

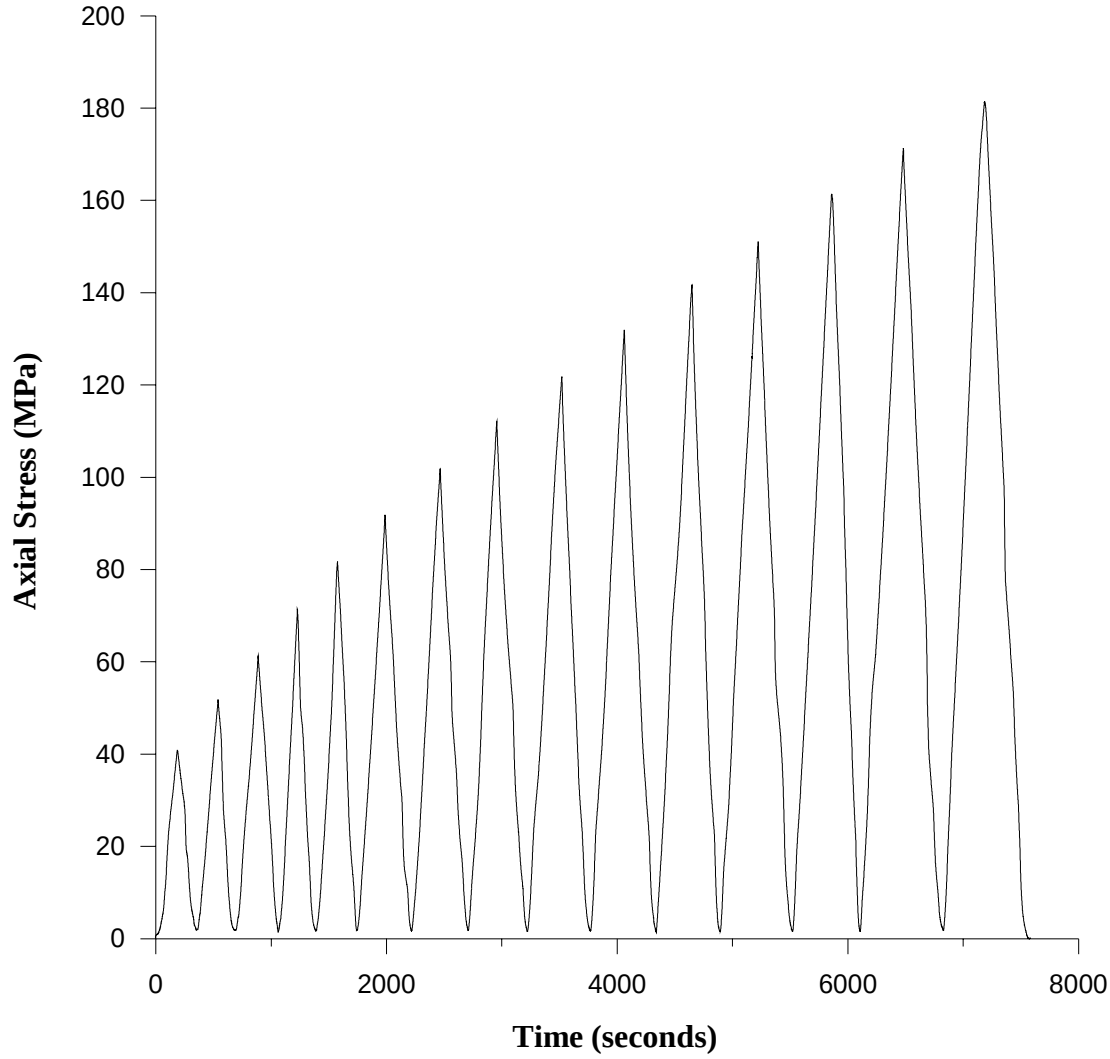

Figure 7.23 Axial stress -*vs*- time showing the load history for an incremental cyclic loading test performed on a sample of 130 m level URL pink granite.

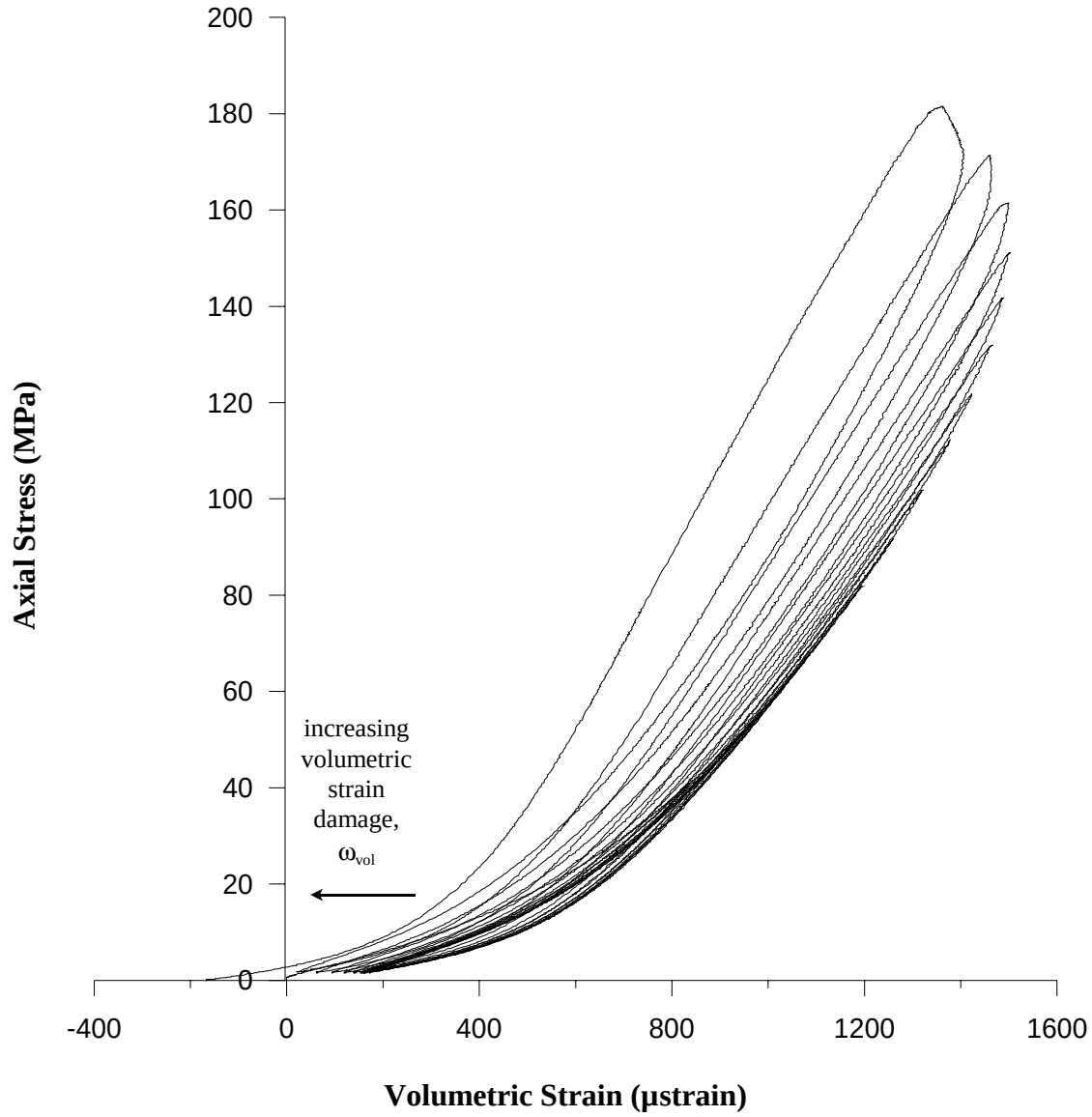

Figure 7.24 Axial stress -*vs*- volumetric strain showing the migration of the volumetric strain curve with each cycle and load increment for a 130 m level URL pink granite.

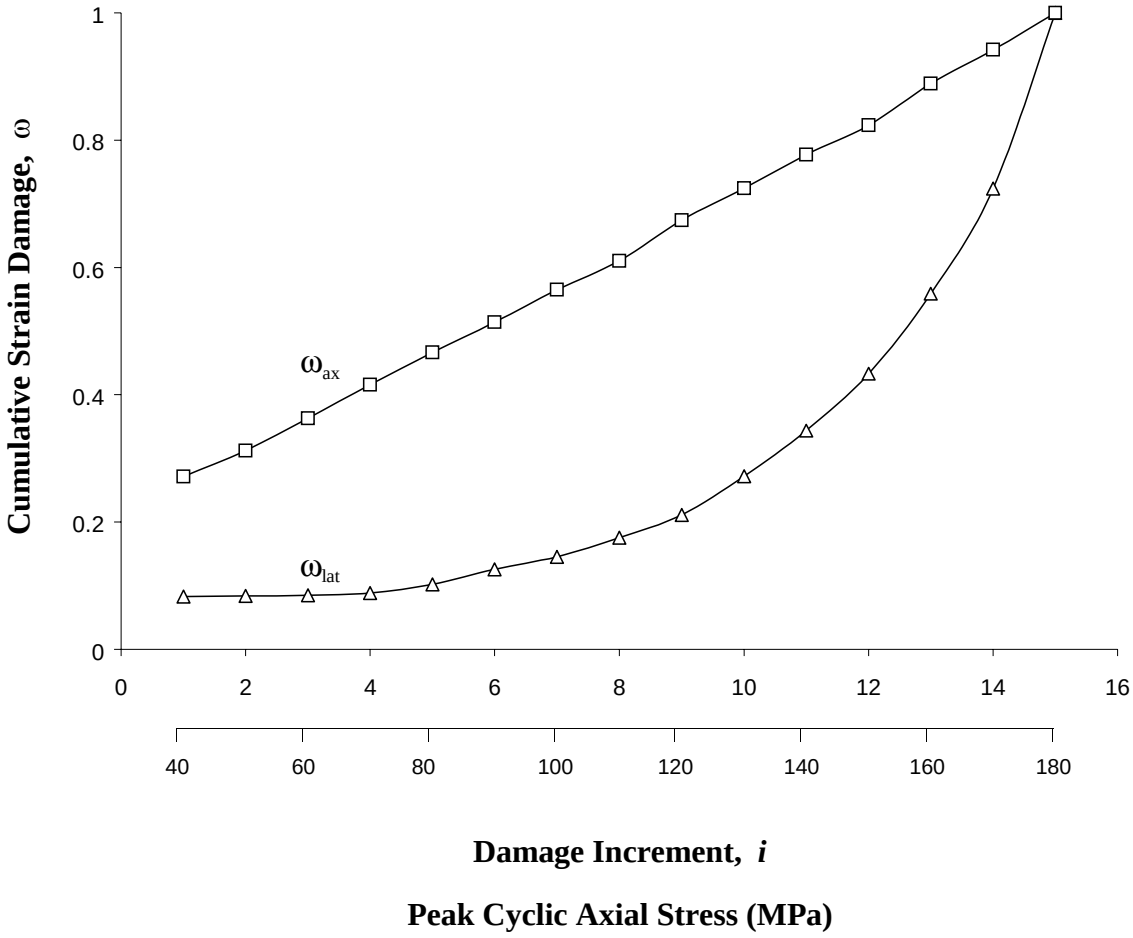

Figure 7.25 Cumulative strain damage -*vs*- damage increment (and peak cyclic axial stress) for an incremental cycling test performed on a 130 m level URL pink granite.

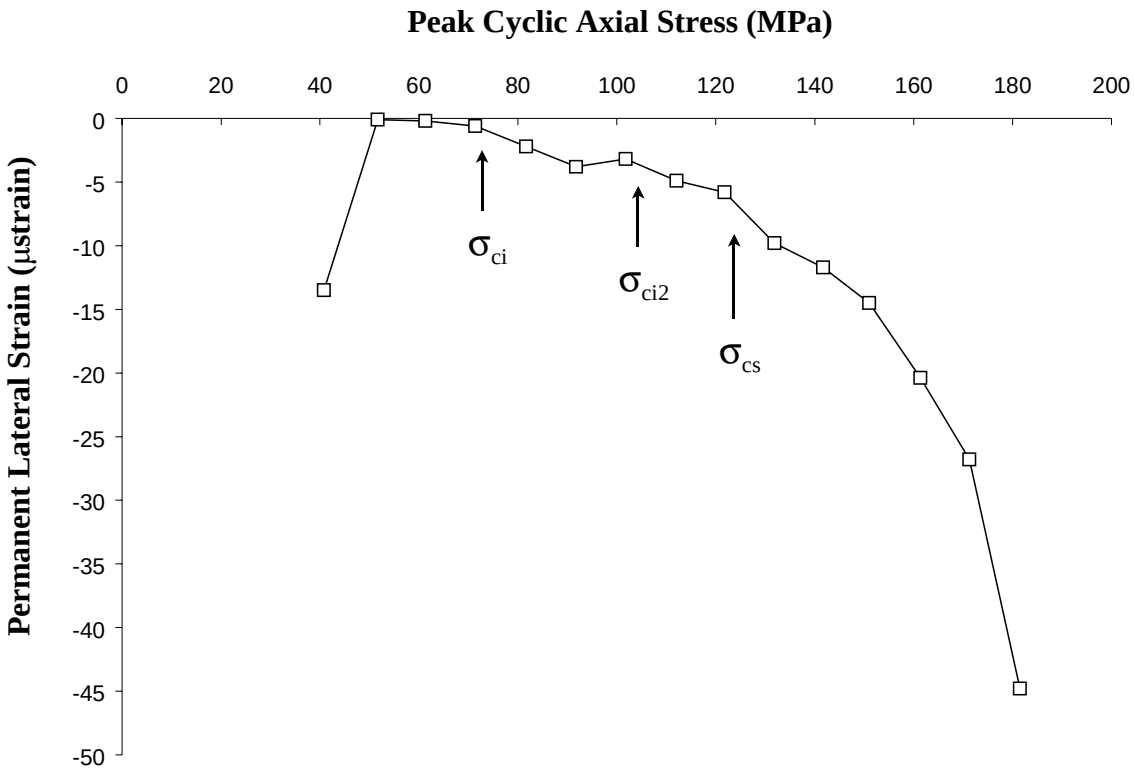

Figure 7.26 Permanent lateral strain -*vs*- peak cyclic axial load showing the correlation between absolute lateral strain damage and the crack thresholds for a 130 m level URL pink granite.

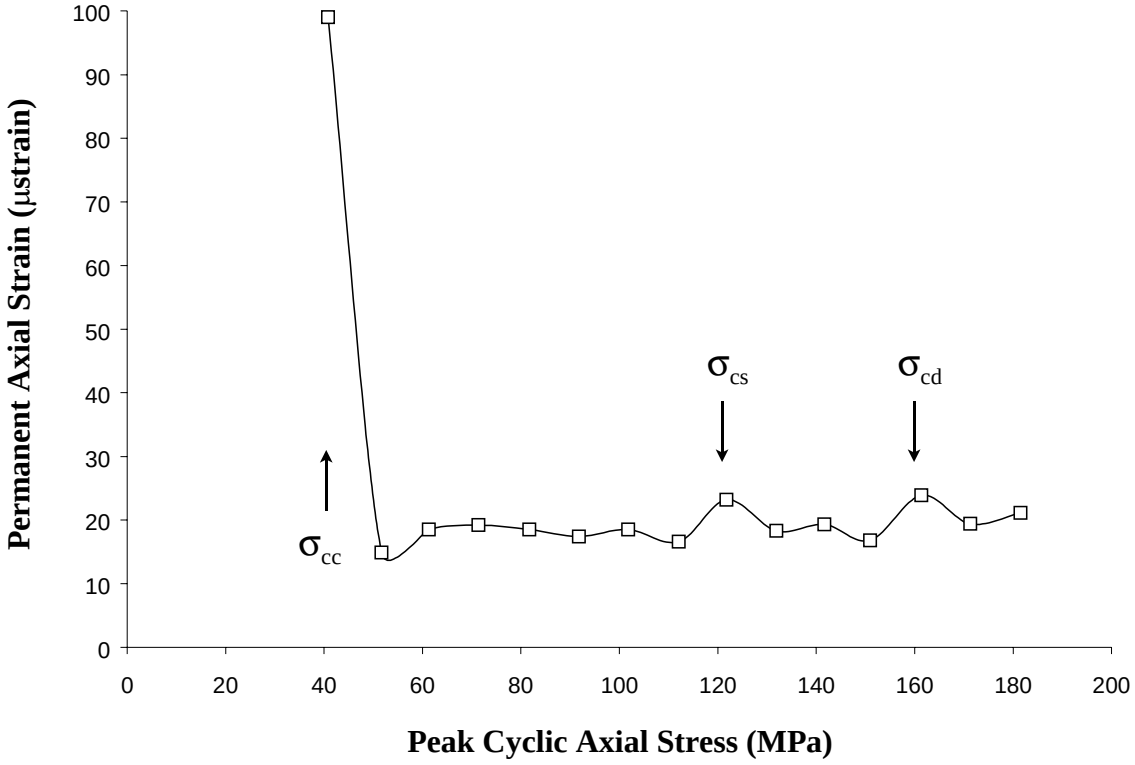

Figure 7.27 Permanent axial strains -*vs*- peak cyclic axial load showing the correlation between absolute axial strain damage and the crack thresholds for a 130 m level URL pink granite.

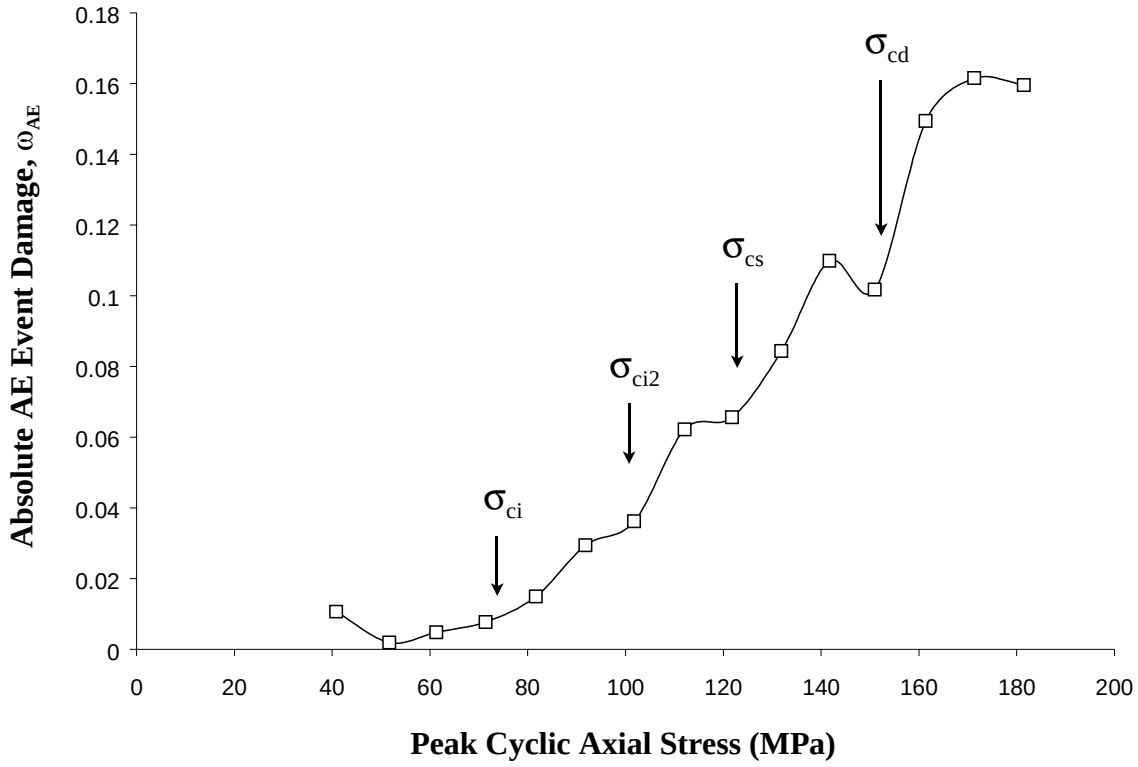

Figure 7.28 Absolute AE event damage -*vs*- peak cyclic axial stress showing the correlation between absolute AE damage and the crack thresholds for a 130 m level URL pink granite.

Table 7.6 Comparison of permanent axial and lateral strains from monotonic loading tests and the incremental cyclic loading test for the 130 m level URL pink granite (standard deviation is provided in parentheses).

Test Type	Permanent Axial Strain (μstrain)	Permanent Lateral Strain (μstrain)
monotonic loading	145 (± 33)	-196 (± 53)
incremental cycling	134	-150

Similarily, average Young's modulus and Poisson ratio values fell within the range of values obtained in Chapter 4. Throughout the loading increments, the Young's modulus value gradually increased until the loads surpassed the secondary cracking threshold, leveled off and remained relatively constant until the crack damage threshold was surpassed, and then gradually decreased (Figure 7.29). This would seem to indicate that between peak cyclic loads of 60 and 110 MPa, initiating cracks did not act to reduce the axial stiffness of the material. Instead, it would appear that open cracks at oblique angles to the load and localized zones of yielded material near propagating crack tips, closed or compressed resulting in increasing Young's modulus values. However, once the crack damage threshold was reached, the unstable propagation and coalescence of existing cracks acted to soften the material. Poisson ratio values were seen to gradually increase with each cycle thus establishing that new cracks initiated and propagated with each cyclic load increment (Figure 7.29).

7.3.2 Incremental-Constant Load Test

Results from the incremental cyclic loading test showed that the development of microfractures followed a similar pattern to that seen in the monotonic loading tests. In essence, the test demonstrated that the effects of unloading the sample between load

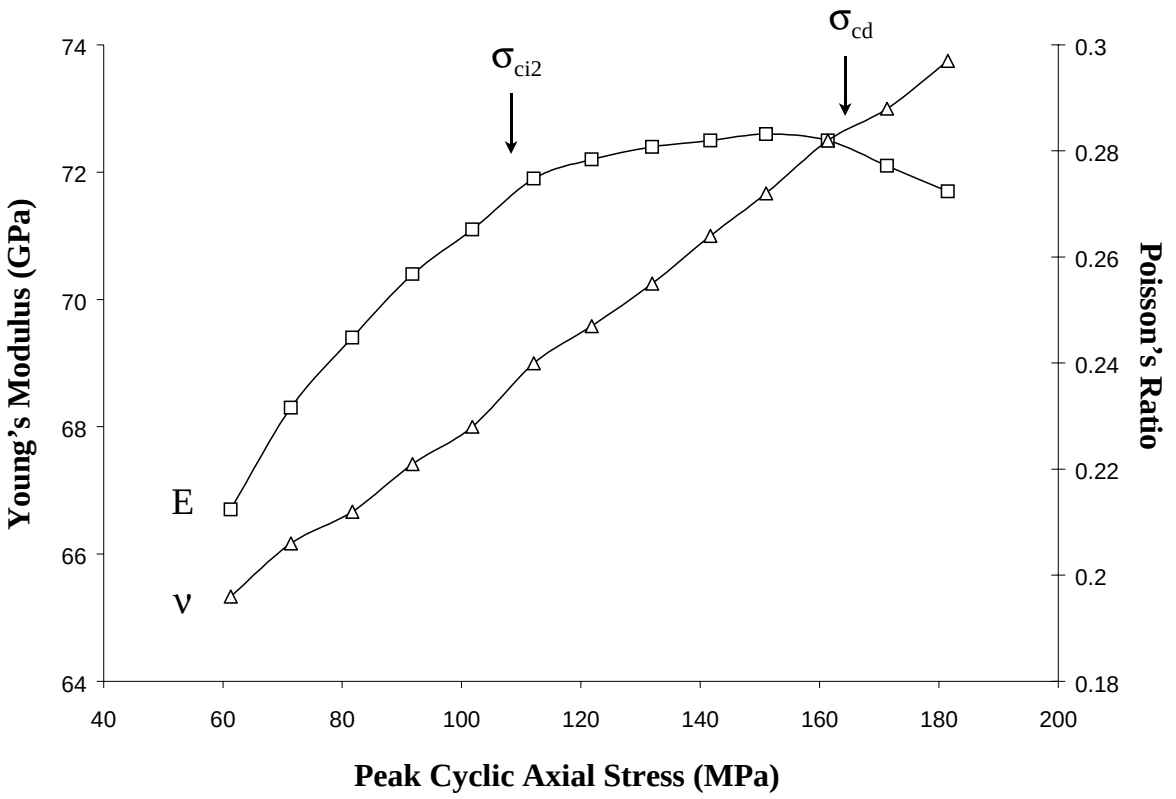

Figure 7.29 Plots of Young's modulus and Poisson's ratio -*vs*- peak cyclic axial stress for a 130 m level URL pink granite.

load increments were minimal. In general, the act of applying a load can be thought of as supplying energy to the crack propagation process. By removing the load, the energy supply disappears and crack propagation ceases as the energy remaining in the system dissipates. However, the dissipation of energy is not instantaneous and therefore some thought should be given to the effects of time with respect to the loading and unloading process. For example, Farmer (1983) found that the mechanics of deformation in a cyclic loading test are similar to that seen in a creep test except that the cycling process represents a direct energy input which satisfies the conditions for crack propagation much more quickly than under a constant load. However, crack propagation can be continued under constant loads if the energy in the system exceeds that required for crack propagation (e.g. unstable crack propagation conditions).

A test was therefore designed to determine what effect short time intervals might have on the microfracturing process and the accumulation of damage with increasing stresses. It was decided that the test should incorporate elements of both monotonic and creep loading. With this in mind, a sample of 130 m level URL pink granite was loaded in 10 MPa increments. At each 10 MPa increment the load was held constant and the AE activity was monitored. Once the detection of AE activity ceased, the load was increased to the next load increment. This procedure was repeated until the rate of AE activity indicated that sample failure was imminent at which point the sample was unloaded. In total, 16 load and constant load intervals were used between loads of 40 and 190 MPa (Figure 7.30).

Results from this test indicate that a significant percentage of the observed microfracturing occurred over periods of constant load as opposed to load increases. This effect was reflected in both measurements of the creep strain and AE activity. However, test results also showed that the overall behaviour of the sample closely followed that seen in other tests of the Lac du Bonnet pink granite. Figure 7.31 shows that the stress-strain curves for the test resembles those seen in the monotonic loading experiments with the exception that large creep strains are detectable at higher constant loads (values of the total permanent strains accumulated for the test are provided in

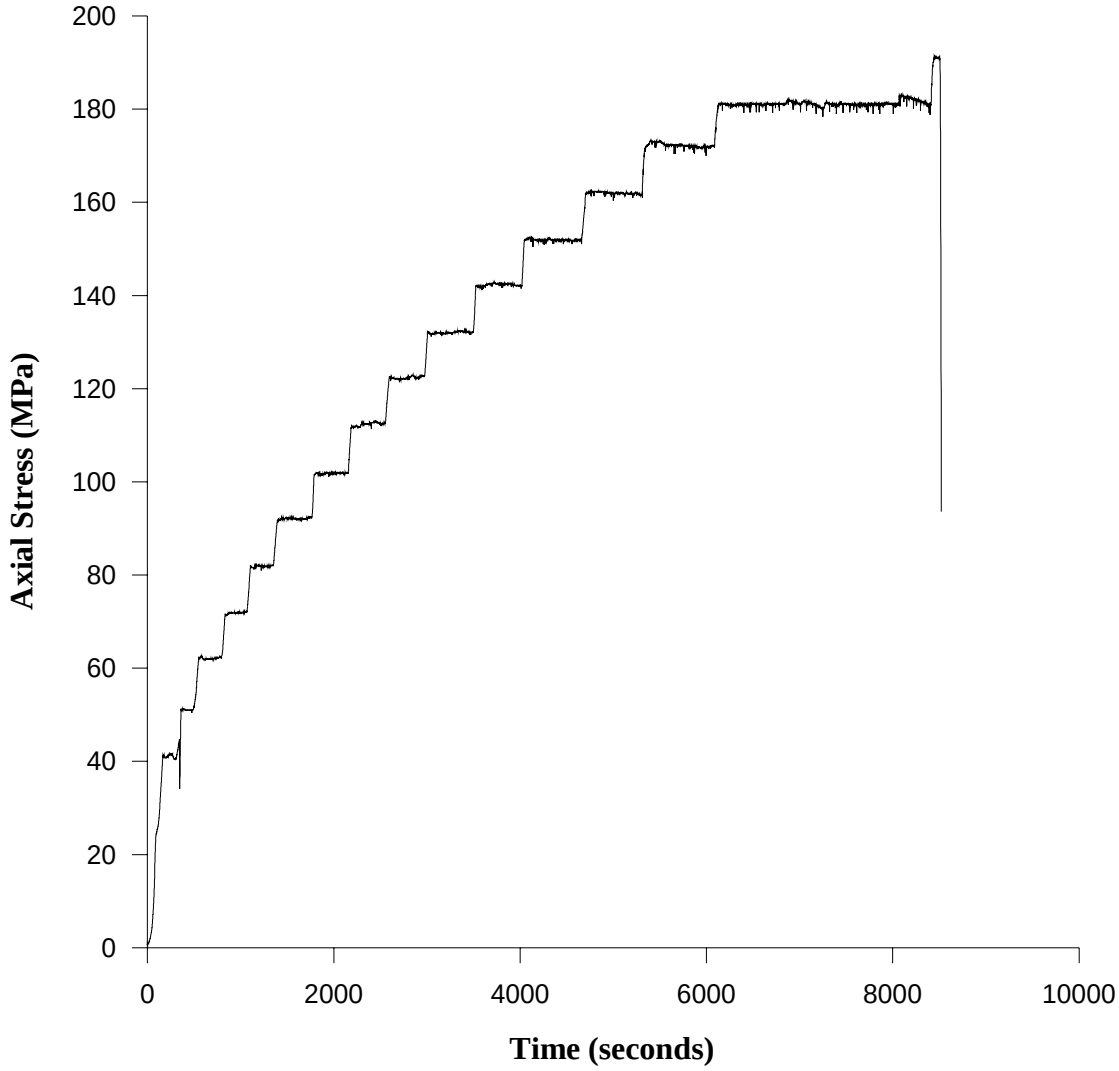

Figure 7.30 Axial stress -*vs*- time showing the load history for an incremental constant loading test performed on a 130 m level URL pink granite.

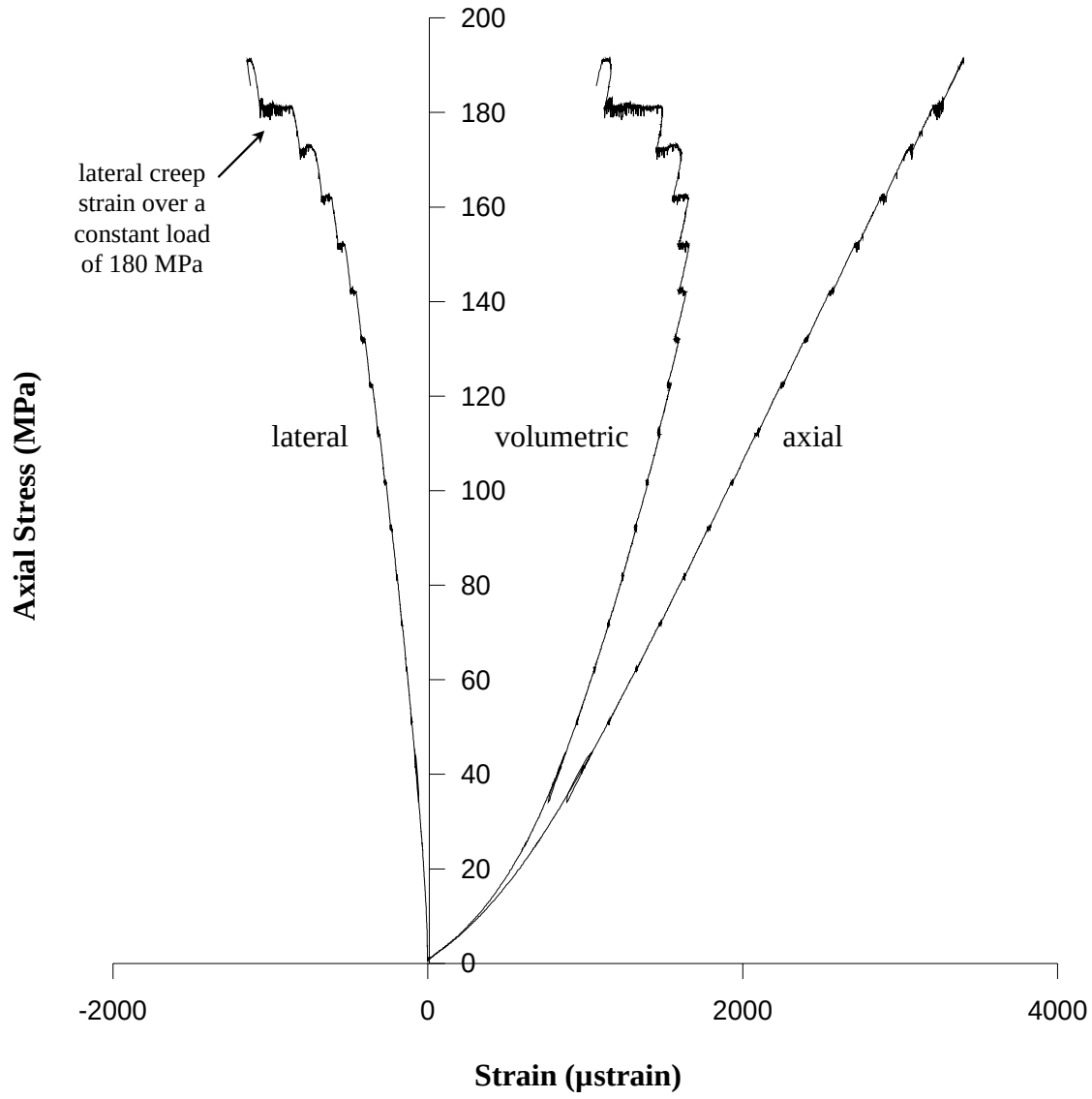

Figure 7.31 Axial stress -*vs*- axial, lateral and volumetric strain showing the development of creep strains with each constant load increment for a 130 m level URL pink granite.

Table 7.7). From this plot it can also be seen that volumetric strain reversal occurs at approximately 160 MPa, thus agreeing with crack damage threshold values determined in the monotonic loading tests.

Creep strains recorded over the constant load intervals revealed that the axial values remained relatively constant whereas lateral values increased with each load increment (Figure 7.32). These creep strains were attributed to the continued initiation and propagation of cracks as the load was held constant. In other words, induced energy levels in the sample continued to incite crack activity after load increases were stopped and held constant. Axial creep strains were attributed to the coalescence and yielding of bridging material between interacting crack tips, whereas lateral creep strains were associated with the initiation and propagation of microfractures. Damage values based on these measured creep strains showed that the accumulation of axial strain damage during creep loading followed a relatively linear trend, whereas lateral values showed an exponential trend (Figure 7.33). These curves emulate trends seen in several of the other tests presented in this chapter (for example Figures 7.10 and 7.25). Similarly, changes in the elastic constants calculated for each load increment followed the same trends seen in previous tests. Figure 7.34 shows that the deformation modulus (i.e. the slope of the axial stress-strain curve between constant load levels), gradually increases as cracks close and yielded material compresses resulting in the stiffening of the material. The curve then approaches a constant value equal to the secant modulus for 130 m level URL pink granite (Table 4.1). Poisson ratio values are seen to continuously increase with each load increment, thus reflecting the progressive accumulation of microfracturing damage.

AE event counts also show increases in the number of detected events with increasing load intervals. In terms of the breakdown of the detected events, Figure 7.35 shows that the majority of the recorded events occur as loads are held constant as opposed to periods of increasing load. This would seem to indicate that a significant percentage of the detected microfractures developed due to the energy remaining in the system once loading was suspended. Figure 7.36 depicts the calculated energy released through AE events with each load level. In correlating this response to the thresholds of

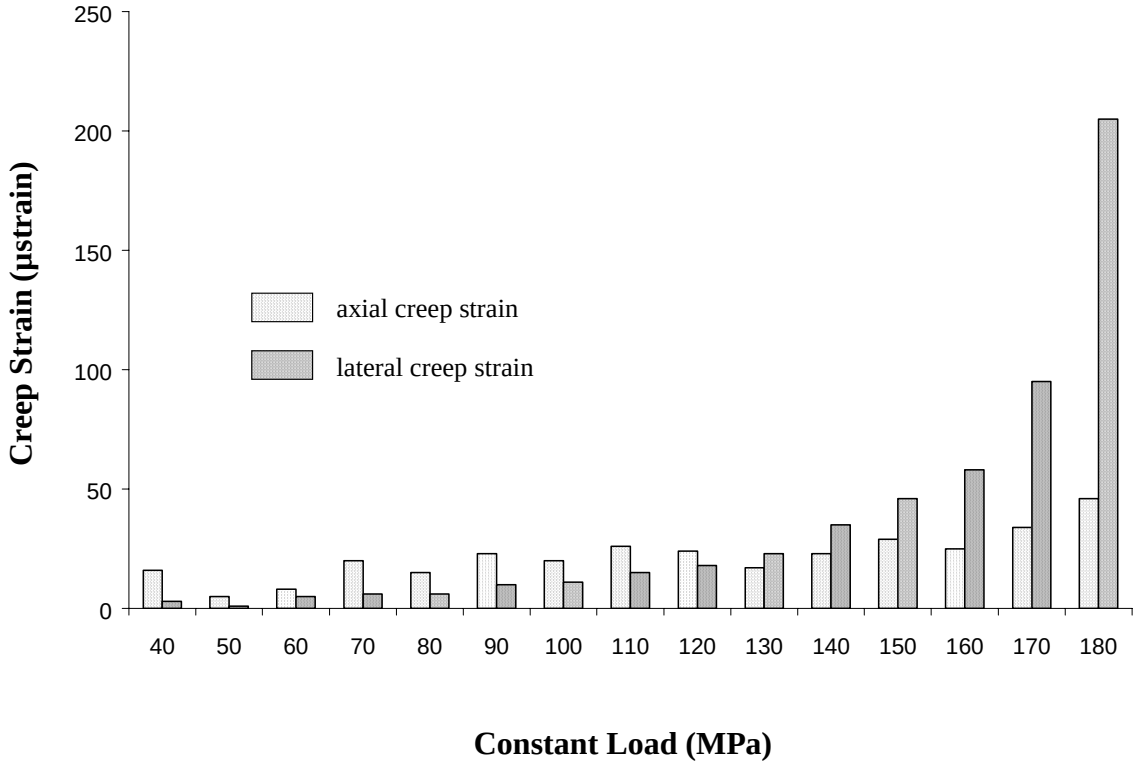

Figure 7.32 Axial and lateral creep strains -*vs*- constant load for a 130 m level URL pink granite.

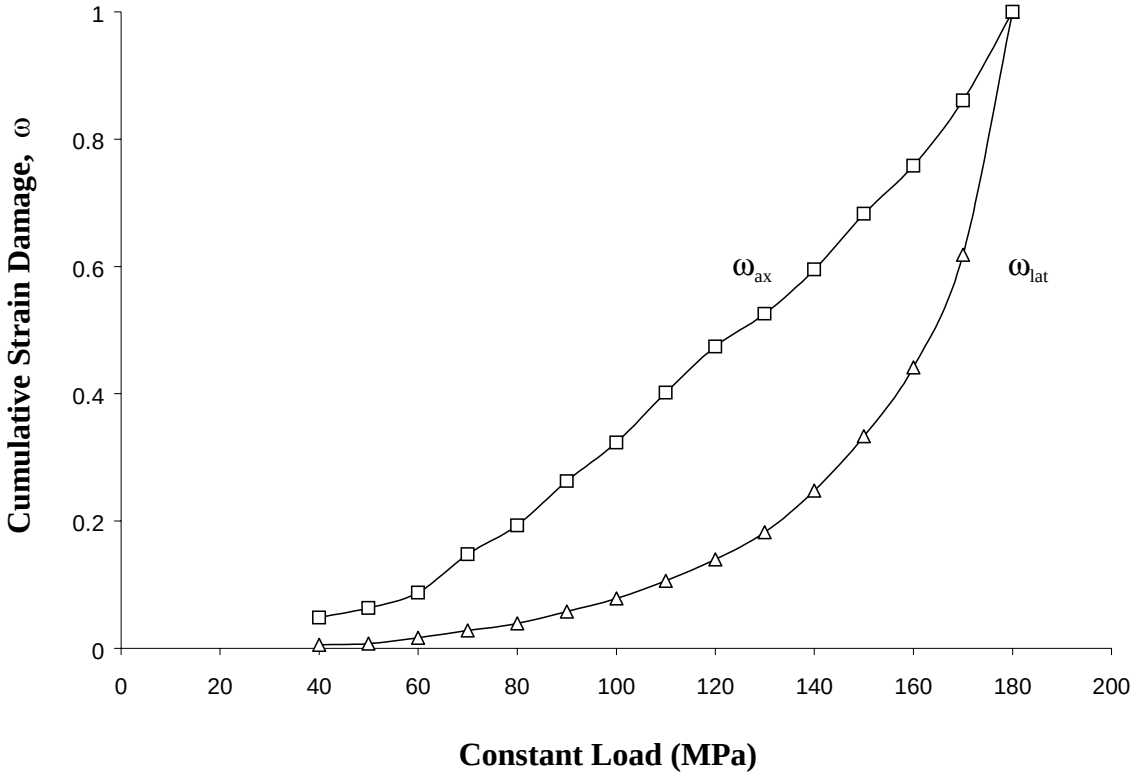

Figure 7.33 Cumulative damage -*vs*- constant load showing the axial (ω_{ax}) and lateral (ω_{lat}) creep strain damage for a 130 m level URL pink granite.

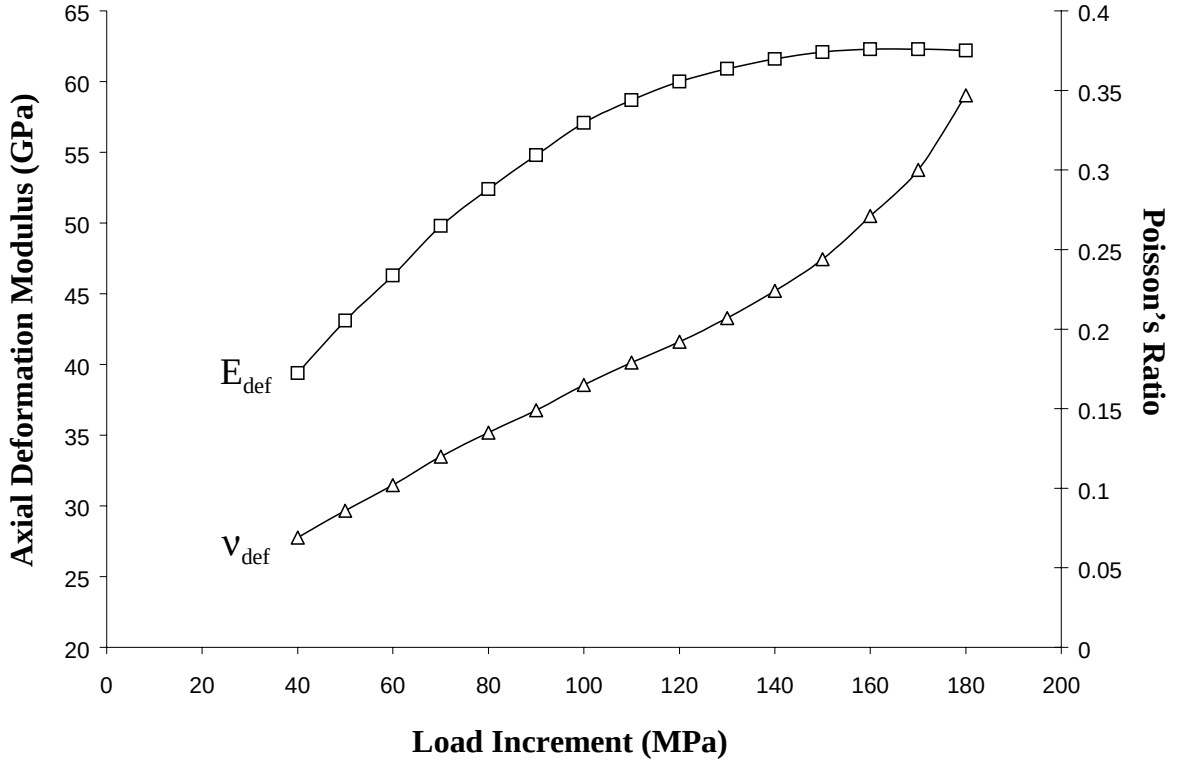

Figure 7.34 Plots of the axial deformation modulus and Poisson's ratio -*vs*- load increment for a 130 m level URL pink granite.

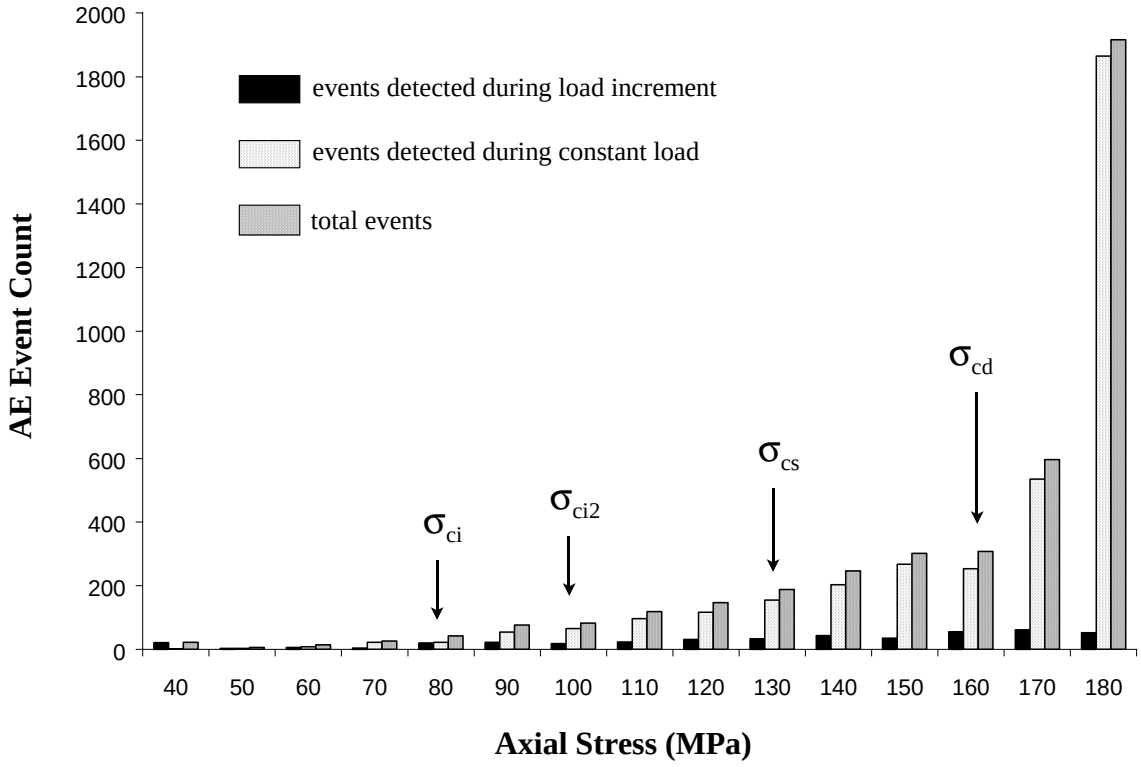

Figure 7.35 Plot of AE event count -*vs*- axial stress showing the breakdown of AE events recorded during load increments and constant loads for a 130 m level URL pink granite.

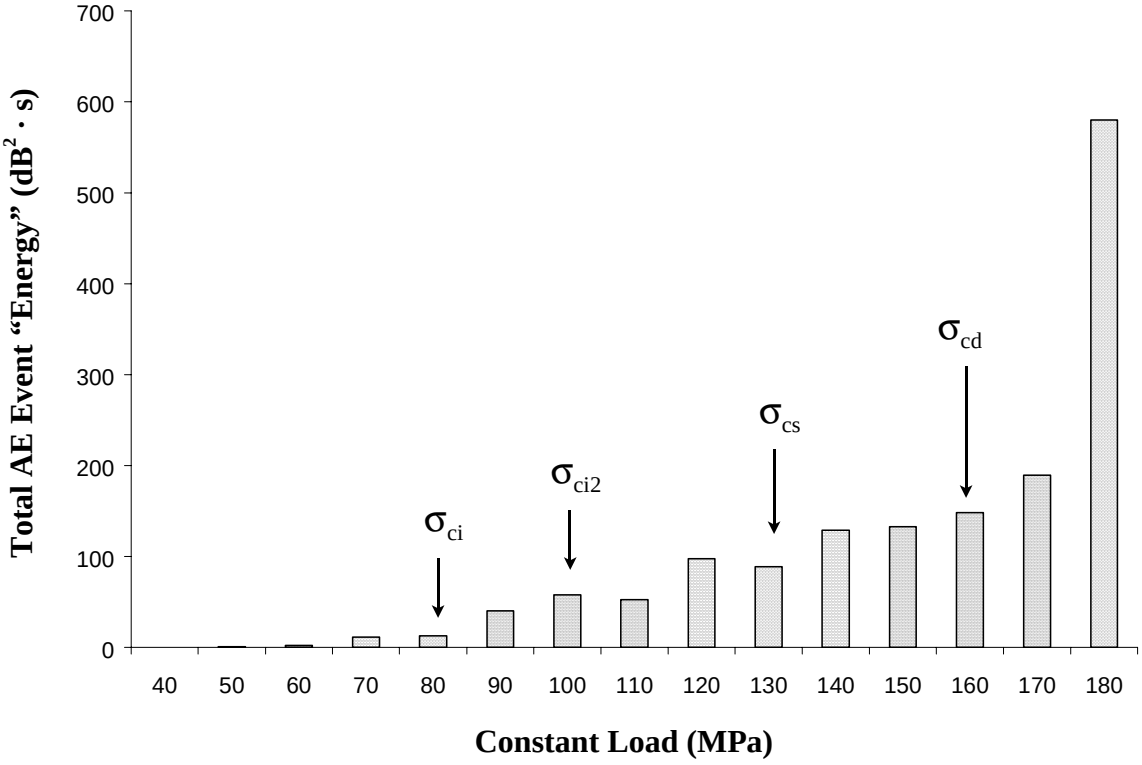

Figure 7.36 Total AE event "energy" -*vs*- constant load for a 130 m level URL pink granite. AE event "energy" was derived from the event peak amplitude and event duration for those events falling within each stress interval.

Table 7.7 Comparison of permanent axial and lateral strains from monotonic loading tests, the incremental cyclic loading test and the incremental/constant load for the 130 m level URL pink granite (standard deviation is provided in parentheses).

Test Type	Permanent Axial Strain (μstrain)	Permanent Lateral Strain (μstrain)
monotonic loading test	145 (± 33)	-196 (± 53)
incremental cycling test	134	-150
Incremental/constant load test	120	-265

crack development, it can be seen that noticeable increases in AE activity and AE event energy follow those load intervals in which the different crack thresholds fall. The most significant increases follow the crack damage threshold, which theoretically marks the beginning of unstable crack propagation. Although the sample did not immediately fail under the constant load, AE activity was detected for 40 minutes before stopping. This was three times longer than that required for the intervals following the crack coalescence threshold. It is also possible that given more time, perhaps on the scale of hours or days, the sample may have failed. However, both AE activity and strain gauge measurements indicated that the sample had reached an approximate state of equilibrium. This would seem to indicate that some uncertainty exists in the use of volumetric strain calculations as an indicator of critical crack propagation. As an approximation, however, results seem to agree that the crack damage threshold is a key parameter in marking the beginning of imminent sample failure.

7.4 Chapter Summary

A number of approaches were explored in an attempt to better quantify the stress-induced microfracturing damage observed in uniaxial compression tests. Results from monocyclic loading tests demonstrated that damage and the subsequent deformation characteristics of the damaged material could be easily quantified by normalizing the stresses and strains required to pass from one stage of crack development to another. Results from this analysis showed that crack initiation and crack damage occurs at $0.39\sigma_{UCS}$ and $0.75\sigma_{UCS}$, respectively. Furthermore, relationships were used to quantify the damage dependent stress-strain relationship for the 130 m level URL pink granite using an axial deformation modulus (E_{def}) and the ratio of lateral to axial deformation (ν_{def}).

Acoustic velocity measurements were analyzed in a further attempt to quantify stress-induced damage. These results showed that both P- and S-wave velocities generally increased throughout loading as existing cracks aligned perpendicular to the wave path closed. Continued increases were observed up to the point where the material appeared to yield, resulting in a sharp decline in velocity values. Large decreases were also observed in the peak S-wave amplitudes prior to this point coinciding with the crack coalescence threshold. However, these results only provided another qualitative check with respect to identifying the different crack thresholds.

Acoustic emissions were found to provide a direct measure of the rapid release of energy associated with damage related mechanisms. Simplified models describing the loss of cohesion and the subsequent development of microfractures leading up to unstable crack propagation were derived using normalized acoustic emission rates. Results indicate that approximately 55% of the damage causing mechanisms leading up to unstable crack propagation occur prior to crack coalescence and 45% occur afterwards. A third order polynomial was used to fit this relationship in terms of a continuous function describing the accumulation of damage leading up to unstable crack propagation.

Damage-controlled cyclic loading tests were used to examine the accumulation of damage and its influence on altering the deformation and fracture characteristics of rock. Results from the first of these damage-controlled test, involving cyclic loads exceeding the crack damage threshold, showed that subsequent to the first damage increment very little in the form of new cracking transpired. Instead existing cracks would reactivate and propagate in an unstable fashion until the load was reduced. Results suggest that failure occurred through a process that involved the coalescence of smaller cracks into larger cracks which, in turn, would coalesce with one another until a critical plane was formed.

Results from the second damage-controlled test, in which cyclic loads were kept below the crack damage threshold, revealed that the slow development of the microcrack population resulted in the initiation and propagation of new cracks with each damage increment. Failure occurred when the crack population reached a state, both in density and size, through which large scale crack interaction, coalescence and unstable propagation ensued. This was marked by a large decrease in material stiffness over the last five damage increments of the test.

The final set of tests performed concentrated on quantifying the different rates of stress-induced damage relating to given changes in the stress state of the sample. The first of these tests involved cyclic loading of a sample whereby the maximum load applied increased with each subsequent cycle. Axial damage values for the test linearly increased with each damage increment. Lateral damage values did not show any signs of increasing until the crack initiation threshold was surpassed, after which a steady increase was observed. Results suggested that in many ways the sample responded to incremental cyclic loading in the same manner as samples loaded monotonically.

The second of these incremental damage tests explored the influence of time on the microfracturing process and the accumulation of damage. Results from this test indicated that a significant percentage of microfracturing damage occurred over periods of constant load. Creep strains were attributed to the continued initiation and propagation of cracks due to the slow dissipation of induced energy levels. Damage values based on these measured creep strains showed that the accumulation of axial

strain damage during creep loading followed a relatively linear trend, whereas lateral values showed an exponential trend. Values of the calculated AE event “energy” showed significant increases following the crack damage threshold, which theoretically marks the beginning of unstable crack propagation. Although the sample did not fail under this constant load, AE activity suggested that the crack damage threshold is a key parameter in marking the beginning of imminent sample failure.

CHAPTER 8

SUMMARY AND CONCLUSIONS

The research presented in this thesis was undertaken to investigate the effects of stress-induced brittle fracturing on the progressive degradation of rock strength under uniaxial compression. Through the combined use of laboratory strain gauge and acoustic emission techniques, rigorous methodologies were developed to aid in the identification and characterization of the different stages of crack development. In addition, elements of numerical modelling were used to aid in the conceptualization of the internal mechanisms acting during the initiation, propagation and interaction of coalescing cracks. The insights gained in these studies primarily concentrated on using a test material which could be considered near isotropic, linear elastic, brittle and relatively undisturbed (i.e. 130 m level URL pink Lac du Bonnet granite from Atomic Energy of Canada Limited's Underground Research Laboratory). The versatility and full potential of the laboratory methodologies developed herein was further established through tests involving rock types of varying grain size, mineralogy, sampling disturbance and rheological behaviour. Once the different processes and mechanisms relating to brittle fracture development were resolved, test results were formulated to quantify the progressive accumulation of stress-induced damage. Additional laboratory tests were designed to aid in this assessment and to establish further the effects of damage on the deformation and strength characteristics of brittle rock. Through these different studies the objectives of the thesis were met. The following sections contain a summary of the major findings and key contributions from this thesis study.

8.1 The Brittle Fracture Process

Recent studies at the URL have shown that high compressive stresses near the tunnel face significantly contribute to the loss of strength, and the eventual failure of the rock, through stress-induced brittle fracturing. By integrating the use of strain gauge measurements, acoustic emission monitoring and scanning electron imaging, new laboratory techniques and rigorous methodologies were developed to aid in the identification and characterization of several mechanisms relating to stress-induced brittle fracturing. These include:

- The implementation of a moving point regression technique reduced the degree of subjectivity incorporated into the analysis of stress-strain data and acted to highlight small changes in sample deformation, which can be correlated with the closure and opening of microfractures.

- Several parameters relating to the characteristics of an acoustic emission event (i.e. ringdown count, event duration, peak amplitude and rise time) were used to identify different mechanisms relating to crack development. In addition, approximations of the AE event energy was used to accentuate larger events.

Initial testing concentrated on establishing the different thresholds of crack development for brittle rock as defined by Brace (1964), Bieniawski (1967a) and Martin (1993). These include the crack closure, crack initiation, crack damage and peak strength thresholds. In addition, two supplementary thresholds (i.e. the secondary crack and crack coalescence thresholds) were added, thereby providing a complete picture of the evolution of brittle crack development in Lac du Bonnet granite. These thresholds were identified and characterized as follows:

- Initial loading of the test samples saw the closure of existing cracks, largely attributable to sampling disturbance, resulting in non-linear axial deformation

and increasing axial stiffness values. The crack closure threshold (σ_{cc}) was reached when the majority of these cracks had closed. Observations suggested that the initial stages of crack closure predominantly involved the simple movement of preferentially aligned crack walls towards one another, parallel to the direction of the applied load. Decreases in lateral stiffness values possibly signified the shear or slippage of crack faces upon closure. The average crack closure threshold for the 130 m level URL pink granite was 47.3 MPa (i.e. $0.23\sigma_{UCS}$).

- The crack closure threshold marked the point where near linear elastic deformation began. However, test results revealed that this behaviour was only truly seen in the axial direction, whereas non-linear behaviour in the lateral direction was seen throughout the test. This complicates the calculation of the Poisson's ratio and its use as an elastic parameter. Results suggested that both the Young's modulus and Poisson's ratio should be calculated over the stress interval between crack closure and crack initiation. These values for the 130 m level URL pink granite were 66.5 GPa and 0.25, respectively.

- The initiation of new fractures was seen to be predominantly dependent on the mineralogy of the sample. In the case of Lac du Bonnet granite, samples were primarily composed of feldspar and quartz grains. Initial cracking seemed to originate along grain boundaries between neighbouring quartz and feldspar grains, and intragranularly within the feldspar grains. The point where the majority of these fractures began to initiate was defined as the crack initiation threshold (σ_{ci}). This point was detectable in both strain gauge and acoustic emission measurements. In more complex cases, the combined use of acoustic emission response and moving point regression analysis performed on the lateral and volumetric stress-strain curves provided the most accurate and reliable method of identifying crack initiation. In addition, analysis of the acoustic event properties and the calculation of the event energies provided a means to verify

results. Subjectivity, variability and uncertainty in the calculation of the Poisson's ratio value indicated that the use of the crack volume calculation, as described by Martin (1993), may not provide the most reliable method to identify crack initiation. The crack initiation threshold for the 130 m level URL pink granite was 81.5 MPa (i.e. $0.39\sigma_{UCS}$).

- At increased loads, cracks began to originate within the quartz grains. This point was referred to as the secondary cracking threshold (σ_{ci2}) and was characterized by increases in the AE event rate, the AE event "energy" and a notable break in the volumetric stiffness curve. In rocks with a more varied composition and with grains of starkly contrasting strengths, it may be possible that a number of these points exist, each marked by a stress level required to initiate intergranular cracking within that mineral constituent. The secondary cracking threshold for the 130 m level URL pink granite was detected at 103.9 MPa (i.e. $0.50\sigma_{UCS}$).

- Cracking was seen to progress in a stable fashion following both the crack initiation and secondary cracking thresholds. Analysis of both the axial and lateral stiffness curves, however, indicated that a significant rate change occurred in strain well before volumetric strain reversal. The point also coincided with an increase in the rate of AE events. The departure of the axial strain behaviour from linear to non-linear hinted that some fracture mechanism was acting in the lateral direction, possibly the destruction of material between interacting cracks, the "stepping out" of propagating cracks or possibly an element of shear fracturing which, in turn, would frictional effects. It was concluded that this point marked the small-scale coalescence of cracks and was referred to as the crack coalescence threshold (σ_{cs}). This behaviour was studied using numerical modelling techniques which showed that as the number of propagating cracks increased both in number and size, the stress fields surrounding the crack tips will begin to interact with one another. In terms of crack propagation, these interactions can act either to suppress or promote crack

growth depending on the size of the neighbouring cracks, the distance separating them and the loading conditions (i.e. uniaxial or triaxial). The crack coalescence threshold for the 130 m level URL pink granite was determined to be 132.8 MPa (i.e. $0.64\sigma_{UCS}$).

- The continued coalescence and interaction between propagating cracks eventually resulted in a point where the volumetric strain curve reversed. This point was referred to as the crack damage threshold (σ_{cd}). Theoretically, crack propagation beyond this point occurs in an unstable fashion. The crack damage threshold was therefore considered to be the intermediate-term strength of the material. Observations of the failed samples seems to indicate that the final mode of failure may be linked to a complex combination of shear and buckling of columnar pieces delineated by large coalesced cracks orientated parallel to the loading direction (i.e. post-localization). Movement of these interlocked columnar pieces may result in the appearance of strain hardening as irregularities and newly-shaped crack faces "lock-up", thereby providing some additional short-term strength. The crack damage threshold for the 130 m level URL pink granite was detected at 156.0 MPa (i.e. $0.75\sigma_{UCS}$). The uniaxial compressive strength was determined to be 206.9 MPa (±13.5 MPa).

8.2 Rock Microstructure and the Brittle Fracture Process

A number of factors relating to the microstructure and composition of rock are known to have an adverse effect on their strength and deformation characteristics. The first of these factors tested was grain size. *In situ* observations at the URL revealed that the severity of stress-induced spalling following tunnel advances was more pronounced in regions comprised predominantly of granite as opposed to finer-grained granodiorite. Grain size effects were tested using samples of fine-grained granodiorite, medium-grained grey granite and coarse-grained pegmatite from the 240 m level of the URL. The following observations and conclusions were made:

- An inverse relationship was found between grain size and acoustic velocity, Young's modulus and secant modulus. P- and S-wave velocities generally decreased with grain size. However, the pegmatite, with the largest grain size, had velocity values similar to the finer-grained granodiorite. These high velocity values were attributed to the presence of large feldspar crystals dominating the sample matrix and the subsequently smaller number of grain boundaries which act to impede the acoustic pulse. Modulus values were found to decrease with increasing grain size. Large discrepancies between the secant and Young's modulus values for the grey granite and pegmatite were attributed to stress-induced sampling disturbance owing to their weaker nature relative to the granodiorite.

- Analysis of the fracture characteristics of the samples showed that grain size had relatively little influence on the crack initiation and secondary cracking thresholds. This was likely due to the large number of cracks that developed within grain boundaries (i.e. intergranularly). These cracks were found to be more dependent on the strength of the constituent minerals than their grain size. Grain size was seen to have more of an influence on cracks originating along grain boundaries. These effects were found to be minimal, with respect to sample deformation and stiffness, although the number of detected AE events drastically increased with increasing grain size.

- Grain size was found to have a detrimental effect on the crack coalescence and crack damage thresholds. Relative values for these thresholds drastically decreased with increasing grain size. It was reasoned that longer grain boundaries and larger intergranular cracks, due to increased grain size, provided longer paths of weakness for growing cracks to propagate along. This resulted in the quicker degradation of material strength once these longer cracks began to coalesce and interact. Thus, rock strength was found to decrease with increasing

grain size, not by inducing crack initiation sooner (as dictated by Griffith's empirical relationship), but through a process where longer cracks propagating along longer planes of weakness coalesce at lower stresses, resulting in failure at lower loads.

Previous studies at the URL have also shown that sample disturbance can have a significant effect on the mechanical properties of Lac du Bonnet granite. Sampling disturbance effects were tested using granite and granodiorite samples taken from three different *in situ* stress regimes of the URL (i.e. 130 m, 240 m and 420 m levels corresponding to σ_1-σ_3 values of 7.5, 13 and 41 MPa, respectively). The following observations were made based on these tests:

- Acoustic velocities and material stiffnesses decreased with depth of sampling. These decreases were attributed to increased stress-induced sampling disturbance. Substantial damage was found in samples obtained from the 420 m level (it was also noted that some cracking in these samples may have occurred *in situ* prior to sampling due to the high deviatoric stresses). These observations were further confirmed through SEM images which showed that crack densities in the samples drastically increased with sampling depth. Values of P- and S-wave velocity, and Young's and secant modulus decreased with increased sampling disturbance.

- Identification of the crack initiation threshold became more complicated when test samples underwent a large degree of sampling disturbance prior to testing. In such cases, crack initiation thresholds based on the calculated crack volumes and elastic constants (e.g. Martin, 1993) are highly inaccurate. The acoustic emission response and the stress-strain stiffness curves, however, provided a reliable means to ascertain crack initiation and propagation processes.

- Results indicated that sampling disturbance had only minor effects on the initiation of new fractures. As loads approached the crack initiation and secondary cracking thresholds, new fracturing began within those grains and along those grain boundaries that had not been damaged during sampling disturbance. Increasing AE counts with increased sample disturbance prior to these points suggested that higher crack densities resulted in more AE activity related to grain boundary movements and the collapse of crack structures.

- Further analysis showed that values for the crack coalescence and crack damage thresholds significantly decreased with increased sampling disturbance. The presence of numerous stress relief cracks in the 420 m level samples were seen to weaken the rock by providing an increased number of existing planes of weakness for active cracks to propagate along. It was found that in the highly damaged sample more cracks may propagate more easily, resulting in their coalescence and ultimately the failure of the sample at lower than expected compressive stresses.

- The extent of damage seen in the 420 m level granite was not reflected in samples of the 420 m level granodiorite. The fine-grained nature of the granodiorite helped to limit the extent of crack propagation and interaction, thereby resulting in higher compressive strengths than the granite. However, the presence of sampling disturbance did act to reduce the granodiorite's strength relative to the 240 m level granodiorite.

Brittle fracture theories have been applied to a wide variety of materials representing a number of different deformation characteristics. It was found that the laboratory techniques and methodologies developed for the brittle crystalline rocks of the URL could also be utilized in analyzing the fracture characteristics of more ductile and porous materials. Ductile behaviour and porosity effects were tested using samples of Saskatchewan potash and Berea sandstone. The following observations were made:

- Test results demonstrate that brittle fracture characteristics can be detected in potash under appropriate loading rates. Saskatchewan potash samples, upon loading, were seen to behave initially as an elasto-plastic material. The process of crack closure seen in the URL samples was not detected in the potash samples, possibly due to the viscous nature of the material or the low stresses under which they may have closed/healed. At approximately $0.21\sigma_{UCS}$ significant cracking and plastic deformation occurred. A decrease in the deformation modulus and an increase in both the AE event count and AE event energy rate marked this point. Crack propagation was found to be stable until approximately $0.53\sigma_{UCS}$ at which point crack propagation became unstable. This point was marked by a reversal in the volumetric stiffness curve and an increase in the acoustic event properties, which in turn reflected an increase in the size of the measured AE events. Visible signs of brittle fracture were observed upon failure of the Saskatchewan potash samples. The uniaxial compressive strength was determined to be 23.2 MPa. This observed behaviour, however, would likely be influenced by a number of factors related to the time-dependent nature of the rock. Further in-depth study would be required to determine the sensitivity of these points to loading rate, temperature and humidity.

- Testing of the Berea sandstone revealed that the behaviour and fracture characteristics of porous materials are dominated by mechanisms relating to pore collapse. Pore collapse and grain compaction was seen to result in the development of axial cracks along grain boundaries, through the weaker segments of the cement matrix, and the rotation or movement of the intact grains into a tighter alignment parallel to the direction of loading. Crack initiation for these processes was observed at 10.0 MPa (i.e. $0.21\sigma_{UCS}$). Decreases in lateral stiffness were detected as grain boundary cracks opened, and increases in axial stiffness were seen as grain structures compacted. Following grain compaction at 14.0 MPa (i.e. $0.29\sigma_{UCS}$), contact was established between the constituent grains and an interval of approximate linear elastic behaviour was observed in the axial

direction. However, a high degree of non-linearity associated with stress-induced microfracturing was observed in the lateral direction, resulting in questionable Poisson's ratio calculations. Once a general state of compaction was reached, stress-induced cracking relating to grain contact loading was observed. Stable crack propagation and constant AE activity continued in the samples up to the crack damage threshold at 32.0 MPa ($0.66\sigma_{UCS}$). Following the crack damage threshold, AE activity continued to increase until the unstable development and propagation of coalescing cracks resulted in the small scale spalling of the sample at $0.89\sigma_{UCS}$. Failure occurred in a brittle manner at a uniaxial compressive strength of 48.6 MPa. Inspection of the failed samples suggested that the boundary of the samples failed first under uniaxial conditions, but the interior of the samples failed at slightly higher stresses due to confining pressures induced by the opening of numerous grain boundary cracks owing to the very fine-grained nature of the material.

8.3 Quantifying Stress-Induced Fracture Damage

The contrivance of a mechanistic-based criterion describing the gradual loss of cohesion in a material through progressive fracturing is of primary interest with regards to the *in situ* analysis of brittle rock failure around underground excavations. A number of approaches were explored in an attempt to better quantify the stress-induced microfracturing damage observed in laboratory uniaxial compression tests. The following observations were made based on both monotonic and cyclic loading tests of the 130 m level URL pink granite:

- Results from monocyclic loading tests demonstrated that damage and the subsequent deformation characteristics of the damaged material could be quantified by normalizing the stresses and strains required to pass from one stage of crack development to another. Relationships were derived for uniaxial compressive loading to allow for their incorporation into analytical, empirical or

numerical models. Results revealed that approximately 30% of the measured axial strain recorded occurred during crack closure and nearly half occurred before any cracking was detected. In contrast, only 7% of the total lateral strains were recorded during the crack closure interval, demonstrating that crack closure predominantly involves cracks preferentially aligned perpendicular to the applied load. The largest proportion of total lateral strain was recorded in the interval following crack coalescence. Approximately 66% of the lateral strains may be attributed to the coalescence and unstable propagation of growing cracks. These relationships were further quantified in terms of the damage dependent stress-strain relationship using an axial deformation modulus (E_{def}) and the ratio of lateral to axial deformation (ν_{def}).

- Acoustic velocity measurements were analyzed in a further attempt to quantify stress-induced damage. These results showed that both P- and S-wave velocities generally increased throughout loading as existing cracks aligned perpendicular to the wave path closed. Continued increases were observed up to the point where the material appeared to yield, resulting in a sharp decline in velocity values. Large decreases were also observed in the peak S-wave amplitudes prior to this point coinciding with the crack coalescence threshold. The lack of any changes in amplitude values following the crack initiation threshold, however, suggested that the method was not sensitive enough to detect the development of smaller individual cracks. In general, these results did little more than to serve as another qualitative check with respect to identifying the various thresholds of crack behaviour. A number of difficulties were also encountered throughout testing as the explosive nature of the brittle failure process at high stresses had an adverse effect on the P- and S-wave crystals (this in turn was partly dependent on the stiffness of the loading frame used). In addition, size limitations associated with the crystal housings did not allow for comparisons to be made with respect to directional fracture anisotropy.

- Acoustic emissions were found to provide a direct measure of the rapid release of energy associated with damage-related mechanisms. Empirical equations describing the loss of cohesion and the subsequent development of microfractures leading up to unstable crack propagation were derived using normalized acoustic emission rates. Relationships were derived with respect to both the compressive strength of the material and the crack damage threshold. Results indicate that approximately 55% of the damage-causing mechanisms leading up to unstable crack propagation occur prior to crack coalescence and 45% occur afterwards. A third order polynomial was used to fit this relationship in terms of a continuous function describing the accumulation of damage leading up to unstable crack propagation (i.e. the crack damage threshold).

Damage-controlled cyclic loading tests were used to examine the accumulation of damage and its influence on altering the detected crack processes. Several damage parameters were derived with respect to the measured permanent axial (ω_{ax}), lateral (ω_{lat}) and volumetric (ω_{vol}) strains and the recorded number of acoustic events (ω_{AE}), induced with each damage increment (*i*). Relationships based on these parameters were provided for two load histories: cyclic loads which *exceeded* the crack damage threshold with each damage increment; and cyclic loads restricted to levels *below* the crack damage threshold. The following results from these tests were obtained:

- Results from the first damage-control test, involving cyclic loads *exceeding* the crack damage threshold, showed that subsequent to the first damage increment very little in the form of new cracking transpired. Instead existing cracks would reactivate and propagate in an unstable fashion until loads were reduced. In terms of material strength, results revealed that values for the crack damage threshold slowly increased up to damage increment 26 before rapidly dropping to values well below the initial crack initiation threshold for the rock. Values for the crack coalescence threshold followed a similar pattern with the exception that a small-scale fluctuation could be seen throughout the test. These

fluctuations reflected an internal mechanism which suggested that the coalescence of interacting cracks involves large plastic strains as bridging material between cracks weakens and collapses. The progressive accumulation of damage in the sample also resulted in the degradation of the material stiffness. Young's modulus and Poisson's ratio values reflected the gradual softening of the material up until damage increment 26, coinciding with the peak crack damage threshold, where a sharp decline in stiffness was observed. In terms of the induced damage, only 30% of the permanent lateral strains occurred before the peak crack damage threshold was reached. In contrast, over 60% of the axial strain damage was induced prior to this point. Results indicate that at some point in the load history of the sample, the state of crack development reached a point whereby the continued generation of damage results in a magnified effect in terms of reducing the cohesion of the sample. Failure of the sample appeared to occur through a process that involved the coalescence of smaller cracks into larger cracks which, in turn, would coalesce with one another until a critical plane was formed.

- Results from the second damage-controlled test, in which cyclic loads were kept *below* the crack damage threshold, revealed that the slow development of the microcrack population resulted in the initiation and propagation of new cracks with each damage increment. The axial damage curve for the test showed a linear rate of increase with each damage increment, whereas the lateral damage curve followed an exponential rate of increase. The lateral damage was found to reflect the opening (i.e. initiation and propagation) of new cracks with each damage increment. Furthermore, AE results revealed that those damage increments showing increases in AE activity correlated to large increases in the lateral damage curve but not the axial damage curve. Deformation constants calculated for the test showed that Young's modulus and Poisson ratio values remained fairly constant with each damage increment, with the exception of a large increase in the Young's modulus observed between damage increments 27

and 33. This rapid increase in material stiffness suggested that some form of strain hardening may have occurred within the sample, possibly as angular asperities along coalesced crack faces locked-up. These results suggested that by limiting the cyclic loads to stresses below the crack damage threshold, the degree of plastic yielding exhibited by bridging material was greatly reduced. It was conjectured that the internal breakdown in material stiffness does not occur until the crack population reaches a state, both in density and size, through which large scale crack interaction and coalescence can occur. This was not observed until the last four or five damage increments of the test.

The final set of tests performed for this thesis study concentrated on quantifying the different rates of stress-induced damage relating to given changes in the stress state of the sample. These tests were designed to incorporate unique loading paths and elements from the previous monotonic and cyclic loading tests in order isolate incremental changes in fracture damage. Tests were also devised to isolate time-dependent fracture characteristics that may be related to the changing state of stress and the added energy available to drive crack propagation. Observations and conclusions from these tests are as follows:

- The first of these tests involved cyclic loading of a sample whereby the maximum load applied increased with each subsequent cycle. Axial damage values for the test increased linearly with each damage increment. Lateral damage values did not show any signs of increasing until the crack initiation threshold was surpassed, after which a steady increase was observed. Results suggested that in many ways the sample responded to incremental cyclic loading in the same manner as samples loaded monotonically. Load cycles over which the rate of permanent lateral strain increased corresponded with the crack initiation, secondary cracking and crack coalescence thresholds, i.e. crack thresholds marking the initiation and opening of cracks. Increases in measurements of permanent axial strain coincided with those thresholds which

were observed to significantly influence the axial component of deformation, i.e. crack closure, crack coalescence and crack damage. Young's modulus and Poisson ratio values for the test fell within the range of values obtained in monotonic loading tests. Young's modulus values were seen to gradually increase until the crack damage threshold was surpassed, and then gradually decreased. Poisson ratio values were seen to gradually increase with each cycle thus establishing that new cracks initiated and propagated with each cyclic load increment.

- The second incremental damage test explored the influence of time on the microfracturing process and the accumulation of damage. Results from this test indicated that a significant percentage of microfracturing damage occurred over periods of constant load. This effect was reflected in both measurements of the creep strain and AE activity. Axial creep strains were attributed to the coalescence and yielding of bridging material between interacting crack tips, whereas lateral creep strains were associated with the initiation and propagation of microfractures. Damage values based on these measured creep strains showed that the accumulation of axial strain damage during creep loading followed a relatively linear trend, whereas lateral values showed an exponential trend. Values of the calculated AE event "energy" showed significant increases following the crack damage threshold, which theoretically marks the beginning of unstable crack propagation. Although the sample did not fail under this constant load, AE activity suggested that the crack damage threshold is a key parameter in marking the beginning of imminent sample failure.

8.4 Further Research

The insights gained through this study have provided major contributions into understanding how stress-induced microfracturing results in the degradation of material strength leading up to failure. Extension of this work and continued studies relating the fracture process in laboratory tested samples to *in situ* behaviour could be addressed as follows:

- Test results from this thesis study revealed that fracture damage induced through sampling disturbance had a markedly different effect on material strength than damage induced through monotonic or cyclic loading. Tensile stress gradients induced during the sampling process, and the subsequent destruction of quartz grains within the rock matrix, were seen to have a significant effect in terms of the degradation of material strength. Furthermore, cyclic loading tests revealed that the rate at which damage accumulates in the sample could be controlled through the load path used. Further testing could be performed to determine the effects load path has on the initiation and propagation of fractures. Tests incorporating stress rotation and load paths more indicative of that experienced by the near-field rock surrounding an excavation would allow for better understanding of the *in situ* brittle fracture process responsible for compressive failures.

- The damage relationships derived in this thesis study were developed so as to allow for their easy incorporation into any number of analytical, empirical or numerical design models. An extensive numerical modelling study would provide insight into the effectiveness and applicability of laboratory test data to *in situ* observations. Preliminary work with discrete element models has shown that great potential exists in correlating the fracture processes observed in the laboratory to those observed *in situ*.

- The numerical modelling study performed in this thesis demonstrated that confining stresses significantly influences the initiation and development of microfractures. The tests performed in this study could be duplicated so as to include confining stresses. This would allow for the derivation of more extensive damage relationships that incorporate the different stress states encountered *in situ*.

BIBLIOGRAPHY

Adams, M. and Sines, G. (1978). Crack extension from flaws in a brittle material subjected to compression. *Tectonophysics*. **49** (1/2): 97-118.

Andreev, G.E. (1995). *Brittle Failure of Rock Materials: Test Results and Constitutive Models*. A.A. Balkema, Rotterdam, 446 pp.

anonymous (1988). International Society for Rock Mechanics Commission on Testing Methods: Suggested methods for determining the fracture toughness of rock. *International Journal of Rock Mechanics and Mining Sciences & Geomechanical Abstracts*. **25** (2): 71-96.

ASTM Designation E1820-96 (1997). Standard test method for measurement of fracture toughness. *In* Annual Book of ASTM Standards. Edited by American Society for Testing and Materials, West Conshohocken. **03.01**.

ASTM Designation D4543-85 (1997). Standard practice for preparing rock core specimens and determining dimensional and shape tolerances. *In* Annual Book of ASTM Standards. Edited by American Society for Testing and Materials, West Conshohocken. **04.08**.

ASTM Designation D3148-93 (1997). Standard test method for elastic moduli of intact rock core specimens in uniaxial compression. *In* Annual Book of ASTM Standards. Edited by American Society for Testing and Materials, West Conshohocken. **04.08**.

Atkinson, B.K. (1987). Introduction to fracture mechanics and its geophysical applications. *In* Fracture Mechanics of Rock. Edited by B.K. Atkinson, Academic Press Inc. Ltd., London, 1-26.

Aubertin, M., Sgaoula, J. and Gill, D.E. (1993). A damage model for rocksalt: Application to tertiary creep. *In* Seventh Symposium on Salt, Kyoto. Edited by H. Kakihana, H.R. Hardy Jr., T. Hoshi and K. Tookura, Elsevier Science Publishers B.V., Amsterdam, 117-125.

Batzle, M.L., Simmons, G. and Siegfried, R.W. (1980). Microcrack closure in rocks under stress: Direct observations. *Journal of Geophysical Research*. **85** (B12): 7072-7090.

Beattie, A.G. (1983). Acoustic emission, principles and instrumentation. *Journal of Acoustic Emission*. **2** (1/2): 95-128.

Bernabe, Y. and Brace, W.F. (1990). Deformation and fracture of Berea sandstone. *In* The Brittle-Ductile Transition in Rocks, Geophysical Monograph 56. Edited by A.G. Duba, W.B. Durham, J.W. Handin and H.F. Wang, American Geophysical Union, Washington, 91-101.

Berry, J.P. (1960a). Some kinetic considerations of the Griffith criterion for fracture - I: Equations of motion at constant force. *Journal of the Mechanics and Physics of Solids*. **8** (3): 194-206.

Berry, J.P. (1960b). Some kinetic considerations of the Griffith criterion for fracture - II: Equations of motion at constant deformation. *Journal of the Mechanics and Physics of Solids*. **8** (3): 207-216.

Bessinger, B.A. and Cook, N.G.W. (1996). Laboratory comparison of rock properties controlling geologic compression-driven extensile fracturing. *In* Proceedings of the 2nd North American Rock Mechanics Symposium: Rock Mechanics Tools and Techniques, Montreal. Edited by M. Aubertin, F. Hassani and H. Mitri, A.A. Balkema, 1137-1144.

Bezys, R. (1984). Fracture Initiation, Propagation and Arrest Produced by Compressive Loading and Unloading in the Lac du Bonnet Batholith. B.Sc. thesis, Department of Earth Sciences, University of Manitoba, Winnipeg, 72pp.

Bieniawski, Z.T. (1967a). Mechanism of brittle rock fracture: Part I - Theory of the fracture process. *International Journal of Rock Mechanics and Mining Sciences & Geomechanical Abstracts*. **4** (4): 395-406.

Bieniawski, Z.T. (1967b). Mechanism of brittle rock fracture: Part II - Experimental studies. *International Journal of Rock Mechanics and Mining Sciences & Geomechanical Abstracts*. **4** (4): 407-423.

Bobet, A. and Einstein, H.H. (1996). Fracture coalescence in rock material under uniaxial and biaxial loading. *In* Proceedings of the 2nd North American Rock Mechanics Symposium: Rock Mechanics Tools and Techniques, Montreal. Edited by M. Aubertin, F. Hassani and H. Mitri, A.A. Balkema, Rotterdam, 1603-1609.

Bombolakis, E.G. (1968). Photoelastic study of initial stages of brittle fracture in compression. *Tectonophysics*. **6** (6): 461-473.

Bombolakis, E.G. (1973). Study of the brittle fracture process under uniaxial compression. *Tectonophysics*. **18**: 231-248.

Bortolucci, A.A. and Celestino, T.B. (1996). Probabilistic model for failure of brittle materials under compression based on fracture mechanics. *In* Proceedings of the 2nd North American Rock Mechanics Symposium: Rock Mechanics Tools and Techniques, Montreal. Edited by M. Aubertin, F. Hassani and H. Mitri, A.A. Balkema, Rotterdam, 1715-1720.

Brace, W.F. (1961). Dependence of fracture strength of rocks on grain size. *Bulletin of the Mineral Industries Experiment Station, Mining Engineering Series, Rock Mechanics*. **76**: 99-103.

Brace, W.F. (1964). Brittle fracture of rocks. *In* State of Stress in the Earth's Crust: Proceedings of the International Conference, Santa Monica. Edited by W.R. Judd, American Elsevier Publishing Co., New York, 110-178.

Brace, W.F. and Bombolakis, E.G. (1963). A note on brittle crack growth in compression. *Journal of Geophysical Research*. **68** (12): 3709-3713.

Brace, W.F., Paulding, B.W., Jr. and Scholz, C. (1966). Dilatancy in the fracture of crystalline rocks. *Journal of Geophysical Research*. **71** (16): 3939-3953.

Brace, W.F., Silver, E., Hadley, K. and Goetze, C. (1972). Cracks and pores: A closer look. *Science*. **178** (4057): 162-164.

Broek, D. (1986). *Elementary Engineering Fracture Mechanics*. Martinus Nijhoff Publishers, Boston, 469 pp.

Brown, A., Soonawala, N.M., Everitt, R.A. and Kamineni, D.C. (1989). Geology and geophysics of the Underground Research Laboratory site, Lac du Bonnet Batholith, Manitoba. *Canadian Journal of Earth Sciences*. **26** (2): 404-425.

Brown, E.T. (1981). *Rock Characterization Testing and Monitoring: ISRM Suggested Methods*. Pergamon Press Ltd., Oxford, 211 pp.

Cannon, N.P., Schulson, E.M., Smith, T.R. and Frost, H.J. (1990). Wing cracks and brittle compressive fracture. *Acta Metallurgica et Materialia*. **38** (10): 1955-1962.

Carpinteri, A., Scavia, C. and Yang, G.P. (1996). Microcrack propagation, coalescence and size effects in compression. *Engineering Fracture Mechanics*. **54** (3): 335-347.

Carter, B.J., Duncan, E.J.S. and Lajtai, E.Z. (1991). Fitting strength criteria to intact rock. *Geotechnical and Geological Engineering*. **9** (1): 73-81.

Chengyong, W., Peide, L., Rongsheng, H. and Xiutang, S. (1990). Study of the fracture process zone in rock by laser speckle interferometry. *International Journal of Rock Mechanics and Mining Sciences & Geomechanical Abstracts*. **27** (1): 65-69.

Chow, T.M., Meglis, I.L. and Young, R.P. (1995). Progressive microcrack development in tests on Lac du Bonnet granite - II. Ultrasonic tomographic imaging. *International Journal of Rock Mechanics and Mining Sciences & Geomechanical Abstracts*. **32** (8): 751-761.

Chudnovsky, A. and Kunin, B. (1987). A probabilistic model of brittle crack formation. *Journal of Applied Physics*. **62** (10): 4124-4129.

Cook, N.G.W. (1965). The failure of rock. *International Journal of Rock Mechanics and Mining Sciences & Geomechanical Abstracts*. **2** (4): 389-403.

Cox, S.J.D. and Meredith, P.G. (1993). Microcrack formation and material softening in rock measured by monitoring acoustic emissions. *International Journal of Rock Mechanics and Mining Sciences & Geomechanical Abstracts*. **30** (1): 11-24.

Deflandre, J.-P., Vincke, O. and Rebut, E. (1995). Contribution of the acoustic emission analysis to the interpretation of the uniaxial compression test. *In* Rock Mechanics, Proceedings of the 35th U.S. Symposium, Reno. Edited by J.J.K. Daemen and R.A. Schultz, A.A. Balkema, Rotterdam, 867-872.

Dey, T.N. and Wang, C. (1981). Some mechanisms of microcrack growth and interaction in compressive rock failure. *International Journal of Rock Mechanics and Mining Sciences & Geomechanical Abstracts*. **18** (3): 199-209.

Dowding, C.H. and Mueller, C.G. (1987). Factors affecting the relative magnitude of acoustic emissions generated during the fracture of granite. *In* Proceedings of the 28th U.S. Symposium on Rock Mechanics, Tuscon. Edited by I.W. Farmer, J.J.K. Daemen, C.S. Desai, C.E. Glass and S.P. Neuman, A.A. Balkema, Rotterdam, 359-366.

Dowla, N., Hayatdavoudi, A., Ghalambor, A., Okoye, C. and Alcocer, C. (1990). Laboratory investigation of saturation effect on mechanical properties of rocks. *In* Transactions of the SPWLA Thirty-First Annual Logging Symposium, Lafayette. The Society of Professional Well Log Analysts, Inc., Houston, EE1-EE10.

Du, Y. and Aydin, A. (1991). Interaction of multiple cracks and formation of echelon crack arrays. *International Journal for Numerical and Analytical Methods in Geomechanics*. **15** (3): 205-218.

Dyskin, A.V., Germanovich, L.N., Lee, K.K., Ring, L.M. and Ingraffea, A.R. (1994). Modelling crack propagation in compression. *In* Rock Mechanics: Models and Measurements, Challenges from Industry, Proceedings of the 1st North American Rock Mechanics Symposium, Austin. Edited by P.P. Nelson and S.E. Laubach, A.A. Balkema, Rotterdam, 451-460.

Dyskin, A.V., Ustinov, K.B. and Korsunsky, A.M. (1995). On modelling of defect interaction. *International Journal of Fracture*. **71** (4): R79-R83.

Dzik, E.J. and Lajtai, E.Z. (1998). Modeling the axial tensile fractures of the compressive stress field. *In Press*.

Eberhardt, E., Stead, D. and Szczepanik, Z. (1996). Crack Initiation and Propagation in Granite and Granodiorite from the 130m and 420m Levels of the URL. Atomic Energy of Canada Limited, Contract Report #122567, University of Saskatchewan, Saskatoon, 263pp.

Einstein, H.H. and Dershowitz, W.S. (1990). Tensile and shear fracturing in predominantly compressive stress fields - a review. *Engineering Geology*. **29** (2): 149-172.

Everitt, R.A., Brown, A., Davison, C., Gascoyne, M. and Martin, C.D. (1990). Regional and local settings of the Underground Research Laboratory. *In* Proceedings: International Symposium on Unique Underground Structures, Denver. Edited by R.S. Sinha, CSM Press, Denver, 64:1-23.

Farmer, I. (1983). *Engineering Behaviour of Rocks*. Chapman and Hall, New York, 208 pp.

Franklin, J.A. and Dusseault, M.B. (1989). *Rock Engineering*. McGraw-Hill Publishing Company, New York, 600 pp.

Fredrich, J.T., Evans, B. and Wong, T-F. (1990). Effect of grain size on brittle and semibrittle strength: Implications for micromechanical modelling of failure in compression. *Journal of Geophysical Research*. **95** (B7): 10907-10920.

Freeze, R.A. and Cherry, J.A. (1979). *Groundwater*. Prentice-Hall, Inc., Englewood Cliffs, 604 pp.

Goodman, R.E. (1989). *Introduction to Rock Mechanics*. John Wiley & Sons, New York, 562 pp.

Gorelic, M., Chudnovsky, A. and Shlyapobersky, J. (1996). Application of statistical fracture mechanics in hydraulic fracture. *In* Proceedings of the 2nd North American Rock Mechanics Symposium: Rock Mechanics Tools and Techniques, Montreal. Edited by M. Aubertin, F. Hassani and H. Mitri, A.A. Balkema, Rotterdam, 1261-1268.

Griffith, A.A. (1920). The phenomena of rupture and flow in solids. *Philosophical Transactions of the Royal Society of London, Series A, Mathematical and Physical Sciences*. **221** (587): 163-198.

Griffith, A.A. (1924). The theory of rupture. *In* Proceedings of the First International Congress for Applied Mechanics, Delft. Edited by C.B. Biezeno and J.M. Burgers, J. Waltman Jr., Delft, 55-63.

Guessous, Z., Ladanyi, B. and Gill, D.E. (1984). Effect of sampling disturbance on laboratory determined properties of rock salt. *In* The Mechanical Behaviour of Salt, Proceedings of the Second Conference, Hanover. Edited by H.R. Hardy Jr. and M. Langer, Trans Tech Publications, Clausthal-Zellerfeld, 137-158.

Hallbauer, D.K., Wagner, H. and Cook, N.G.W. (1973). Some observations concerning the microscopic and mechanical behaviour of quartzite specimens in stiff, triaxial compression tests. *International Journal of Rock Mechanics and Mining Sciences & Geomechanical Abstracts*. **10** (6): 713-726.

Hamajima, R., Kawai, T., Kusabuka, M. and Yamashita, K. (1984). Crack propagation analysis of cracked rock media. *In* Numerical Methods in Fracture Mechanics: Proceedings of the Third International Conference, Swansea. Edited by A.R. Luxmoore and D.R.J. Owen, Pineridge Press, Swansea, 751-764.

Hardy, H.R., Jr. (1977). Emergence of acoustic emission/microseismic activity as a tool in geomechanics. *In* Proceedings of the First Conference on Acoustic Emission/Microseismic Activity in Geologic Structures and Materials, University Park. Edited by H.R. Hardy and L.W. Leighton, Trans Tech Publications, Clausthal-Zellerfeld, 3-31.

Hardy, H.R., Jr. (1981). Applications of acoustic emission techniques to rock and rock structures: A state-of-the-art review. *In* Acoustic Emissions in Geotechnical Engineering Practice, STP 750. Edited by V.P. Drnevich and R.E. Gray, American Society for Testing and Materials, Philadelphia, 4-92.

Hoek, E. (1965). Rock Fracture Under Static Stress Conditions. National Mechanical Engineering Research Institute, Council for Scientific and Industrial Research, CSIR Report MEG 383, Pretoria, 228pp.

Hoek, E. and Bieniawski, Z.T. (1965). Brittle fracture propagation in rock under compression. *International Journal of Fracture Mechanics*. **1** (3): 137-155.

Hoek, E. and Brown, E.T. (1980). *Underground Excavations in Rock*. The Institution of Mining and Metallurgy, London, 527pp.

Holcomb, D.J. (1993). General theory of the Kaiser effect. *International Journal of Rock Mechanics and Mining Sciences & Geomechanical Abstracts*. **30** (7): 929-935.

Holcomb, D.J., Stone, C.M. and Costin, L.S. (1990). Combining acoustic emission locations and a microcrack damage model to study development of damage in brittle materials. *In* Rock Mechanics and Challenges: Proceedings of the 31st U.S. Symposium, Golden. Edited by W.A. Hustrulid and G.A. Johnson, A.A. Balkema, Rotterdam, 645-651.

Horii, H. and Okui, Y. (1994). Micromechanics-based continuum theory and numerical analysis of localized phenomena. *In* Proceedings of the Eighth International Conference on Computer Methods and Advances in Geomechanics, Morgantown. Edited by H.J. Siriwardane and M.M. Zaman, A.A. Balkema, Rotterdam, 1687-1692.

Huang, J., Wang, Z. and Zhao, Y. (1993). The development of rock fracture from microfracturing to main fracture formation. *International Journal of Rock Mechanics and Mining Sciences & Geomechanical Abstracts*. **30** (7): 925-928.

Hugman, R.H.H. and Friedman, M. (1979). Effects of texture and composition on mechanical behavior of experimentally deformed carbonate rocks. *The American Association of Petroleum Geologists Bulletin*. **63** (9): 1478-1489.

Inglis, C.E. (1913). Stresses in a plate due to the presence of cracks and sharp corners. *Transactions of the Institution of Naval Architects*. **55**: 219-230.

Ingraffea, A.R. (1979). The strength ratio effect in the fracture of rock structures. *In* Proceedings of the 20th U.S. Symposium on Rock Mechanics, Austin. University of Texas at Austin, 153-162.

Ingraffea, A.R. (1987). Theory of crack initiation and propagation in rock. *In* Fracture Mechanics of Rock. Edited by B.K. Atkinson, Academic Press Inc. Ltd., London, 71-110.

Ingraffea, A.R., Boone, T.J. and Swenson, D.V. (1993). Computer simulation of fracture processes. *In* Comprehensive Rock Engineering: Principles, Practice and Projects. Edited by J.A. Hudson, Pargamon Press, New York. **1**: 545-573.

Ingraffea, A.R. and Heuze, F.E. (1980). Finite element models for rock fracture mechanics. *International Journal for Numerical and Analytical Methods in Geomechanics*. **4** (1): 25-43.

Ingraffea, A.R. and Wawrzynek, P.A. (1985). Modelling of the fracture process zone in rock. *In* Rock Masses: Modelling of Underground Openings/Probability of Slope Failure/Fracture of Intact Rock, Proceedings of the Symposium, Denver. Edited by C.H. Dowding, American Society of Civil Engineers, New York, 151-157.

Itasca (1995). FLAC - Fast Lagrangian Analysis of Continua, version 3.3. Itasca Consulting Group, Minneapolis.

Jackson, R., Lau, J.S.O. and Annor, A. (1989). Mechanical, thermo-mechanical & joint properties of rock samples from the site of AECL's Underground Research Laboratory, Lac du Bonnet, Manitoba. *In* Proceedings of the 42nd Canadian Geotechnical Conference, Materials: From Theory to Practice, Winnipeg. Canadian Geotechnical Society, Toronto, 41-49.

Jackson, R. and Lau, J.S.O. (1990). The effect of specimen size on the laboratory mechanical properties of Lac du Bonnet grey granite. *In* Proceedings of the First International Workshop on Scale Effects in Rock Masses, Loen. Edited by A. Pinto da Cunha, A.A. Balkema, Rotterdam, 165-174.

Jeremic, M.L. (1994). *Rock Mechanics in Salt Mining*. A.A. Balkema, Rotterdam, 532 pp.

Johnston, I.W. (1985). Strength of intact geomechanical materials. *Journal of Geotechnical Engineering*. **111** (6): 730-749.

Kachanov, M. and Laures, J.P. (1989). Three-dimensional problems of strongly interacting arbitrarily located penny-shaped cracks. *International Journal of Fracture*. **41** (4): 289-313.

Kemeny, J.A. and Cook, N.G.W. (1991). Micromechanics of deformation in rocks. *In* Toughening Mechanisms in Quasi-Brittle Materials. Edited by S.P. Shah, Kluwer Academic Publishers, Netherlands, 155-188.

Kemeny, J.M. and Tang, F.F. (1990). A numerical damage model for rock based on microcrack growth, interaction, and coalescence. *In* Damage Mechanics in Engineering Materials. Edited by J.W. Ju, D. Krajcinovic and H.L. Schreyer, The American Society of Mechanical Engineers, New York, 103-116.

Khair, A.W. (1984). Acoustic emission pattern: An indicator of mode of failure in geologic materials as affected by their natural imperfections. *In* Proceedings, Third Conference on Acoustic Emission/Microseismic Activity in Geologic Structures and Materials, University Park. Edited by H.R. Hardy, Jr. and F.W. Leighton, Trans Tech Publications, Clausthal-Zellerfeld, 45-66.

Knudsen, F.P. (1959). Dependence of mechanical strength of brittle polycrystalline specimens on porosity and grain size. *Journal of the American Ceramic Society*. **42** (8): 376-387.

Kranz, R.L. (1979). Crack-crack and crack-pore interactions in stressed granite. *International Journal of Rock Mechanics and Mining Sciences & Geomechanical Abstracts*. **16** (1): 37-47.

Kranz, R.L. (1983). Microcracks in rocks: A review. *Tectonophysics*. **100** (1-3): 449-480.

Kwong, L.S. (1983). Photomicrographic Analysis of Cracks Produced by Compression in Lac du Bonnet Quartz Monzonite. B.Sc. thesis, Department of Earth Sciences, University of Manitoba, Winnipeg, 71pp.

Lajtai, E.Z. (1971). A theoretical and experimental evaluation of the Griffith theory of brittle fracture. *Tectonophysics*. **11**: 129-156.

Lajtai, E.Z., Carter, B.J. and Duncan, E.J.S. (1994). En echelon crack-arrays in potash salt rock. *Rock Mechanics and Rock Engineering*. **27** (2): 89-111.

Lajtai, E.Z. and Dzik, E.J. (1996). Searching for the damage threshold in intact rock. *In* Proceedings of the 2nd North American Rock Mechanics Symposium: Rock Mechanics Tools and Techniques, Montreal. Edited by M. Aubertin, F. Hassani and H. Mitri, A.A. Balkema, Rotterdam, 701-708.

Lajtai, E.Z. and Lajtai, V.N. (1974). The evolution of brittle fracture in rocks. *Journal of the Geological Society of London*. **130** (1): 1-18.

Lemaitre, J. and Chaboche, J.-L. (1990). *Mechanics of solid materials*. Cambridge University Press, Cambridge, 556pp.

Li, C. (1995). Micromechanics modelling for stress-strain behaviour of brittle rocks. *International Journal for Numerical and Analytical Methods in Geomechanics*. **19** (5): 331-344.

Li, C. and Nordlund, E. (1993). Assessment of damage in rock using the Kaiser effect of acoustic emission. *International Journal of Rock Mechanics and Mining Sciences & Geomechanical Abstracts*. **30** (7): 943-946.

Lockner, D. (1993). The role of acoustic emission in the study of rock. *International Journal of Rock Mechanics and Mining Sciences & Geomechanical Abstracts*. **30** (7): 883-899.

Lockner, D.A., Byerlee, J.D., Kuksenko, V., Ponomarev, A. and Sidorin, A. (1991). Quasi-static fault growth and shear fracture energy in granite. *Nature*. **350** (6313): 39-42.

Ma, Q., Scott, J., T.E. and Roegiers, J.-C. (1995). Modelling induced acoustic velocity anisotropy during triaxial tests of rocks. *In* Rock Mechanics, Proceedings of the 35th U.S. Symposium, Reno. Edited by J.J.K. Daemen and R.A. Schultz, A.A. Balkema, Rotterdam, 813-818.

Mansurov, V.A. (1994). Acoustic emission from failing rock behaviour. *Rock Mechanics and Rock Engineering*. **27** (3): 173-182.

Martin, C.D. (1993). Strength of Massive Lac du Bonnet Granite Around Underground Openings. Ph.D. thesis, Department of Civil and Geological Engineering, University of Manitoba, Winnipeg, 278pp.

Martin, C.D. (1997). Seventeenth Canadian Geotechnical Colloquium: The effect of cohesion loss and stress path on brittle rock strength. *Canadian Geotechnical Journal*. **34** (5): 698-725.

Martin, C.D. and Chandler, N.A. (1994). The progressive fracture of Lac du Bonnet granite. *International Journal of Rock Mechanics and Mining Sciences & Geomechanical Abstracts*. **31** (6): 643-659.
Martin, C.D. and Read, R.S. (1996). AECL's Mine-by Experiment: A test tunnel in brittle rock. *In* Proceedings of the 2nd North American Rock Mechanics Symposium: Rock Mechanics Tools and Techniques, Montreal. Edited by M. Aubertin, F. Hassani and H. Mitri, A.A. Balkema, Rotterdam, 13-24.

Martin, C.D. and Stimpson, B. (1994). The effect of sample disturbance on laboratory properties of Lac du Bonnet granite. *Canadian Geotechnical Journal*. **31** (5): 692-702.

Mazars, J. and Pijaudier-Cabot, G. (1996). From damage to fracture mechanics and conversely: A combined approach. *International Journal of Solids and Structures*. **33** (20-22): 3327-3342.

McClintock, F.A. and Walsh, J.B. (1962). Friction on Griffith cracks in rocks under pressure. *In* Proceedings of the Fourth U.S. National Congress of Applied Mechanics, Berkeley. Edited by R.M. Rosenberg, The American Society of Mechanical Engineers, New York, 1015-1021.

Meglis, I.L., Chow, T.M. and Young, R.P. (1995). Progressive microcrack development in tests of Lac du Bonnet granite - I. Acoustic emission source location and velocity measurements. *International Journal of Rock Mechanics and Mining Sciences & Geomechanical Abstracts*. **32** (8): 751-761.

Menendez, B., Zhu, W. and Wong, T.-F. (1996). Micromechanics of brittle faulting and cataclastic flow in Berea sandstone. *Journal of Structural Geology*. **18** (1): 1-16.

Mlakar, V., Hassani, F.P. and Momayez, M. (1993). Crack development and acoustic emission in potash rock. *International Journal of Rock Mechanics and Mining Sciences & Geomechanical Abstracts*. **30** (3): 305-319.

Myer, L.R., Kemeny, J.M., Zheng, Z., Suarez, R., Ewy, R.T. and Cook, N.G.W. (1992). Extensile cracking in porous rock under differential compressive stress. *Applied Mechanics Reviews*. **45** (8): 263-280.

Mosher, S., Berger, R.L. and Anderson, D.E. (1975). Fracturing characteristics of two granites. *Rock Mechanics*. **7** (3): 167-176.

Munson, D.E., Holcomb, D.J., DeVries, K.L., Brodsky, N.S. and Chan, K.S. (1995). Correlation of theoretical calculations and experimental measurements of damage around a shaft in salt. *In* Proceedings of the 35th U.S. Symposium on Rock Mechanics, Reno. Edited by J.J.K. Daemen and R.A. Schultz, A.A. Balkema, Rotterdam, 491-496.

Nemat-Nasser, S. and Horii, H. (1982). Compression-induced nonplanar crack extension with application to splitting, exfoliation and rockburst. *Journal of Geophysical Research*. **87** (B8): 6805-6821.

Ohnaka, M. and Mogi, K. (1982). Frequency characteristics of acoustic emissions in rocks under uniaxial compression and its relation to the fracturing process to failure. *Journal of Geophysical Research*. **87** (B5): 3873-3884.

Olsson, W.A. (1974). Grain size dependence of yield stress in marble. *Journal of Geophysical Research*. **79** (32): 4859-4862.

Peng, S. and Johnson, A.M. (1972). Crack growth and faulting in cylindrical specimens of Chelmsford granite. *International Journal of Rock Mechanics and Mining Sciences & Geomechanical Abstracts*. **9** (1): 37-86.

Peng, S.S. and Oritz, C.A. (1973). Crack propagation and fracture of rock specimens loaded in compression. *In* Proceedings of an International Conference on Dynamic Crack Propagation, Bethlehem. Edited by G.C. Sih, Noordhoff International Publishers, Leyden, 113-129.

Pollock, A.A. (1977). Metals and rocks: AE physics and technology in common and in contrast. *In* Proceedings of the First Conference on Acoustic Emission/Microseismic Activity in Geologic Structures and Materials, University Park. Edited by H.R. Hardy and F.W. Leighton, Trans Tech Publications, Clausthal-Zellerfeld, 383-403.

Rao, M.V.M.S. (1988). A study of acoustic emission activity in granites during stress cycling experiments. *Journal of Acoustic Emission*. **7** (3): S29-S34.

Read, R.S. (1994). Interpreting Excavation-Induced Displacements Around a Tunnel in Highly Stressed Granite. Ph.D. thesis, Department of Civil and Geological Engineering, University of Manitoba, Winnipeg, 328pp.

Reyes, O. and Einstein, H.H. (1991). Failure mechanisms of fractured rock - A fracture coalescence model. *In* Proceedings of the Seventh International Congress on Rock Mechanics, Aachen. Edited by W. Wittke, A.A. Balkema, Rotterdam, 333-340.

Rossmanith, H.P. (1983). Modelling of fracture process zones and singularity dominated zones. *Engineering Fracture Mechanics*. **17** (6): 509-525.

Sack, R.A. (1946). Extension of Griffith's theory of rupture to three dimensions. *The Proceedings of the Physical Society*. **58** (6): 729-736.

Sammis, C.G. and Ashby, M.F. (1986). The failure of brittle porous solids under compressive stress states. *Acta Metallurgica*. **34** (3): 511-526.

Sayers, C.M. and van Munster, J.G. (1991). Microcrack-induced seismic anisotropy of sedimentary rocks. *Journal of Geophysical Research*. **96** (B10): 16529-16533.

Scholz, C.H. (1968). Microfracturing and the inelastic deformation of rock in compression. *Journal of Geophysical Research*. **73** (4): 1417-1432.

Schulson, E.M. (1990). The brittle compressive fracture of ice. *Acta Metallurgica et Materialia*. **38** (10): 1963-1976.

Schulson, E.M., Kuehn, G.A., Jones, D.A. and Fifolt, D.A. (1991). The growth of wing cracks and the brittle compressive failure of ice. *Acta Metallurgica et Materialia*. **39** (11): 2651-2655.

Shah, K.R. and Labuz, J.F. (1995). Damage mechanisms in stressed rock from acoustic emission. *Journal of Geophysical Research*. **100** (B8): 15527-15539.

Shakoor, A. and Bonelli, R.E. (1991). Relationship between petrographic characteristics, engineering index properties, and mechanical properties of selected sandstones. *Bulletin of the Association of Engineering Geologists*. **XXVIII** (1): 55-71.

Shao, J.F. and Khazraei, R. (1994). Wellbore stability analysis in brittle rocks with continuous damage model. *In* Eurock '94: Rock Mechanics in Petroleum Engineering, Delft. A.A. Balkema, Rotterdam, 215-222.

Shao, J.F., Khazraei, R. and Henry, J.P. (1996). Application of continuum damage theory to borehole failure modelling in brittle rock. *In* Proceedings of the 2nd North American Rock Mechanics Symposium: Rock Mechanics Tools and Techniques, Montreal. Edited by M. Aubertin, F. Hassani and H. Mitri, A.A. Balkema, Rotterdam, 1721-1728.

Shen, B. and Stephansson, O. (1993). Numerical analysis of mixed mode I and mode II fracture propagation. *International Journal of Rock Mechanics and Mining Sciences & Geomechanical Abstracts*. **30** (7): 861-867.

Simmons, G.R. and Baumgartner, P. (1994). The Disposal of Canada's Nuclear Fuel Waste: Engineering for a Disposal Facility. Atomic Energy of Canada Limited, Research Report AECL-10715, Whiteshell Laboratories, Pinawa, 384pp.

Simmons, G. and Richter, D. (1976). Microcracks in rocks. *In* The Physics and Chemistry of Minerals and Rocks. Edited by R.G.J. Strens, John Wiley & Sons, Toronto, 105-137.

Singh, U.K. and Digby, P.J. (1989). A continuum damage model for simulation of the progressive failure of brittle rocks. *International Journal of Solids and Structures*. **25** (6): 647-663.

Sondergeld, C.H. and Estey, L.H. (1981). Acoustic emission study of microfracturing during the cyclic loading of Westerly granite. *Journal of Geophysical Research*. **86** (B4): 2915-2924.

Sondergeld, C.H., Granryd, L.A. and Estey, L.H. (1984). Acoustic emissions during compression testing of rock. *In* Proceedings of the Third Conference on Acoustic Emission/Microseismic Activity in Geologic Structures and Materials, University Park. Edited by H.R. Hardy and F.W. Leighton, Trans Tech Publications, Clausthal-Zellerfeld, 131-145.

Spanner, J.C., Brown, A., Hay, D.R., Mustafa, V., Notvest, K. and Pollock, A. (1987). Fundamentals of acoustic emission testing. *In* Nondestructive Testing Handbook: Acoustic Emission Testing. Edited by P. McIntire, American Society for Nondestructive Testing, United States, 11-61.

Sprunt, E.S. and Brace, W.F. (1974). Direct observation of microcavities in crystalline rock. *International Journal of Rock Mechanics and Mining Sciences & Geomechanical Abstracts*. **11** (4): 139-150.

Sun, X., Hardy Jr., H.R. and Rao, M.V.M.S. (1991). Acoustic emission monitoring and analysis procedures utilized during deformation studies on geologic materials. *In* Acoustic Emission: Current Practice and Future Directions, STP 1077. Edited by W. Sachse, J. Roget and K. Yamaguchi, American Society for Testing and Materials, Philadelphia, 365-380.

Svab, M. and Lajtai, E.Z. (1981). Microstructural control of crack growth in Lac du Bonnet granite. *In* Proceedings of the Fifth Canadian Fracture Conference: Fracture Problems and Solutions in the Energy Industry, Winnipeg. Edited by L.A. Simpson, Pergamon Press, New York, 219-228.

Swanson, P.L. and Spetzler, H. (1984). Ultrasonic probing of the fracture process zone in rock using surface waves. *In* Proceedings of the 25th U.S. Symposium on Rock Mechanics, Evanston. Edited by C.H. Dowding and M.M. Singh, A.A. Balkema, Rotterdam, 67-76.

Talebi, S. and Young, R.P. (1992). Microseismic monitoring in highly stressed granite: Relation between shaft-wall cracking and *in situ* stress. *International Journal of Rock Mechanics and Mining Sciences & Geomechanical Abstracts*. **29** (1): 25-34.

Tapponnier, P. and Brace, W.F. (1976). Development of stress-induced microcracks in Westerly granite. *International Journal of Rock Mechanics and Mining Sciences & Geomechanical Abstracts*. **13** (4): 103-112.

Tomecka-Suchon, S. and Rummel, F. (1992). Fracture-induced resistivity changes in granite. *International Journal of Rock Mechanics and Mining Sciences & Geomechanical Abstracts*. **29** (6): 583-587.

Vallejo, L.E. (1987). The brittle and ductile behavior of a material containing a crack under mixed-mode loading. *In* Proceedings of the 28th U.S. Symposium on Rock Mechanics, Tuscon. Edited by I.W. Farmer, J.J.K. Daemen, C.S. Desai, C.E. Glass and S.P. Neuman, A.A. Balkema, Rotterdam, 383-390.

Walsh, J.B. (1984). Precursors to rock failure observed in laboratory experiments. *In* Proceedings of the 1st International Congress on Rockbursts and Seismicity in Mines, Johannesburg. Edited by N.C. Gay and E.H. Wainwright, South African Institute of Mining and Metallurgy, Johannesburg, 269-275.

Watters, R.J. and Chuck, D.M. (1989). Acoustic emission signatures of Yucca Mountain tuffs, Nevada. *In* Rock Mechanics as a Guide for Efficient Utilization of Natural Resources: Proceedings of the 30th U.S. Symposium on Rock Mechanics, Morgantown. Edited by A.W. Khair, A.A. Balkema, Rotterdam, 245-252.

Wawersik, W.R. and Brace, W.F. (1971). Post-failure behavior of a granite and diabase. *Rock Mechanics*. **3** (2): 5-85.

Wawersik, W.R. and Fairhurst, C. (1970). A study of brittle rock fracture in laboratory compression experiments. *International Journal of Rock Mechanics and Mining Sciences & Geomechanical Abstracts*. **7** (5): 561-575.

Wen, Z., Gorelik, M., Chudnovsky, A., Dudley II, J.W. and Shlyapobersky, J. (1996). Observation and characterization of crack growth in porous rocks. *In* Proceedings of the 2nd North American Rock Mechanics Symposium: Rock Mechanics Tools and Techniques, Montreal. Edited by M. Aubertin, F. Hassani and H. Mitri, A.A. Balkema, Rotterdam, 1269-1277.

Wong, R.H.C., Chau, K.T. and Wang, P. (1996). Microcracking and grain size effect in Yeun Long marbles. *International Journal of Rock Mechanics and Mining Sciences & Geomechanical Abstracts*. **33** (5): 479-485.

Xiao, Q., Xiaomin, Y. and Wentao, L. (1991). Micro-experimental study on damage behaviour and investigation of damage variable in rock. *In* Rock Mechanics as a Multidisciplinary Science: Proceedings of the 32nd U.S. Symposium, Norman. Edited by J.-C. Roegiers, A.A. Balkema, Rotterdam, 675-682.

Yanagidani, T., Ehara, S., Nishizawa, O., Kusunose, K. and Terada, M. (1985). Localization of dilatancy in Ohshima granite under constant uniaxial stress. *Journal of Geophysical Research*. **90** (B8): 6840-6858.

Zhao, Y., Huang, J. and Wang, R. (1993). Real-time SEM observations of the microfracturing process in rock during a compression test. *International Journal of Rock Mechanics and Mining Sciences & Geomechanical Abstracts*. **30** (6): 643-652.

Appendix I

Strain Gauge Analysis for Individual Test Results

Laboratory Test Notes :

The following notes refer to the laboratory test results presented in this and the following appendix (i.e. Appendix I and II). With the exception of those tests noted below, samples were not loaded to failure but to a point just beyond the crack damage threshold.

Samples Loaded to Failure :

130-1-3	240-3-2	Potash 1
130-1-9	420-1-2	Potash 2
130-1-10	420-1-3	Potash 3
130-1-12	420-2-1	Potash 4
130-1-13	420-3-4	Potash 5
130-1-14	420-3-5	SS 1
130-1-22	420-4-3	SS 2
130-1-23	420-4-4	SS 3
130-1-24	420-4-5	SS 4
130-1-25		SS 5
130-1-26		
130-1-27		
130-1-28		
130-2-2		

Test stopped prematurely before crack damage threshold was reached :

130-1-6
130-1-11
240-2-4

Other :

130-1-1	Test stopped following failure of large feldspar phenocryst near surface of sample.
240-2-4	Sample failed along pre-existing discontinuity\fracture.
Potash 2	Sudden increase in load between 6 and 12 MPa due to testing error.
SS 1	Bedding parallel to core axis (samples SS 2 to SS 4 are orientated with the bedding perpendicular to the core axis).

Axial Stiffness Curves - AECL 130m Pink Granite

130-1-1

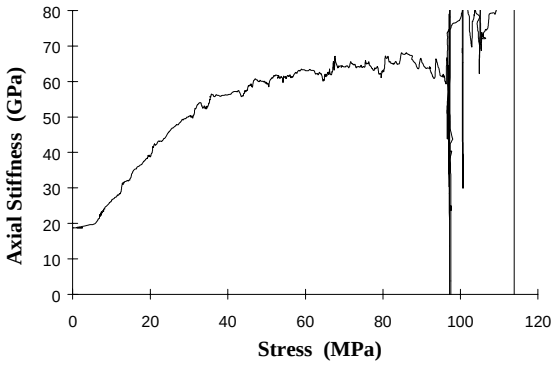

130-1-2

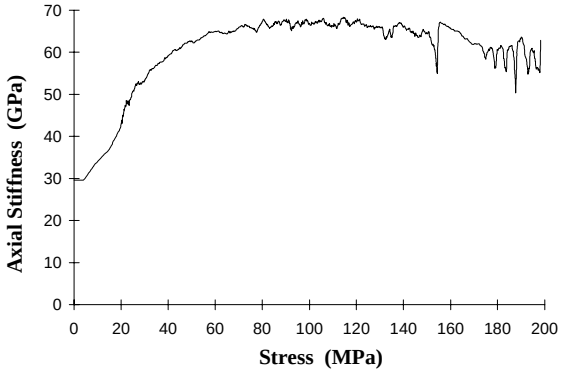

130-1-3

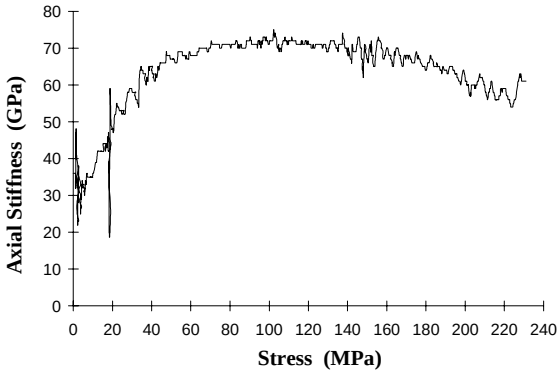

130-1-4

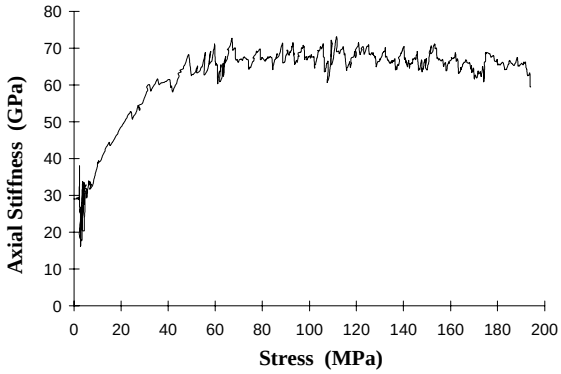

130-1-5

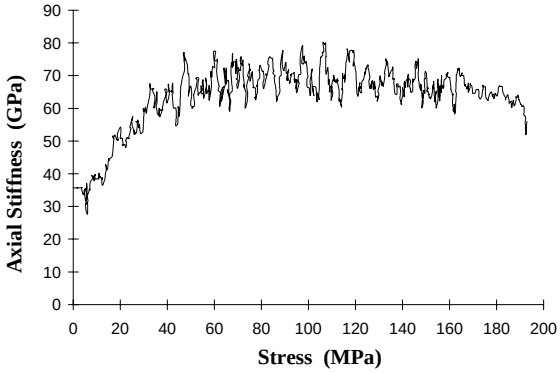

130-1-6

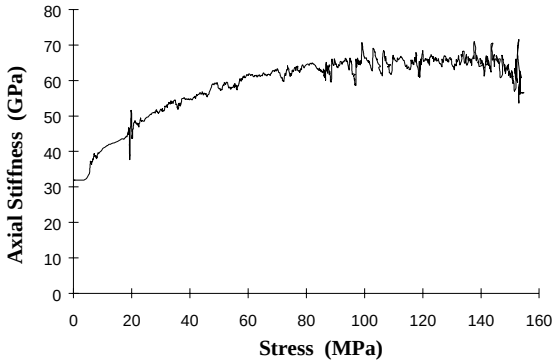

Axial Stiffness Curves - AECL 130m Pink Granite

130-1-7

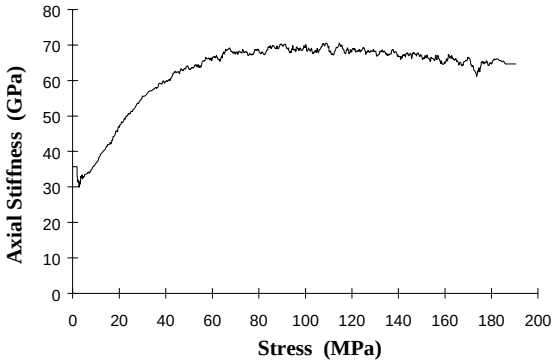

130-1-8

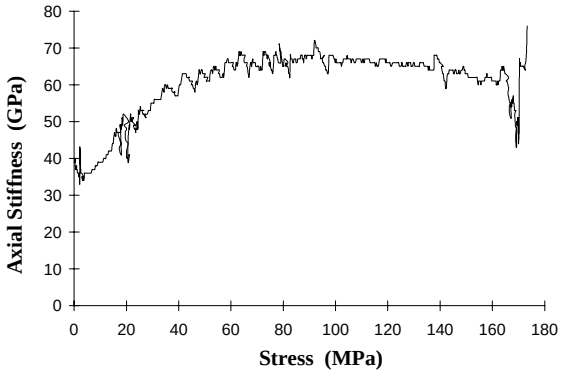

130-1-9

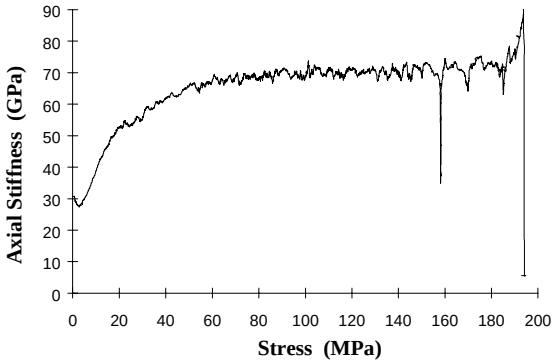

130-1-10

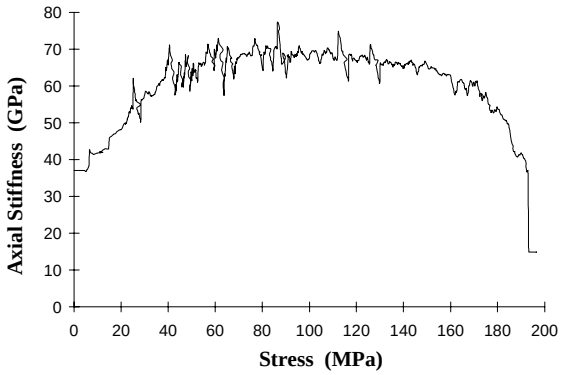

130-1-11

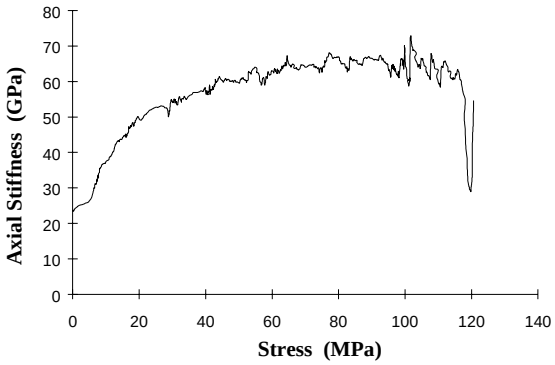

130-1-12

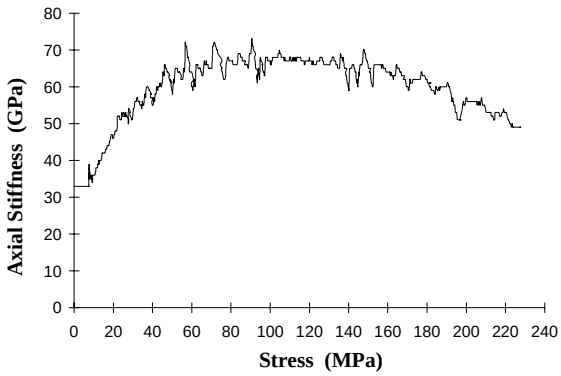

Axial Stiffness Curves - AECL 130m Pink Granite

130-1-13

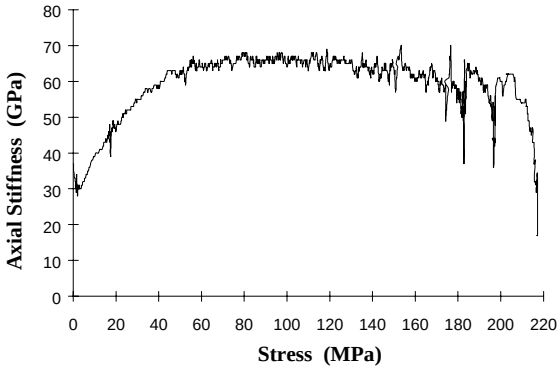

130-1-14

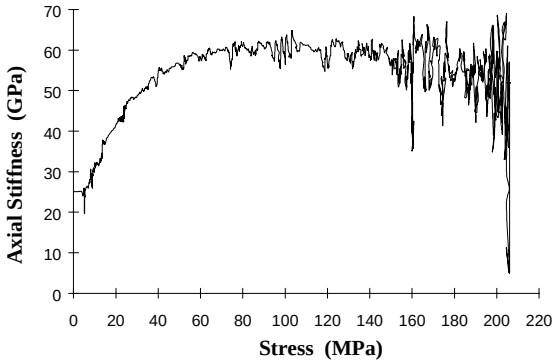

130-1-15

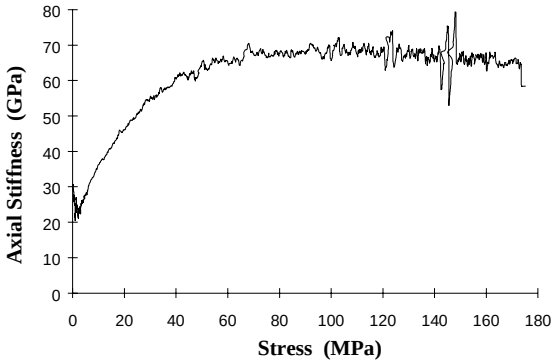

130-1-16

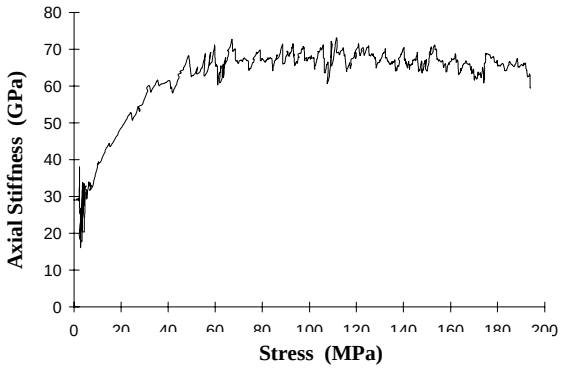

130-1-17

Cyclic loading test.

130-1-18

Cyclic loading test.

Axial Stiffness Curves - AECL 130m Pink Granite

130-1-19

Cyclic loading test.

130-1-20

Sample not tested.

130-1-21

Sample not tested.

130-1-22

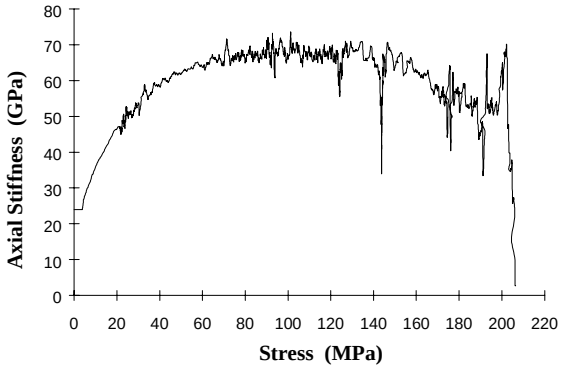

130-1-23

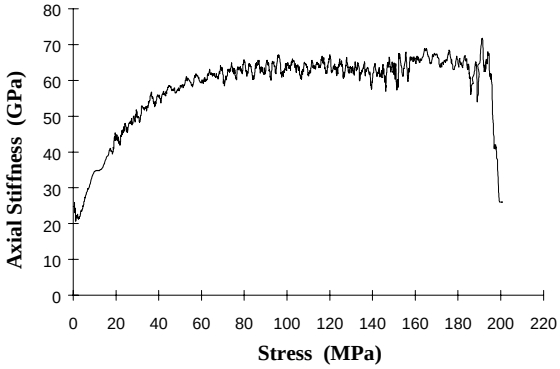

130-1-24

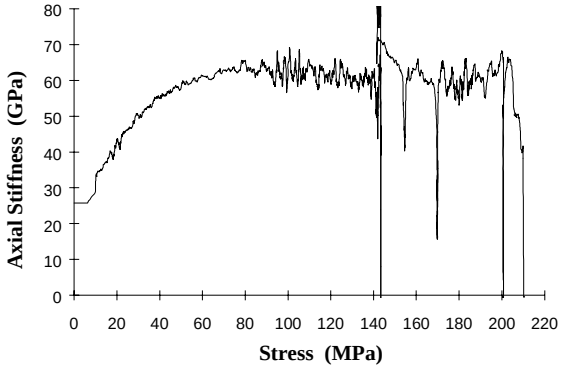

Axial Stiffness Curves - AECL 130m Pink Granite

130-1-25

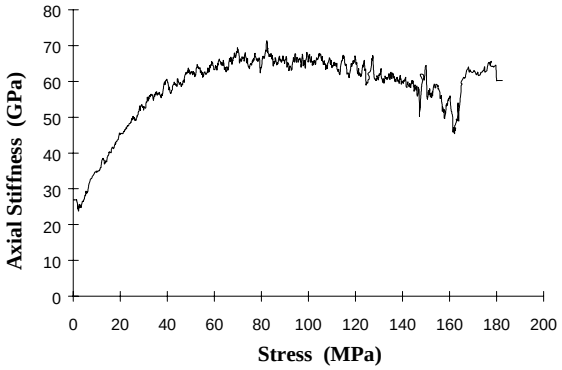

130-1-26

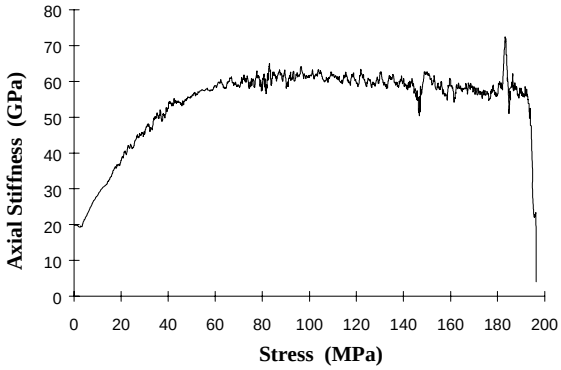

130-1-27

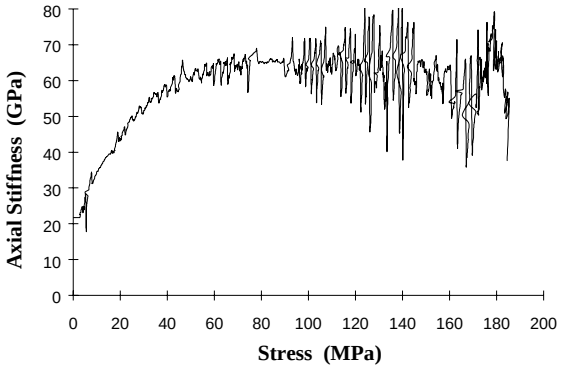

130-1-28

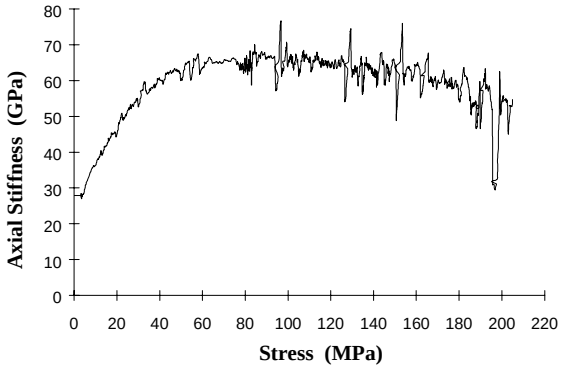

130-2-2

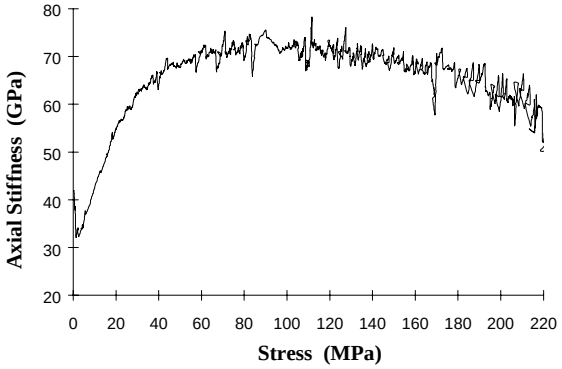

130-2-4

Cyclic loading test.

Axial Stiffness Curves - AECL 240m Grey Granite

240-1-1

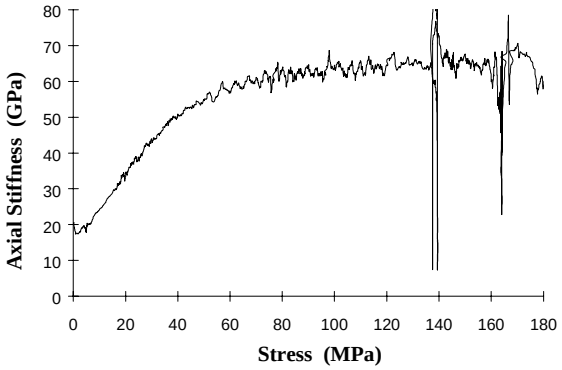

240-1-2

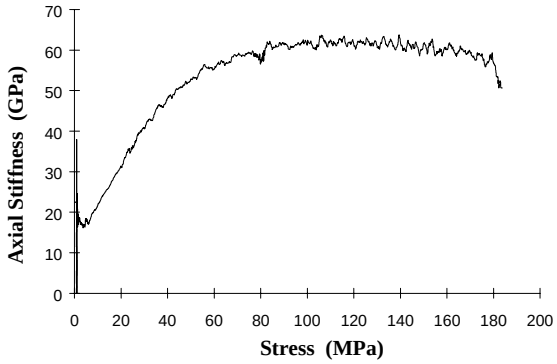

240-1-3

Sample not tested.

240-1-4

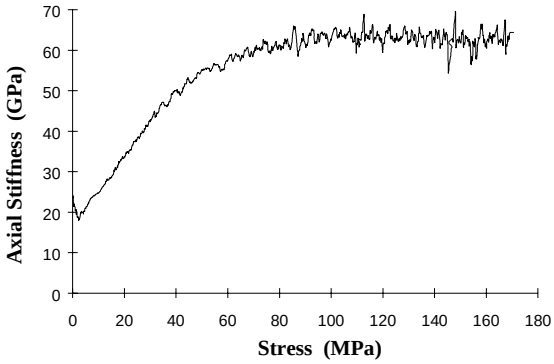

240-1-5

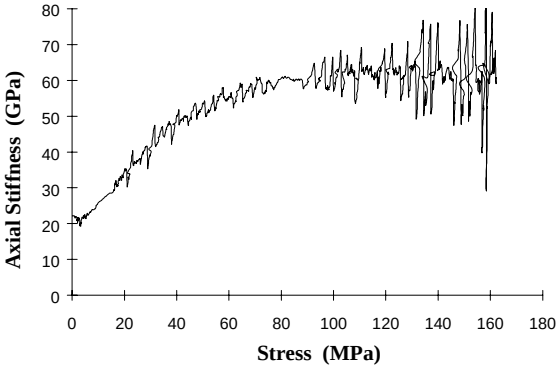

240-1-6

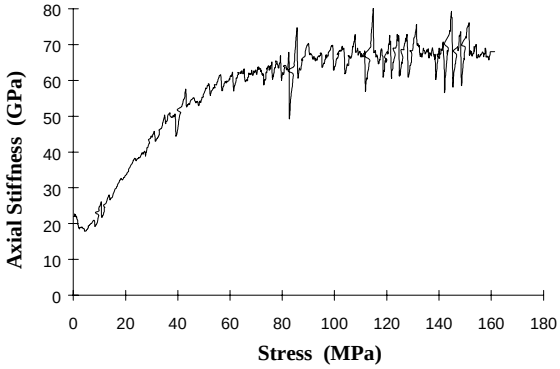

Axial Stiffness Curves - AECL 240m Granodiorite

240-2-1

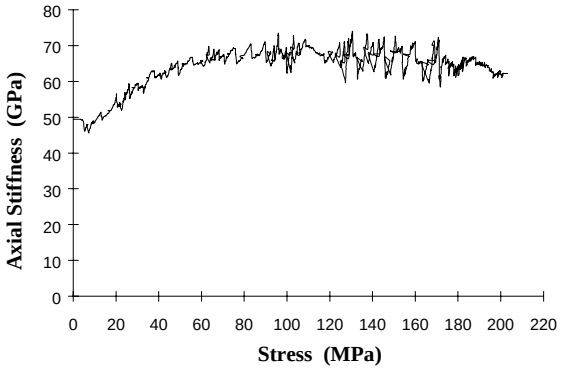

240-2-2

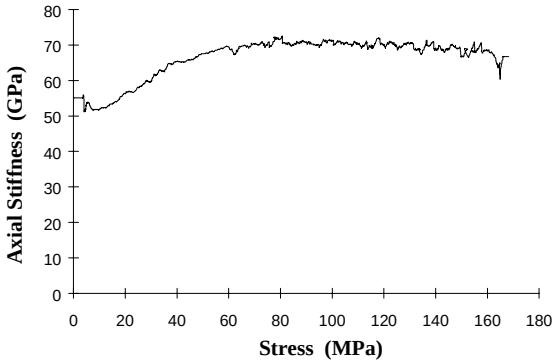

240-2-3

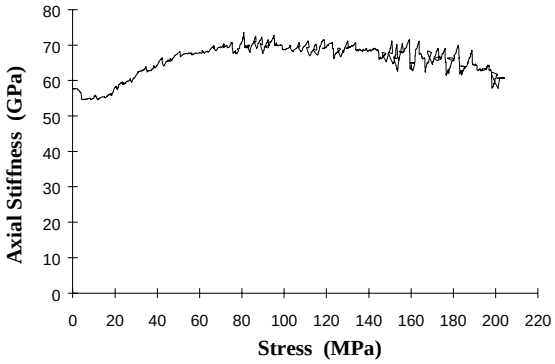

240-2-4

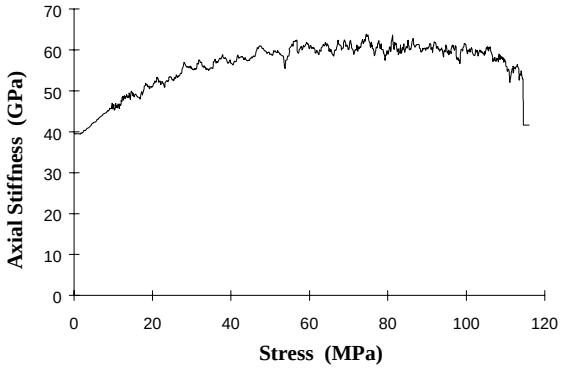

240-2-5

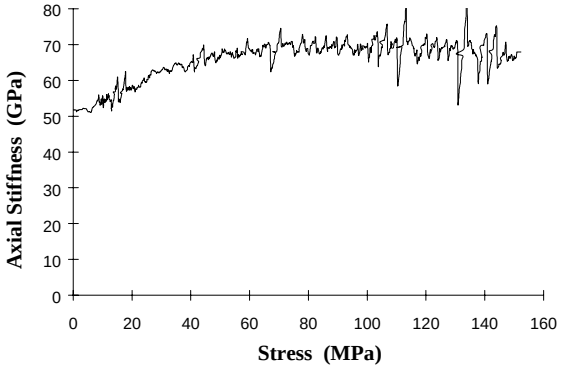

Axial Stiffness Curves - AECL 240m Pegmatite

240-3-1

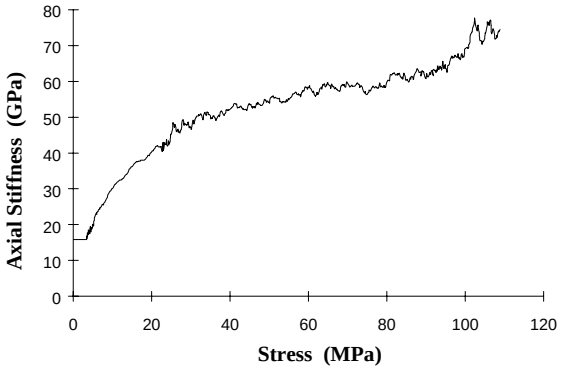

240-3-2

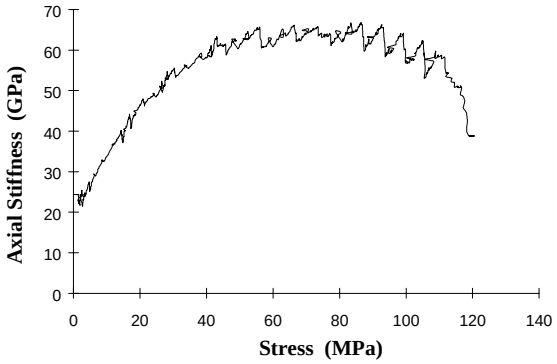

240-3-3

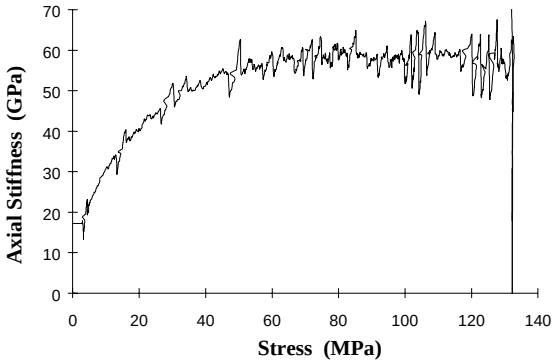

240-3-4

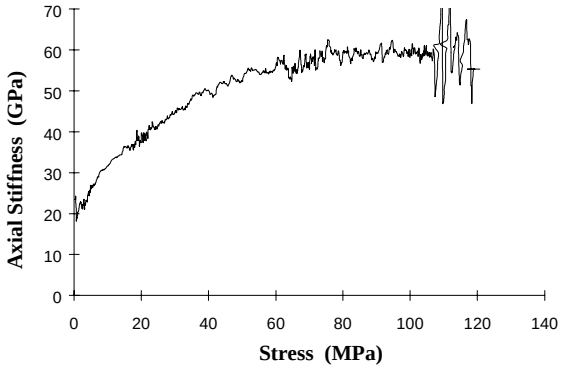

240-3-5

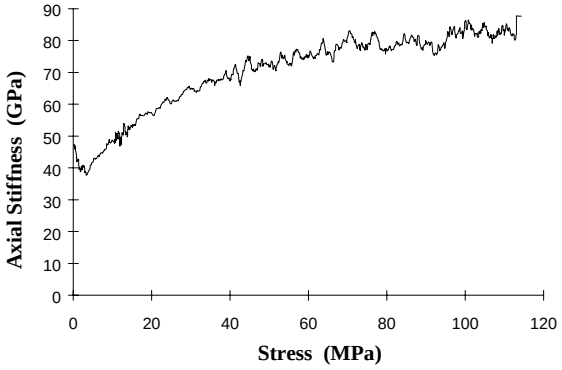

Axial Stiffness Curves - AECL 420m Granodiorite

420-1-2

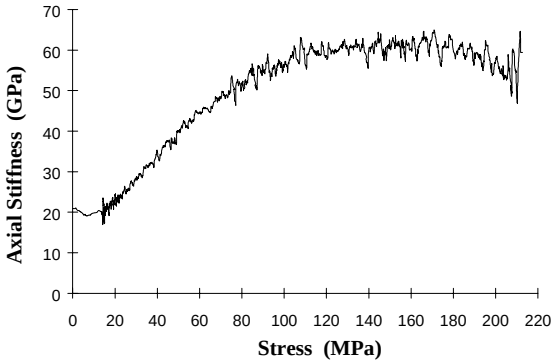

420-1-3

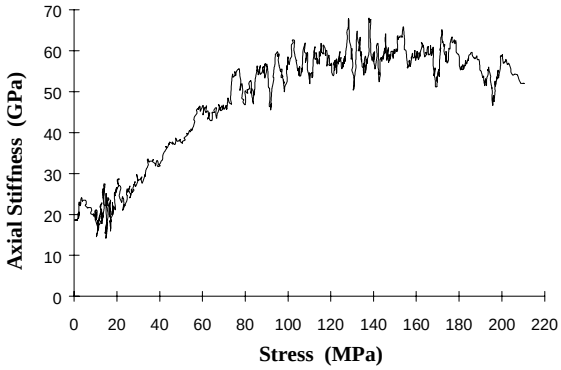

420-2-1

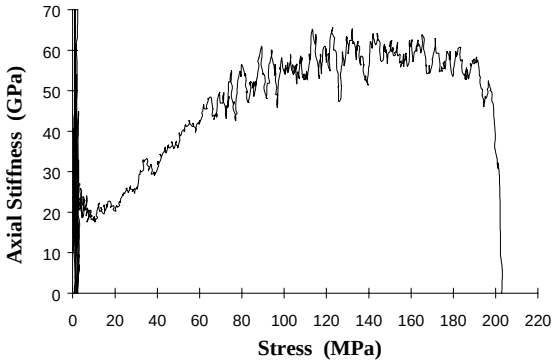

420-3-4

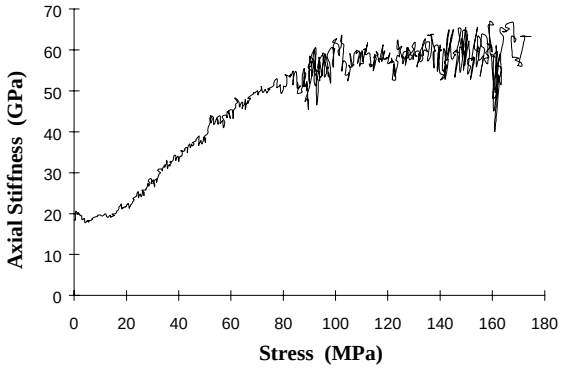

420-3-5

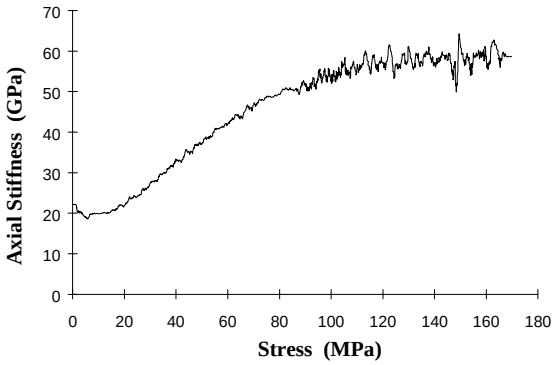

Axial Stiffness Curves - AECL 420m Grey Granite

420-4-1

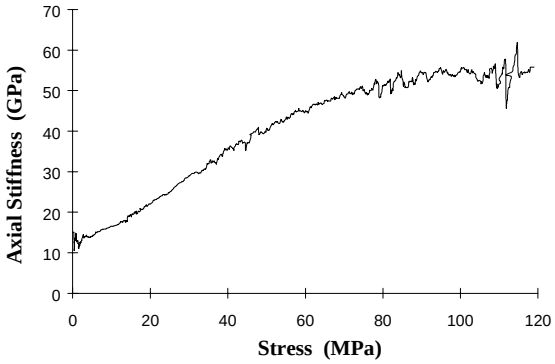

420-4-2

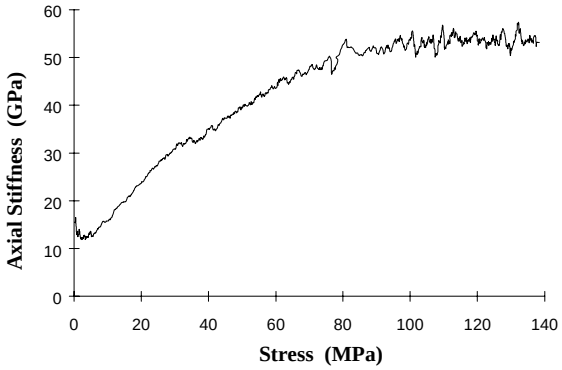

420-4-3

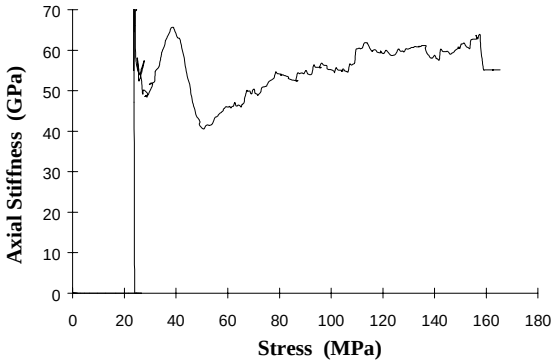

420-4-4

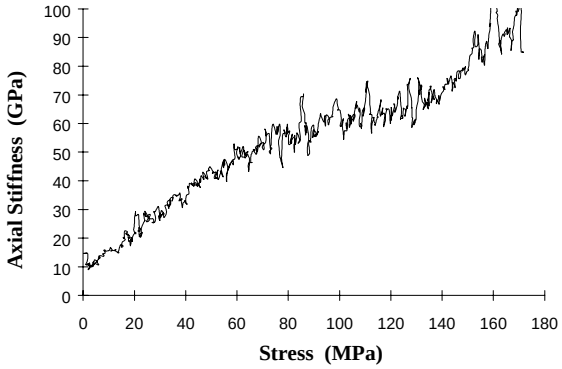

420-4-5

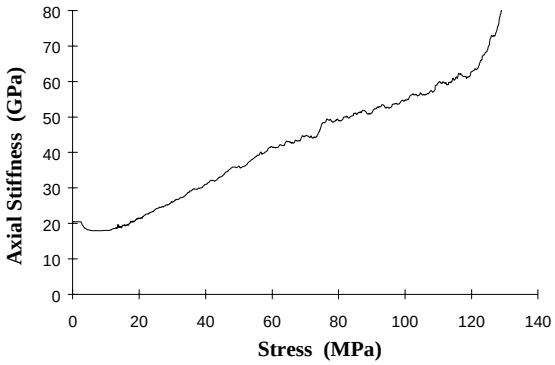

Axial Stiffness Curves - Saskatchewan Potash

Potash 1

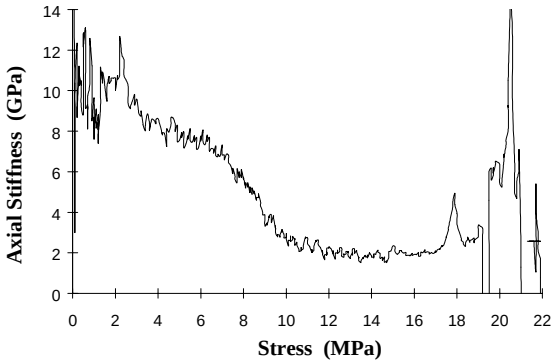

Potash 2

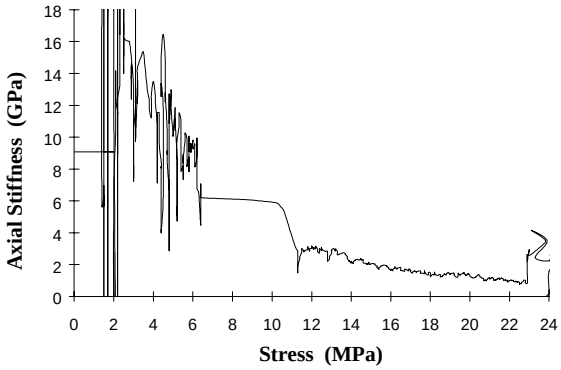

Potash 3

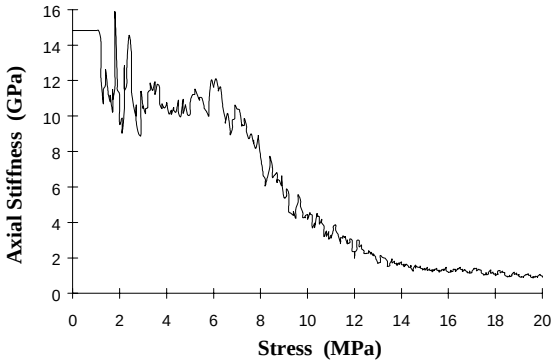

Potash 4

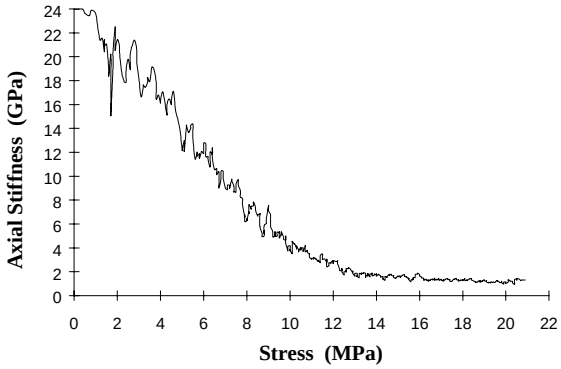

Potash 5

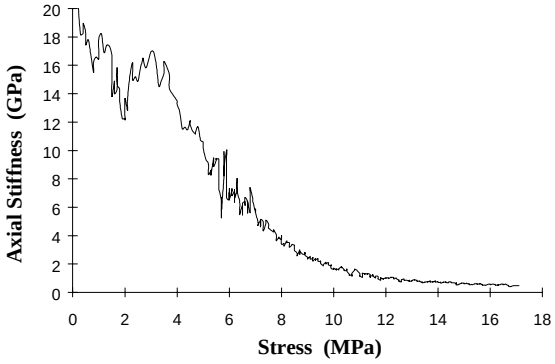

Axial Stiffness Curves - Berea Sandstone

SS 1

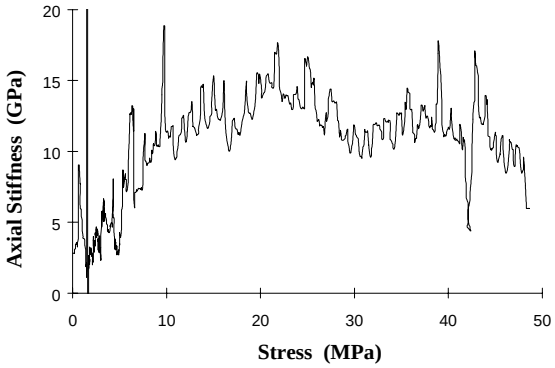

SS 2

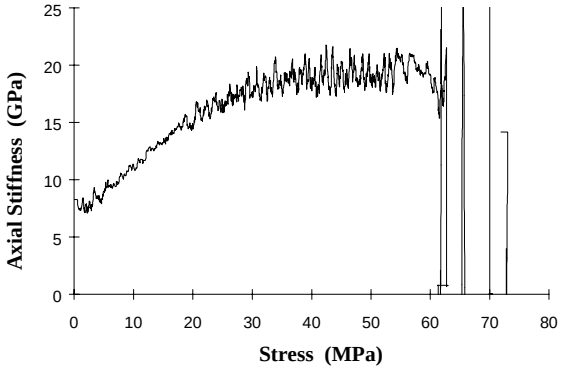

SS 3

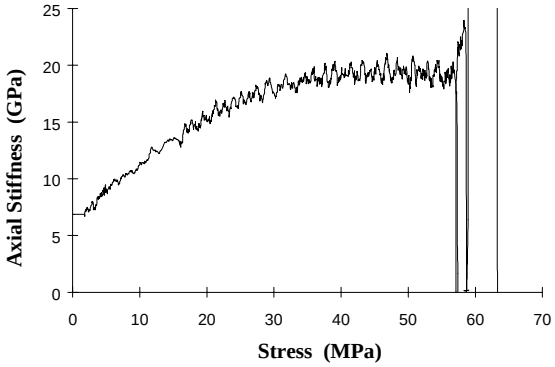

SS 4

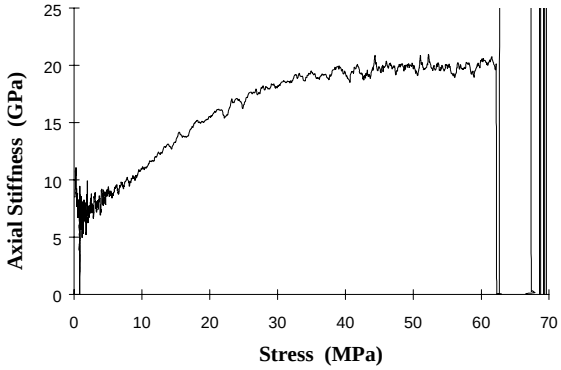

SS 5

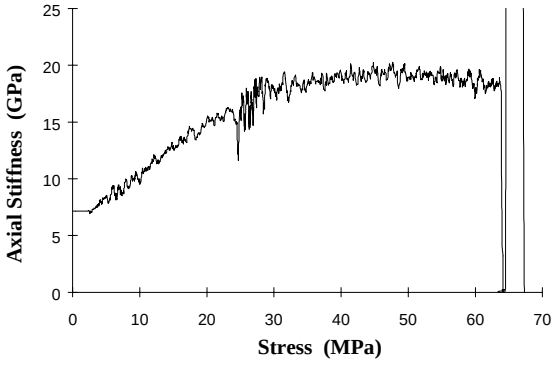

Lateral Stiffness Curves - AECL 130m Pink Granite

130-1-1

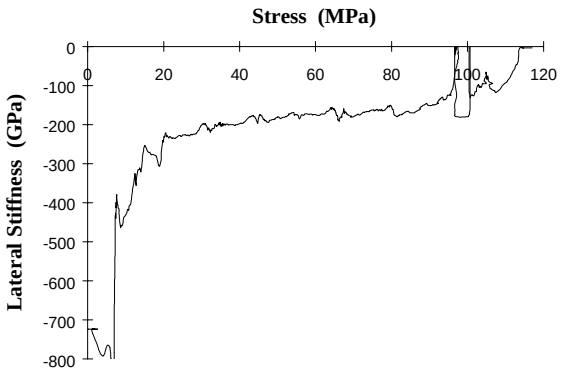

130-1-2

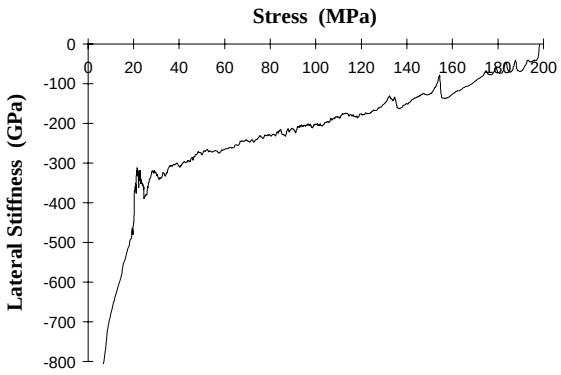

130-1-3

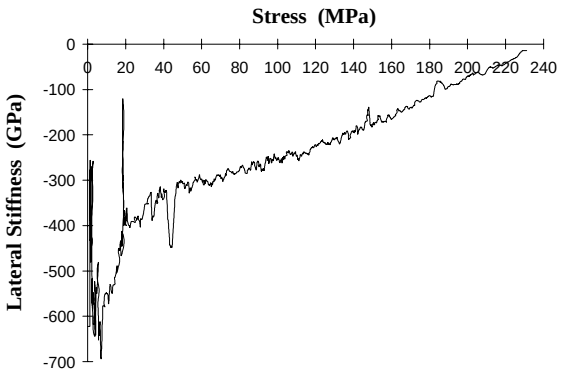

130-1-4

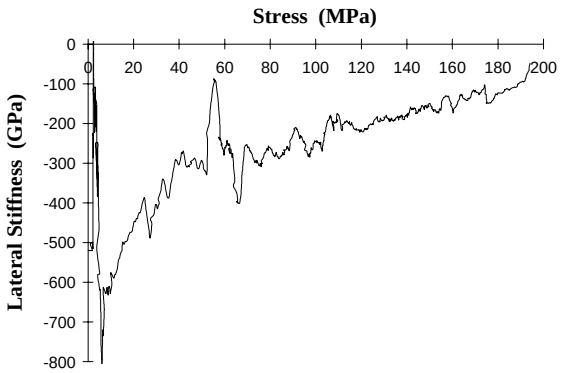

130-1-5

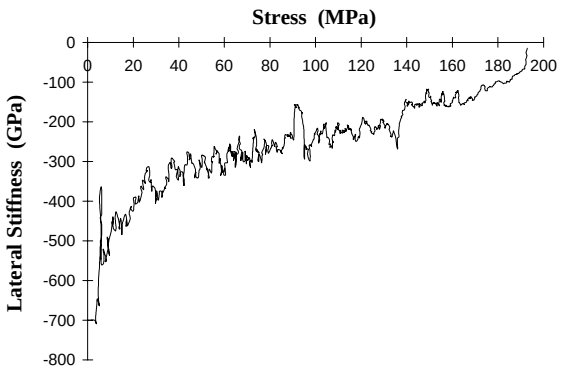

130-1-6

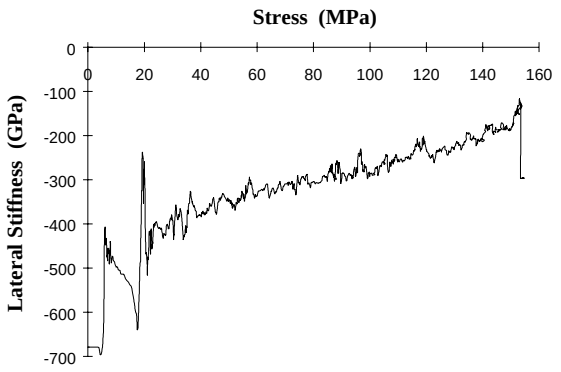

Lateral Stiffness Curves - AECL 130m Pink Granite

130-1-7

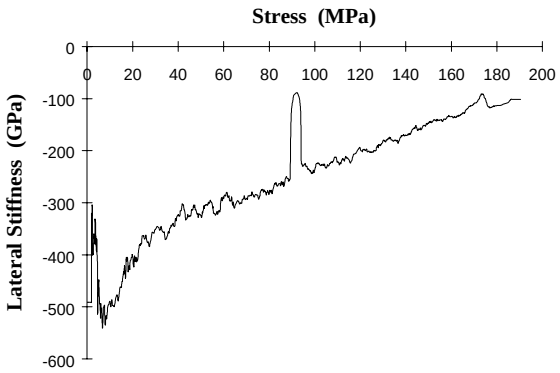

130-1-8

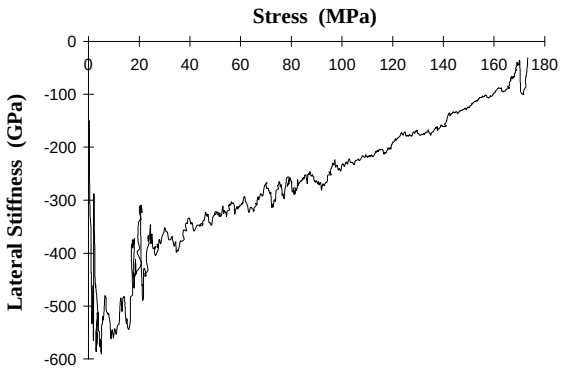

130-1-9

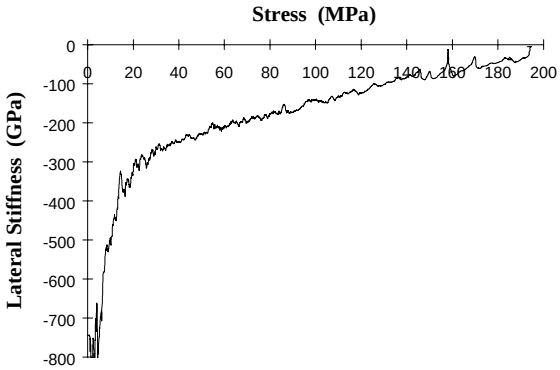

130-1-10

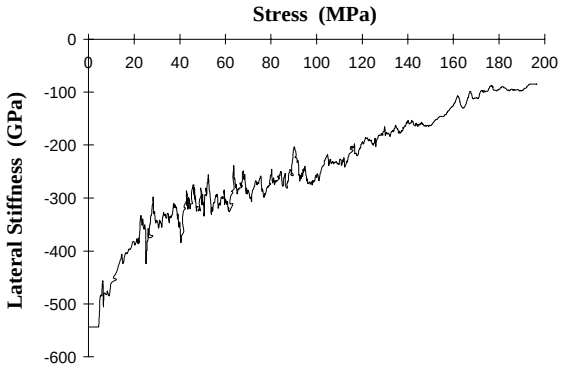

130-1-11

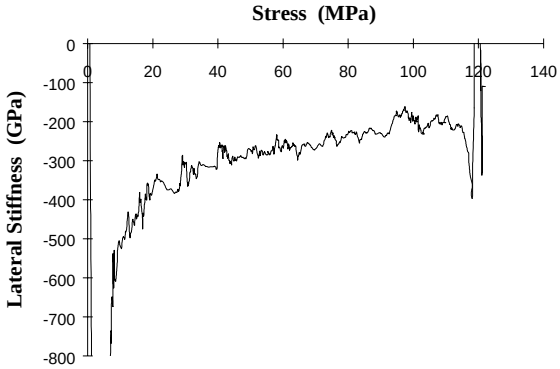

130-1-12

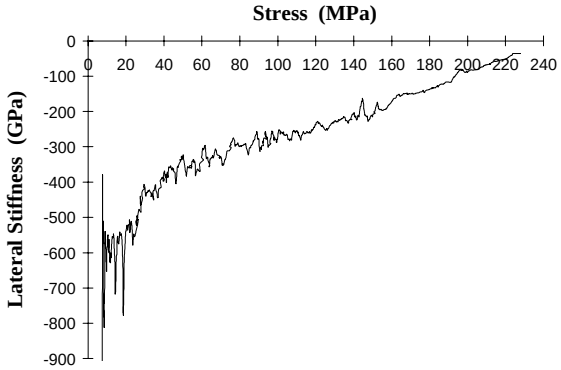

Lateral Stiffness Curves - AECL 130m Pink Granite

130-1-13

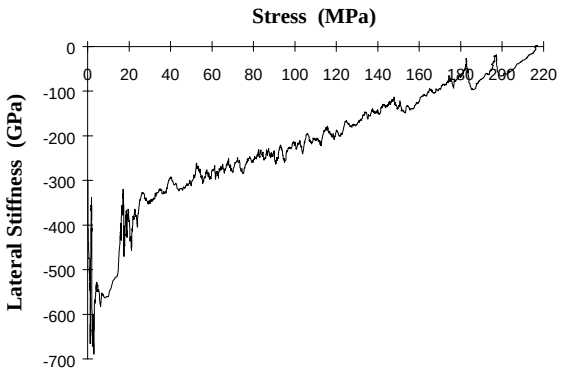

130-1-14

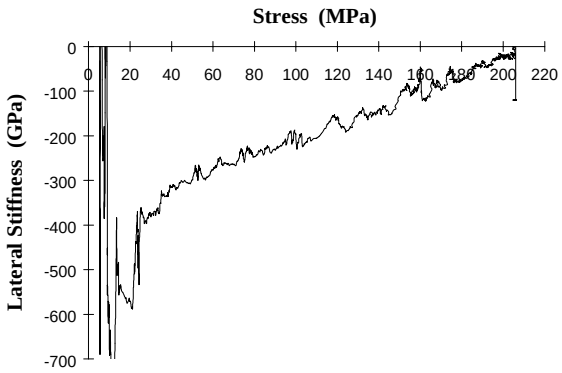

130-1-15

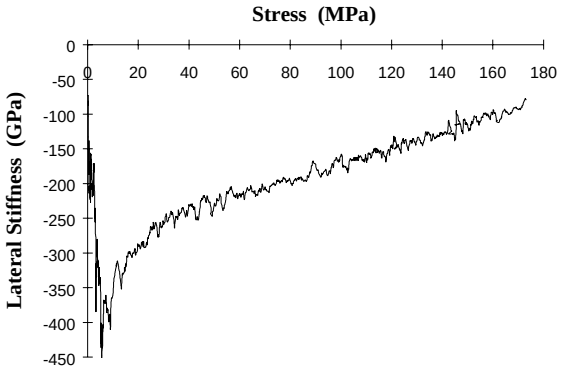

130-1-16

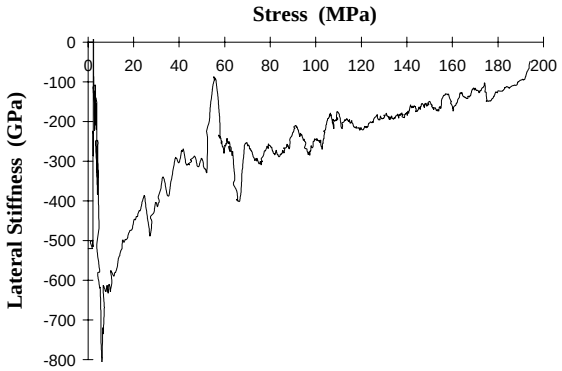

130-1-17

Cyclic loading test.

130-1-18

Cyclic loading test.

Lateral Stiffness Curves - AECL 130m Pink Granite

130-1-19

Cyclic loading test.

130-1-20

Sample not tested.

130-1-21

Sample not tested.

130-1-22

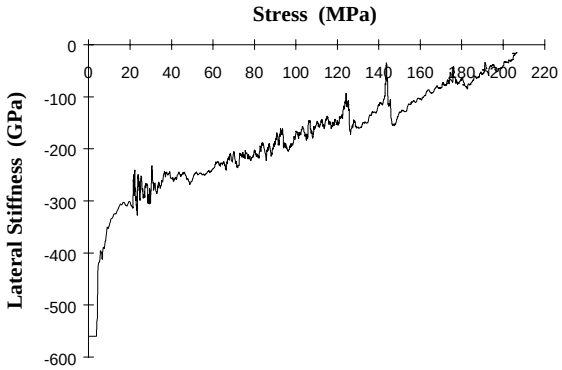

130-1-23

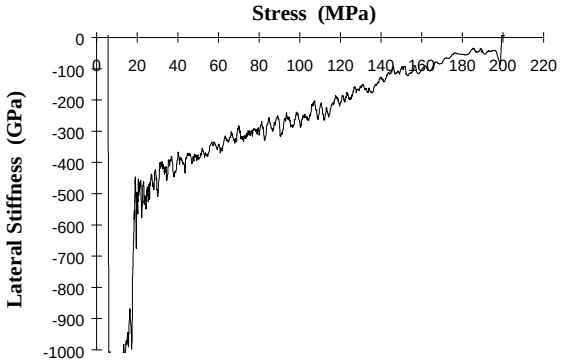

130-1-24

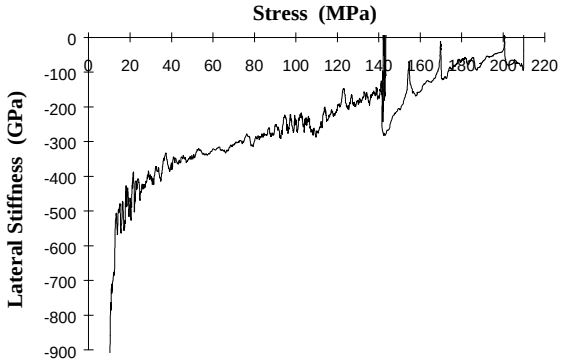

Lateral Stiffness Curves - AECL 130m Pink Granite

130-1-25

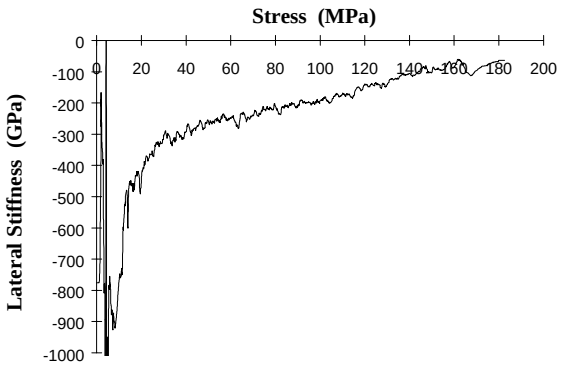

130-1-26

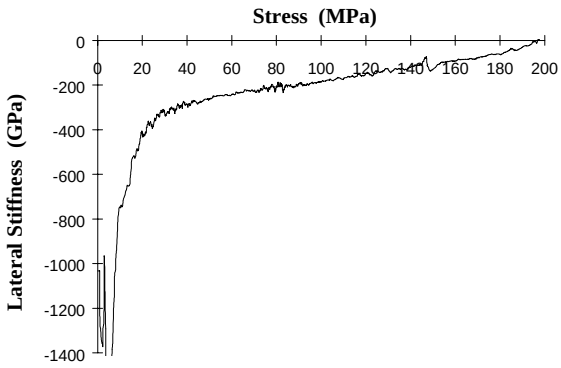

130-1-27

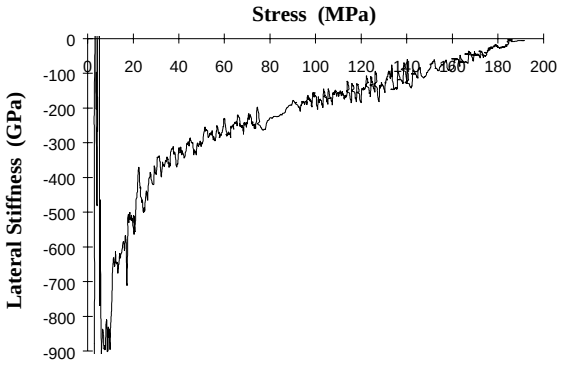

130-1-28

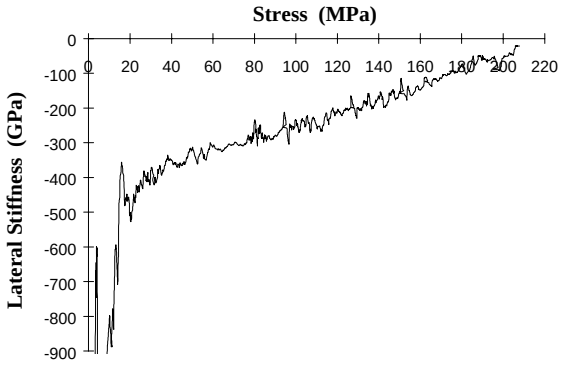

130-2-2

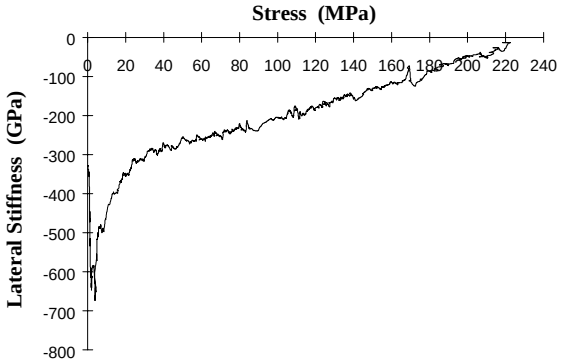

130-2-4

Cyclic loading test.

Lateral Stiffness Curves - AECL 240m Grey Granite

240-1-1

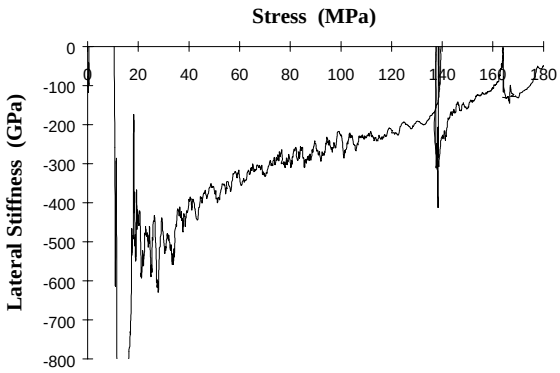

240-1-2

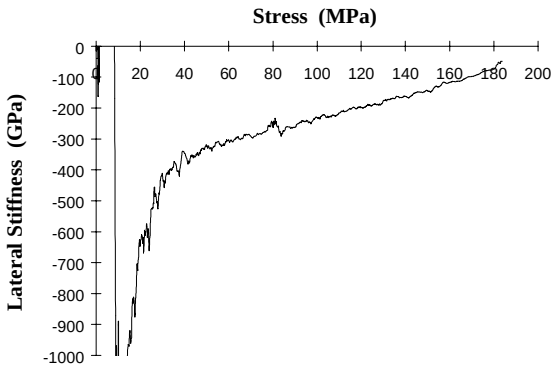

240-1-3

Sample not tested.

240-1-4

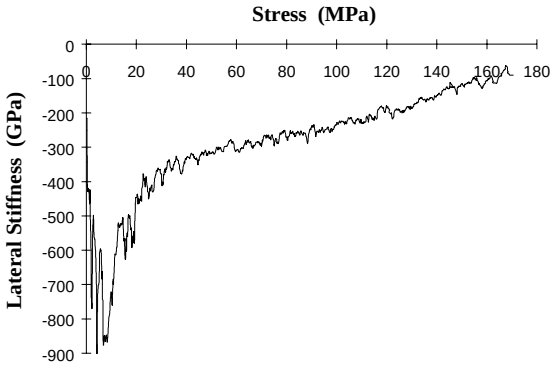

240-1-5

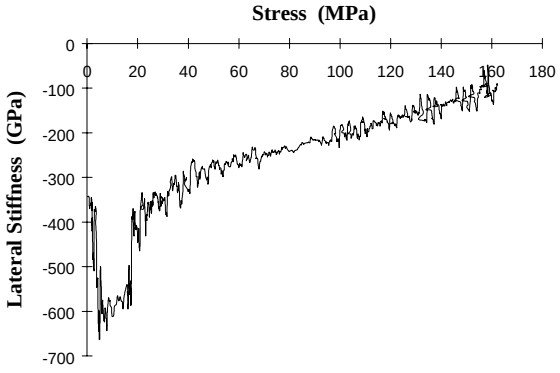

240-1-6

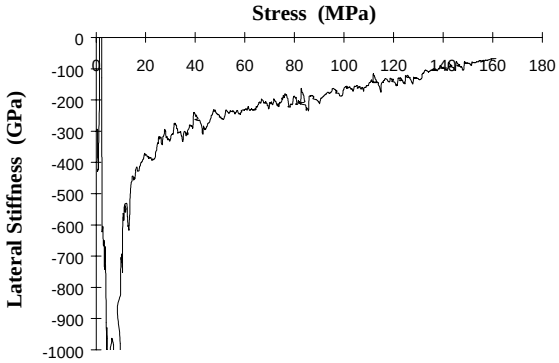

Lateral Stiffness Curves - AECL 240m Granodiorite

240-2-1

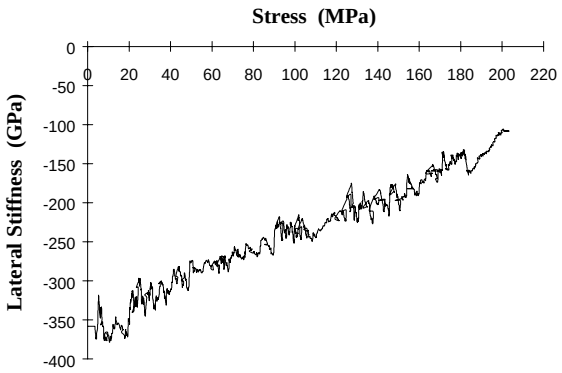

240-2-2

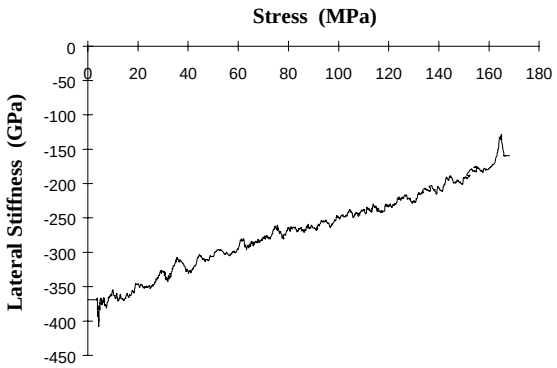

240-2-3

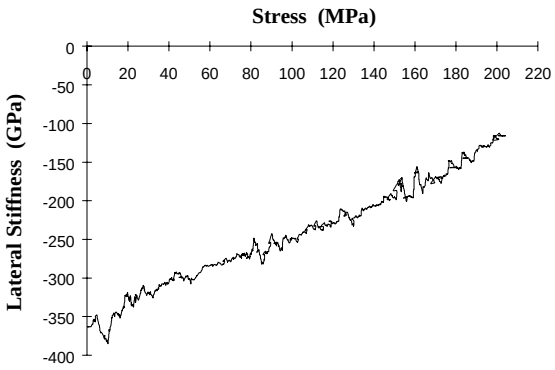

240-2-4

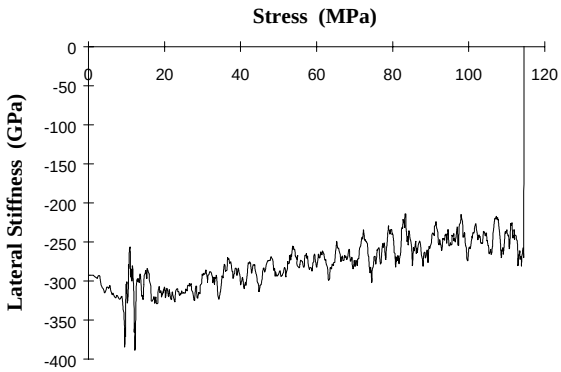

240-2-5

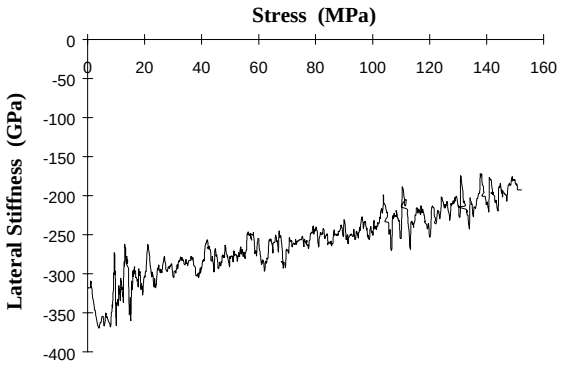

Lateral Stiffness Curves - AECL 240m Pegmatite

240-3-1

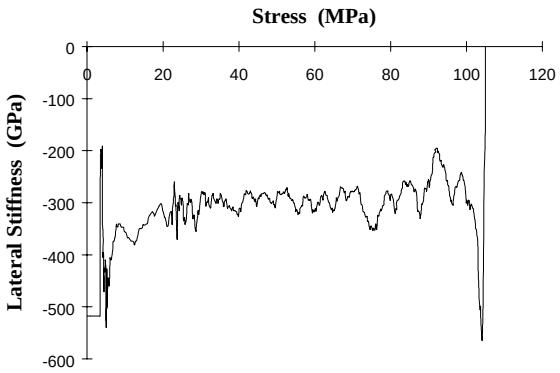

240-3-2

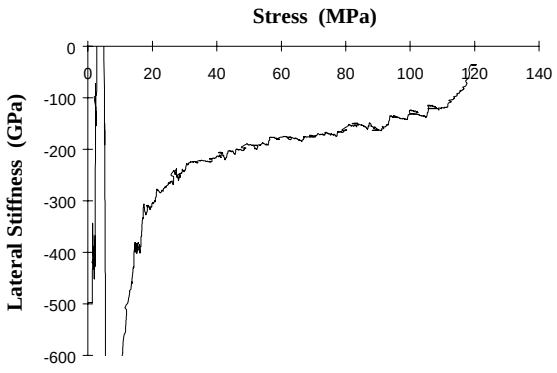

240-3-3

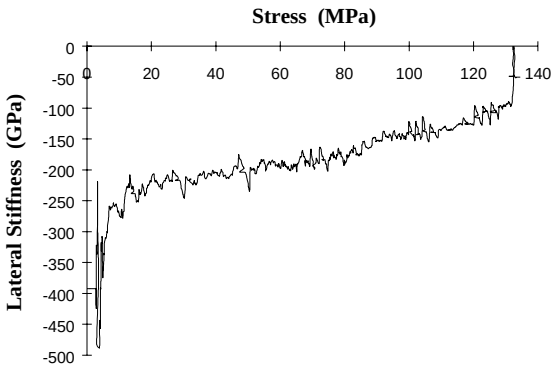

240-3-4

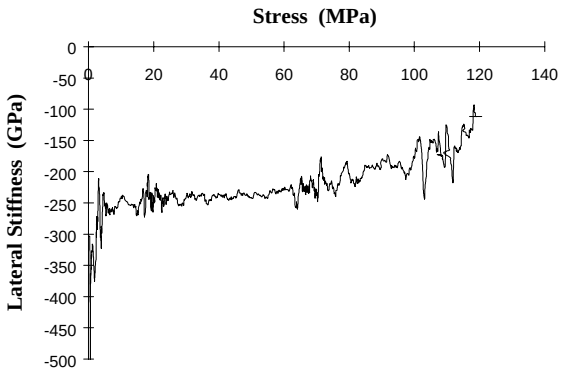

240-3-5

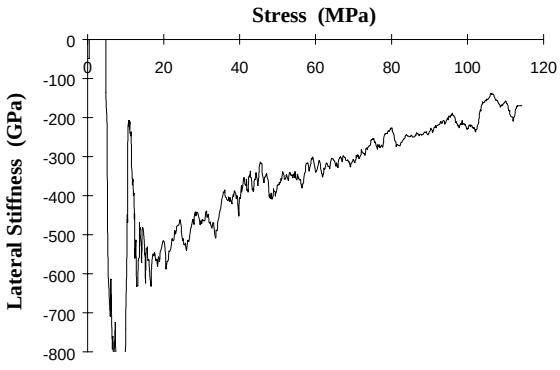

Lateral Stiffness Curves - AECL 420m Granodiorite

420-1-2

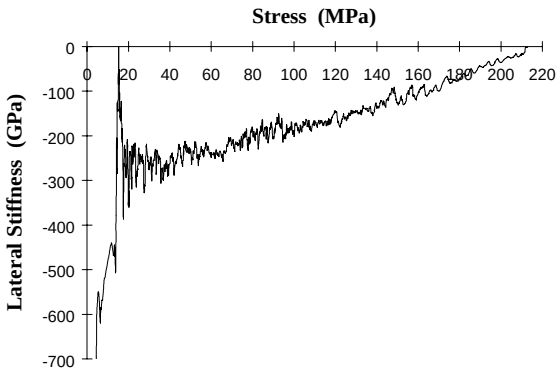

420-1-3

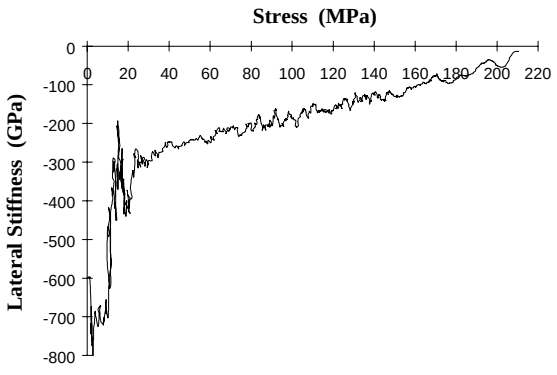

420-2-1

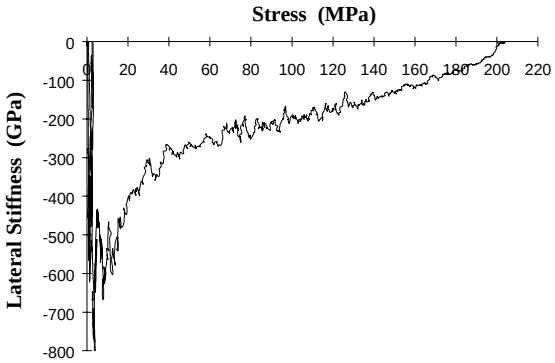

420-3-4

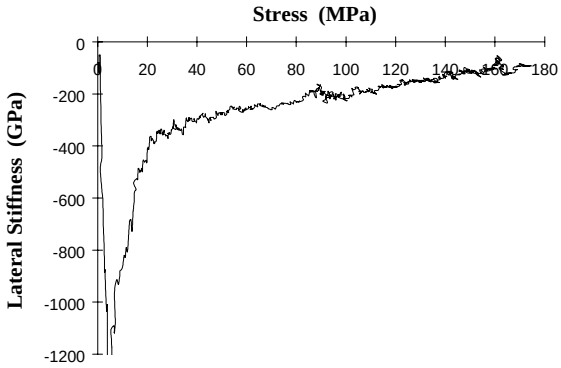

420-3-5

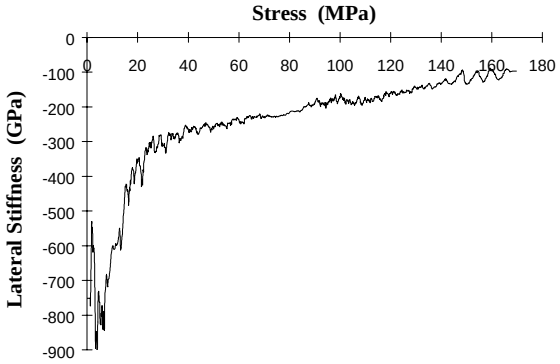

Lateral Stiffness Curves - AECL 420m Grey Granite

420-4-1

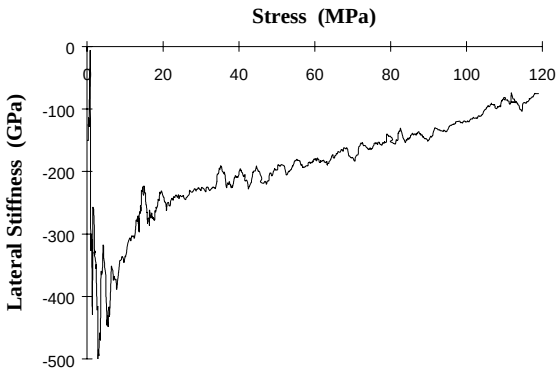

420-4-2

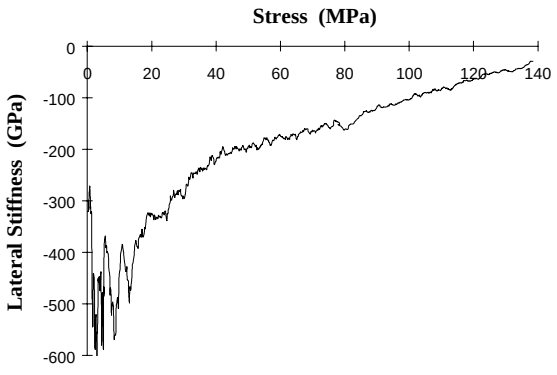

420-4-3

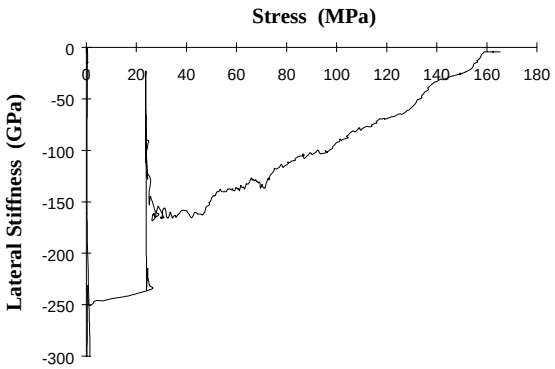

420-4-4

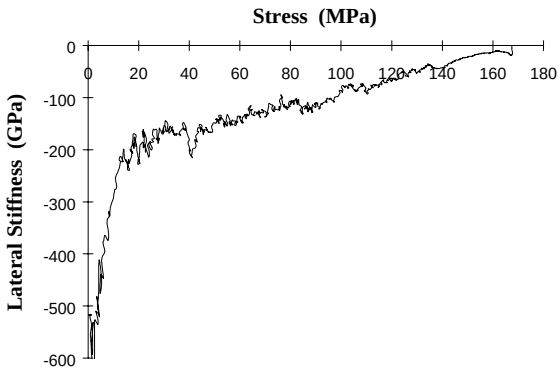

420-4-5

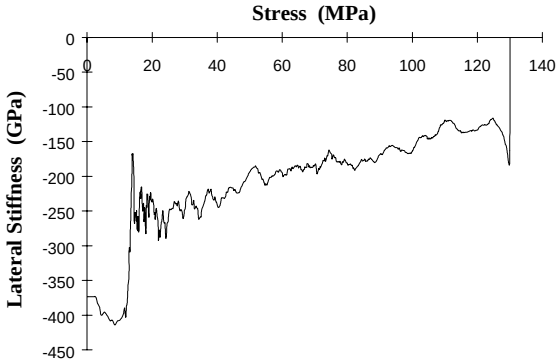

Lateral Stiffness Curves - Saskatchewan Potash

Potash 1

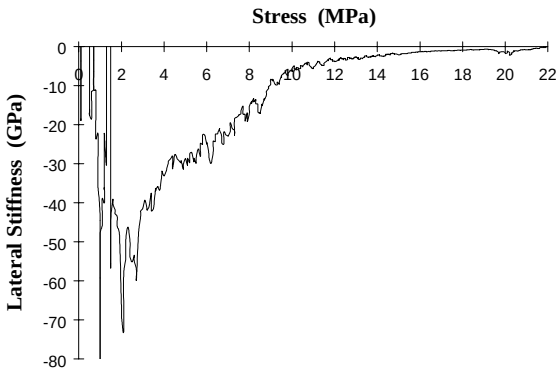

Potash 2

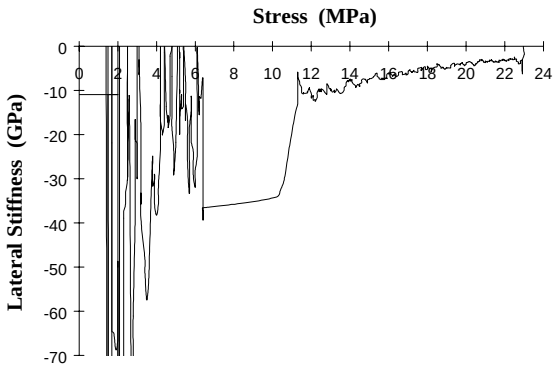

Potash 3

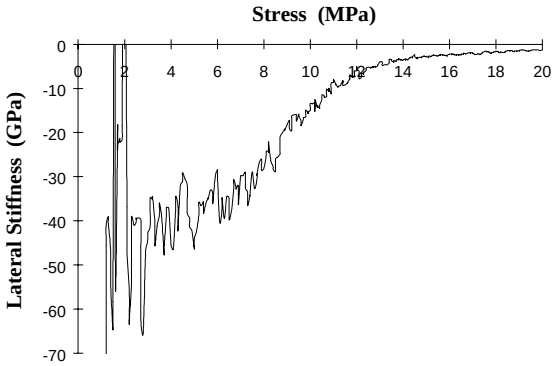

Potash 4

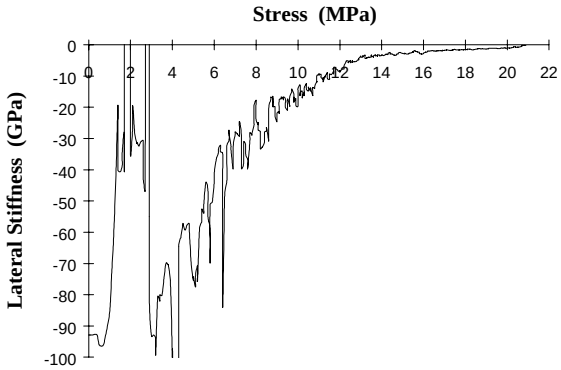

Potash 5

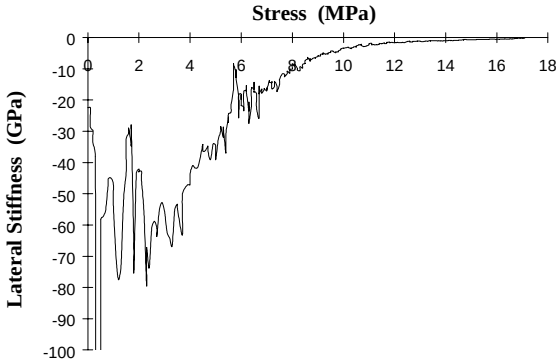

Lateral Stiffness Curves - Berea Sandstone

SS 1

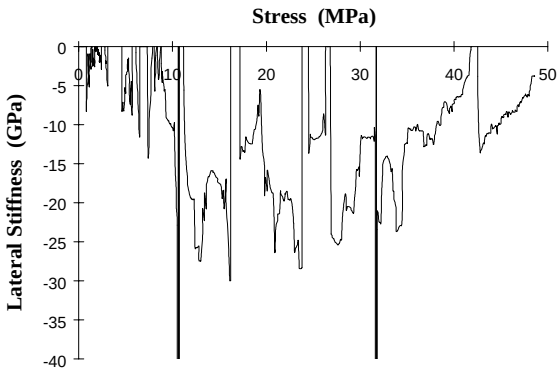

SS 2

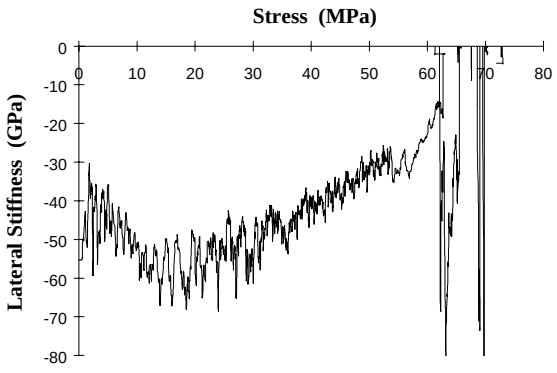

SS 3

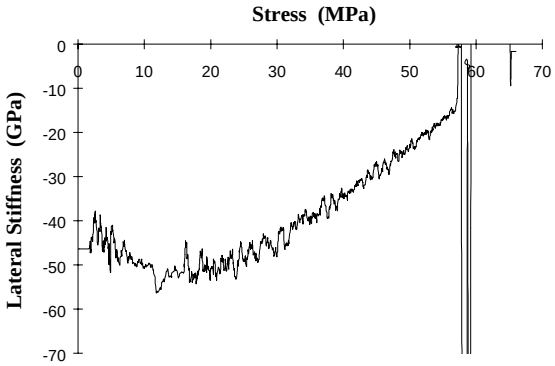

SS 4

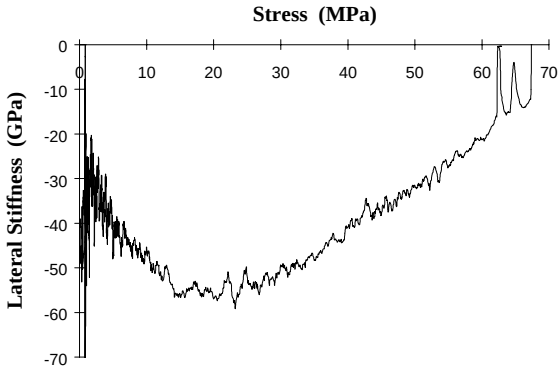

SS 5

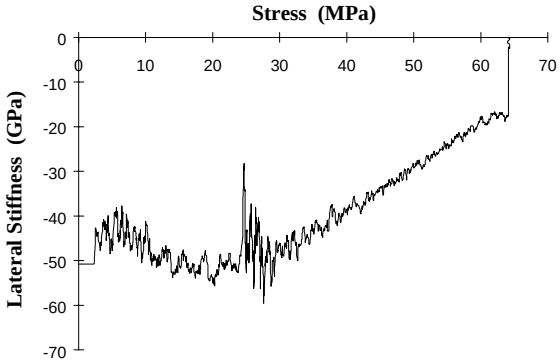

Volumetric Stiffness Curves - AECL 130m Pink Granite

130-1-1

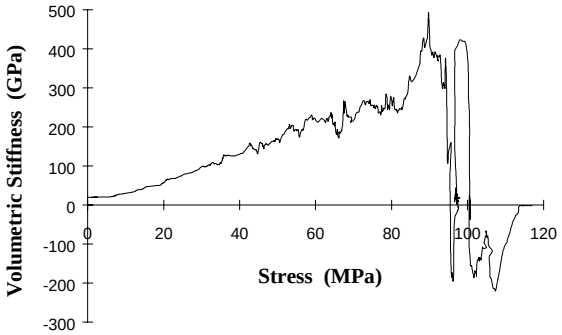

130-1-2

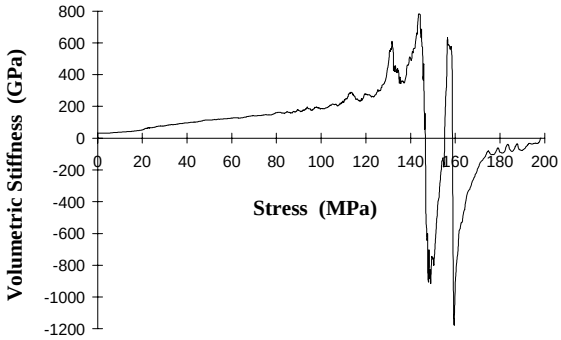

130-1-3

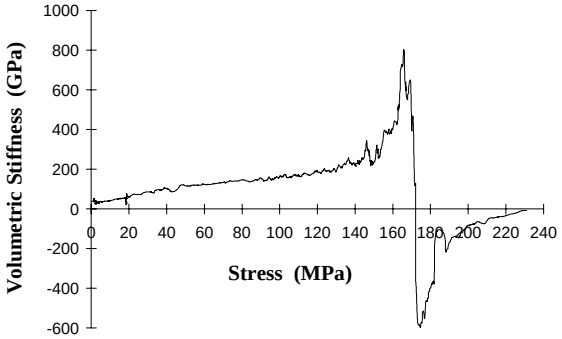

130-1-4

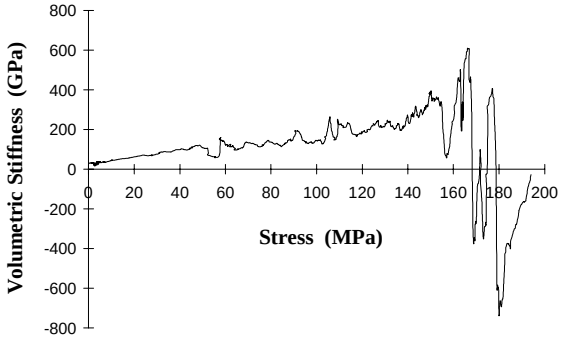

130-1-5

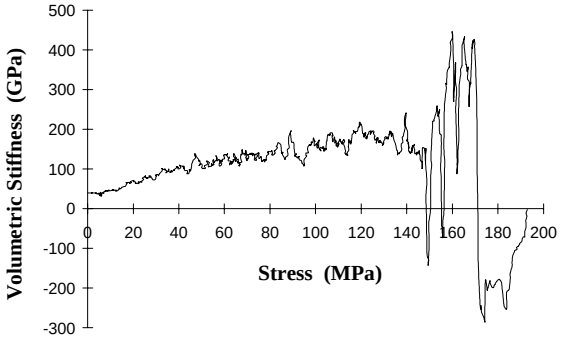

130-1-6

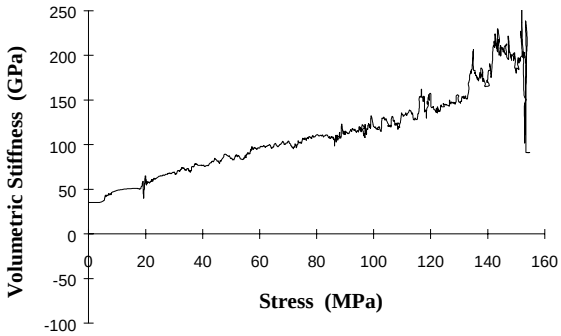

Volumetric Stiffness Curves - AECL 130m Pink Granite

130-1-7

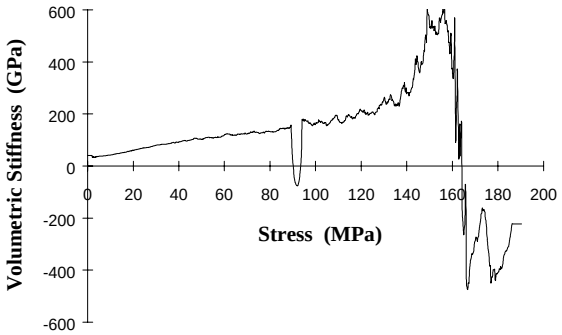

130-1-8

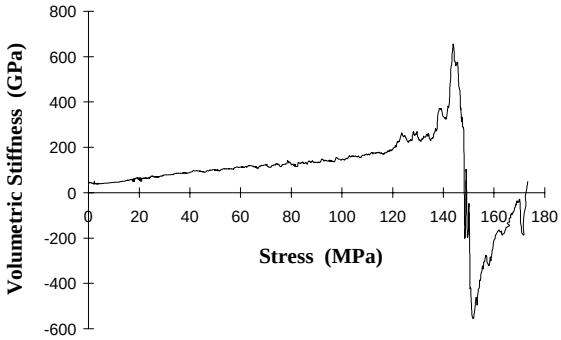

130-1-9

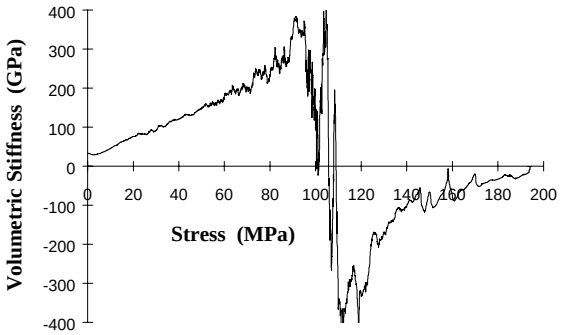

130-1-10

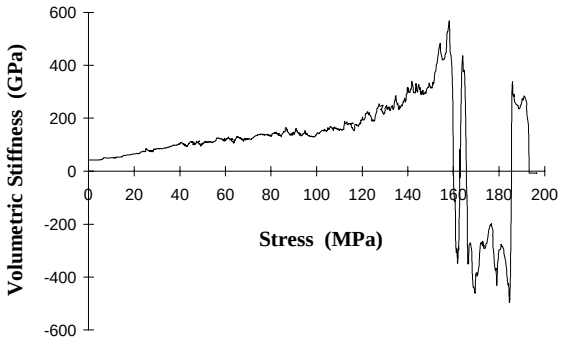

130-1-11

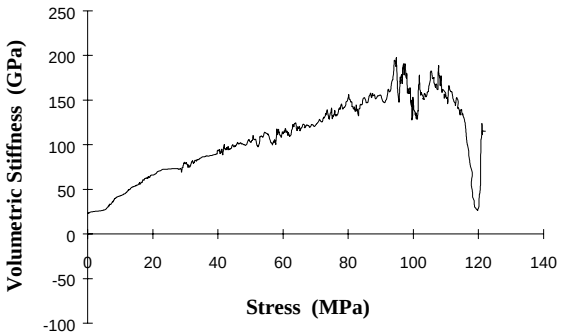

130-1-12

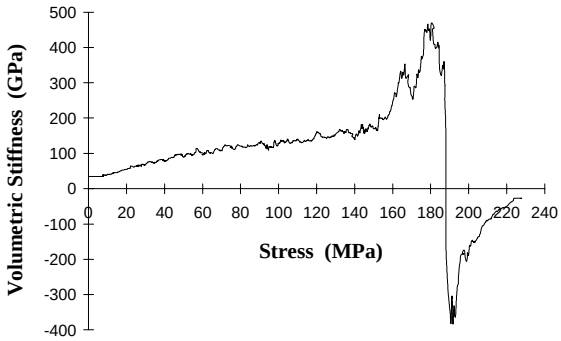

Volumetric Stiffness Curves - AECL 130m Pink Granite

130-1-13

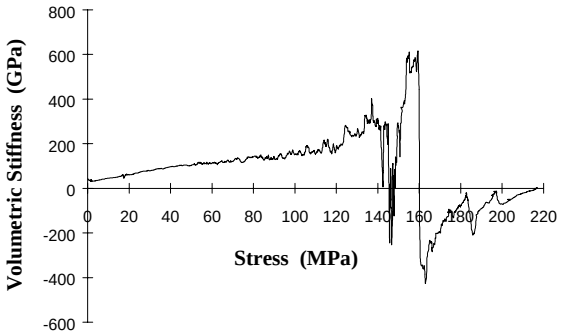

130-1-14

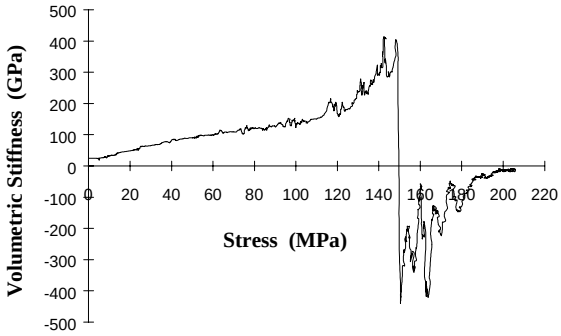

130-1-15

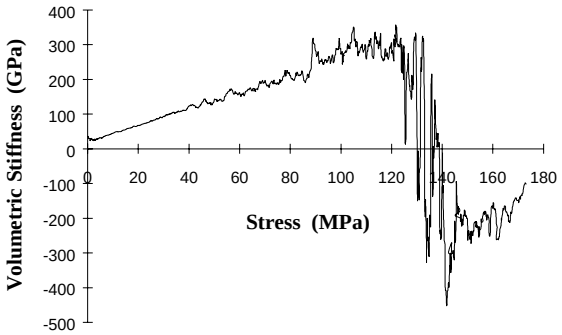

130-1-16

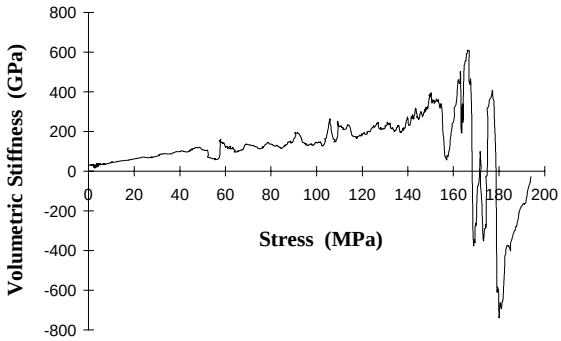

130-1-17

Cyclic loading test.

130-1-18

Cyclic loading test.

Volumetric Stiffness Curves - AECL 130m Pink Granite

130-1-19

Cyclic loading test.

130-1-20

Sample not tested.

130-1-21

Sample not tested.

130-1-22

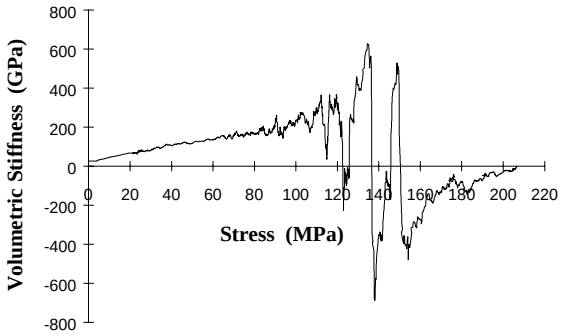

130-1-23

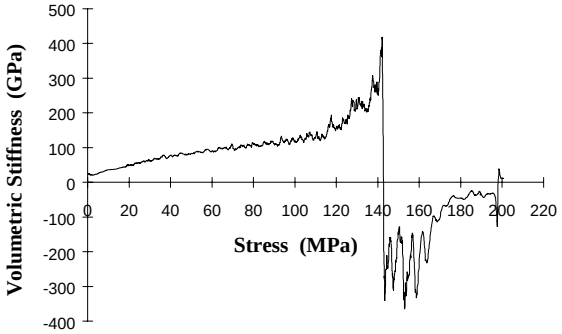

130-1-24

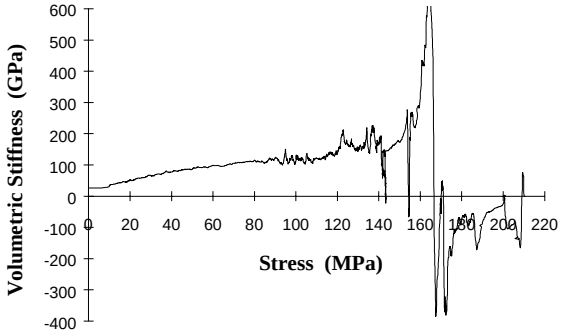

Volumetric Stiffness Curves - AECL 130m Pink Granite

130-1-25

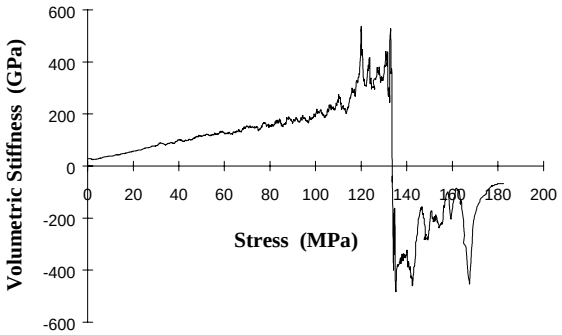

130-1-26

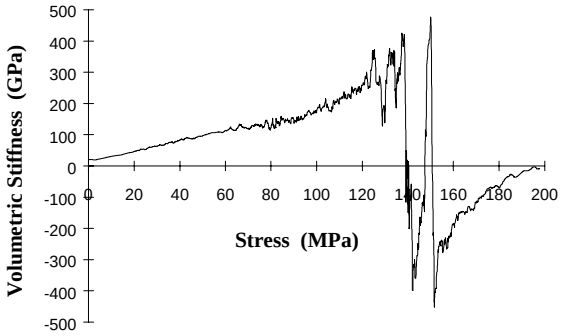

130-1-27

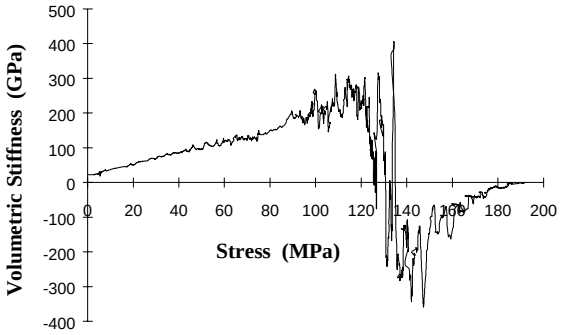

130-1-28

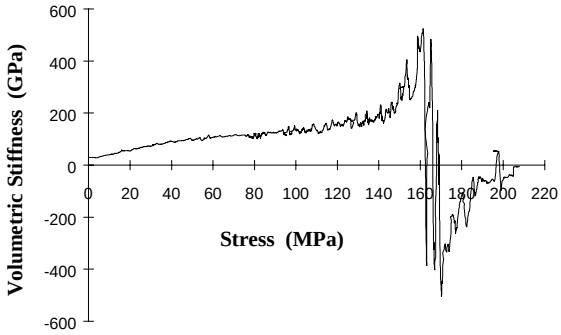

130-2-2

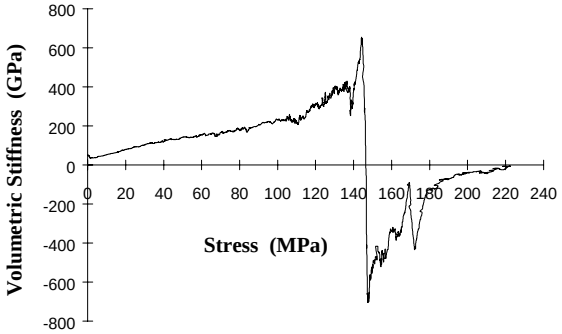

130-2-4

Cyclic loading test.

Volumetric Stiffness Curves - AECL 240m Grey Granite

240-1-1

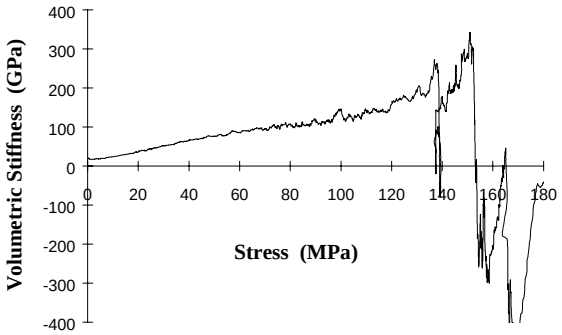

240-1-2

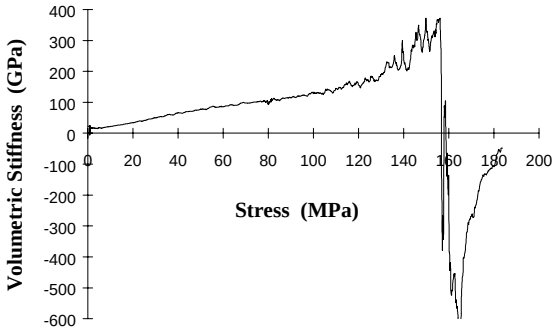

240-1-3

Sample not tested.

240-1-4

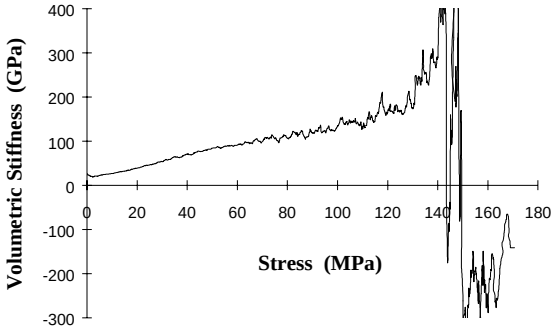

240-1-5

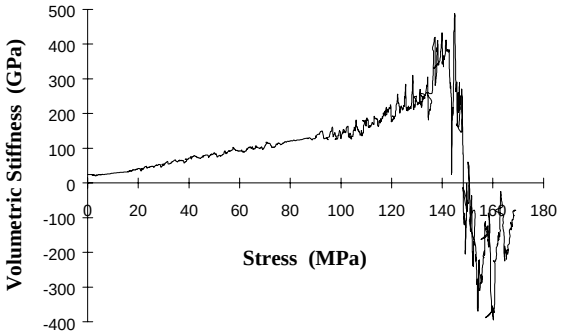

240-1-6

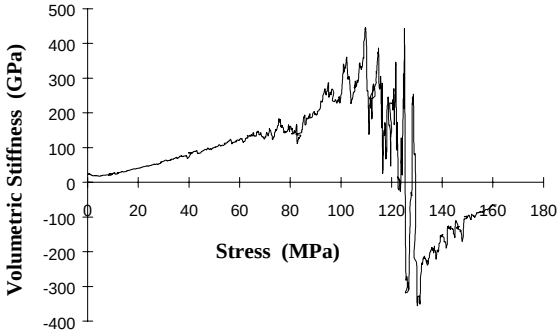

Volumetric Stiffness Curves - AECL 240m Granodiorite

240-2-1

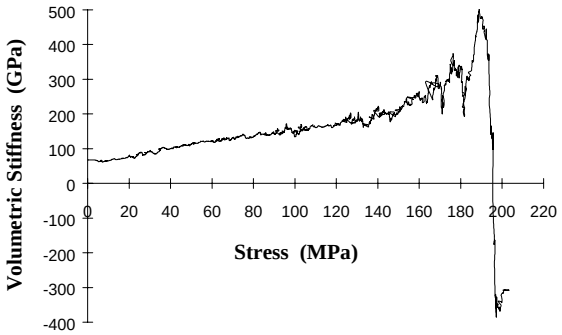

240-2-2

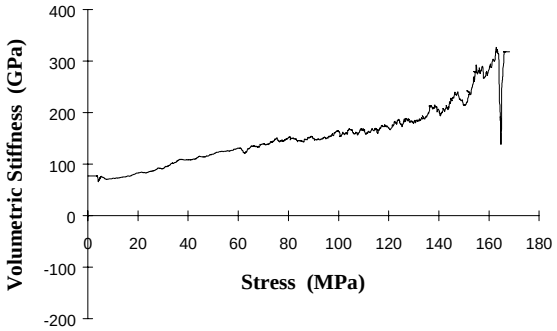

240-2-3

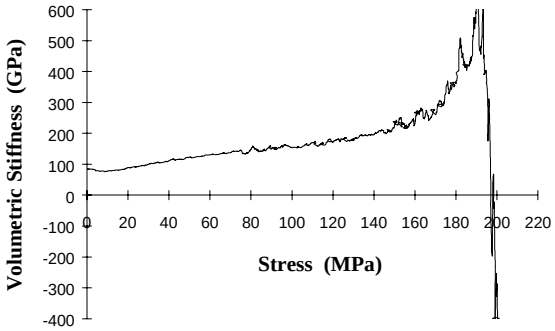

240-2-4

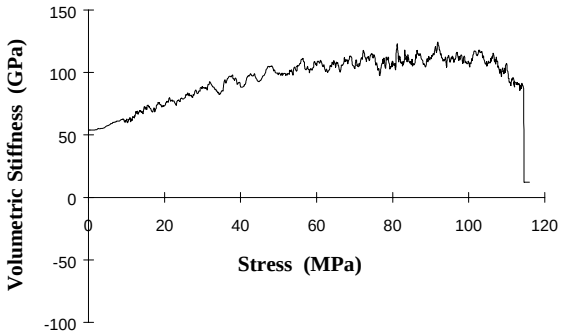

240-2-5

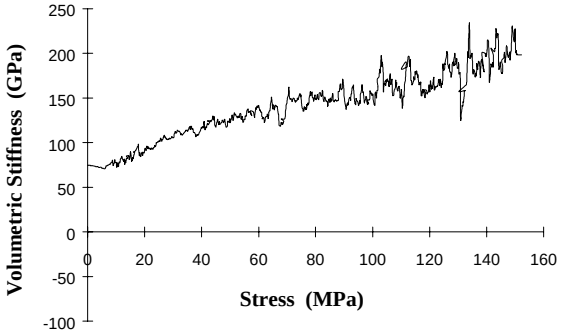

Volumetric Stiffness Curves - AECL 240m Pegmatite

240-3-1

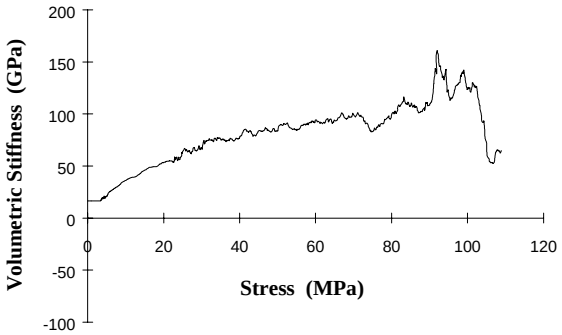

240-3-2

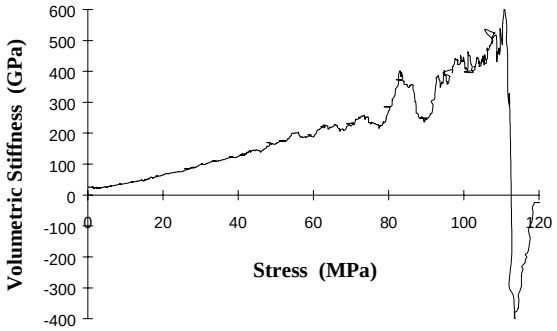

240-3-3

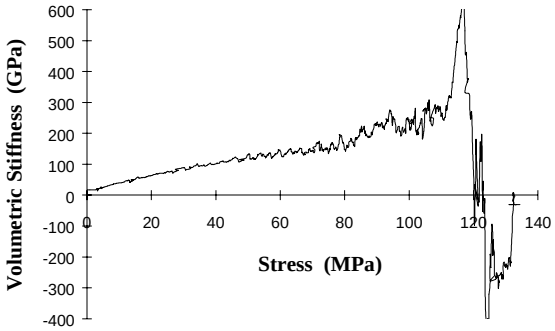

240-3-4

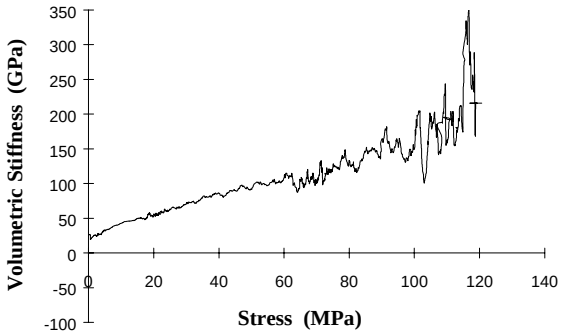

240-3-5

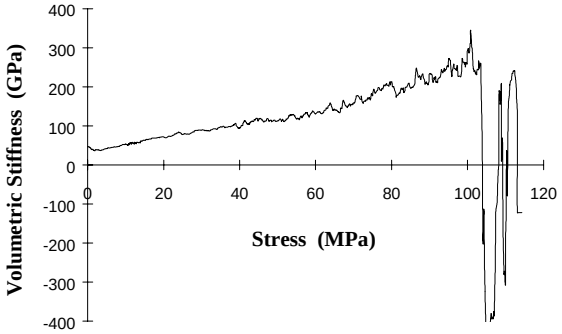

Volumetric Stiffness Curves - AECL 420m Granodiorite

420-1-2

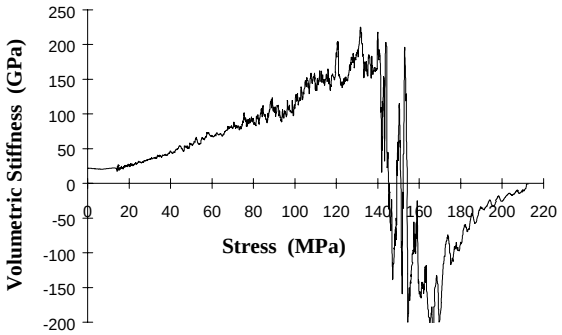

420-1-3

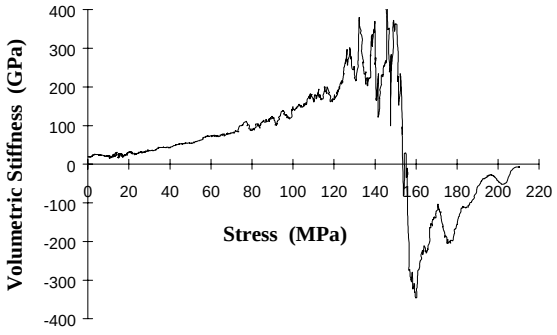

420-2-1

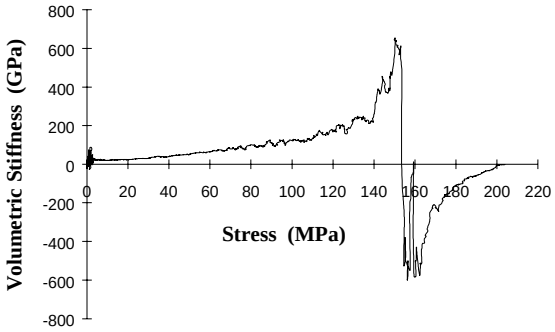

420-3-4

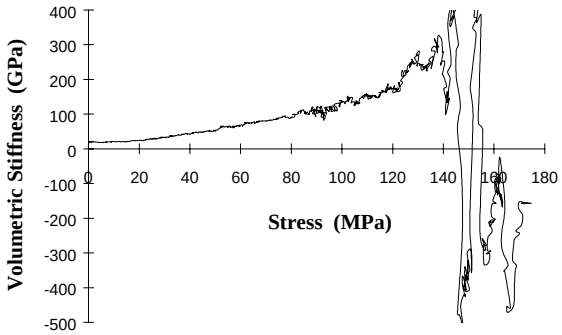

420-3-5

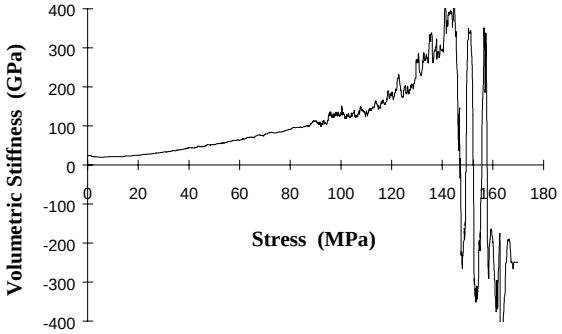

Volumetric Stiffness Curves - AECL 420m Grey Granite

420-4-1

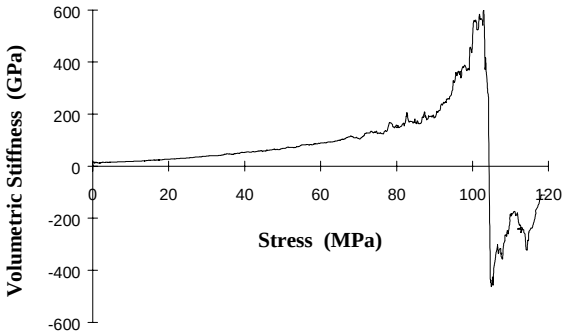

420-4-2

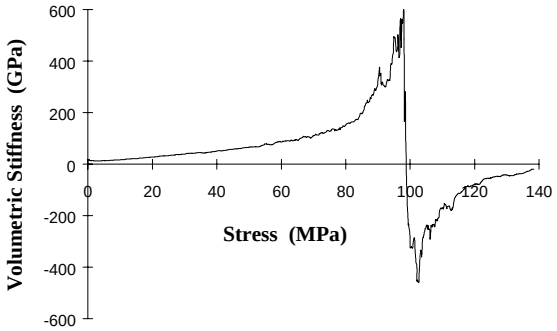

420-4-3

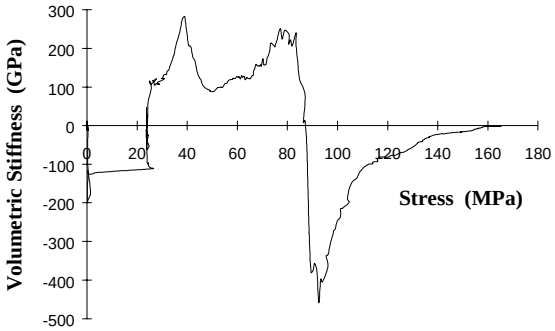

420-4-4

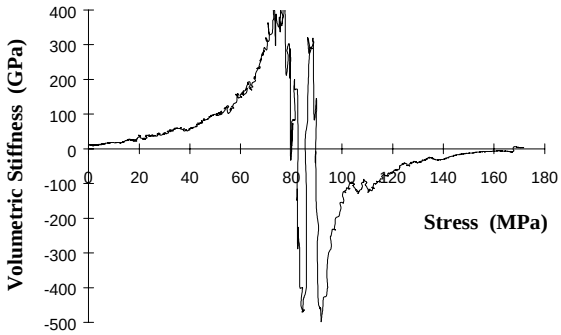

420-4-5

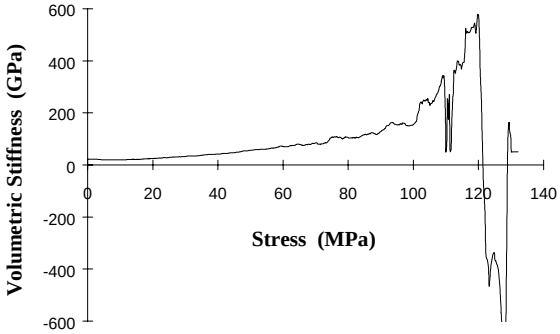

Volumetric Stiffness Curves - Saskatchewan Potash

Potash 1

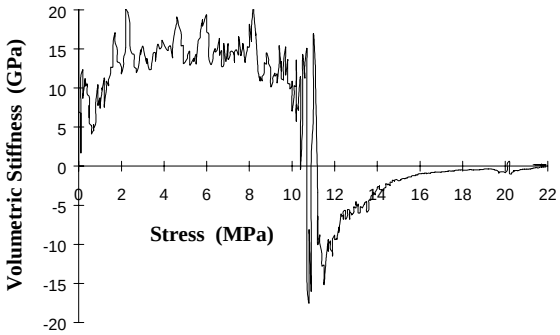

Potash 2

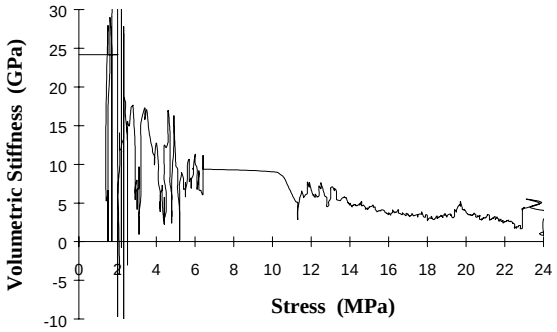

Potash 3

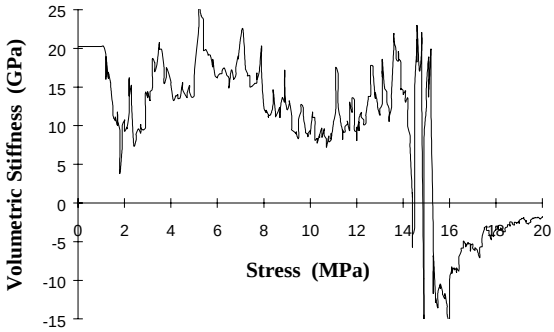

Potash 4

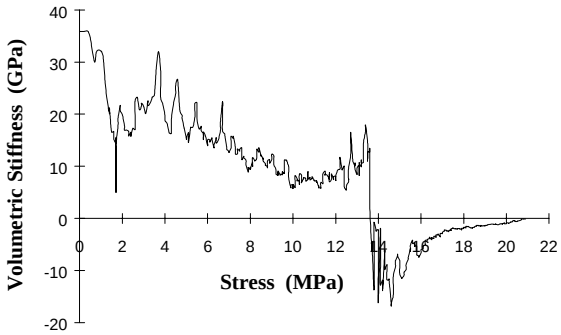

Potash 5

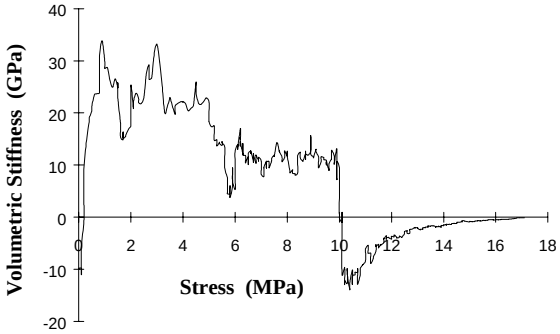

Volumetric Stiffness Curves - Berea Sandstone

SS 1

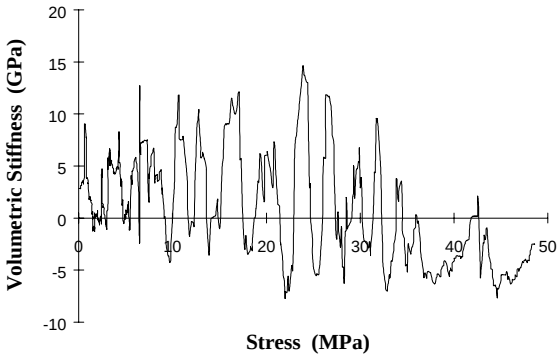

SS 2

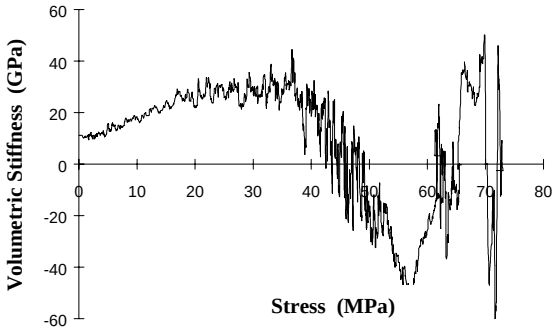

SS 3

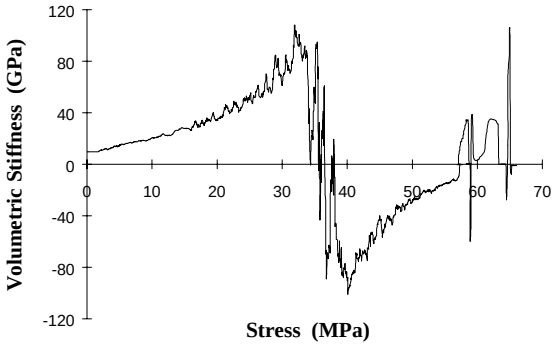

SS 4

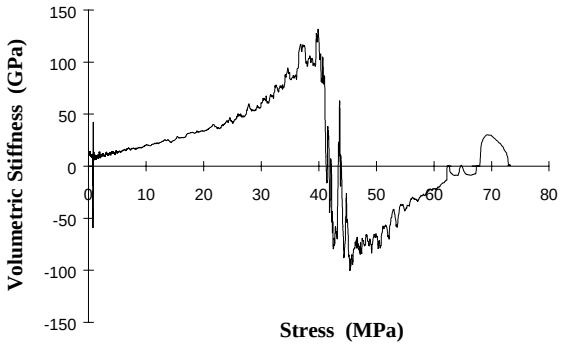

SS 5

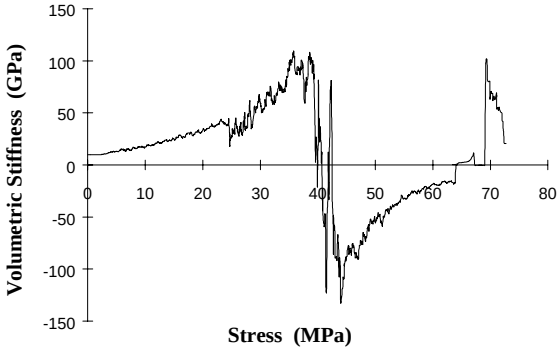

Appendix II

Acoustic Emission Response for Individual Tests

Log Acoustic Emission Event Counts - AECL 130m Pink Granite

130-1-1

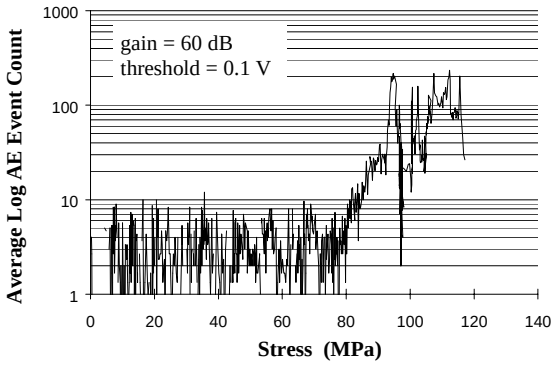

130-1-2

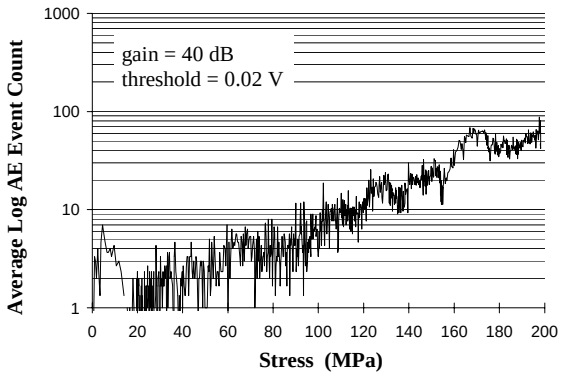

130-1-3

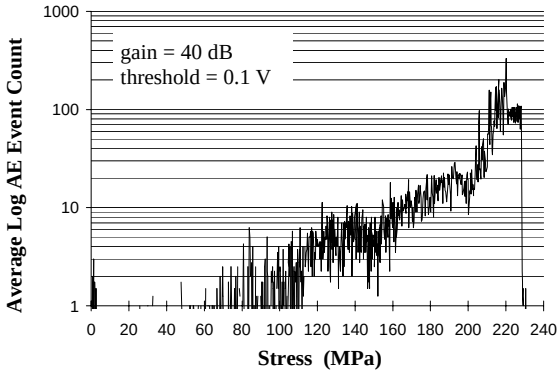

130-1-4

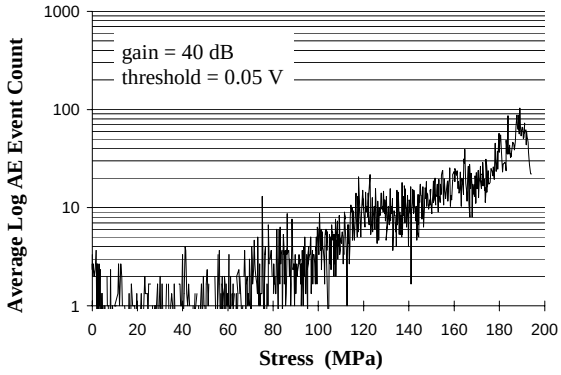

130-1-5

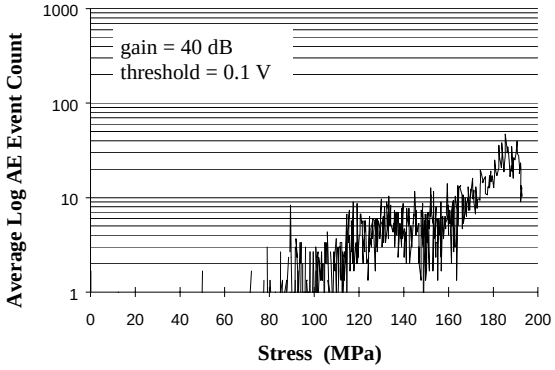

130-1-6

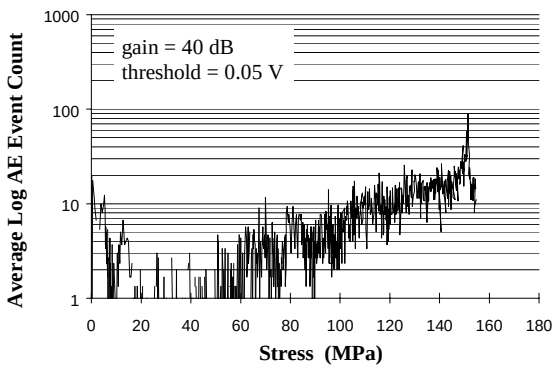

Log Acoustic Emission Event Counts - AECL 130m Pink Granite

130-1-7

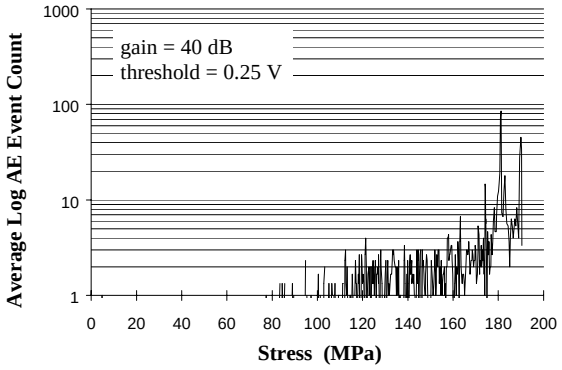

130-1-8

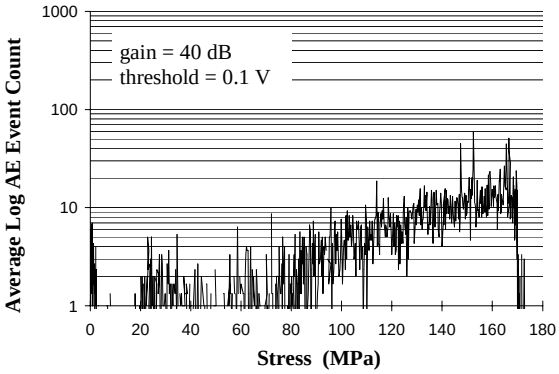

130-1-9

AE not recorded.

130-1-10

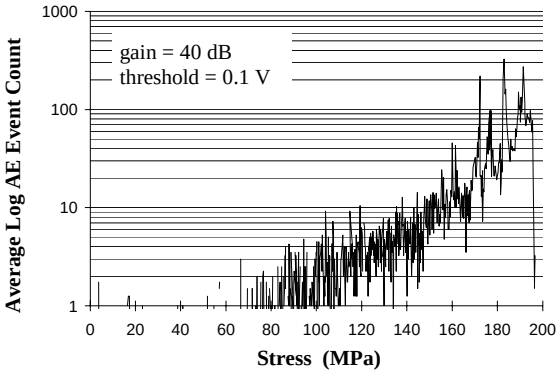

130-1-11

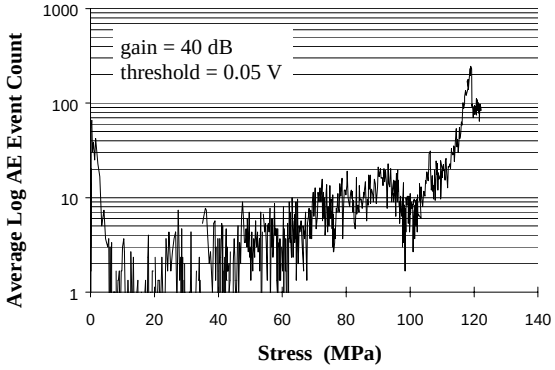

130-1-12

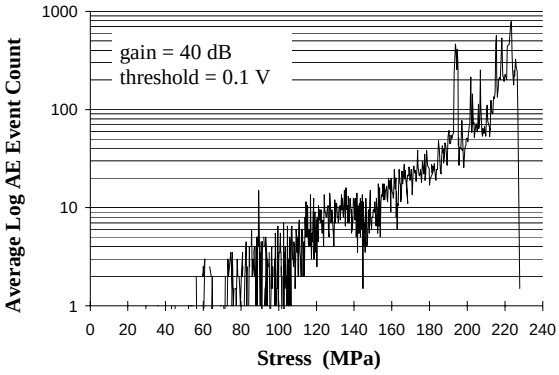

Log Acoustic Emission Event Counts - AECL 130m Pink Granite

130-1-13

AE not recorded.

130-1-14

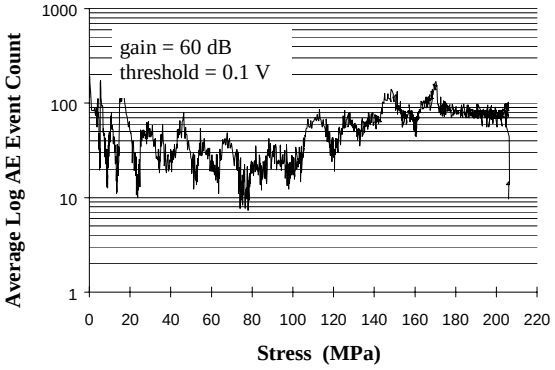

130-1-15

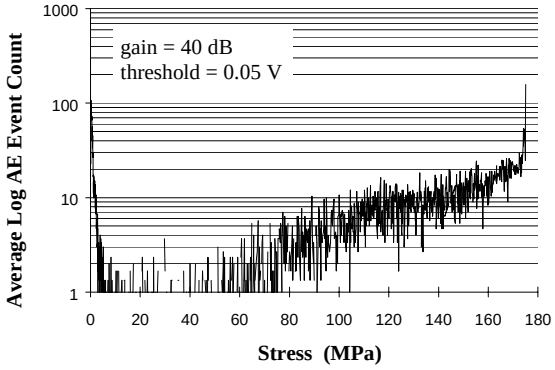

130-1-16

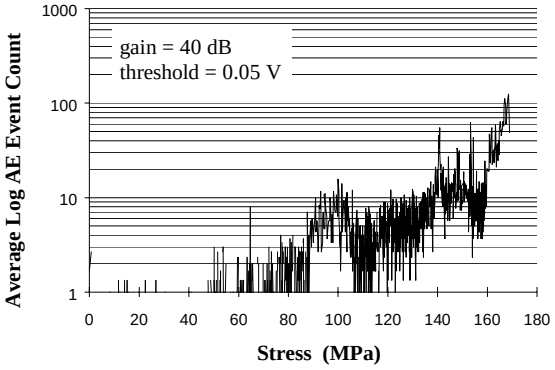

Samples 130-1-17 to 130-1-19, 130-2-4 - used in cyclic loading tests.
Samples 130-1-20 to 130-1-28, 130-2-2 - AE not recorded.

Log Acoustic Emission Event Counts - AECL 240m Grey Granite

240-1-1

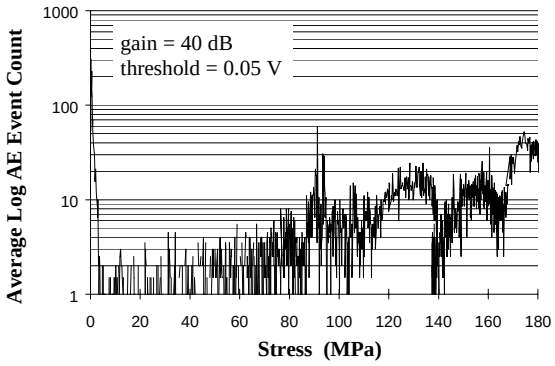

240-1-2

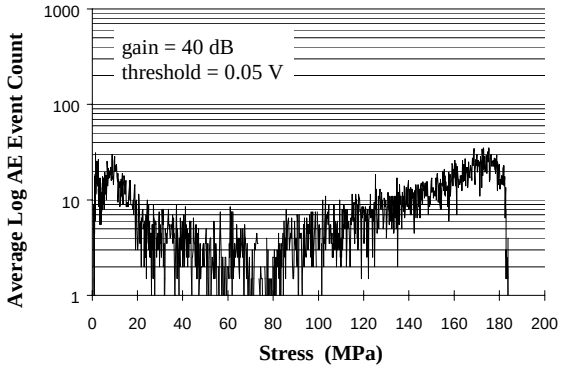

240-1-3

Sample not tested.

240-1-4

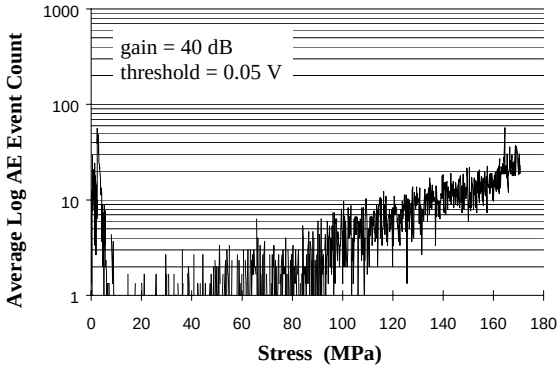

240-1-5

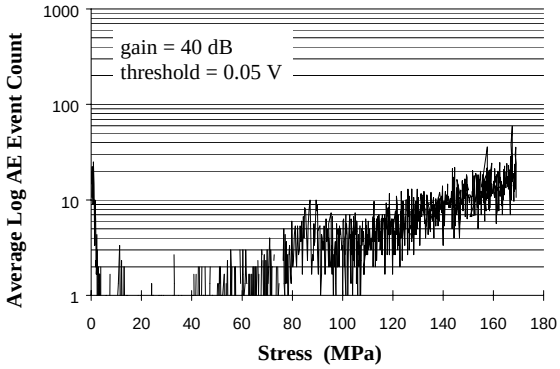

240-1-6

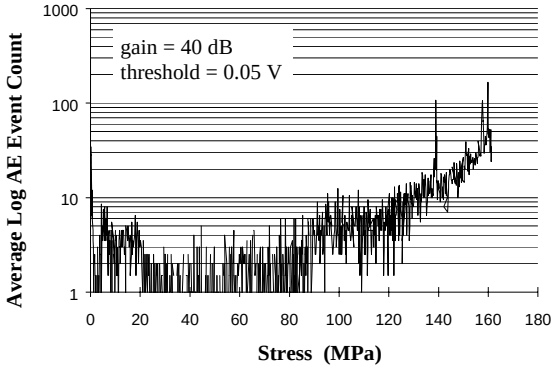

Log Acoustic Emission Event Counts - AECL 240m Granodiorite

240-2-1

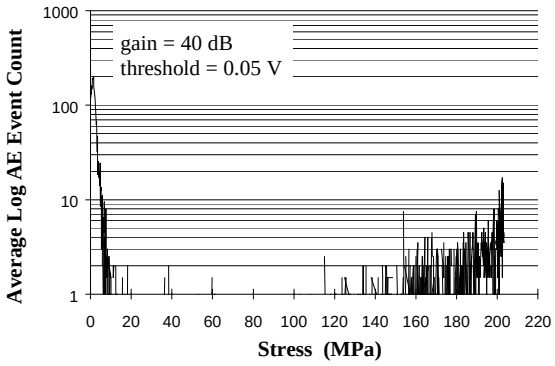

240-2-2

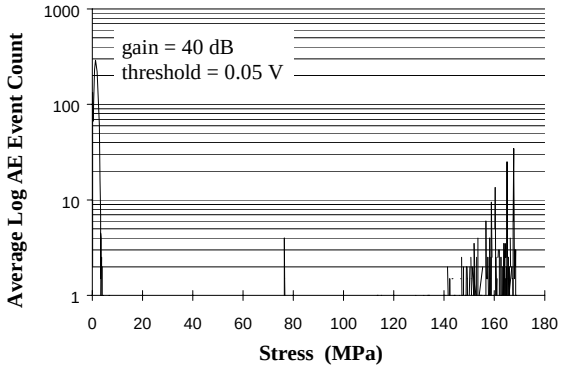

240-2-3

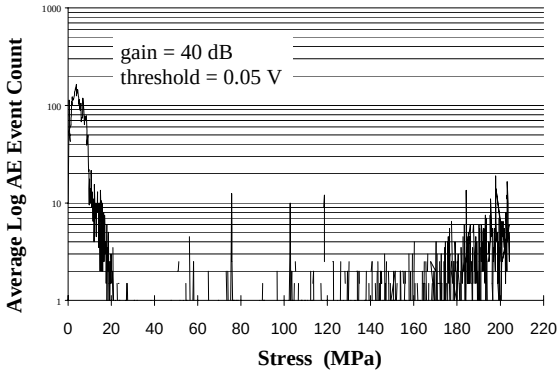

240-2-4[1]

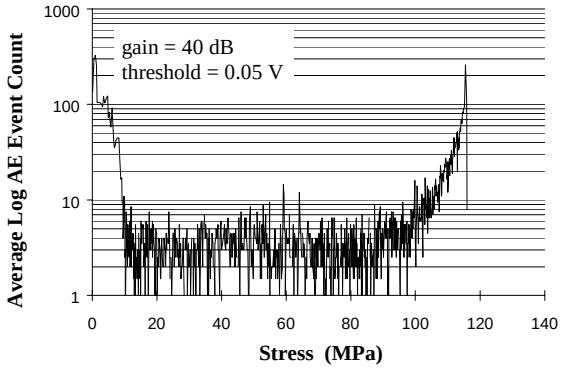

240-2-5

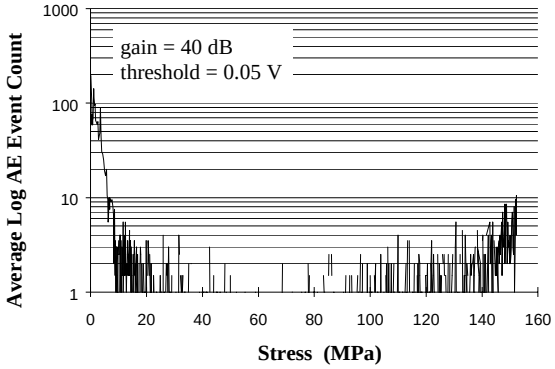

Log Acoustic Emission Event Counts - AECL 240m Pegmatite

240-3-1

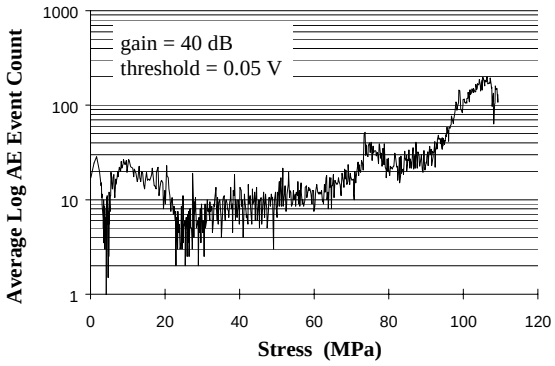

240-3-2

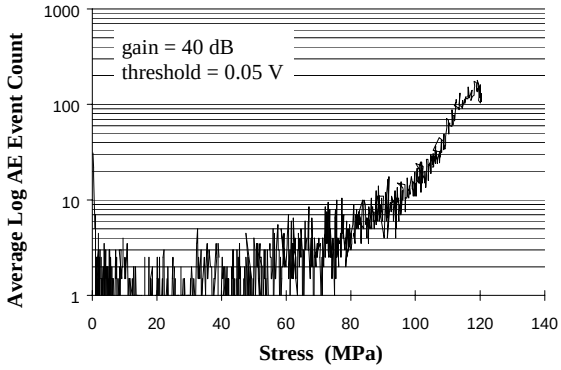

240-3-3

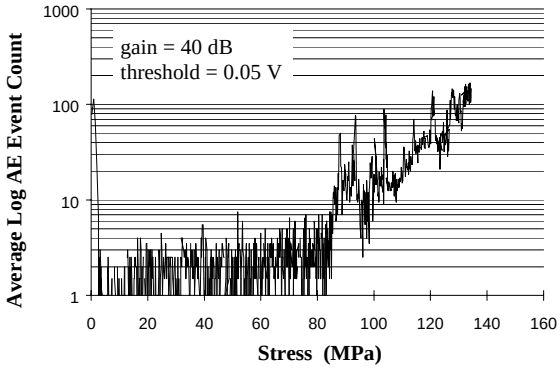

240-3-4

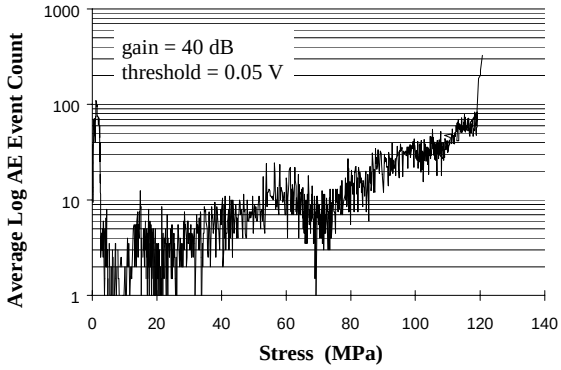

240-3-5

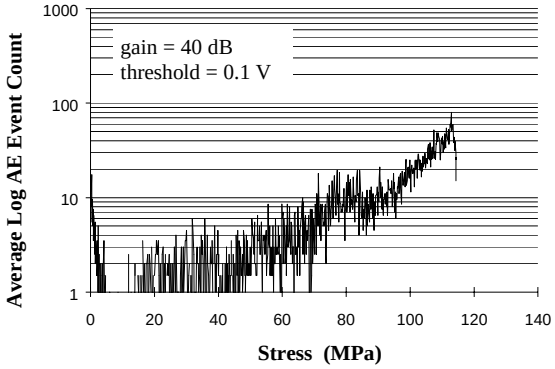

Log Acoustic Emission Event Counts - AECL 420m Granodiorite

420-1-2

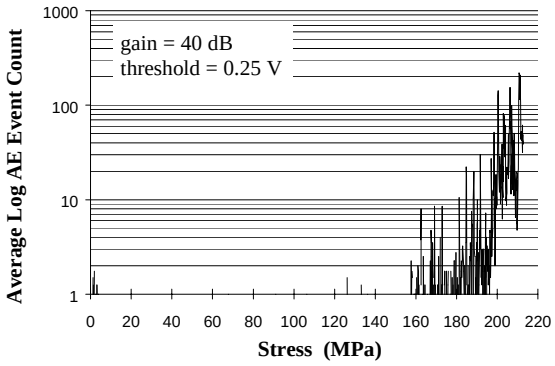

420-1-3

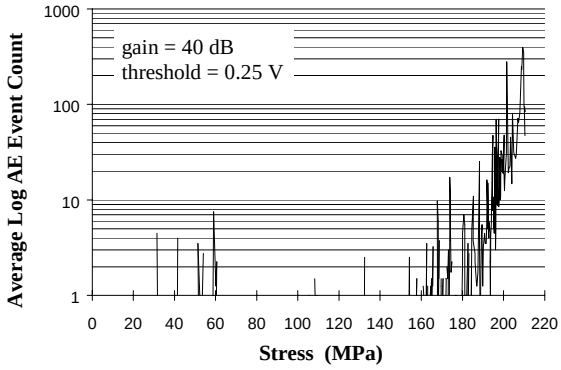

420-2-1

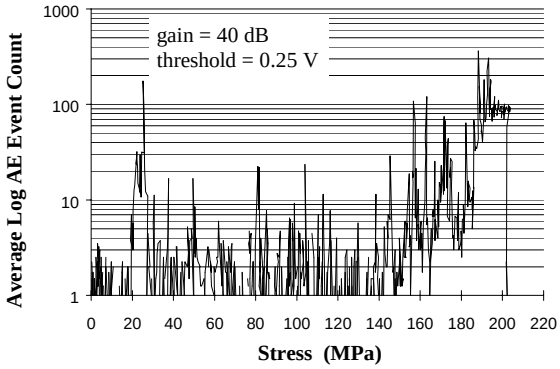

420-3-4

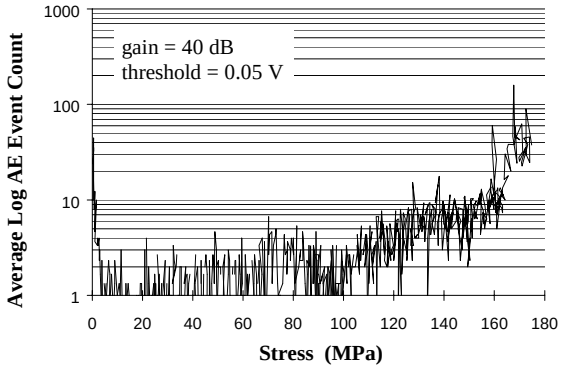

420-3-5

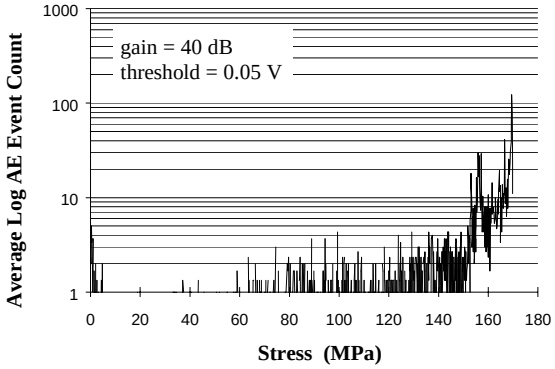

Log Acoustic Emission Event Counts - AECL 420m Grey Granite

420-4-1

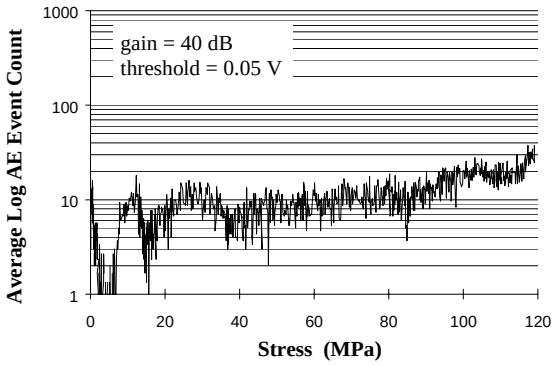

420-4-2

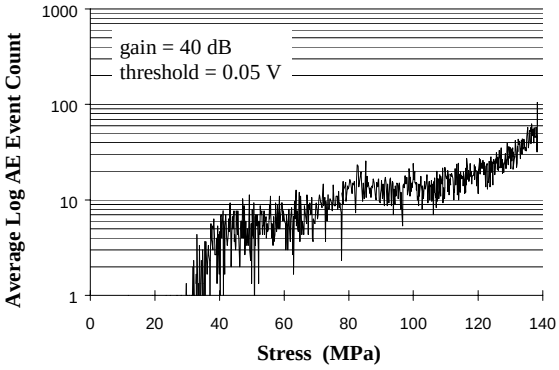

420-4-3

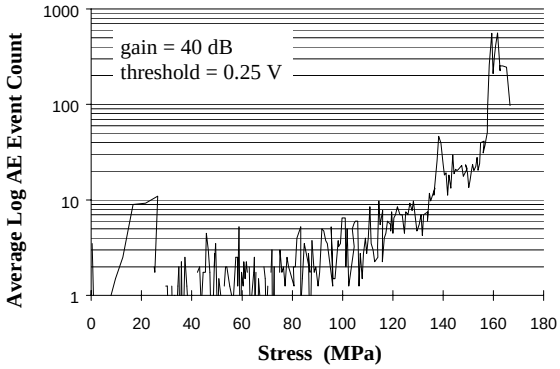

420-4-4

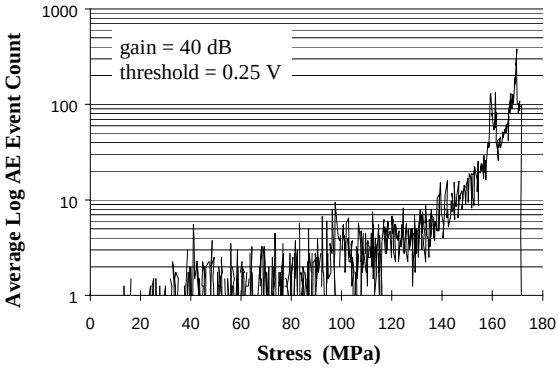

420-4-5

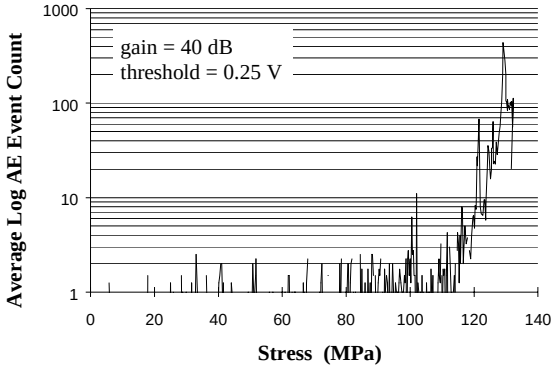

Log Acoustic Emission Event Counts - Saskatchewan Potash

Potash 1

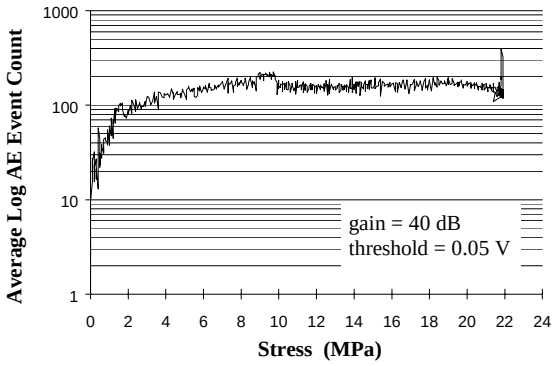

Potash 2

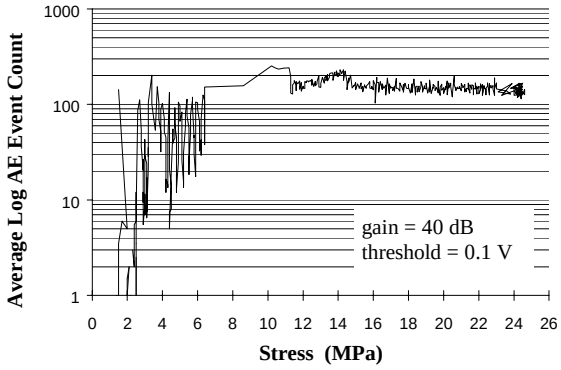

Potash 3

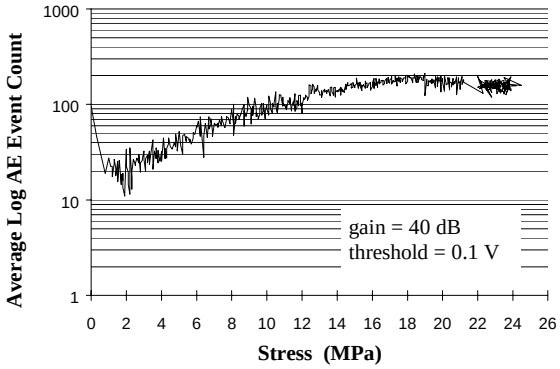

Potash 4

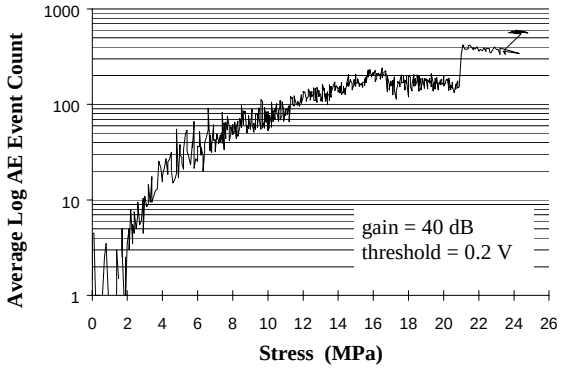

Potash-5

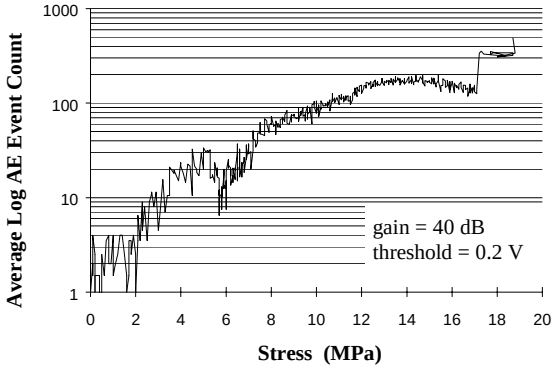

Log Acoustic Emission Event Counts - Berea Sandstone

SS 1

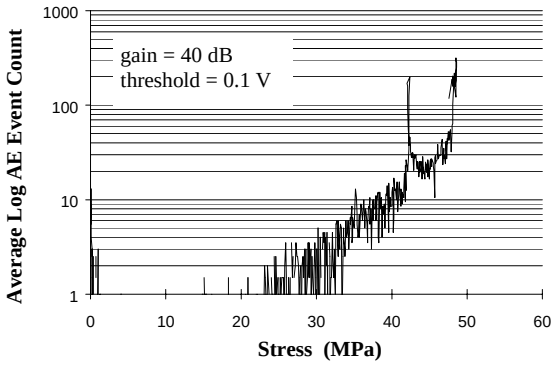

SS 2

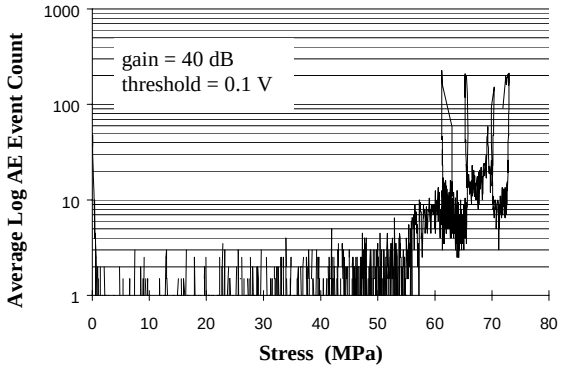

SS 3

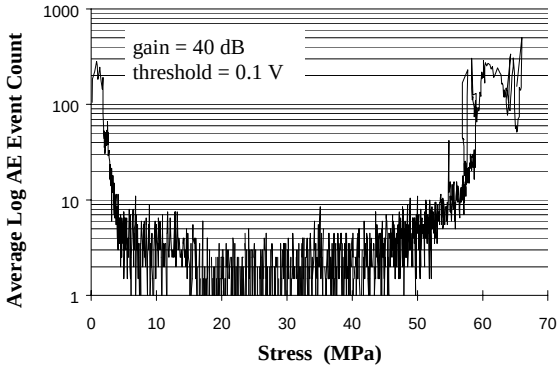

SS 4

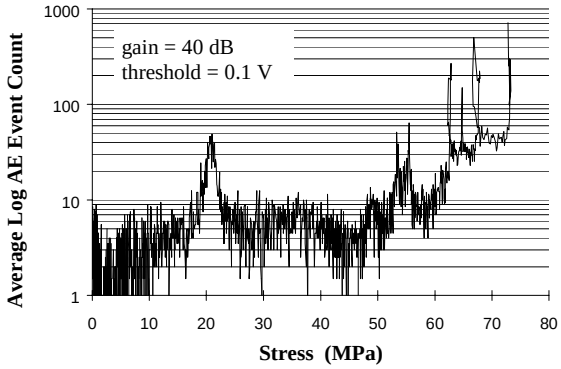

SS-5

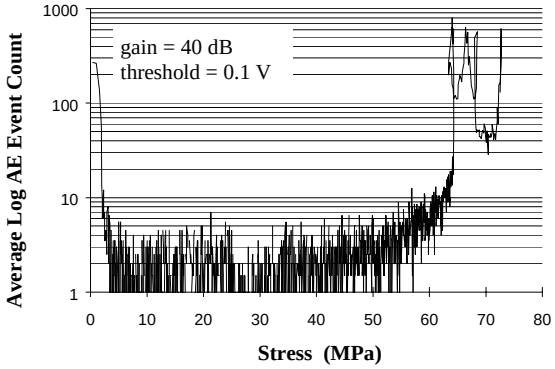

AE Elastic Impulse "Energy" Rate - AECL 130m Pink Granite

130-1-1

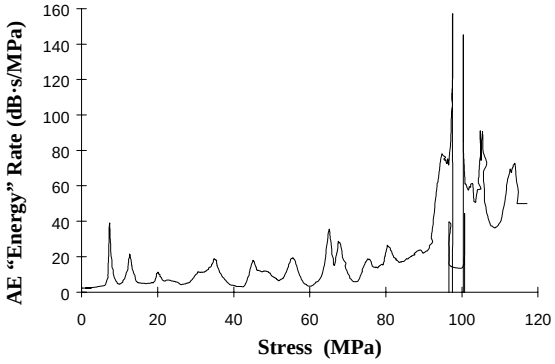

130-1-2

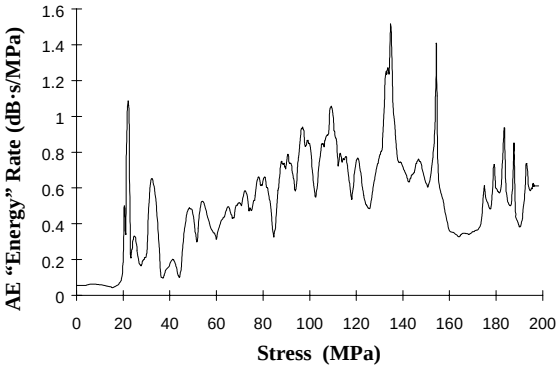

130-1-3

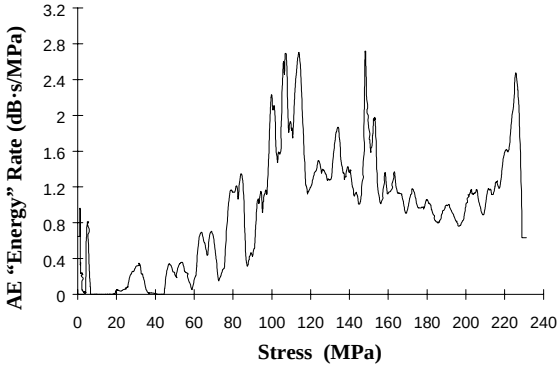

130-1-4

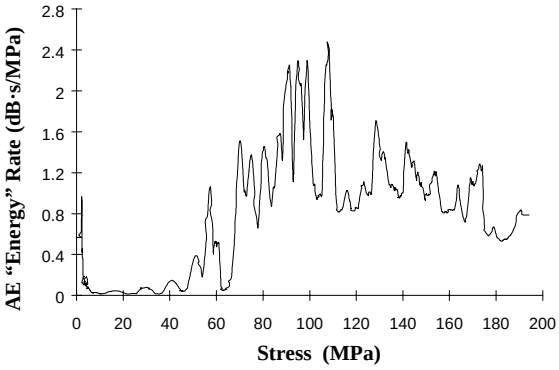

130-1-5

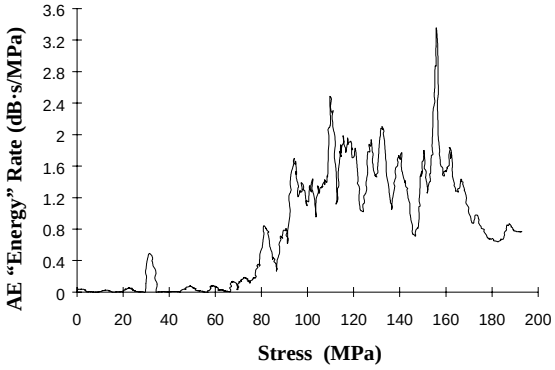

130-1-6

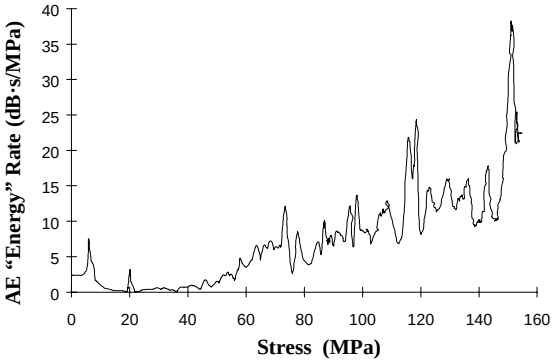

AE Elastic Impulse "Energy" Rate - AECL 130m Pink Granite

130-1-7

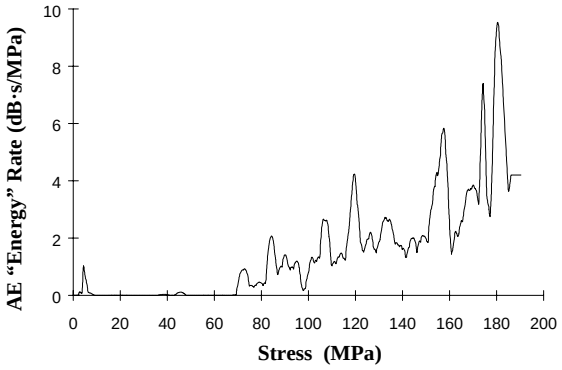

130-1-8

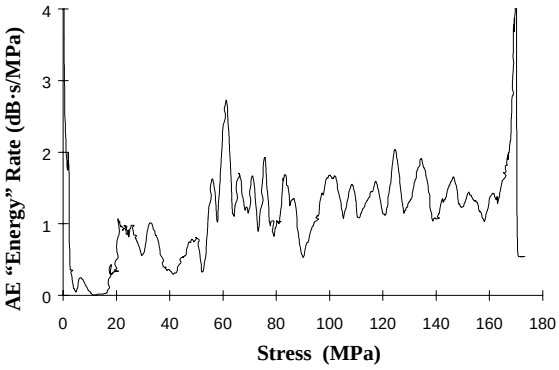

130-1-9

AE not recorded.

130-1-10

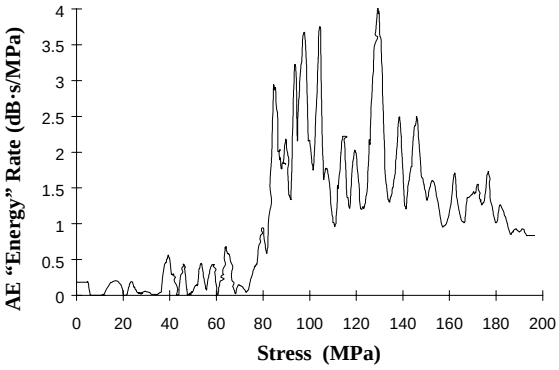

130-1-11

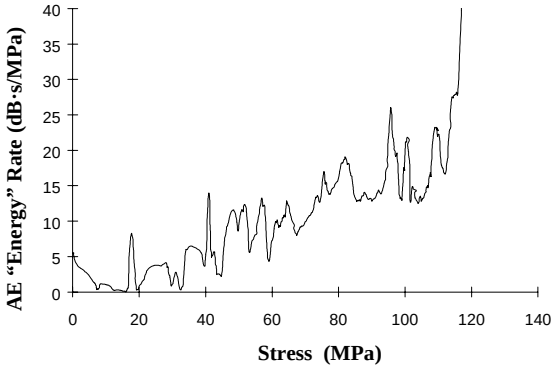

130-1-12

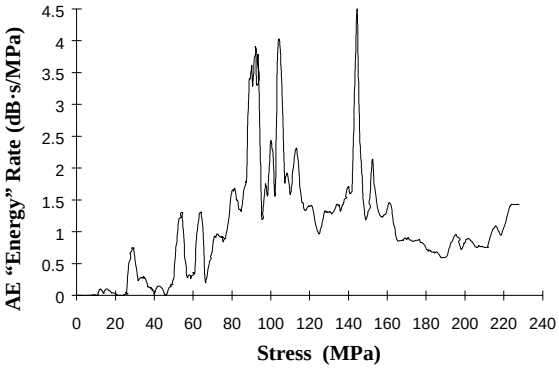

AE Elastic Impulse "Energy" Rate - AECL 130m Pink Granite

130-1-13

AE not recorded.

130-1-14

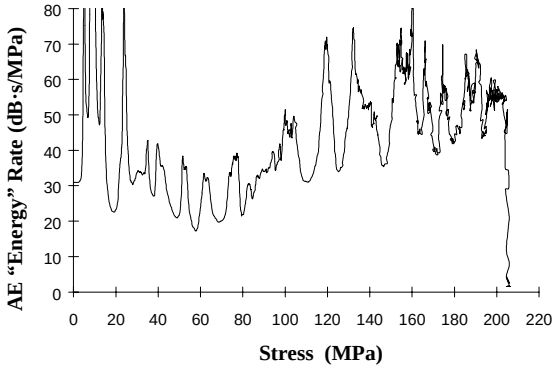

130-1-15

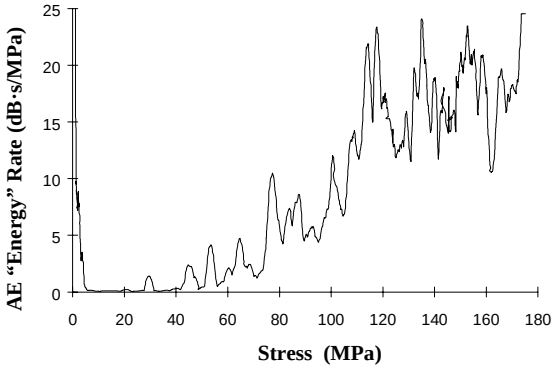

130-1-16

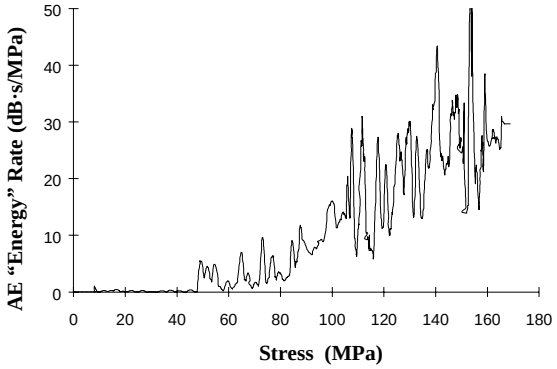

Samples 130-1-17 to 130-1-19, 130-2-4 - used in cyclic loading tests.
Samples 130-1-20 to 130-1-28, 130-2-2 - AE not recorded.

AE Elastic Impulse "Energy" Rate - AECL 240m Grey Granite

240-1-1

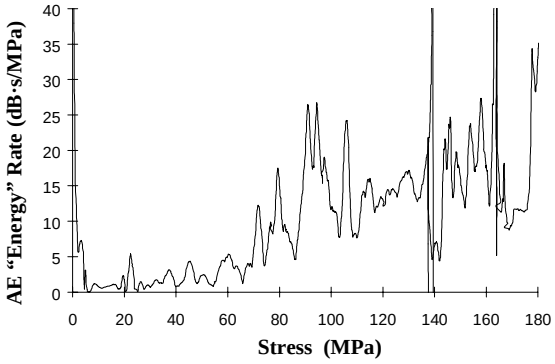

240-1-2

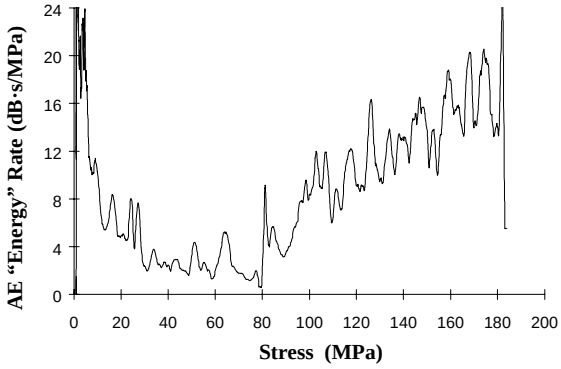

240-1-3

Sample not tested.

240-1-4

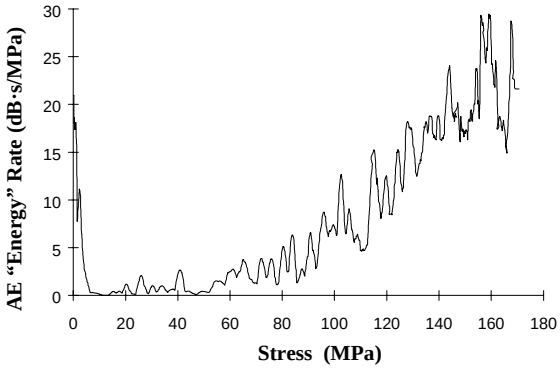

240-1-5

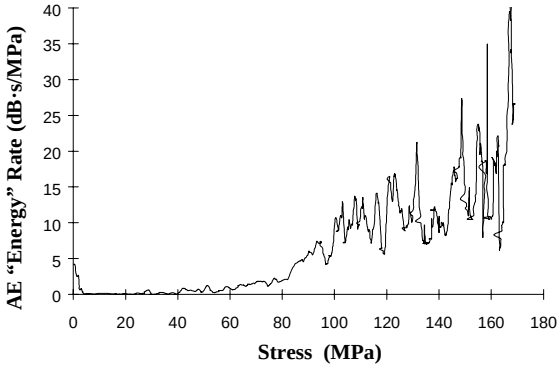

240-1-6

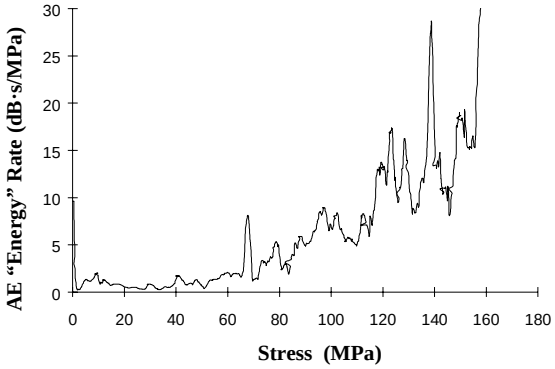

AE Elastic Impulse “Energy” Rate - AECL 240m Granodiorite

240-2-1

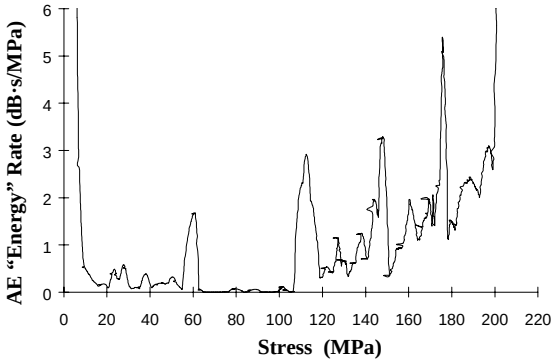

240-2-2

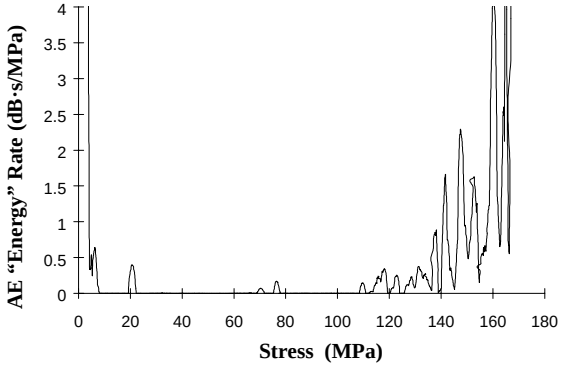

240-2-3

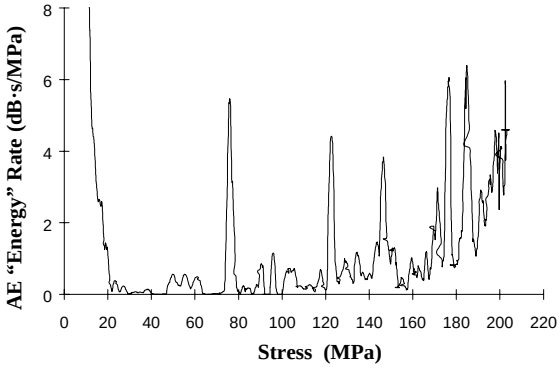

240-2-4

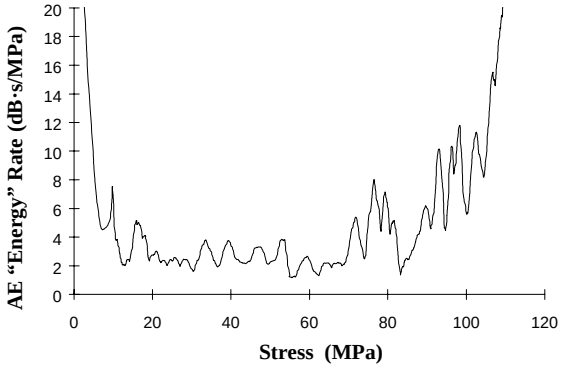

240-2-5

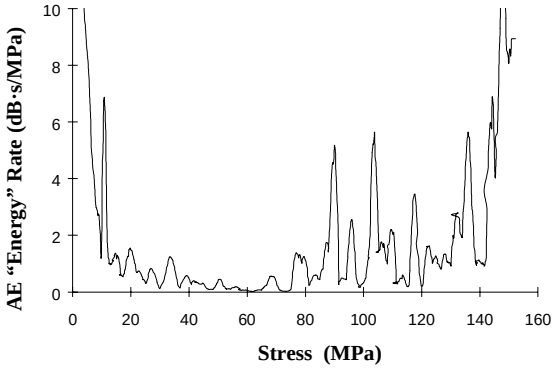

AE Elastic Impulse "Energy" Rate - AECL 240m Pegmatite

240-3-1

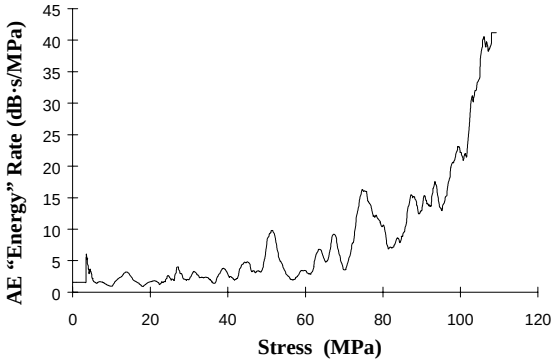

240-3-2

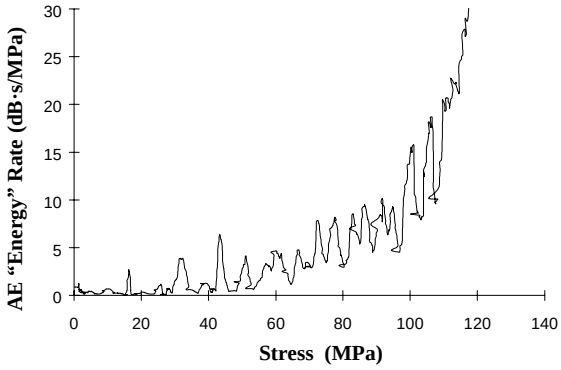

240-3-3

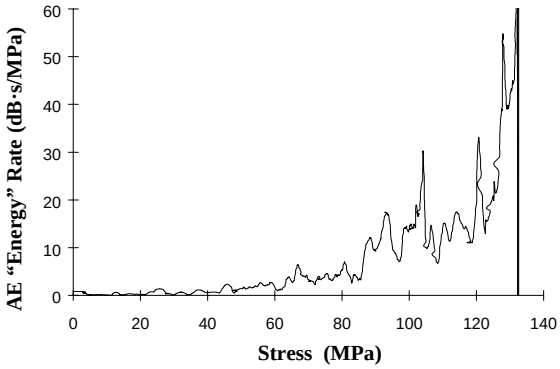

240-3-4

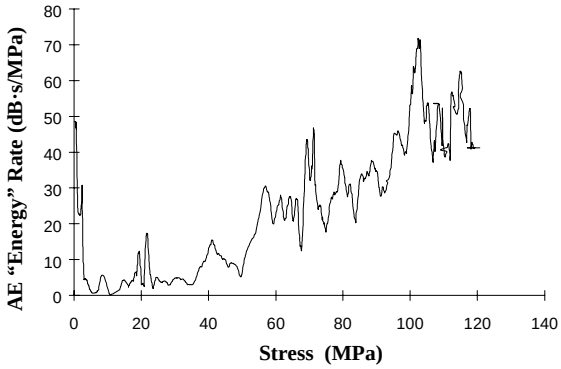

240-3-5

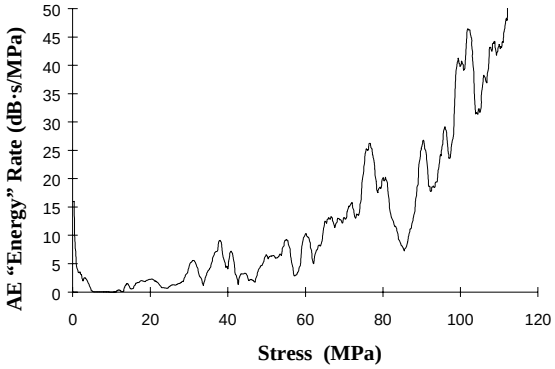

AE Elastic Impulse "Energy" Rate - AECL 420m Granodiorite

420-1-2

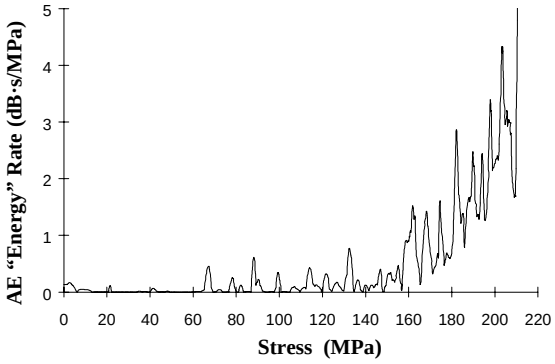

420-1-3

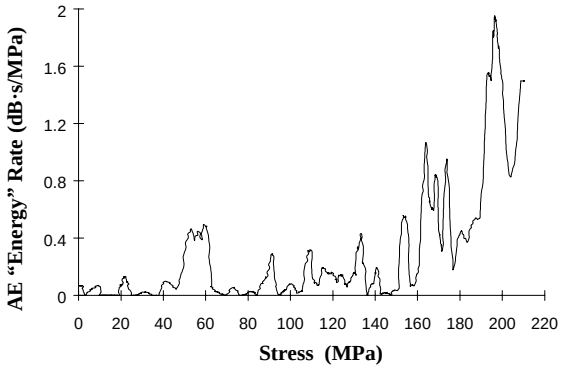

420-2-1

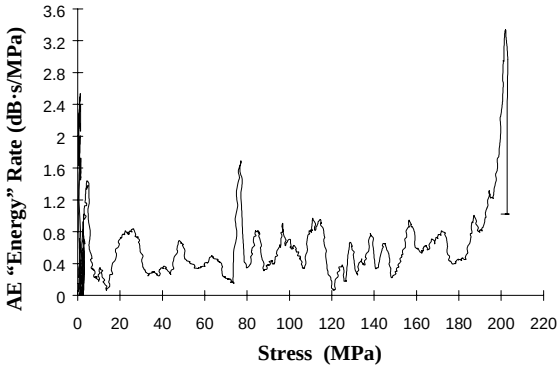

420-3-4

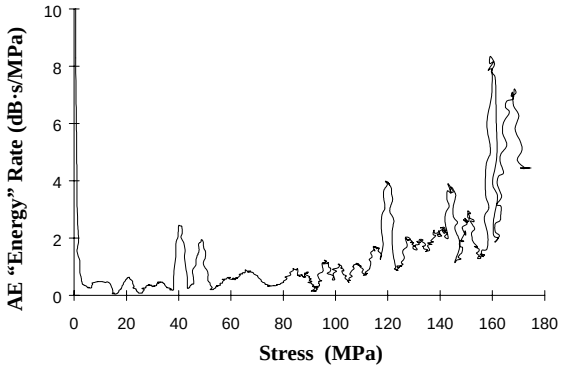

420-3-5

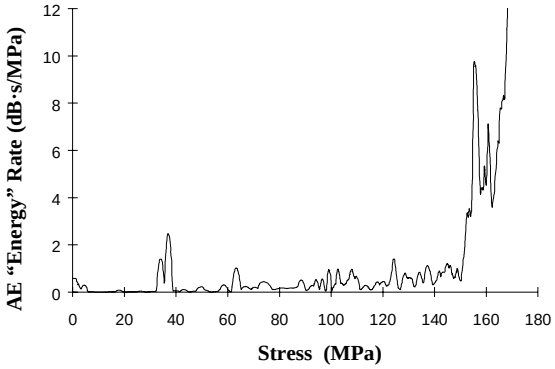

AE Elastic Impulse "Energy" Rate - AECL 420m Grey Granite

420-4-1

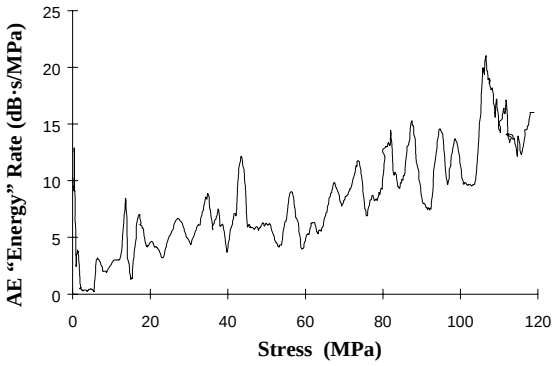

420-4-2

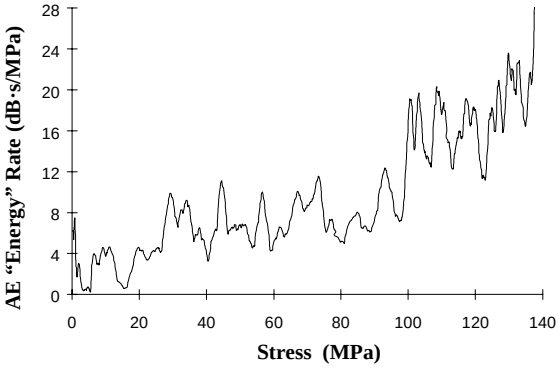

420-4-3

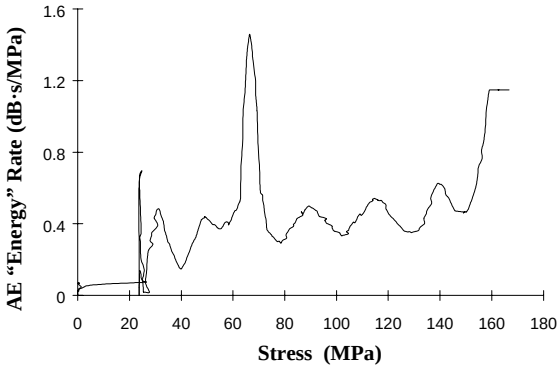

420-4-4

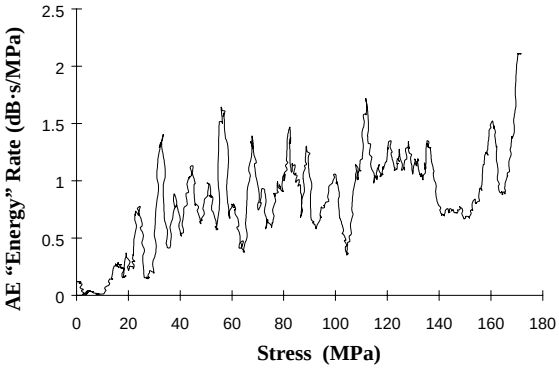

420-4-5

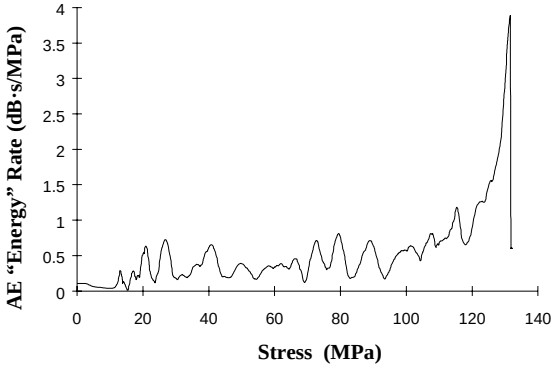

AE Elastic Impulse "Energy" Rate - Saskatchewan Potash

Potash 1

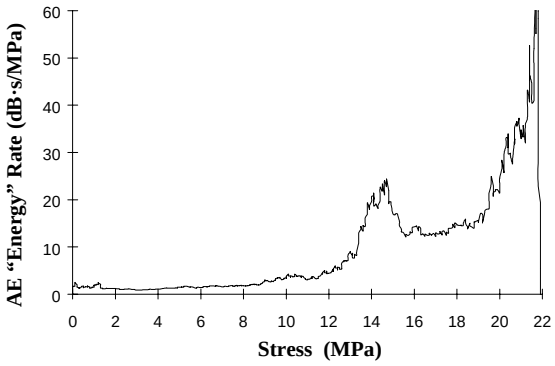

Potash 2

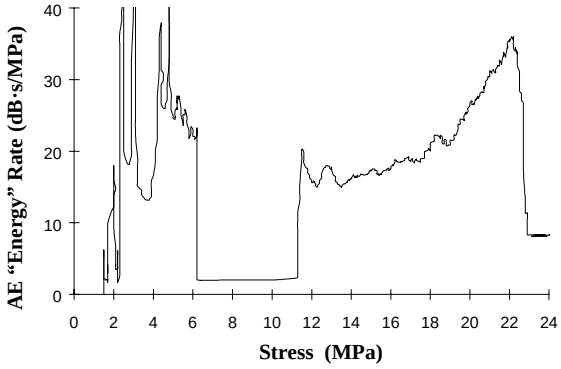

Potash 3

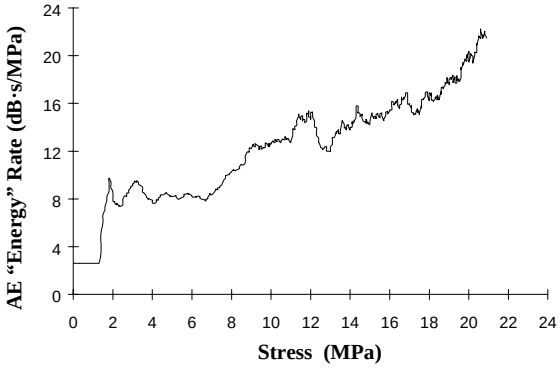

Potash 4

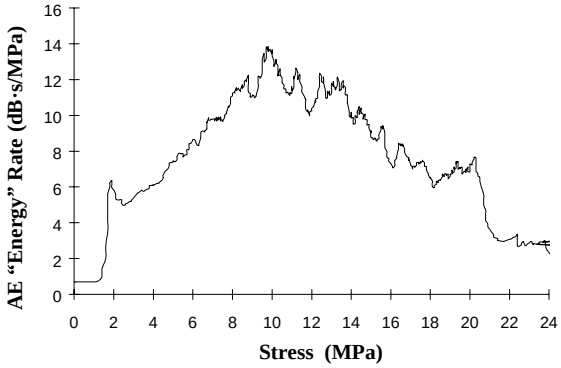

Potash 5

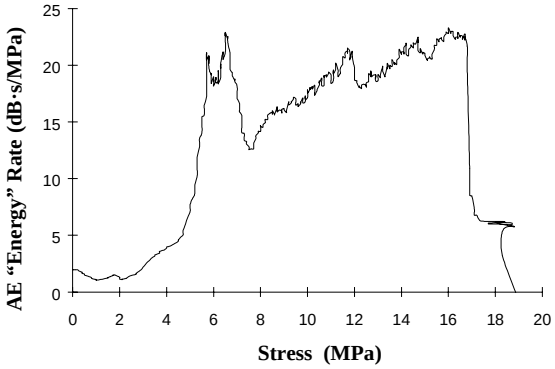

AE Elastic Impulse "Energy" Rate - Berea Sandstone

SS 1

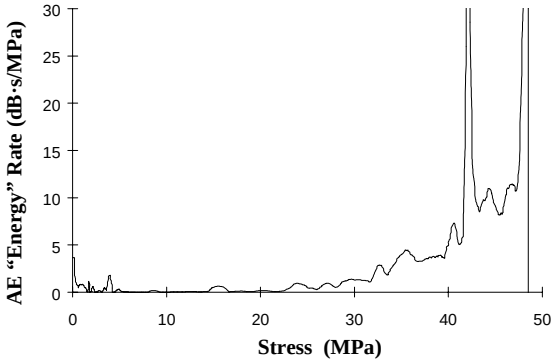

SS 2

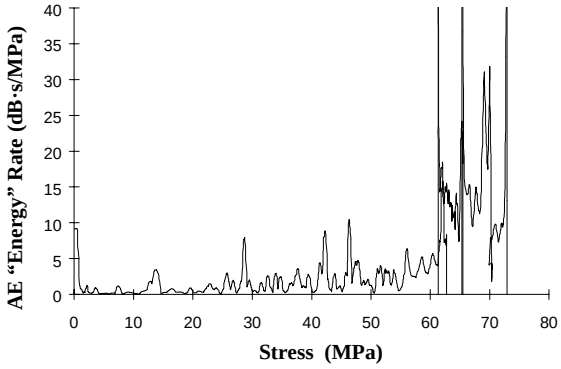

SS 3

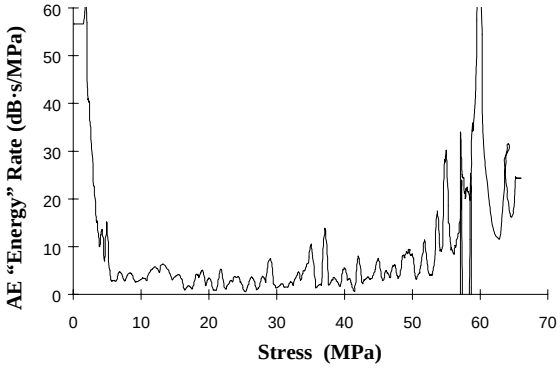

SS 4

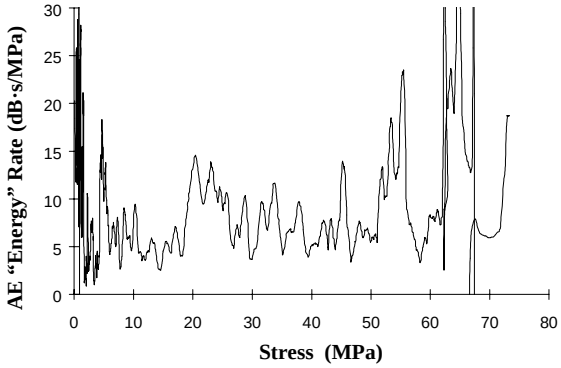

SS 5